UNIVERSITY OF BIRMINGHAM

Synthesis and Characterisation of Mn^{3+} Condensed Phosphate Phases and Fe^{3+} Substituted Analogues

by
Yasmin Begum

A thesis submitted to
the University of Birmingham
for the degree of
Doctor of Philosophy

School of Chemistry
College of Engineering and Physical Sciences
University of Birmingham
August 2012

Abstract

This thesis describes the synthesis, properties and structural characterisation of a series of Mn^{3+} condensed phosphate phases and Fe^{3+} substituted analogues. To date, the synthesis of such mixed cation compositions has been unexplored, but this work has highlighted that they present an interesting array of properties.

α-$NH_4MnP_2O_7$ was successfully synthesised in pure phase form and found to adopt a type I pyrophosphate structure (space group $P2_1/c$). A second polymorph β-$NH_4MnP_2O_7$ was also identified and appears to be the first pyrophosphate to crystallise in space group $P\bar{1}$. Both of these polymorphs were found to be key components of a commercial manganese violet pigment and were stable to *ca.* 340°C. The α-$NH_4Mn_xFe_{1-x}P_2O_7$ solid solution was also characterised, with the introduction of Fe^{3+} resulting in a distinct colour change, an increase in thermal stability to *ca.* 500°C for x = 0 and a change in the magnetic properties of these materials. Similar changes were seen in the isostructural $RbMn_xFe_{1-x}P_2O_7$ system but a marked improvement in thermal stability (*ca.* 1000°C for x = 0), with an unusual decomposition mechanism involving manganese expulsion observed for the intermediate members. Analogous studies were performed on compounds of $RbMn_xFe_{1-x}HP_3O_{10}$, $Mn_xFe_{1-x}H_2P_3O_{10}$ ($x \leq 0.5$), $Mn_xFe_{1-x}P_3O_9$ ($0 \leq x \leq 0.4$ and $0.75 \leq x \leq 1$) and β-$HMnP_2O_7$.

Many of these compounds showed unusual and intense colourations, which has been attributed to the Jahn-Teller active Mn^{3+} being able to exhibit a “plastic” coordination sphere. The magnetic structures of a number of compounds have also been solved and show antiferromagnetic ordering overall. The nature of the exchange interactions was found to largely rely on orbital occupancy, with geometries of the interacting species not found to have a significant influence.

The layered compound $MnH_2P_3O_{10}\cdot 2H_2O$ was also investigated and found to readily undergo monoamine intercalation. Attempts to incorporate additional transition metal ions into the interlayer region of this compound proved inconclusive.

Acknowledgements

Firstly I would like to thank my supervisor, Dr Adrian Wright, for his support, advice and encouragement over the last 4 years.

I would also like to show my gratitude to Professor Frank Berry, not only for the many discussions on my research and collection of the Mössbauer data, but also for his genuine kindness and optimism. I must also extend my thanks to other members of staff in the department, namely Dr Jackie Deans for her help with UV-Vis, XRD, TGA, XRF and general floor matters and Dr Louise Male for her help with XRD. Externally, I would like to thank Dr Emma Suard (ILL) and Dr Denis Cheptiakov (SINQ) for their help in collection of neutron diffraction data and Dr Andrew Dent (Diamond) for kindly running EXAFS and XANES measurements.

I would also like to thank fellow “labbies” Evin and Tom for the fun times and being fantastic friends; their support and advice have been appreciated more than they know. Thank you to other past and present members of the 5th floor for making it an enjoyable place to work and for always being willing to help with the odd problem.

Lastly I would like to thank my friends Lucy, Harpz, Tanz, Nagina and Khatija for their support and friendship and my family, particularly Mum, for the unconditional support and patience.

This thesis is dedicated to the late Gulab Khan, Fatima Bibi and Ali Muhammad

“Death is a bridge, uniting lover with Beloved.”

-Hadith

Abbreviations

AFM	Antiferromagnetic
BVS	Bond Valence Sum
DTA	Differential Thermal Analysis
EXAFS	Extended X-ray Absorption Fine Structure
FCFW	Field Cooled/ Field Warmed
FM	Ferromagnetic
GII	Global Instability Index
GSAS	General Structure Analysis System
IR	Infrared
MnTP	$MnH_2P_3O_{10}\cdot 2H_2O$
MnTP-hex	Hexylamine intercalate of MnTP
MPMS	Magnetic Properties Measurement System
ND	Neutron Diffraction
PXRD	Powder X-ray Diffraction
SEM	Scanning Electron Microscopy
SQUID	Superconducting QUantum Interference Device
TGA-MS	Thermogravimetric Analysis-Mass Spectrometry
TM	Transition Metal
UV-Vis	Ultraviolet-Visible
VU	Valence Units
XAFS	X-ray Absorption Fine Structure
XANES	X-ray Absorption Near Edge Structure
XRD	X-ray Diffraction
XRF	X-ray Fluorescence
ZFCFW	Zero-Field Cooled/ Field Warmed

Contents

Chapter Three: Synthesis and Characterisation of α-$NH_4MnP_2O_7$, Manganese Violet and Substitutional Analogues

Appendices

Chapter One

Introduction

This thesis describes a detailed study into a number of mixed Mn^{3+}, Fe^{3+} condensed phosphate systems, principally discussing their synthesis, structure, thermal stability, electronic properties and magnetic behaviour. Where possible, further studies have been conducted that are justified by the nature of the material.

The basis of this first chapter is to provide a general background to phosphate chemistry, with a particular focus on the aspects that are relevant to this research. A more detailed introduction will then be given at the beginning of each individual chapter, concerning the purpose of the research that has been conducted there.

1.1 General Overview of Phosphate Chemistry

The area of phosphate chemistry is incredibly diverse, with inorganic phosphates currently being used in food and beverage products, pharmaceuticals, fire extinguishers, detergents, fertilisers and for water treatment, to name a few examples. Most of these applications employ compounds containing Na^{+}, K^{+}, Ca^{2+} and Mg^{2+} cations, which are generally known to be biologically friendly; indeed, calcium and magnesium phosphates often find themselves central to studies conducted within the biomaterials field.[1-2] There is also much research undertaken

on phosphate systems for their uses as ferroelectric materials[3], immobilisers of radioactive waste[4-5] and as components in lithium ion batteries.[6] A prime example of this is $LiFePO_4$, which was first reported in 1997 as a potential cathode material for rechargeable lithium batteries and has since been the subject of much investigation.[7-8] A great deal of interest also lies in the catalytic,[9] magnetic[10] and luminescent[11] properties of various phosphate materials. It is thus clear that inorganic phosphates possess a relatively rich chemistry that gives them the potential to be used in a number of applications.

The term “phosphate” refers to a unit consisting of phosphorus (V) bound to four oxygen atoms, and can be regarded as a salt of phosphoric acid. There are three main groupings used in the classification of phosphates: orthophosphates (or monophosphates), condensed phosphates (or polyphosphates) and oxyphosphates. Orthophosphates consist of one phosphate anion (PO_4^{3-}) which has a tetrahedral configuration and is thus analogous to silicate (SiO_4^{4-}), sulphate (SO_4^{2-}) and perchlorate (ClO_4^-) ions. Many orthophosphate compounds can be synthetically derived, though some are also found to naturally exist as minerals or within biological systems, such as triphylite ($LiFePO_4$) and adenosine triphosphate (ATP), respectively. Condensed phosphates are defined as possessing one or more P-O-P linkage and having an O:P ratio < 4. This group of phosphates will be discussed in greater detail in section 1.2 below. Finally, oxyphosphates can be described as entities that possess an anionic phosphate unit as well as additional oxygen atoms that do not belong to this, thus having an overall O:P ratio > 4. For example, $Li_xCo_yTiO(PO_4)$[12] is an oxyphosphate in which the transition metals are octahedrally

coordinated by four oxygen atoms of the phosphate unit as well as to two other oxygen atoms.

1.2 Condensed Phosphates

All materials reported in this research consist of a condensed phosphate unit, and so it is important to clearly define here the terminology that will be used throughout this thesis. Condensed phosphates may be formed from the condensation of two or more PO_4 groups, most commonly through the elimination of a water molecule, as shown in Figure 1.1. This gives rise to P-O-P linkages in which the PO_4 tetrahedra are corner-shared *via* a common oxygen atom. In this way, polymerised chains, sheets, rings or cages can be built *cf.* silicate chemistry.

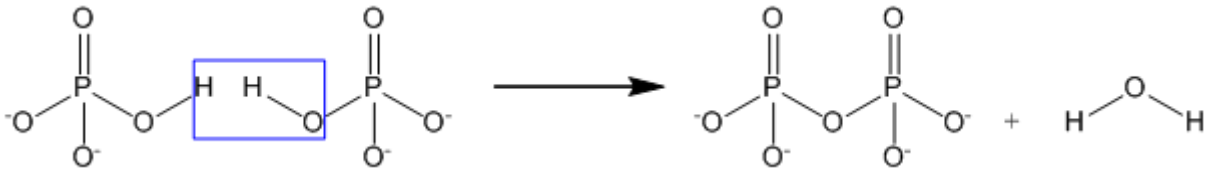

Figure 1.1: *Schematic showing the formation of a condensed phosphate*

Some notable structural features attributed to condensed phosphates are[13]: -

a) Any PO_4 tetrahedron can share a maximum of three of its corner oxygens with neighbouring tetrahedra, giving rise to three types of building unit, shown below in Figure 1.2.

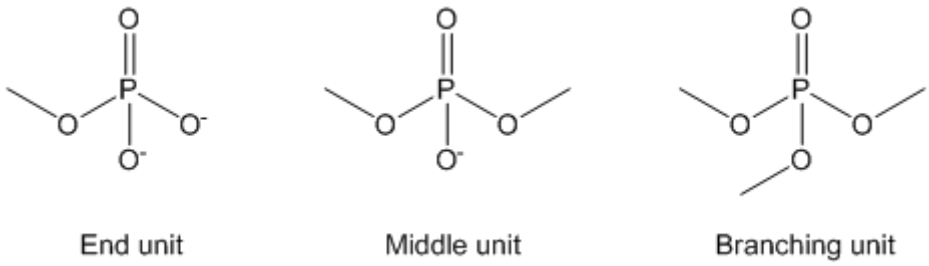

Figure 1.2: *The three main building units in condensed phosphates*

b) Structural isomerism is a definite possibility as tetrahedra can be linked in different arrangements.

c) Differences in packing can give rise to polymorphs.

d) The P-O-P bond angle of corner sharing tetrahedra lies between 120-180°.

e) As expected, P-O (terminal) bond lengths are shorter than P-O-(P) bridging bond lengths.

Condensed phosphates can form crystalline solids as well as amorphous glass-type structures, both of which are well studied. Clearly the structure of phosphate glasses is not well known, and so often they are just described as consisting of random three dimensional networks of PO_4 tetrahedra linked through three corners, with cations occupying interstitial sites within the structure. Generally all condensed phosphates are found to be quite resistant to chemical attack, as each phosphorus atom is in its fully oxidised state. However, under certain conditions (*e.g.* a change in temperature, pH or concentration) hydrolysis can occur just as readily as condensation does, breaking up the P-O-P linkages. The rate of hydrolysis can be influenced by a variety of factors such as crystal structure and the steric accessibility of moisture.

In the past, classification of condensed phosphates has been a somewhat confusing issue, with numerous individuals providing an input. However, development of techniques such as XRD, IR spectroscopy, NMR and paper chromatography have helped in clarifying the issue, and nowadays crystalline condensed phosphates can be divided into four general categories[13-15]. -

1) Finite chain phosphates

Finite chain phosphates are built up from the linear linkage of PO_4 units to give a condensed entity of general formula $P_nO_{3n+1}^{(n+2)-}$. Where n = 1 and 2, we have an orthophosphate and pyrophosphate respectively, though it must be explicitly noted that the former is not a condensed phosphate. Although such phosphates have been isolated up to n = 16, *crystalline* linear phosphates with a value of n > 3 are generally difficult to prepare. This is possibly because the highly charged anions attach randomly to growing crystals, making the continuation of ordered growth difficult. There could also be geometrical constraints: it may not be spatially possible for the cations and anions to achieve their ideal coordination number. Thus size, charge and coordination number are dominant factors in determining whether a stable lattice is formed or not.

2) Infinite chain phosphates

For large values of n, say > 15, a linear condensed phosphate tends to be termed a “metaphosphate” with general formula $(P_nO_{3n})^{n-}$. Sometimes such infinite chain phosphates are also referred to as “polyphosphates”.[16]

3) Cyclic phosphates

Simple phosphate rings with n > 3 have the metaphosphate composition and consist of alternating phosphorus and oxygen atoms, analogous to the rings formed by silicates.

4) Ultraphosphates

Ultraphosphates, also known as branched phosphates, are those which contain triply linked PO_4 tetrahedra. They tend to from when the metal:phosphorus ratio is

less than unity. Possessing triply linked tetrahedra (*i.e.* branching points) renders these phosphates somewhat unstable, meaning that they hydrolyse very rapidly.

1.2.1 Structure Types

It is generally found that condensed phosphate compounds adopt two main structure types. The first is a three-dimensional network consisting of MO_6 units partially or fully coordinated by condensed phosphate anions. The latter may be further coordinated to counter cations to give a reasonably rigid structure. It is worth noting that this type of structure is common for pyrophosphates, triphosphates and polyphosphates, all of which have been investigated in this research. The second structure type is composed of layers of MO_6 octahedra, again partially or fully coordinated by the condensed phosphate unit. Acidic protons and/ or water of crystallisation are often situated in between these layers for the purpose of holding them together through weak interlayer bonding (see Figure 1.3). This topology is found amongst various pyrophosphate and triphosphate compounds.

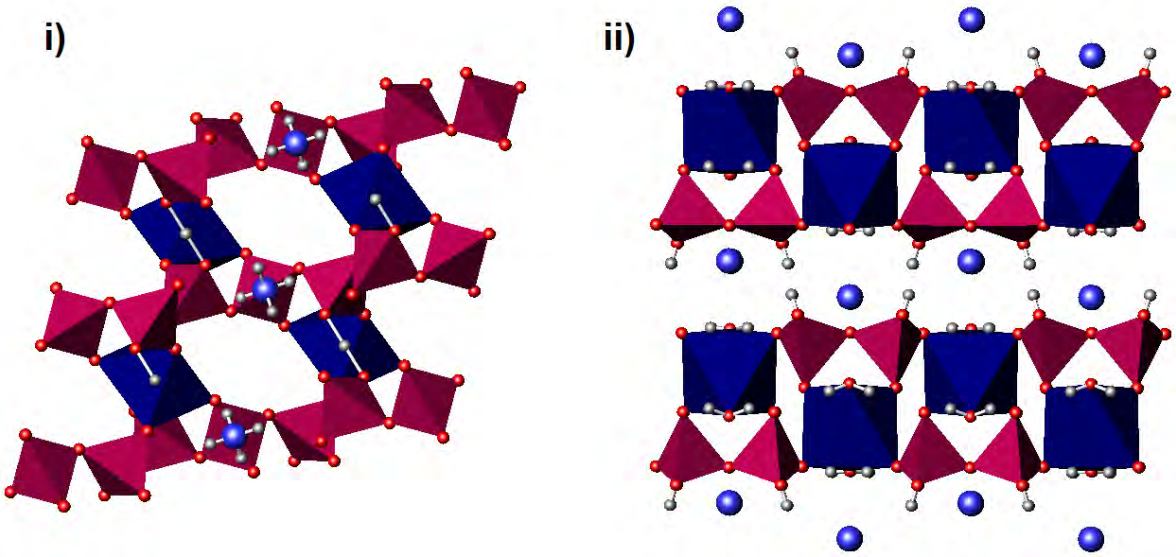

Figure 1.3: *The two structure types present in condensed phosphates: i) a 3D framework, as seen in $NH_4FeHP_3O_{10}$[17] and ii) a layered structure, as seen for $KMnHP_2O_7{\cdot}2H_2O$.[18] MO_6 octahedra are shown in blue, PO_4 tetrahedra in pink, oxygen atoms as red spheres, nitrogen/ potassium atoms as blue spheres and hydrogen atoms as grey spheres.*

It should be apparent that many types of condensed phosphate compounds can be formed, through having varying degrees of condensation of the anion as well as the possibility of incorporating a number of different cations into the structure. The number of potential stoichiometries can be further increased should the crystal lattice be able to accommodate waters of hydration.

1.2.2 The History of Condensed Phosphates

Condensed phosphates have been the subject of investigations for almost 200 years, with the early focus being on characterising the chain length of such materials and trying to derive a logical nomenclature. One of the largest obstacles to advancement in this area was that often studies were carried out on compounds that were not known to be free of impurities.

The earliest report of condensed inorganic phosphates was given by Berzelius[19] in 1816, who observed the phenomenon of condensation upon conducting studies on the ignition of orthophosphoric acid. In 1848, Fleitmann and Henneberg[20] proposed a chemical scheme (1.1) for this, which led to the generalised formula for linear condensed phosphates being developed.

$$nH_3PO_4 + (n-1)H_2O \rightarrow H_{n+2}P_nO_{3n+1} \qquad \textbf{(1.1)}$$

By 1895, Schwarz[21] had described the preparation of sodium triphosphate as well as a number of mixed triphosphates. Shortly after this, Knorre[22] reviewed the work that had been carried out in the field of condensed phosphates, as well as reporting the results from his own investigations into the preparation of sodium cyclophosphate and double salts. Further work was carried out on water soluble cyclotriphosphates and cyclohexaphosphates by Boulle,[23] whose procedure is still

used for synthesising such salts. In 1938, Bonneman-Bemia[24] described a number of new triphosphate compounds and was the first to use X-ray diffraction to characterise these as well as previously reported triphosphate phases.

By the 1950s, the pace in this field had significantly accelerated due to progression in X-ray structural analysis as well as Westman and Scott[25] and Ebel[26] demonstrating that thin layer chromatography could be used as a key technique in determining chain length. Indeed, these advances now made it possible to ascertain the purity of a sample as well as to accurately establish the degree of condensation of the phosphate unit. Although many of the previously described phosphates were actually found to be mixtures of various condensed phosphates, this only served as motivation to develop well-controlled, reproducible synthetic procedures that yielded pure phases.

By the late 1960s condensed phosphates had finally been unambiguously categorised, mainly as a result of the systematic investigations conducted by Thilo[27-29] and van Wazer and Griffith.[14] A huge wealth of information on the synthesis and properties of condensed phosphates, aided by chromatographic and X-ray analysis was published, leading to this becoming the fundamental basis of phosphate chemistry. X-ray diffraction analysis continued to become a powerful tool in the subsequent development of phosphate chemistry, in particular allowing a number of structural determinations to be performed in order to prove the geometrical configurations of condensed phosphate anions.

1.2.3 Pyrophosphates

Pyrophosphates (or diphosphates) are found to be the most common type of condensed phosphate, and have received much attention since first discovered by Berzelius.[19] Indeed, their existence was readily accepted during this time period, unlike triphosphates which remained disputed up until the 1940s. Chemical preparations include solid state reactions, flux methods and exchange reactions, with compounds of general formula $M_4^{I}P_2O_7$, $M_2^{I}M^{II}P_2O_7$, $M^{I}M^{III}P_2O_7$, $M_2^{II}P_2O_7$ and $M^{IV}P_2O_7$ known to exist. Within these categories, the existence of acidic anions such as $[HP_2O_7]^{3-}$, $[H_2P_2O_7]^{2-}$ and $[H_3P_2O_7]^{-}$ has been long established and typified by strong hydrogen-bonding between the anions to give infinite chains, ribbons or planes.

A significant part of this research is concerned with monovalent-trivalent cation pyrophosphates, which serve as an interesting family of condensed phosphates. Stoichiometries of $M^{I}M^{III}P_2O_7$, $M^{I}M^{III}(H_2P_2O_7)_2$, $M^{I}M_2^{III}H(P_2O_7)_2$ and $M_6^{I}M_2^{III}(P_2O_7)_3$ can be taken up, though the former is found to be the most numerous amongst these and is the subject of this research.

1.2.3.1 The Pyrophosphate Anion

The pyrophosphate anion is the simplest condensed phosphate anion, built up from two corner-sharing PO_4 tetrahedra. When discussing the geometrical features of this unit, the P-O-P bridging angle is considered as well as the relative orientation of the two PO_4 groups with respect to each other. For the latter case the terminology of “staggered” (trans) and “eclipsed” (cis) was developed, though it is very rare for any P_2O_7 group to be purely one or the other, unless the constituent atoms are found to be situated on symmetry elements within the structure. Much of the observed P_2O_7

groups have no internal symmetry, but there are some cases in which internal symmetries of 2, *m*, $\bar{1}$ or *mm* have been reported.

Figure 1.4 shows the average values found for various distances and bond angles in the P_2O_7 unit. Within each PO_4 tetrahedron, the P-O distances and O-P-O bond angles are often compared. Amongst the P-O distances, it is commonly found that P-O (bridging) > P-OH > P-O (terminal).

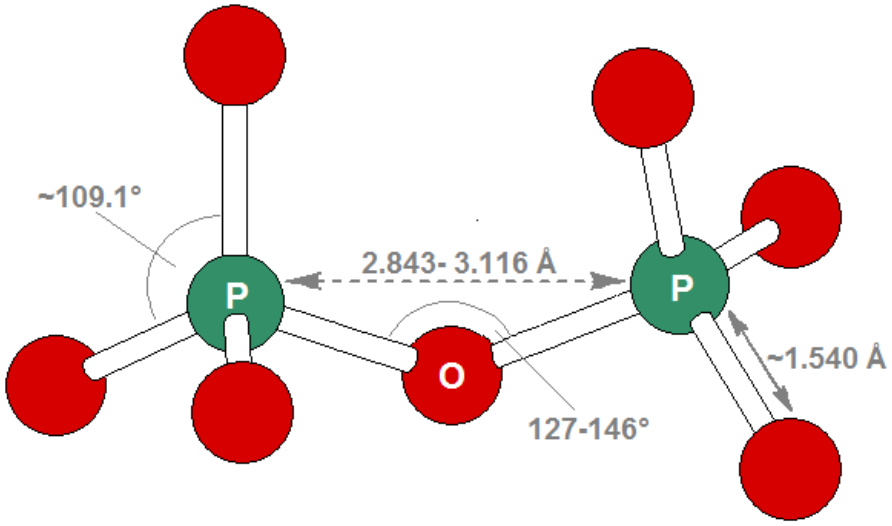

Figure 1.4: *Average bond distances and bond angles observed for the pyrophosphate anion*[30]

1.2.3.2 $M^{I}M^{III}P_2O_7$ Monovalent-Trivalent Cation Pyrophosphates

The first characterisation of a $M^{I}M^{III}P_2O_7$ compound was performed by D'Yvoire,[31] who presented findings on $KAlP_2O_7$. A subsequent structural determination led to this compound being eventually referred to as a type-I pyrophosphate.[32] At around the same time, another polymorph of $NaFeP_2O_7$[33] was identified and the structural details of this type-II pyrophosphate were later reported by Gabelica-Robert *et al*.[34] A third structure type for $LiFeP_2O_7$[35] was reported shortly after and led to a number of compounds being categorised into these three

different structure types. Sometime later an isolated structure type was reported for α-$NaTiP_2O_7$[36] and more recently for KYP_2O_7[37] and $NaYP_2O_7$.[38]

All of these frameworks consist of $M^{III}O_6$ octahedra corner-linked to P_2O_7 tetrahedra (see Figure 1.5). The six corners of each octahedron are shared with either five or six different P_2O_7 groups, creating channels in which the monovalent cation is situated. The main difference amongst these structure types is in the conformation of the pyrophosphate group, which can range from staggered to eclipsed.

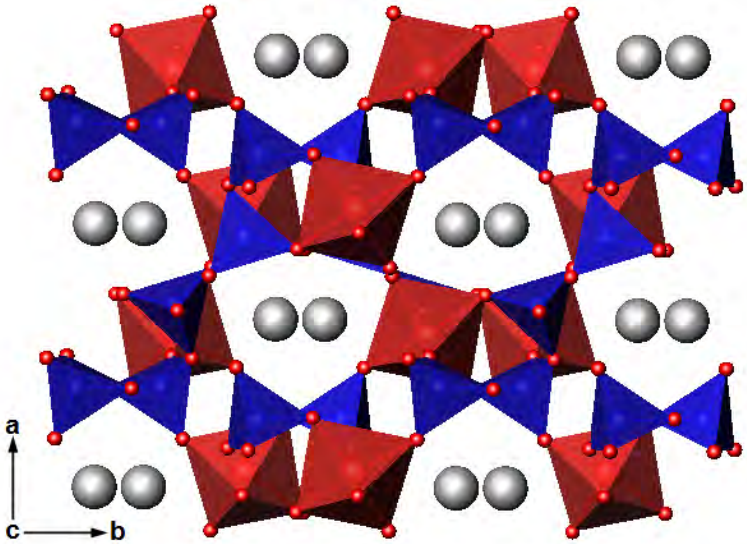

Figure 1.5: *Structure of $KAlP_2O_7$,[32] a type-I $M^IM^{III}P_2O_7$ pyrophosphate. AlO_6 octahedra are shown in red, PO_4 tetrahedra in blue and K^+ cations as grey spheres.*

The size of the M^I cation appears to strongly influence the structure type that crystallises, with type-I being frequently observed for M^I = K, Rb and Cs (also, to a lesser extent for Na), type-II being most common for M^I = Na and Ag and type-III being encountered for Li containing compounds. Clearly there are exceptions to this, notably for some Na and K containing compounds ($NaYP_2O_7$ and KYP_2O_7). Furthermore, studies on the $NaEuP_2O_7$[39] compound show that it adopts a structure

type not previously described, consisting of EuO_8 polyhedra that are seemingly defined by the nature and size of the M^{III} cation. Therefore this suggests that the individual requirements of the trivalent cation can also have an influence on structure type.

1.2.3.3 $HM^{III}P_2O_7$ Trivalent Cation Pyrophosphates

At this stage it is also worth discussing the family of $HM^{III}P_2O_7$ compounds, which do not belong to any of the structure types that have already been detailed here. As briefly mentioned, the acidic pyrophosphate units allow for strong hydrogen-bonding between the anions, which results in the formation of infinite chains within these structures. For many of the reported compounds of this composition, it is found that the pyrophosphate units do not completely isolate the metal octahedra from each other, with such phases consisting of isolated $M_2^{III}O_{10}$ dimers formed from two octahedra that are edge-shared and then further corner-linked to the pyrophosphate groups (see Figure 1.6). Interestingly, three different structure types have been reported to date, but only concerning M^{III} = Mn,[40-41] Fe,[42-43] Tl[44] and Yb.[45]

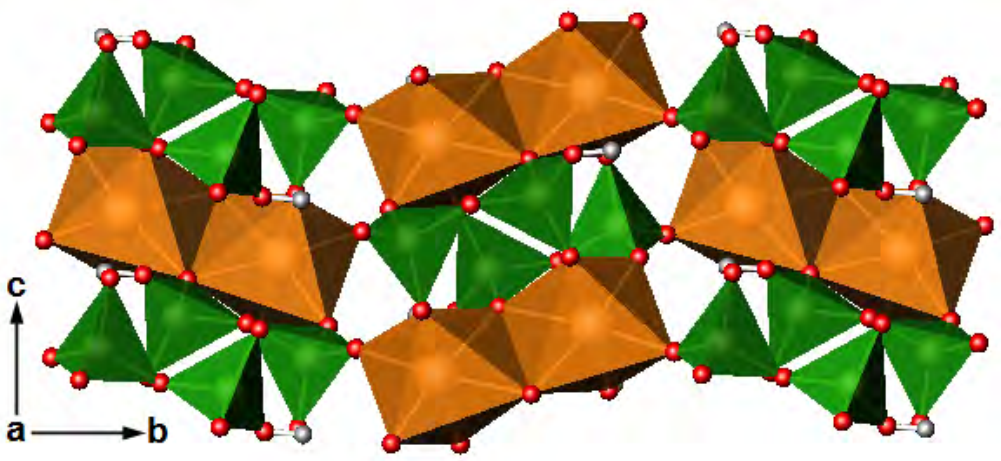

Figure 1.6: *Structure of $HFeP_2O_7$[43] showing FeO_6 octahedra in orange, PO_4 tetrahedra in green and protons as grey spheres.*

1.2.4 Triphosphates

The development of triphosphate chemistry was relatively slow compared to that of pyrophosphates, with the existence of n > 2 condensed phosphates disputed for some time. Works by Morey and Ingerson[46-48] on the $NaPO_3$-$Na_4P_2O_7$ and KPO_3-$K_4P_2O_7$ phase equilibrium diagrams clearly showed the existence of $Na_5P_3O_{10}$ and $K_5P_3O_{10}$, respectively, but it was not until the development of paper chromatography and XRD analysis that the disagreement ended. In 1958, Davies and Corbridge[49] conducted the first structural investigation on a triphosphate and solved the crystal structure of one form of $Na_5P_3O_{10}$. Following this, there was a steady increase in the amount of literature regarding triphosphate systems.

Unlike the case of pyrophosphates, there are relatively few synthetic routes that lead to the formation of crystalline triphosphates. Crystallisation in aqueous media is rare, with many of the well-characterised triphosphates discovered through investigations of various systems by flux methods. Compounds of general formula $M_5^{I}P_3O_{10}$, $M_3^{I}M^{II}P_3O_{10}$, $M_2^{I}M^{III}P_3O_{10}$ and $M^{I}M_2^{II}P_3O_{10}$ are known to exist, and where present, $[HP_3O_{10}]^{4-}$ and $[H_2P_3O_{10}]^{3-}$ acidic triphosphate anions are characterised by strong hydrogen-bonding that can lead to infinite anionic networks.

A relatively poorly studied area of triphosphate chemistry is that in which a trivalent cation is present. Although there have been a few structural characterisations, the applications of these materials have been seldom investigated. Trivalent cation triphosphates of the type $M^{I}M^{III}HP_3O_{10}\cdot xH_2O$ and $M_5^{III}(P_3O_{10})_3\cdot xH_2O$ are known to exist, where M^{I} can also be a proton. The former class of compounds (x = 0 and 2) have been investigated in this research and will be detailed in the sections that follow.

1.2.4.1 The Triphosphate Anion

The main features used to describe a triphosphate anion are the P-P distances and the P-O-P and P-P-P bond angles. In assessing compounds where the atomic arrangements have been determined, P-P distances are found to range from 2.818-2.991 Å, P-O-P angles are found to lie between 112.6-139.0° and P-P-P angles can vary from 84.5-151.3°.[30] A similar range of values is also observed for longer chain condensed phosphates and in large ring cyclophosphates. Approximately half of these P_3O_{10} units have no internal symmetry; whereas the other half possess a twofold symmetry in which the central phosphorus atom is located on the diad (see Figure 1.7). As with pyrophosphates, within each PO_4 tetrahedron the P-O distances are found to average to ~1.540 Å and O-P-O angles to ~109.1°.

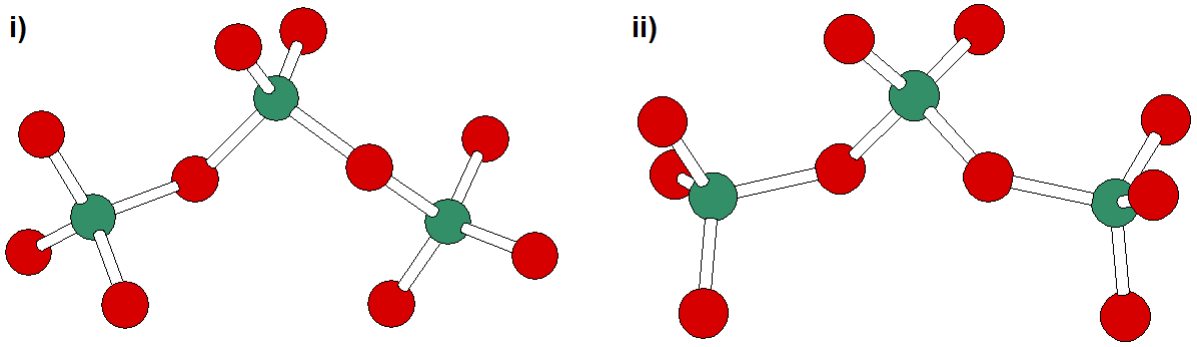

Figure 1.7: *Some examples of triphosphate anions, with phosphorus and oxygen atoms shown as green and red spheres, respectively: i) a P_3O_{10} group with no symmetry and ii) a P_3O_{10} group with binary symmetry*

1.2.4.2 $M^{III}H_2P_3O_{10}$ Trivalent Cation Triphosphates

With regards to these x = 0 dihydrogen triphosphates, D'Yvoire[50] was the first to characterise two forms of $AlH_2P_3O_{10}$, through XRD analysis and paper chromatography. Two analogous iron salts were also reported, and shortly after

Remy and Boulle[51] described three hydrated forms of $CrH_2P_3O_{10}$. $GaH_2P_3O_{10}$ and $GaH_2P_3O_{10}\cdot 2H_2O$ were reported by Chudinova *et al*[52] and Mel'nikov *et al*[53] during their investigations into the thermal decomposition of $Ga(H_2PO_4)_3$. Later, Guzeeva *et al*[54] and Selevich and Lyutsko[55] identified two analogous manganese forms as products of the P_2O_5-MnO (or Mn_2O_3) reaction system.

Genkina *et al*[56] and Lutsko and Johansson[57] were the first to report structural details on $AlH_2P_3O_{10}$ and $FeH_2P_3O_{10}$, respectively, confirming their three-dimensional frameworks. Since then, structural studies on a number of similar $M^{III}H_2P_3O_{10}$ phases (M^{III} = V,[58] Ga,[59] In,[60] Cr[60]) have corroborated the existence of an isostructural family.

1.2.4.3 $M^{I}M^{III}HP_3O_{10}$ Monovalent-Trivalent Cation Triphosphates

Another class of anhydrous triphosphates are those containing monovalent-trivalent cations, with the majority that have been synthesised having a general formula of $M^{I}M^{III}HP_3O_{10}$. The synthesis of a number of these phases has been described in the literature, with many reported to be dimorphous. Averbuch-Pouchot and Durif[61] compiled a concise review of all phases described in the literature up to 1991, many of which still do not have their structures solved. Table 1.1 summarises the compounds to date that have had their structures reported. It is worth noting that structure types 1-3 are of a layered nature whereas types 4-6 are three-dimensional frameworks. The general topology of these structure types was discussed in section 1.2.1, though structure type 6 is an exception to this. Indeed, it has been exclusively observed that this structure type consists of $M^{III}O_8$ polyhedra edge-shared with two adjacent polyhedra to form infinite chains.

Table 1.1: *Summary of the confirmed structure types that various $M^{I}M^{III}HP_3O_{10}$ compounds belong to*

Structure Type and Space Group	Compounds belonging to the series
Type 1 (*P*2/*a*)	$NH_4AlHP_3O_{10}$[62]
	$KAlHP_3O_{10}$[62]
Type 2 (*P*2/*n*)	1M-$CsGaHP_3O_{10}$[63]
Type 3 (*Pca*2$_1$)	$CsGaHP_3O_{10}$-III[64]
Type 4 (*C*2/*c*)	$NH_4FeHP_3O_{10}$[17]
	$CsVHP_3O_{10}$[65]
	α-$RbMnHP_3O_{10}$[66]
	$KMnHP_3O_{10}$[67]
	$RbFeHP_3O_{10}$[68]
Type 5 (*C*2)	$CsMnHP_3O_{10}$[69]
	α-$CsGaHP_3O_{10}$[70]
	β-$RbMnHP_3O_{10}$[71]
	$CsFeHP_3O_{10}$[68]
Type 6 ($P\bar{1}$)	$NH_4BiHP_3O_{10}$[72]
	$NH_4SmHP_3O_{10}$[73]
	$KSmHP_3O_{10}$[73]

1.2.4.4 $M^{III}H_2P_3O_{10}\cdot 2H_2O$ Trivalent Cation Triphosphates

Compounds of the general formula $M^{III}H_2P_3O_{10}\cdot 2H_2O$ also make up an interesting family of materials, and have been well studied by the Wright group.[68,74-75] Despite the syntheses of a number of phases being described, it was only in 2006 that the structure of $AlH_2P_3O_{10}\cdot 2H_2O$[76] was solved. Prior to this, the layered nature of such materials was assumed owing to their ability to undergo ion exchange and intercalation. These structures are now known to consist of metal triphosphate layers held together by weak hydrogen-bonding between the acidic protons and interlayer

water molecules (see Figure 1.8). An understanding of the structure type has allowed detailed studies into the ion exchange, intercalation and exfoliation properties of these materials.

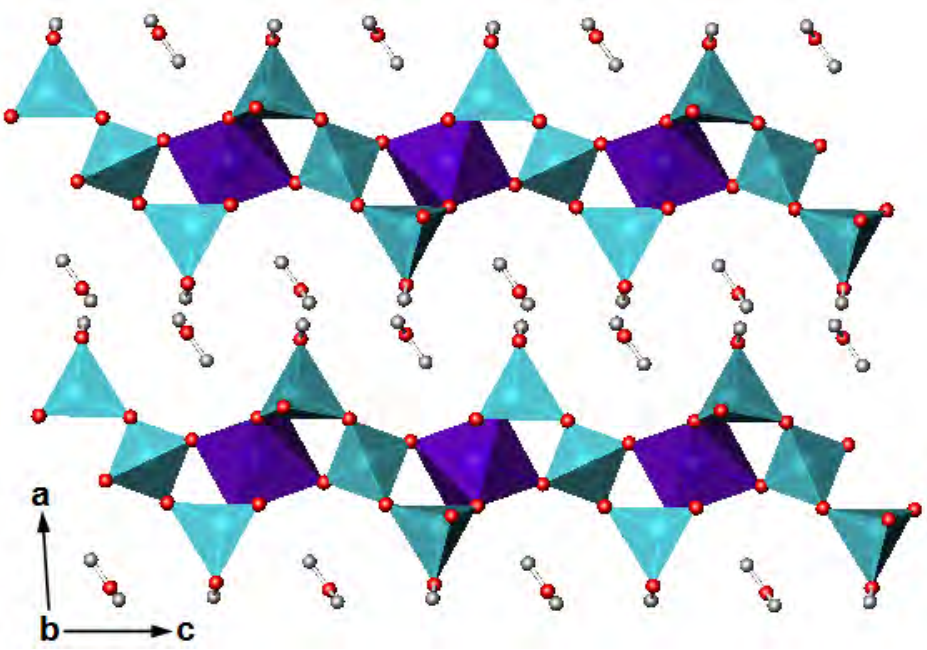

Figure 1.8: *Structure of $AlH_2P_3O_{10}\cdot 2H_2O$[76] showing AlO_6 octahedra in dark blue, PO_4 tetrahedra in light blue, oxygen atoms as red spheres and hydrogen atoms as grey spheres.*

1.2.5 Long Chain Polyphosphates

One of the earliest reports of a long chain polyphosphate was by Graham[77], who obtained sodium polyphosphate by heating the dihydrogen orthophosphate salt:-

$$NaH_2PO_4 \rightarrow NaPO_3 + H_2O \qquad \textbf{(1.2)}$$

KPO_3 was synthesised in an analogous fashion, and soon after various different forms of these two polyphosphates were described, with apparent differences in chemical reactivity, crystallinity and fibrous morphology. For a long time these forms became referred to as Graham, Maddrell or Kurrol salts, and it was only relatively recently that they were found to actually contain a mixture of different chain lengths.

Indeed, only the existence of two crystalline forms of $NaPO_3$ has been clearly established to date.

It is now known that long chain polyphosphates tend to a metaphosphate composition of $P_nO_{3n}^{3-}$, as opposed to maintaining a composition of $P_nO_{3n+1}^{(n+2)-}$. The degree of polymerisation of the anion is very high, with molecular weights ranging from 500,000 to several million. This value can be strongly influenced by the thermal history of the sample as well as its stoichiometry; for example, a small change in the theoretical O:P ratio of 3 can lead to large variations in the extent of polymerisation. Due to their large molecular weights, polyphosphates are not water-soluble and can remain stable for many years.

Polyphosphates of general formula $M^{I}PO_3$, $M^{III}P_3O_9$, $M^{I}M^{III}P_4O_{12}$, $M^{III}HP_4O_{12}$ and $M_2^{I}M^{III}P_5O_{15}$ (for the latter, M^{III} = lanthanide) are known to exist. A number of different routes can be employed for their synthesis, such as the dehydration of dihydrogen orthophosphates, flux methods, hydrothermal methods and thermally induced phase transitions of existing polyphosphates.

1.3 Magnetic Analysis of Condensed Phosphate Frameworks

The presence of transition metal ions within a condensed phosphate framework can give rise to magnetic ordering through the intervening phosphate units. Such exchange interactions have been relatively unexplored compared with say those of oxide systems.

Magnetic exchange interactions can occur through two types of pathway: direct and indirect exchange. Direct exchange occurs where the magnetic ions are situated close enough such that sufficient, direct orbital overlap can occur. Depending on the nature of each magnetic ion, the electron spins will align parallel

(ferromagnetically) or antiparallel (antiferromagnetically) with respect to each other. In many materials there is often insufficient overlap between neighbouring magnetic orbitals, and so it is also necessary to consider indirect exchange interactions. Such interactions occur between magnetic ions when they are separated by intervening species; in the case of solids it is the intervening ligands. This exchange mechanism is referred to as “superexchange”, the nature of which has been well-studied. Where the intervening ligand is a diamagnetic ion, detailed works by Goodenough[78] and Kanamori[79] have allowed much of the interactions to be predicted. Clearly, there is also the possibility of superexchange in phosphate systems, though now *via* a longer M-O-P-O-M pathway. As there are now three intervening ligands rather than one, this exchange mechanism is currently poorly understood.

1.3.1 Superexchange

Superexchange occurs where an intermediate, non-magnetic ligand facilitates the coupling of electron spins on adjacent metal centres. The outcome of the interaction depends on the number of electrons at the two metal centres as well as the arrangement of their orbitals with respect to those of the intervening ligand. If we consider a linear M^{n+}-O^{2-}-M^{n+} transition metal array, then the overlap between each metal d-orbital and the (filled) p-orbital of the intermediate ligand leads to partial transfer of electron density to the metal sites. Figure 1.9 shows a very simple case where the d-orbitals have one d-electron each. If electron density is to be transferred from the intervening ligand to the adjacent metal centres, then the two metal centres must have their spins aligned antiparallel so that they can accept this electron density whilst obeying the Pauli exclusion principle. This exchange is mediated by σ-bonding

between the metal d-orbitals and the ligand p-orbitals; an analogous but weaker interaction can also occur *via* the π-overlap of these orbitals.

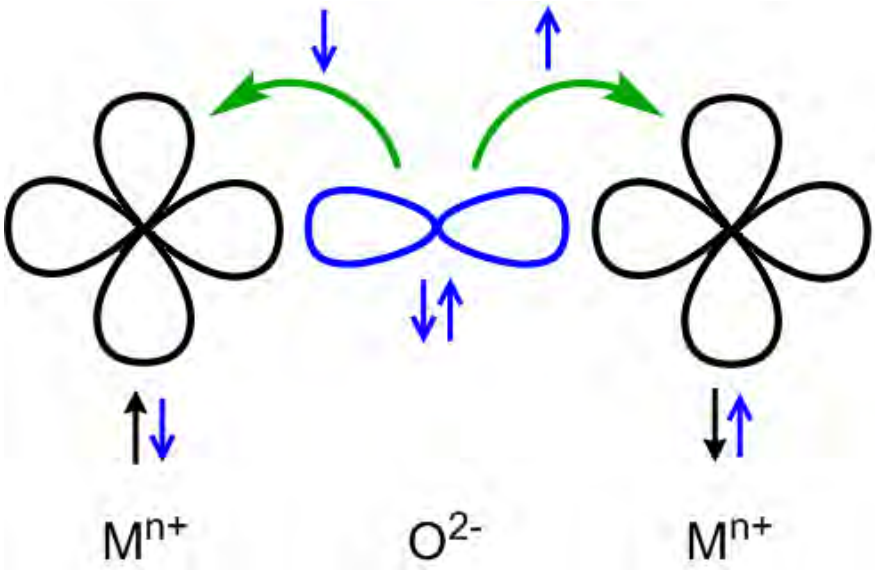

Figure 1.9: *Superexchange in a linear M-L-M system, giving rise to antiferromagnetic ordering*

The strength of interaction can vary with the degree of covalency, but is also highly dependent on the M-L-M bond angle. If we consider a 90° M-L-M configuration (Figure 1.10), then now each d-orbital overlaps with a different p-orbital on the ligand. The transfer of electron density from the ligand to the adjacent metal d-orbitals occurs such that the ligand obeys Hund's rule of maximum multiplicity. In order for the metal cations to receive this electron density, the Pauli exclusion principle ensures that their spins are opposite to that of the incoming electron density. Overall, the metal spins are aligned parallel with respect to each other, now giving rise to ferromagnetic ordering. Such 90° interactions are common in the layer lattices of chlorides.

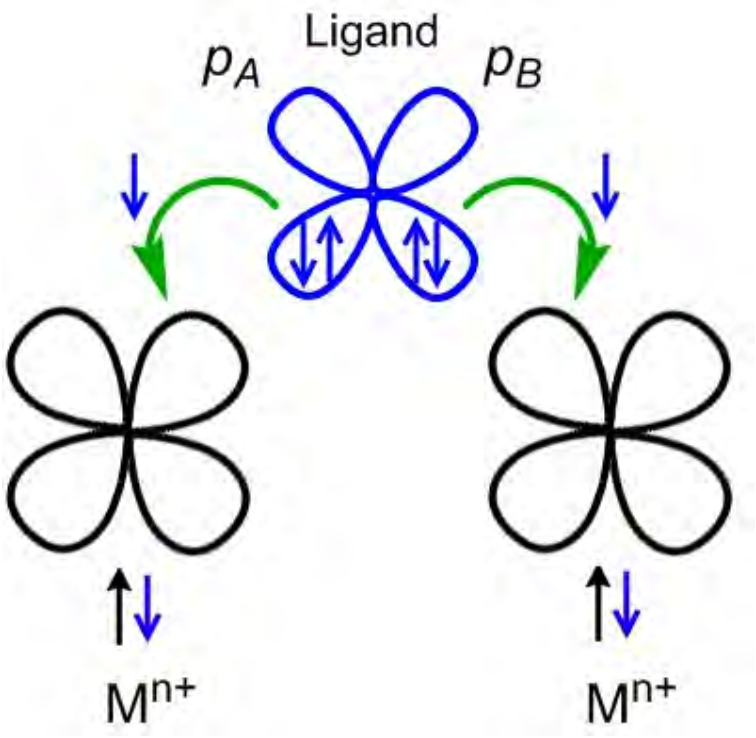

Figure 1.10: *Superexchange in a 90° M-L-M array, giving rise to ferromagnetic ordering*

1.3.2 Trivalent Cation Condensed Phosphates

It is relatively rare for trivalent cation condensed phosphate systems to possess M-L-M superexchange pathways, and so consequently those interactions occurring through extended M-L---L-M linkages, often termed "super-superexchange", need to be considered. There are a number of magnetic solids that possess both superexchange and super-superexchange pathways, though in this instance the latter interactions are often neglected due to being much weaker.

Although there have been a number of structural determinations of trivalent transition metal condensed phosphates, there has been relatively little reported on the magnetic properties of these systems, with reports of magnetic structures being even rarer. The magnetic structures of $LiFeP_2O_7$[80] and $NaFeP_2O_7$[81] have been studied by neutron diffraction and found to consist of both ferromagnetic and

antiferromagnetic interactions. However, in the case of $LiFeP_2O_7$, the authors ignored those super-superexchange pathways in which the Fe atoms were separated by a distance greater than 6 Å. As a follow up of this work, Whangbo *et al*[82] used spin dimer analysis to estimate the strengths of all Fe-O---O-Fe interactions in these two compounds, though ignored the ferromagnetic contributions to the exchange parameters on the assumption that they would be small. Their results suggested that it is the L---L distance that is critical to the strength of interaction, with a shorter contact giving rise to a stronger interaction between the magnetic ions. Indeed, in their calculations on $LiFeP_2O_7$ and $NaFeP_2O_7$, it was found that the strongest exchange interactions were expected to occur within Fe-O---O-Fe pathways possessing reasonably short O---O distances (~2.5 Å) but large Fe---Fe distances (> 6 Å). Furthermore, the strongest interactions appeared to be correlated with larger Fe-O---O angles.

For those compounds studied in this research, where super-superexchange interactions exist, the approach used is to only consider those interactions which occur through M-O-P-O-M pathways *i.e.* through an orthophosphate unit. Indeed, this is the shortest possible exchange route, and in accordance with Whangbo *et al*,[82] gives rise to the shortest O---O contact. A number of magnetic structures have analysed in this way, particularly for compounds of the type $M^IM^{III}HP_3O_{10}$ (M^I = α-Rb and Cs, M^{III} = Mn and Fe).[66,68,83] The exchange pathways show a number of resemblances due to the similarities in the metal phosphate frameworks amongst these members. In brief, each M^{III} spin has been found to be linked to six others *via* M-O-P-O-M pathways. Where M^{III} = Mn, four of these interactions appear to be ferromagnetic and two antiferromagnetic, whereas with M^{III} = Fe, all of these

interactions appear to be antiferromagnetic in nature. Despite its structural similarities, the magnetic structure of $KMnHP_3O_{10}$[84] has been found to be much more complex, due the presence of two manganese sublattices. In this case, all interactions mediated by the orthophosphate units have been found to be antiferromagnetic in nature, but a weak ferromagnetic component arises due to a small canting of these moments.

More recently, Coomer *et al*[71] have performed a detailed magnetic analysis on β-$RbMnHP_3O_{10}$ and $RbMnP_2O_7$. Whilst the former compound possesses a similar magnetic structure to those triphosphates already described, $RbMnP_2O_7$ has been found to exhibit relatively complex magnetic pathways. In addition to its apparent ferromagnetic and antiferromagnetic Mn-O-P-O-Mn exchange pathways, it has been found that each PO_4 unit simultaneously connects three Mn centres in an overall antiferromagnetic fashion, a feature not observed for the triphosphates.

It is fair to say that only the magnetic structures of a distinct few compounds are known. Despite there being some unusual features, there also appears to be a number of similarities, suggesting that it may be possible to derive some empirical rules from these observations.

1.4 Inorganic Pigments

A pigment is generally considered to be a substance that is virtually insoluble in the applied medium and that can be utilised for its colouring or protective properties. Inorganic pigments make up approximately 97% of the whole pigments industry, with the most common areas of use being in paints, inks, plastics, cosmetics, building materials, ceramic glazes and enamels. The suitability of a

pigment for a particular application is based on a number of factors,[85] some of which are listed below: -

a) Chemical and Physical Properties: composition, moisture and salt content, particle size, density and hardness.
b) General Stability: resistance to light, heat, weather and chemicals and anticorrosive properties.
c) Stability in Binding Mediums: interaction with the binder, dispersibility and compatibility.
d) Colouring Properties: colour, tinting strength, lightening power and hiding power.

Inorganic pigments may be categorised into groups according to their observed colour and the manner in which it is generated. Table 1.2 below shows one type of classification scheme.

Table 1.2: *Classification of Inorganic Pigments*[85]

Type of Pigment	Generation of Optical Effect
White	Non-selective light scattering
Coloured	Selective light absorption and light scattering
Black	Non-selective light absorption
Lustre	Regular reflection or interference of light
Luminescent	Following the absorption of radiation, it is emitted as light of a longer wavelength

The colour of a substance is commonly characterised using the CIE (*Commision Internationale d'Eclairage*) system, which is a universally accepted standard for colour specification and measurement. This is based on determining the

relative amounts of three characteristic wavelengths present in a colour. The wavelengths are 435.8, 546.1 and 700.0 nm, which correspond to the blue, green and red regions of the visible spectrum, respectively. This leads to tristimulus values *X*, *Y* and *Z*, from which coordinates for chromaticity, lightness and hue can be obtained by performing a mathematical transformation.

A range of pigment compositions are currently used, based on oxides, hydroxides, sulfides, sulfates, selenides, phosphates, carbonates, oxyhalides and more, with the titanium dioxide pigment dominating the trade. One of the largest obstacles facing the industry today is that many inorganic pigments contain toxic metals such as lead, cadmium, cobalt, bismuth and barium. If certain levels are exceeded then the use of such compounds can have an adverse effect on the environment and human health, which has resulted in a drive to develop safer substitutes.

1.4.1 Transition Metal Phosphates

There are few well known transition metal phosphates currently used as pigments. The mineral vivianite, $Fe_3(PO_4)_2 \cdot (H_2O)_8$, and its various hydrated forms are used as blue colourants in oils and paints. The “manganese violet” pigment, reported to be an ammonium manganese pyrophosphate, and “cobalt violet”, ($Co_3(PO_4)_2$), are widely used in artists’ colours. Transition metal phosphates are perhaps better known for their anticorrosion properties, with zinc and chromium orthophosphates of composition $Zn_3(PO_4)_2 \cdot 4H_2O$ and $CrPO_4 \cdot 3H_2O$, respectively, used as anticorrosion pigments in metal surface coatings. Such compounds work by their interaction with water, which is able to hydrolyse them to release soluble phosphate. A reaction then occurs between the phosphate ions and metal surface, producing a coating that

either strengthens or chemically modifies the existing oxide film already present on the iron surface. As a consequence, the iron is prevented from participating in electrochemical reactions that result in the formation of rust.

Relatively recently there has been a renewed interest in developing non/less-toxic transition metal phosphate pigments. Whilst the phosphate unit is optically inactive, its coordination to a transition metal centre can have structural implications which result in unusual or enhanced properties of the material. A recent structural study by Coomer *et al*[71] showed the compounds $RbMnP_2O_7$ and β-$RbMnHP_3O_{10}$ to exhibit intense violet colourations, correlated with the Mn^{III} cation adopting an unusual octahedral coordination environment, beyond the [4+2] Jahn-Teller distortion normally observed. It was postulated that this effect was driven by the steric requirements of the condensed phosphate anions, though the optical properties of these materials were not further investigated. In fact, there are relatively few studies in the literature that are concerned with the structural aspects of phosphate pigment compounds, with the focus being more so on the synthesis, optical characteristics and optimisation of such materials. In this respect, some attention has been guided towards transition metal phosphate solid solutions, with $Co_{1-x}Cu_xFeOPO_4$,[86] $Mn_{3-x}Mg_xFe_4(PO_4)_6$,[87] $Co_{2-x}Mg_xP_2O_7$,[88] $Cu_{2-x}Mn_xP_4O_{12}$,[89] $Cd_{2-x}Zn_xP_4O_{12}$[90] and $Zn_{2-x}Ni_xP_4O_{12}$[91] all investigated as potential pigment materials. Other work has focused on doping existing transition metal phosphates with rare earth cations in order to enhance the properties of the host material.[92-94]

1.5 Research Aims

The primary aim of this research was to investigate the synthesis, structure and properties of a number of Mn^{III} condensed phosphate phases. This particular

cation was chosen within a condensed phosphate environment as previous studies suggested that it is able to exhibit a “plastic” coordination sphere in order to fulfil the steric requirements of the phosphate unit, so giving the potential for unusual structural features.[71] With this in mind, the synthesis and characterisation of the manganese violet pigment (referred to as $NH_4MnP_2O_7$) was to be first explored. Following on from this, we would aim to investigate the effects of substituting Mn^{III} for similarly sized Fe^{III}. With each cation showing its own individual electronic requirements, it would be of interest to see if a solid solution could be formed, and also whether this was accompanied by a change in oxidation state. Furthermore, there was also scope here to alter the optical and magnetic properties of these materials. If successful, this approach would be extended to other Mn^{III} condensed phosphate systems.

After consulting the literature, we also chose to investigate the $MnPO_4$-Fe_2O_3-H_3PO_4 reaction system as a route to other (Mn,Fe) condensed phosphates. A product of this reaction system, $MnH_2P_3O_{10}\cdot 2H_2O$, was further studied with regards to its intercalation properties.

In all cases, principal characterisation would be attempted through X-ray and neutron diffraction, TGA-MS, UV-Vis spectroscopy and SQUID magnetometry. Where possible, the magnetic exchange interactions of the phases isolated would also be investigated in order to supplement the existing literature on magnetically dilute frameworks.

References

[1] C. Combes and C. Rey, *Acta Biomater.*, 2010, **6**, 3362-3378.

[2] G. Mestres and M. P. Ginebra, *Acta Biomater.*, 2011, **7**, 1853-1861.

[3] V. A. Isupov, *Ferroelectrics*, 2002, **274**, 203-283.

[4] I. W. Donald, B. L. Metcalfe and R. N. J. Taylor, *J. Mater. Sci.*, 1997, **32**, 5851-5887.

[5] I. W. Donald, B. L. Metcalfe, S. K. Fong, L. A. Gerrard, D. M. Strachan and R. D. Scheele, *J. Nucl. Mater.*, 2007, **361**, 78-93.

[6] M. Tang, W. C. Carter and Y. M. Chiang, *Annu. Rev. Mater. Res.*, 2010, **40**, 501-529.

[7] A. K. Padhi, K. S. Nanjundaswamy and J. B. Goodenough, *J. Electrochem. Soc.*, 1997, **144**, 1188-1194.

[8] W. J. Zhang, *J. Power Sources*, 2011, **196**, 2962-2970.

[9] I. S. Cho, D. W. Kim, D. H. Kim, S. S. Shin, T. H. Noh, D. W. Kim and K. S. Hong, *Eur. J. Inorg. Chem.*, 2011, **14**, 2206-2210.

[10] H. Wen, M. H. Cao, G. B. Sun, W. G. Xu, D. Wang, X. Q. Zhang and C. W. Hu, *J. Phys. Chem.*, 2008, **C112**, 15948-15955.

[11] N. Niu, P. Yang, Y. Wang, W. Wang, F. He, S. Gai and D. Wang, *J. Alloy. Compd.*, 2011, **509**, 3096-3102.

[12] R. Essehli, B. El Bali, H. Ehrenberg, I. Svoboda, N. Bramnik and H. Fuess, *Mat. Res. Bull.*, 2009, **44**, 817-821.

[13] D. E. C. Corbridge, *The Structural Chemistry of Phosphorus*; Elsevier Scientific Publishing Company: Amsterdam, 1974.

[14] J. R. van Wazer, *Phosphorus and its Compounds, Volume I: Chemistry*; Interscience Publishers Inc: New York, 1958.

[15] J. R. van Wazer and E. J. Griffith, *J. Am. Chem. Soc.*, 1955, **77**, 6140-6144.

[16] M. Bagieu-Beucher, *Acta Crystallogr.*, 1978, **B34**, 1443-1446.

[17] V. V. Krasnikov, Z. A. Konstant and V. S. Fundamenskii, *Inorg. Mater.*, 1983, **19**, 1231-1235.

[18] H. Assaaoudi, A. Ennaciri, M. Harcharras, B. El Bali, F. Reinauer, R. Glaum, A. Rulmont and M. R. Spirlet, *Acta Crystallogr.*, 2002, **C58**, I79-I81.

[19] J. Berzelius, *Ann. Physik*, 1816, **54**, 31.

[20] T. Fleitmann and W. Henneberg, *Liebigs Ann. Chem.*, 1848, **65**.

[21] F. Schwarz, *Z. Anorg. Chem.*, 1895, **9**, 249.

[22] G. Knorre, *Z. Anorg. Chem.*, 1900, **24**, 369.

[23] A. Boulle, *C. R. Acad. Sci.*, 1938, **206**, 517.

[24] P. Bonneman-Bémia, *Anal. Chim.*, 1941, **16**, 395.

[25] A. E. R. Westman and A. E. Scott, *Nature*, 1951, **168**, 740.

[26] J. P. Ebel, *Bull. Soc. Chim. Fr.*, 1968, 1663.

[27] E. Thilo, *Angew. Chem. Int. Edit.*, 1955, **67**, 141-145.

[28] E. Thilo, *Angew. Chem. Int. Edit.*, 1965, **4**, 1061-1071.

[29] E. Thilo, *Bull. Soc. Chim. Fr.*, 1968, 1726.

[30] M. T. Averbuch-Pouchot and A. Durif, *Topics in Phosphate Chemistry*; World Scientific Publishing Co. Pte. Ltd.: Singapore, 1996.

[31] F. D'Yvoire, *Bull. Soc. Chim. Fr.*, 1962, 1224.

[32] H. N. Ng and C. Calvo, *Can. J. Chem.*, 1973, **51**, 2613-2620.

[33] J. P. Gamondès, F. D'Yvoire and A. Boulle, *C. R. Acad. Sci.*, 1969, **C269**, 1532.

[34] M. Gabelica-Robert, M. Goreaud, P. Labbe and B. Raveau, *J. Solid State Chem.*, 1982, **45**, 389-395.

[35] E. A. Genkina, B. A. Maximov, V. A. Timofeeva, A. B. Bykov and O. K. Melnikov, *Dokl. Akad. Nauk SSSR*, 1985, **284**, 864-867.

[36] A. Leclaire, A. Benmoussa, M. M. Borel, A. Grandin and B. Raveau, *J. Solid State Chem.*, 1988, **77**, 299-305.

[37] A. Hamady, M. F. Zid and T. Jouini, *J. Solid State Chem.*, 1994, **113**, 120-124.

[38] A. Hamady and T. Jouini, *Acta Crystallogr.*, 1996, **C52**, 2949-2951.

[39] M. Ferid, K. Horchani and J. Amami, *Mat. Res. Bull.*, 2004, **39**, 1949-1955.

[40] P. A. Durif and M. T. Averbuch-Pouchot, *Acta Crystallogr.*, 1982, **B38**, 2883-2885.

[41] L. S. Ivashkevich, K. A. Selevich, A. I. Lesnikovich, A. F. Selevich and A. S. Lyakhov, *Z. Kristallogr.*, 2006, **221**, 115-121.

[42] E. A. Genkina, N. S. Triodina, B. A. Maksimov and O. K. Melnikov, *J. Struct. Chem.*, 1988, **29**, 323-326.

[43] K. A. Selevich, L. S. Ivashkevich, A. F. Selevich and A. I. Lesnikovich, *Russ. J. Inorg. Chem.*, 2007, **52**, 1125-1130.

[44] L. S. Ivashkevich, K. A. Selevich, A. S. Lyakhov and A. F. Selevich, *Acta Crystallogr.*, 2007, **E63**, I38-I40.

[45] A. F. Selevich, K. Khurs, A. S. Lyakhov and A. I. Lesnikovich, *Phos. Res. Bull.*, 2005, **19**, 234.

[46] E. Ingerson and G. W. Morey, *Am. Mineral.*, 1943, **28**, 448-455.

[47] G. W. Morey and E. Ingerson, *Am. J. Sci.*, 1944, **242**, 1-6.

[48] G. W. Morey, *J. Am. Chem. Soc.*, 1954, **76**, 4724-4726.

[49] D. R. Davies and D. E. C. Corbridge, *Acta Crystallogr.*, 1958, **11**, 315-319.

[50] F. D'Yvoire, *Bull. Soc. Chim. Fr.*, 1962, **6**, 1224.

[51] P. Remy and A. Boulle, *C. R. Hebd. Acad. Sci.*, 1964, **258**, 927-929.

[52] N. N. Chudinova, M. A. Avaliani and L. S. Guzeeva, *Inorg. Mater.*, 1977, **13**, 1774-1777.

[53] P. P. Mel'nikov, V. A. Efremov, A. K. Stepanov, T. S. Romanova and L. N. Komissarova, *Zh. Neorg. Khim.*, 1976, **21**, 46-50.

[54] L. S. Guzeeva, A. V. Lavrov and I. V. Tananaev, *Inorg. Mater.*, 1982, **18**, 1590-1594.

[55] A. F. Selevich and V. D. Lyutsko, *Russ. J. Inorg. Chem.*, 1984, **29**, 364-369.

[56] E. A. Genkina, Y. A. Gorbunov, B. A. Maximov, A. A. Shternberg and O. K. Melnikov, *Kristallografiya*, 1984, **29**, 215-219.

[57] V. Lutsko and G. Johansson, *Acta Chem. Scand. Ser. A*, 1984, **38**, 663-669.

[58] A. S. Lyakhov, K. K. Palkina, V. A. Lyutsko, S. I. Maksimova and N. T. Chibiskova, *Inorg. Mater.*, 1990, **26**, 895-899.

[59] A. S. Lyakhov, V. A. Lyutsko, G. K. Tuchkovskii and K. K. Palkina, *Russ. J. Inorg. Chem.*, 1991, **36**, 803-805.

[60] K. A. Selevich, L. S. Ivashkevich and A. F. Selevich, *Russ. J. Inorg. Chem.*, 2006, **51**, 1565-1570.

[61] M. T. Averbuch- Pouchot and A. Durif, *Annu. Rev. Mater. Sci.*, 1991, **21**, 65-92.

[62] M. T. Averbuch- Pouchot, A. Durif and J. C. Guitel, *Acta Crystallogr.*, 1977, **B33**, 1436-1438.

[63] J. X. Mi, H. Borrmann, Y. X. Huang, J. T. Zhao and R. Kniep, *Z. Kristallogr.*, 2003, **218**, 169-170.

[64] N. Anisimova, M. Bork, R. Hoppe and M. Meisel, *Z. Anorg. Allg. Chem.*, 1995, **621**, 1069-1074.

[65] B. Klinkert and M. Jansen, *Z. Anorg. Allg. Chem.*, 1988, **567**, 77-86.

[66] A. J. Wright and J. P. Attfield, *Inorg. Chem.*, 1998, **37**, 3858-3861.

[67] J. Mechergui and W. Belam, *Mat. Res. Bull.*, 2008, **43**, 3358-3367.

[68] N. J. Checker, *The Synthesis and Properties of Novel Condensed Phosphates*, PhD Thesis, University of Birmingham, 2006.

[69] E. V. Murashova and N. N. Chudinova, *Kristallografiya*, 1995, **40**, 476-484.

[70] J. X. Mi, H. Borrmann, Y. X. Huang, J. T. Zhao and R. Kniep, *Z. Kristallogr.*, 2003, **218**, 167-168.

[71] F. C. Coomer, N. J. Checker and A. J. Wright, *Inorg. Chem.*, 2010, **49**, 934-942.

[72] M. T. Averbuch- Pouchot and M. Bagieu-Beucher, *Z. Anorg. Allg. Chem.*, 1987, **552**, 171-180.

[73] N. Zouari, T. Mhiri, A. Daoud, P. Gravereau and E. Lebraud, *Int. J. Inorg. Mater.*, 2000, **2**, 379-387.

[74] S. K. Rishi, *Synthesis and Characterisation of a series of layered trivalent metal triphosphates*, PhD Thesis, University of Birmingham, 2006.

[75] T. P. Marsh, *Studies into the Ion Exchange and Intercalation Properties of $AlH_2P_3O_{10}\cdot 2H_2O$*, PhD Thesis, University of Birmingham, 2011.

[76] S. K. Rishi, B. M. Kariuki, N. J. Checker, J. Godber and A. J. Wright, *Chem. Commun.*, 2006, 747-749.

[77] T. Graham, *Philos. T. Roy. Soc.*, 1833, **123**, 253-284.

[78] J. B. Goodenough, *Phys. Rev.*, 1955, **100**, 564-573.

[79] J. Kanamori, *J. Phys. Chem. Solids*, 1959, **10**, 87-98.

[80] G. Rousse, J. Rodríguez-Carvajal, C. Wurm and C. Masquelier, *Solid State Sciences*, 2002, **4**, 973-978.

[81] R. C. Mercader, L. Terminiello, G. J. Long, D. G. Reichel, K. Dickhaus, R. Zysler, R. Sanchez and M. Tovar, *Phys. Rev. B*, 1990, **42**, 25-32.

[82] M. H. Whangbo, D. Dai and H. J. Koo, *Dalton Trans.*, 2004, 3019-3025.

[83] A. J. Wright and J. P. Attfield, *J. Solid State Chem.*, 1998, **141**, 160-163.

[84] A. J. Wright, C. Ruiz-Valero and J. P. Attfield, *J. Solid State Chem.*, 1999, **145**, 479-483.

[85] G. Buxbaum, *Industrial Inorganic Pigments*; Wiley-VCH: Weinheim, 1998.

[86] S. Meseguer, M. A. Tena, C. Gargori, R. Galindo, J. A. Badenes, M. Llusar and G. Monros, *Ceram. Int.*, 2008, **34**, 1431-1438.

[87] M. Llusar, J. A. Badenes, A. Garcia, C. Gargori, R. Galindo and G. Monros, *Ceram. Int.*, 2011, **37**, 493-504.

[88] M. Llusar, A. Zielinska, M. A. Tena, J. A. Badenes and G. Monros, *J. Eur. Ceram. Soc.*, 2010, **30**, 1887-1896.

[89] M. Trojan and P. Sulcova, *Dyes Pigments*, 2000, **47**, 291-294.

[90] M. Trojan and P. Sulcova, *Thermochim. Acta*, 2000, **343**, 135-138.

[91] M. Trojan, P. Sulcova and P. Mosner, *Dyes Pigments*, 2000, **44**, 161-164.

[92] H. Onoda, K. Tange and I. Tanaka, *J. Mater. Sci.*, 2008, **43**, 5483-5488.

[93] H. Onoda, K. Kojima and H. Nariai, *J. Alloy. Compd.*, 2006, **408**, 568-572.

[94] H. Onoda, K. Yokouchi, K. Kojima and H. Nariai, *Mater. Sci. Eng.*, 2005, **B116**, 189-195.

Chapter Two

Experimental Techniques

2.1 Introduction

The main experimental techniques employed in this research were concerned with the synthesis of materials and their subsequent characterisation. The phosphates studied here were all prepared by acid flux synthesis, and some materials then further modified through ion exchange and intercalation. A number of different characterisation techniques were employed, including powder X-ray and neutron diffraction, SQUID magnetometry, TGA-MS, UV-Vis spectroscopy, Mössbauer spectroscopy, EXAFS, XANES, XRF, SEM and IR spectroscopy.

2.2 Synthesis

All condensed phosphate materials synthesised in this research were produced using the acid flux method. In essence, this technique involved the slow addition of intimately mixed metal source(s) to an excess of phosphoric acid held in a porcelain crucible. The reaction mixture was then heated at the required temperature either in an oven or on a hotplate for a fixed duration of time. The product was then isolated by suction filtration and washed with water to remove any excess acid. The exact reaction conditions *i.e.* reagent ratios, reaction temperature and reaction

duration were dependent on the nature of the condensed phosphate system, and will be described in more detail in the relevant sections of Chapters 3-7.

2.3 Modification of Condensed Phosphates

2.3.1 Ion Exchange

Ion exchange in α-$NH_4MnP_2O_7$ was attempted as a route to access previously unreported $M^IMnP_2O_7$ phases. A nitrate melt method was employed, which involved intimately mixing the host with alkali metal nitrates in a molar ratio of 1:10, respectively, and then heating the mixture for 4 h at a range of temperatures that depended on the alkali cation. The resulting mixture was then washed with water and recovered *via* vacuum filtration. More details on this will be provided in the relevant sections.

2.3.2 Intercalation

The introduction of magnetic species into the layered structure of MnTP was investigated by means of an intercalation route. Intercalation with monoamines was achieved by stirring MnTP with the respective amine in a sealed reaction vessel at room temperature. The resulting product was recovered by suction filtration and washed with acetone and water. After appropriate characterisation, the hexylamine intercalate was further refluxed with aqueous and methanolic transition metal acetate solutions at fixed molar ratios. Again, the products from this reaction were isolated *via* suction filtration. More details on this will be provided in the relevant section of Chapter 7.

2.4 Characterisation Techniques

2.4.1 Diffraction

Diffraction is used to describe the mutual scattering of waves when they encounter a sequence of regularly arranged obstacles separated by distances similar to the wavelength of the incoming waves. If we consider a series of waves targeted at an object, then clearly, once these waves leave the object they will traverse different paths, and so it is the phase relationship between the scattered waves that becomes important. If the waves remain in-phase, then they are said to mutually reinforce or constructively interfere with one another, giving rise to diffraction. The other extreme is where the scattered waves are out-of-phase with one another, leading to destructive interference to give no net effect (Figure 2.1). Intermediate phase relationships can also exist, resulting in partial reinforcement of the waves.

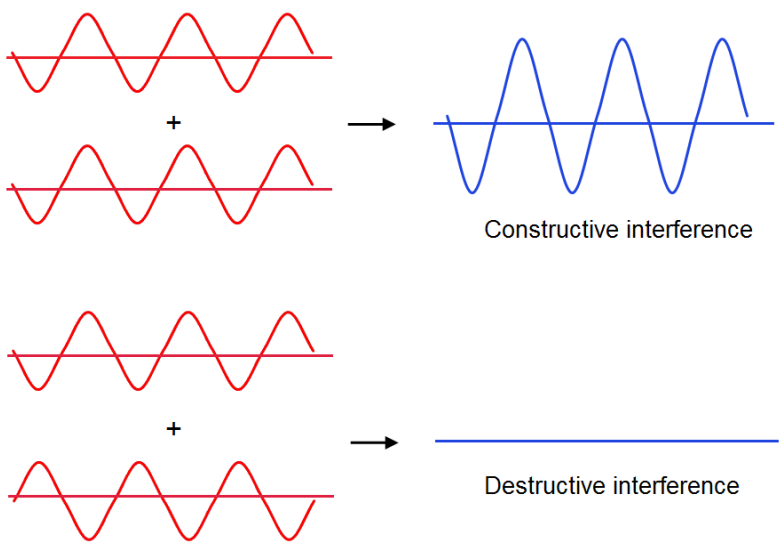

Figure 2.1: *Schematic showing the in-phase and out-of-phase relationships between two waves*

2.4.1.1 Fundamentals of the Crystalline State

An ideal crystalline solid consists of a periodic repetition of atoms, ions or molecules in space, with their long range order extending over a distance of ~10^3-10^{20} atomic or molecular dimensions. The periodic nature of a crystal is often described in terms of a *lattice*, which is further defined as consisting of a number of unit cells equal in their size and content. The unit cell is taken to be the simplest parallelepiped that contains all of the symmetry such that it can generate the entire lattice through replication and translation. The three lengths of the unit cell are conventionally defined by the vectors *a*, *b* and *c*, and the angles by *α*, *β* and *γ* such that *α* lies between *b* and *c* and so on. In three-dimensions each unit cell can have a different combination of these lengths and angles, giving rise to seven crystal systems consisting of specific symmetry elements (see Table 2.1 below).

Table 2.1: *The seven crystal systems and their corresponding symmetry elements*

Crystal System	Characteristic Symmetry Element(s)
Triclinic: $a \neq b \neq c$; $\alpha \neq \beta \neq \gamma \neq 90°$	None or centre of inversion
Monoclinic: $a \neq b \neq c$; $\alpha = \gamma = 90°$, $\beta \neq 90°$	Unique two-fold axis and/ or mirror plane
Orthorhombic: $a \neq b \neq c$; $\alpha = \beta = \gamma = 90°$	Three perpendicular two-fold axes
Trigonal: $a = b \neq c$; $\alpha = \beta = 90°$, $\gamma = 120°$	Unique three-fold axis
Tetragonal: $a = b \neq c$; $\alpha = \beta = \gamma = 90°$	Unique four-fold axis
Hexagonal: $a = b \neq c$; $\alpha = \beta = 90°$, $\gamma = 120°$	Unique six-fold axis
Cubic: $a = b = c$; $\alpha = \beta = \gamma = 90°$	Four three-fold axes

It is worth noting that trigonal and hexagonal crystal systems are usually described in the same type of lattice, resulting in six crystal families overall. Combining these six crystal systems with the different possible types of lattice centring (primitive, base-centred, body-centred and face-centred) gives 14 different types of unit cells, referred to as Bravais lattices (Figure 2.2). A consideration of the translational symmetry of the entire lattice, the 14 Bravais lattices and 32 crystallographic point groups gives a total of 230 crystallographic space groups which can be used to describe the symmetry of the entire crystal.

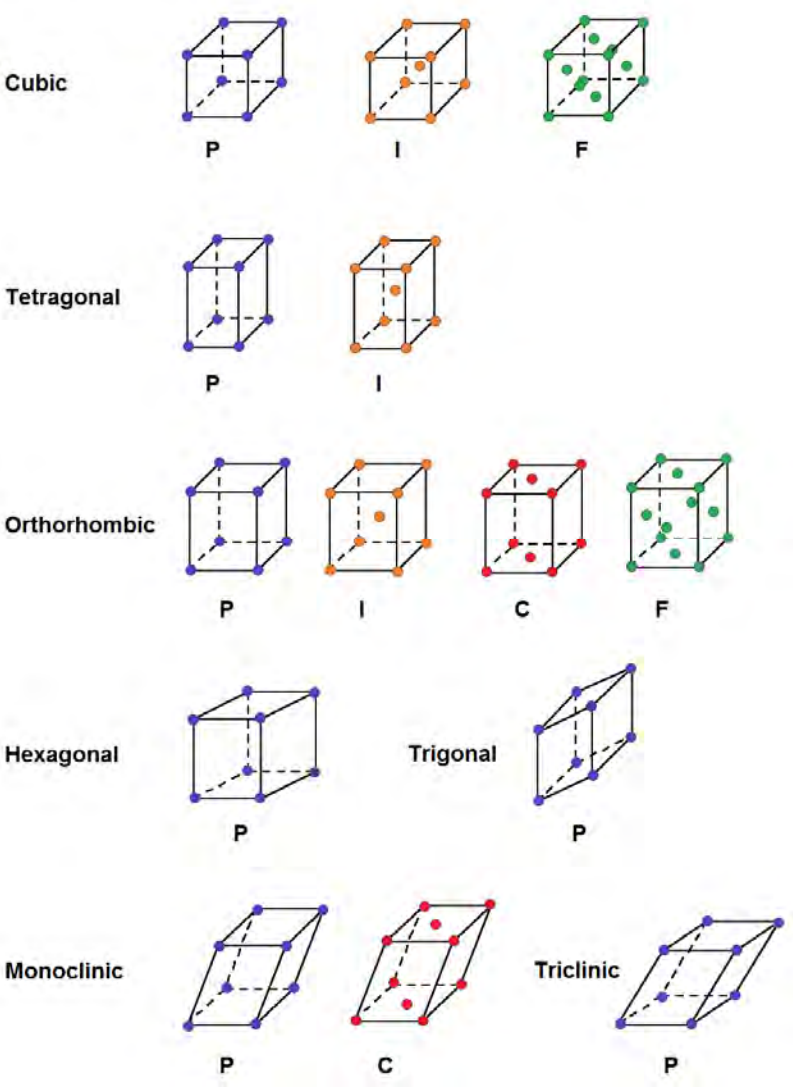

Figure 2.2: *The 14 Bravais Lattices*[1]

To understand the phenomenon of diffraction from a crystal, the imaginary concept of crystallographic lattice planes has been developed. Each set of lattice planes must run parallel to each other, be equally spaced and intersect lattice points within the crystal. Each plane is described using three Miller indices, *h*, *k* and *l*, which indicate that the planes divide the unit cell edges *a*, *b* and *c* into *h*, *k* and *l* equal parts, respectively. If a plane runs parallel to a particular crystallographic axis, then it will only intersect that axis at infinity, so the corresponding Miller index is set to 0 in this instance (see Figure 2.3).

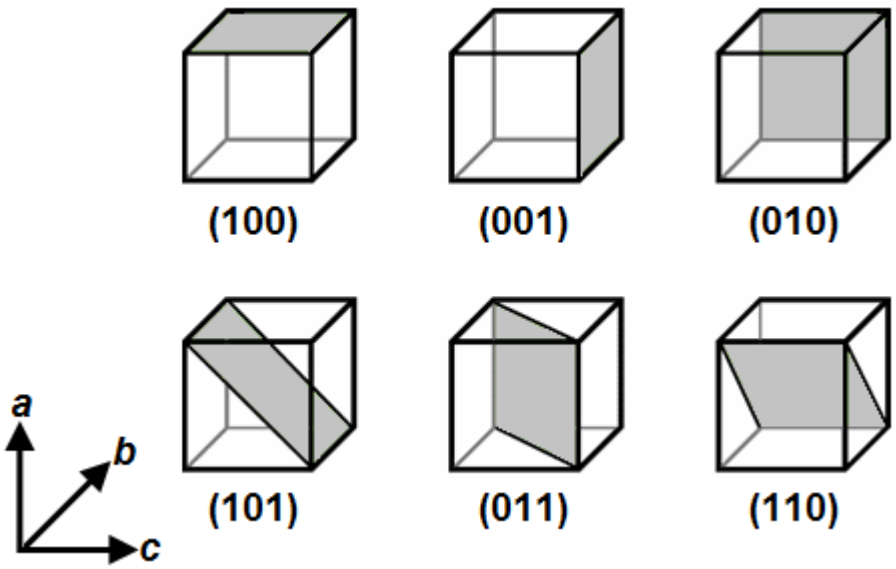

Figure 2.3: *Examples of some Miller indices representations*[2]

The perpendicular distance between adjacent planes is termed the interplanar *d*-spacing. For a monoclinic system, the main crystal system encountered in this research, the *d*-spacing between any set of planes is given by: -

$$\frac{1}{d_{hkl}^2} = \frac{1}{\sin^2\beta}\left(\frac{h^2}{a^2} + \frac{k^2\sin^2\beta}{b^2} + \frac{l^2}{c^2} - \frac{2hl\cos\beta}{ac}\right) \qquad \text{[Equation 2.1]}$$

2.4.1.2 Bragg's Law

In 1912, it was discovered by Max von Laue[3-4] that the regular arrangement of atoms within a crystal could allow them to act as a diffraction grating to X-rays, provided that their interatomic separations were comparable in magnitude to the wavelength of the applied radiation. Shortly after this discovery, W. L. Bragg[5] formulated a law that is now widely used to interpret diffraction from a crystalline sample. Bragg proposed that a crystal contains a discrete set of parallel planes separated by an interplanar distance, *d*. Figure 2.4 shows that as an X-ray wave enters the crystal, some of it will be "reflected" by the first plane but the rest will continue through to the next plane.

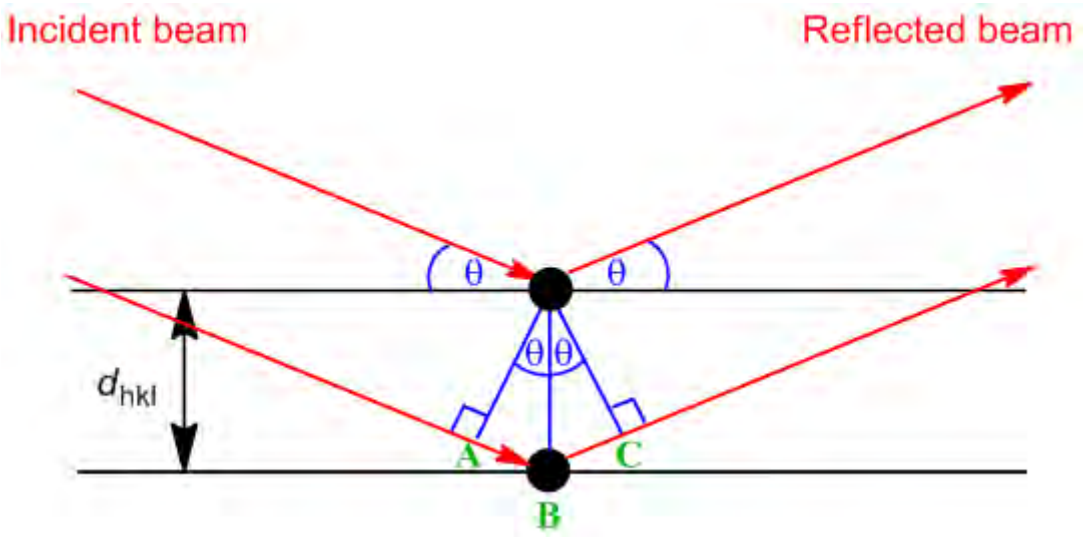

Figure 2.4: *Derivation of Bragg's Law*

For constructive interference to occur between the diffracted waves, the difference in the path length of each wave (equivalent to AB + BC) must be equal to an integer multiple of the wavelength, and so Bragg showed that: -

$$AB + BC = n\lambda = 2d\sin\theta$$

[Equation 2.2]

Where n is the order of reflection (an integer value), λ is the wavelength of the incident radiation, *d* is the interplanar spacing and θ is the angle of incidence. Waves that satisfy this condition interfere constructively and result in a scattered wave of significant intensity. However, Bragg's Law places restrictions on the angles at which reflection may occur. The equation can be simplified by letting n = 1 always. To do this, scattering from planes with a reduced spacing of *d*/n is included. So for example, if n = 2 then the *d*-spacing is halved by doubling the number of planes in that set.

2.4.2 X-ray Diffraction

Diffraction is an incredibly powerful technique that allows the structural information of crystalline compounds to be derived. In this research, X-ray diffraction was used as the first point of characterisation for all materials, with a short scan being able to readily reveal the success, or otherwise, of a reaction. Further means of phase identification was then conducted through a search of the JCPDS[6] database. Initial indexing and structural refinements were carried out with the data before proceeding to neutron diffraction data for a more accurate location of the lighter atoms and magnetic analyses. In both cases the powder technique was found to be especially valuable as all compounds encountered in this research could only be prepared in polycrystalline form, ruling out the possibility of using single crystal diffraction experiments. Providing one collects good quality data and has access to a suitable structural model, the Rietveld[7] method can be used in conjunction with powder diffraction experiments to obtain a reliable details on the crystal structure.

2.4.2.1 Generation of X-rays[8]

X-rays are radiation with wavelengths ranging from ~0.1-100 Å. The conventional laboratory source of X-rays is the X-ray tube. The sealed tube consists of an anode (a metal target) and a cathode (typically a tungsten filament) held under vacuum inside a metal/ glass or metal/ ceramic container. The cathode is electrically heated to emit electrons which are accelerated towards the anode by a high electrostatic potential maintained between the anode and cathode. X-rays are generated upon impact of these electrons with the metal target, and exit the tube through beryllium windows. Although relatively simple, sealed tubes have a very poor efficiency due to much of the supplied energy being converted into heat rather than X-rays, meaning that the anode must be continuously cooled. Alternatively, a rotating anode X-ray source can be used which allows the heat to be dissipated.

A typical X-ray spectrum generated by a tube is shown schematically in Figure 2.5. The spectrum consists of intense peaks characteristic of the metal target superimposed over a continuous background, known as white radiation or Bremsstrahlung radiation. This continuous X-ray spectrum arises due to the sudden deceleration of electrons upon impact with the metal target, giving a distribution of wavelengths that are not dependent on the nature of the target.

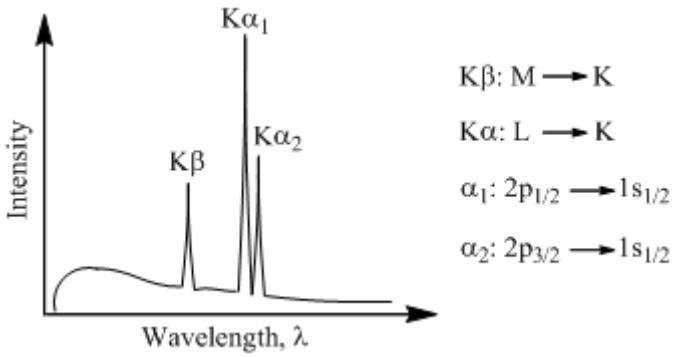

Figure 2.5: *Schematic of a typical X-ray emission spectrum*

The three characteristic spectral lines are due to transitions of electrons from higher energy levels to lower energy levels, which results in characteristic X-rays being emitted, as described in Figure 2.6.

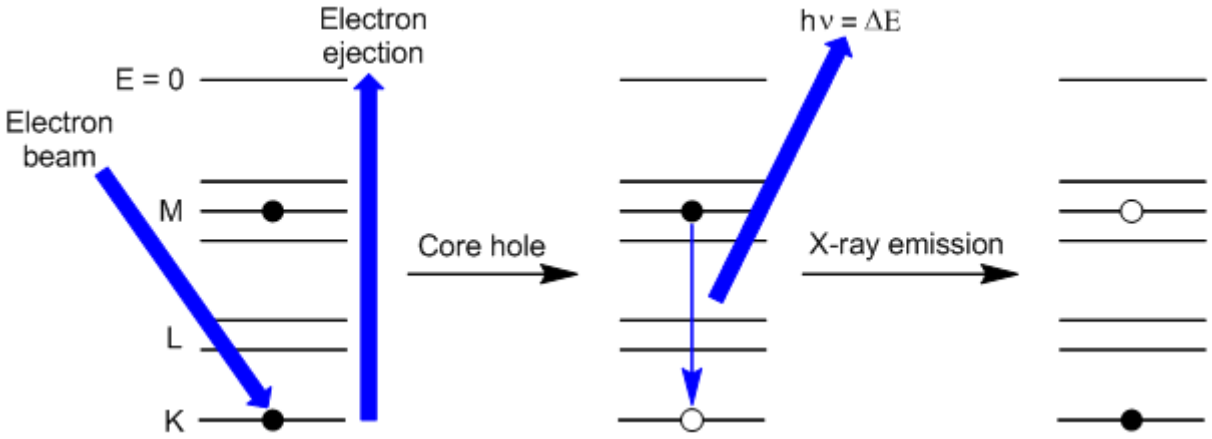

Figure 2.6: *The generation of characteristic X-rays*

The most common metal targets are copper (used exclusively in this project) and molybdenum. Other targets include chromium, iron and cobalt. Monochromatisation of radiation is critical for most diffraction experiments, with the Kα radiation often selected due its intensity superseding that of the other spectral lines present. Crystal monochromators or β-filters are employed to eliminate unwanted wavelengths, which would otherwise result in multiple Bragg peaks appearing in the diffraction pattern.

2.4.2.2 Powder X-ray Diffraction

A powder or polycrystalline sample consists of multiple crystallites that are randomly arranged to give a whole range of possible orientations. When such a sample is irradiated by an X-ray beam, the beam is diffracted in all possible directions allowed by the Bragg equation. Each crystallite within the powdered

sample will scatter the beam to give a diffraction dot, and so given the numerous crystallites present, a large number of closely spaced dots arise, giving the appearance of a diffraction cone, as shown in Figure 2.7. Diffraction cones are generated by each lattice spacing in the crystal, with the innermost cones corresponding to those planes with the largest *d*-spacings. A detector is rotated around the sample and cuts through these diffraction cones, scanning the intensity of the diffracted X-rays as a function of detector angle, 2θ. The resulting information can be used to determine unit cell dimensions and possible cell symmetry.

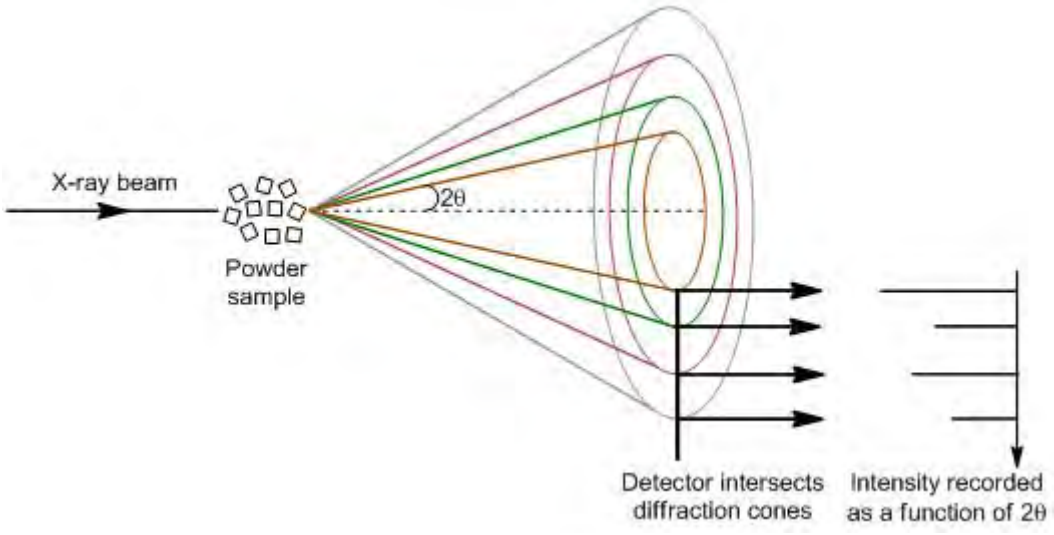

Figure 2.7: *Schematic representation of the formation of diffraction cones and the collection of a powder pattern*

A powder diffraction pattern can be regarded as a series of diffraction peaks overlaid on a background. The background arises due to instrumental and experimental factors, such as detector noise, sample holder and sample packing. Sample effects can also make a contribution, including the presence of amorphous components, incoherent scattering, local effects, X-ray absorbance and X-ray fluorescence. In many cases it is only the Bragg reflections that are of concern,

meaning that the background is often disregarded. However, sometimes the detail hidden in the background can become extremely useful, as is the case for Pair Distribution Function analysis.

With regards to Bragg reflections, peak positions, shapes and intensities can reveal information about crystal structure as well as indicate properties of the sample. The main factors influencing each of these will be discussed in more detail below.[8]

a) Peak positions

Peak positions are determined by Bragg's law. For a fixed wavelength, peak position will be dependent on the interplanar separation, which in turn is dictated by the unit cell size and symmetry. Various other factors can also affect the position at which a peak is observed, including instrument/ sample alignment, axial divergence of the beam, specimen absorption and specimen porosity.

b) Peak shapes

The observed peak shapes in a diffraction pattern can be a combination of several instrumental and specimen properties. Instrumental effects include the location and geometry of the source, monochromator(s), slits and specimen. Physical properties of the specimen such as crystallite size and microstrains can also have a significant influence on peak shape, as well as the crystallinity of the phase, disorder and defects.

c) Peak intensities

Peak intensities are principally a function of the periodicity of the scattering centres, but can also be affected by a number of other factors. The calculated intensity of a peak, I_{hkl} is given by equation 2.3: -

$$I_{hkl} = K \times p_{hkl} \times L_\theta \times P_\theta \times A_\theta \times T_{hkl} \times E_{hkl} \times |F_{hkl}|^2 \qquad \text{[Equation 2.3]}$$

Where: -

- K is the scale factor. This is a multiplier that normalises observed intensities with calculated intensities.
- p_{hkl} is the multiplicity factor. This accounts for the presence of symmetrically equivalent points in the lattice, and is dependent on lattice symmetry and the combination of Miller indices. For example, in a cubic system, the reflections (123), (132), (213), (231), (312) and (321) will all have the same *d*-spacing and therefore contribute to the same line in the diffraction pattern. The multiplicity factor takes the intensity of one of these reflections and then multiplies it by the number of equivalent reflections.
- L_θ is the Lorentz factor, defined by the geometry of diffraction. This accounts for effects such as the finite size of reciprocal lattice points and the variable radii of the Debye rings, both of which are functions of θ: -

$$L_\theta \propto \frac{1}{\cos\theta \sin^2\theta} \qquad \text{[Equation 2.4]}$$

- P_θ is the polarisation factor (often combined with the Lorentz factor). This accounts for a partial polarisation of the scattered beam, which will have two components, one with its amplitude parallel to the sample axis and the other with its amplitude perpendicular to this. The diffracted intensity is proportional to the square of the amplitude, and given that $(A_\parallel)^2 \propto 1$ and $(A_\perp)^2 \propto \cos^2 2\theta$, then: -

$$P_\theta \propto \frac{1+\cos^2 2\theta}{2} \qquad \text{[Equation 2.5]}$$

- A_θ is the absorption factor. This accounts for absorption of the incident beam and the non-zero porosity of the sample. Absorption effects depend on the geometry of the sample as well as its thickness, x, and linear absorption coefficient, μ. The intensity of the beam, I, after passing through a sample with incident intensity I_0 is given by: -

$$I = I_0 \exp(-\mu x) \qquad \text{[Equation 2.6]}$$

- T_{hkl} is the preferred orientation factor. This accounts for deviations from a completely random crystallite distribution in the powder. When crystallite shapes are isotropic (*e.g.* spherical), a random distribution of their orientations can often be achieved. However, in the case of anisotropic shapes (*e.g.* platelet-like or needle-like), natural preferences in packing can mean that a preferred orientation of the crystallites occurs, leading to some reflections being significantly more intense than others.
- E_{hkl} is the extinction multiplier. This takes into account extinction effects that cause a reduction in the scattered intensity. This mainly occurs when the scattered wave is back-reflected into the crystal and is then out-of-phase with the incident wave, causing destructive interference. This effect is quite small in powders and so the extinction factor is often neglected.
- $|F_{hkl}|^2$ is the structure factor. This is dependent on the crystal structure and is the most important parameter affecting peak intensities. It represents the sum of the scattering power of all of the atoms present in the unit cell: -

$$F_{hkl} = \sum_{j=1}^{n} g_j f_j \exp\left[2\pi i \left(hx_j + ky_j + lz_j\right)\right] \exp\left(-\frac{B_j \sin^2\theta}{\lambda^2}\right) \qquad \text{[Equation 2.7]}$$

where: n is the total number of atoms in the unit cell, g_j is the population factor of the j^{th} atom, f_j is the atomic scattering factor for the j^{th} atom (this describes the interaction of the incident wave with the specific atom type), $i = \sqrt{-1}$, h, k and l are the indices of reflection, x_j, y_j and z_j represent the fractional coordinates of the j^{th} atom in the unit cell and B_j is the isotropic displacement parameter of the j^{th} atom.

The Phase Problem

By applying a Fourier transformation, the structure factors for various points on the reciprocal lattice can provide information about electron density distribution within the unit cell. In order to reconstruct the electron density and hence locate atoms within the structure, two components of each reflection are required: the amplitude of the structure factor and its corresponding phase angle. However, when a diffraction pattern is recorded, it is the intensity of each reflection that is measured, which is proportional to the square of the structure factor *i.e.* $I_{hkl} \propto |F_{hkl}|^2$. This means that the absolute value of the structure factor can be determined, but information on its phase is lost during the experiment, leading to the so-called “phase problem”. As a consequence of this, a simple Fourier transformation cannot be applied to derive the crystal structure.

A number of methods have been developed in order to solve crystal structures from powder diffraction data. These include modelling the structure on similar frameworks, reciprocal space methods (*e.g.* the Patterson technique) and direct methods.

2.4.2.3 Laboratory Diffractometers

The main X-ray diffractometers used in this research were the Siemens D5000 and a Bruker AXS: D8 Advance diffractometer fitted with an automatic sample changer, both of which operate in transmission mode. The powdered samples were placed in between two pieces of Scotch® 3M Magic Tape™ (known to give negligible scattering) and then attached to the respective sample holders of each diffractometer. Variable temperature XRD measurements were carried out on a Bruker AXS: D8 Advance diffractometer fitted with a Materials Research Instruments (MRI) heating stage. This instrument operates in reflection mode, with samples being loaded into an alumina holder and flattened with a glass slide.

2.4.2.3.1 Siemens D5000

The Siemens D5000 generates X-rays using the standard X-ray tube with a copper metal target. A germanium monochromator is used to select $K\alpha_1$ radiation with $\lambda = 1.5406$ Å. Samples are attached to an aluminium disc holder and rotated in the plane perpendicular to the incident beam. The position of the X-ray source remains fixed while a Position Sensitive Detector (PSD) covering 8° 2θ rotates in small increments (~0.02°) around a circumference of $5 \leq 2\theta \leq 100°$ about the sample. The sample and detector have a θ-2θ setup, where they move through angles of θ and 2θ, respectively. As was shown schematically in Figure 2.7, the detector moves through the diffraction cones generated by the sample and records the intensity at various points to produce a diffraction pattern.

2.4.2.3.2 Bruker D8 Advance with Automatic Sample Changer

The Bruker D8 is very much similar to the Siemens D5000, employing a copper X-ray tube and Ge monochromator to give Cu $K\alpha_1$ radiation. Samples are attached to a plastic disc holder and again rotated in the plane perpendicular to X-ray beam. The position of the X-ray source remains fixed while a PSD covering 3° 2θ rotates in small steps through a circumference of $2 \leq 2\theta \leq 90°$ around the sample. A step size of ~0.018° was used for all samples. The PSD is a high performance solid state LynxEye detector which increases measured intensities whilst still maintaining a good resolution, allowing for much faster data collection. The sample magazine has 9 positions which are changed during measurement by moving the magazine through the central opening of the goniometer body.

2.4.2.3.3 Bruker D8 Advance with MRI Heating Stage

This instrument is equipped with a MRI heating stage attached to the goniometer body. Samples are placed into an alumina crucible and loaded into the heating chamber. An X-ray tube is used to generate Cu $K\alpha_1$ radiation which is directed at the sample. The heating stage consists of X-ray transparent Kapton windows which allow X-ray entrance and exit to a LynxEye PSD. The sample remains static while the X-ray source and detector operate in a θ-θ setup, moving in a synchronised fashion through angles of θ_1 and θ_2, respectively. The sample heater itself is made of Ta foil with a laser-welded thermocouple. A temperature range of 20-1000°C is possible, with stage components water-cooled to allow careful control of the temperature. The stage is able to operate under various atmospheres such as air, nitrogen and oxygen.

In this research, variable temperature XRD measurements were carried out under a N_2 atmosphere. Samples were heated from 30-750°C at a rate of 10°C/ min, with diffraction patterns collected in 25°C increments. The actual sample temperature at every set point temperature was determined from a temperature calibration curve of the stage.

2.4.2.4 Powder XRD Analysis

Following the collection of XRD data on a sample, a "search and match" against compounds held in the JCPDS[6] database was conducted in order to identify the phases present and to ascertain sample purity. The next step taken was to assign a unit cell to the phase of interest. In most cases we were able to find isostructural phases to those synthesised, which gave us an indication of unit cell size and symmetry. These parameters were entered into the program DSPACE[9], which was able to calculate the allowed reflections and their expected positions. This information was then matched with the observed data so that all of the peaks could be indexed. Following this, the rough unit cell size, cell symmetry, observed peak positions and their corresponding (*hkl)* assignments were inputted into the CELL[10] program for refinement. Through a least squares minimisation method, CELL[10] was able to give more accurate unit cell parameters for the phase of interest.

Where there was no prior knowledge of unit cell size and symmetry, the Crysfire[11] program was employed to calculate possible unit cells. This program is essentially a DOS based suite that incorporates eight major indexing programs (ITO[12], DICVOL[13-14], TREOR[15], TAUP[16], KOHL[17-18], FJZN6[19], LZON[20] and LOSH[20]), each of which have their own different criteria for use. These programs use complex algorithms to calculate unit cells based on the observed data. Each unit

cell is given a figure of merit, which can be used as an indication of its credibility. The complimentary program CHEKCELL[21] can then be used to assign probable space groups to these unit cells and to further refine the parameters against the observed data.

2.4.3 Neutron Diffraction[22-23]

Neutron diffraction (ND) can be used in a similar fashion to X-ray diffraction to determine the atomic structure of a material, provided that the neutron wavelength is similar in magnitude to the interatomic separations found within the solid. A neutron itself is a subatomic hadron particle with a spin of 1/2. It consists of three quarks, two of which are down-quarks with a charge of -1/3 e and one up-quark with a charge of +2/3 e. Despite being electrically neutral, a neutron possesses a magnetic moment of *ca.* 1.913 nuclear magnetons due to the presence of these three charged particles. The consequences of this are that two different types of scattering with neutrons can take place: nuclear scattering and magnetic scattering. The former occurs due to interaction between the neutron and atomic nucleus, whereas the latter is a result of the interaction between the neutron magnetic moment and a magnetic field generated by the atom.

In the case of nuclear scattering, the diameter of the atomic nucleus is often much smaller than the neutron wavelength, meaning that the nucleus behaves as a point scatterer and any scattering that occurs is isotropic. As such, data can be collected at higher angles. On the other hand, the extension of magnetic shells is comparable to the wavelength of neutrons, and so magnetic scattering is found to be dependent on $\sin\theta/\lambda$. This variation is described by the magnetic form factor, and due to having no contribution from the core electrons of an atom, it falls off much more

rapidly with increasing angle than is the case with X-rays. The magnetic scattering amplitude, *D*, is given by: -

$$D = \left(\frac{e^2}{mc^2} \right) \gamma \times g(J/2) f \qquad \text{[Equation 2.8]}$$

where *e* and *m* are the charge and mass of an electron, respectively, *c* is the velocity of light, γ is the magnetic moment of the neutron in nuclear magnetons, *g* is the Landé splitting factor, *J* is the total angular momentum quantum number and *f* is the magnetic form factor. For transition metals, where the orbital contribution to the magnetic moment is often quenched, *g*(*J*/2) is replaced with *S*, the spin angular momentum quantum number.

As with X-ray diffraction, the intensity of a diffracted neutron beam is proportional to the square of the structure factor. Most neutron diffraction experiments involve an unpolarised neutron beam where all possible spin directions are present, meaning that nuclear and magnetic scattering intensities are additive. In this instance the structure factor for a given reflection, F_{hkl}, is given by: -

$$\left|F_{hkl}\right|^2 = \left|F_N\right|^2 + \left|F_M\right|^2 \qquad \text{[Equation 2.9]}$$

where F_N and F_M are the structure factors for the nuclear and magnetic scattering, respectively. The intensity, I_{hkl} of a given reflection can then be represented by the general expression: -

$$I_{hkl} = p_{hkl} \times \left|F_{hkl}\right|^2 \times L \times A \times C \qquad \text{[Equation 2.10]}$$

where p_{hkl} is the multiplicity factor, *L* is the Lorentz factor, *A* is an absorption coefficient and *C* is an instrumental constant.

2.4.3.1 Comparison of X-ray diffraction and Neutron diffraction

The cost of neutron diffraction equipment is considerably higher than that of X-ray diffraction, meaning that there is limited access to ND facilities, which are only available at national facilities. As scattering of neutrons occurs through their interaction with atomic nuclei, much larger sample sizes and/ or longer data collection times are required *cf.* X-ray diffraction in order to increase the probability of this interaction occurring.

Whilst ND allows the position of atomic nuclei and their thermal motion to be reliably determined, XRD only gives the electron density distribution of an atom, from which positions are to be inferred. This is because the scattering of X-ray radiation occurs through the interaction of its electric vector with the electron densities of atoms. However, it is possible to use a combination of the two techniques to accurately determine the electron density distribution about various atomic nuclei within the crystal structure.

As briefly mentioned, no trend is observed in the scattering of neutrons with nuclear mass, nuclear charge or atomic number. In addition, the diameter of the atomic nucleus is much smaller than typical neutron wavelengths, meaning that there is no direct relationship between the atomic form factor (scattering factor) and neutron wavelength. This differs to the case with X-rays, where the atomic form factor is directly proportional to atomic number *i.e.* the number of electrons present. Furthermore, the atomic form factor shows a dependence on the wavelength of the incident radiation and the diffraction angle, 2θ, with the variation specifically being with $\sin\theta/\lambda$. The irregular behaviour of neutron atomic form factors means that ND can be used to distinguish both light and heavy atoms, and is particularly useful for

locating hydrogen positions. Furthermore, ND can differentiate neighbouring atoms in the periodic table as well as different isotopes of the same element. In contrast, XRD is better suited to heavier elements and cannot distinguish between atoms possessing a similar number of electrons.

An important advantage of ND is that it also allows magnetically ordered materials to be investigated. The interaction between the neutron magnetic moment and the magnetic moment generated by the presence of unpaired electrons gives rise to extra peaks in the diffraction pattern, potentially allowing magnetic structures to be solved.

2.4.3.2 Neutron diffraction experiments

Neutrons can be created by the process of spallation or by nuclear fission in a reactor. Once produced, they are slowed down to the appropriate energy by being passed through moderators which are ideally low in mass, possess a high scattering cross section and a low absorption cross section. Common moderator materials include water, heavy water, liquid hydrogen, liquid methane, graphite and beryllium.

Spallation involves accelerating negatively charged ions (typically H^-) to very high velocities and then passing them through a foil which removes the electrons to generate a beam of protons. The protons are then fired at a heavy metal target such as tantalum, uranium, lead or liquid mercury to initiate nuclear processes that result in the production of neutrons. Most methods of acceleration tend to give intense pulses of high energy protons, and so a pulsed neutron beam results.

Nuclear fission is a reaction where the nucleus of an atom splits into lighter nuclei, producing neutrons, γ-rays and a large amount of thermal energy in the process. The nuclear reaction is either initiated by impact with a neutron or through

the spontaneous radioactive decay of an unstable isotope. The neutrons that are released can cause further nuclear fission of other nuclei present to give a self-sustaining chain reaction. The nuclear reaction can be controlled by using neutron moderators or neutron absorbers to reduce the amount of neutrons that go on to cause more fission. Uranium-235, uranium-233, plutonium-239 and thorium-232 are examples of fissile nuclei that are capable of sustaining a chain reaction with neutrons. Such large nuclei are also used because they are able to release a huge amount of energy during the fission process.

There are two main types of neutron powder diffraction experiment, each of which will be briefly discussed below.

1) Time of Flight (TOF) Neutron Diffraction

In the TOF technique, a sample is bombarded by neutrons with a wide range of energies (typically from a pulsed source). The velocity (v) of a neutron can be related to its wavelength (λ) through the de Broglie relationship (see equation 2.11). As all neutrons leave the source at the same time, then the time (*t*) taken for a neutron to travel the distance from the source (L_1) to the sample (L_2) allows its wavelength to be determined: -

$$\lambda = \frac{h}{mv} = \frac{h}{m}\,\frac{t}{L_1 + L_2} \qquad \text{[Equation 2.11]}$$

where *h* is Planck's constant.

The time taken for the neutrons to reach the sample can be easily resolved by modern detection systems. In order for the neutron wavelength to be in an appropriate range to give rise to diffraction, the beam is passed through a moderator to slow the neutrons down. The detector is fixed at a specific 2θ angle and collects

the diffracted beams as a function of time of flight. Given that the scattering is measured at a fixed angle and that the neutron wavelength can be determined, the *d*-spacing of each reflection can then be established using Bragg's law (equation 2.2).

2) Continuous Wave (CW) Neutron Diffraction

The CW technique employs a neutron beam of fixed wavelength. A nuclear reactor is frequently used to generate a continuous source of neutrons which are then passed through a pyrolytic graphite, Ge or Cu monochromator to give neutrons of a set energy. This allows the diffracted beam to be measured as a function of θ and means that the detector does not have to remain stationary. The main disadvantage with this approach is that there is a high loss of neutron flux due to producing a monochromatic beam, resulting in longer data collection times being required.

In this research, neutron powder diffraction data were collected in CW mode at two neutron diffraction facilities: the Institut Laue-Langevin (ILL) in Grenoble and the Paul Scherrer Institute (PSI) in Switzerland.

2.4.3.2.1 ILL, Grenoble

The ILL employs a high flux nuclear reactor to generate an intense source of neutrons which are passed through moderators before being directed at a number of different instruments. All experiments here were conducted on the high resolution D2B powder diffractometer (see Figure 2.8). This instrument uses a Ge monochromator to focus the beam onto the sample and provide a fixed wavelength of radiation. Wavelengths can be selected by computer control since they are obtained by a straightforward rotation within the Ge (*hkl*) plane. Samples are loaded

into vanadium cylinders and may be placed on up to 9 sample positions that can be set up for automatic measurement. A cryostat or cryofurnace can be added to the sample positions to perform variable temperature experiments.

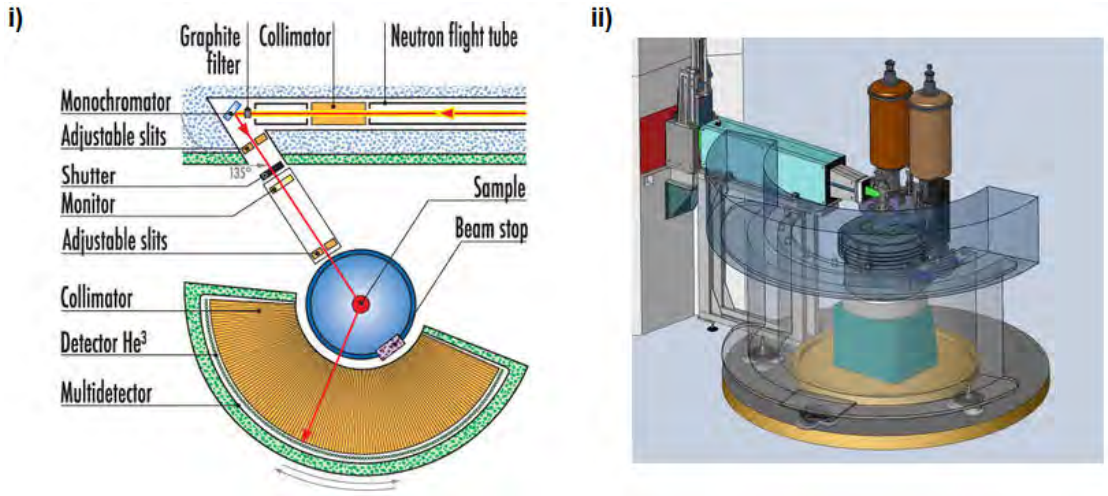

Figure 2.8: *Layout of the D2B instrument at the ILL[24]: i) Schematic aerial view and ii) 3D layout*

In this research, diffraction patterns of the samples of interest were recorded with λ = 1.5943 Å over 100 steps of 0.05° 2θ with 128 detectors (^{3}He counting tubes) spaced at 1.25° intervals.

2.4.3.2.2 PSI, Switzerland

The PSI is host to the SINQ spallation neutron source. A continuous source of neutrons is generated by striking a block of lead with a fast beam of protons. Each lead nucleus ejects 10-20 neutrons which are then passed through a liquid deuterium moderator prior to being directed at a number of different instruments. All experiments at the PSI were conducted on the high resolution powder diffractometer for thermal neutrons (HRPT) with a wavelength of 1.494 Å. The instrument employs a wafer-type Ge monochromator to achieve a constant wavelength. Various types of

sample environments can be employed, including an 8-position sample changer for room temperature measurements and a 4-position sample changer for measurements in the temperature range of 1.5-315 K. An oscillating radial collimator prevents Bragg peaks from the sample environment appearing in the diffraction pattern.

The high resolution of the instrument is achieved by thermal neutrons and the large scattering angles of the monochromator and sample (up to 165°). The detector is a large position sensitive ^{3}He detector consisting of 1600 wires with an angular spacing of 0.1° and a scattering angle range of 160°.

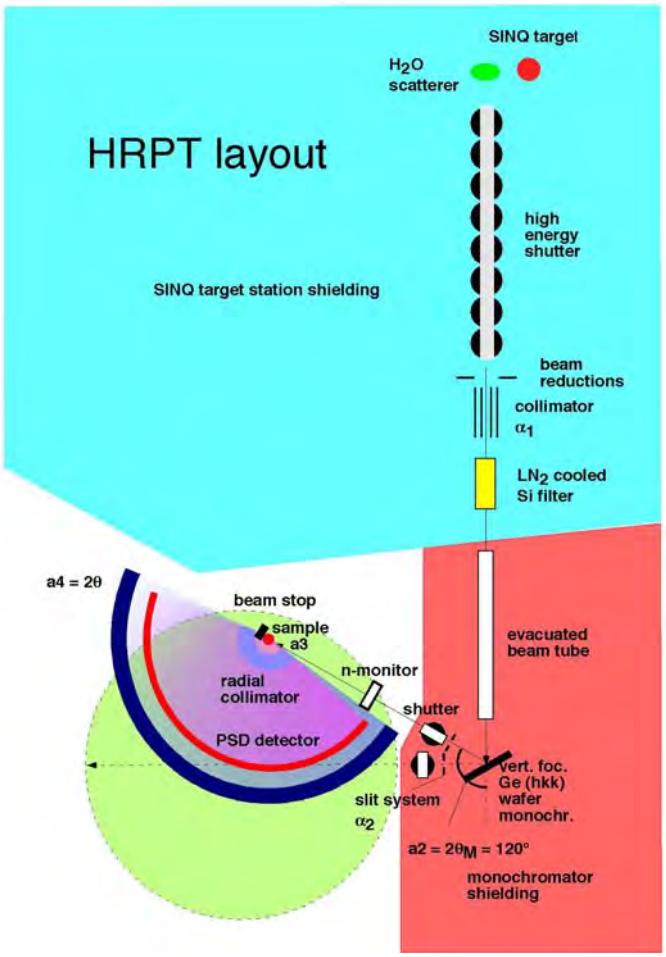

Figure 2.9: *Schematic layout of the HRPT instrument at SINQ*[25]

2.4.4 Rietveld Analysis[26]

The Rietveld method was used in this research to obtain structural details from both X-ray and neutron powder diffraction data. When applied properly, the Rietveld method can provide accurate structural details on materials that cannot otherwise be prepared as adequate single crystals. Furthermore, as the powder diffraction method employs larger sample sizes than a single crystal measurement, the resulting structural details are better representative of the bulk material.

The development of this technique by Hugo Rietveld[7,27] in the 1960s marked a turning point in the analysis of powder diffraction data. Prior to this, many structural determinations relied on single crystal diffraction, as this allowed three-dimensional data to be extracted from the diffraction pattern without the difficulty of overlapping reflections. The problem that powder samples posed was that the individual structure factors could not be resolved from the diffraction patterns due to their one-dimensional nature and the presence of overlapping peaks.

In order to conduct a Rietveld analysis, one firstly requires a structural model that includes initial approximations of a number of variables such as peak shape parameters, unit cell dimensions and atomic coordinates. Other factors such as background and atomic displacement parameters can be estimated and then later refined. For computational analysis, the diffraction pattern needs to be recorded in digitised form- normally a record of the intensity, y_i, at each of several thousand increments, i, in the diffraction pattern suffices for this. As all diffraction experiments in this research used a fixed wavelength of radiation, the increments used were 2θ steps. The basis of the Rietveld method is then to use a least squares minimisation method to obtain the best fit between the observed diffraction pattern and the

calculated pattern, the latter being based on the structural model. Specifically, the quantity that is minimised is termed the residual, S_y: -

$$S_y = \sum_i w_i \left[y_i(obs) - y_i(calc) \right]^2 \qquad \text{[Equation 2.12]}$$

where $y_i\ (obs)$ is the observed intensity at the i^{th} point, $y_i\ (calc)$ is the calculated intensity at the i^{th} point and w_i is the weighting of each data point, i, equivalent to $[y_i\ (obs)]^{-1}$, summed over all data points.

Most powder diffraction patterns are a collection of overlapping reflection profiles, each of which have their own peak height, peak position, peak shape and integrated area that is proportional to the Bragg intensity, I_{hkl}. Many Bragg reflections can contribute to the observed intensity at any point, i. Calculated intensities, $y_i\ (calc)$, are therefore calculated from the structural model by summing the calculated contributions from close range Bragg reflections plus the background: -

$$y_i(calc) = \left[s \sum_{hkl} L_{hkl} \left| F_{hkl} \right|^2 \phi(2\theta_i - 2\theta_{hkl}) T_{hkl} A \right] + y_{bi} \qquad \text{[Equation 2.13]}$$

where s is the scale factor, L_{hkl} is a term for the Lorentz, polarisation and multiplicity factors, F_{hkl} is the structure factor for the (hkl) reflection, ϕ is the reflection profile function, T_{hkl} is the preferred orientation function, A is the absorption factor and y_{bi} is the background intensity at the i^{th} step.

In order to improve the agreement between the observed and calculated data, calculated shifts are applied to the initial parameters in the structural model and then the whole procedure is repeated. A number of model parameters can be refined and optimised to improve the fit, including atomic coordinates, displacement factors, site occupancies, background, lattice parameters, instrumental features, specimen reflection profiles, *etc*. It is important to note that the procedure is iterative, with the

result from one iteration being used as the starting point for the next. As each shift is applied, ideally there is an improved knowledge of the structure and a better allocation of the observed intensity to the partially overlapping individual Bragg reflections. The Rietveld refinement process is continued until the residual (S_y) is minimised as much as possible in order to obtain the best fit. There are various numerical criteria of fit that allow the progress of the refinement to be assessed, some of which are given below: -

R-profile: $$R_p = \frac{\sum_{i=1}^{n} |y_i(obs) - y_i(calc)|}{\sum_{i=1}^{n} y_i(obs)}$$ [Equation 2.14]

R-weighted profile: $$R_{wp} = \left[\frac{\sum_{i=1}^{n} w_i [y_i(obs) - y_i(calc)]^2}{\sum_{i=1}^{n} w_i [y_i(obs)]^2} \right]^{1/2}$$ [Equation 2.15]

R-expected: $$R_{exp} = \left[\frac{(N - P - C)}{\sum_{i=1}^{n} w_i [y_i(obs)]^2} \right]^{1/2}$$ [Equation 2.16]

[*N* = total number of data points measured in the diffraction pattern, *P* = the number of refined parameters and *C* = number of constraints].

Chi-squared: $$\chi^2 = \left[\frac{R_{wp}}{R_{\exp}} \right]^2$$ [Equation 2.17]

R-structure factor: $$R_F = \frac{\sum_{hkl} \left| F_{hkl}(obs) - F_{hkl}(calc) \right|}{\sum_{hkl} F_{hkl}(obs)}$$ [Equation 2.18]

R_{wp} is commonly reported as it includes the residual that is to be minimised. R_{exp} characterises the quality of the experimental data, with a larger denominator meaning better counting statistics. The goodness of fit, χ^2, should therefore tend to unity as R_{wp} approaches R_{exp}. The R_F value is based on the Bragg intensities calculated from the model, and so this can be used as an indication of the reliability of the structural model.

Although numerical criteria are very important, it is also necessary to use graphical criteria of fit such as difference plots. Indeed, many figures of merit can be easily influenced by factors such as impurity lines and the number of data points collected. Graphical plots are able to provide an indication of where the source of any problems with the refinement lies and also whether the refinement has reached a false minimum.

A number of different software packages can be used to carry out Rietveld refinements. In this research, the GSAS[28] suite of programs was used. GSAS[28] is able to work with both powder and single crystal X-ray and neutron diffraction data from both CW and TOF measurements. Importantly, it is also able to model both the nuclear and magnetic structures of a material. A linear interpolated background function and an asymmetry-corrected pseudo-Voigt peak function were used to refine the background and peak shape, respectively.

2.4.4.1 Linear interpolated background function

In the Rietveld method, the background of a powder diffraction pattern is accounted for by adding its contribution to the calculated intensity. In this research it was approximated using function number 7 within GSAS[28], which calculates the background using a linear interpolation formula suggested by Rietveld[7] in his early work. Up to 36 background coefficients can be refined, with the scan range of the diffraction pattern equally partitioned based on the number of parameters chosen. In effect, a straight line is then constructed between these points.

2.4.4.2 Asymmetry-corrected pseudo-Voigt peak shape[8]

It is necessary to fit peak shapes to a suitable function in order to obtain both the positions and intensities of the individual Bragg peaks. Peak profile function number 2 within GSAS[28], the so-called Thompson modified pseudo-Voigt function[29-30], was used to model peak shape.

The basic pseudo-Voigt function is a linear combination of the centrosymmetric Gauss and Lorentz functions, mixed in a η: 1-η ratio such that η varies from 0 (pure Lorentz) to 1 (pure Gauss): -

$$y(x) = PV(x) = \left[\eta \frac{\sqrt{C_G}}{\sqrt{\pi} H} exp\left(-C_G x^2\right) \right] + \left[(1-\eta) \frac{\sqrt{C_L}}{\pi H} \left(1 + C_L x^2\right)^{-1} \right] \quad \text{[Equation 2.19]}$$

Gauss **Lorentz**

where: -

- H = FWHM = $(U \tan^2\theta + V \tan\theta + W)^{1/2}$; the full width at half maximum as a function of θ. U, V and W are free variables.
- $C_G = 4\ln 2$ and $C_L = 4$; used as normalisation constants.

- $x = (2\theta_i - 2\theta_k)/H_k$. This is the difference between the Bragg angle of the i^{th} point and the calculated Bragg angle of the k^{th} reflection, divided by the peak's full width at half maximum.
- $\eta = \eta_0 + \eta_1 2\theta + \eta_2 2\theta^2$; the pseudo-Voigt mixing parameter. η_0, η_1 and η_2 are free variables.

The benefit of using this function is that the FWHMs due to Gaussian and Lorentzian contributions to the peak shape can be separated. There are various modifications of this function that seek to improve precision and to better model anisotropic peak broadening and peak asymmetry. The Thompson modified pseudo-Voigt function[29-30] is identical to equation 2.19 but employs a multi-term Simpson's integration. The Gaussian FWHM is modified by an additional broadening parameter whilst the Lorentzian FWHM incorporates two anisotropic broadening parameters for crystallite size and strain. The asymmetry of a peak is modelled by incorporating an asymmetrisation function into this symmetric peak shape profile.

2.4.5 Magnetic Analysis of Materials

Magnetisation in solids arises from atoms that possess unpaired electrons. The orbital and spin angular momenta of these electrons generate a magnetic field that can be influenced to different extents by neighbouring magnetic fields and applied fields, sometimes resulting in unusual properties of the material.

2.4.5.1 Basic Principles

The magnetisation, *M*, of a sample can be defined as the field that it generates when placed in an applied field, *H*. This can be related to the magnetic susceptibility, χ, through the following relationship: -

$$\chi = \frac{M}{H} \qquad \text{[Equation 2.20]}$$

There are two main types of bulk magnetism in solids: diamagnetism and paramagnetism. Diamagnetism occurs for atoms with closed shells *i.e.* paired electrons, and is therefore present in most materials. Purely diamagnetic substances are repelled by magnetic fields and possess negative susceptibilities. If other effects are present then they dominate over diamagnetism, which is found to be relatively weak. Paramagnetism arises from the presence of unpaired electrons in atoms. The individual magnetic moments are randomly orientated and do not interact strongly with each other. If an external magnetic field is applied, the moments will attempt to line up with the field, but may be hindered by the presence of excess thermal energy. In many cases the Curie law can be used to describe the dependence of the paramagnetic susceptibility on temperature: -

$$\chi = \frac{C}{T} \qquad \text{[Equation 2.21]}$$

where C is the Curie constant and T is the temperature in degrees Kelvin.

At certain temperatures characteristic of the material, it may become possible for the magnetic moments on individual atoms to overcome thermal randomisation and interact with one another. If the moments interact so as to align their spins parallel, ferromagnetism arises, whereas if the moments align antiparallel, antiferromagnetism results (see Figure 2.10). The temperatures at which these orderings occur are referred to as the Curie temperature (T_C) and Néel temperature (T_N), respectively.

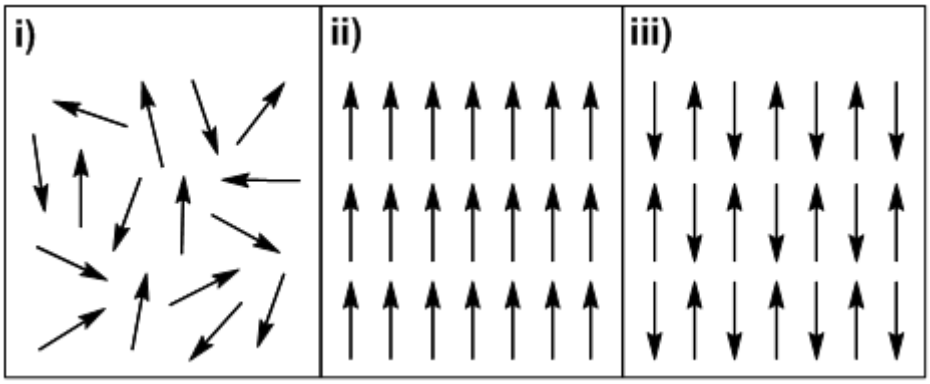

Figure 2.10: *Various arrangements of unpaired electron spins: i) paramagnetic, ii) ferromagnetic and iii) antiferromagnetic*

The Curie-Weiss law can be used to describe the high temperature, paramagnetic behaviour of ferromagnets and antiferromagnets: -

$$\chi = \frac{C}{T - \theta} \qquad \text{[Equation 2.22]}$$

where θ is the Weiss constant, the sign of which indicates whether interactions are ferromagnetic or antiferromagnetic (see Figure 2.11).

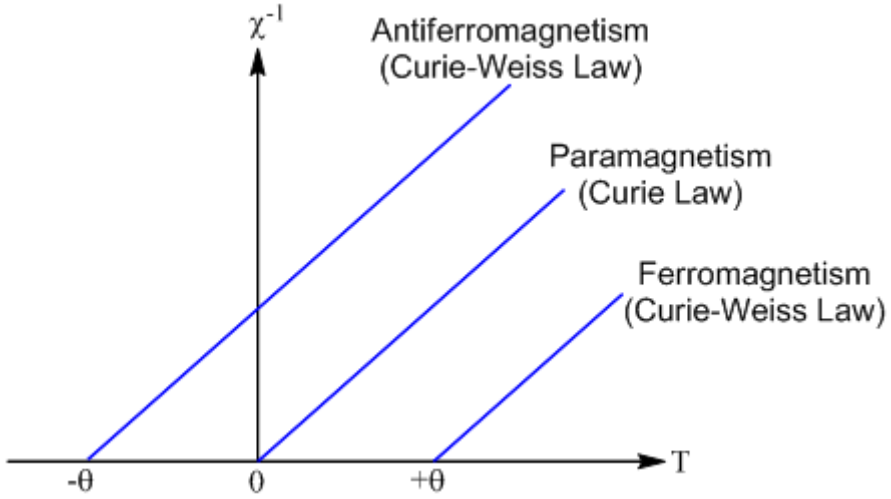

Figure 2.11: *Trends in magnetic behaviour with the Curie and Curie-Weiss laws*

In some cases, antiparallel arrangements of the moments do not lead to a net cancellation. Ferrimagnetism occurs when different sized moments interact and

canted antiferromagnetism occurs when the moments are not completely collinear. In both instances a net ferromagnetic moment is observed (see Figure 2.12). Frustrated interactions can also occur, for example, when there is more than one magnetic ground state possible or when a random arrangement of the moments is fixed.

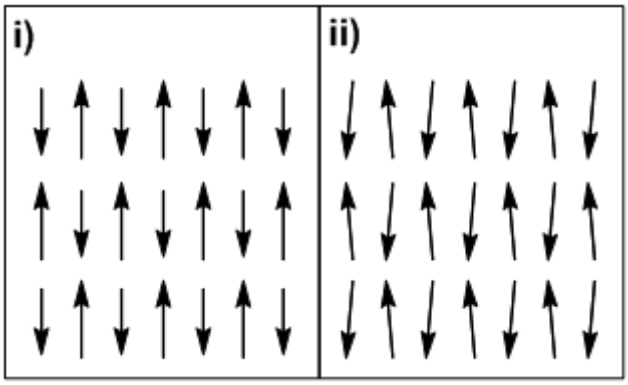

Figure 2.12: *i) Ferrimagnetism and ii) Canted Antiferromagnetism*

The magnetic properties of compounds are often expressed in terms of the effective magnetic moment, μ_{eff}, which can be related to the molar susceptibility (χ_m) through: -

$$\chi_m = \frac{N\mu_0\mu_{eff}^2}{3kT} \qquad \text{[Equation 2.23]}$$

where N is the Avogadro constant, μ_0 is the permeability of free space, k is the Boltzmann constant and T is the temperature. Thus a plot of χ_m *vs.* T^{-1} should give a gradient equal to the Curie constant.

The magnetic moment of an atom arising from the spin of unpaired electrons is given by: -

$$\mu_S = g\sqrt{S(S+1)} = \sqrt{n(n+2)} \quad \mu_B \qquad \text{[Equation 2.24]}$$

where *g* is the gyromagnetic ratio (usually two), *S* is the sum of the individual spin quantum numbers, *n* is the number of unpaired electrons and μ_B is units of the Bohr magneton. Similarly, the moment generated by the orbital motion of electrons is given by: -

$$\mu_L = \sqrt{L(L+1)} \quad \mu_B \qquad \text{[Equation 2.25]}$$

where *L* is the sum of the orbital angular momentum quantum numbers. If both of these factors contribute to the overall magnetic moment, then it may be represented by:-

$$\mu_{atom} = g_j \sqrt{J(J+1)} \quad \mu_B \qquad \text{[Equation 2.26]}$$

where: -

- The Landé factor, $g_J = 1 + \frac{J(J+1) - L(L+1) + S(S+1)}{2J(J+1)}$
- $J = L + S$, the total angular momentum quantum number.

Equation 2.26 is particularly useful for the lanthanides, where in most cases both the spin and orbital angular momentum make almost a full contribution to the observed moment. However, in the case of the 3d transition metals, the orbital contribution to the moment is often partially or wholly quenched through interaction with surrounding atoms. Thus here, moments are better represented by the spin-only value (equation 2.24).

2.4.5.2 Magnetisation Measurements

Magnetic susceptibility measurements were performed on a Quantum Design Magnetic Properties Measurements System (MPMS).[31] The magnetometer can

measure magnetisation of a sample as a function of temperature or applied field. Temperature is varied using an inbuilt heater and liquid helium cooling system. Magnetic fields are generated by a superconducting magnet wound in a solenoidal fashion. The magnet is charged to a particular current and can then carry on operating during the measurement with the desired magnetic field, with no need for any external current or power source.

Each sample was accurately weighed before being placed in a gelatine capsule and fixed in the centre of a plastic straw. A zero-field cooled/ field warmed (ZFCFW) measurement was first performed where the sample was cooled to the lowest measurement temperature in the absence of a magnetic field. Magnetisation was then measured as a function of temperature up to the highest desired temperature, which was room temperature. A field cooled/ field warmed (FCFW) measurement was also performed, which was similar to the ZFCFW measurement except that this time the sample was initially cooled in the presence of an applied magnetic field. In both cases fields of 100 Oe were used. The two measurements were carried out in order to investigate whether an applied field alongside minimum thermal energy resulted in an ordering of magnetic moments.

The MPMS consists of a number of superconducting components. The sample itself is moved by small amounts through superconducting detection coils, where its magnetic moment, if any, induces an electrical current in these coils and then causes a current to flow into the SQUID input coil (see Figure 2.13). SQUID electronics produce an output voltage that is directly proportional to the current flowing into it, and hence is also proportional to the magnetic flux.

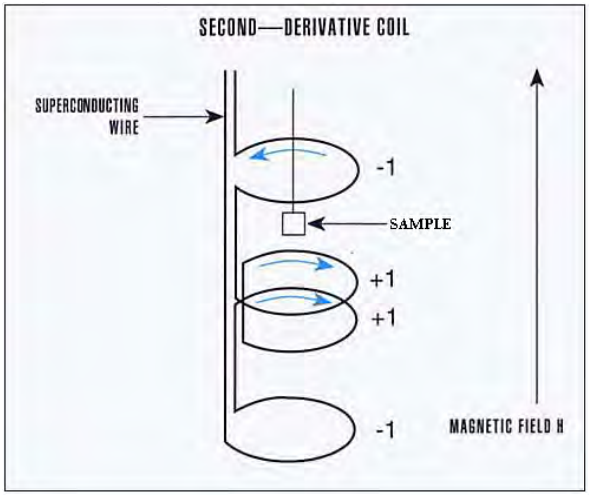

Figure 2.13: *The configuration of the superconducting detection coil*[31]

The SQUID itself is made up of a superconducting loop which has been connected by two insulating layers (Josephson junctions). When a magnetic field is applied through the ring, it interferes with the quantised magnetic flux induced by the current applied across the SQUID.[32] This effect results in the maximum current tunnelling through the two junctions and consequently it oscillates between two values. The ensuing voltage across the SQUID is very sensitive to small changes in the magnetic flux signal from samples. Due to this extreme sensitivity, the SQUID detector is shielded from surrounding magnetic fields (*e.g.* those present in the lab or generated from the superconducting magnet) *via* a superconducting shield.

2.4.5.3 Magnetic Structure Determination from NPD

The long range ordering of unpaired electrons within a solid causes coherent scattering of neutrons, giving rise to magnetic reflections in the diffraction pattern. In order to interpret this information, a basic understanding of magnetic symmetry is required. In this research, spin colours were used to describe magnetic symmetry.

In a magnetically ordered solid, the spin associated with each atom is considered to be an axial vector possessing a current loop. The effect of a symmetry

operation on a magnetic vector may be different to its effect on a normal object, as now the direction of the current loop also needs to be considered. To account for this, crystallographic space groups have been extended using colour (or Shubnikov) space group theory. This approach gives magnetic symmetry operations a colour of either “black” or “red” (the latter indicated by a prime after the space group symbol) in addition to the actual operation. In a black symmetry operation, the loop direction is unchanged and therefore the direction of the vector remains the same. In a red symmetry operation (also known as an antisymmetry operation or time-reversal), the loop direction changes and so this requires the spin to be inverted. Some examples of these operations are given in Figure 2.14.

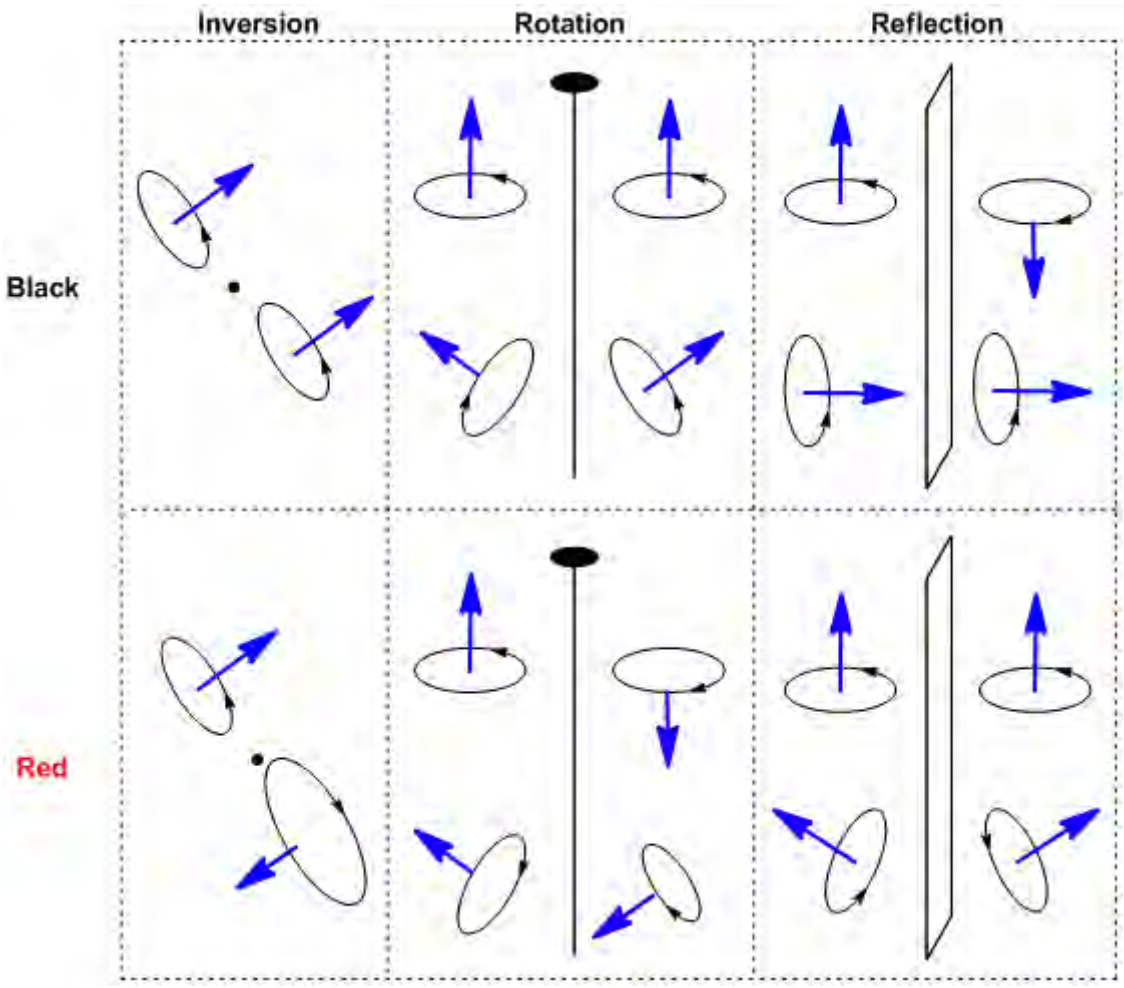

Figure 2.14: *Examples of symmetry and antisymmetry operations*

In simple cases, the magnetic unit cell is an integral multiple of the nuclear unit cell, meaning that it is relatively straightforward to derive a magnetic structural model. Furthermore, magnetisation measurements can assist in deciding what type of ordering is observed overall. In this research, initially the nuclear and magnetic phases contributing to a given diffraction pattern were modelled separately within GSAS.[28] A trial and error approach was used to deduce the orientation of the magnetic moments and hence the magnetic symmetry of the system. The scattering of various arrangements of magnetic moments was correlated with the experimental data until the best fit was obtained.

2.4.6 Thermogravimetric Analysis-Mass Spectrometry

Thermogravimetric analysis monitors the change in mass of a sample whilst it is subjected to variations in temperature. The technique can be used to investigate the thermal stability of a sample, decomposition temperatures, composition, uptake of moisture, *etc*.

The thermogravimetric analyser is a delicate instrument consisting of a precise balance. A small amount of the sample (typically ~20-40 mg) is weighed in an alumina boat and placed in a furnace, with a thermocouple accurately measuring the temperature whilst the weight change is monitored with the balance. This may be done in a number of different atmospheres depending on the nature of the sample.

In this research, all samples were heated at a rate of 10°C/min under a N_2 atmosphere in a Netzsch STA 449 F1 Jupiter instrument. This is coupled to a Quadrupole Mass Spectrometer (QMS) system, which allows for the qualitative analysis of evolved gases. Gases given off as the sample is heated are transferred directly into the electron impact ion source of the mass spectrometer, *via* a preheated

fused silica capillary. The mass of the evolved species is detected as a function of temperature, which can be particularly useful in clarifying the thermal decomposition scheme of a given material.

The instrument can also compare the sample crucible temperature to that of a reference crucible *via* a Differential Thermal Analysis (DTA) unit. This allows heat flow and energy changes within the sample to be detected, which may not necessarily involve a change in mass, for example, if there is a phase change, crystallisation of a phase or collapse of crystallinity. The technique is able to indicate whether thermal events are exothermic or endothermic, and can also be used to calculate heats of formation if calibration with known standards has been performed.

2.4.7 Electronic Spectroscopy

Electronic transitions occur in the UV-visible region (200-750 nm) of the electromagnetic spectrum and can provide information about structure and bonding. Where transition metal complexes are concerned, their colour arises because they absorb light in the visible region. Two main types of transition are possible: -

1) d→d transitions: these occur between metal orbitals possessing d-character.
2) Charge transfer transitions: these occur between metal- and ligand-centred molecular orbitals, where charge is either transferred from metal to ligand or *vice versa*. As such, these transitions are labelled metal to ligand charge transfer (MLCT) or ligand to metal charge transfer (LMCT), respectively.

The following selection rules apply to electronic transitions: -

- Spin selection rule: $\Delta S = 0$ (where S is the spin multiplicity). Transitions are allowed between states of the same multiplicity such that the spin of the electron involved is not changed.

- Laporte selection rule: this depends on the symmetry of the complex. Where there is a centre of inversion present, transitions are only allowed between energy levels of different parity. This means that *g*→*u* and *u*→*g* transitions are allowed but *g*→*g* and *u*→*u* forbidden, where *g* refers to "*gerade*" or symmetric with respect to inversion and *u* refers to "*ungerade*" or antisymmetric with respect to inversion. This leads to $\Delta l = \pm 1$ (where *l* is the orbital angular momentum quantum number), meaning that d→d transitions are formally forbidden. Such transitions can become allowed due to molecular vibrations, which result in a temporary loss of the centre of inversion.

It should be noted that charge transfer transitions are fully allowed by these selections rules, so give very intense absorptions. These transitions often occur at higher energies than d→d transitions, though can sometimes also mask them. Table 2.2 shows typical intensities seen for various types of transition.

Table 2.2: *Typical molar extinction coefficients (ε_{max}) for various types of transition occurring in transition metal complexes*[33]

Type of transition	Typical ε_{max} ($dm^3\ mol^{-1}\ cm^{-1}$)	Comments
Spin forbidden d→d	<1	Seen for high spin d^5 complexes
Spin allowed, Laporte forbidden d→d	1-10	Centrosymmetric complex
	10-1000	Non-centrosymmetric complex
Charge transfer	1000-50000	

2.4.7.1 Term Symbols

The ground state of a free ion can be described using a spectroscopic term symbol according to the Russell-Saunders coupling scheme. This is appropriate for first row transition metal elements, where spin-orbit coupling is small. According to Hund's rules, electrons will occupy orbitals in order to first maximise spin multiplicity and thereafter to maximise orbital angular momentum. The resulting term symbol is then written as ^{2S+1}X, where S is the total spin angular momentum quantum number and X is a label which depends on the total orbital angular momentum quantum number, L: -

L	0	1	2	3	4	5 ...
X	S	P	D	F	G	H ...

This research focuses exclusively on Mn^{3+} (d^4) and Fe^{3+} (d^5) complexes, and so a brief description of how their ground states are derived is given in Figure 2.15. This gives a simple representation of such ions and shows how respective ground state terms of ^5D and ^6S are obtained for the free ions according to Hund's rules.

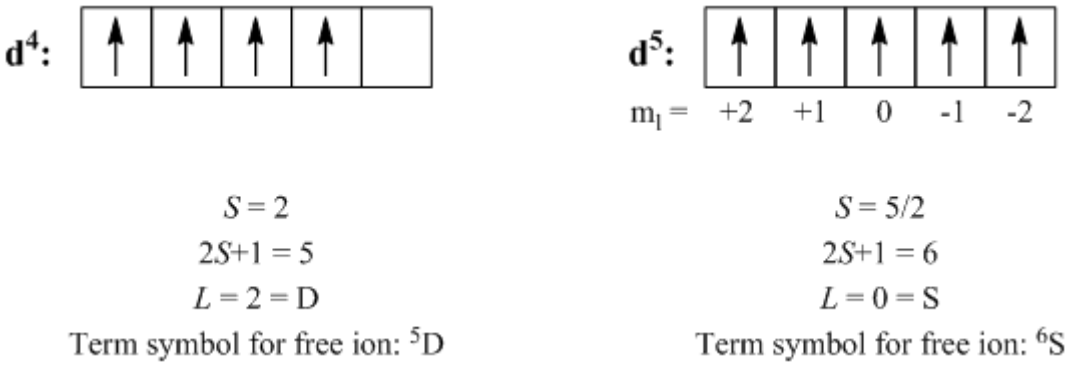

Figure 2.15: *Schematic showing how ground state terms of ^5D and ^6S are derived for free d^4 and d^5 ions, respectively*

When ligands are coordinated to the metal ion, there is a loss in degeneracy of the d-orbitals, with P, D, F, G and H terms splitting into the levels shown below.

$$P \rightarrow T_1$$

$$D \rightarrow E + T_2$$

$$F \rightarrow A_2 + T_1 + T_2$$

$$G \rightarrow A_1 + E + T_1 + T_2$$

$$H \rightarrow E + 2T_1 + T_2$$

It should be noted that an S term possesses no orbital degeneracy and so does not actually split in a crystal field, with the corresponding level labelled A_1. Therefore a high spin octahedral Fe^{3+} complex will have a ground state of $^6A_{1g}$, where the "g" subscript is added to indicate that the complex possesses a centre of inversion. Due to the absence of low-lying excited states with the same spin, all transitions are formally spin and Laporte forbidden.

For high spin octahedral Mn^{3+} complexes, three electrons occupy the t_{2g} orbitals and the fourth an e_g orbital, of which there are two possible permutations (Figure 2.16). This is therefore a doubly degenerate state, giving rise to a ground state of ^5E_g and an excited state of $^5T_{2g}$. Thus one spin-allowed but Laporte forbidden transition is expected. However, Jahn-Teller distortions can further remove orbital degeneracy to give rise to more transitions, which is discussed further in the relevant sections of subsequent chapters.

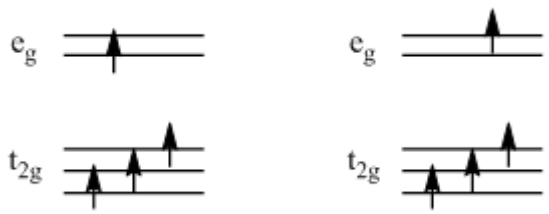

Figure 2.16: *Doubly degenerate states occurring for high spin octahedral d^4 complexes*

2.4.7.2 Spectroscopic Measurements

Ultraviolet-Visible (UV-Vis) spectroscopy was carried out on a Cary 5000 UV-Vis-NIR spectrophotometer accommodated with a praying mantis accessory.[34] The instrument uses a deuterium and mercury lamp to generate UV-Vis radiation and a photomultiplier tube detector.

The praying mantis attachment (Figure 2.17) is designed to allow powders to be examined by diffuse reflection spectroscopy. The accessory contains six aluminium mirrors, two of which are 90° off axis ellipsoid mirrors that are arranged 60° away from the direction of specularly reflected radiation. The near focal points of these two mirrors meet at the sample (held in a cup), where the beam forms a spot <2 mm in diameter. A beam balancer with an integral attenuator is used to balance out the reflections of all six mirrors, while a separate adjustable attenuator can be used to balance out sample reflectance. All measurements were carried out on the undiluted solid samples relative to a Teflon standard.

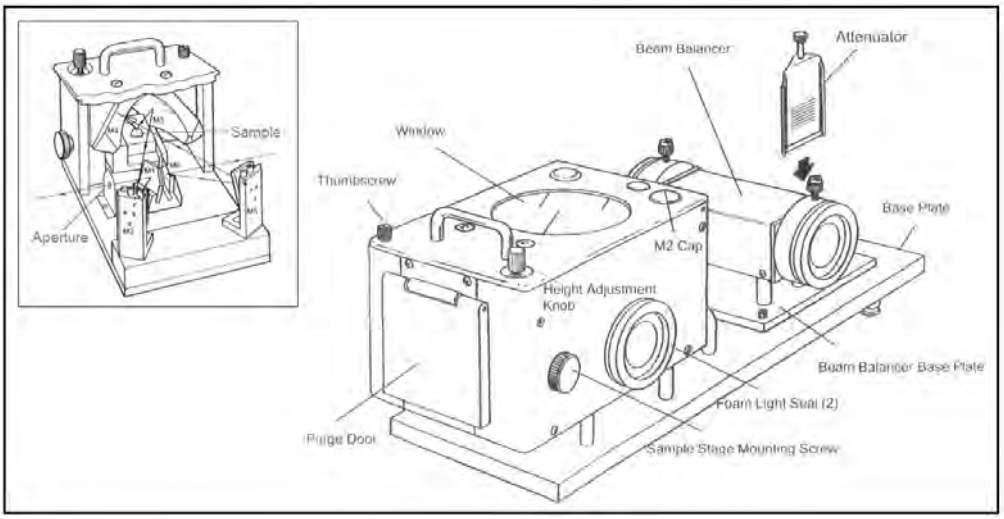

Figure 2.17: *Front view of the praying mantis, with inset showing the interior of the sample compartment*[34]

2.4.7.3 Mathematical Fitting of Electronic Spectra

All electronic spectra obtained consisted of broad features and it was clear that these were not just due to one transition, but rather the result of a number of overlapping peaks. Such broad features can occur due to the vibration of ligands in the complex, which constantly changes the crystal field splitting and means that absorption occurs over a broad energy range. Other reasons for broad features can be due to spin-orbit coupling or Jahn-Teller distortions, both of which cause a further splitting of energy levels and give rise to more transitions which may not be fully distinguishable from each other.

A significant part of this research was based on investigating the Jahn-Teller distortion that occurs within the octahedral Mn^{3+} complexes studied. Indeed, the number of transitions seen in the electronic spectra can be related to the extent of this distortion.[35] To obtain more details on this, the PeakFit[36] software was used for the mathematical fitting of the electronic spectra, and allowed for the detection and separation of individual peaks. A similar approach has been used by a number of groups in the analysis of Mn^{3+} spectra.[37-39]

The PeakFit[36] program requires the input of electronic spectra *i.e.* the raw data in a digitised format. A hidden peak is defined as one which does not produce a local maximum in the spectrum but which may be apparent through visual inspection, for example, as a shoulder to a broader peak. The “AutoFit Peaks III Deconvolution” option was selected, which can allow hidden peaks to be detected by using an algorithm to deconvolute a Gaussian instrument response function from the raw data. Once this is done, peak maxima are automatically placed in the spectrum. In some cases the automatic deconvolution is not successful in identifying all of the peaks that

are visually apparent to the user, or it may be that the user knows how many peaks are expected in the spectrum. As such there is the option to manually place peak maxima in the spectrum. Baseline and peak shape parameters can also be selected and for all spectra considered here, in accordance with the literature, a constant baseline was chosen and a Gaussian peak shape function in which the widths were allowed to freely vary. Least squares refinement cycles were then performed until the best fit between the observed data and the calculated electronic spectrum was obtained. This was monitored by a graphical inspection of the fit as well as consulting the r^2 (goodness of fit) value, where $r^2 = 1$ corresponded to a perfect fit and $r^2 = 0$ a complete lack of fit. For all of the spectra fitted in this research, the value of r^2 was ≥ 0.998.

2.4.8 Mössbauer Spectroscopy[40]

Mössbauer spectroscopy can be used to give information on the chemical, structural and magnetic properties of a material. The technique is based on the transitions that nuclei make between different nuclear energy levels, which correspond to the absorption or emission of a γ-ray. These energy levels can be split or influenced by the surrounding environment of the nucleus, thus allowing information to be derived about the atom's local environment. However, a sensitive technique is required as the strength of interaction between a nucleus and its environment is very small ("hyperfine"), typically being the order of billionths of an electronvolt.

When a free nucleus absorbs or emits a γ-ray, it recoils due to conservation of momentum, taking a recoil energy, E_R, from the γ-ray. The γ-ray can then be absorbed by another nucleus, which too will recoil. After a short while, the γ-ray loses

energy such that it no longer corresponds to the energy of the nuclear transition, meaning that resonance does not occur. Mössbauer discovered that the atoms in a solid matrix are much closer together, and if the γ-ray energy is small enough, then the recoil energy is very small. In this situation, the emitting and absorbing nuclei absorb and emit the γ-ray at practically the same energy, giving rise to resonance.

There are only a select few isotopes such as ^{57}Fe, ^{99}Ru, ^{119}Sn that show the Mössbauer effect, with the energy of the transition, ΔE, and the lifetime of the excited state, Δt, being critical factors in determining whether the effect is observed or not.

$$\Delta E \Delta t \leq \frac{h}{4\pi} \qquad \text{[Equation 2.27]}$$

If we recall that the γ-ray energy needs to be small in order to minimise the recoil effect, then the Mössbauer effect is only detected in isotopes with very low lying excited states. Furthermore, the longer the lifetime of the excited state, the smaller is the linewidth, giving a better resolution *cf.* the γ-ray energy. A good resolution is required to detect the hyperfine interactions in the nucleus.

Experiments use a radioactive γ-ray source that is oscillated towards and away from the sample by a few mm/s. This allows the γ-ray energy to be varied so that when it matches the nuclear transition energy of the absorber, the γ-rays are resonantly absorbed. The Mössbauer spectrum is therefore recorded as a function of source velocity. If the source nucleus and the absorber nucleus are in identical environments, then a single peak occurs a 0 mm/s. However, if this is not the case then the energy levels of the absorbing nuclei can be influenced by their environment in three ways: -

1) Isomer Shift

The isomer shift influences the position that a peak is observed at. It arises due to the Coulombic interaction between the nucleus and its s-electrons. If the s-electron environment is different between source and absorber, then the resonance energy of the transition shifts either positively or negatively, the shift being quoted relative to a known absorber. Isomer shift can be used to determine oxidation states, ligand bonding states, electron shielding and electron withdrawing power of ligands, which will all have an influence on the s-electron charge density at the nucleus.

2) Quadrupole Splitting

Nuclei in states with angular momentum quantum number, $I > 1/2$ have a non-spherical positive charge distribution. The resulting nuclear quadrupole moment can be influenced by an asymmetric electric field (*e.g.* generated by an asymmetric electronic charge distribution or asymmetric ligand arrangement), which may cause a splitting of the nuclear energy levels. ^{57}Fe and ^{119}Sn isotopes have an excited state with $I = 3/2$ that is split into two substates with $m_I = \pm 1/2$ and $m_I = \pm 3/2$, giving rise to a two-line spectrum or a doublet: -

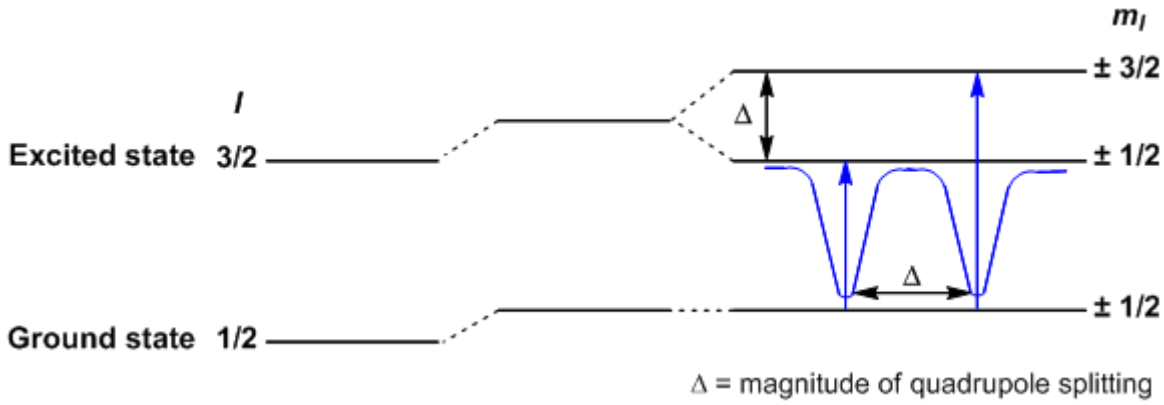

Figure 2.18: *Quadrupole splitting for an excited state with nuclear spin of I = 3/2*

3) Magnetic Splitting

A nucleus can experience various types of magnetic field given by: -

$$B_{eff} = (B_{contact} + B_{orbital} + B_{dipolar}) + B_{applied} \qquad \text{[Equation 2.28]}$$

where B_{eff} is the total effective magnetic field at the nucleus, $B_{contact}$ is the field generated by electron spin, $B_{orbital}$ is the field generated by orbital angular momentum of electrons, $B_{dipolar}$ is the dipolar field that arises from electron spin and $B_{applied}$ is the applied field.

The nuclear spin undergoes an interaction with the magnetic field, causing a Zeeman splitting of its spin state. Where there is no applied field, the magnetic field generated by the first three terms in equation 2.28 causes nuclear levels with a spin of I to split into $(2I+1)$ substates where $m_I = +I \ldots -I$. Transitions can occur between these substates provided that $\Delta m_I = 0, \pm 1$, giving rise to more lines in the Mössbauer spectrum. For single crystals or under applied fields, the relative intensities of these lines can give information on moment orientation and magnetic ordering.

For this research, ^{57}Fe Mössbauer spectra were recorded by Dr Allen Bowden (Open University, UK) at 298 K with a constant acceleration spectrometer in transmission geometry using a 400 MBq ^{57}Co/ Rh source. The drive velocity was calibrated with the source and a natural iron foil. Chemical isomer shift data were reported relative to that of metallic iron at 298 K. All data interpretation was conducted by Professor Frank Berry (Open University, UK).

2.4.9 X-ray Absorption Fine Structure[41]

X-ray Absorption Fine Structure (XAFS) can be used to investigate the local structure about specific elements within a material. XAFS occurs when sufficiently energetic X-rays are absorbed by an atom and cause the ejection of core level electrons. An X-ray beam is directed at the sample and its energy increased until it passes the absorption edge of the element of interest. Absorption is low below the edge but suddenly increases at and past the edge, where the incident photons become energetic enough to cause ionisation. Any remaining energy is transferred as kinetic energy to the ejected photoelectrons. The resulting XAFS spectrum is divided into the X-ray Absorption Near Edge Structure (XANES), which is typically within 40 eV of the edge and the Extended X-ray Absorption Fine Structure (EXAFS), which extends to ~1000 eV above the absorption edge (Figure 2.19). XAFS experiments require synchrotron radiation in order to provide an intense source of tuneable radiation.

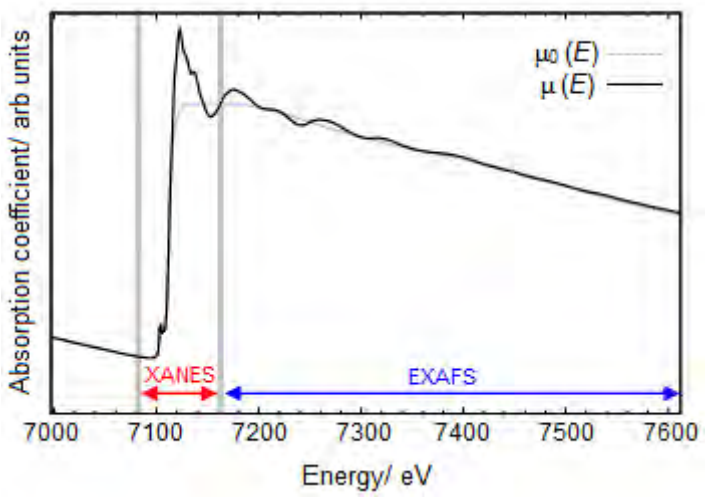

Figure 2.19: *An XAFS spectrum showing the XANES and EXAFS regions*[42]

In this research, XAFS measurements and data analysis were performed by Dr Andrew Dent on the B18 beamline at the Diamond Light Source (UK) in Rapid Access.[43] This beamline provides X-ray energies in the range of 2.05-35 keV using a fixed-exit, double-crystal monochromator that holds two pair of crystals, Si (111) and Si (311). Experiments here used the Si (111) pair to provide an energy resolution of 2 x 10^{-4} eV. Approximately 20 mg of each sample was finely ground with ~80 mg of cellulose powder, before being pressed into 8 mm diameter pellets of ~2 mm thickness. For each sample, 20 × 1 minute QEXAFS data were collected at the Mn K- and Fe K-edges in transmission mode, with ion chambers before and behind the sample filled with appropriate mixtures of inert gases to optimize sensitivity. The spectra were measured with a step size equivalent to approximately 1 eV. Data were normalized using the program Athena[44], with a linear pre-edge and polynomial post-edge background subtracted from the raw summed $\ln(I/I_0)$ data. Curved wave first shell EXAFS analysis was carried out using the DL_EXCURV[45-46] package.

2.4.9.1 EXAFS

EXAFS can be used to determine the coordination number of an atom, bond distances to neighbouring atoms and the atomic numbers of neighbouring atoms. Following the ejection of photoelectrons from the atom of interest, interference occurs between the outgoing electron waves and backscattered electron waves from surrounding atoms (see Figure 2.20). This creates regions of constructive and destructive interference that are seen as oscillations of local maxima and minima, respectively.

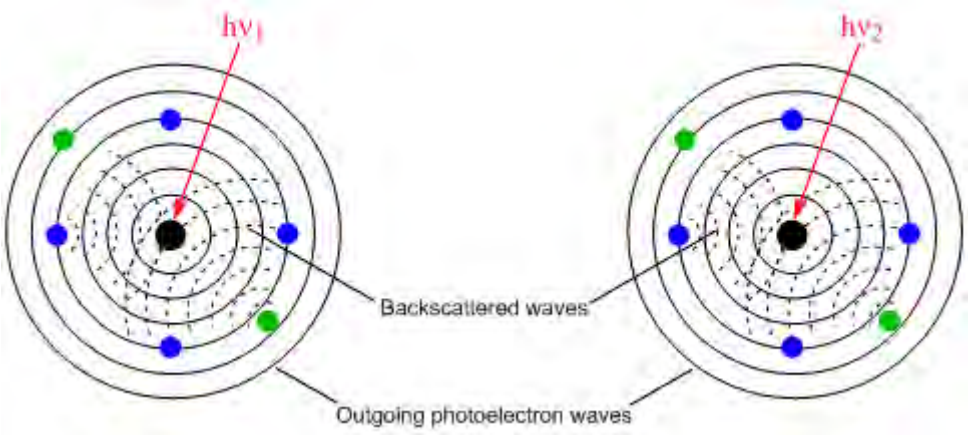

Figure 2.20: *Interference between the outgoing photoelectron waves from a central atom and backscattered waves from neighbouring atoms*

The quantity of interest is the X-ray absorption coefficient, μ, which is related to the sample thickness (*x*) and the intensity of the incident (I_0) and transmitted (*I*) beams through equation 2.29. The measured spectrum records the absorption coefficient as a function of energy *i.e.* μ(*E*), giving an average of the snapshot spectra (femtosecond timescale) of all of the atoms that have been probed.

$$I = I_0 \exp(-\mu x) \qquad \text{[Equation 2.29]}$$

The EXAFS fine-structure function, χ(*E*) can then be defined as: -

$$\chi(E) = \frac{\mu(E) - \mu_0(E)}{\Delta\mu_0(E)} \qquad \text{[Equation 2.30]}$$

where μ_0 (*E*) is a background function for the absorption of an isolated atom and $\Delta\mu_0(E)$ is the measured jump in absorption, μ(*E*) at the threshold energy, E_0.

EXAFS is more often interpreted in terms of the wave-behaviour of the photoelectron, and so the X-ray energy is frequently converted into the wave number of the photoelectron, *k*: -

$$k = \sqrt{\frac{2m(E - E_0)}{(h/2\pi)^2}} \qquad \text{[Equation 2.31]}$$

where E_0 is the absorption edge energy and m is the electron mass. The EXAFS fine structure then becomes a function of photoelectron wave number, $\chi(k)$. The different frequencies that occur within the oscillations of $\chi(k)$ are due to different near-neighbour coordination shells, and can be described and modelled using the "EXAFS equation": -

$$\chi(k) = \sum_j \frac{N_j f_j(k) \exp\left(-2k^2\sigma_j^2\right)}{kR_j^2} \sin\left[2kR_j + \delta_j(k)\right] \qquad \text{[Equation 2.32]}$$

where $f_j(k)$ is the scattering amplitude from each of N_j atoms of the j^{th} type with a Debye-Waller factor of σ_j^2 (mean square displacement in the bond distance which accounts for thermal vibration and static disorder) at a distance R_j away. $\delta(k)$ is the total phase shift experienced by the photoelectron. It is worth noting that a Fourier transformation is often used to extract the different coordination spheres surrounding the absorbing atom. The scattering functions f(k) and $\delta(k)$ are either theoretically calculated or empirically measured, allowing interatomic distances, the number of neighbouring atoms and disorder to be determined.

2.4.9.2 XANES

The XANES region of the XAFS spectrum is not as well understood as that of EXAFS. XANES is concerned with the near-edge and pre-edge features, with absorption peaks at the pre-edge occurring due to excitation of core electrons to vacant nd, (n+1)s or (n+1)p atomic orbitals or intramolecular/ intermolecular molecular orbitals. The excitation of a 1s electron to these levels is referred to as the

K-edge, a 2s electron as the L_I-edge and a 2p electron as the L_{II}- or L_{III}-edge. The core hole is filled by a bound electron from a higher energy level, which loses energy either as a fluorescent photon or by causing the ejection of another electron from the atom (Auger electron), both of which can be used for signal recording. The region immediately past the edge is thought to arise from a number of effects such as many-body interactions, multiple scatterings of the photoelectron, distortion of excited states by Coulombic interactions, *etc*.

There are no physical expressions that can be used to describe XANES, with the “EXAFS equation” (equation 2.32) breaking down at low *k*. As a consequence of this, model spectra and linear algebraic techniques are required to interpret the edge features. The edge position, shape and intensity can provide details on the oxidation state of an element, charge transfer, surrounding ligand type and coordination environment.

2.4.10 X-ray Fluorescence

X-ray Fluorescence (XRF) was used in this research for the semi-quantitative elemental analysis of materials. Measurements were performed on a Bruker AXS: S8 Tiger wavelength dispersive XRF spectrometer with internal instrument calibration (“standard-less” analysis). Powdered samples were placed in plastics cups with a Mylar film cover and then transferred to metallic holders with an exposure diameter of 13 mm. Measurements were conducted in a helium atmosphere in order to prevent air from absorbing the fluorescent X-rays.

The S8 Tiger directs high energy X-rays towards the sample of interest, causing excitation of core electrons within the elements present. As electrons from

higher energy levels relax down, X-rays characteristic of the elements present are emitted. A typical spectrum will display multiple peaks with different intensities. Various monochromator crystals are used to separate the multiple frequency signals into the specific wavelengths of the elements. A proportional counter and scintillation counter are then used for the detection of light elements and heavy elements, respectively.

2.4.11 Scanning Electron Microscopy[47]

Scanning Electron Microscopy (SEM) is used to study the surface or near surface structure of a sample. It can represent the three-dimensional nature of a surface in two dimensions, giving an indication of height, width, depth and relative distances. General information can be obtained on topography, morphology and crystallography. All electron microscopes use a beam of electrons to form an image of the object of interest. Primary electrons enter the sample and then the same or different electrons leave the sample to form an image. If a core level electron is ejected from an atom then an electron from a higher energy level can fill the electron hole and release energy in the process. Visible light, a characteristic Auger electron or a characteristic X-ray may be emitted. The latter is the basis of Energy Dispersive X-ray (EDX) analysis.

In this research, SEM was performed using a JEOL-JSM6060LV operating under vacuum with a 20.0 kV electron beam. The powdered samples were dispersed onto an adhesive carbon pad and then coated with carbon in order to aid their conductivity.

2.4.12 Fourier Transform Infrared Spectroscopy

Infrared (IR) spectroscopy deals with transitions that occur within the infrared region of the electromagnetic spectrum, which are predominantly vibrational or rotational in nature. A molecule can vibrate in a number of different ways, with linear molecules having 3*N* – 5 vibrational modes and non-linear molecules having 3*N* – 6 vibrational modes, where *N* is the total number of atoms present. For a vibrational mode to be IR active, it must result in a change in the dipole moment of the molecule.

A Fourier transform infrared (FTIR) spectrometer passes a beam of IR light through the sample, which is absorbed by molecules and causes them to vibrate. The frequencies at which vibrations occur can be related to the strength of the absorbing bond and the reduced mass of the atoms forming it, which means that absorptions are characteristic of chemical groups and the bonds present. A whole wavelength range is measured and the signal recorded in terms of light output from the sample as a function of mirror position *i.e.* an interferogram. A Fourier transform then converts this data into transmittance *vs.* infrared wavenumber.

In this research FTIR measurements were carried out on solid samples using a Varian 660-IR FTIR spectrometer fitted with a Pike MIRacle attenuated total reflectance (ATR) attachment.[48] A ceramic Mid-IR source fitted with a KBr beam splitter is used to provide radiation over the range 7900-375 cm^{-1}. Inside the ATR accessory, samples are loaded onto the surface of a zinc selenide crystal and pressure is applied *via* a clamp in order to maximise the contact between the two. The infrared beam is directed onto the crystal to create an evanescent wave which is partly absorbed by the sample to give an attenuated wave; this is then passed back

to the IR beam and exits to a DLaTGS (deuterated L-alanine doped TriGlycine Sulfate) detector.

References

[1] Figure adapted from http://cnx.org/content/m16927/latest/.

[2] Figure adapted from http://www.diracdelta.co.uk/science/source/m/i/miller%20indices/source.html.

[3] M. von Laue, *Phys. Z.*, 1913, **14**, 1075-1079.

[4] M. von Laue, *Ann. Physik*, 1913, **41**, 989-1002.

[5] W. L. Bragg, *Proc. Camb. Phil. Soc.*, 1913, **17**, 43-57.

[6] JCPDS, *International Centre for Diffraction Data*, 1999, P.1., Swathmore, Pennsylvania, PA 19081, USA, 11990.

[7] H. M. Rietveld, *J. Appl. Crystallogr.*, 1969, **2**, 65-71.

[8] V. K. Pecharsky and P. Y. Zavalij, *Fundamentals of Powder Diffraction and Structural Characterisation of Materials*; Springer: New York, 2005.

[9] C. Greaves, *DSPACE*; School of Chemistry, University of Birmingham, 1982.

[10] *CELL*; based on the original code by M. F. Pye, I. C. L., Oxford.

[11] R. Shirley, *The CRYSFIRE System for Automatic Powder Indexing: User's Manual*, 2002, The Lattice Press, 41 Guildford Park Avenue, Guildford, Surrey, GU2 7NL, England.

[12] J. W. Visser, *J. Appl. Crystallogr.*, 1969, **2**, 89-95.

[13] D. Louer and R. Vargas, *J. Appl. Crystallogr.*, 1982, **15**, 542-545.

[14] A. Boultif and D. Louer, *J. Appl. Crystallogr.*, 1991, **24**, 987-993.

[15] P. E. Werner, L. Eriksson and M. Westdahl, *J. Appl. Crystallogr.*, 1985, **18**, 367-370.

[16] D. Taupin, *J. Appl. Crystallogr.*, 1973, **6**, 380-385.

[17] F. Kohlbeck and E. M. Horl, *J. Appl. Crystallogr.*, 1976, **9**, 28-33.

[18] F. Kohlbeck and E. M. Horl, *J. Appl. Crystallogr.*, 1978, **11**, 60-61.

[19] R. Shirley, 2002, Unpublished.

[20] R. Shirley and D. Louer, *Acta Crystallogr.*, 1978, **A34**, S382.

[21] J. Laugier and B. Bochu, *LMGP Suite of Programs for the Interpretation of X-ray Experiments*; ENSP/Laboratoire des Matériaux et du Génie Physique, BP 46. 38042 Saint Martin d'Hères, France, www.ccp14.ac.uk/tutorial/lmgp/

[22] G. E. Bacon, *Neutron Diffraction*; Clarendon Press: Oxford, 1955.

[23] G. E. Bacon, *Neutron Diffraction*; Clarendon Press: Oxford, 1975.

[24] www.ill.eu/instruments-support/instruments-groups/instruments/d2b/.

[25] *HRPT User Guide*, 2002.

[26] R. A. Young, *The Rietveld Method, IUCr Monographs on Crystallography*; Oxford University Press: New York, 1993.

[27] H. M. Rietveld, *Acta Crystallogr.*, 1967, **22**, 151.

[28] A. C. Larson and R. B. von Dreele, *General Structure Analysis System*; Los Alamos National Laboratory, 1994.

[29] C. J. Howard, *J. Appl. Crystallogr.*, 1982, **15**, 615-620.

[30] P. Thompson, D. E. Cox and J. B. Hastings, *J. Appl. Crystallogr.*, 1987, **20**, 79-83.

[31] M. McElfresh, *Fundamentals of Magnetism and Magnetic Measurements featuring Quantum Design's Magnetic Property Measurement System*; Quantum Design: San Diego, 1994.

[32] Z. S. Teweldemedhin, R. L. Fuller and M. Greenblatt, *J. Chem. Ed.*, 1996, **73**, 906-909.

[33] C. E. Housecroft and A. G. Sharpe, *Inorganic Chemistry*; Pearson Education: Harlow, 2001.

[34] Harrick Scientific Products, *Solutions in Optical Spectroscopy Manual*, 141 Tompkins Avenue, Box 277, Pleasantville, New York, 10562 (914) 747 7202.

[35] R. G. Burns, *Mineralogical Applications of Crystal Field Theory*; Cambridge University Press: New York, 1993.

[36] *PeakFit Version 4.12*; Seasolve, 1999-2003.

[37] D. M. Sherman and N. Vergo, *Am. Mineral.*, 1988, **73**, 140-144.

[38] U. Halenius, *Mineralog. Mag.*, 2004, **68**, 335-341.

[39] D. R. Gamelin, M. L. Kirk, T. L. Stemmler, P. Samudranil, W. H. Armstrong, J. E. Penner-Hahn and E. I. Solomon, *J. Am. Chem. Soc.*, 1994, **116**, 2392-2399.

[40] www.rsc.org/Membership/Networking/InterestGroups/MossbauerSpect/.

[41] M. Newville, *Fundamentals of XAFS*; Consortium of Advanced Radiation Sources: University of Chicago, 2004.

[42] Figure adapted from http://magicspin.jku.at/synchrotron.php.

[43] A. J. Dent, G. Cibin, S. Ramos, A. D. Smith, S. M. Scott, L. Varandas, M. R. Pearson, N. A. Krumpa, C. P. Jones and P. E. Robbins, *J. Phys.: Conf. Ser.*, 2009, **190 012039**, 1-4.

[44] B. Ravel and M. Newville, *J. Synchrotron Radiat.*, 2005, **12**, 537-541.

[45] N. Binsted, *EXCURV98*; CCLRC Daresbury Laboratory, 1998.

[46] S. Tomic, B. G. Searle, A. Wander, N. M. Harrison, A. J. Dent, J. F. W. Mosselmans and J. E. Inglesfield, CCLRC Technical Report DL-TR-2005-001, ISSN 1362-0207, 2005.

[47] G. Lawes and A. M. James, *Scanning Electron Microscopy and X-ray Microanalysis*; Wiley: Chichester, 1987.

[48] Varian Inc., *FT-IR Spectroscopy Solutions, 660/ 670/ 680-IR Manual*.

Chapter Three

Synthesis and Characterisation of α-$NH_4MnP_2O_7$, Manganese Violet and Substitutional Analogues

3.1 Introduction

Manganese (III) condensed phosphate materials and substitutional analogues have been the subject of various patents claiming rights to their use as anticorrosion agents, antimicrobial agents and as non-toxic pigments for use in metal coatings, plastics, cosmetics and toys.[1-3] Their main industrial application is as pigments, where the manganese violet pigment, given by an empirical formula of $NH_4MnP_2O_7$, was reported in 1988 to represent ~2.5% of the synthetic inorganic pigments market, with titanium dioxide pigments accounting for approximately 66%.[4] Its key characteristics of durability, non-toxicity, light-fastness, weather resistance and being readily dispersed[4] mean it finds many applications, particularly in cosmetics. Despite this, surprisingly little is known about the structural aspects of $NH_4MnP_2O_7$.

Available literature reveals that manganese violet is generally synthesised by heating a manganese salt, diammonium hydrogen phosphate and phosphoric acid at elevated temperatures.[5] Lee and Browne[6] studied this compound in detail and were the first to report a more specific synthetic procedure involving heating exact quantities of MnO_2, $NH_4H_2PO_4$ and H_3PO_4 at 120°C for 30 minutes in order to obtain

a melt. This was then further heated at 300°C for 1 hour followed by excess water being added to the hot product. The resulting suspension was then boiled for 30 minutes and allowed to cool before being filtered. Although X-ray diffraction was employed, the product possessed significant amorphous character as well as impurities such as MnO_2 and $Mn_4(P_2O_7)_3$, which limited the opportunity to obtain detailed structural information.

Due to the recent structural determination of the chemically similar $RbMnP_2O_7$[7] and general advances in characterisation techniques, it was deemed an opportune time to further investigate the manganese violet pigment. This chapter initially details our investigations into the synthesis of manganese violet, the potential presence of polymorphs and comparison to a commercially available version of this pigment. Following this, attempts to chemically modify the pigment through exchanging the NH_4^+ cation for other species and substituting the Mn^{3+} cation for other transition metal ions, notably Fe^{3+}, are described. In all cases the study emphasises the structural, optical, thermal and magnetic properties of the materials obtained.

3.2 Experimental

3.2.1. Synthesis of Manganese Violet

Initially, in order to synthesise $NH_4MnP_2O_7$, the method reported by Lee and Browne[6] was repeated, as well as a similar method previously used to synthesise $RbMnP_2O_7$,[8] which involved heating $(NH_4)_2HPO_4$, Mn_2O_3 and H_3PO_4 with a NH_4:Mn:P molar ratio of 9:1:15 at 250°C for 48 h and cooling to RT over 24 h. Whilst the former approach and variations of it yielded poorly crystalline products, the latter resulted in a mixture of more crystalline phases that could not be fully identified using

the JCPDS[9] database, but were found to include $NH_4MnHP_3O_{10}$. Therefore, a systematic exploration of synthetic conditions was undertaken using a phosphoric acid melt method, with the reagents $(NH_4)_2HPO_4$, Mn_2O_3 and H_3PO_4 (86.5 wt %). A number of conditions were explored, including variations in reagent ratios, reaction temperatures and reaction durations, over the course of which two $NH_4MnP_2O_7$ polymorphs were identified. Further details on this are given in section 3.3.

3.2.2. Synthesis of α-$NH_4MnP_2O_7$ substitutional analogues

Ion exchange in α-$NH_4MnP_2O_7$ was attempted as a route to access previously unreported $M^IMnP_2O_7$ phases. Aqueous ion exchange methods were found to be unsuccessful, which was in part expected given the rigid, three-dimensional framework of the material. Therefore a nitrate melt method was employed which involved grinding the host with alkali metal nitrates in the molar ratio of 1:10, respectively. The resulting mixture was placed in a porcelain crucible and heated in an oven at various temperatures for up to 4 h. Following the reaction, excess nitrate was removed by washing the product with copious amounts of water and recovering the ion-exchanged product by suction filtration.

α-$NH_4Mn_{1-x}Fe_xP_2O_7$ compounds were synthesised in a similar fashion to the pure Mn end member, using the reagents $(NH_4)_2HPO_4$, Mn_2O_3, Fe_2O_3 and H_3PO_4 (86.5 wt %) in a NH_4:TM:P molar ratio of 2.5:1:3 and heating at temperatures ranging from 250-300°C for 1 h. Attempts to form solid solutions with vanadium (III) and chromium (III) under similar conditions were unsuccessful, with the acid melts yielding poorly crystalline products that could not be identified.

3.2.3. Collection of Diffraction Data

Powder X-ray diffraction (XRD) data were collected on a Bruker AXS: D8 Advance diffractometer in transmission mode with a 2θ scan range of 5-80°. Room temperature neutron powder diffraction (NPD) data for both α-$NH_4MnP_2O_7$ and a commercial sample were recorded on the D2B instrument at the Institut Laue-Langevin, Grenoble. An incident neutron wavelength of 1.5943 Å was employed over the range $5 \leq 2\theta \leq 160°$, with a 3 h collection time for the former compound and a 4 h collection time for the latter sample. Data were also collected on α-$NH_4MnP_2O_7$ at 2 K in a similar fashion. RT NPD data on the α-$NH_4Mn_xFe_{1-x}P_2O_7$ (x = 0, 0.25, 0.5 and 0.75) compounds were recorded on the HRPT instrument at the Paul Scherrer Institute, Switzerland. A wavelength of 1.494 Å was employed over the range $5 \leq 2\theta \leq 160°$, with a 2 h collection time for all samples. Due to the relatively high proton content of these phases, Debye-Scherrer absorption corrections were applied to the cylindrical samples within GSAS,[10] using attenuation factors calculated from the NIST neutron attenuation calculator.[11] Such attenuation factors accounted for the large incoherent scattering cross section of the protons as well the relatively large absorption cross section of manganese.

3.3 Results and Discussion

During our investigations into the synthesis of manganese violet, it was found that one polymorph, hereby designated as α-$NH_4MnP_2O_7$, could be isolated by heating $(NH_4)_2HPO_4$, Mn_2O_3 and H_3PO_4 in the NH_4:Mn:P molar ratio of 2.5:1:3 in a porcelain crucible at a rate of 1°C/ min up to 205°C for 1 h. The reaction mixture was allowed to cool to room temperature before the product was washed with water and

recovered *via* vacuum filtration. This yielded a deep violet microcrystalline powder. Reaction temperatures higher than 205°C led to a second polymorph (designated as β-$NH_4MnP_2O_7$) being observed that gave a similar X-ray diffraction pattern to α-$NH_4MnP_2O_7$. Despite attempting various reaction conditions, β-$NH_4MnP_2O_7$ could not be isolated as a single phase. Often, only a mixture of the two polymorphs could be obtained and indeed, this was the reason for the short reaction time being employed for the synthesis of α-$NH_4MnP_2O_7$. Therefore a commercial manganese violet pigment (grade VM42), which also contained a mixture of both polymorphs, was used to further investigate the structure of β-$NH_4MnP_2O_7$.

3.3.1 Crystal Structure of α-$NH_4MnP_2O_7$

Structural details on α-$NH_4MnP_2O_7$ were obtained from a Rietveld refinement of the neutron powder diffraction data, using $NH_4YbP_2O_7$[12] as a starting model to allow the positions of the protons to be accurately determined. The refinement converged to a relatively low R_{wp} value of 1.18%, which was in part due to the dataset possessing a relatively high background from the proton content (Figure 3.1). The refinement confirmed that α-$NH_4MnP_2O_7$ adopts a type-I [13] pyrophosphate structure with space group $P2_1/c$ and lattice parameters of a = 7.4252(3) Å, b = 9.6990(4) Å, c = 8.6552(4) Å and β = 105.627(3)°. The final refined structural parameters are shown in Table 3.1, with selected bond lengths and angles given in Table 3.2.

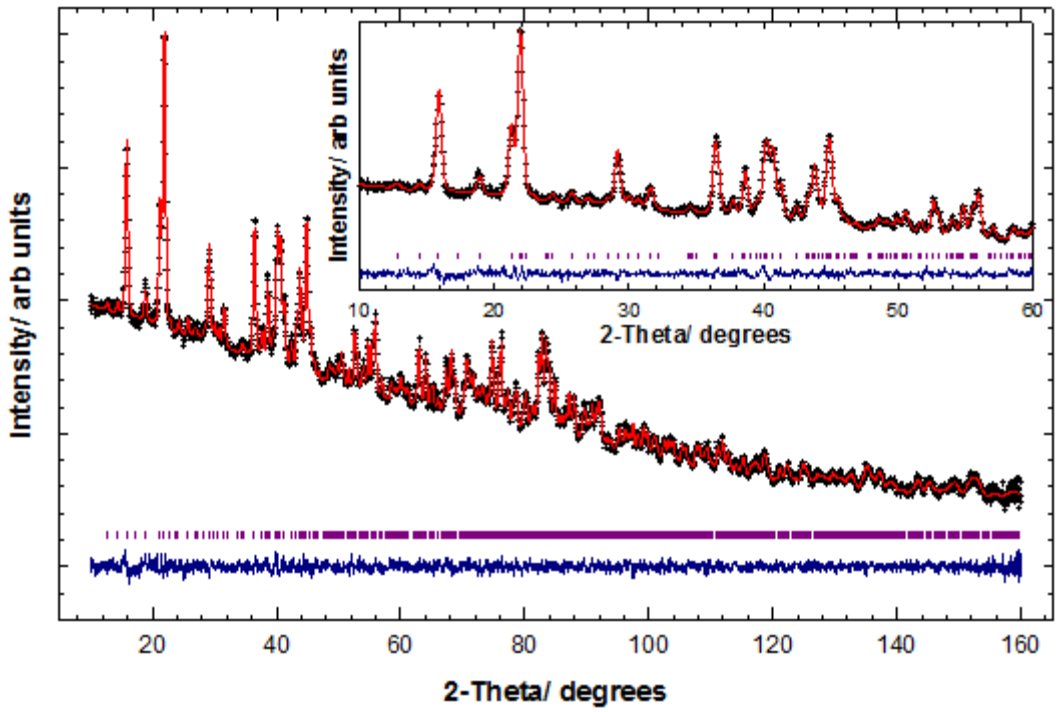

Figure 3.1: *Observed (+), calculated (-), difference profiles (-) and reflection positions (|) for the Rietveld refinement on α-$NH_4MnP_2O_7$. The 10-60° 2θ region is expanded in the inset.*

The structure, as shown in Figure 3.2, can be described as a three-dimensional network of MnO_6 octahedra corner-linked to five P_2O_7 units, one of them in a bidentate fashion, resulting in hexagonal tunnels running along the *c*-direction of the structure. These tunnels accommodate the ammonium cations, which possess relatively high thermal displacement factors (U_{iso}). This is not unexpected as these NH_4 species may possess some disorder in the channel sites, which could be static and/ or dynamic. The two PO_4 tetrahedra that form the P_2O_7 unit have quite an irregular arrangement of bond lengths, but are in a semi-staggered configuration with respect to each other, which is clearly sterically favourable. Generally the two tetrahedra constituting the diphosphate groups are often found to be highly distorted, but with average P-O distances of around 1.540 Å.[14] Here the average P-O distance was found to be similar at ~1.55 Å.

Table 3.1: *Refined structural parameters from the 300 K neutron diffraction data on α-$NH_4MnP_2O_7$. Proton displacement factors (U_{iso}) were constrained to be equal.*

Atom	Site	Occupancy	*x*	*y*	*z*	U_{iso}/ Å^2	BVS[15]
Mn	4*e*	1.0	0.738(2)	0.099(1)	0.755(2)	0.015(2)	3.28
P(1)	4*e*	1.0	0.625(1)	0.4078(9)	0.8300(9)	0.011(2)	5.08
P(2)	4*e*	1.0	0.926(1)	0.3761(9)	0.6870(9)	0.010(2)	4.63
O(1)	4*e*	1.0	0.586(1)	0.2576(8)	0.7508(9)	0.018(2)	1.74
O(2)	4*e*	1.0	0.639(1)	0.4051(9)	1.0007(9)	0.018(2)	1.94
O(3)	4*e*	1.0	0.822(1)	0.4525(8)	0.8013(9)	0.011(2)	2.09
O(4)	4*e*	1.0	0.483(1)	0.4986(8)	0.7266(9)	0.010(2)	2.05
O(5)	4*e*	1.0	0.945(1)	0.2191(8)	0.7434(8)	0.011(2)	1.68
O(6)	4*e*	1.0	0.827(1)	0.3978(8)	0.5133(9)	0.014(2)	1.72
O(7)	4*e*	1.0	1.134(1)	0.4293(8)	0.740(1)	0.013(2)	1.79
N	4*e*	1.0	0.3183(8)	0.3124(6)	0.4520(8)	0.018(1)	3.27
H(1)	4*e*	1.0	0.274(4)	0.384(3)	0.496(3)	0.076(3)	0.96
H(2)	4*e*	1.0	0.404(3)	0.348(2)	0.379(3)	0.076(3)	0.62
H(3)	4*e*	1.0	0.215(3)	0.274(2)	0.379(2)	0.076(3)	0.89
H(4)	4*e*	1.0	0.406(2)	0.266(2)	0.538(2)	0.076(3)	0.82

Space group $P2_1/c$, a = 7.4252(3) Å, b = 9.6990(4) Å, c = 8.6552(4) Å and β = 105.627(3)°. Figures of merit: R_{wp} = 1.18%, R_p = 0.95%, χ^2 = 1.543.

Table 3.2: *Selected Bond Distances (Å) and Angles (degrees) for α-$NH_4MnP_2O_7$*

Mn-O(1)	1.90(2)	**Mn-O(5)**	1.95(1)
Mn-O(2)	2.13(2)	**Mn-O(6)**	2.15(2)
Mn-O(4)	1.95(2)	**Mn-O(7)**	1.90(2)
O(1)-Mn-O(2)	87.5(6)	**O(2)-Mn-O(7)**	92.0(7)
O(1)-Mn-O(4)	84.2(6)	**O(4)-Mn-O(5)**	173.3(9)
O(1)-Mn-O(5)	89.3(7)	**O(4)-Mn-O(6)**	87.4(6)
O(1)-Mn-O(6)	91.5(7)	**O(4)-Mn-O(7)**	89.6(6)
O(1)-Mn-O(7)	173.7(9)	**O(5)-Mn-O(6)**	91.2(7)
O(2)-Mn-O(4)	90.5(7)	**O(5)-Mn-O(7)**	97.0(7)
O(2)-Mn-O(5)	90.8(6)	**O(6)-Mn-O(7)**	88.9(6)
O(2)-Mn-O(6)	177.7(8)		
P(1)-O(1)	1.60(1)	**P(2)-O(3)**	1.59(1)
P(1)-O(2)	1.45(1)	**P(2)-O(5)**	1.593(9)
P(1)-O(3)	1.61(1)	**P(2)-O(6)**	1.50(1)
P(1)-O(4)	1.48(1)	**P(2)-O(7)**	1.58(1)
O(1)-P(1)-O(2)	112.0(7)	**O(3)-P(2)-O(5)**	105.8(6)
O(1)-P(1)-O(3)	104.2(6)	**O(3)-P(2)-O(6)**	111.8(7)
O(1)-P(1)-O(4)	105.4(6)	**O(3)-P(2)-O(7)**	105.3(6)
O(2)-P(1)-O(3)	110.1(6)	**O(5)-P(2)-O(6)**	114.9(7)
O(2)-P(1)-O(4)	118.1(7)	**O(5)-P(2)-O(7)**	103.0(7)
O(3)-P(1)-O(4)	106.1(6)	**O(6)-P(2)-O(7)**	115.1(7)
N-H(1)	0.90(3)	**H(1)---O(6)**	2.24(3)
N-H(2)	1.07(3)	**H(2)---O(1)**	2.22(3)
N-H(3)	0.93(2)	**H(2)---O(4)**	2.04(3)
N-H(4)	0.96(2)	**H(3)---O(5)**	2.03(2)
		H(4)---O(1)	1.97(2)

The MnO_6 octahedra appear to display a [2+2+2] Jahn-Teller distortion, with two long bonds of 2.13 Å and 2.15 Å to the trans ligands O(2) and O(6), two intermediate bond lengths of 1.95 Å and two shorter bonds 1.90 Å in length. However, it should be noted that the four shorter bond lengths are within two standard errors of each other (95% confidence interval), suggesting that the MnO_6 coordination sphere may be better described by a [4+2] distortion. Bond Valence Sum (BVS) calculations according to the values provided by Brown and Altermatt[15] show that the Mn^{3+} in the structure is slightly overbonded, with a BVS value of +3.28 (see Table 3.1). On the other hand, calculations at the phosphorus centres reveal that P(2) is slightly underbonded, with BVS (P(1)) = +5.08 and BVS (P(2)) = +4.63. This indicates that there are steric bond strains present in both the MnO_6 and PO_4 units, and so although the Mn^{3+} appears to exhibit a "plastic" coordination sphere, the structural requirements of the pyrophosphate unit are not completely fulfilled by the Mn^{3+} adopting a distorted octahedral environment. The Global Instability Index (GII) (see Appendix 1) can be used to measure the extent of deviation from the valence sum rule, by taking the root mean square of the bond valence sum deviations.[16] Generally, GII values above 0.2 valence units (vu) indicate the structure is unstable and values between 0.1-0.2 vu indicate that there are lattice-induced strains present in the structure. Here a value of 0.23 vu was obtained, indicating that there is a strong degree of lattice strain present due to the distortions in both the MnO_6 and PO_4 units.

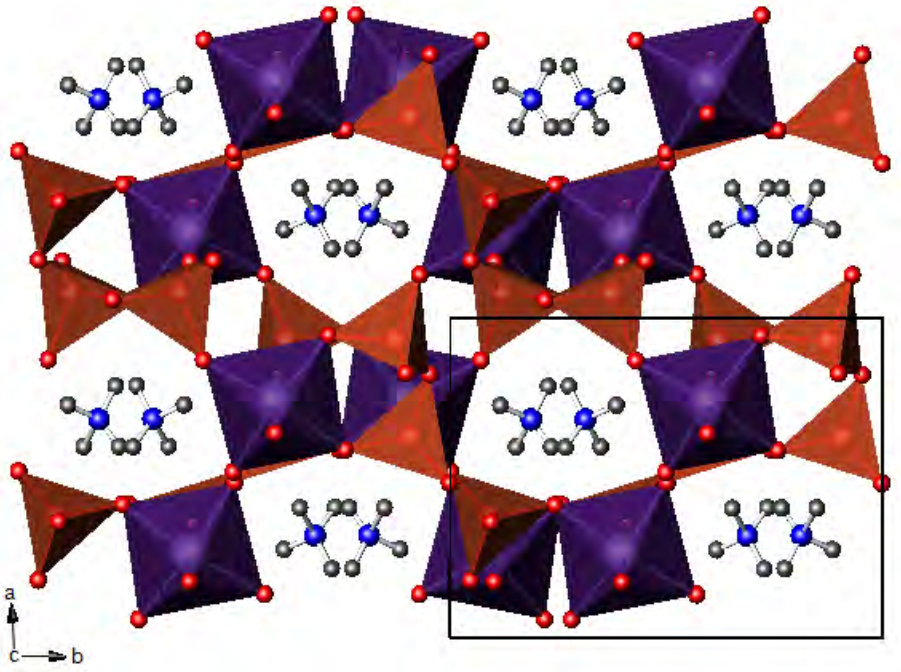

Figure 3.2: *Structure of α-$NH_4MnP_2O_7$ viewed down the c-axis, showing MnO_6 octahedra (purple), P_2O_7 condensed phosphate tetrahedra (red) and ammonium cations located in the intersecting tunnels. The thin black line defines the unit cell.*

3.3.2 α-$NH_4MnP_2O_7$ *cf.* commercial Manganese Violet (grade VM42)

Initial analysis of the X-ray diffraction data on the commercial manganese violet pigment (grade VM42) revealed that the sample contained at least 3 crystalline phases (Figure 3.3): α-$NH_4MnP_2O_7$ (as above), β-$NH_4MnP_2O_7$ and a third unidentified phase. Although the latter two phases could not be identified using the JCPDS[9] database, it was clear from the diffraction data that the peaks arising from the β-$NH_4MnP_2O_7$ polymorph were similar to those of the α-$NH_4MnP_2O_7$ polymorph. This allowed the selection of 26 independent reflections from this phase for input into the Crysfire[17] program. From this, the Kohl[18-19] indexing program was able to successfully assign a triclinic cell and a subsequent search on the ICSD[20] database revealed that these lattice parameters closely matched those of $RbAlAs_2O_7$[21], which then served as the structural model in the Rietveld refinement of this phase.

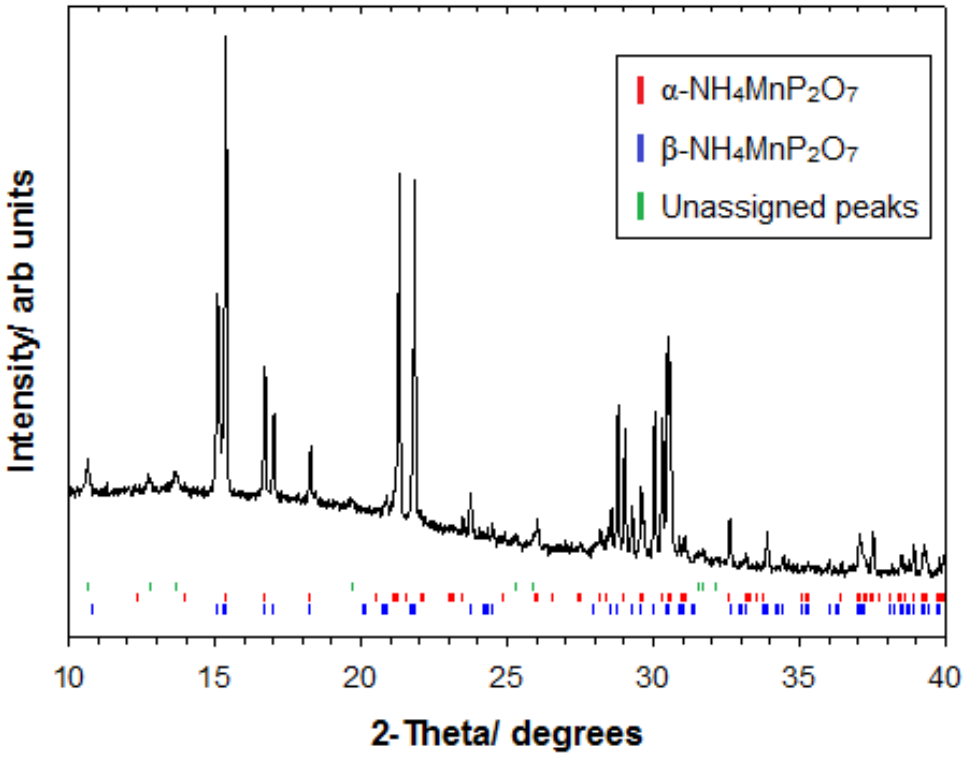

Figure 3.3: *XRD pattern of a commercial manganese violet pigment. Marker positions below the pattern indicate assignment of reflections.*

A two-phase refinement of the neutron diffraction data was employed and converged to an R_{wp} value of 1.55% (Figure 3.4). From this, β-$NH_4MnP_2O_7$ was confirmed as crystallising in space group $P\bar{1}$ with lattice parameters of a = 8.4034(6) Å, b = 6.1498(4) Å, c = 6.1071(4) Å, α = 104.618(5)°, β = 100.748(5)°, γ = 96.802(6)° and V = 295.45(3) $Å^3$, with the refinement suggesting that the α- and β-polymorphs exist within the sample in the approximate ratio of 2:1, respectively. Given the different crystal systems (monoclinic *vs.* triclinic), the volume of the α-phase (V = 600.29(4) $Å^3$) was found to be approximately twice that of the β-phase, though both phases showed similar densities of ~2.73 g cm^{-3}.

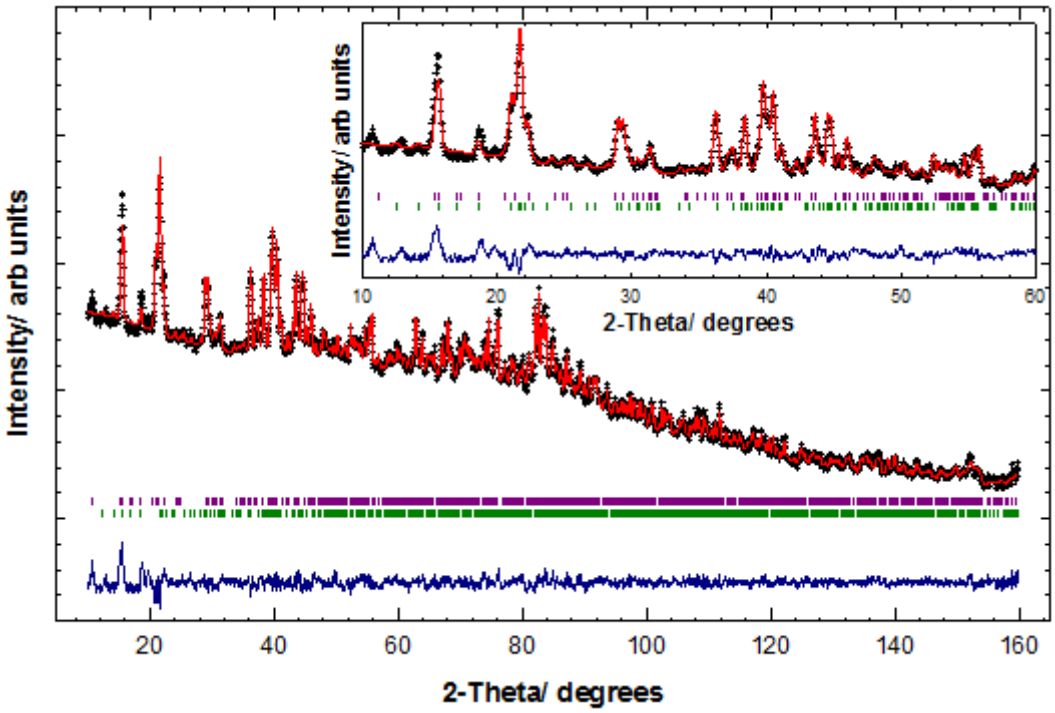

Figure 3.4: *Observed (+), calculated (-) and difference profiles (-) for the Rietveld refinement carried out on VM42. Green and purple markers indicate reflection positions for the α- and β-$NH_4MnP_2O_7$ phases, respectively and the inset shows an expansion of the 10-60° 2θ region.*

It is worth noting at this stage that we were unable to locate the protons in the β-phase, principally due to the complexity of the neutron diffraction pattern for this sample. The $RbAlAs_2O_7$[21] structural model clearly does not account for proton positions, though we would expect the NH_4^+ cations to be located in similar positions to the Rb^+ cations, given their comparable ionic radii of 1.59-1.69 Å[22] and 1.59 Å,[23] respectively. Indeed, refinements indicated that the best fit to the data was when the model was adapted to locate the nitrogens of the NH_4 groups on the rubidium sites. This led to two symmetrically inequivalent nitrogen atoms within the unit cell, found on the (0, 0, 0) and (½, 0, 0) inversion centres. Location of NH_4 cations here clearly violates the T_d point group symmetry of the ammonium cation, but attempts to refine the nitrogen atoms elsewhere within the channels proved unsuccessful. The implications of this are that the polymorph may contain disordered NH_4 groups

compatible with the local symmetry. Alternatively, the quality of the data may not be sufficient to determine the potential subtly in the orientation of the NH_4 groups. This could be as a result of the relatively low β-$NH_4MnP_2O_7$ phase content in this multiphase dataset, compounded by the high background. Therefore, due to this incomplete structural detail, only preliminary findings on the β-$NH_4MnP_2O_7$ phase are reported, for the purpose of comparing to the α-polymorph. The refined structural parameters are shown in Table 3.3, with selected bond lengths and angles given in Table 3.4.

Table 3.3: *Refined structural parameters for β-$NH_4MnP_2O_7$ (global isotropic displacement factor used), obtained from a two-phase Rietveld refinement on VM42.*

Atom	Site	Occupancy	*x*	*y*	*z*	U_{iso} / Å^2
Mn	2*i*	1.0	0.230(4)	0.695(6)	0.377(6)	0.008(1)
P(1)	2*i*	1.0	0.321(3)	0.243(4)	0.476(4)	0.008(1)
P(2)	2*i*	1.0	0.200(3)	0.523(4)	0.816(4)	0.008(1)
O(1)	2*i*	1.0	0.224(2)	-0.021(4)	0.409(4)	0.008(1)
O(2)	2*i*	1.0	0.513(3)	0.255(3)	0.463(4)	0.008(1)
O(3)	2*i*	1.0	0.236(3)	0.359(3)	0.335(4)	0.008(1)
O(4)	2*i*	1.0	0.320(2)	0.370(3)	0.738(3)	0.008(1)
O(5)	2*i*	1.0	0.035(3)	0.371(3)	0.779(4)	0.008(1)
O(6)	2*i*	1.0	0.203(2)	0.689(3)	0.683(4)	0.008(1)
O(7)	2*i*	1.0	0.274(2)	0.656(4)	0.072(4)	0.008(1)
N(1)	1*a*	1.0	0	0	0	0.008(1)
N(2)	1*d*	1.0	0.5	0	0	0.008(1)

Space group $P\bar{1}$, a = 8.4034(6) Å, b = 6.1498(4) Å, c = 6.1071(4) Å, α = 104.618(5)°, β = 100.748(5)° and γ = 96.802(6)°. Figures of merit: R_{wp} = 1.55%, R_p = 1.18%, χ^2 = 4.852.

Table 3.4: *Selected Bond Distances (Å) and Angles (degrees) for β-$NH_4MnP_2O_7$.*

Mn-O(1)	1.72(4)	**Mn-O(5)**	2.02(4)
Mn-O(2)	2.15(4)	**Mn-O(6)**	1.93(4)
Mn-O(3)	2.02(4)	**Mn-O(7)**	1.93(4)
P(1)-O(1)	1.64(3)	**P(2)-O(4)**	1.52(3)
P(1)-O(2)	1.63(3)	**P(2)-O(5)**	1.52(3)
P(1)-O(3)	1.40(3)	**P(2)-O(6)**	1.46(3)
P(1)-O(4)	1.59(3)	**P(2)-O(7)**	1.55(3)
O(1)-Mn-O(2)	95(2)	**O(2)-Mn-O(7)**	92(2)
O(1)-Mn-O(3)	179(2)	**O(3)-Mn-O(5)**	93(2)
O(1)-Mn-O(5)	87(2)	**O(3)-Mn-O(6)**	83(2)
O(1)-Mn-O(6)	98(2)	**O(3)-Mn-O(7)**	88(2)
O(1)-Mn-O(7)	91(2)	**O(5)-Mn-O(6)**	95(2)
O(2)-Mn-O(3)	85(2)	**O(5)-Mn-O(7)**	89(2)
O(2)-Mn-O(5)	177(2)	**O(6)-Mn-O(7)**	170(2)
O(2)-Mn-O(6)	83(2)		

Similarly to α-$NH_4MnP_2O_7$, Figures 3.5 and 3.6 show that the structure of β-$NH_4MnP_2O_7$ also consists of a three-dimensional network of distorted MnO_6 octahedra corner-linked to five P_2O_7 units, one of them in a bidentate fashion. This results in alternating hexagonal tunnels running along the *b*- and *c*-directions of the structure, which contain the N(2) and N(1) ammonium cations, respectively. This feature is a notable structural difference between the two polymorphs: whilst α-$NH_4MnP_2O_7$ possesses one pore type of approximate dimensions ~4.0 × ~4.0 Å, β-$NH_4MnP_2O_7$ possesses two similar pore types, one ~2.8 × ~4.2 Å in size and the other ~3.2 × ~4.9 Å in size.

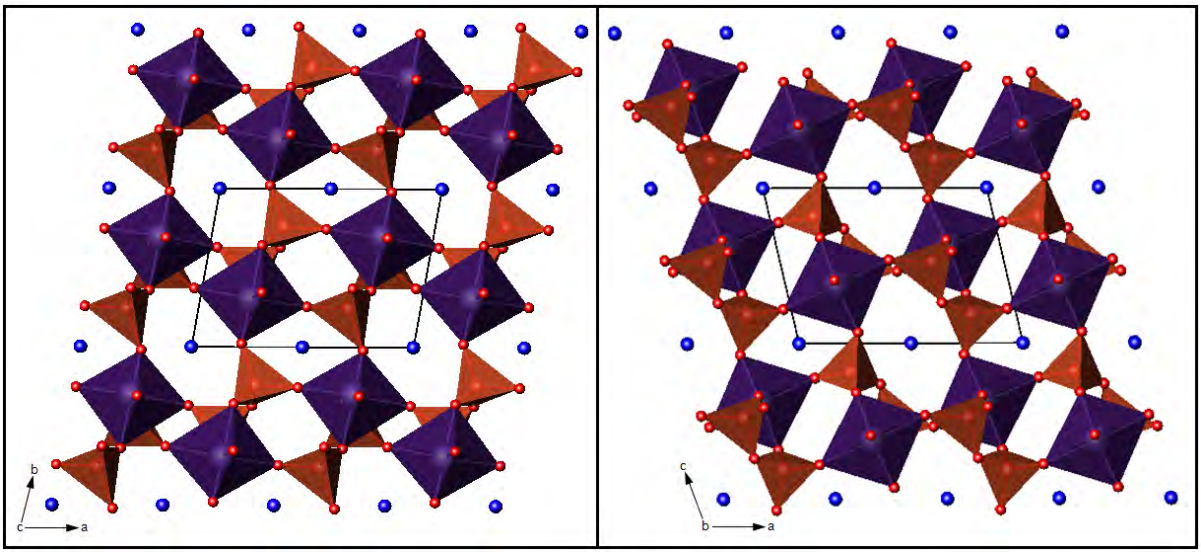

Figure 3.5: *Structure of β-$NH_4MnP_2O_7$ viewed down the b- and c-axes, showing MnO_6 octahedra (purple), P_2O_7 condensed phosphate tetrahedra (red) and ammonium cations located in the intersecting tunnels (nitrogen atoms as blue spheres). The thin black lines define the unit cell.*

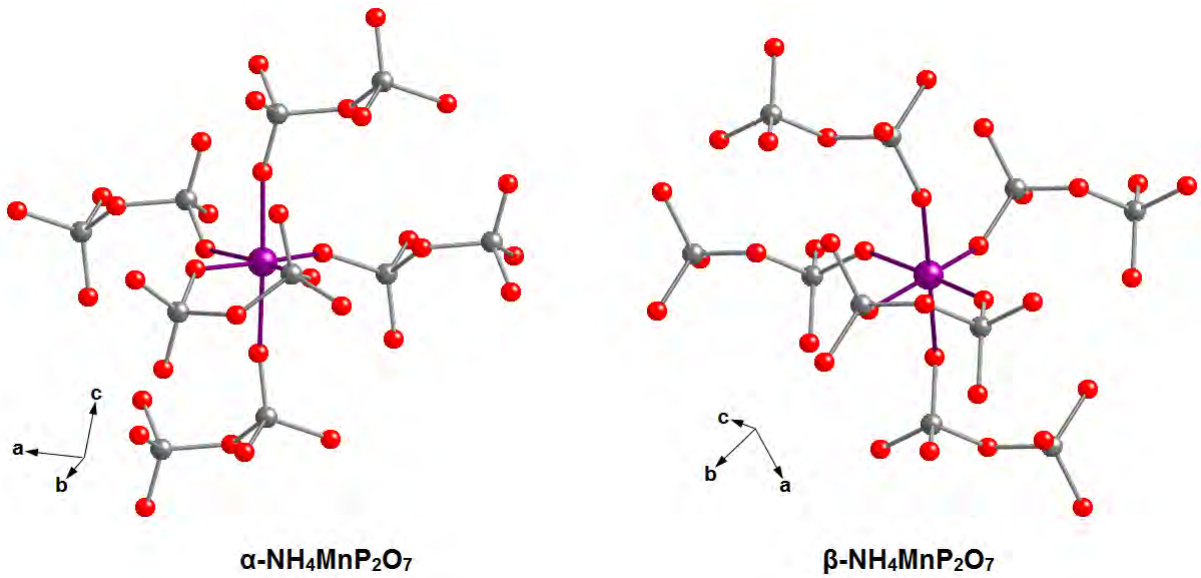

Figure 3.6: *Orientation of the diphosphate groups about the Mn^{3+} centres in the α- and β-polymorphs. The manganese, phosphorus and oxygen atoms are shown as purple, grey and red spheres, respectively.*

The two PO_4 tetrahedra that constitute the P_2O_7 unit in β-$NH_4MnP_2O_7$ are also reasonably distorted, though the averaged P-O distance comes to the expected value of ~1.54 Å. From our initial results it seems that there are no obvious

differences in the relative configuration of these units between the two polymorphs, with both showing a semi-staggered arrangement and O---O dihedral angles of a similar magnitude (see Figure 3.7 and Table 3.5). Furthermore, for both polymorphs the O-P-O angles lie in the range of 103-118° and the P-O-P bridging angles are approximately 126°. It is therefore likely to be subtle differences in the MnO_6 octahedra and PO_4 tetrahedra that contribute to driving the β-$NH_4MnP_2O_7$ polymorph to adopt a triclinic symmetry; indeed, we believe that this is the first reported $M^{I}M^{III}P_2O_7$ system that crystallises in such low symmetry.

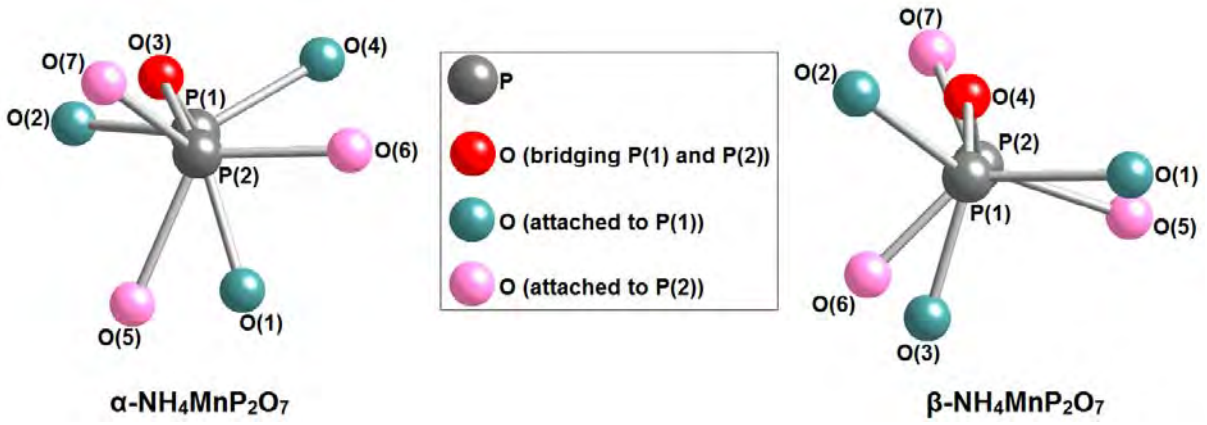

Figure 3.7: *Comparison of the relative P_2O_7 configurations in the α- and β-polymorphs*

Table 3.5: *O-P-O angles and approximate P-O-P bridging and O---O dihedral angles (degrees) within the P_2O_7 units of the α- and β-$NH_4MnP_2O_7$ polymorphs. Oxygen labels are not directly comparable between the two structures (see Figure 3.7) and errors associated with O---O dihedral angles have been estimated.*

α-$NH_4MnP_2O_7$		**β-$NH_4MnP_2O_7$**	
O(1)-P(1)-O(2)	112.0(7)	**O(1)-P(1)-O(2)**	112(2)
O(1)-P(1)-O(3)	104.2(6)	**O(1)-P(1)-O(3)**	109(2)
O(1)-P(1)-O(4)	105.4(6)	**O(1)-P(1)-O(4)**	109(2)
O(2)-P(1)-O(3)	110.1(6)	**O(2)-P(1)-O(3)**	113(2)
O(2)-P(1)-O(4)	118.1(7)	**O(2)-P(1)-O(4)**	106(2)
O(3)-P(1)-O(4)	106.1(6)	**O(3)-P(1)-O(4)**	107(2)
O(3)-P(2)-O(5)	105.8(6)	**O(4)-P(2)-O(5)**	108(2)
O(3)-P(2)-O(6)	111.8(7)	**O(4)-P(2)-O(6)**	105(2)
O(3)-P(2)-O(7)	105.3(6)	**O(4)-P(2)-O(7)**	107(2)
O(5)-P(2)-O(6)	114.9(7)	**O(5)-P(2)-O(6)**	116(2)
O(5)-P(2)-O(7)	103.0(7)	**O(5)-P(2)-O(7)**	113(2)
O(6)-P(2)-O(7)	115.1(7)	**O(6)-P(2)-O(7)**	107(2)
P(1)-O(3)-P(2)	125.6(7)	**P(1)-O(4)-P(2)**	125.9(2)
O(1)---O(5)	65.2(1)	**O(1)---O(5)**	85.4(1)
O(2)---O(7)	116.7(1)	**O(2)---O(7)**	111.1(1)
O(4)---O(6)	80.6(1)	**O(3)---O(6)**	58.4(1)

3.3.2.1 UV-Vis Spectroscopy

Figure 3.8 shows that the electronic absorption spectra of α-$NH_4MnP_2O_7$ and the commercial manganese violet sample were quite similar. This was expected given that the commercial sample contained approximately twice as much of the α-$NH_4MnP_2O_7$ polymorph than the β-form, which would result in the characteristics of the former dominating the spectrum. Mn^{3+} exists as a high spin d^4 ion and when in a regular octahedral coordination environment, we would expect to see one spin-allowed absorbance band in the visible region due to the $^5E_g \rightarrow {}^5T_{2g}$ transition. The absorbance spectra shown in Figure 3.8 each show a broad peak that is in general agreement with this, although a closer inspection reveals that there are shoulders

towards the left hand side of these broad features, representative of a Jahn-Teller splitting of the energy levels, as was also suggested by the neutron diffraction data.

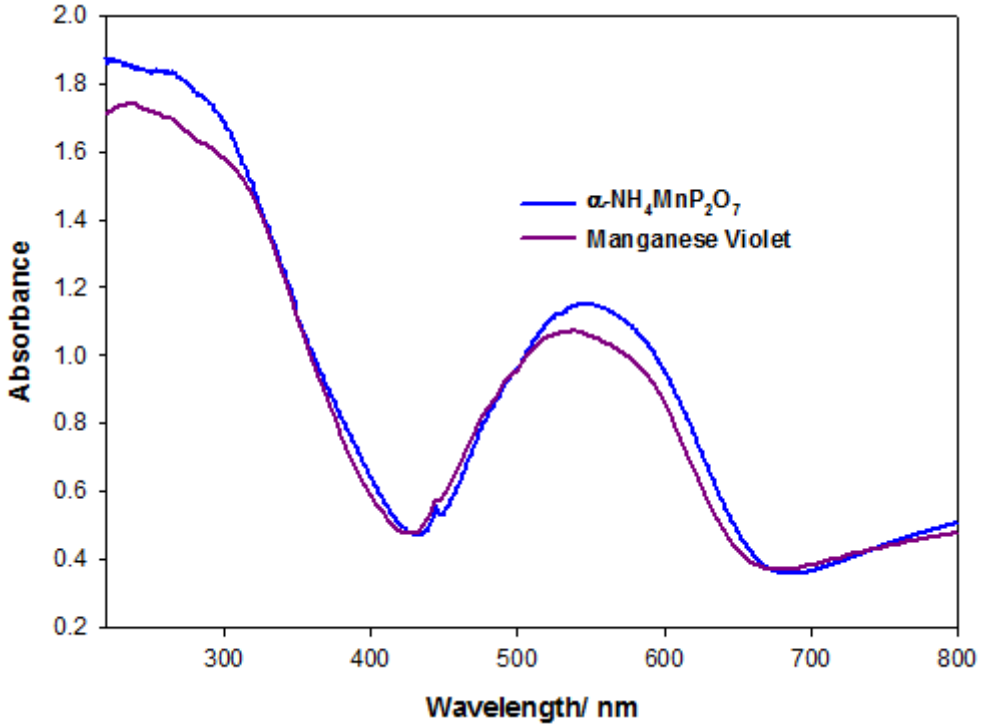

Figure 3.8: *UV-Vis absorbance spectra for α-$NH_4MnP_2O_7$ and a commercial manganese violet pigment*

The electronic properties of α-$NH_4MnP_2O_7$ are discussed in more detail in section 3.3.4.2, where this compound is compared to other members of the α-$NH_4Mn_xFe_{1-x}P_2O_7$ solid solution.

3.3.2.2 Thermal Stability

3.3.2.2.1. α-$NH_4MnP_2O_7$

The variable temperature XRD measurements in N_2 (Figure 3.9) showed that α-$NH_4MnP_2O_7$ remained present up to 342°C, but began to lose crystallinity at this stage and extra unidentified peaks appeared in the diffraction pattern. By 370°C complete loss of peaks belonging to α-$NH_4MnP_2O_7$ occurred to leave only this other unidentified phase present in a poorly crystalline state. Above 445°C, the final decomposition product of manganese (II) cyclotetraphosphate ($Mn_2P_4O_{12}$) began to crystallise and remained up to the last measurement temperature of 752°C. The TGA-MS plot given in Figure 3.10 indicated that an apparent mass loss of both H_2O and NH_3 had occurred in two almost simultaneous endothermic steps between 340-436°C and then 436-520°C. This is likely to correspond to the formation of the unidentified phase and then the formation of $Mn_2P_4O_{12}$, respectively.

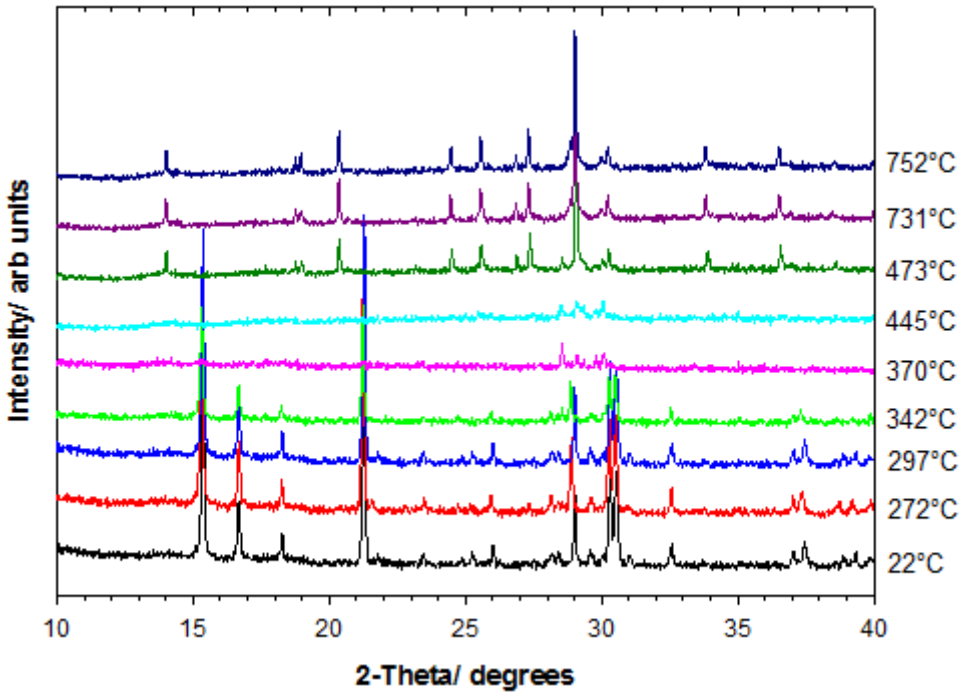

Figure 3.9: *Variable Temperature XRD of α-$NH_4MnP_2O_7$ showing thermal decomposition to manganese (II) cyclotetraphosphate.*

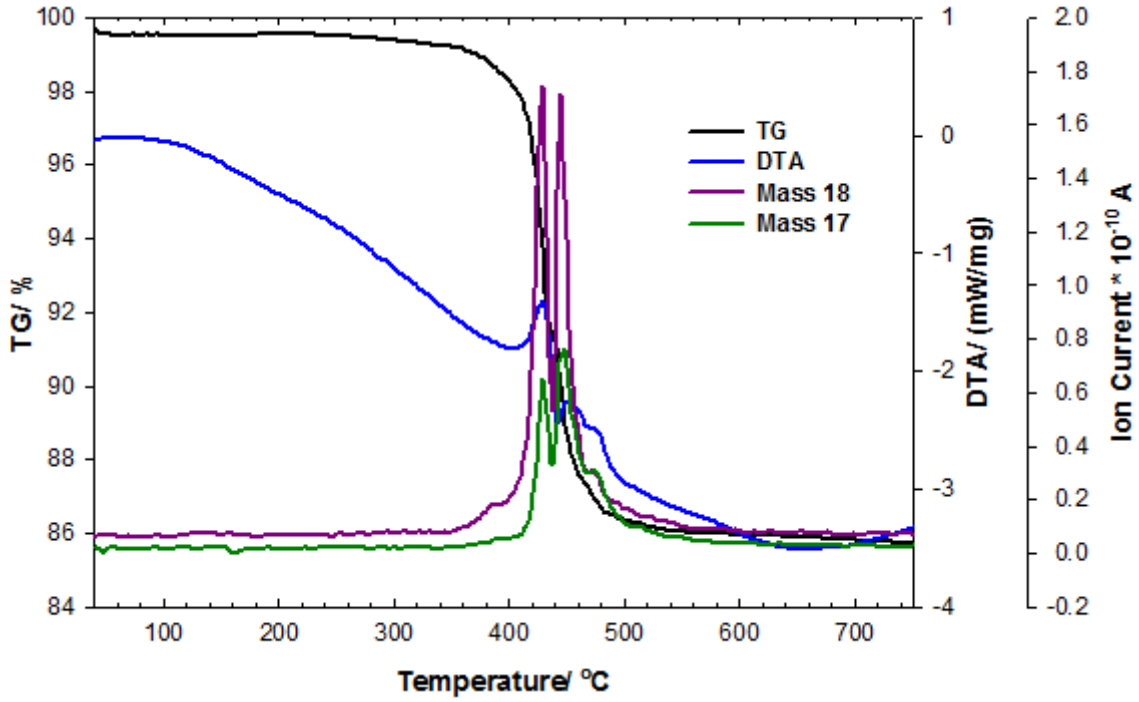

Figure 3.10: *TGA-MS Plot for α-$NH_4MnP_2O_7$.*

An overall mass loss of 13.75% was observed, which is consistent with the expected 13.79% for formation of $Mn_2P_4O_{12}$. At present it is unclear as to how exactly the cyclotetraphosphate is formed, as the poor crystallinity of the intermediate phase meant that it could not be identified using the JCPDS[9] database. Furthermore, independent heat treatments failed to isolate this phase, suggesting that it is metastable; indeed, after α-$NH_4MnP_2O_7$ had been heated to temperatures between 340-440°C and then cooled, subsequent room temperature XRD data found the samples to be either the reformed host material or in some cases, $Mn_2P_4O_{12}$.

3.3.2.2.2. VM42

Upon heating the VM42 compound, disappearance of the third, unknown phase was observed by 127°C, as indicated by the loss of peaks below 2θ = 15° in the variable temperature XRD measurements (Figure 3.11). The TGA-MS measurement in Figure 3.12 showed that a small endothermic mass loss of 2.21%

occurred between 127-240°C, which was assigned as water loss from this unknown phase, with the variable temperature measurements confirming that no change occurred to the α- and β-$NH_4MnP_2O_7$ polymorphs across this temperature range.

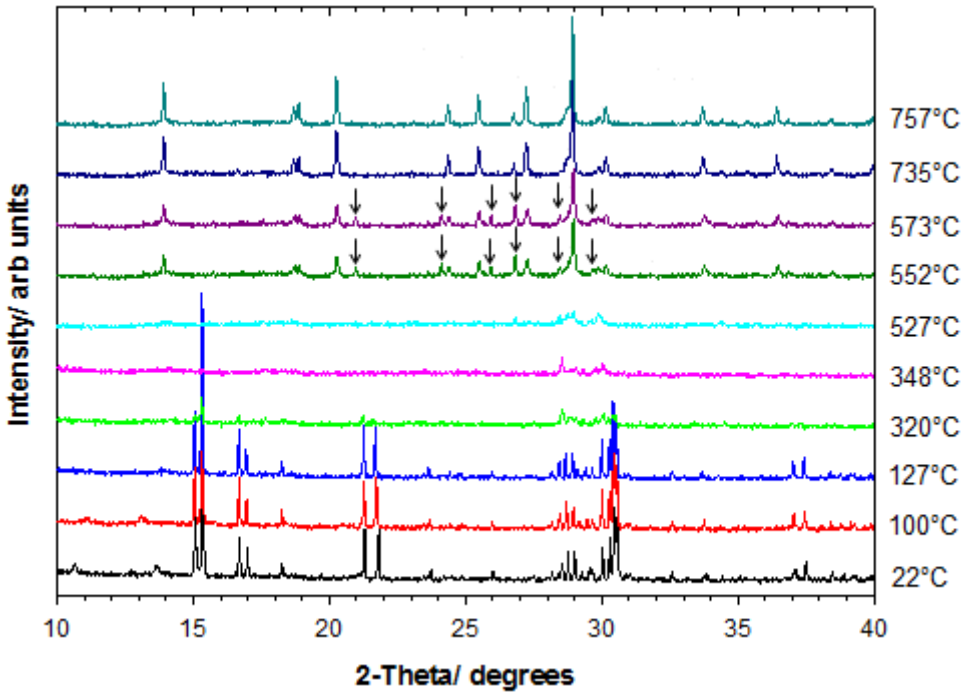

Figure 3.11: *Variable temperature XRD of the commercial manganese violet compound. Arrows indicate peaks that do not belong to the $Mn_2P_4O_{12}$ phase.*

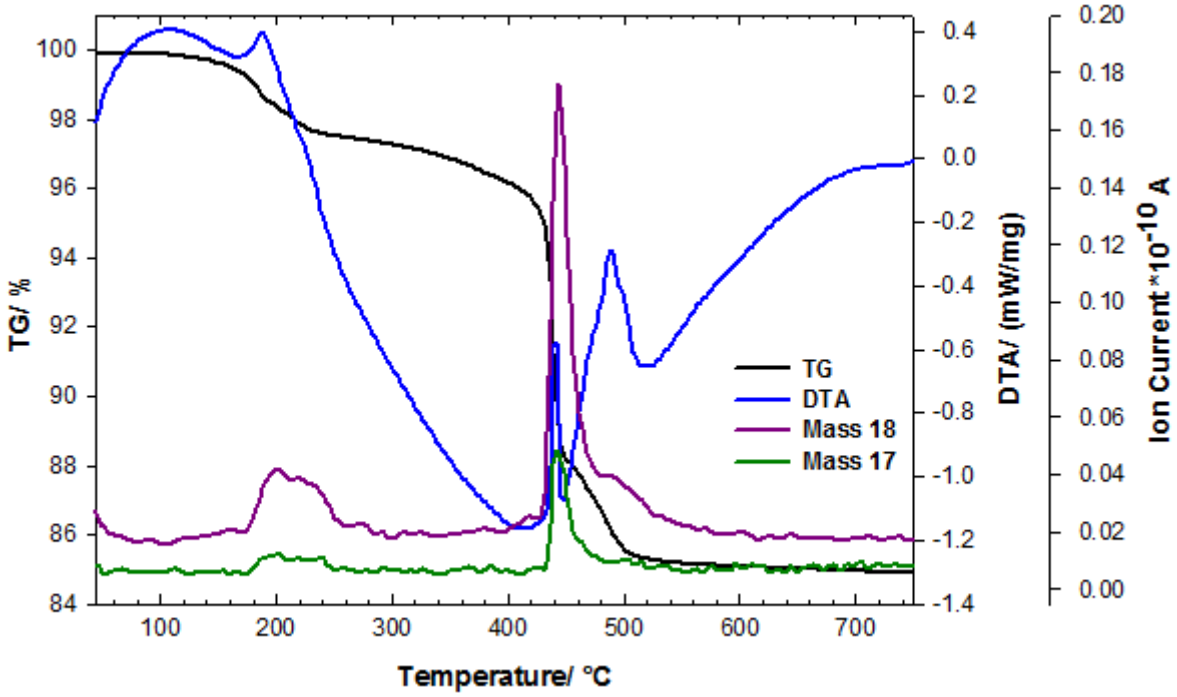

Figure 3.12: *TGA-MS Plot for the commercial manganese violet compound*

By 320°C, the α- and β-polymorphs were still present but with drastically reduced crystallinity. The relative intensities of their peaks with respect to each other remained the same as they were at 30°C, indicating that both polymorphs have a similar thermal stability. At this stage it also appeared that a similar intermediate phase to that observed after breakdown of the pure α-$NH_4MnP_2O_7$ compound (Figure 3.9) was formed. By 348°C we observed the apparent breakdown of both polymorphs, but the intermediate phase remained stable up to 527°C. The TGA-MS measurement showed that two further consecutive endothermic mass losses of H_2O and NH_3 occurred from ~320-448°C and then from 448-560°C. Again, these two mass loss steps are likely to correspond to formation of the intermediate phase and then the formation of $Mn_2P_4O_{12}$, respectively. It is worth noting that compared to the pure α-$NH_4MnP_2O_7$ phase, the mixture of polymorphs decomposed at a slightly lower temperature and the intermediate phase was observed over a wider temperature range. In the variable temperature XRD measurement, $Mn_2P_4O_{12}$ and at least one other unidentified phase (likely to have crystallised from the third phase) were observed at 552°C, but by 735°C only $Mn_2P_4O_{12}$ was observed as a crystalline phase. A total mass loss of 11.94% was observed between ~320-560°C, but as we do not know the exact composition of VM42 before and after the heat treatments, we were unable to establish what percentage mass loss would be expected. The measurements do however indicate that β-$NH_4MnP_2O_7$ exhibits similar thermal behaviour to α-$NH_4MnP_2O_7$.

3.3.3 Ion exchange in α-$NH_4MnP_2O_7$

Ion exchange in the α-$NH_4MnP_2O_7$ compound was investigated as a potential route to synthesise other $M^IMnP_2O_7$ phases (M^I = alkali metal cation). Given that the NH_4 cations reside in the channels of the structure, attempts to remove and replace these with other species were undertaken. An approach was employed that has been reported to give M^I exchange in various polymorphs of $HMnP_2O_7$.[24-26] In brief, the host and an alkali metal nitrate were heated to temperatures close to the melting points of the nitrates, which are relatively low compared to those of other alkali metal salts (see Table 3.6). In theory, such elevated temperatures should result in enhanced mobility of the species involved, allowing the ammonium cation to be more readily exchanged, as detailed in equation 3.1 below. Any excess nitrate can then be removed from the reaction by washing with copious amounts of water.

$$\alpha\text{-}NH_4MnP_2O_7 + M^INO_3 \rightarrow \alpha\text{-}M^IMnP_2O_7 + NH_4NO_3 \qquad \text{[Equation 3.1]}$$

Table 3.6: *Melting points of various monovalent nitrate and chloride salts*[27]

Cation	Nitrate	Chloride
NH_4^+	170°C	520°C (triple point; decomposes)
Li^+	253°C	610°C
Na^+	307°C	801°C
K^+	334°C	771°C
Rb^+	310°C	724°C
Cs^+	409°C	646°C

Clearly there are other factors to be considered here, such as the size of the alkali cation to be exchanged. The ionic radius of an NH_4^+ cation in 5-9 fold coordination

ranges from 1.59-1.69 Å[22] and is comparable in size to K^+ and Rb^+, which have ionic radii of 1.59 Å and 1.66 Å, respectively, when in 10-fold coordination.[23] Indeed, this serves to explain why partial K^+ and Rb^+ exchange occurred. Li^+ and Na^+ exchange proved unsuccessful, with the host phase appearing to decompose to give a mixture of different phases. The melting point of $CsNO_3$ proved too high to attempt an ion exchange reaction, with the host phase decomposing before any change was observed.

Due to the melting points of KNO_3 and $RbNO_3$ being close to the temperature at which α-$NH_4MnP_2O_7$ begins to decompose (340°C), there was a limit to the reaction temperatures that could be used for ion exchange. Furthermore, it was found that the reaction was accompanied by the formation of a considerable amount of amorphous material. The most significant change in the diffraction pattern of the host was observed when it was heated with KNO_3 at 330°C and with $RbNO_3$ at 440°C, suggesting that these might be the optimum temperatures for exchange. Clearly the temperature at which the potential Rb exchange occurred was much higher than anticipated; indeed, at this temperature our variable temperature XRD suggests that the metastable intermediate (discussed in section 3.3.2.2.1) would be present. It is therefore likely that upon reaction with rubidium nitrate, this intermediate reverts to a structure type similar to the host. Figure 3.13 shows the change in diffraction pattern of the host when these reaction conditions were employed while Table 3.7 lists the corresponding lattice parameters. Due to the limited quality of the datasets for the exchanged phases, reliable structural detail could not be obtained from XRD Rietveld refinements. However, in varying the K and Rb fractional occupancies, we were able to confirm that these cations had been incorporated into

the host, with the refinements suggesting occupancies of 30(1)% and 79(1)%, respectively (see Appendix 2).

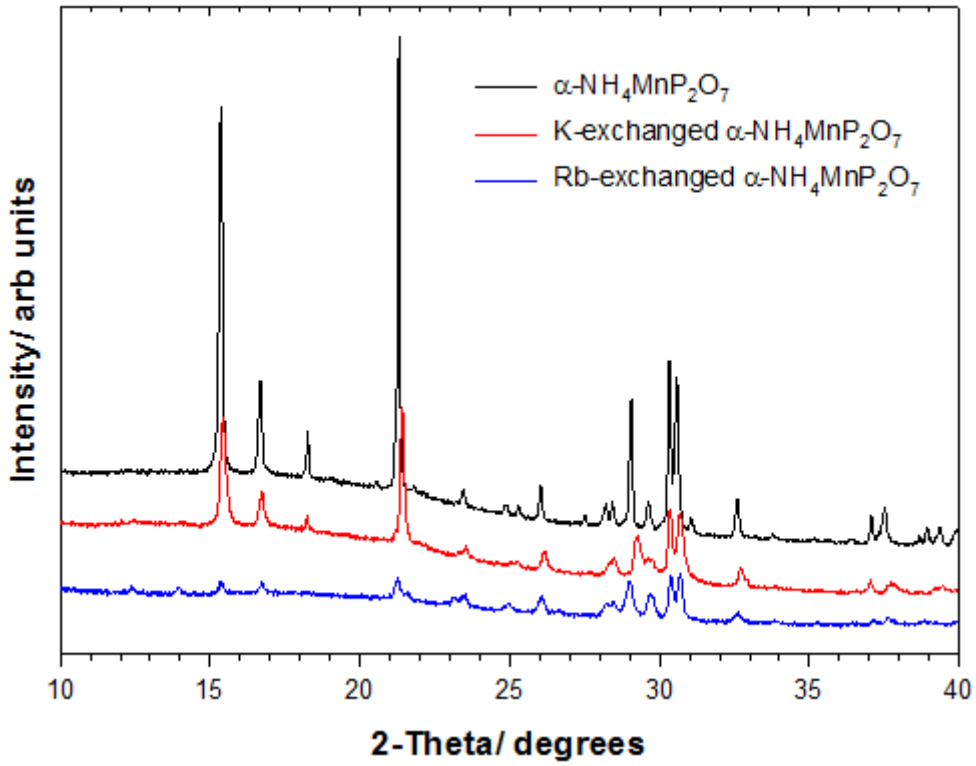

Figure 3.13: *X-ray Diffraction Patterns of α-$NH_4MnP_2O_7$ and K- and Rb-exchanged phases*

Table 3.7: *XRD lattice parameters of α-$NH_4MnP_2O_7$, K- and Rb-exchanged phases. The lattice parameters of as-synthesised $RbMnP_2O_7$ are also given for comparison.*

	a/ Å	**b/ Å**	**c/ Å**	**β/ °**	**Volume/ Å^3**
α-$NH_4MnP_2O_7$	7.4133(2)	9.6828(3)	8.6414(2)	105.651(2)	597.30(5)
K-exchanged α-$NH_4MnP_2O_7$	7.3494(5)	9.6847(6)	8.5955(5)	105.905(5)	588.38(9)
Rb-exchanged α-$NH_4MnP_2O_7$	7.3778(8)	9.6656(9)	8.6463(9)	105.423(5)	594.4(2)
$RbMnP_2O_7$	7.3905(1)	9.6755(1)	8.6610(1)	105.335(1)	597.27(2)

Further evidence for exchange was obtained from XRF measurements on the loose powders and TGA measurements. The XRF measurements were performed with internal instrument calibration ("standard-less" analysis), so should be treated more as a qualitative rather than quantitative analysis. The data obtained (Table 3.8) clearly confirms that K^+ and Rb^+ were indeed incorporated into the final product, though XRF cannot differentiate between the crystalline and amorphous components of the sample. Figure 3.14 shows that upon heating, a total mass loss of 6.80% was observed for the K-exchanged phase and 3.58% for the Rb-exchanged phase, *cf.* 13.79% that would be expected if all of the ammonium cation were retained in the host. Moreover, the phases formed after thermal decomposition were found to contain potassium and rubidium, though all of the decomposition products could not be identified. In the case of K-exchange, the main decomposition products were found to be $KMnP_3O_9$ and $Mn_2P_4O_{12}$ and in the case of Rb-exchange, $RbMnP_2O_7$ and $Mn_2P_2O_7$.

Table 3.8: *XRF results for α-$NH_4MnP_2O_7$, K- and Rb-exchanged phases. Theoretical values for the latter two are based on full exchange.*

		Elemental Weight %			
		Mn	**P**	**K**	**Rb**
α-$NH_4MnP_2O_7$	Measured	31.2	22.8	0	0
	Theoretical	22.3	25.1	0	0
K-exchanged α-$NH_4MnP_2O_7$	Measured	29.6	22.2	4.9	0
	Theoretical	20.5	23.1	14.6	0
Rb-exchanged α-$NH_4MnP_2O_7$	Measured	25.0	16.4	0	20.1
	Theoretical	17.5	19.7	0	27.2

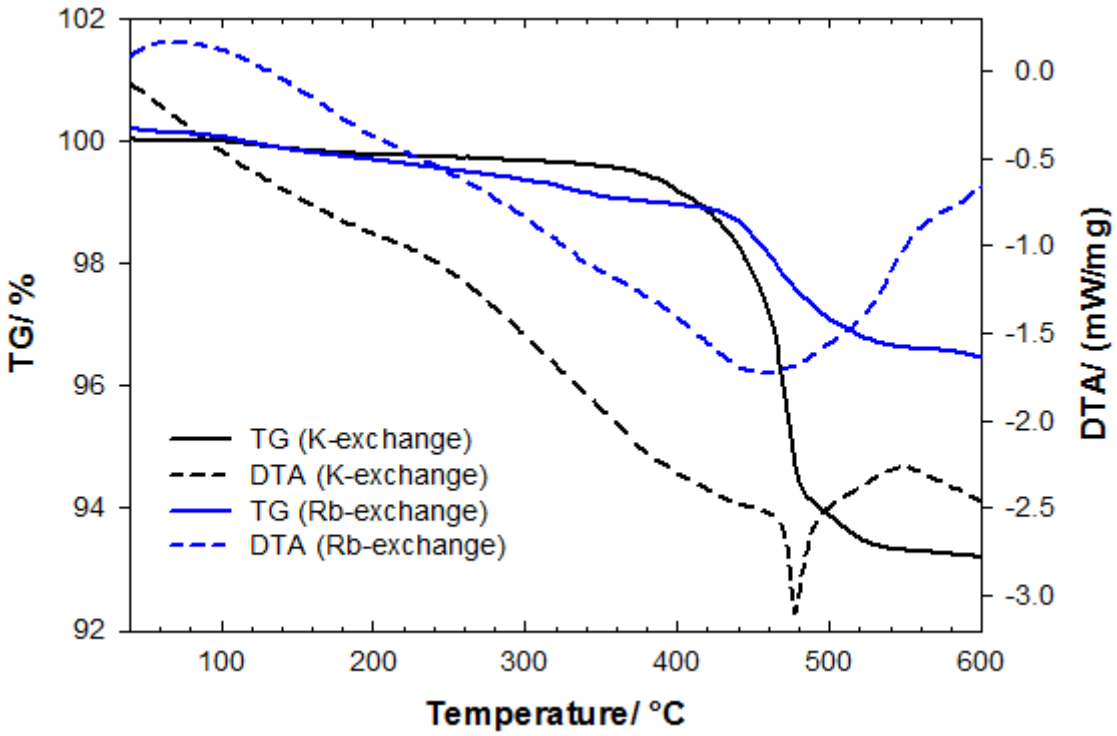

Figure 3.14: *TGA plots for K- and Rb-exchanged phases*

3.3.4 The α-$NH_4Mn_xFe_{1-x}P_2O_7$ System

In order to explore the potential impact of replacing manganese with other species, a study of the α-$NH_4Mn_xFe_{1-x}P_2O_7$ system was undertaken and the effects on the structural, optical, thermal and magnetic properties of the materials investigated. All members of the solid solution were successfully synthesised as pure phase compounds, with ND refinements shown in Figure 3.15, atomic coordinates in Table 3.9 and selected bond lengths and angles in Table 3.10. It is worth noting at this stage that for x = 0.75, a joint ND/ XRD refinement was performed in order to accurately locate the manganese and iron atoms within the structure. This is because at this composition the bound coherent scattering length of neutrons[28] from the transition metal (TM) site is approximately -0.3125 fm [(-3.73 fm × 0.75) + (9.94 fm × 0.25)], *cf.* the vanadium sample cylinder with a scattering length of -0.402 fm, used to

give negligible neutron scattering. A detailed structural description was given in section 3.3.1 and as such the focus here will lie with the change in properties of these materials as the series is traversed.

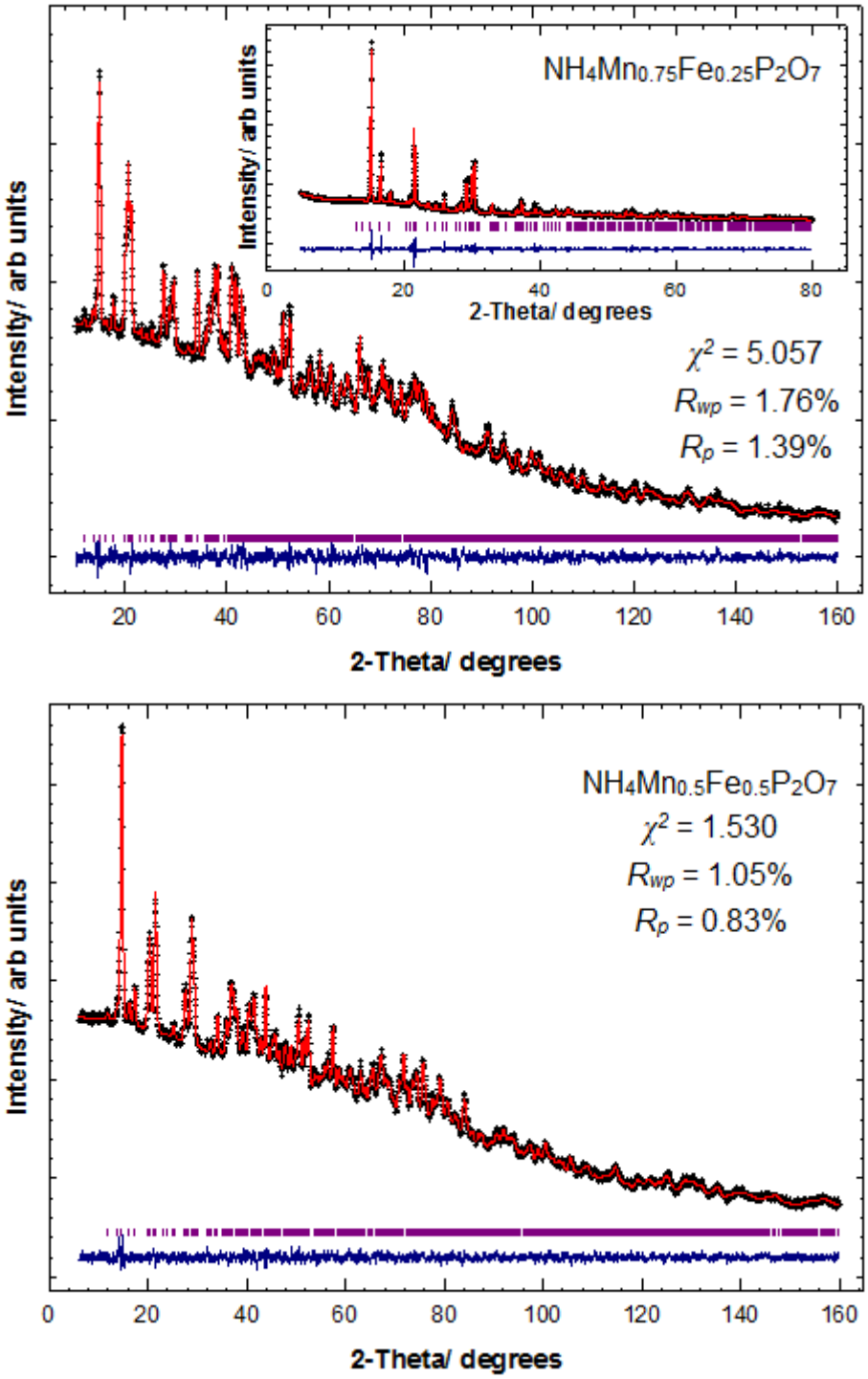

Figure 3.15: *Observed (+), calculated (-), difference profiles (-) and reflection positions (l) for the 300 K Rietveld refinements carried out on the $NH_4Mn_xFe_{1-x}P_2O_7$ (x = 0.75, 0.5, 0.25 and 0) series. The inset for x = 0.75 shows the XRD data refinement.*

Figure 3.15 continued...

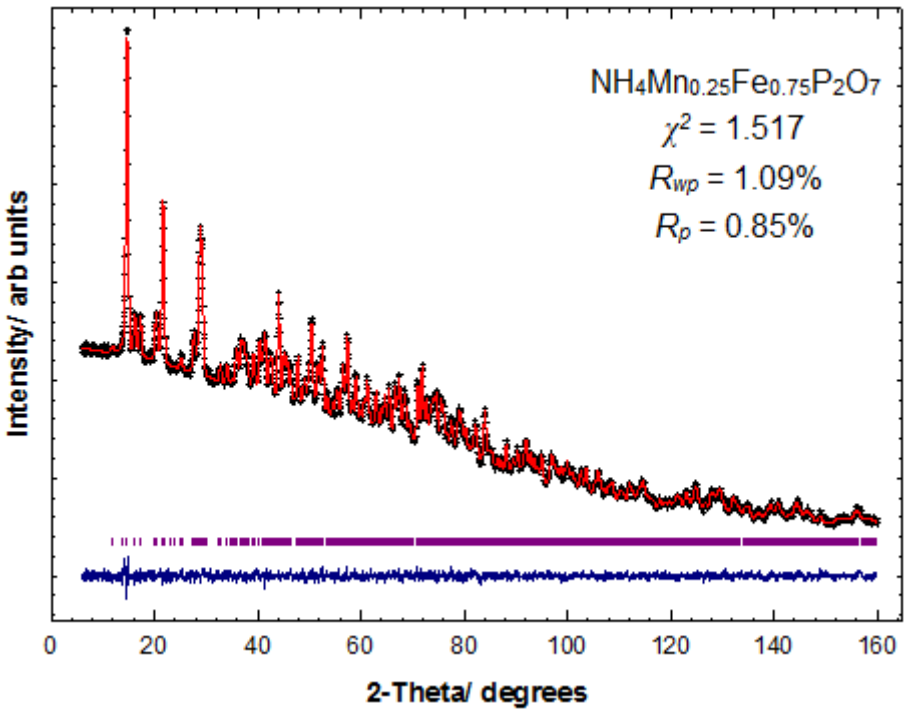

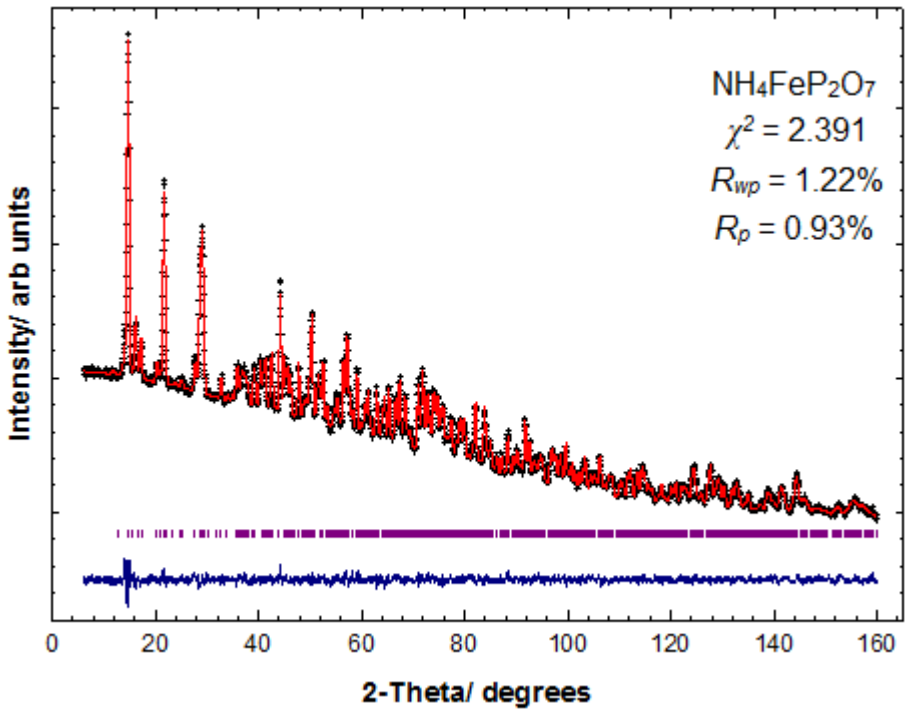

Table 3.9: *Refined structural parameters at 300 K for the α-$NH_4Mn_xFe_{1-x}P_2O_7$ series (x = 1, 0.75, 0.5, 0.25 and 0) with Bond Valence Sums[15]. Proton displacement factors (U_{iso}) were constrained to be equal for each compound.*

		x = 1	x = 0.75	x = 0.5	x = 0.25	x = 0
Space group $P2_1/c$	***a*/ Å**	7.4252(3)	7.4322(5)	7.5022(6)	7.5141(3)	7.5212(2)
	***b*/ Å**	9.6990(4)	9.7748(5)	9.9347(7)	9.9807(4)	10.0094(3)
	***c*/ Å**	8.6552(4)	8.4974(4)	8.3344(6)	8.2948(3)	8.2756(2)
	***β*/ °**	105.627(3)	105.672(4)	105.824(6)	105.872(3)	105.933(2)
Mn/ Fe 4*e*	***x***	0.738(2)	0.736(1)	0.737(1)	0.7391(7)	0.7390(4)
	y	0.099(1)	0.1027(7)	0.107(1)	0.1008(5)	0.1010(3)
	z	0.755(2)	0.763(1)	0.755(2)	0.7577(7)	0.7564(4)
	U_{iso}/ Å^2	0.015(2)	0.020(3)	0.002(3)	0.007(1)	0.0113(7)
	Occupancy	1/ 0	0.734(5)/ 0.266(5)	0.465(6)/ 0.535(6)	0.224(6)/ 0.776(6)	0/ 1
	BVS	3.28	3.36/ 3.35	3.22/ 3.21	3.18/ 3.17	3.23
P(1) 4*e*	***x***	0.625(1)	0.629(1)	0.633(1)	0.6287(9)	0.6284(7)
	y	0.4078(9)	0.407(1)	0.4071(7)	0.4082(6)	0.4064(5)
	z	0.8300(9)	0.843(1)	0.841(1)	0.8311(8)	0.8274(6)
	U_{iso}/ Å^2	0.011(2)	0.020(2)	0.009(2)	0.019(1)	0.016(1)
	Occupancy	1	1	1	1	1
	BVS	5.08	4.79	4.87	4.92	4.79
P(2) 4*e*	***x***	0.926(1)	0.925(1)	0.936(1)	0.931(1)	0.9326(9)
	y	0.3761(9)	0.3706(8)	0.369(1)	0.3706(7)	0.3664(6)
	z	0.6870(9)	0.6835(9)	0.696(1)	0.6883(9)	0.6925(8)
	U_{iso}/ Å^2	0.010(2)	0.006(2)	0.019(3)	0.024(2)	0.020(1)
	Occupancy	1	1	1	1	1
	BVS	4.63	4.95	4.73	4.88	4.95
O(1) 4*e*	***x***	0.586(1)	0.588(1)	0.588(1)	0.5863(7)	0.5870(6)
	y	0.2676(8)	0.2626(8)	0.2601(8)	0.2636(5)	0.2641(5)
	z	0.7508(9)	0.748(1)	0.753(1)	0.7577(8)	0.7550(7)
	U_{iso}/ Å^2	0.018(2)	0.013(2)	0.021(2)	0.022(1)	0.019(1)
	Occupancy	1	1	1	1	1
	BVS	1.74	1.73	1.68	1.69	1.76
O(2) 4*e*	***x***	0.639(1)	0.643(1)	0.642(1)	0.6480(9)	0.6488(8)
	y	0.4051(9)	0.4073(9)	0.4138(9)	0.4131(6)	0.4129(5)
	z	1.0007(9)	1.011(1)	1.011(1)	1.0141(8)	1.0174(7)
	U_{iso}/ Å^2	0.018(2)	0.014(2)	0.027(2)	0.024(1)	0.024(1)
	Occupancy	1	1	1	1	1
	BVS	1.94	2.19	2.32	2.02	1.90
O(3) 4*e*	***x***	0.822(1)	0.831(1)	0.831(1)	0.8266(9)	0.8273(7)
	y	0.4525(8)	0.4510(8)	0.4489(7)	0.4477(5)	0.4506(5)
	z	0.8013(9)	0.812(1)	0.813(1)	0.8042(8)	0.8024(7)
	U_{iso}/ Å^2	0.011(2)	0.013(2)	0.024(2)	0.020(1)	0.019(1)
	Occupancy	1	1	1	1	1
	BVS	2.09	1.83	1.98	2.07	2.02
O(4) 4*e*	***x***	0.483(1)	0.484(1)	0.492(1)	0.4903(8)	0.4895(7)
	y	0.4986(8)	0.5039(8)	0.5046(8)	0.5036(6)	0.5045(5)
	z	0.7266(9)	0.7245(9)	0.725(1)	0.7229(7)	0.7290(6)
	U_{iso}/ Å^2	0.010(2)	0.010(2)	0.023(2)	0.018(2)	0.016(1)
	Occupancy	1	1	1	1	1
	BVS	2.05	1.74	1.64	1.82	1.88

Table 3.9 continued...

		x = 1	x = 0.75	x = 0.5	x = 0.25	x = 0
	x	0.951(1)	0.941(1)	0.953(1)	0.9456(9)	0.9425(7)
O(5)	***y***	0.2191(8)	0.2252(8)	0.217(1)	0.2210(7)	0.2218(5)
4*e*	***z***	0.7434(8)	0.741(1)	0.746(1)	0.7376(8)	0.7369(6)
	U_{iso}/ Å^2	0.011(2)	0.008(2)	0.028(2)	0.024(1)	0.015(1)
	Occupancy	1	1	1	1	1
	BVS	1.68	1.91	1.74	1.75	1.95
	x	0.827(1)	0.825(1)	0.822(1)	0.8215(9)	0.8183(7)
O(6)	***y***	0.3978(8)	0.3972(9)	0.395(1)	0.3936(7)	0.3940(6)
4*e*	***z***	0.5133(9)	0.513(1)	0.513(1)	0.5083(9)	0.5102(7)
	U_{iso}/ Å^2	0.014(2)	0.011(2)	0.029(3)	0.029(2)	0.023(1)
	Occupancy	1	1	1	1	1
	BVS	1.72	1.99	1.63	1.85	1.72
	x	1.134(1)	1.128(1)	1.126(1)	1.1286(9)	1.1277(8)
O(7)	***y***	0.4293(8)	0.431(1)	0.429(1)	0.4258(7)	0.4245(5)
4*e*	***z***	0.740(1)	0.732(1)	0.730(1)	0.7353(8)	0.7340(7)
	U_{iso}/ Å^2	0.013(2)	0.021(2)	0.028(2)	0.024(1)	0.023(1)
	Occupancy	1	1	1	1	1
	BVS	1.79	1.72	1.85	1.79	1.77
	x	0.3183(8)	0.3156(9)	0.3121(9)	0.3141(6)	0.3160(6)
N	***y***	0.3124(6)	0.3158(6)	0.3102(6)	0.3103(4)	0.3126(4)
4*e*	***z***	0.4520(8)	0.450(1)	0.448(1)	0.4495(7)	0.4482(6)
	U_{iso}/ Å^2	0.018(1)	0.015(1)	0.025(2)	0.028(1)	0.030(1)
	Occupancy	1	1	1	1	1
	BVS	3.27	3.24	3.18	3.20	3.19
	x	0.274(4)	0.256(3)	0.279(3)	0.275(3)	0.269(2)
H(1)	***y***	0.384(3)	0.385(3)	0.390(2)	0.402(2)	0.392(2)
4*e*	***z***	0.496(3)	0.484(3)	0.500(3)	0.511(3)	0.508(2)
	U_{iso}/ Å^2	0.076(3)	0.063(4)	0.096(5)	0.092(3)	0.079(2)
	Occupancy	1	1	1	1	1
	BVS	0.96	0.96	0.79	0.53	0.64
	x	0.404(3)	0.392(3)	0.386(4)	0.386(3)	0.398(2)
H(2)	***y***	0.348(2)	0.365(2)	0.344(3)	0.339(2)	0.343(2)
4*e*	***z***	0.379(3)	0.384(3)	0.359(3)	0.373(3)	0.383(2)
	U_{iso}/ Å^2	0.076(3)	0.063(4)	0.096(5)	0.092(3)	0.079(2)
	Occupancy	1	1	1	1	1
	BVS	0.62	0.70	0.57	0.77	0.79
	x	0.215(3)	0.207(3)	0.199(4)	0.217(3)	0.212(3)
H(3)	***y***	0.274(2)	0.275(2)	0.279(2)	0.275(2)	0.279(2)
4*e*	***z***	0.379(2)	0.392(3)	0.401(4)	0.386(3)	0.389(2)
	U_{iso}/ Å^2	0.076(3)	0.063(4)	0.096(5)	0.092(3)	0.079(2)
	Occupancy	1	1	1	1	1
	BVS	0.89	0.92	1.02	1.10	1.05
	x	0.406(2)	0.420(3)	0.390(3)	0.397(3)	0.404(2)
H(4)	***y***	0.266(2)	0.274(2)	0.261(2)	0.269(2)	0.281(2)
4*e*	***z***	0.538(2)	0.543(3)	0.540(4)	0.547(3)	0.557(2)
	U_{iso}/ Å^2	0.076(3)	0.063(4)	0.096(5)	0.092(3)	0.079(2)
	Occupancy	1	1	1	1	1
	BVS	0.82	0.69	0.82	0.80	0.72

Table 3.10: *Selected Bond Distances (Å) and Angles (degrees) for the α-$NH_4Mn_xFe_{1-x}P_2O_7$ series (x = 1, 0.75, 0.5, 0.25 and 0) and Global Instability Index[16] Values*

	x = 1	x = 0.75	x = 0.5	x = 0.25	x = 0
TM-O(1)	1.90(2)	1.89(1)	1.89(2)	1.990(8)	1.991(6)
TM-O(2)	2.13(2)	2.06(1)	1.97(2)	1.953(9)	1.911(7)
TM-O(4)	1.95(2)	1.93(1)	2.04(1)	2.023(7)	2.004(6)
TM-O(5)	1.95(1)	1.99(1)	1.97(2)	2.004(8)	1.991(6)
TM-O(6)	2.15(2)	2.05(1)	2.07(2)	2.00(1)	2.021(7)
TM-O(7)	1.90(2)	1.96(1)	2.03(2)	2.002(8)	2.022(6)
O(1)-TM-O(2)	87.5(6)	86.7(5)	91.5(7)	91.1(4)	90.8(3)
O(1)-TM-O(4)	84.2(6)	86.2(6)	83.7(6)	83.5(3)	84.0(2)
O(1)-TM-O(5)	89.3(7)	86.7(5)	92.5(6)	88.4(3)	87.4(2)
O(1)-TM-O(6)	91.5(7)	95.1(5)	91.6(7)	89.5(4)	89.5(3)
O(1)-TM-O(7)	173.7(9)	176.0(7)	172.5(8)	173.8(4)	173.8(3)
O(2)-TM-O(4)	90.5(7)	89.0(5)	87.6(7)	89.0(3)	87.7(3)
O(2)-TM-O(5)	90.8(6)	89.2(5)	95.3(6)	91.0(3)	91.3(3)
O(2)-TM-O(6)	177.7(8)	177.2(6)	172.8(8)	176.5(4)	175.5(3)
O(2)-TM-O(7)	92.0(7)	90.7(5)	90.6(6)	90.0(3)	90.5(3)
O(4)-TM-O(5)	173.3(9)	172.7(6)	175.3(8)	171.9(4)	171.3(3)
O(4)-TM-O(6)	87.4(6)	89.1(6)	86.4(5)	87.7(3)	87.8(2)
O(4)-TM-O(7)	89.6(6)	90.7(5)	89.2(6)	90.4(3)	90.0(2)
O(5)-TM-O(6)	91.2(7)	93.0(5)	91.0(7)	92.5(3)	93.2(3)
O(5)-TM-O(7)	97.0(7)	96.4(6)	94.5(6)	97.8(4)	98.6(3)
O(6)-TM-O(7)	88.9(6)	87.3(5)	85.5(6)	89.1(3)	88.8(3)
P(1)-O(1)	1.60(1)	1.61(1)	1.63(1)	1.565(8)	1.544(7)
P(1)-O(2)	1.45(1)	1.41(1)	1.41(1)	1.486(9)	1.539(7)
P(1)-O(3)	1.61(1)	1.65(1)	1.62(1)	1.613(8)	1.627(7)
P(1)-O(4)	1.48(1)	1.58(1)	1.56(1)	1.511(8)	1.501(7)
P(2)-O(3)	1.59(1)	1.65(1)	1.62(1)	1.597(9)	1.600(8)
P(2)-O(5)	1.593(9)	1.50(1)	1.56(2)	1.54(1)	1.491(8)
P(2)-O(6)	1.50(1)	1.46(1)	1.55(1)	1.513(9)	1.542(8)
P(2)-O(7)	1.58(1)	1.57(1)	1.50(1)	1.529(9)	1.527(8)
O(1)-P(1)-O(2)	112.0(7)	117.6(8)	116.4(7)	112.4(6)	112.9(4)
O(1)-P(1)-O(3)	104.2(6)	101.9(7)	104.7(6)	105.7(4)	107.6(4)
O(1)-P(1)-O(4)	105.4(6)	101.8(7)	104.7(7)	108.4(5)	110.9(4)
O(2)-P(1)-O(3)	110.1(6)	110.0(7)	110.1(8)	107.2(5)	106.1(5)
O(2)-P(1)-O(4)	118.1(7)	119.6(7)	115.6(6)	116.5(5)	112.6(4)
O(3)-P(1)-O(4)	106.1(6)	103.7(7)	104.2(6)	105.9(5)	106.2(4)
O(3)-P(2)-O(5)	105.8(6)	104.3(6)	109.4(8)	108.5(5)	112.0(5)
O(3)-P(2)-O(6)	111.8(7)	112.3(6)	106.6(7)	107.3(5)	103.5(4)
O(3)-P(2)-O(7)	105.3(6)	101.4(6)	106.5(8)	106.0(6)	105.3(4)
O(5)-P(2)-O(6)	114.9(7)	118.0(7)	113.9(9)	112.8(6)	113.1(5)
O(5)-P(2)-O(7)	103.0(7)	106.6(7)	109.2(7)	106.6(6)	109.3(5)
O(6)-P(2)-O(7)	115.1(7)	112.6(7)	111.0(8)	115.2(6)	113.2(5)
N-H(1)	0.90(3)	0.90(2)	0.97(3)	1.12(3)	1.05(2)
N-H(2)	1.07(3)	1.02(3)	1.10(3)	0.98(2)	0.97(2)
N-H(3)	0.93(2)	0.92(3)	0.88(3)	0.85(3)	0.87(2)
N-H(4)	0.96(2)	1.03(3)	0.96(4)	0.97(3)	1.01(2)
GII	0.23	0.22	0.26	0.21	0.20

3.3.4.1 Trends and Jahn-Teller distortions

High spin octahedral Mn^{3+} and Fe^{3+} cations have similar ionic radii of 0.65 Å,[23] which can in part explain the existence of a solid solution across the whole α-$NH_4Mn_xFe_{1-x}P_2O_7$ range. The electronic requirements of these two cations are also important; whilst Mn^{3+} (d^4) is a Jahn-Teller active cation showing a preference for a [4+2] elongation, Fe^{3+} (d^5) is expected to show a more regular octahedral coordination sphere in which the six bond lengths are more similarly matched in length. Figure 3.16 shows the average transition metal to oxygen (TM-O) bond lengths obtained from the diffraction data. As was discussed earlier, for x = 1 the data suggests a [4+2] elongation of bond lengths (Figure 3.17). As the amount of iron in the system is increased, the bond lengths of the TM octahedron become more similar in length.

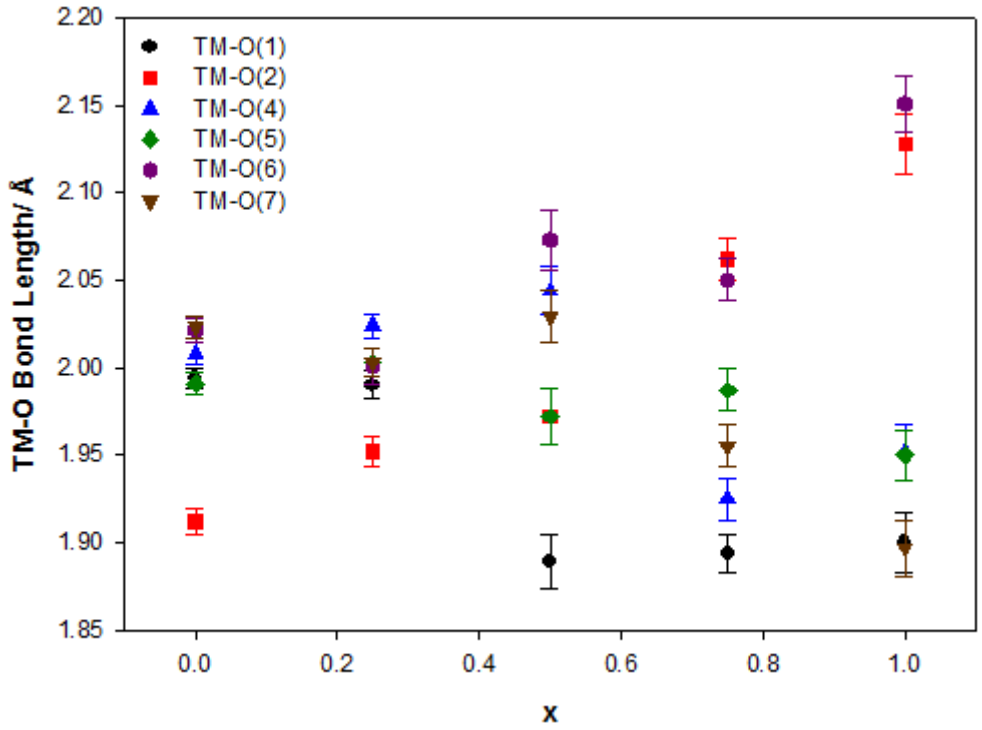

Figure 3.16: *Average bond lengths of the TM-O_6 octahedron as a function of varying Mn^{3+} content in the α-$NH_4Mn_xFe_{1-x}P_2O_7$ solid solution.*

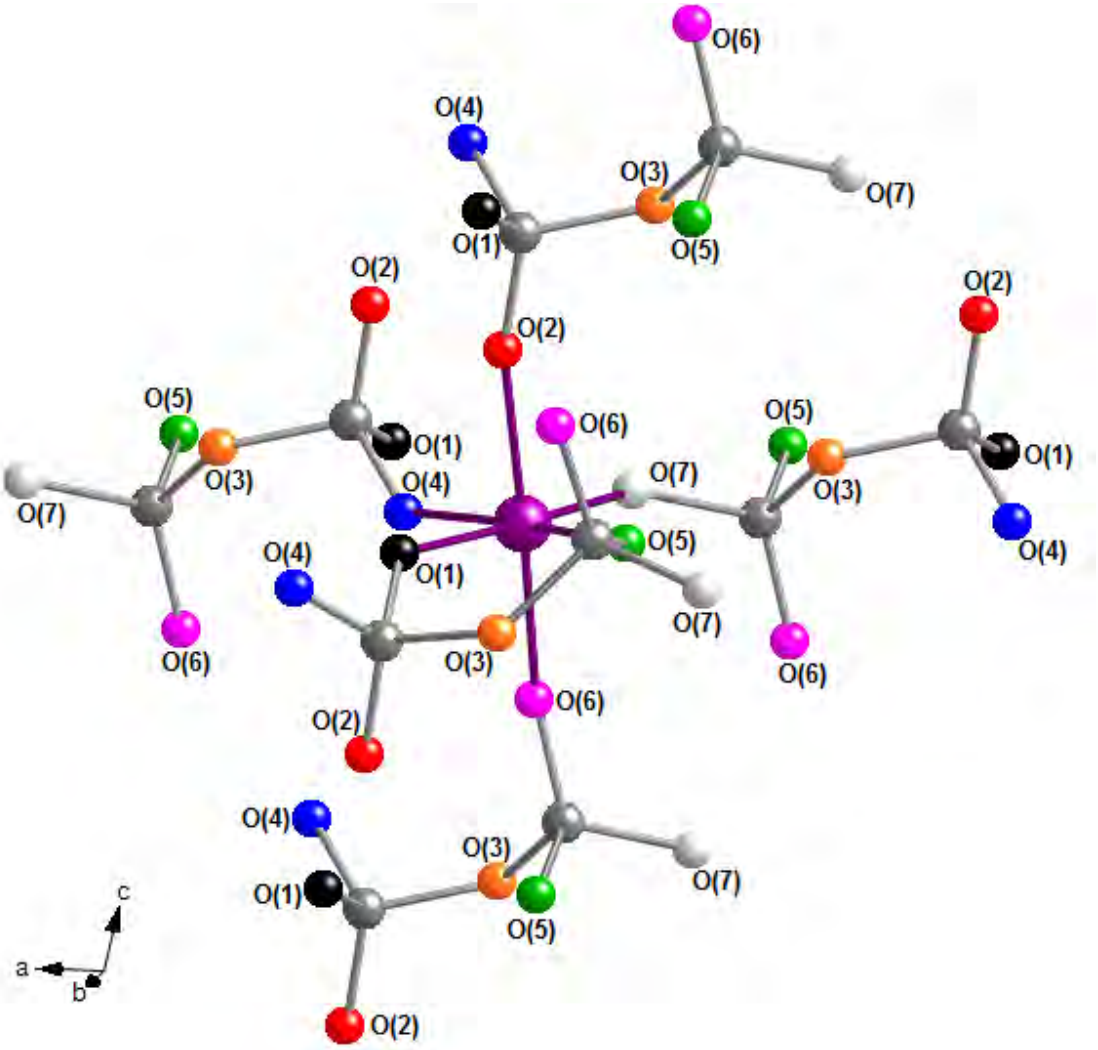

Figure 3.17: *Orientation of the pyrophosphate ligands about the TM centre in the α-$NH_4Mn_xFe_{1-x}P_2O_7$ structure type. The TM and phosphorus atoms are shown as purple and dark grey spheres, respectively.*

For x = 0.25 and 0, the TM-O(2) bond lengths are noticeably shorter than the other five, particularly for x = 0. The reason for this is at present unclear, with BVS values (Table 3.9) showing that the oxidation state of O(2) remained close to the expected value of -2. Although the P(1)-O(2) bond lengths are closer to the expected 1.54 Å for these two members, further inspection across the series (Figures 3.18 and 3.19) shows that these bond lengths are relatively long when compared with the other members of the solid solution. This may not necessarily be unusual but does

indicate that while the TM-O(2) bond becomes markedly shorter for x = 0.25 and 0, the P(1)-O(2) bond length becomes longer, perhaps in order to fulfil the bonding requirements of O(2). Similarly, the TM-O(1) bond is generally observed to become longer for these two members while the P(1)-O(1) bond length becomes shorter. A general increase in the P(1)-O(2) and P(2)-O(6) bond lengths with increasing Fe content is also observed, which can be related to a shortening of the TM-O(2) and TM-O(6) bonds as the transition metal coordination sphere becomes less distorted. It is also worth commenting that the P-O bond lengths to the bridging oxygen, O(3), do not significantly differ across the series and are generally found to be longer than P-O bonds to the terminal oxygens- this is a common observation in condensed phosphate systems.[14]

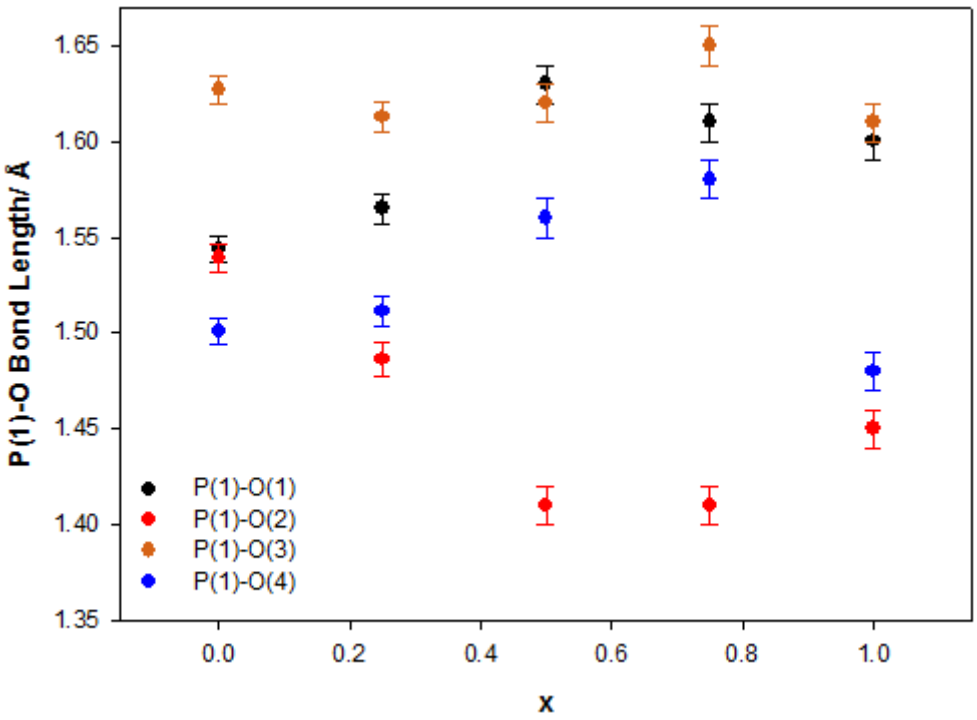

Figure 3.18: *Change in P(1)-O bond lengths as a function of varying Mn^{3+} content in the α-$NH_4Mn_xFe_{1-x}P_2O_7$ solid solution.*

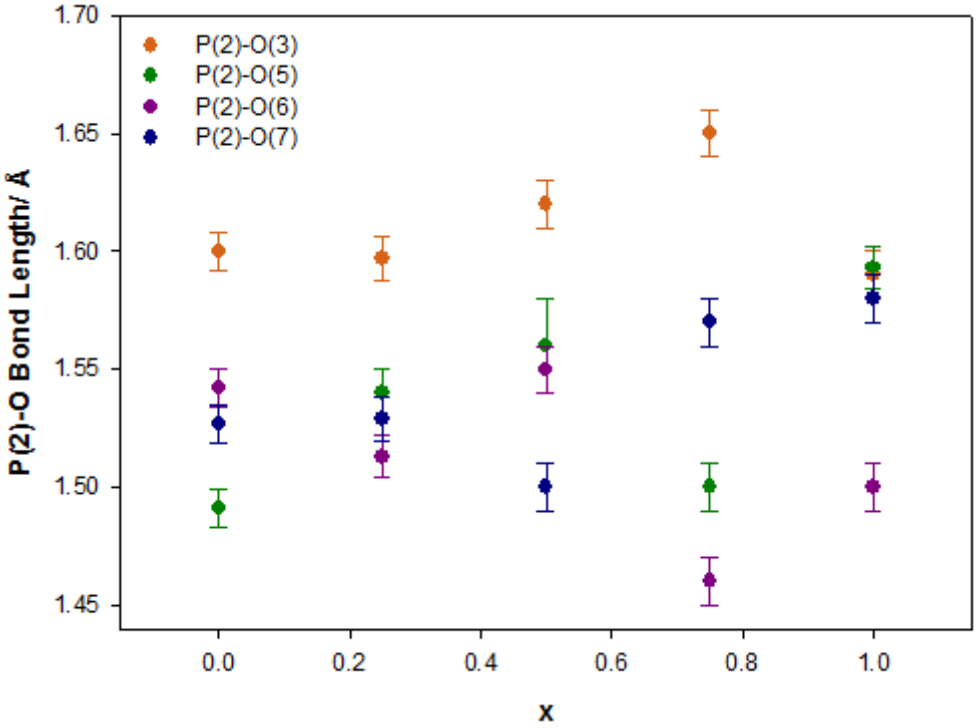

Figure 3.19: *Change in P(2)-O bond lengths as a function of varying Mn^{3+} content in the α-$NH_4Mn_xFe_{1-x}P_2O_7$ solid solution.*

Interestingly, all compounds gave similar GII values, ranging between 0.20-0.26 vu (Table 3.10), suggesting that the introduction of Fe into the system does relatively little to relieve the strains present in the structure. A maximum value of 0.26 vu was seen for x = 0.5 however, suggesting that this composition gives the least stable structure.

Figures 3.20 and 3.21 show that a general increase in the *c*-lattice parameter is observed with increasing Mn content, but a decrease is seen in the *a*-, *b*- and *β*-parameters.

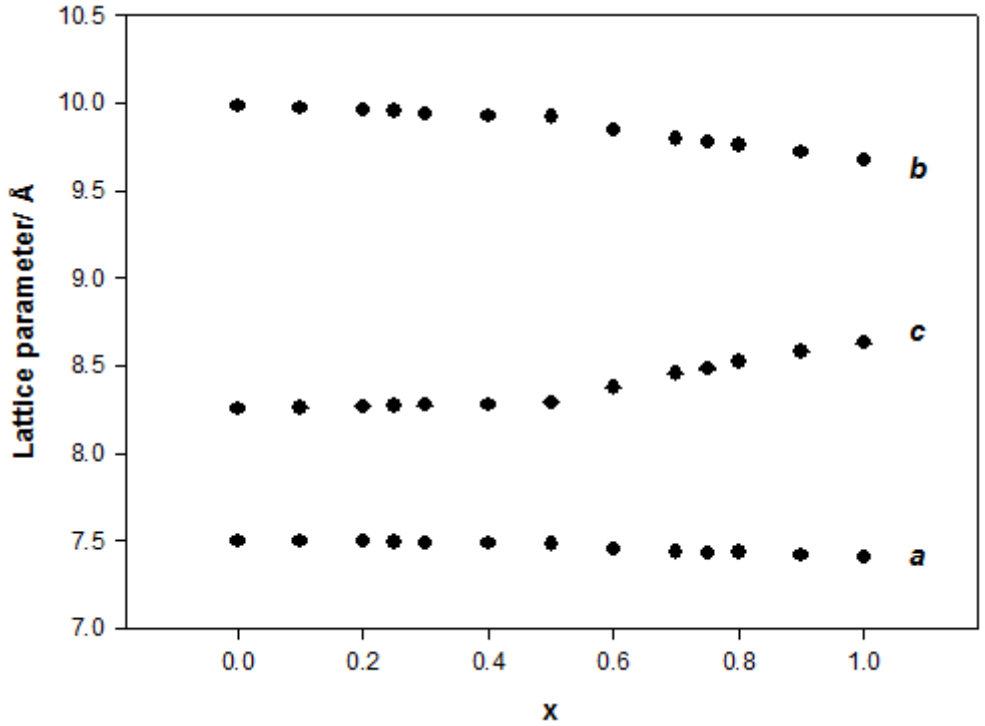

Figure 3.20: *Change in the a-, b- and c-lattice parameters with varying Mn^{3+} content in the α-$NH_4Mn_xFe_{1-x}P_2O_7$ solid solution (XRD data).*

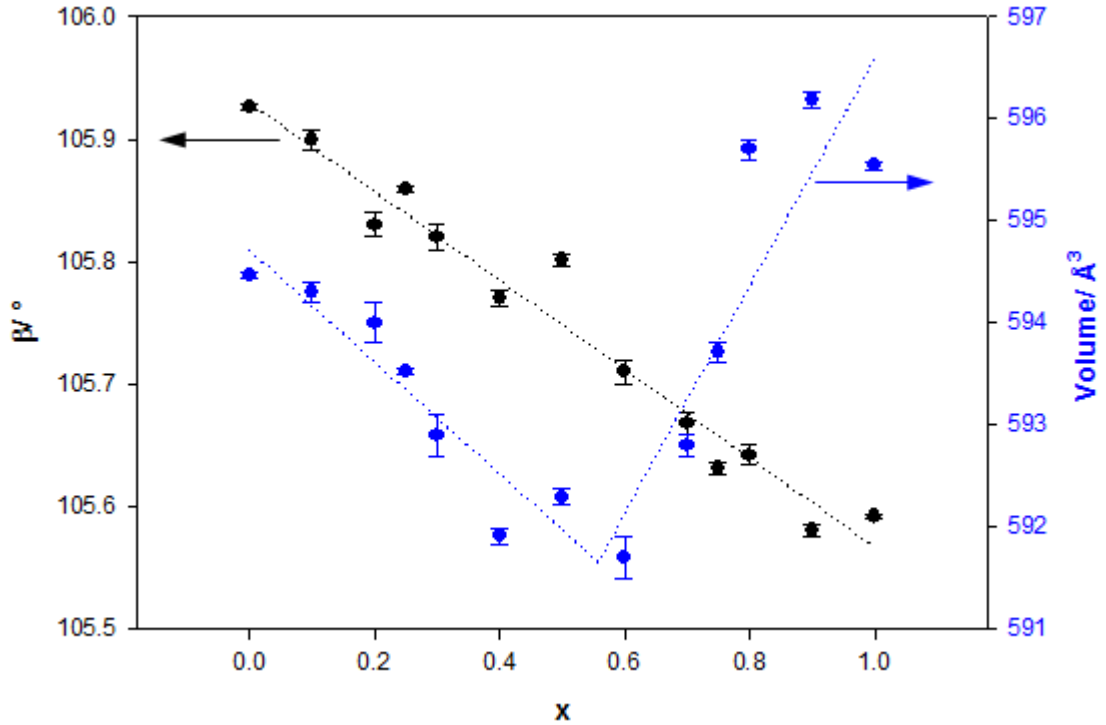

Figure 3.21: *Change in the β-parameter (●) and volume (●) of the unit cell with varying Mn^{3+} content in the α-$NH_4Mn_xFe_{1-x}P_2O_7$ solid solution (XRD data).*

A closer inspection of the structure (as shown in Figure 3.17) shows that the directions of the TM-O(2) and TM-O(6) bonds, which are those that are in particular elongated for x > 0.5, are closely correlated with the *c*-axis of the structure, whereas the remaining four bonds of the octahedron lie in between the trajectories of the unit cell axes. Referring back to Figure 3.16, generally it is observed that with increasing Mn content the TM-O(2) and TM-O(6) bond lengths become longer in length while the remaining four bonds become shorter. This can therefore explain the increase in *c* coupled to the decrease in the *a*- and *b*- unit cell parameters with increasing Mn content. A decrease in the *β*-angle can then occur because the largest difference between the *a*- and *c*- axes occurs for those compounds containing a greater amount of manganese, giving less repulsion between the oxygen ligands forming the transition metal octahedron. Thus it appears that the electronic requirements of the transition metal ions *i.e.* the extent of the Jahn-Teller effect dictates the trend in unit cell parameters. However, this effect is limited by the internal flexibility of the diphosphate unit, for which the P-O bonds need to remain within a certain range for effective covalent bonding to occur. The volume of the unit cell is at its lowest at x ≈ 0.5, where these competing effects are at a minimum and where it is likely that the electronic preferences of neither transition metal ion dominates.

3.3.4.2 UV-Vis Spectroscopy

The UV-Vis spectra of the α-$NH_4Mn_xFe_{1-x}P_2O_7$ series are shown in Figure 3.22. In all cases, absorbance bands were seen in the visible region. Octahedral Fe^{3+} has a $^6A_{1g}$ ground state for which intense d→d transitions are not expected to occur due to the absence of low lying excited states of the same spin. Transitions occurring due to octahedral Mn^{3+} on the other hand are spin-allowed and are therefore expected to be relatively intense, obscuring any bands exhibited by Fe^{3+}. Thus the bands observed in the visible region can provide information on the local Mn^{3+} environment. The PeakFit[29] program was used to resolve the spectra of these compounds in order to further investigate this and to obtain estimates of the transition energies, with the data being fitted to a sum of Gaussian bands on a constant baseline (see Chapter 2, section 2.4.7.3 for more details). It should be noted that such modelling of octahedral Mn^{3+} electronic spectra has also been reported in the literature.[30-32]

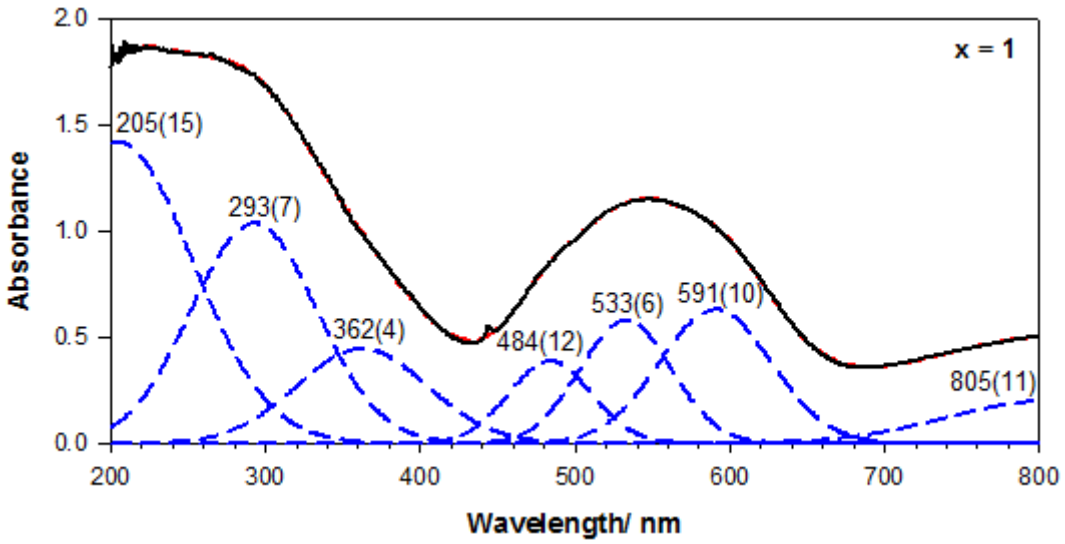

Figure 3.22: *UV-Vis spectra of the α-$NHMn_xFe_{1-x}P_2O_7$ series, showing raw data (—), fitted Gaussian bands (---) and sum of the fitted Gaussian bands (---). Peak positions are marked.*

Figure 3.22 continued...

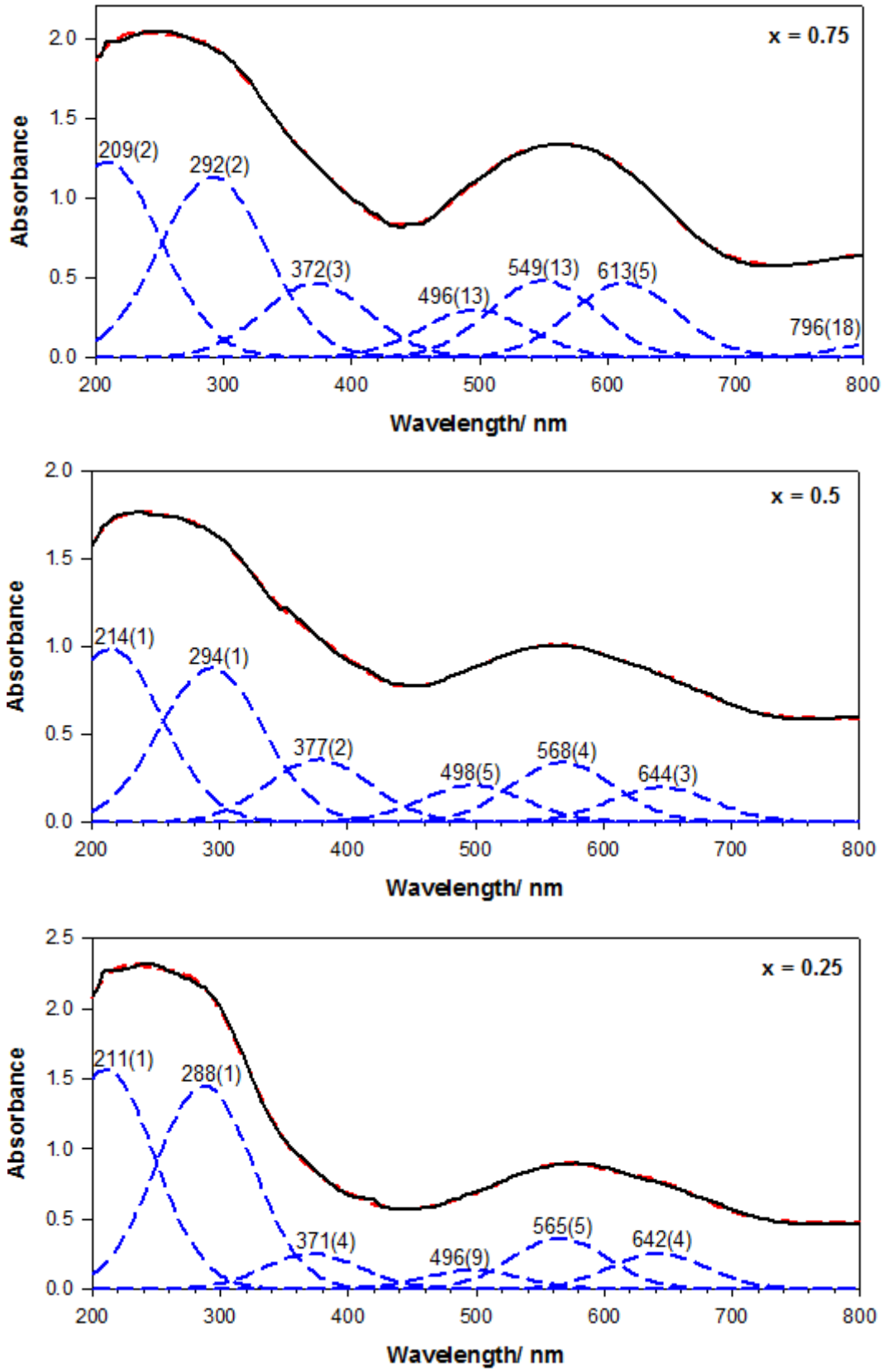

Figure 3.22 continued...

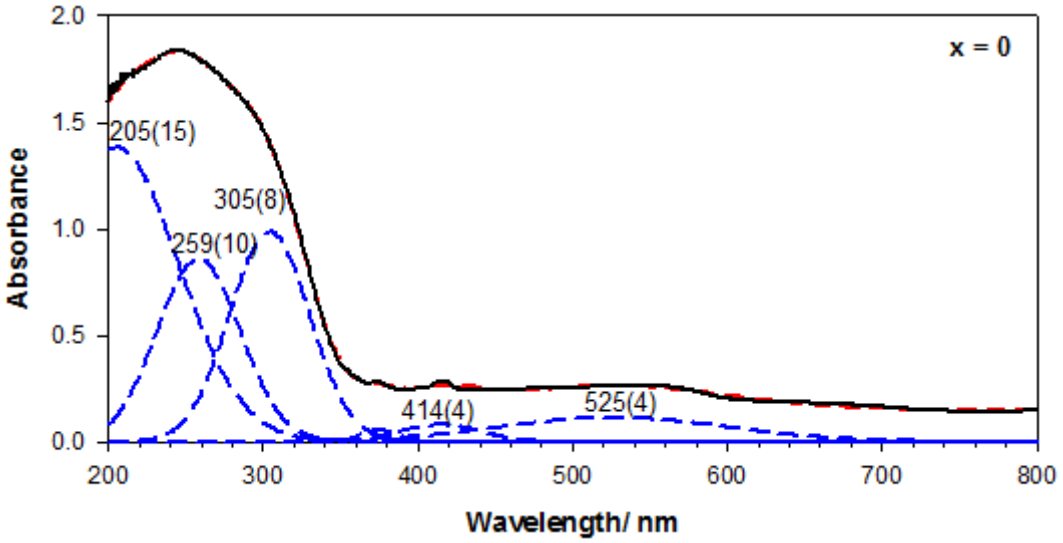

As can be seen from Figure 3.23, when Mn^{3+} is in a regular octahedral environment, only one d→d transition is expected to occur. If there is a tetragonal elongation, then the symmetry of the MnO_6 unit is reduced to D_{4h} and the energy levels further split, in which case three d→d transitions would be expected. In the case of a highly distorted MnO_6 coordination sphere, any remaining degeneracy is removed to give five non-degenerate energy levels in which four d→d transitions would be expected to occur from the ground state. The MnO_6 site now possesses lower symmetry in which the centre of inversion no longer remains, meaning that d→d transitions become both spin and Laporte allowed.

For compounds with x > 0, visual inspection of the broad feature in the region of *ca.* 400-700 nm suggested that this was not just due to one band, but that it consisted of overlapping peaks. During the least squares refinement process an initial model consisting of three peaks in this region was used, consistent with Mn^{3+} not existing in a regular octahedral coordination environment, as evidenced by diffraction data on compounds with x > 0.5. However, as it is not clear how many

bands might be expected in the UV region of these spectra or the visible region of x = 0, the software was allowed to provide the best fit to these spectral data using an unlimited number of peaks. Once completed, the results were scrutinised by eye to ensure that the peaks suggested by the software appeared justified in improving the overall fit.

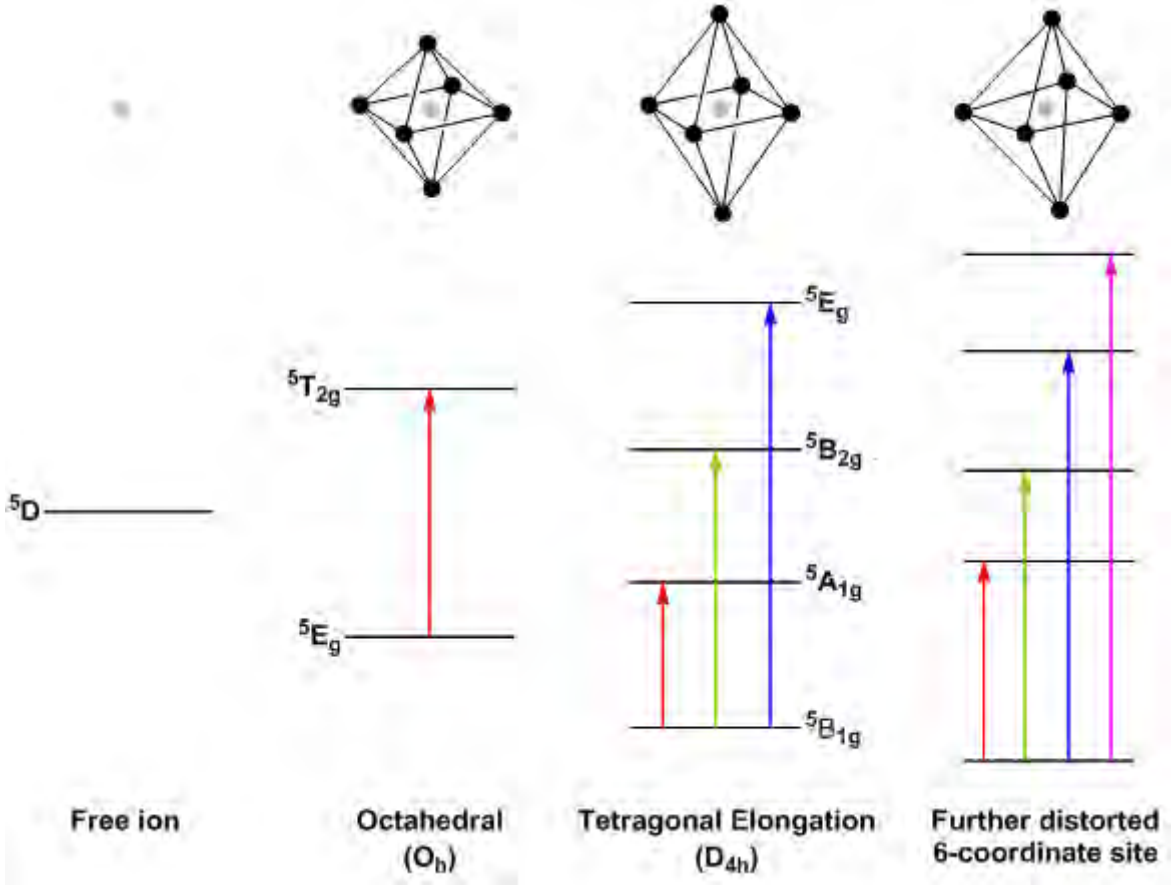

Figure 3.23: *Ligand field energy separations for a Mn^{3+} ion in various 6-coordinate environments*

For x = 1 and 0.75, three d→d transitions were modelled in the visible region and a fourth transition modelled towards the near-IR region. Such highly distorted 6-coordinate sites have been reported for Mn^{3+} present in various minerals, with the fourth transition also occurring in the far-visible/ near IR region.[31-33] Indeed, this loss of inversion symmetry explains the intense violet colouration exhibited by the x = 1

and 0.75 members, as can be seen in Figure 3.24. For x = 0, two relatively weak d→d transitions were modelled in the visible region, consistent with the $^6A_{1g}$ ground state of Fe^{3+}.

Figure 3.24: *Colouration of the α-$NH_4Mn_xFe_{1-x}P_2O_7$ series.*

A colour change from violet to blue was observed for the compounds containing Mn, with the intensity in colouration decreasing with the greater amount of Fe in the system. This appeared to occur in accordance with the Mn content and its surrounding octahedral environment becoming more regular. Indeed, for x = 0.5 and 0.25, three d→d transitions were modelled in the visible region but a fourth was not observed in the far-visible/ near IR region, consistent with a [4+2] tetragonal elongation of the MnO_6 octahedra. The average value of 10*Dq* coincides with the second ($^5B_{1g}$→$^5B_{2g}$) transition (Figure 3.25), and based on the resolved spectra, was estimated to be 211(1) and 212(2) kJ mol^{-1} for x = 0.5 and 0.25, respectively. These values lie within the general 10*Dq* range of 191-251 kJ mol^{-1} that is often found for high spin Mn^{3+} complexes.[34]

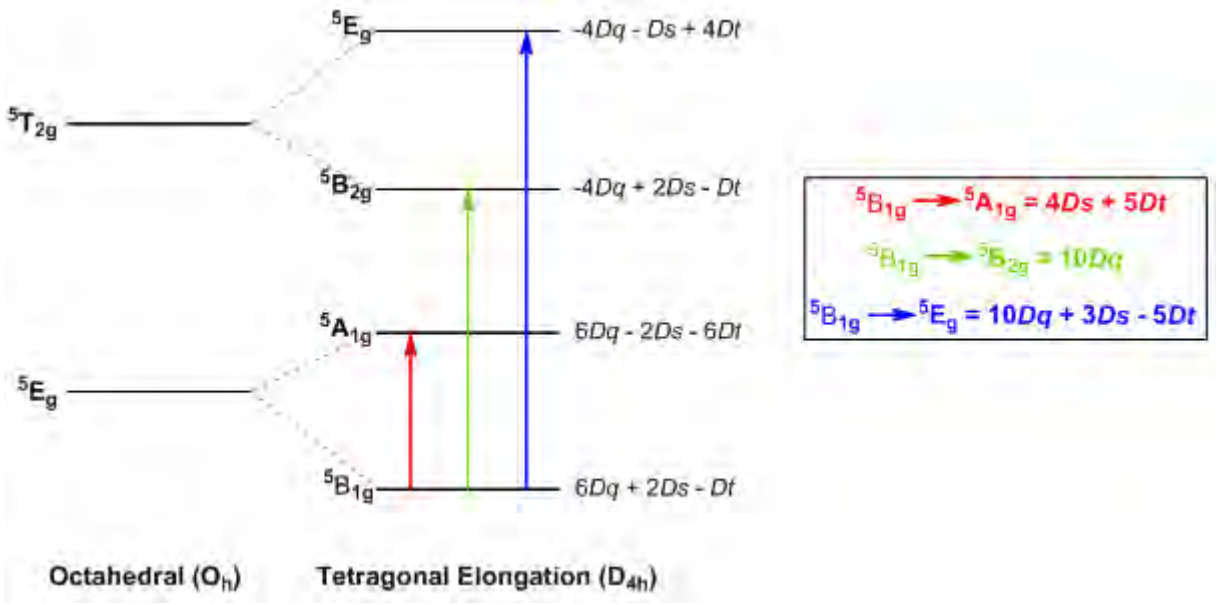

Figure 3.25: *Ligand field energy separations for a Mn^{3+} ion in a tetragonally elongated octahedron. Dq describes the crystal field splitting while Ds and Dt are parameters used to describe the energies of the 3d orbitals in a tetragonal field.*

In all cases, the bands occurring in the UV region were tentatively assigned as charge transfer (CT) bands, most likely ligand to metal charge transfer (LMCT) given that Mn^{3+} and Fe^{3+} are in relatively high oxidation states and are directly coordinated to oxygen anions possessing lone pairs. CT bands are generally found to be orders of magnitude more intense than d→d bands, though for the spectra recorded here, such a difference was not observed. The measured spectra show that the CT bands have a strong absorbance of ~1.6-2.3 absorbance units, and so it is possible that it is actually the d→d transitions that are more intense than we would expect. The reason for this is at present unclear, though is likely in part to be due to a strong Jahn-Teller effect significantly reducing the symmetry of the MnO_6 unit. A similar assignment of bands has been made for the Mn^{3+} spectra of $MnPO_4 \cdot 1.3H_2O$[35] and $K_xMn_yHf_{1-y}(PO_4)_3$[36] compounds, where a significant difference in intensity between

the LMCT and d→d bands was also not observed, perhaps suggesting that this is a feature of Mn^{3+} phosphate compounds.

3.3.4.3 Thermal Stability

Figure 3.26 shows that the thermal stability of the α-$NH_4Mn_xFe_{1-x}P_2O_7$ phases increased with the greater amount of Fe present in the system, with Table 3.11 giving approximate decomposition temperatures, the total mass loss observed and the identified products after decomposition. In all cases the mass spectrometer showed that a loss of both water and ammonia had occurred from the host.

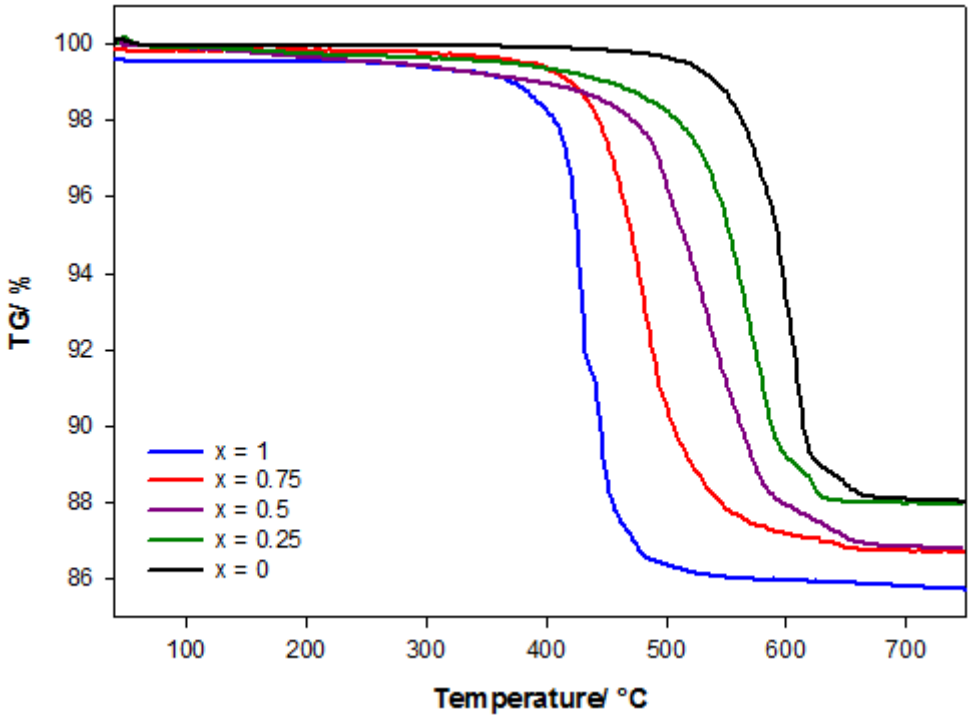

Figure 3.26: *TGA plots for the α-$NH_4Mn_xFe_{1-x}P_2O_7$ series.*

Table 3.11: *Summary of thermal decomposition of α-$NH_4Mn_xFe_{1-x}P_2O_7$ phases*

x	Approximate decomposition temperature/ °C	% mass loss observed	Product(s) after thermal decomposition
1	340	13.75	$Mn_2P_4O_{12}$
0.75	380	13.30	$Mn_2P_4O_{12}$*
0.5	420	13.22	$Mn_2P_4O_{12}$ + $Fe(PO_3)_3$*
0.25	440	11.98	$Mn_2P_4O_{12}$ + $Fe(PO_3)_3$*
0	500	11.94	$Fe(PO_3)_3$*

**Other phases also present but not identified*

Due to the poor crystallinity of the final phases, particularly for $0 < x < 1$, all of the decomposition products could not be identified using the JCPDS[9] database. From the products that were identified, it would seem that Mn^{3+} has a tendency to reduce to Mn^{2+} in a N_2 atmosphere whereas Fe^{3+} remains stable in its oxidation state at these measurement temperatures, allowing the host structure to remain stable up to higher temperatures. A similar situation has been observed in manganese oxide molecular sieves, where substitution of Fe^{3+} for Mn^{3+}/ Mn^{4+} has been shown to enhance the thermal stability of these materials.[37] It is worth noting that α-$NH_4MnP_2O_7$ was also heated in air and found to form $Mn_2P_4O_{12}$, suggesting that a Mn^{2+} phase forms regardless of whether decomposition occurred in N_2 or air.

3.3.4.4 Magnetic Analysis

Figure 3.27 shows the magnetic susceptibility measurements for the α-$NH_4Mn_xFe_{1-x}P_2O_7$ series and the Curie-Weiss fits to the data, while Table 3.12 summarises the parameters calculated from the latter. α-$NH_4MnP_2O_7$ showed a sharp antiferromagnetic transition at T_N = 21.3 K, indicative of weak three-dimensional magnetic ordering. Above its Néel temperature the sample behaved as a Curie-Weiss paramagnet, with a Weiss temperature (θ) similar in magnitude to the Néel temperature. The effective magnetic moment of 5.14(1) μ_B was found to be in good agreement with the spin-only moment and experimentally observed moments for Mn^{3+} complexes. Interestingly, upon introducing iron into the system, all materials showed apparent paramagnetic behaviour, though the susceptibility data for the Fe end member was more indicative of frustrated magnetic interactions. There also appeared to be a very small curvature to the Curie-Weiss fits of the data, suggesting deviations from the ideal Curie-Weiss law. This was further reflected in the fact that θ (which suggested the presence of antiferromagnetic interactions) increased rapidly in traversing the series.

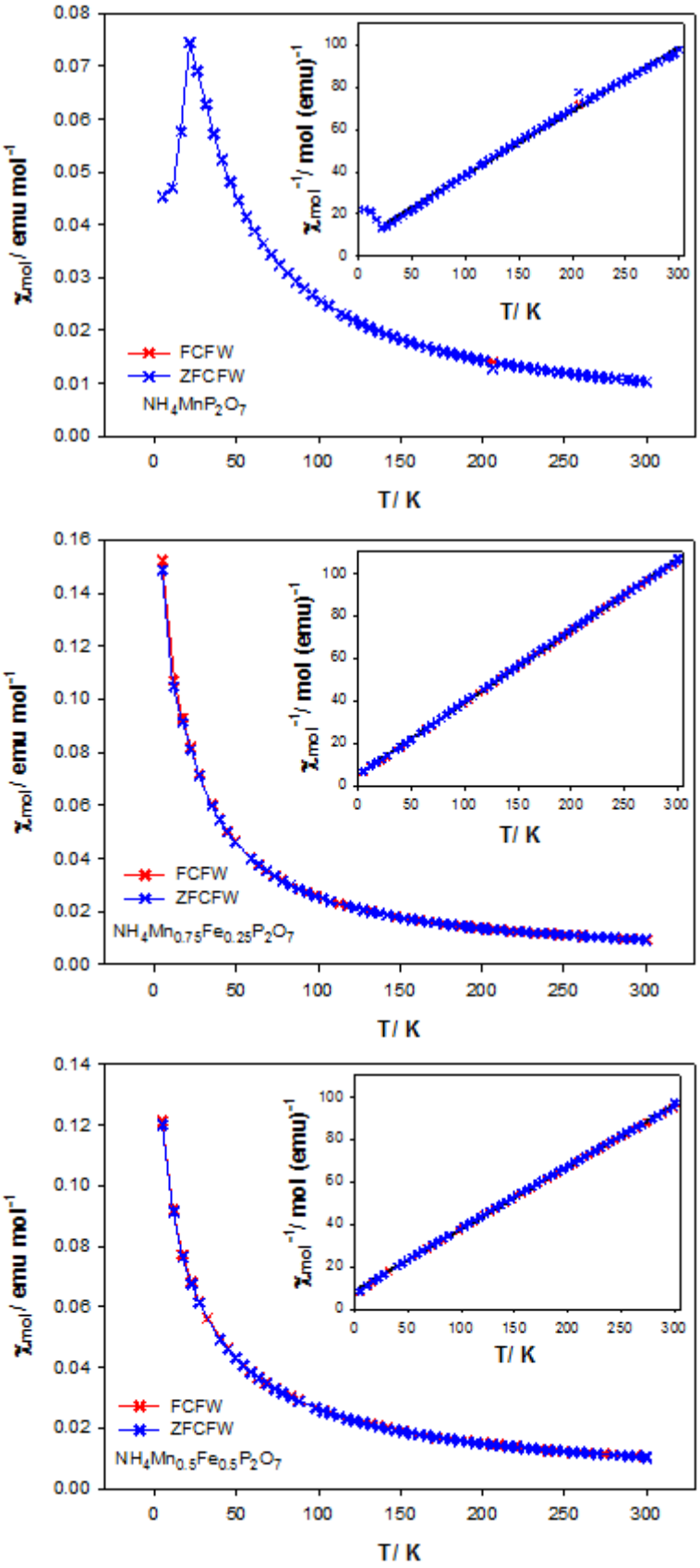

Figure 3.27: *Plots of molar susceptibility against temperature for the α-$NH_4Mn_xFe_{1-x}P_2O_7$ series, with insets showing Curie-Weiss fits.*

Figure 3.27 continued...

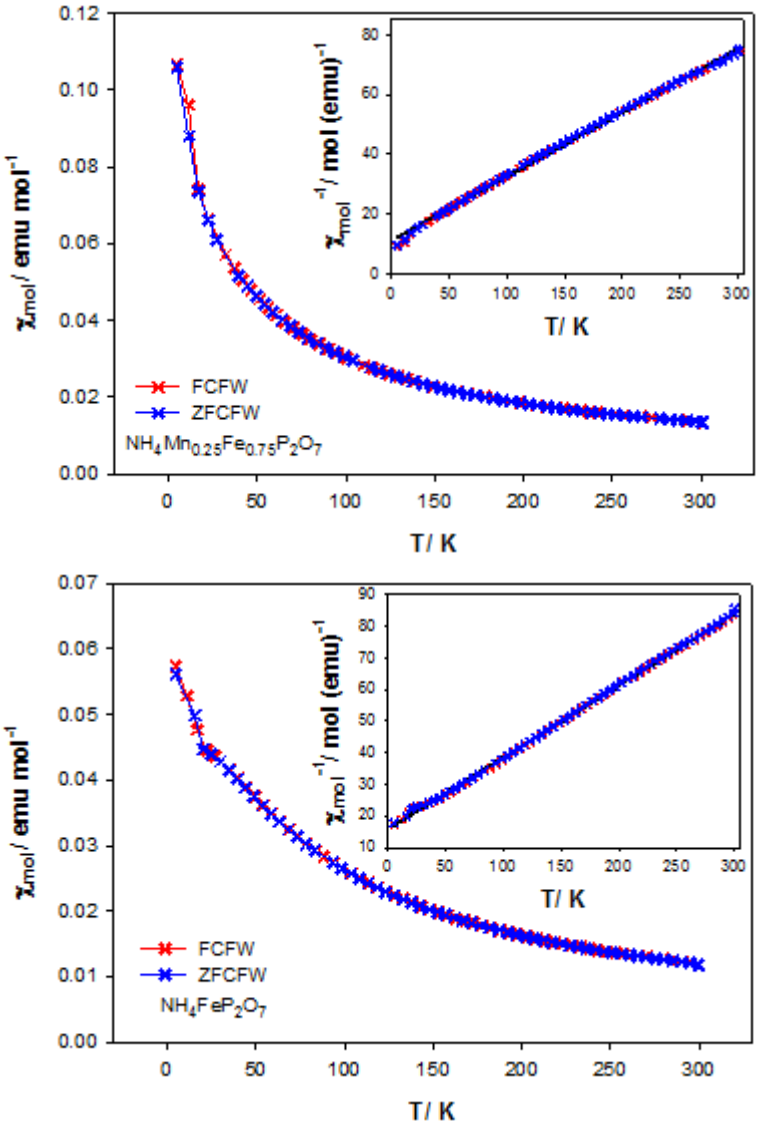

Table 3.12: *Summary of parameters determined from the susceptibility data on the α-$NH_4Mn_xFe_{1-x}P_2O_7$ series*

x	θ/ K	$\mu_{eff}/\ \mu_B$	$\mu_{so}/\ \mu_B$	$\mu_{obs}/\ \mu_B$ [38]
1	-26(1)	5.14(1)	4.90	4.80-4.90
0.75	-15.3(3)	4.866(4)	5.16	
0.5	-29.3(5)	5.236(6)	5.41	
0.25	-51(1)	6.11(2)	5.67	
0	-69.2(6)	5.934(9)	5.92	5.70-6.00

3.3.4.4.1 Magnetic Structure of α-$NH_4MnP_2O_7$

After the nuclear contribution was fitted to the 2 K neutron diffraction data on α-$NH_4MnP_2O_7$, the diffraction pattern showed evidence for additional peaks and intensity (Figure 3.28). This allowed a magnetic unit cell to be determined which was found to be commensurate with the nuclear cell and consistent with the magnetic space group $P2_1'/c$. The relative orientations of the four Mn spins in the unit cell were found to be (0.736, 0.104, 0.755)+, (0.243, 0.604, 0.713)+, (0.243, 0.890, 0.213)- and (0.736, 0.390, 0.255)-, with the magnetic intensities fitted with a calculated form factor for Mn^{3+}.[39] The magnitude of the moments was found to be 3.79(7) μ_B, which is close to the saturated moment of 4.0 μ_B expected for high spin Mn^{3+} ions. The final refined structural parameters are shown in Table 3.13, with selected bond lengths and angles given in Table 3.14.

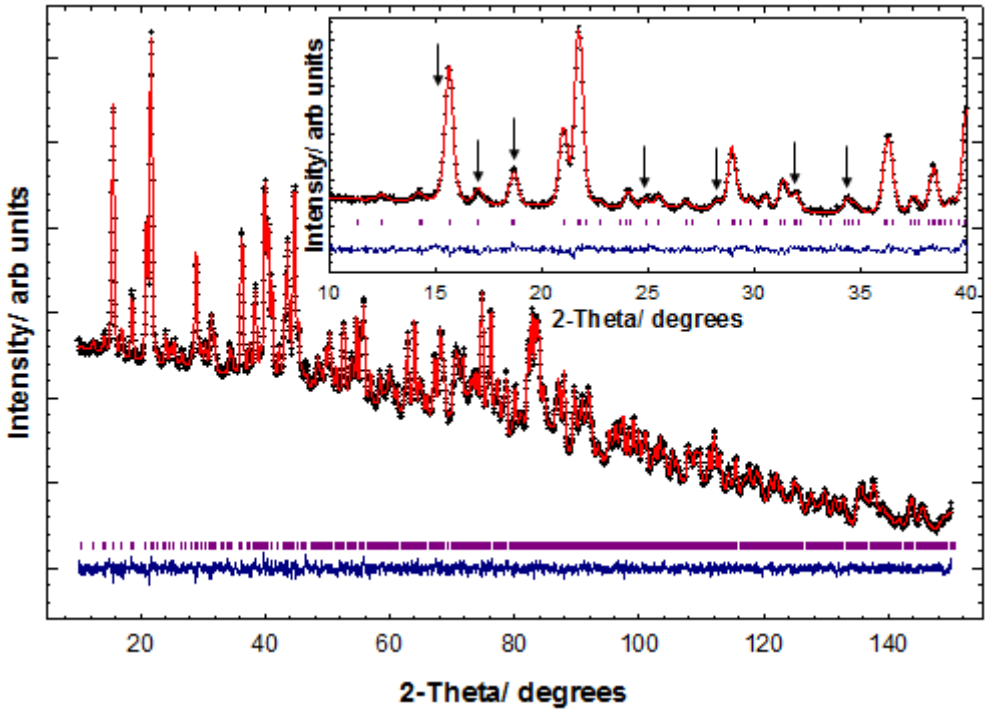

Figure 3.28: *Observed (+), calculated (-), difference profiles (-) and reflection positions (l) for the 2 K Rietveld refinement carried out on α-$NH_4MnP_2O_7$. The low angle region is enlarged in the inset, with arrows indicating peaks with significant magnetic intensity.*

Table 3.13: *Refined structural parameters for α-$NH_4MnP_2O_7$, obtained from a Rietveld refinement of the 2 K neutron diffraction data*

Atom	Site	Occupancy	*x*	*y*	*z*	U_{iso}/ Å^2	BVS[15]
Mn	4*e*	1.0	0.736(1)	0.1038(7)	0.755(1)	0.004(1)	3.32
P(1)	4*e*	1.0	0.6253(7)	0.4058(6)	0.8308(6)	0.002(1)	4.94
P(2)	4*e*	1.0	0.9300(8)	0.3725(6)	0.6892(6)	0.004(1)	4.77
O(1)	4*e*	1.0	0.5863(7)	0.2574(5)	0.7507(6)	0.005(1)	1.89
O(2)	4*e*	1.0	0.6403(7)	0.4046(5)	1.0047(6)	0.005(1)	1.87
O(3)	4*e*	1.0	0.8234(8)	0.4529(5)	0.8037(6)	0.005(1)	2.00
O(4)	4*e*	1.0	0.4845(7)	0.5007(5)	0.7258(6)	0.004(1)	1.97
O(5)	4*e*	1.0	0.9431(6)	0.2181(6)	0.7420(6)	0.003(1)	1.83
O(6)	4*e*	1.0	0.8284(7)	0.4005(5)	0.5190(6)	0.005(1)	1.73
O(7)	4*e*	1.0	1.1355(7)	0.4265(5)	0.7431(6)	0.003(1)	1.75
N	4*e*	1.0	0.3241(4)	0.3143(3)	0.4501(5)	0.0063(7)	2.84
H(1)	4*e*	1.0	0.252(1)	0.391(1)	0.486(1)	0.030(3)	0.71
H(2)	4*e*	1.0	0.403(1)	0.357(1)	0.380(1)	0.030(2)	0.66
H(3)	4*e*	1.0	0.240(2)	0.243(1)	0.387(1)	0.029(2)	0.75
H(4)	4*e*	1.0	0.416(1)	0.2720(8)	0.547(1)	0.015(2)	0.72

Space group $P2_1'/c$, a = 7.4198(2) Å, b = 9.6670(4) Å, c = 8.6344(3) Å, β = 105.588(2)°

Magnetic moments: M_x = 0.3(2) μ_B, M_y = 0.0 μ_B, M_z = 3.78(7) μ_B, $|M|$ = 3.79(7) μ_B

Figures of merit: R_{wp} = 0.94%, R_p = 0.75%, χ^2 = 1.826

Overall α-$NH_4MnP_2O_7$ was found to adopt the same magnetic structure type as $RbMnP_2O_7$[7], with the easy axis of magnetisation found to be orientated along the *c*-axis of the structure; the direction also associated with the elongated bonds of the MnO_6 octahedra (Figure 3.29). It is worth noting that although the elongation is still along the Mn-O(2) and Mn-O(6) bonds, the MnO_6 octahedra do not show a simple [4+2] or [2+2+2] Jahn-Teller distortion, as was the case for the room temperature structure. Upon reducing the temperature, the Mn^{3+} octahedral coordination sphere becomes more irregular, with only three bond lengths within three standard errors of each other. Despite this, BVS values for both the 300 K and 2 K structures were

found to be reasonably similar, giving GII values of 0.23 vu and 0.22 vu, respectively. This suggests that although temperature plays a role in changing the extent of the Jahn-Teller distortion at the MnO_6 octahedra, this has little effect on the lattice-induced strains present in these units, which still remain. No phase transitions or change in crystal symmetry were evident upon reducing temperature, indicating that the observed pattern of Mn-O bond lengths are merely a consequence of Mn^{3+} being able to exhibit a "plastic" coordination sphere. Indeed, such plasticity has also been reported for a number of other Mn^{3+} complexes.[40-42]

Table 3.14: *Selected Bond Distances (Å) and Angles (degrees) for α-$NH_4MnP_2O_7$ at 2 K*

Mn-O(1)	1.851(9)	**Mn-O(5)**	1.917(9)
Mn-O(2)	2.09(1)	**Mn-O(6)**	2.200(9)
Mn-O(4)	1.96(1)	**Mn-O(7)**	1.957(9)
O(1)-Mn-O(2)	88.6(1)	**O(2)-Mn-O(7)**	90.3(1)
O(1)-Mn-O(4)	84.1(3)	**O(4)-Mn-O(5)**	175.1(1)
O(1)-Mn-O(5)	91.3(3)	**O(4)-Mn-O(6)**	86.3(2)
O(1)-Mn-O(6)	93.0(1)	**O(4)-Mn-O(7)**	88.2(2)
O(1)-Mn-O(7)	172.2(1)	**O(5)-Mn-O(6)**	92.3(2)
O(2)-Mn-O(4)	90.4(2)	**O(5)-Mn-O(7)**	96.4(3)
O(2)-Mn-O(5)	91.1(2)	**O(6)-Mn-O(7)**	87.6(1)
O(2)-Mn-O(6)	176.2(1)		
P(1)-O(1)	1.584(7)	**P(2)-O(3)**	1.620(7)
P(1)-O(2)	1.476(6)	**P(2)-O(5)**	1.556(6)
P(1)-O(3)	1.615(7)	**P(2)-O(6)**	1.485(7)
P(1)-O(4)	1.499(7)	**P(2)-O(7)**	1.560(7)
O(1)-P(1)-O(2)	113.1(5)	**O(3)-P(2)-O(5)**	106.5(4)
O(1)-P(1)-O(3)	105.0(4)	**O(3)-P(2)-O(6)**	108.4(4)
O(1)-P(1)-O(4)	105.9(4)	**O(3)-P(2)-O(7)**	104.8(4)
O(2)-P(1)-O(3)	109.1(4)	**O(5)-P(2)-O(6)**	116.1(4)
O(2)-P(1)-O(4)	118.0(4)	**O(5)-P(2)-O(7)**	104.8(4)
O(3)-P(1)-O(4)	104.7(4)	**O(6)-P(2)-O(7)**	115.5(4)
N-H(1)	1.01(1)	**O(1)---H(4)**	1.87(1)
N-H(2)	1.04(1)	**O(4)---H(2)**	1.96(1)
N-H(3)	0.99(1)		
N-H(4)	1.01(1)		

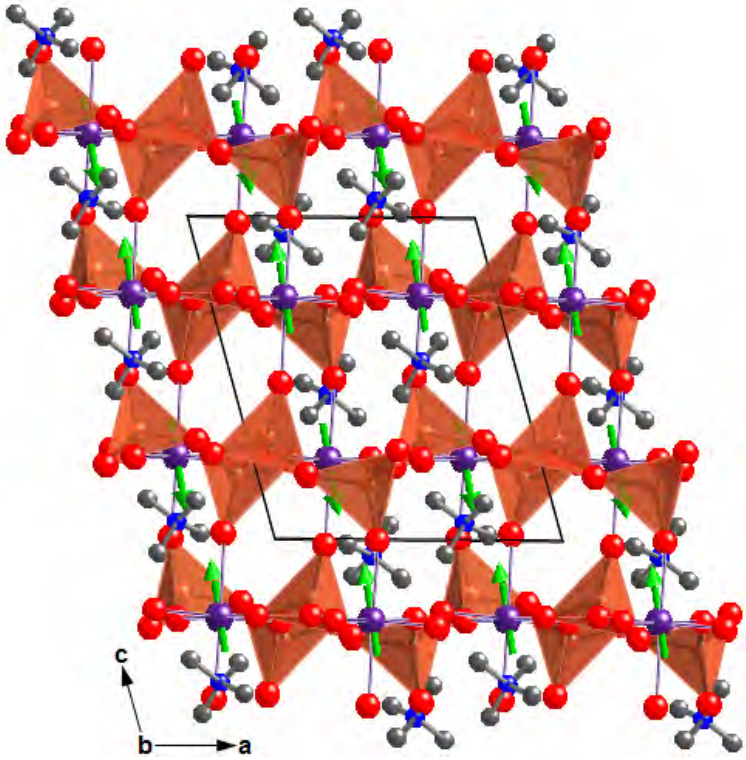

Figure 3.29: *Magnetic structure of α-$NH_4MnP_2O_7$ viewed down the b-direction, with the orientation of magnetic moments on the Mn^{3+} ions (purple spheres) shown with green arrows and condensed phosphate tetrahedra shown in orange.*

The Mn---Mn distances (> 5 Å) within the structure are too long for direct exchange to occur, with the shortest entity separating these ions being an orthophosphate unit. As such, only interactions occurring through Mn-O-P-O-Mn linkages were considered, which is in accordance with the suggestion by Whangbo *et al*[43] that the strongest interactions occur through the shortest O---O separations. Exchange interactions occurring through multiple phosphate groups are likely to be much weaker and so were not considered here.

Each Mn spin is linked to eight other spins in total *via* twelve different Mn-O-P-O-Mn "super-superexchange" pathways. Four of these interactions appear to be ferromagnetic (FM) in nature and occur within the *ab*-plane of the structure, while the remaining eight appear to be antiferromagnetic (AFM) and occur along the *c*-axis

(see Figure 3.30). However, a closer inspection of the structure reveals that each PO_4 unit within the diphosphate group simultaneously connects three Mn centres *via* the terminal oxygen atoms, clearly seen towards the top of Figure 3.30. The spin directions of this triad are such that each pair of Mn ions linked in a ferromagnetic fashion are also linked to a third Mn ion in an antiferromagnetic fashion, giving rise to antiferromagnetic ordering overall, as was also suggested by the magnetic susceptibility data for this compound. Similar triads have also been observed in the structures of $LiFeP_2O_7$[44] and $NaFeP_2O_7$.[45]

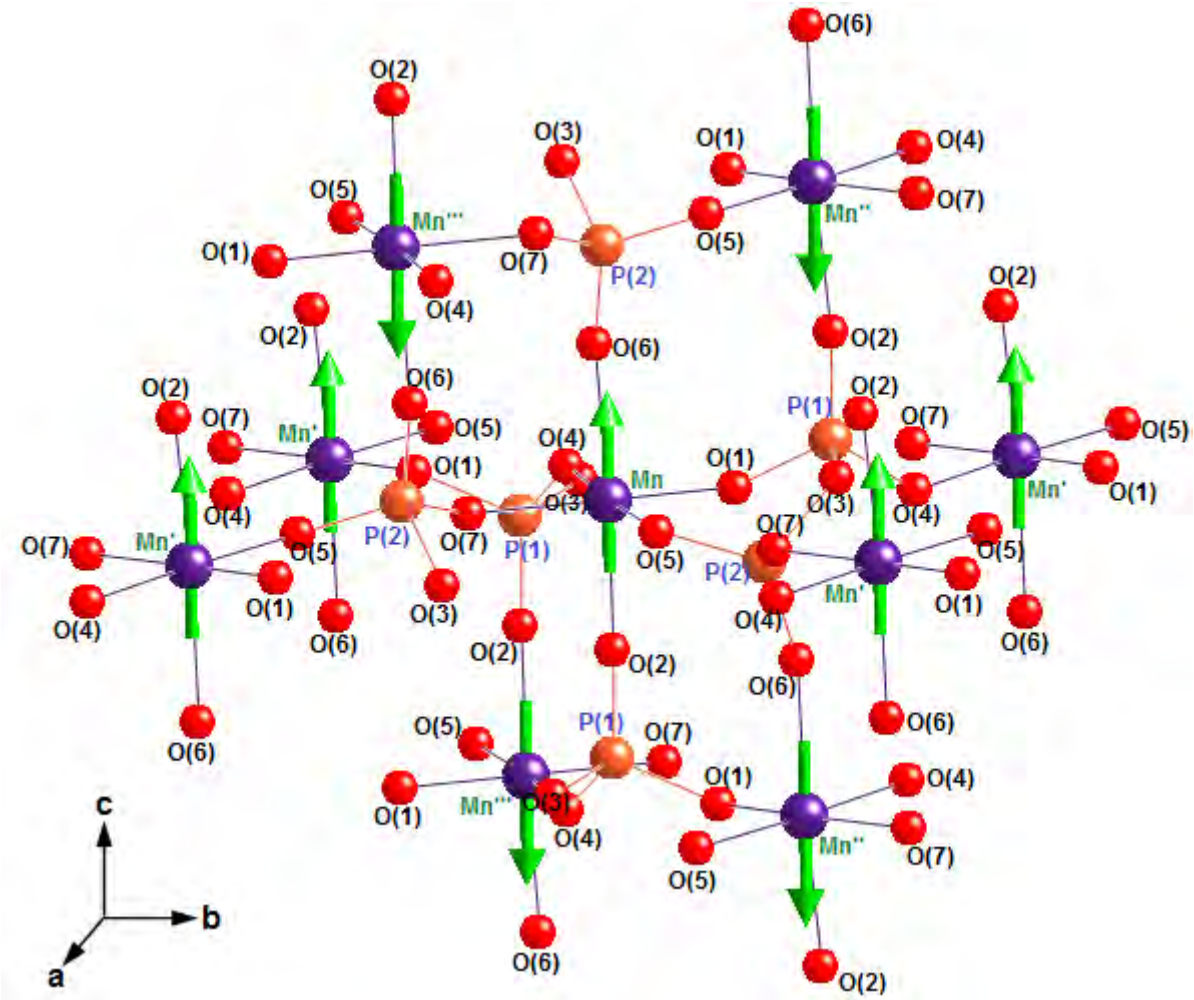

Figure 3.30: *Nearest neighbour Mn---Mn interactions in α-$NH_4MnP_2O_7$. Manganese, phosphorus and oxygen atoms are shown as purple, orange and red spheres, respectively.*

Given that we observe twice as many AFM pathways than FM, it is likely that the AFM interactions are either stronger or weakly preferred over FM interactions. Indeed, if FM interactions were stronger, then we would expect the triad of interactions presented by each PO_4 unit to be solely FM, which would give no obvious reason for AFM interactions to be present in the structure (see Figure 3.31). However, if AFM interactions dominate, then FM interactions would be imposed on the structure simply because the triad cannot be purely AFM.

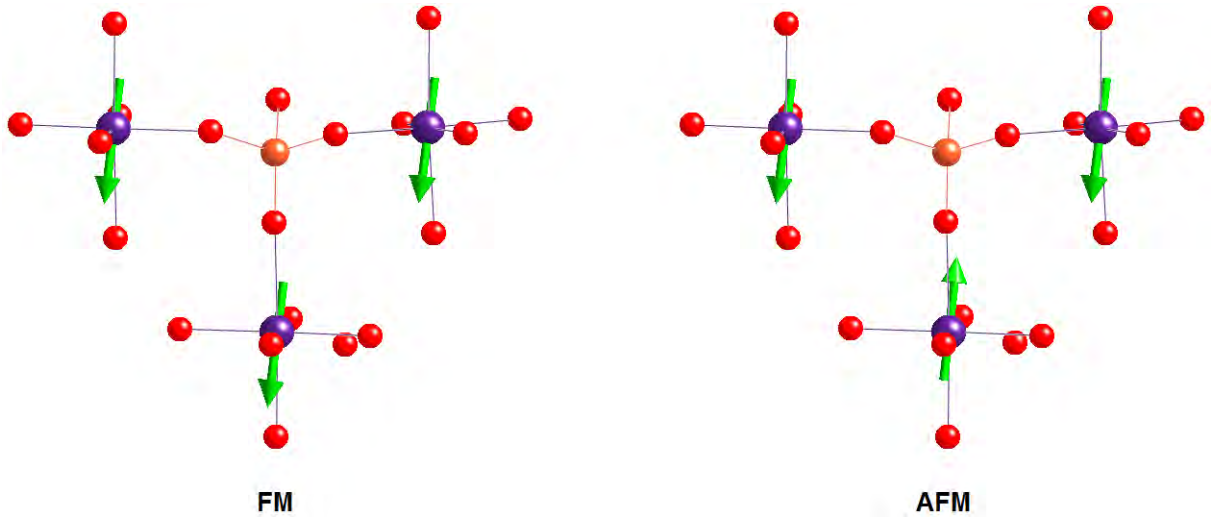

Figure 3.31: *Different possibilities for the triad of interactions occurring through the orthophosphate unit. Manganese, phosphorus and oxygen atoms are shown as purple, orange and red spheres, respectively.*

Within the structure it is evident that the equatorial Mn-O bonds mediate the apparent ferromagnetic interactions while one axial and one equatorial Mn-O bond mediate the antiferromagnetic interactions. This suggests that FM interactions involve the unoccupied $d_{x^2-y^2}$ orbitals of two Mn ions while AFM interactions are the result of interaction between an unoccupied $d_{x^2-y^2}$ orbital and a singly occupied d_{z^2} orbital. Whilst the actual Mn-O and P-O bond lengths do not appear to correlate with the sign of interaction, the angles within the Mn-O-P-O-Mn linkage do show some

correlations with this. From Table 3.15 it can be seen that FM interactions involve O-P-O angles < 105.9° and O---O separations < 2.5 Å, while AFM interactions involve O-P-O angles > 113.1° and O---O separations > 2.5 Å; a similar case was also noted for $RbMnP_2O_7$.[7] In the case of equatorial Mn-O bonds, the Mn-O-P angles for both FM and AFM interactions range from 125.8-137.4°. However, for the axial Mn-O bonds an almost linear Mn-O-P array is observed with angles of 163.6° and above. Furthermore, FM interactions involve Mn---Mn separations > 6.0 Å whereas for AFM interactions this separation is slightly shorter, being < 5.3 Å.

Table 3.15: *Summary of the exchange pathways present in α-$NH_4MnP_2O_7$ and geometries of the interacting species.*

Mn-O(1)-P(1)-O(4)-Mn' **Mn-O(4)-P(1)-O(1)-Mn'**	O(1)-P(1)-O(4) = 105.9(4)° Mn-O(1)-P(1) = 132.2° Mn'-O(4)-P(1) = 137.2°	O(1)---O(4) = 2.455 Å Mn---Mn' = 5.955 Å	FM
Mn-O(7)-P(2)-O(5)-Mn' **Mn-O(5)-P(2)-O(7)-Mn'**	O(5)-P(2)-O(7) = 104.8(4)° Mn-O(7)-P(2) = 137.4° Mn'-O(5)-P(2) = 125.8°	O(5)---O(7) = 2.475 Å Mn---Mn' = 6.239 Å	FM
Mn-O(2)-P(1)-O(1)-Mn'' **Mn-O(1)-P(1)-O(2)-Mn''**	O(1)-P(1)-O(2) = 113.1(5)° Mn-O(2)-P(1) = 164.7° Mn''-O(1)-P(1) = 132.2°	O(1)---O(2) = 2.554 Å Mn---Mn'' = 5.162 Å	AFM
Mn-O(2)-P(1)-O(4)-Mn''' **Mn-O(4)-P(1)-O(2)-Mn'''**	O(2)-P(1)-O(4) = 118.0(4)° Mn-O(2)-P(1) = 164.7° Mn'''-O(4)-P(1) = 137.2°	O(2)---O(4) = 2.544 Å Mn---Mn''' = 5.247 Å	AFM
Mn-O(6)-P(2)-O(5)-Mn'' **Mn-O(5)-P(2)-O(6)-Mn''**	O(5)-P(2)-O(6) = 116.1(4)° Mn-O(6)-P(2) = 163.6° Mn''-O(5)-P(2) = 125.8°	O(5)---O(6) = 2.579 Å Mn---Mn'' = 5.162 Å	AFM
Mn-O(6)-P(2)-O(7)-Mn''' **Mn-O(7)-P(2)-O(6)-Mn'''**	O(6)-P(2)-O(7) = 115.5(4)° Mn-O(6)-P(2) = 163.6° Mn'''-O(7)-P(2) = 137.4°	O(6)---O(7) = 2.567 Å Mn---Mn''' = 5.312 Å	AFM

It is therefore possible that a combination of orbital occupancy effects and geometrical factors influence the degree of overlap between adjacent orbitals, giving rise to different exchange pathways. Clearly the mechanism for exchange here is more complex than in the case of simple oxide systems, for which exchange interactions can be predicted using Goodenough's[46] and Kanamori's[47] rules. Although some empirical observations for condensed phosphate systems have been noted, these have yet to be validated by further examples of magnetically dilute frameworks.

3.4 Conclusions

In investigating the synthesis of the manganese violet pigment, two polymorphs of $NH_4MnP_2O_7$ were identified, both of which have been shown to be key components of commercial samples. A reliable synthetic route was developed for the preparation of α-$NH_4MnP_2O_7$, which allowed a structural details to be obtained. The structure adopted is that of a type-I pyrophosphate (monoclinic), consisting of Jahn-Teller distorted MnO_6 octahedra corner-linked to pyrophosphate tetrahedra, with ammonium cations located in the intersecting tunnels. β-$NH_4MnP_2O_7$ has been found to be the first $M^IM^{III}P_2O_7$ system that adopts a triclinic structure. A unit cell was determined but due to being unable to synthesise the compound in single phase form, reliable structural details could not be obtained. Some general observations regarding the two polymorphs are that both consist of a very similar framework topology, with the main difference being that the β-polymorph possesses two different pore types whereas the α-polymorph only contains one pore type. Both polymorphs appear to have a similar thermal stability of ~340°C.

Substitution of the ammonium and manganese cations in α-$NH_4MnP_2O_7$ was also investigated. Whilst partial K-exchange and Rb-exchange are possible by a nitrate melt reaction, the process is accompanied by the formation of a significant amount of amorphous material, suggesting that this route is not ideal for forming other $M^IMnP_2O_7$ phases. The α-$NH_4Mn_xFe_{1-x}P_2O_7$ solid solution was successfully synthesised in a similar fashion to the Mn end member and the effects of introducing Fe into the system were examined. Diffraction showed that the average distortion at the TM centre is reduced with increasing Fe content, which can in turn be correlated with the change in unit cell parameters across the series. The UV-Vis spectra for x = 1 and 0.75 showed four d→d transitions occurring in the visible-near IR region, suggesting that the MnO_6 octahedra were distorted beyond a [4+2] elongation. For x = 0.5 and 0.25, three d→d transitions were observed in the visible region, consistent with a [4+2] MnO_6 tetragonal elongation. This suggested that the Mn coordination sphere became more regular with an increasing amount of Fe in the system. Indeed, this was also accompanied by a colour change in these materials and an improvement in their thermal stability. As such, these compounds have the potential to be used as pigment materials, being expected to show a similar chemical stability to manganese violets. GII values did not significantly differ across the series and were relatively large, indicating that lattice-induced strains are present in this structure type irrespective of the electronic properties of the transition metal ion. This results in unusual bond lengths within the TM-O_6 and PO_4 units and possibly contributes to the intense/ unusual colouration generated by the Mn^{3+} centres.

The magnetic properties of the α-$NH_4Mn_xFe_{1-x}P_2O_7$ system were investigated and only the Mn end member was found to show magnetic ordering (T_N = 21.3 K). It

was somewhat surprising to find that the presence of Fe in the structure was substantial enough even to lead to the x = 0.75 member exhibiting paramagnetic behaviour. Indeed, here the Mn---Mn interactions would be expected to dominate and give rise to some magnetic ordering, as was observed for the parent material.

The magnetic structure of α-$NH_4MnP_2O_7$ was solved and found to consist of both ferromagnetic and antiferromagnetic Mn-O-P-O-Mn "super-superexchange" pathways. Furthermore, each PO_4 unit within the structure simultaneously connects three Mn centres to give AFM ordering overall, with the moment directions being along the axial direction of the Jahn-Teller distorted MnO_6 octahedra. The sign of interaction appears to be strongly correlated with orbital occupancy, with FM interactions seemingly involving two unoccupied $d_{x^2-y^2}$ orbitals but AFM interactions involving an unoccupied $d_{x^2-y^2}$ orbital and a singly occupied d_{z^2} orbital. Empirical observations suggest that geometrical factors are also related to the sign of interaction, though the extent of their influence is at present unclear.

References

[1] F. Hund, *Pyrophosphathaltige Violett- und Blaupigmente*, **DE4122448**, 1993.

[2] Bayer, *Verwendung von Kaliummanganpyrophosphat zur Herstellung gefärbter Metallic-Lackierungen und so hergestellte, gefärbte Metallic-Lacke*, **DE4314268**, 1994.

[3] M. Müller, *Anticorrosion Agents*, **WO0249960A2**, 2002.

[4] P. A. Lewis, *Pigment Handbook: Properties and Economics Volume 1*; Wiley: New York, 1988.

[5] Holliday Pigments, http://www.holliday-pigments.com/manganese-violets.

[6] J. D. Lee and L. S. Browne, *J. Chem. Soc. (A), Inorg. Phys. Theor.*, 1968, 559-561.

[7] F. C. Coomer, N. J. Checker and A. J. Wright, *Inorg. Chem.*, 2010, **49**, 934-942.

[8] N. J. Checker, *The Synthesis and Properties of Novel Condensed Phosphates*, PhD Thesis, University of Birmingham, 2006.

[9] JCPDS, *International Centre for Diffraction Data*, 1999, P.1., Swathmore, Pennsylvania, PA 19081, USA, 11990.

[10] A. C. Larson and R. B. von Dreele, *General Structure Analysis System*; Los Alamos National Laboratory, 1994.

[11] Data accessed from NIST, *Neutron Attenuation and Activation*, www.ncnr.nist.gov/instruments/bt1/neutron.html.

[12] K. Fejfarova, R. Essehli, B. El Bali and M. Dusek, *Acta. Crystallogr.*, 2008, **E64**, I85-I86.

[13] H. N. Ng and C. Calvo, *Can. J. Chem.*, 1973, **51**, 2613-2620.

[14] M. T. Averbuch-Pouchot and A. Durif, *Topics in Phosphate Chemistry*; World Scientific Publishing Co. Pte. Ltd.: Singapore, 1996.

[15] I. D. Brown and D. Altermatt, *Acta Crystallogr.*, 1985, **B41**, 244-247.

[16] A. Salinas-Sanchez, J. L. Garcia-Munoz, J. Rodriguez-Carvajal, R. Saez-Puche and J. L. Martinez, *J. Solid State Chem.*, 1992, **100**, 201-211.

[17] R. Shirley, *The CRYSFIRE System for Automatic Powder Indexing: User's Manual*, 2000, The Lattice Press, 41 Guildford Park Avenue, Guildford, Surrey, GU2 7NL, England.

[18] F. Kohlbeck and E. M. Horl, *J. Appl. Crystallogr.*, 1976, **9**, 28-33.

[19] F. Kohlbeck and E. M. Horl, *J. Appl. Crystallogr.*, 1978, **11**, 60-61.

[20] Data accessed from ICSD, *Inorganic Crystal Structure Database*, www.cds.dl.ac.uk/cds/datasets/crys/icsd/llicsd.html.

[21] H. Boughzala, A. Driss and T. Jouini, *Acta Crystallogr. Sect. C*, 1993, **49**, 425-427.

[22] A. A. Khan and W. H. Baur, *Acta Crystallogr.*, 1972, **B28**, 683-693.

[23] R. D. Shannon, *Acta Crystallogr.*, 1976, **A32**, 751-767.

[24] L. S. Ivashkevich, K. A. Selevich, A. I. Lesnikovich, A. F. Selevich and A. S. Lyakhov, *Z. Kristallogr.*, 2006, **221**, 115-121.

[25] V. A. Lyutsko and O. G. Pap, *Russ. J. Inorg. Chem.*, 1993, **38**, 1043-1046.

[26] V. A. Lyutsko and T. I. Prisedskaya, *Russ. J. Inorg. Chem.*, 1986, **31**, 1026-1028.

[27] SLAC National Accelerator Laboratory, *Physical Constants of Inorganic Compounds*.

[28] Data accessed from NIST, *Neutron Scattering Lengths and Cross Sections*, www.ncnr.nist.gov/resources/n-lengths/.

[29] *PeakFit Version 4.12*; Seasolve, 1999-2003.

[30] E. Jonsson and U. Halenius, *Geol. Foren. Stock. For.*, 2010, **132**, 167-172.

[31] D. M. Sherman and N. Vergo, *Am. Mineral.*, 1988, **73**, 140-144.

[32] U. Halenius, *Mineralog. Mag.*, 2004, **68**, 335-341.

[33] U. Halenius, *Geol. Foren. Stock. For.*, 1984, **106**, 51-57.

[34] A. B. P. Lever, *Inorganic Electronic Spectroscopy*; Elsevier: Amsterdam, 1984.

[35] M. A. G. Aranda and S. Bruque, *Inorg. Chem.*, 1990, **29**, 1334-1337.

[36] I. V. Ogorodnyk, I. V. Zatovsky, V. N. Baumer, N. S. Slobodyanik, O. V. Shishkin and I. P. Vorona, *J. Solid State Chem.*, 2007, **180**, 2838-2844.

[37] X. Shen, A. M. Morey, J. Liu, Y. Ding, J. Cai, J. Durand, Q. Wang, W. Wen, W. A. Hines, J. C. Hanson, J. Bai, A. I. Frenkel, W. Reiff, M. Aindow and S. L. Suib, *J. Phys. Chem.*, 2011, **C115**, 21610-21619.

[38] C. E. Housecroft and A. G. Sharpe, *Inorganic Chemistry*; Pearson Education: Harlow, 2001.

[39] P. J. Brown, *International Tables of Crystallography, Vol.C*; Kluwer: Dordrecht, 1992.

[40] A. J. Edwards, *J. Chem. Soc. (A), Inorg. Phys. Theor.*, 1971, 2653-2655.

[41] J. P. Fackler Jr and A. Avdeef, *Inorg. Chem.*, 1974, **13**, 1864-1875.

[42] A. Avdeef, J. A. Costamagna and J. P. Fackler Jr, *Inorg. Chem.*, 1974, **13**, 1854-1863.

[43] M. H. Whangbo, D. Dai and H. J. Koo, *Dalton Trans.*, 2004, 3019-3025.

[44] G. Rousse, J. Rodríguez-Carvajal, C. Wurm and C. Masquelier, *Solid State Sciences*, 2002, **4**, 973-978.

[45] R. C. Mercader, L. Terminiello, G. J. Long, D. G. Reichel, K. Dickhaus, R. Zysler, R. Sanchez and M. Tovar, *Phys. Rev. B*, 1990, **42**, 25-32.

[46] J. B. Goodenough, *Phys. Rev.*, 1955, **100**, 564-573.

[47] J. Kanamori, *J. Phys. Chem. Solids*, 1959, **10**, 87-98.

Chapter Four

Structure and Properties of the $RbMn_xFe_{1-x}P_2O_7$ System

4.1 Introduction

Condensed phosphate phases within the Rb-Mn-P-O and Rb-Fe-P-O systems have been the subject of a number of studies. Guzeeva and Tananaev[1] were the first to explore the Rb-Mn-P-O system in 1988 and reported three phases to exist, $RbMnP_2O_7$ and two polymorphs of $RbMnHP_3O_{10}$. Subsequent structural and magnetic characterisations of all three phases were carried out by Coomer *et al*[2] and Wright and Attfield.[3] $RbFeP_2O_7$ was first investigated in 1991 by Millet and Mentzen,[4] who reported the crystal structure for this compound and the caesium analogue. Further crystal structure reports on these two phases as well as magnetic susceptibility measurements were given by Dvoncova and Lii[5] in 1993, with both phases shown to order antiferromagnetically at $T_N \approx 25$ K. Checker[6] conducted further work on these phases, collecting neutron diffraction data in an attempt to solve the magnetic structures. Though both phases exhibited similar magnetic peaks in the 2 K diffraction patterns, magnetic unit cells could not be identified.

Although $RbMnP_2O_7$ and $RbFeP_2O_7$ have been studied extensively, it was of interest to us to ascertain whether a $RbMn_xFe_{1-x}P_2O_7$ solid solution could be formed and to compare this to the isostructural α-$NH_4Mn_xFe_{1-x}P_2O_7$ series (discussed in Chapter 3). As before, the focus would be on the structural, optical, thermal and magnetic properties of the materials obtained. The disparity in the M^I cation would be expected to have subtle effects on the structural properties of these materials but more marked effects on say the thermal properties. Despite the different M^I cations, the Mn end members are known to possess the same magnetic structures, yet the Fe end members show different responses to applied magnetic fields, *i.e.* $NH_4FeP_2O_7$ appears to show some evidence for frustrated magnetic interactions whereas $RbFeP_2O_7$ exhibits antiferromagnetic behaviour. It would also be worthwhile to compare the magnetic behaviour of the intermediate members of these solid solutions.

4.2 Experimental

$RbMn_xFe_{1-x}P_2O_7$ compounds were prepared by a phosphoric acid melt method using a Rb:TM:P molar ratio of 9:1:15. Rb_2CO_3, Mn_2O_3 and Fe_2O_3 were ground together before being added to H_3PO_4 (86.5 wt %) in a porcelain crucible. The resulting mixture was transferred to an oven and heated at 250°C for 48 h and then cooled to RT over 24 h. The resulting products were collected by suction filtration and washed with water.

Powder X-ray diffraction data were collected on a Bruker AXS: D8 Advance diffractometer in transmission mode with a 2θ scan range of 5-80°. Both RT and 2 K neutron diffraction data were recorded on the x = 0.75, 0.5 and 0.25 compounds on the HRPT instrument at the Paul Scherrer Institute, Switzerland. RT data were also

collected on the latter compound heated to 1100°C in air. An incident neutron wavelength of 1.494 Å was employed over the range 5 ≤ 2θ ≤ 160°. RT neutron diffraction data on $RbMnP_2O_7$ were recorded in a similar fashion on the D2B instrument at the Institut Laue-Langevin, Grenoble, using a wavelength of 1.5943 Å.

4.3 Results and Discussion

4.3.1 Nuclear Structure of the $RbMn_xFe_{1-x}P_2O_7$ System

Structural details on the x = 1, 0.75, 0.5 and 0.25 compounds were obtained from Rietveld refinements of the 300 K neutron diffraction data, using the 100 K data on $RbMnP_2O_7$[2] as a starting model (Figure 4.1). A joint XRD/ ND refinement was employed for x = 0.75, due to a cancellation of the coherent scattering of neutrons from the transition metal (TM) site at this composition. The final refined structural parameters are shown in Table 4.1, with selected bond lengths and angles given in Table 4.2. Structural details on $RbFeP_2O_7$ from 300 K neutron diffraction data have been previously reported by Checker.[6]

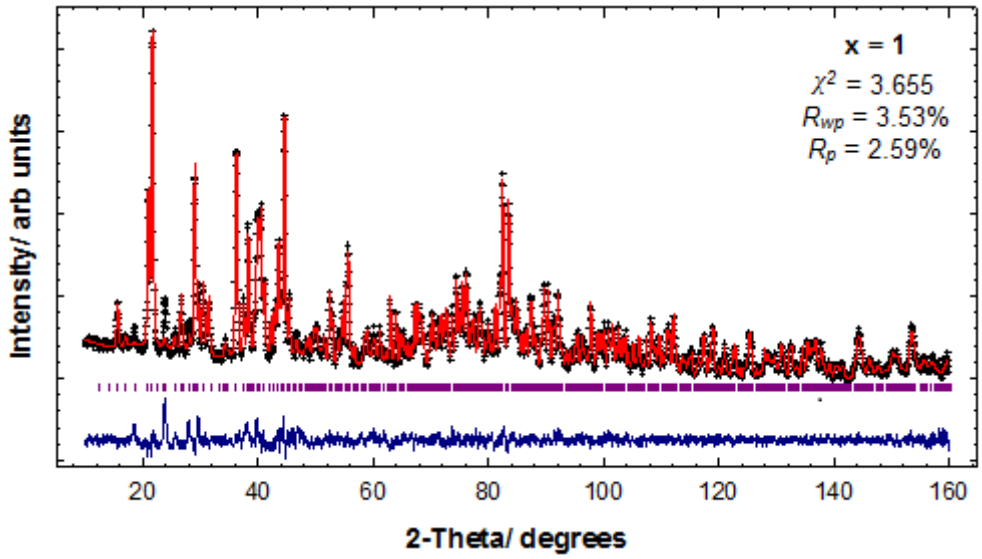

Figure 4.1: *Observed (+), calculated (-), difference profiles (-) and reflection positions (|) for the 300 K Rietveld refinements carried out on the $RbMn_xFe_{1-x}P_2O_7$ (x = 1, 0.75, 0.5 and 0.25) series. The inset for x = 0.75 shows the XRD data refinement.*

Figure 4.1 continued...

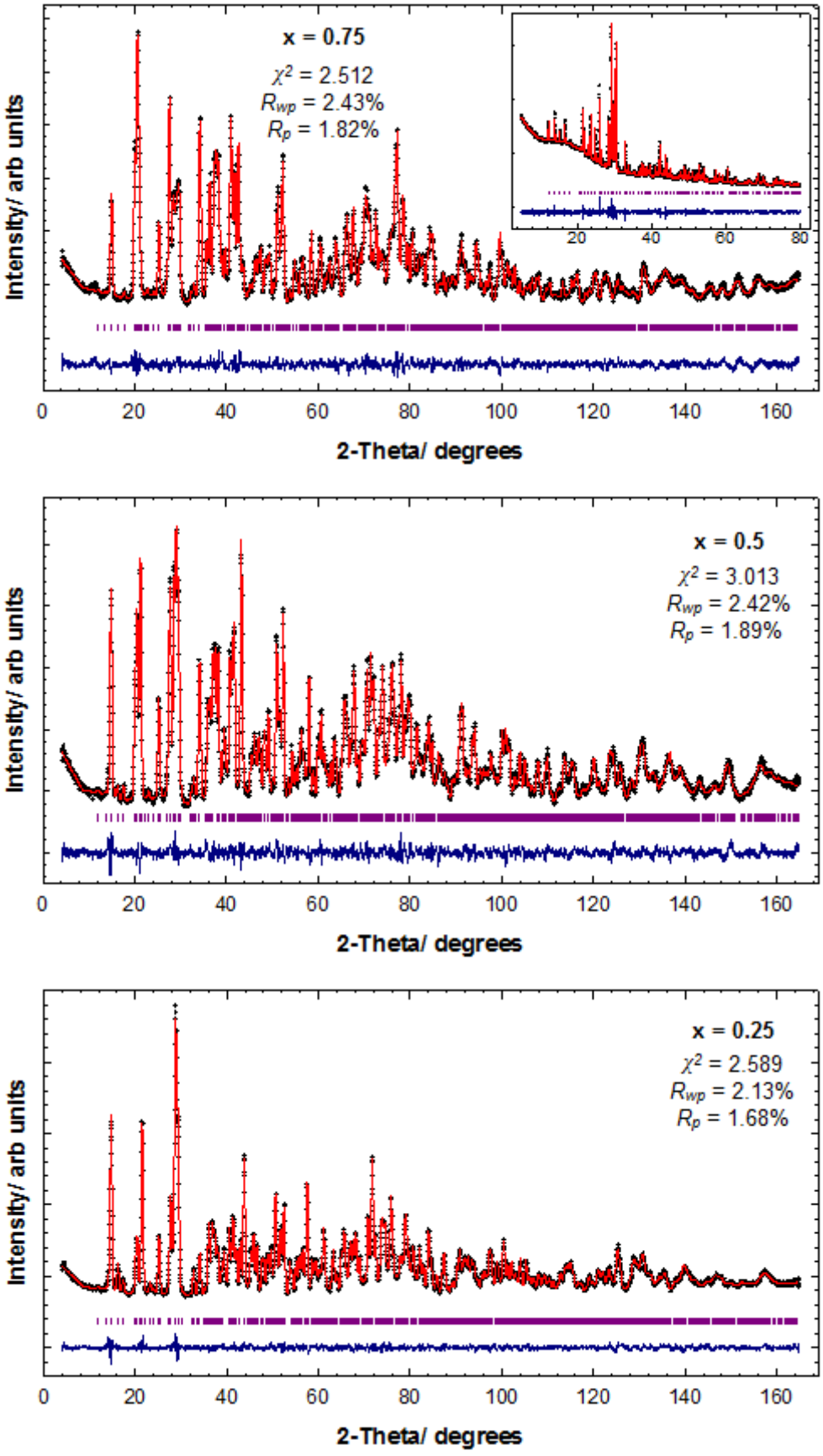

Table 4.1: *Refined structural parameters at 300 K for the $RbMn_xFe_{1-x}P_2O_7$ series (x = 1, 0.75, 0.5, 0.25 and 0) with Bond Valence Sums[7]*

		x = 1	x = 0.75	x = 0.5	x = 0.25	x = 0*
Space group $P2_1/c$	***a*/ Å**	7.3879(2)	7.4080(2)	7.4546(3)	7.4856(2)	7.4989(2)
	***b*/ Å**	9.6723(3)	9.7376(3)	9.8469(4)	9.9370(2)	9.9890(3)
	***c*/ Å**	8.6573(3)	8.5407(3)	8.4464(3)	8.3405(2)	8.2843(2)
	β/ °	105.343(2)	105.378(1)	105.488(3)	105.621(2)	105.714(2)
Mn 4*e*	***x***	0.236(1)	0.2367(6)	0.241(1)	0.2380(4)	
	y	0.6001(8)	0.6004(5)	0.5988(9)	0.6002(3)	
	z	0.755(1)	0.7575(5)	0.762(1)	0.7601(3)	
	U_{iso}/ Å^2	0.001(1)	0.027(2)	0.004(2)	0.0011(7)	
	Occ	1	0.761(2)	0.507(3)	0.251(2)	
	BVS	3.26	3.18	3.16	3.15	
Fe 4*e*	***x***		0.2367(6)	0.241(1)	0.2380(4)	0.2379(5)
	y		0.6004(5)	0.5988(9)	0.6002(3)	0.5996(4)
	z		0.7575(5)	0.762(1)	0.7601(3)	0.7594(5)
	U_{iso}/ Å^2		0.027(2)	0.004(2)	0.0011(7)	0.0061(8)
	Occ		0.239(2)	0.493(3)	0.749(2)	1
	BVS		3.17	3.15	3.15	3.23
Rb 4*e*	***x***	0.1834(6)	0.1857(3)	0.1838(5)	0.1865(3)	0.1857(8)
	y	0.3096(5)	0.3087(2)	0.3084(3)	0.3096(2)	0.3105(5)
	z	0.0417(6)	0.0423(3)	0.0426(5)	0.0462(3)	0.0452(7)
	U_{iso}/ Å^2	0.015(1)	0.0175(7)	0.0170(9)	0.0132(6)	0.019(1)
	Occ	1	1	1	1	1
	BVS	1.22	1.23	1.22	1.23	1.23
P(1) 4*e*	***x***	0.4341(8)	0.4337(4)	0.4330(6)	0.4361(5)	0.4351(7)
	y	0.6299(6)	0.6303(4)	0.6317(4)	0.6313(3)	0.6339(5)
	z	0.1905(6)	0.1893(4)	0.1880(5)	0.1871(4)	0.1858(7)
	U_{iso}/ Å^2	0.005(1)	0.0071(9)	0.0053(9)	0.0084(8)	0.006(1)
	Occ	1	1	1	1	1
	BVS	4.79	4.97	5.00	4.98	4.94
P(2) 4*e*	***x***	0.1311(8)	0.1315(4)	0.1319(5)	0.1319(4)	0.1361(7)
	y	0.9059(6)	0.9072(3)	0.9081(4)	0.9064(3)	0.9090(6)
	z	0.8308(6)	0.8312(3)	0.8320(5)	0.8301(4)	0.8304(7)
	U_{iso}/ Å^2	0.005(1)	0.0032(8)	0.007(1)	0.0092(7)	0.004(1)
	Occ	1	1	1	1	1
	BVS	5.12	5.13	4.83	4.97	4.82
O(1) 4*e*	***x***	0.3297(8)	0.3294(5)	0.3308(5)	0.3291(4)	0.3334(9)
	y	0.9528(5)	0.9509(3)	0.9497(3)	0.9468(2)	0.9425(5)
	z	0.8039(6)	0.8050(4)	0.8055(5)	0.8043(3)	0.8045(8)
	U_{iso}/ Å^2	0.006(1)	0.0081(9)	0.0075(9)	0.0079(6)	0.013(1)
	Occ	1	1	1	1	1
	BVS	2.11	2.14	2.09	2.12	2.22

Table 4.1 continued...

		x = 1	x = 0.75	x = 0.5	x = 0.25	x = 0*
	x	0.0879(7)	0.0888(5)	0.0878(5)	0.0861(4)	0.0863(7)
O(2)	***y***	0.7382(5)	0.7366(3)	0.7365(4)	0.7356(3)	0.7348(6)
4*e*	***z***	0.2584(6)	0.2580(4)	0.2561(5)	0.2578(4)	0.2580(8)
	U_{iso}/ Å^2	0.011(1)	0.0075(8)	0.0074(9)	0.0083(6)	0.012(1)
	Occ	1	1	1	1	1
	BVS	2.25	2.21	2.06	2.13	2.03
	x	0.6337(7)	0.6325(5)	0.6302(6)	0.6283(4)	0.6295(8)
O(3)	***y***	0.5729(5)	0.5753(4)	0.5764(4)	0.5757(3)	0.5742(6)
4*e*	***z***	0.2360(6)	0.2312(4)	0.2320(4)	0.2305(3)	0.2281(7)
	U_{iso}/ Å^2	0.008(1)	0.0103(8)	0.0109(8)	0.0106(7)	0.011(1)
	Occ	1	1	1	1	1
	BVS	2.11	2.09	2.08	2.11	2.01
	x	0.1445(7)	0.1466(5)	0.1461(6)	0.1509(5)	0.1486(9)
O(4)	***y***	0.5902(6)	0.5871(4)	0.5880(4)	0.5855(3)	0.5850(6)
4*e*	***z***	0.5032(6)	0.5053(5)	0.5141(5)	0.5128(4)	0.5157(7)
	U_{iso}/ Å^2	0.013(1)	0.017(1)	0.021(1)	0.0152(7)	0.016(1)
	Occ	1	1	1	1	1
	BVS	1.96	2.02	1.88	1.99	1.97
	x	0.3264(7)	0.3250(5)	0.3227(5)	0.3232(4)	0.3236(8)
O(5)	***y***	0.6048(6)	0.6050(4)	0.6043(5)	0.6043(3)	0.6062(6)
4*e*	***z***	0.0175(6)	0.0173(4)	0.0146(5)	0.0115(4)	0.0060(7)
	U_{iso}/ Å^2	0.013(1)	0.0125(9)	0.016(1)	0.0149(8)	0.013(1)
	Occ	1	1	1	1	1
	BVS	1.74	1.85	1.92	1.94	1.94
	x	0.9872(7)	0.9894(5)	0.9904(6)	0.9925(4)	0.9920(7)
O(6)	***y***	0.4979(5)	0.4957(3)	0.4959(4)	0.4951(3)	0.4960(5)
4*e*	***z***	0.2289(6)	0.2261(4)	0.2275(4)	0.2253(3)	0.2215(7)
	U_{iso}/ Å^2	0.003(1)	0.0088(9)	0.0096(9)	0.0095(7)	0.005(1)
	Occ	1	1	1	1	1
	BVS	2.22	2.16	2.13	2.09	2.05
	x	0.4448(7)	0.4439(4)	0.4434(5)	0.4426(4)	0.4426(8)
O(7)	***y***	0.7832(5)	0.7811(3)	0.7798(4)	0.7802(3)	0.7806(6)
4*e*	***z***	0.2457(6)	0.2413(4)	0.2379(5)	0.2396(4)	0.2360(7)
	U_{iso}/ Å^2	0.007(1)	0.0074(9)	0.015(1)	0.0113(7)	0.010(1)
	Occ	1	1	1	1	1
	BVS	2.00	2.04	2.05	1.97	2.01

**Data on x = 0 was collected by Checker[6]*

Table 4.2: *Selected Bond Distances (Å) and Angles (degrees) for the $RbMn_xFe_{1-x}P_2O_7$ series (x = 1, 0.75, 0.5, 0.25 and 0) and Global Instability Index[8] Values*

	x = 1	x = 0.75	x = 0.5	x = 0.25	x = 0*
TM-O(2)	1.91(1)	1.929(5)	1.978(8)	1.986(4)	2.006(7)
TM-O(3)	1.923(9)	1.956(6)	1.967(9)	2.005(4)	1.989(7)
TM-O(4)	2.11(1)	2.082(6)	2.030(9)	1.994(4)	1.953(7)
TM-O(5)	2.19(1)	2.142(5)	2.053(9)	2.021(4)	1.970(8)
TM-O(6)	1.936(9)	1.956(5)	1.985(9)	2.001(4)	2.015(6)
TM-O(7)	1.932(9)	1.954(5)	1.98(1)	1.982(4)	1.996(7)
O(2)-TM-O(3)	173.7(5)	173.5(3)	173.8(5)	174.3(2)	174.1(3)
O(2)-TM-O(4)	91.4(4)	91.6(2)	88.5(3)	91.3(2)	91.2(3)
O(2)-TM-O(5)	89.3(4)	89.9(2)	90.9(3)	90.8(2)	90.2(3)
O(2)-TM-O(6)	84.3(4)	84.0(2)	83.2(3)	83.6(2)	84.0(3)
O(2)-TM-O(7)	89.4(4)	88.4(2)	87.3(4)	87.7(2)	87.4(3)
O(3)-TM-O(4)	91.1(4)	90.9(2)	90.7(4)	89.8(2)	90.9(3)
O(3)-TM-O(5)	88.0(4)	87.5(2)	89.5(3)	87.8(1)	87.6(3)
O(3)-TM-O(6)	89.9(4)	90.0(2)	90.6(4)	90.8(2)	90.5(3)
O(3)-TM-O(7)	96.4(4)	97.6(2)	98.8(4)	97.9(2)	98.1(3)
O(4)-TM-O(5)	178.4(5)	177.5(3)	176.5(5)	176.9(2)	177.4(4)
O(4)-TM-O(6)	90.3(4)	89.9(2)	87.2(4)	88.9(2)	89.1(3)
O(4)-TM-O(7)	91.2(4)	90.4(2)	89.4(3)	90.0(2)	90.1(3)
O(5)-TM-O(6)	88.3(4)	88.2(2)	89.3(3)	89.0(2)	88.9(3)
O(5)-TM-O(7)	90.3(4)	91.8(2)	94.1(4)	92.4(2)	92.1(3)
O(6)-TM-O(7)	173.5(5)	172.4(3)	170.0(4)	171.2(2)	171.3(3)
P(1)-O(1)	1.612(8)	1.614(4)	1.617(5)	1.619(4)	1.592(7)
P(1)-O(3)	1.525(7)	1.518(4)	1.517(5)	1.492(4)	1.525(7)
P(1)-O(5)	1.517(6)	1.496(4)	1.500(5)	1.505(4)	1.523(8)
P(1)-O(7)	1.554(6)	1.530(4)	1.514(5)	1.540(4)	1.520(8)
P(2)-O(1)	1.611(7)	1.598(4)	1.610(5)	1.600(4)	1.587(8)
P(2)-O(2)	1.527(7)	1.533(5)	1.560(5)	1.537(4)	1.562(7)
P(2)-O(4)	1.470(7)	1.462(5)	1.514(6)	1.494(4)	1.514(8)
P(2)-O(6)	1.509(7)	1.518(4)	1.513(5)	1.523(4)	1.534(7)
O(1)-P(1)-O(3)	104.4(4)	106.0(3)	104.8(3)	106.1(2)	105.0(4)
O(1)-P(1)-O(5)	108.1(4)	107.4(3)	106.6(3)	105.3(2)	106.8(4)
O(1)-P(1)-O(7)	106.2(4)	106.7(3)	107.7(3)	105.8(3)	106.3(4)
O(3)-P(1)-O(5)	114.6(5)	114.2(3)	114.7(3)	115.0(3)	113.0(5)
O(3)-P(1)-O(7)	107.4(4)	107.5(3)	107.6(3)	109.4(3)	110.6(5)
O(5)-P(1)-O(7)	115.3(4)	114.5(3)	114.8(3)	114.5(3)	114.3(4)
O(1)-P(2)-O(2)	107.3(4)	106.5(3)	106.1(3)	107.1(2)	106.1(4)
O(1)-P(2)-O(4)	108.7(4)	107.9(3)	108.5(3)	106.6(3)	109.0(5)
O(1)-P(2)-O(6)	105.6(4)	105.6(2)	106.5(3)	106.0(2)	108.9(4)
O(2)-P(2)-O(4)	113.0(5)	113.7(3)	113.0(3)	113.6(3)	111.6(5)
O(2)-P(2)-O(6)	106.5(5)	107.0(3)	107.0(3)	108.6(3)	106.6(5)
O(4)-P(2)-O(6)	115.2(4)	115.6(3)	115.1(3)	114.4(2)	114.3(4)
GII	0.19	0.14	0.12	0.11	0.14

**Data on x = 0 was collected by Checker[6]*

All compounds were found to adopt a type-I[9] pyrophosphate structure with space group $P2_1/c$. The structure, as shown in Figure 4.2, can be described as a three-dimensional network of TM-O_6 octahedra corner-linked to the PO_4 tetrahedra of five P_2O_7 units, one of them being connected in a bidentate fashion. This results in tunnels running along the *c*-direction of the structure which hold the Rb^+ cations in 10-fold coordination. The two PO_4 tetrahedra that constitute the pyrophosphate unit are in a semi-staggered configuration and are typically distorted to give long P-O bonds to the bridging O(1) atom and shorter bonds to the terminal oxygen atoms.

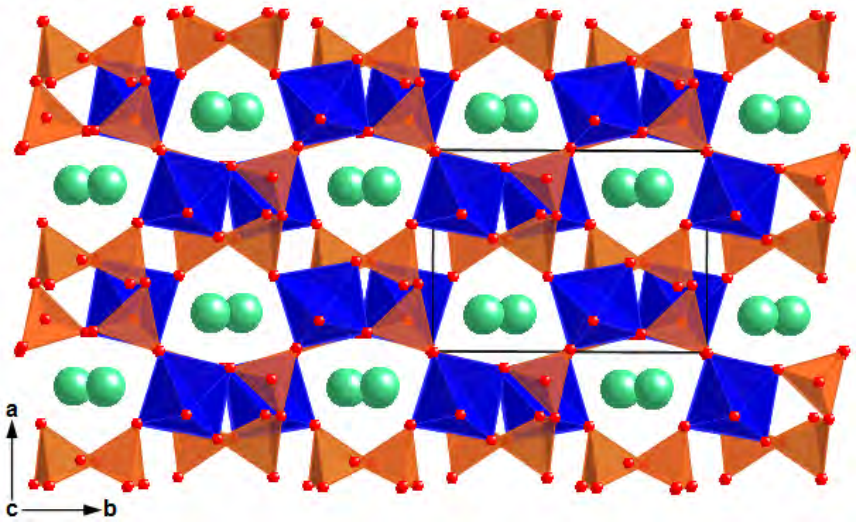

Figure 4.2: *Structure adopted by $RbMn_xFe_{1-x}P_2O_7$ compounds showing TM-O_6 octahedra (blue), P_2O_7 condensed phosphate tetrahedra (orange) and rubidium cations (green spheres) located in the intersecting tunnels. The thin black line defines the unit cell.*

Bond Valence Sum (BVS) calculations according to the values provided by Brown and Altermatt[7] showed that across all compositions, the valencies for most atoms in the $RbMn_xFe_{1-x}P_2O_7$ structure were acceptably close to their expected atomic valence (see Table 4.1). While some ions appeared to be slightly overbonded, others were slightly underbonded. Due to the uncertainties associated with measured bond lengths, it is generally expected that experimental bond valences may not always

exactly match atomic valences. The Global Instability Index[8] (GII) measures the extent to which the valence sum rule is violated, and can provide a good indication of whether discrepancies observed in BVS values are related to the crystal structure of the compound (see Appendix 1). GII values (Table 4.2) were found to range from 0.11-0.19 valence units (vu) for the $RbMn_xFe_{1-x}P_2O_7$ series, with values being ≤0.14 vu for $x < 1$. The magnitude of the values suggests that the structures are stable and that lattice strain is reduced with the introduction of Fe into the system. This can be contrasted to the $NH_4Mn_xFe_{1-x}P_2O_7$ series discussed in the previous chapter, where GII values between 0.20-0.26 vu were obtained, indicating the presence of a greater amount of lattice strain. The increased amount of strain in the ammonium system cannot be explained by a difference in lattice parameters or ionic radii, as they are reasonably similar for both M^I cations.[10-11] The cations do however show differing coordination behaviours towards the surrounding oxygen atoms. In the case of Rb^+, the bonding is predominantly ionic in nature, with this cation found in 10-fold coordination. Conversely, in the case of NH_4^+, N-H---O hydrogen-bonding is observed, giving this cation a coordination number of 3-5, *cf.* the isostructural compound $NH_4YbP_2O_7$,[12] where the ammonium cation is found to be in 4-fold coordination. It has been postulated by Khan and Baur[11] that where the coordination number is small, the hydrogen-bonding character of the ammonium cation dominates, but at larger coordination numbers it begins to show pseudo-alkali character. It is therefore possible that within the ammonium system, the full bonding requirements of the oxygen atoms are not met through a consequence of the NH_4^+ cations adopting a lower coordination number. This would most likely result in the

remaining cations of the structure having to compensate the oxygen atoms, leading to a strained environment.

4.3.2 Trends and Electronic Distortions in the $RbMn_xFe_{1-x}P_2O_7$ System

Similarly to the observation made for the α-$NH_4Mn_xFe_{1-x}P_2O_7$ compounds (Chapter 3), the electronic properties of the two transition metal centres also appear to dictate the trends observed as the $RbMn_xFe_{1-x}P_2O_7$ series is traversed. It should be noted that these rubidium and ammonium analogues are isostructural, but different structural models were used for the refinement of the diffraction data, resulting in different labelling schemes for the atoms. That is, for $x > 0$, in the α-$NH_4Mn_xFe_{1-x}P_2O_7$ series, the TM-O(2) and TM-O(6) bonds are those which show an axial elongation whereas for the $RbMn_xFe_{1-x}P_2O_7$ series discussed here, the TM-O(4) and TM-O(5) bonds are those which are axially elongated.

Octahedral Mn^{3+} and Fe^{3+} have similar ionic radii of 0.65 Å,[10] and as such their size would not be expected to have a significant influence on the lattice. Figure 4.3 shows the average transition metal to oxygen (TM-O) bond lengths. The Mn end member showed a highly distorted [4+2] octahedral coordination sphere, similar to that observed for α-$NH_4MnP_2O_7$. As the amount of Fe in $RbMn_xFe_{1-x}P_2O_7$ increased, the average distortion at the transition metal centre became less pronounced, and for the higher Fe contents a regular octahedral coordination sphere was seen, as would be expected for Fe^{3+} (d^5).

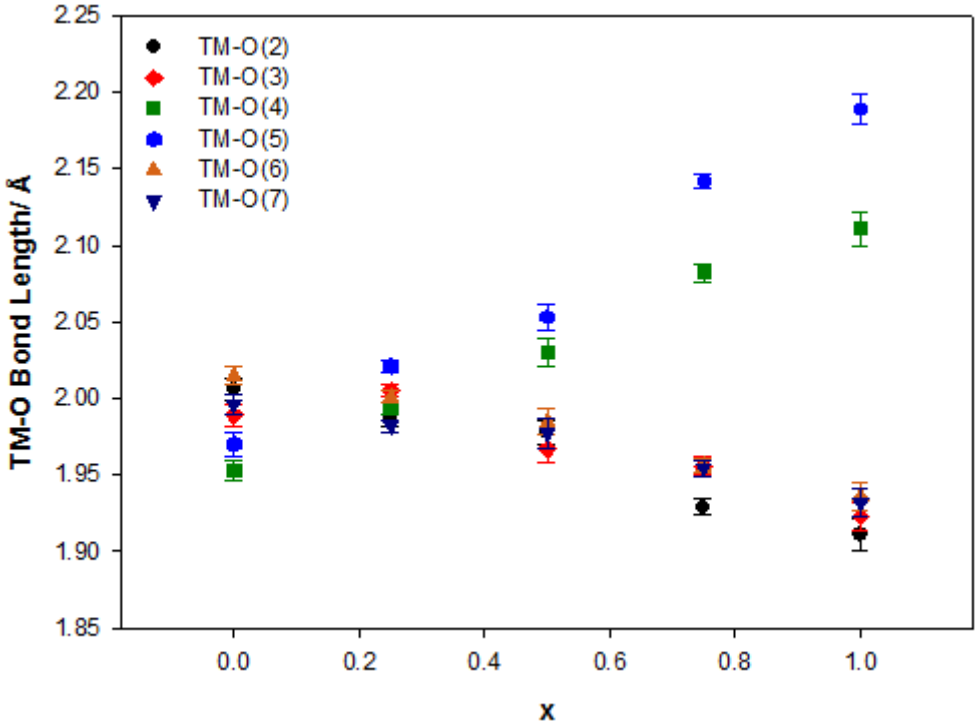

Figure 4.3: *Average bond lengths of the TM-O_6 octahedron as a function of varying Mn^{3+} content in the $RbMn_xFe_{1-x}P_2O_7$ solid solution.*

From the data it can also be seen that with increasing Mn content, the TM-O(4) and TM-(O5) bond lengths became longer whereas the remaining four bonds of the octahedron became shorter. A closer inspection of the transition metal coordination sphere (Figure 4.4) shows that the direction of the elongated bonds is closely correlated with the *c*-axis of the structure while the remaining four bonds lie in between the unit cell axes. From this we would expect an increase to occur in the *c*-parameter with increasing Mn content but a decrease in *a* and *b*, which is confirmed by Figure 4.5.

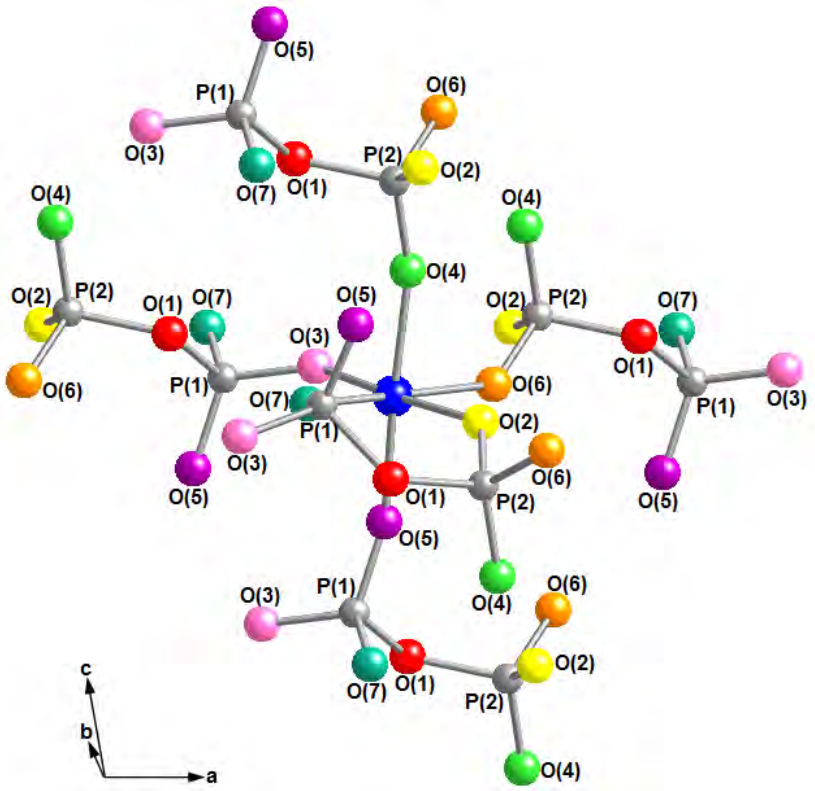

Figure 4.4: *Orientation of the pyrophosphate ligands about the TM centre in the $RbMn_xFe_{1-x}P_2O_7$ structure type. The TM and phosphorus atoms are shown as blue and grey spheres, respectively.*

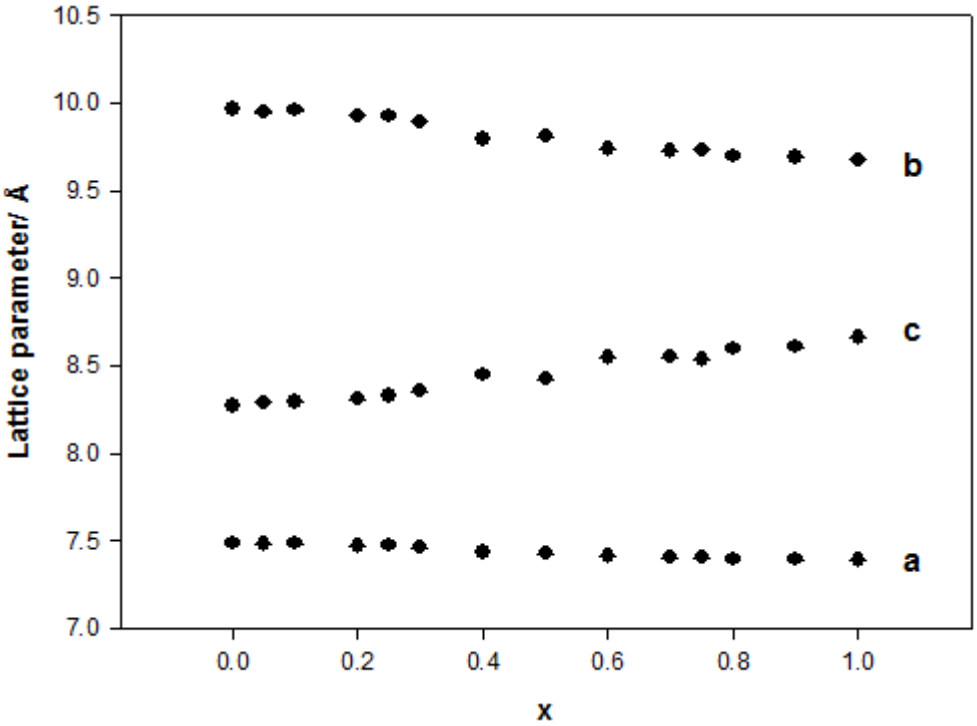

Figure 4.5: *Change in the a-, b- and c-lattice parameters with varying Mn^{3+} content in the $RbMn_xFe_{1-x}P_2O_7$ solid solution (XRD data).*

Figure 4.6 shows that a decrease also occurred in the *β*-angle with increasing Mn content and a minimum in the volume at x ≈ 0.5. The change in *β*-angle can be explained by considering Figure 4.5, which shows that the greatest difference in length between the *a*- and *c*-axes occurs with increasing x. At this point the axial ligands are at their furthest from the TM centre but the equatorial ligands are at their closest, giving increased electrostatic repulsion between the latter. In theory this ligand repulsion can be reduced if the *a*- and *c*-axes are bought closer together *i.e.* if *β* decreases.

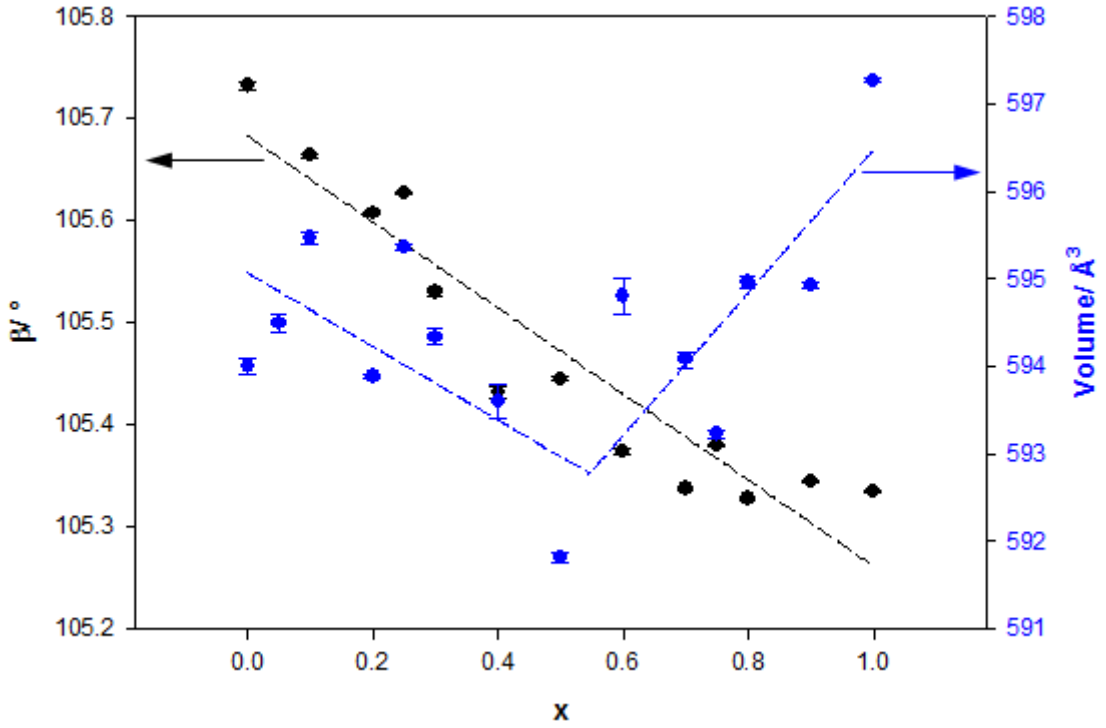

Figure 4.6: *Change in the β-parameter (●) and volume (●) of the unit cell with varying Mn^{3+} content in the $RbMn_xFe_{1-x}P_2O_7$ solid solution (XRD data).*

The electronic spectra of these compounds were used to further investigate the Jahn-Teller effect at the Mn^{3+} centre. The PeakFit[13] program was used to resolve the observed bands into a sum of Gaussian bands on a constant baseline, as can be seen in Figure 4.7. A detailed discussion on how these spectra were

modelled, the bands assigned and the electronic properties of 6-coordinate Mn^{3+} was given in Chapter 3, section 3.3.4.2. For x = 0, only one weak transition was modelled in the visible region, consistent with the $^6A_{1g}$ ground state of Fe^{3+}. This meant that for compounds with x > 0, the transitions occurring in the visible region could be directly related to the MnO_6 coordination sphere.

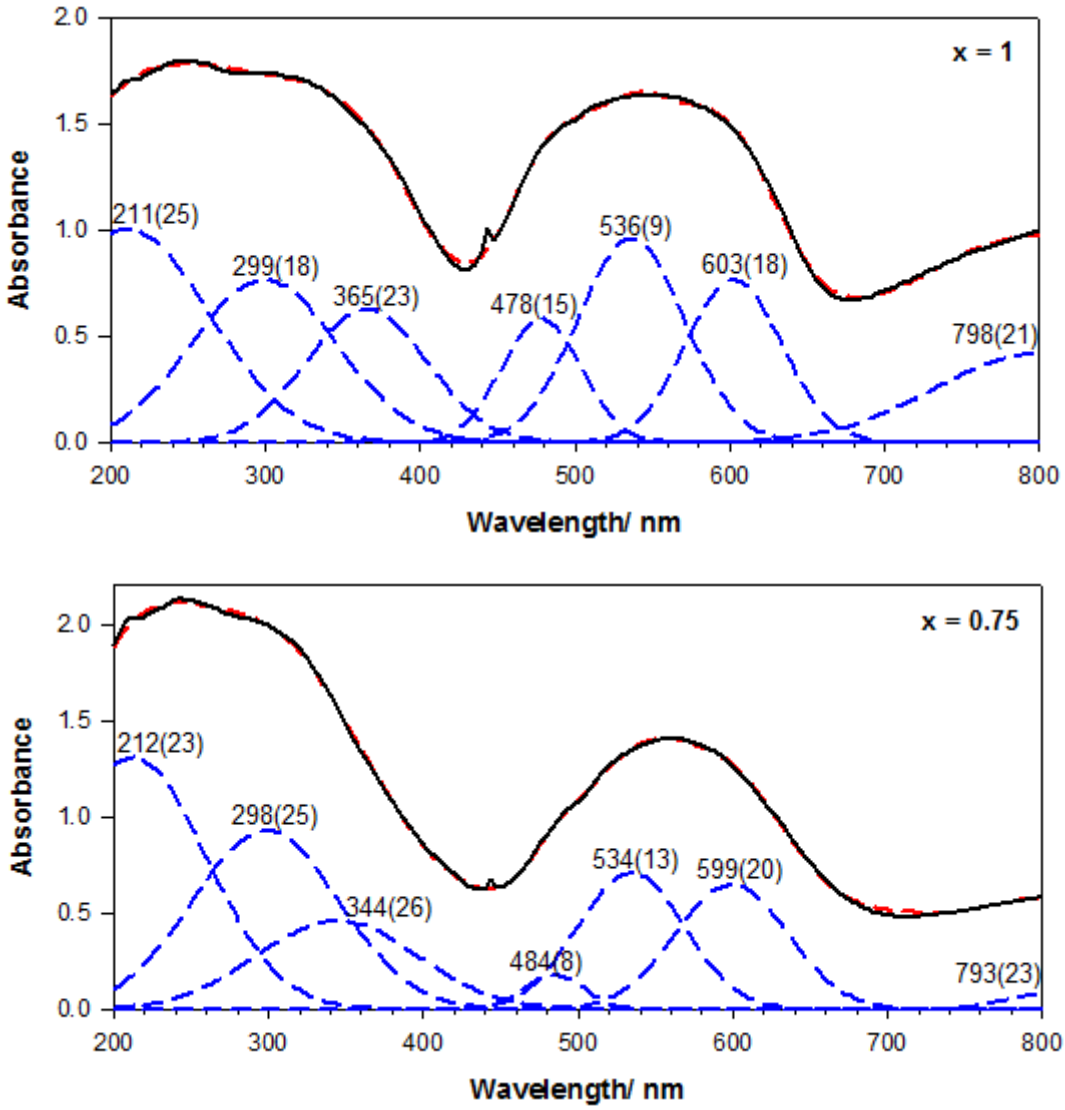

Figure 4.7: *UV-Vis spectra of the $RbMn_xFe_{1-x}P_2O_7$ series, showing raw data (—), fitted Gaussian bands (---) and sum of the fitted Gaussian bands (---). Peak positions are marked.*

Figure 4.7 continued...

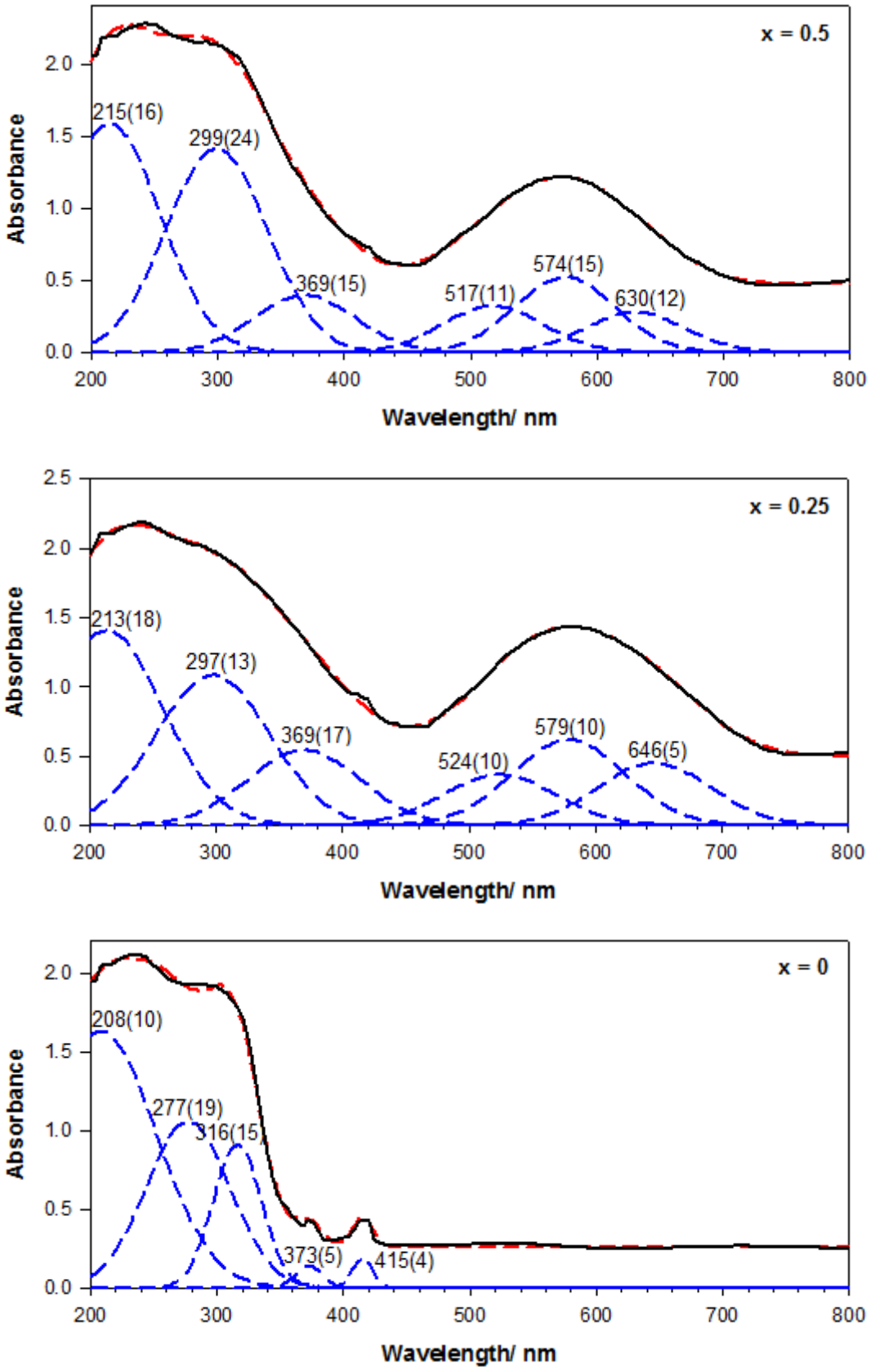

For x = 1 and 0.75, four d→d transitions were modelled in the visible region, suggesting that the MnO_6 coordination sphere was distorted beyond a [4+2] elongation. On the other hand, for x = 0.5 and 0.25, only three d→d transitions were seen, suggesting a [4+2] MnO_6 tetragonal elongation. Given that the second transition ($^5B_{1g}$→$^5B_{2g}$) coincides with the average value of 10*Dq*, values were calculated to be 208(5) and 207(4) kJ mol^{-1} for x = 0.5 and 0.25, respectively. These values were similar to those obtained for the corresponding α-$NH_4Mn_xFe_{1-x}P_2O_7$ compounds (section 3.3.4.2) and are within the range of 191-251 kJ mol^{-1} that is expected for high spin Mn^{3+} complexes.[14] Figure 4.8 shows that a distinct colour change from violet through to blue occurred across the series, which was likely to be related to the subtle changes in the MnO_6 coordination sphere as the series was traversed.

Figure 4.8: *Colouration of the $RbMn_xFe_{1-x}P_2O_7$ series.*

The bond lengths obtained from diffraction (Table 4.2) were consistent with the MnO_6 symmetry suggested by the electronic spectra of these compounds. Indeed, for x = 1 and 0.75, the axial TM-O bond lengths were found to be just outside three standard errors of each other. Normally this would still be described as a [4+2] elongation, but perhaps it can also be interpreted as a [4+1+1] pattern of bond lengths, for which C_{4v} symmetry would be expected. The loss of an inversion centre

would explain the intense colouration exhibited by these two members. For x = 0.5 and 0.25, neutron diffraction showed a [4+2] TM-O_6 elongation, consistent with the D_{4h} symmetry suggested by the electronic spectra. However, the intense colouration also exhibited by these two members suggests deviations from this symmetry, possibly due to local disorder, which was perhaps not detected in the neutron diffraction and spectroscopic measurements.

In an attempt to obtain further details on the TM-O_6 coordination spheres within these samples, XANES, EXAFS and ^{57}Fe Mössbauer measurements were conducted. Indeed, the pre-edge region of an X-ray absorption spectrum can give information on bonding, electronic configuration and site symmetry. Figures 4.9 and 4.10 show that the Mn and Fe edge positions were identical across these compounds and consistent with the elements existing in the +3 oxidation state. The shapes and intensities of the edges were also very similar, giving no reason to suggest a change in the MnO_6 and FeO_6 coordination environments across the series.

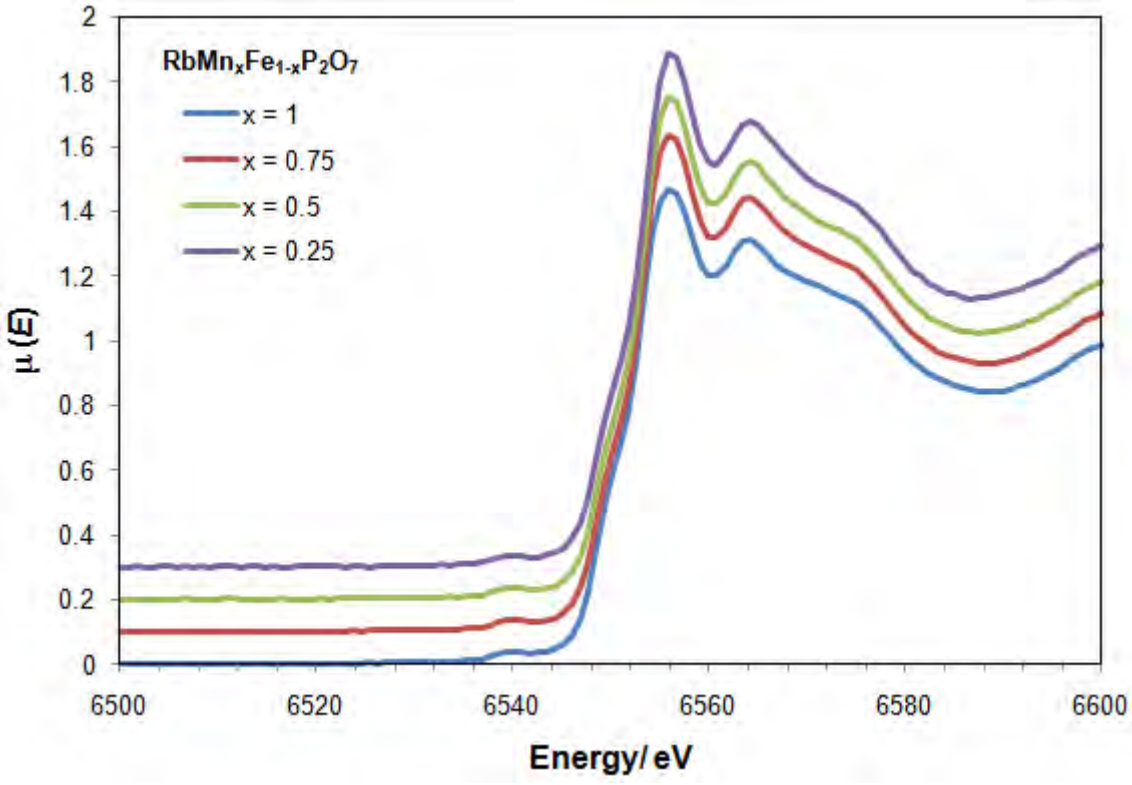

Figure 4.9: *Mn K-edge XANES (stack plots) for the $RbMn_xFe_{1-x}P_2O_7$ series*

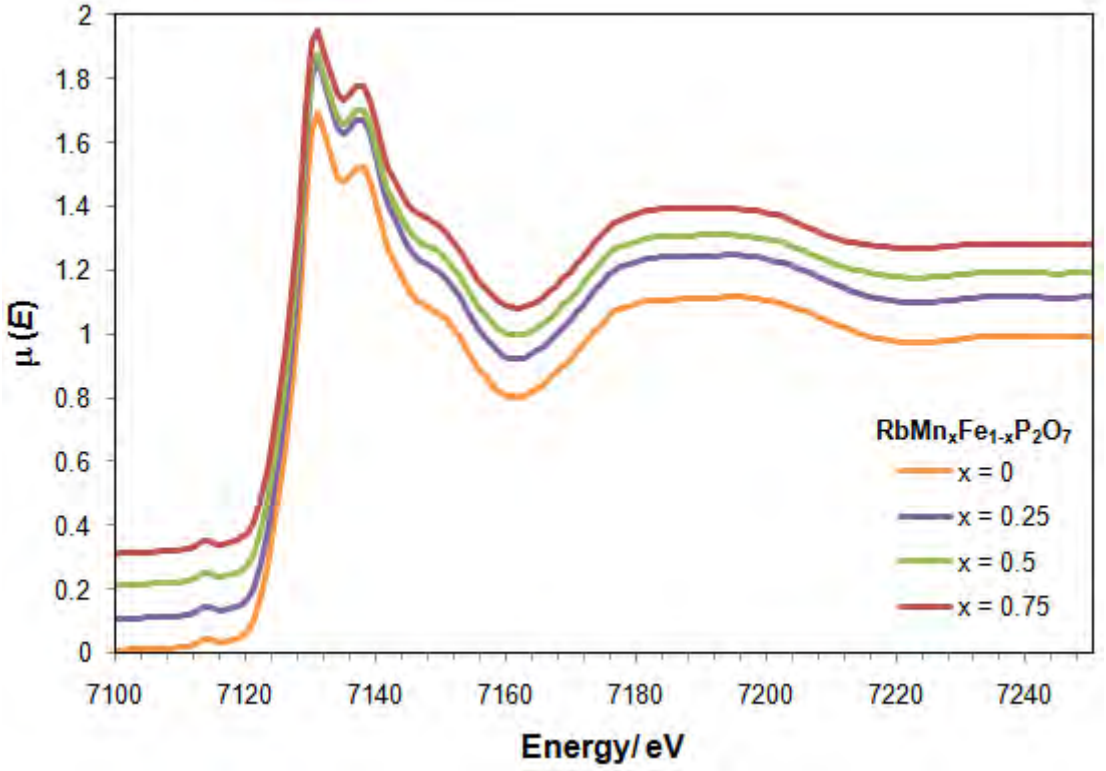

Figure 4.10: *Fe K-edge XANES (stack plots) for the $RbMn_xFe_{1-x}P_2O_7$ series*

The Mn EXAFS spectra are shown in Figure 4.11. All plots were found to be similar and the best fit obtained with four oxygens in the first coordination shell and two in a longer second shell (Table 4.3). The Debye-Waller factors associated with the equatorial bond lengths were normal for samples measured at room temperature and indicated that there was minimal static disorder in these bond lengths. For the axial bond lengths the Debye-Waller factors were a little higher, suggesting a slightly larger spread of these distances from the average value. Although the equatorial bond lengths and axial bond lengths were within error of each other across the series, the former generally became shorter with increasing x while the latter became longer; a trend also seen in the diffraction data. It is possible that this subtle effect is responsible for the colour change that was observed.

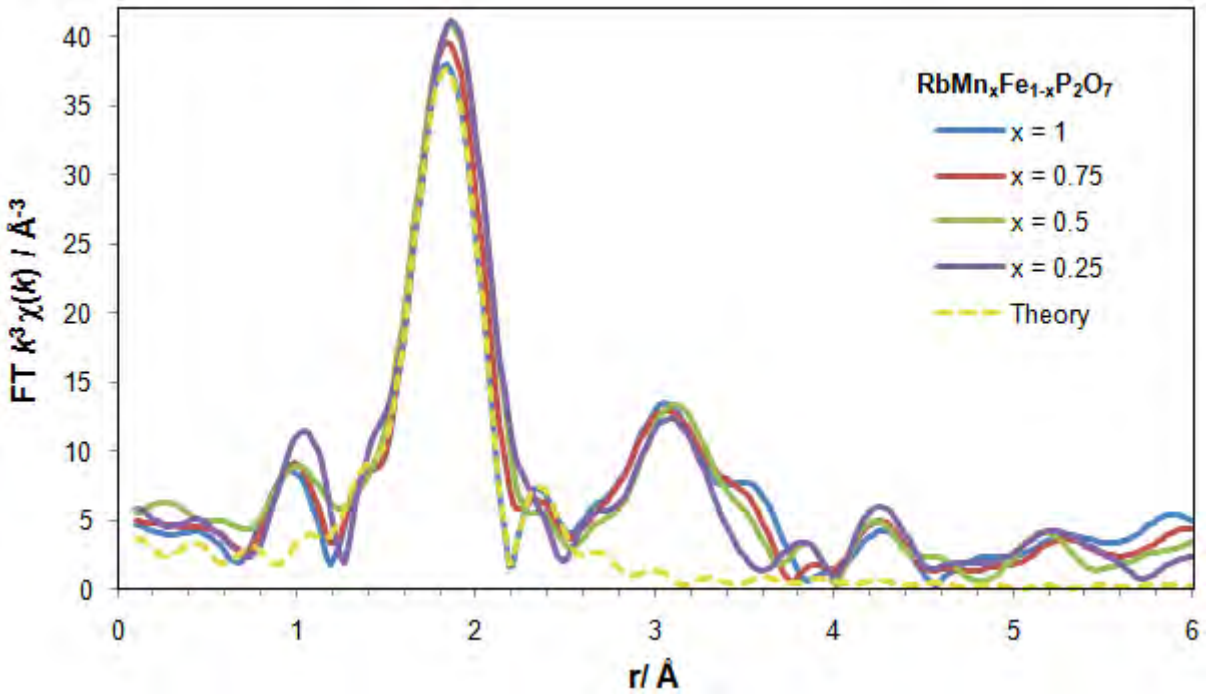

Figure 4.11: *Fourier Transformed Mn K-edge EXAFS for the $RbMn_xFe_{1-x}P_2O_7$ series*

The bond lengths obtained from EXAFS and neutron diffraction for x = 1 were in general agreement. Although EXAFS also only provides average bond distances, the

average is taken over the individual transition metal centres whereas in diffraction, for mixed Mn/ Fe compositions, the average is taken for the site.

Table 4.3: *Mn-O bond lengths (r) and associated Debye-Waller factors (σ^2) obtained from EXAFS measurements on the $RbMn_xFe_{1-x}P_2O_7$ series*

$RbMn_xFe_{1-x}P_2O_7$	r(1)/ Å	σ^2/ Å^2	r(2)/ Å	σ^2/ Å^2
x = 1	1.92(1)	0.010(2)	2.17(3)	0.020(4)
x = 0.75	1.93(1)	0.010(2)	2.12(3)	0.024(4)
x = 0.5	1.93(1)	0.011(2)	2.09(3)	0.027(4)
x = 0.25	1.94(1)	0.011(2)	2.09(3)	0.023(4)

It should be noted that the results from the Mn XANES and EXAFS spectra somewhat contrasted with the UV-Vis data collected. All three techniques would be expected to provide information on the local manganese environment. However, the XANES data indicated no change in site symmetry and the EXAFS data suggested no significant change in the Mn-O bond lengths across the series. On the other hand, UV-Vis data suggested a [4+2] elongation for x = 0.25 and 0.5 and a distortion beyond this for x = 0.75 and 1. These opposing results perhaps reflect differences in the subtleties of these techniques, though the colour change observed across the series does suggest a change in the local manganese environment.

Figure 4.12 and Table 4.4 show that the best fit for the Fe EXAFS spectra was obtained with six oxygens at a distance of 1.99(1) Å from the iron centre, with Debye-Waller factors indicating that there was little static disorder in these bond lengths. Indeed, we would expect Fe^{3+} to take up a regular octahedral environment in which all six bond lengths are closely matched in length. For x = 0 the bond lengths obtained were in agreement with those determined from neutron diffraction.

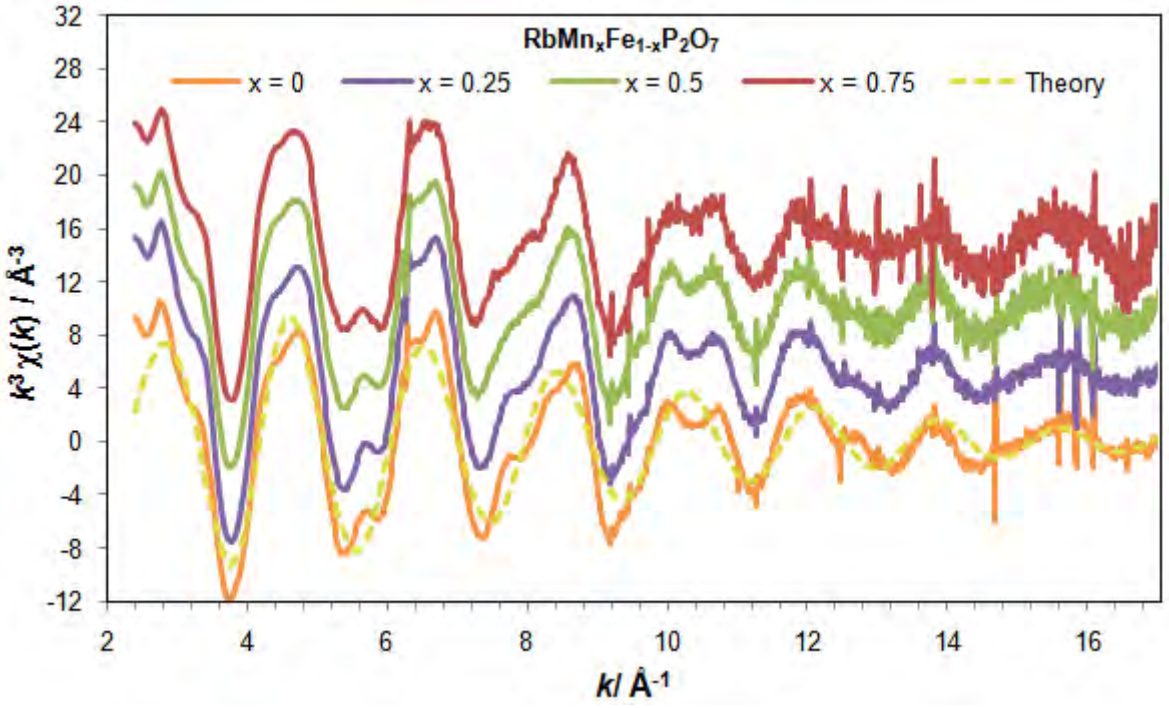

Figure 4.12: *Fe K-edge EXAFS for the $RbMn_xFe_{1-x}P_2O_7$ series*

Table 4.4: *Fe-O bond lengths (r) and associated Debye-Waller factors (σ^2) obtained from EXAFS measurements on the $RbMn_xFe_{1-x}P_2O_7$ series*

$RbMn_xFe_{1-x}P_2O_7$	r(1)/ Å	σ^2/ Å^2
x = 0.75	1.99(1)	0.009(2)
x = 0.5	1.99(1)	0.009(2)
x = 0.25	1.99(1)	0.009(2)
x = 0	1.99(1)	0.010(2)

The local Fe environment within the $RbMn_xFe_{1-x}P_2O_7$ compounds was investigated by ^{57}Fe Mössbauer spectroscopy. The positions of the peaks in the spectra (Figure 4.13) were similar across all compounds (~0.4 mm s^{-1}) and consistent with Fe being in the +3 oxidation state.

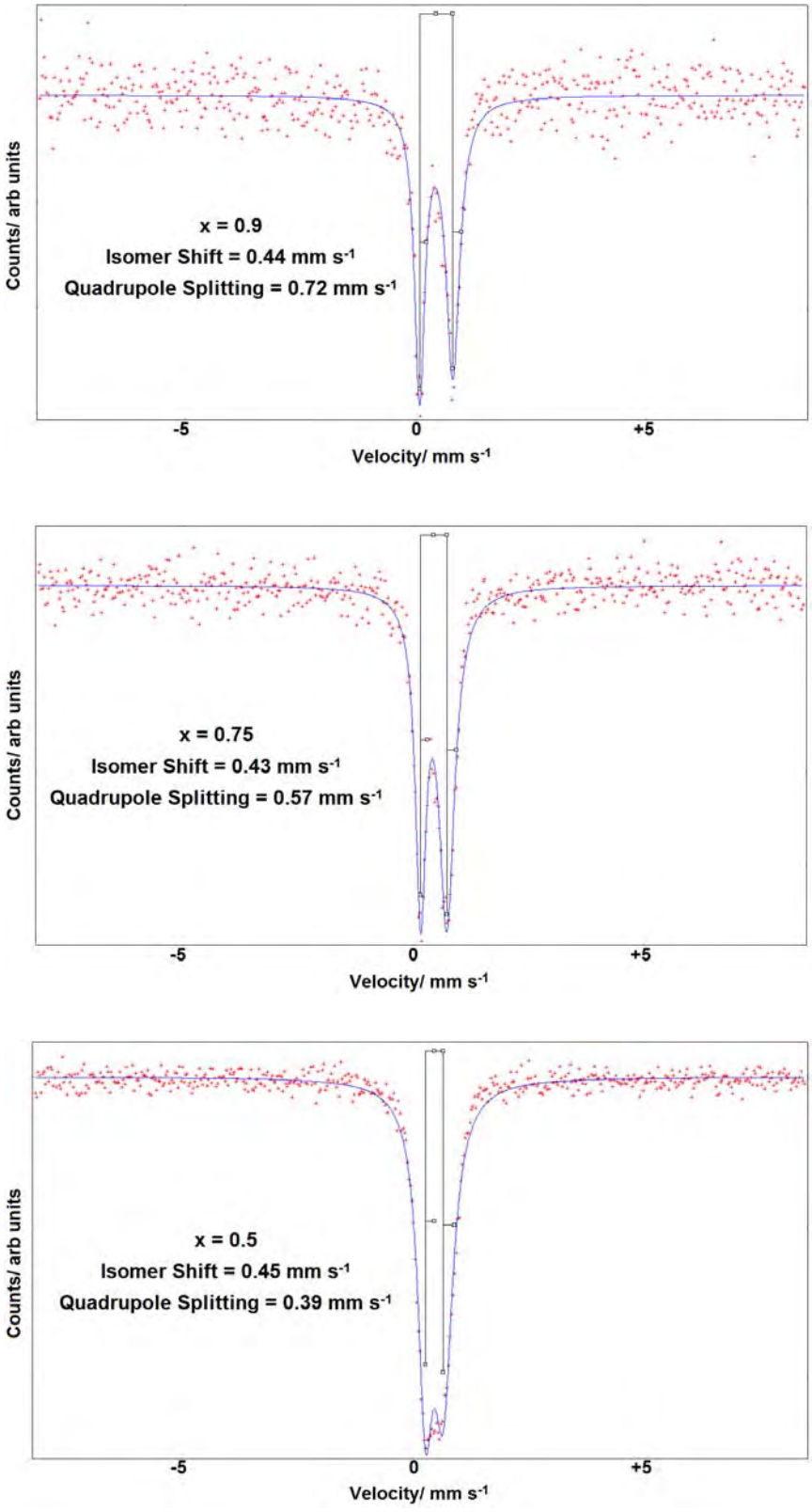

Figure 4.13: *Mössbauer spectra for the $RbMn_xFe_{1-x}P_2O_7$ series*

Figure 4.13 continued...

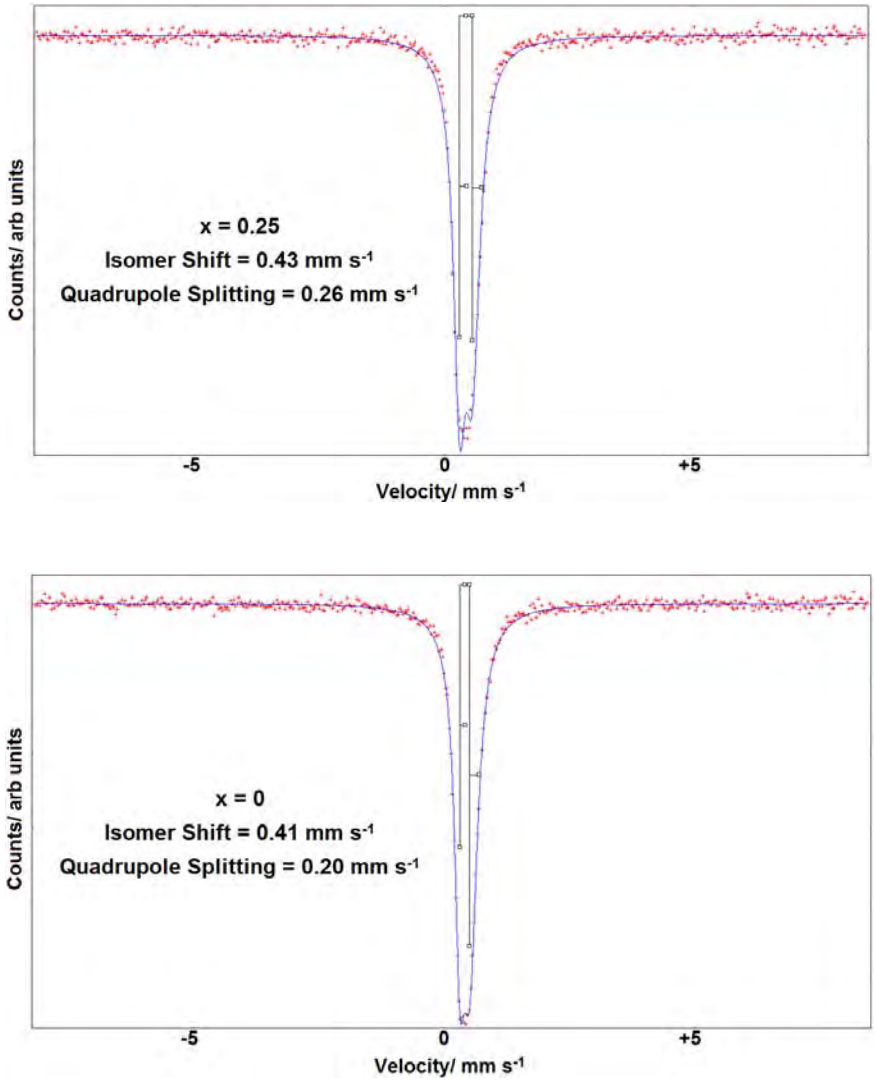

Although a doublet was observed for all compositions, the quadrupole splitting decreased with decreasing x, suggesting that the FeO_6 unit becomes very close to an ideal octahedron when there is less Mn^{3+} present in the system. It is worth noting that such small quadrupole splittings, observed in particular for x = 0 and 0.25, are not often observed. However, an even smaller splitting of 0.14 mm s^{-1} has been reported for $NaFeP_2O_7$,[15] perhaps suggesting that this is a feature of iron pyrophosphate systems.

The magnitude of the quadrupole splitting is related to the extent of the asymmetric electric field (produced by asymmetric electronic charge distribution or asymmetric ligand arrangement) surrounding the Fe^{3+}. All compositions being isostructural have the same ligand arrangement, and so it is assumed that the decrease in quadrupole splitting is caused by the surrounding electronic charge becoming more symmetrically distributed. No evidence for this was seen in the Fe EXAFS data, which suggested that the Fe-O bond lengths remained the same across the series. The O-TM-O bond angles obtained from diffraction measurements also showed no clear trend with decreasing x (see Figures 4.14 and 4.15). It is therefore possible that the change to a more regular FeO_6 octahedron is a subtle effect only detected by the highly sensitive technique of Mössbauer spectroscopy. At higher Mn^{3+} contents, it is likely that the electronic requirements of this cation dominate over those of Fe^{3+}, meaning that the latter cannot take up a highly symmetrical environment. However, as the amount of iron in the system increases, Mn EXAFS to an extent (as evidenced by Debye-Waller factors) and UV-Vis spectroscopy suggest that the MnO_6 coordination sphere becomes more regular, perhaps now in order to satisfy the electronic requirements of Fe^{3+}. This effect appears to manifest itself as a colour change observed across the series.

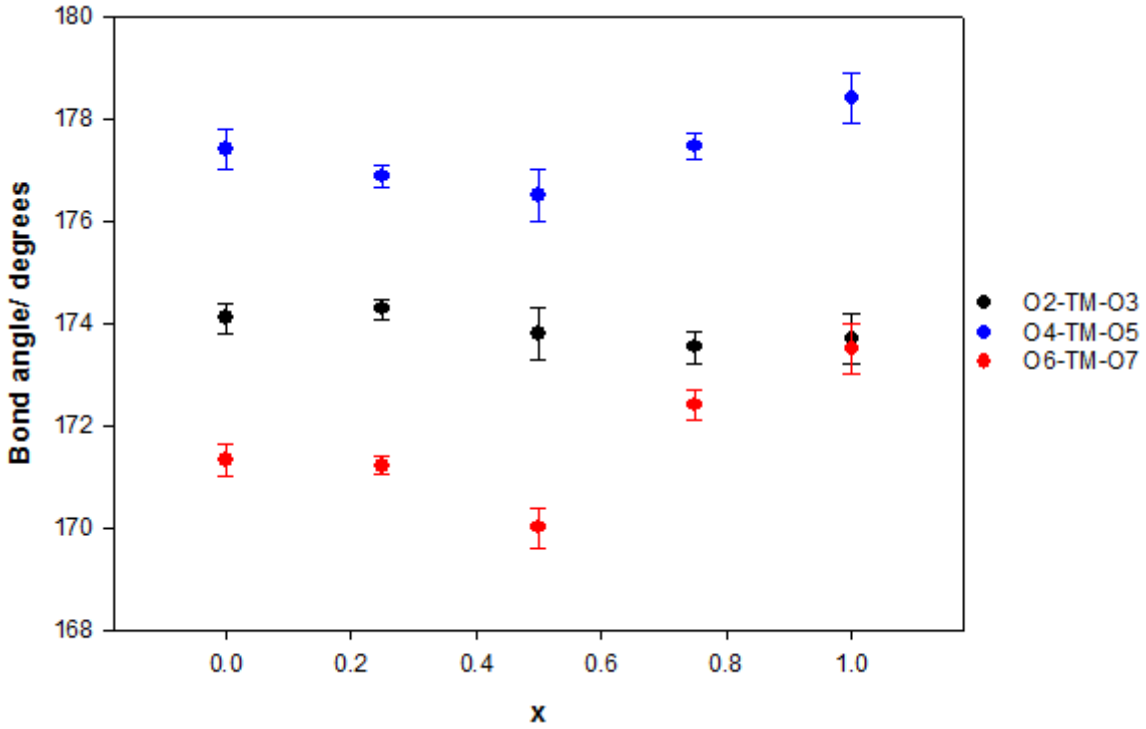

Figure 4.14: *O-TM-O angle of the trans oxygen ligands in the $TM\text{-}O_6$ coordination sphere*

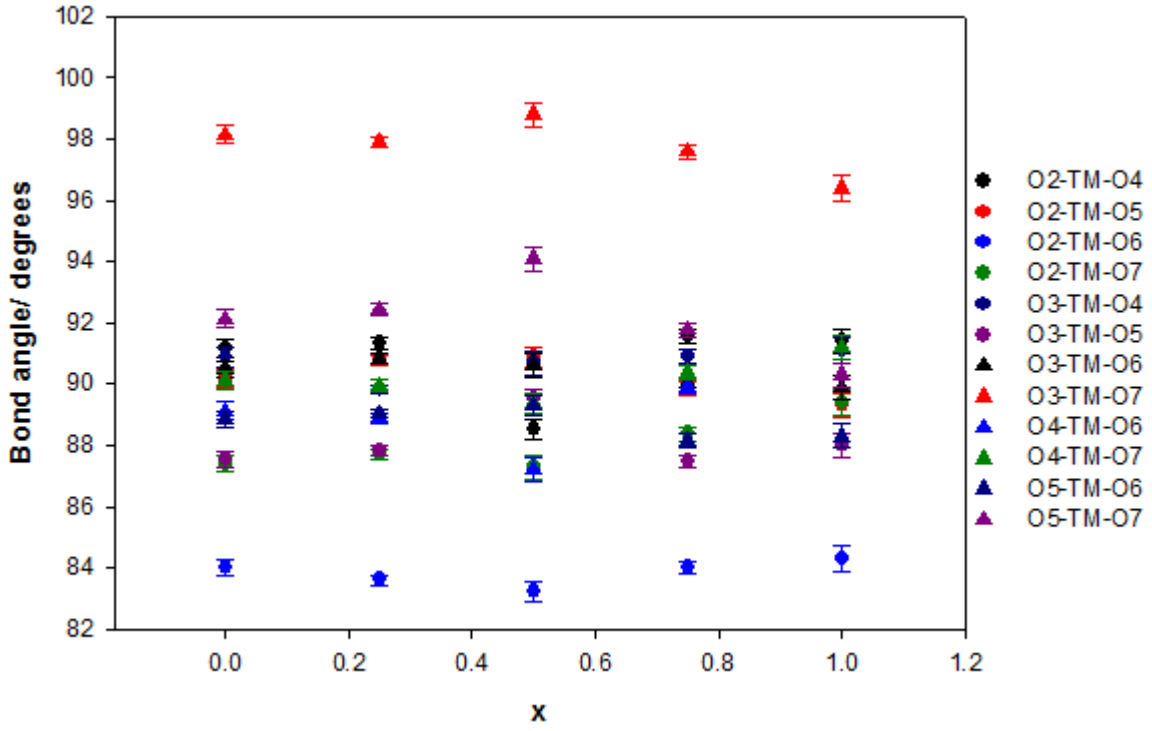

Figure 4.15: *O-TM-O angle of the cis oxygen ligands in the $TM\text{-}O_6$ coordination sphere*

4.3.3 Thermal Stability of the $RbMn_xFe_{1-x}P_2O_7$ System

The thermal behaviour of the x = 1, 0.75, 0.5, 0.25 and 0 members was investigated by TGA-MS under N_2, with the intermediate members additionally heated under an O_2 atmosphere. To explore their colour stability, the compounds were also heated in 100°C increments in a furnace at a rate of 10°C/ min under standard laboratory conditions. After being held at the desired temperature for 30 min, the products were allowed to cool to room temperature before the colour change was monitored by UV-Vis spectroscopy and X-ray diffraction patterns recorded.

x = 1

The TGA plot for $RbMnP_2O_7$ heated under nitrogen is shown in Figure 4.16. The compound remained stable up to 660°C, after which point a mass loss of ~2.2 % was seen. This corresponded to a sharp endothermic event occurring, which was in accordance with the host phase melting. It is possible that rubidium or oxygen were lost from the host at this point, though the mass spectrum showed no significant ions evolved during heating.

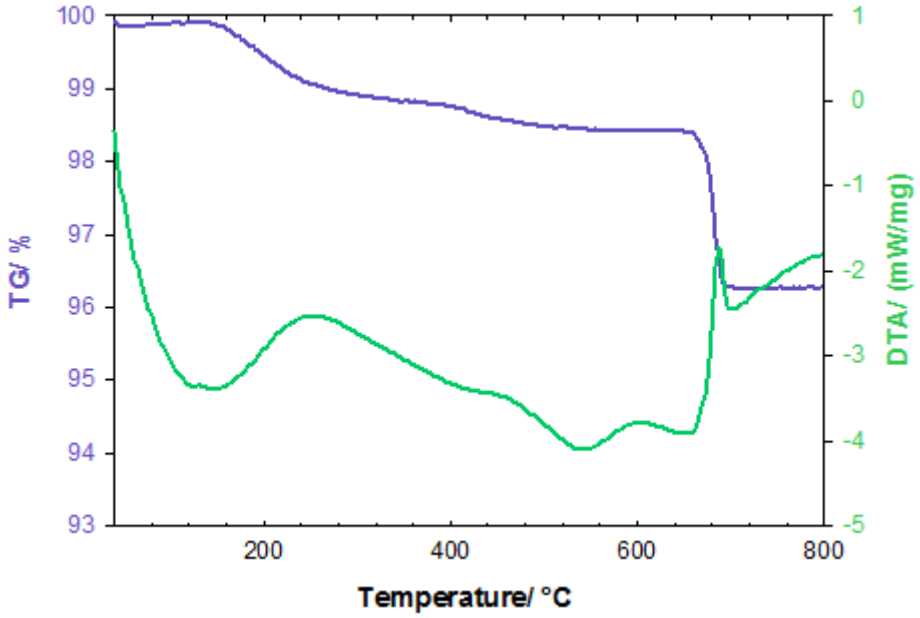

Figure 4.16: *TGA plot for $RbMnP_2O_7$ heated under N_2*

Independent furnace treatments of the host to various temperatures in air showed that the compound exhibited similar thermal behaviour in oxidising atmospheres. It appeared that the host was close to melting between 650-700°C, as evidenced by the sintered nature of the final products over this temperature range. The fact that it did not melt here but did so during the TGA measurement is likely to be due to using a smaller amount of sample in the latter case. Upon cooling after 700°C, three new phases were found to have crystallised, two of which matched $Rb_2Mn(PO_3)_4$ and $RbMnPO_4$ in the JCPDS[16] database (Figure 4.17). Although all of the decomposition products could not be identified, a colour change from intense violet to pale pink was observed, in accordance with a change in the manganese oxidation state to Mn^{2+} (d^5).

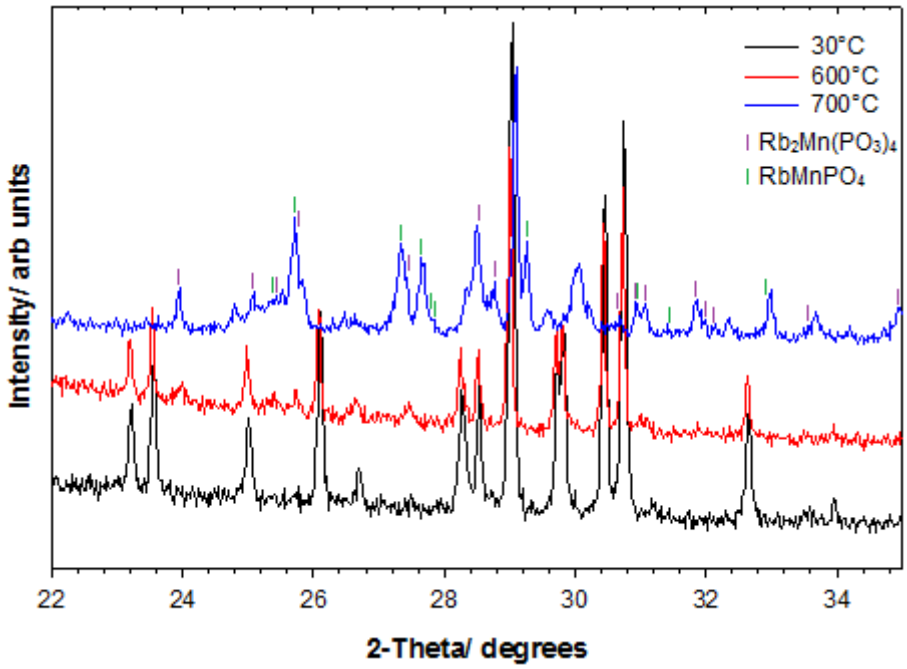

Figure 4.17: *XRD patterns of $RbMnP_2O_7$ heated to various temperatures in air*

x = 0

The TGA measurement in Figure 4.18 shows that $RbFeP_2O_7$ remained stable up to 1050°C, at which point a sharp endothermic event was followed by a broad

exothermic event, corresponding to melting with decomposition. After heating to 1000°C in a furnace, the product remained essentially identical to the host (as evidenced by XRD; Figure 4.19), though melted upon further heating to 1100°C. The increased thermal stability of this phase *cf.* $RbMnP_2O_7$ reflects the fact that Mn^{3+} is more prone to a change in oxidation state at elevated temperatures than is Fe^{3+}.

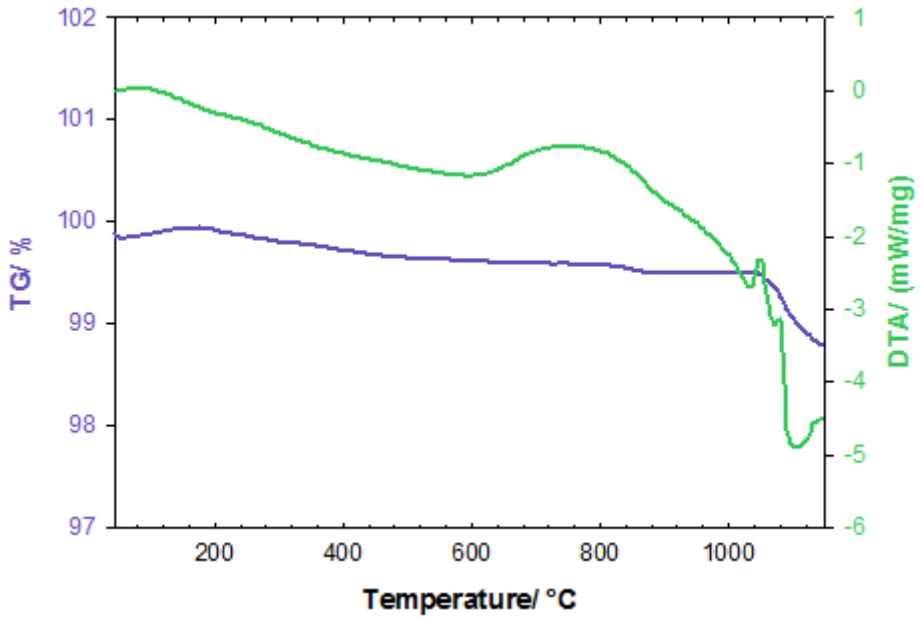

Figure 4.18: *TGA plot for $RbFeP_2O_7$ heated under N_2*

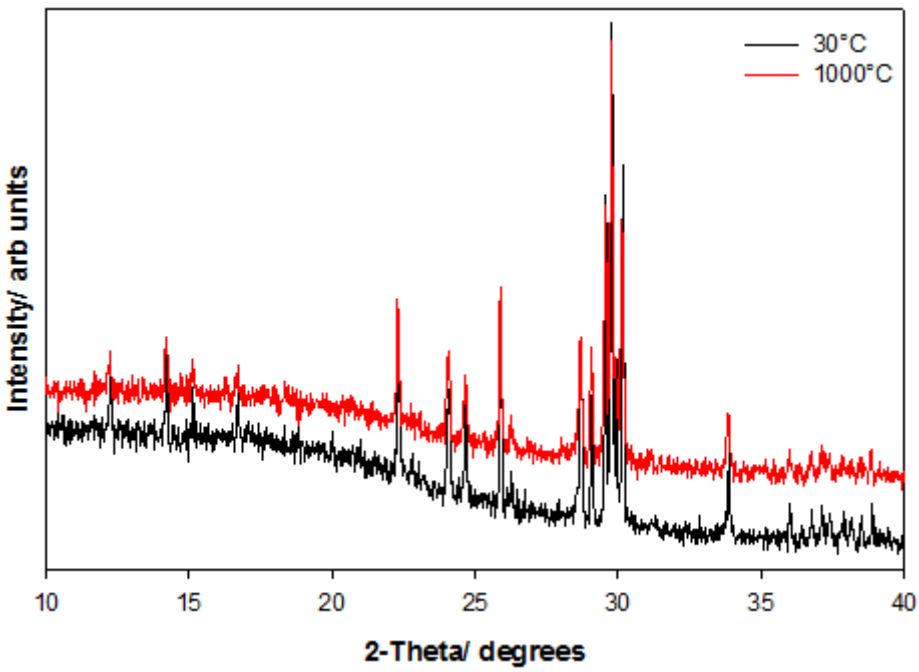

Figure 4.19: *XRD patterns of $RbFeP_2O_7$ before and after being heated to 1000°C in air*

x = 0.25

Similarly to the Fe end member (x = 0), TGA measurements (Figure 4.20) showed that $RbMn_{0.25}Fe_{0.75}P_2O_7$ also remained stable up to *ca.* 1050°C, after which point a mass loss of 0.6% occurred in a broad exothermic process. However, unlike x = 0, the x = 0.25 sample did not melt after the measurements, with analogous behaviour seen in both N_2 and O_2 atmospheres.

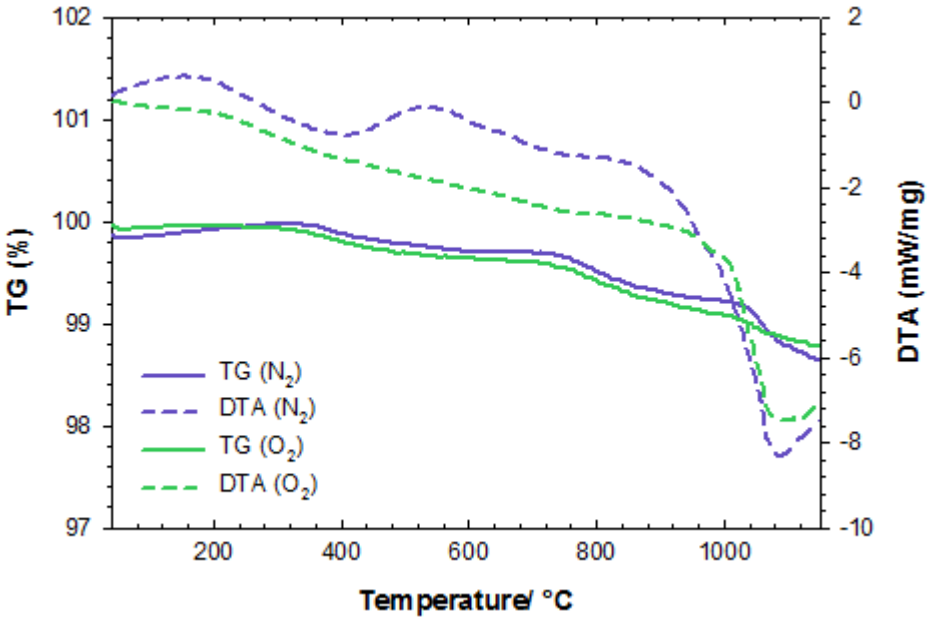

Figure 4.20: *TGA plots for $RbMn_{0.25}Fe_{0.75}P_2O_7$ heated in nitrogen and oxygen*

In order to monitor its colour stability, the compound was heated under air to various temperatures in a furnace and then allowed to cool to rt. The intense blue colour was found to persist up to 1000°C, but by 1100°C a pale blue sintered product was recovered (Figure 4.21) from which it was evident that the compound had been close to melting. Further heating to 1200°C yielded a sintered pale beige product.

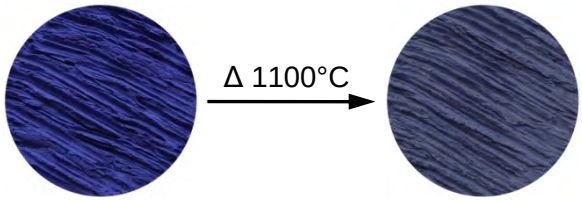

Figure 4.21: *Colour change observed in heating $RbMn_{0.25}Fe_{0.75}P_2O_7$ to 1100°C in air*

X-ray diffraction patterns of the heated compounds (Figure 4.22) showed that although the $RbMn_xFe_{1-x}P_2O_7$ structure type was maintained up to 1100°C, there was a gradual reduction in crystallinity after 800°C. This was accompanied by an irreversible change in the lattice parameters, which was not an effect of thermal expansion. By 1200°C the host had broken down to a poorly crystalline phase which could not be identified using the JCPDS[16] database.

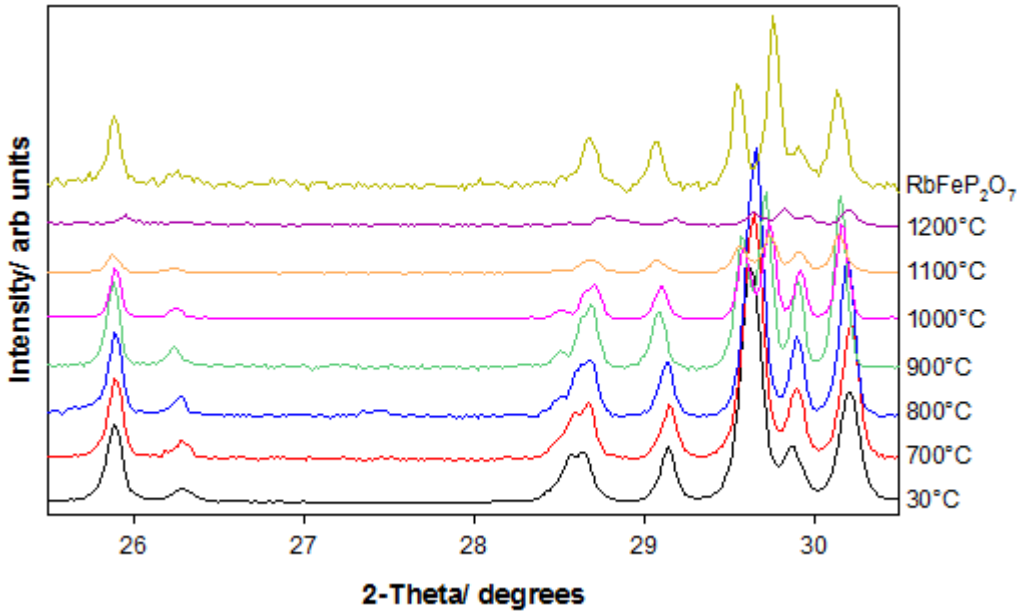

Figure 4.22: *XRD patterns of $RbMn_{0.25}Fe_{0.75}P_2O_7$ heated to various temperatures in air. The pattern of $RbFeP_2O_7$ is shown for comparison.*

The UV-Vis spectra of the host heated to various temperatures (Figure 4.23) showed that there was a decrease in intensity of the d→d transitions, particularly by 1100°C. This was consistent with a reduced amount of Mn^{3+} present, suggesting that a change in oxidation state had occurred. However, we would also expect there to be a variation in particle size amongst the heated compounds, and as this was not further investigated, we cannot be certain about its contribution to the observed spectra. It is worth noting that Mössbauer spectroscopy on the compound heated to 1100°C (Figure 4.24) showed that Fe remained in the +3 oxidation state, confirming

that any features in the UV-Vis spectra were predominantly a consequence of the Mn present in the material.

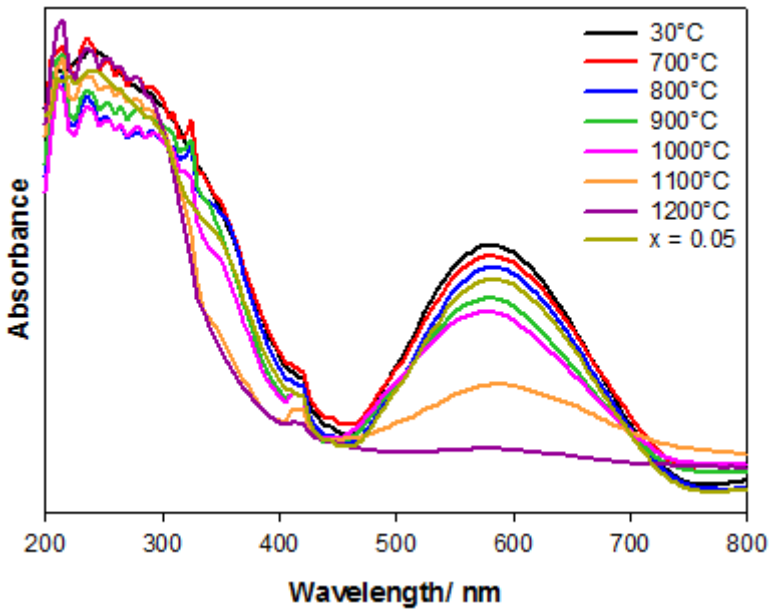

Figure 4.23: *UV-Vis spectra of $RbMn_{0.25}Fe_{0.75}P_2O_7$ heated to various temperatures in air. The spectrum of $RbMn_{0.05}Fe_{0.95}P_2O_7$ is shown for comparison.*

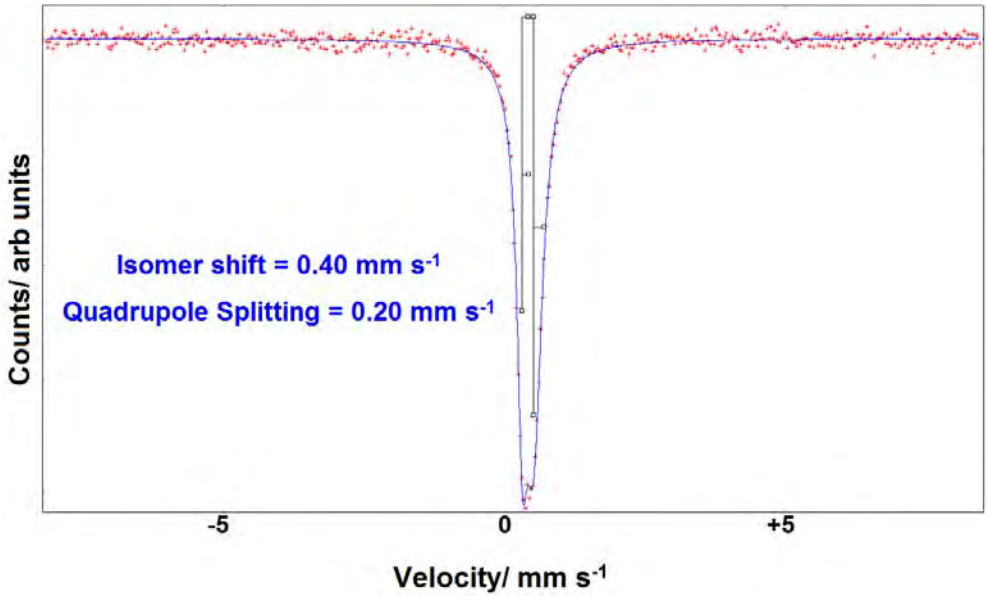

Figure 4.24: *Mössbauer spectrum of $RbMn_{0.25}Fe_{0.75}P_2O_7$ compound heated to 1100°C*

To further investigate the change in lattice parameters and colouration, neutron diffraction data was collected on the compound heated to 1100°C. The Rietveld refinement is shown in Figure 4.25, refined structural parameters in Table 4.5 and selected bond distances and angles in Table 4.6.

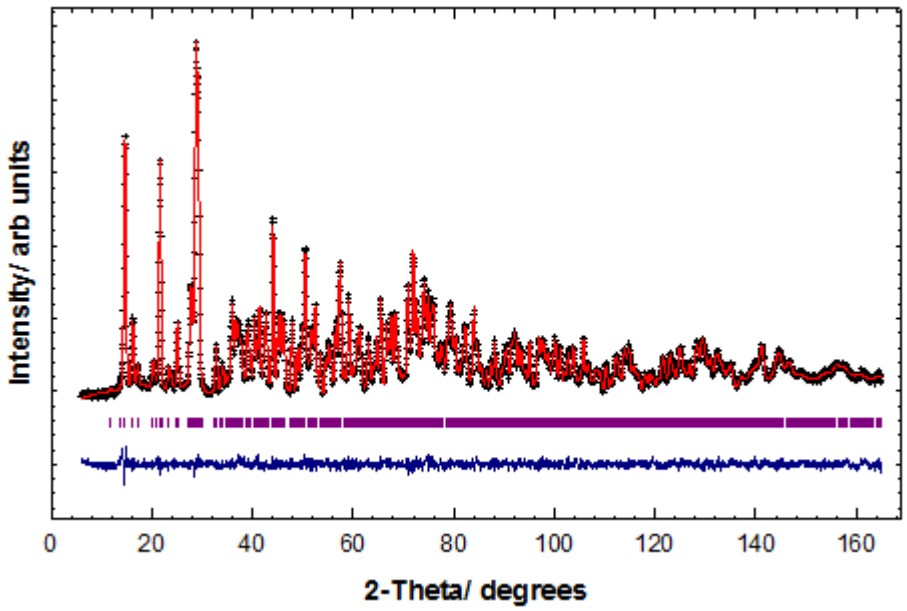

Figure 4.25: *Observed (+), calculated (-), difference profiles (-) and reflection positions (l) for the Rietveld refinement carried out on $RbMn_{0.25}Fe_{0.75}P_2O_7$ heated to 1100°C.*

Table 4.5: *Refined structural parameters for $RbMn_{0.25}Fe_{0.75}P_2O_7$ heated to 1100°C, obtained from a Rietveld refinement of the 300 K neutron diffraction data.*

Atom	Site	Occupancy	*x*	*y*	*z*	U_{iso}/ Å^2	BVS[7]
Mn/ Fe	4*e*	0.042(4)/ 0.958(4)	0.2379(2)	0.5996(2)	0.7606(3)	0.0017(6)	3.18/ 3.17
Rb	4*e*	1.0	0.1862(5)	0.3104(3)	0.0475(5)	0.0141(8)	1.22
P(1)	4*e*	1.0	0.4358(6)	0.6334(4)	0.1890(5)	0.007(1)	4.96
P(2)	4*e*	1.0	0.1339(5)	0.9050(4)	0.8326(5)	0.0056(8)	4.98
O(1)	4*e*	1.0	0.3318(5)	0.9468(3)	0.8057(5)	0.0068(8)	2.10
O(2)	4*e*	1.0	0.0858(5)	0.7341(4)	0.2608(5)	0.0075(8)	2.16
O(3)	4*e*	1.0	0.6274(5)	0.5748(4)	0.2290(5)	0.0107(9)	2.07
O(4)	4*e*	1.0	0.1516(6)	0.5845(4)	0.5151(5)	0.015(1)	2.06
O(5)	4*e*	1.0	0.3220(5)	0.6038(4)	0.0086(5)	0.010(1)	1.89
O(6)	4*e*	1.0	0.9936(5)	0.4948(4)	0.2269(5)	0.007(1)	2.02
O(7)	4*e*	1.0	0.4431(5)	0.7795(4)	0.2374(5)	0.0103(9)	2.04

R_{wp} = 2.63%, R_p = 2.02%, χ^2 = 2.053

Space group $P2_1/c$, a = 7.5019(2) Å, b = 9.9776(3) Å, c = 8.2828(2) Å, β = 105.667(2)°

GII[8] = 0.11 vu

Table 4.6: *Selected Bond Distances (Å) and Angles (degrees) for $RbMn_{0.25}Fe_{0.75}P_2O_7$ heated to 1100°C*

TM-O(2)	2.014(5)	**TM-O(5)**	1.980(5)
TM-O(3)	2.002(5)	**TM-O(6)**	2.003(4)
TM-O(4)	1.966(5)	**TM-O(7)**	2.005(5)
O(2)-TM-O(3)	174.5(2)	**O(3)-TM-O(7)**	97.8(2)
O(2)-TM-O(4)	92.0(2)	**O(4)-TM-O(5)**	176.8(2)
O(2)-TM-O(5)	90.2(2)	**O(4)-TM-O(6)**	88.2(2)
O(2)-TM-O(6)	83.5(2)	**O(4)-TM-O(7)**	89.7(2)
O(2)-TM-O(7)	87.4(2)	**O(5)-TM-O(6)**	89.7(2)
O(3)-TM-O(4)	90.0(2)	**O(5)-TM-O(7)**	92.8(2)
O(3)-TM-O(5)	87.6(2)	**O(6)-TM-O(7)**	170.6(2)
O(3)-TM-O(6)	91.4(2)		
P(1)-O(1)	1.610(5)	**P(2)-O(1)**	1.614(5)
P(1)-O(3)	1.503(5)	**P(2)-O(2)**	1.515(5)
P(1)-O(5)	1.536(5)	**P(2)-O(4)**	1.485(5)
P(1)-O(7)	1.509(6)	**P(2)-O(6)**	1.542(5)
O(1)-P(1)-O(3)	105.3(3)	**O(1)-P(2)-O(2)**	108.3(3)
O(1)-P(1)-O(5)	104.9(3)	**O(1)-P(2)-O(4)**	106.8(4)
O(1)-P(1)-O(7)	108.0(3)	**O(1)-P(2)-O(6)**	105.5(3)
O(3)-P(1)-O(5)	112.8(3)	**O(2)-P(2)-O(4)**	114.2(4)
O(3)-P(1)-O(7)	110.7(4)	**O(2)-P(2)-O(6)**	108.5(3)
O(5)-P(1)-O(7)	114.5(3)	**O(4)-P(2)-O(6)**	113.1(3)

In refining the Mn and Fe occupancies, it was found that the composition of the host had changed to $RbMn_{0.04}Fe_{0.96}P_2O_7$ (the fractional occupancies of all other atoms remained close to one and were therefore not varied in the final refinement). Furthermore, a closer inspection of the XRD lattice parameters for the heated compounds revealed that a marked change occurred after 700°C, leaving the compounds heated to temperatures ≥ 900°C with lattice parameters more similar to the as-synthesised $RbMn_{0.05}Fe_{0.95}P_2O_7$ and $RbFeP_2O_7$ phases (see Figure 4.26).

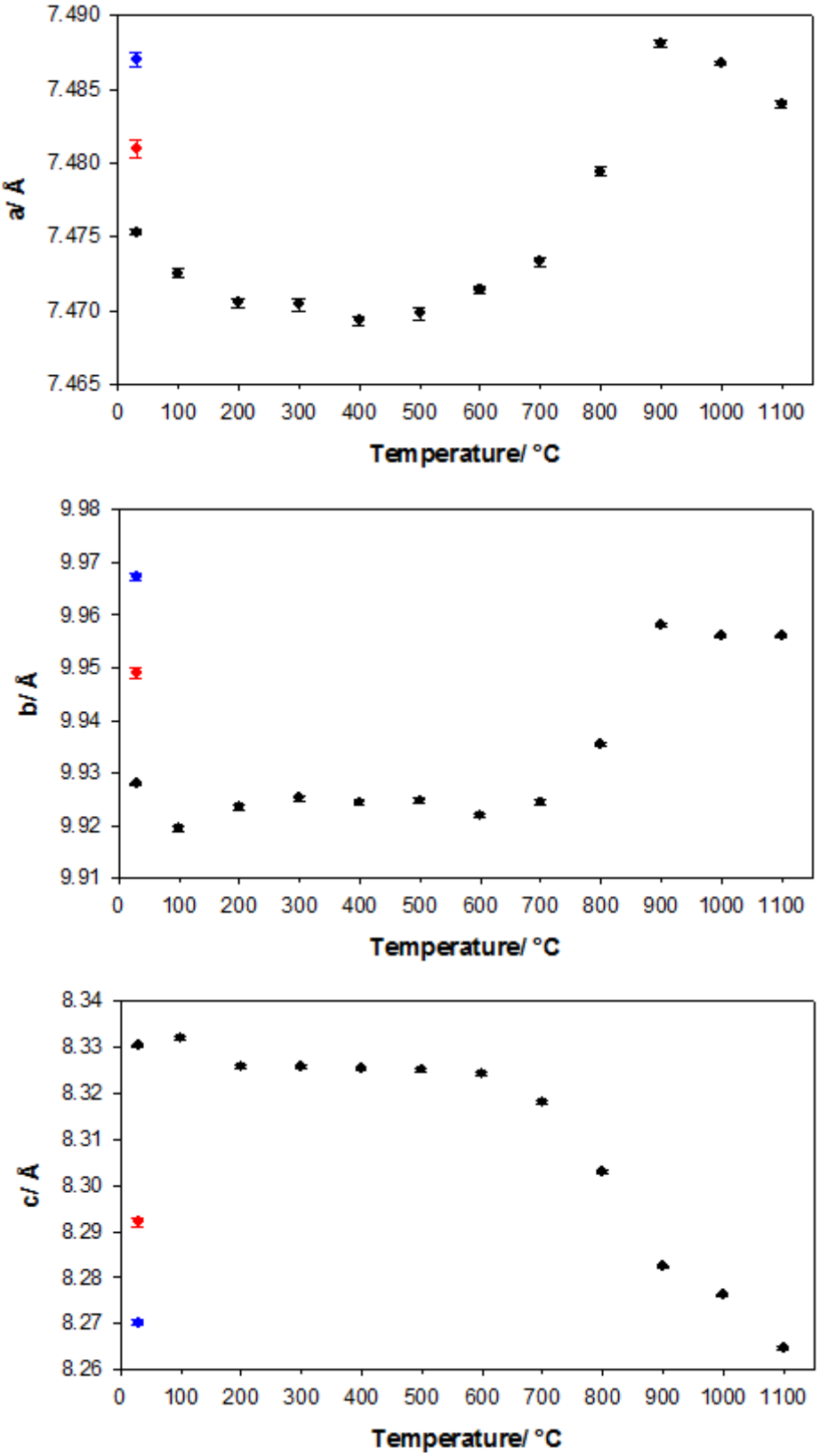

Figure 4.26: *XRD lattice parameters of $RbMn_{0.25}Fe_{0.75}P_2O_7$ heated to various temperatures in air, with those of $RbMn_{0.05}Fe_{0.95}P_2O_7$ (●) and $RbFeP_2O_7$ (●) shown for comparison.*

Figure 4.26 continued...

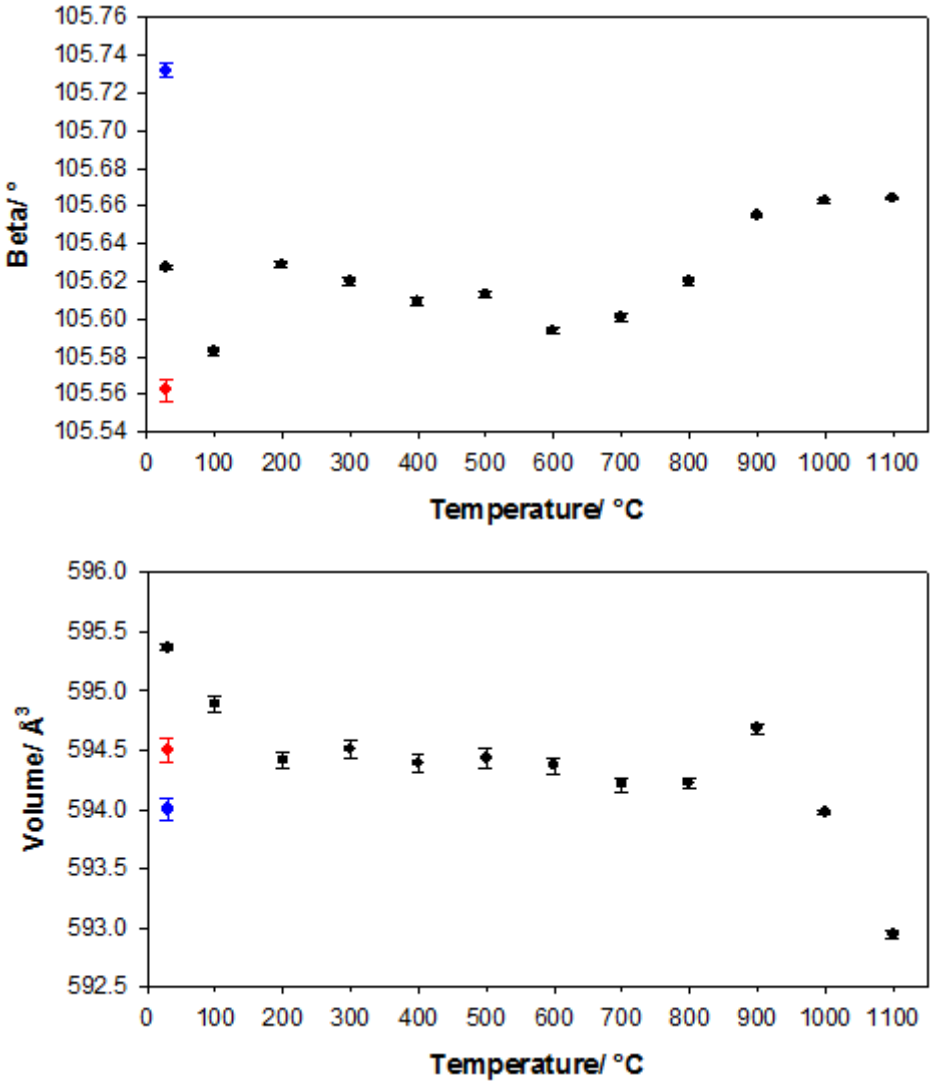

Clearly manganese is expelled from the $RbMn_xFe_{1-x}P_2O_7$ structure, the onset of which occurs after ~700°C. This is not surprising given that $RbMnP_2O_7$ begins to break down at 660°C. However, the TG and DTA signals (Figure 4.20) for the host remained relatively constant over this temperature range, and so the exact mechanism for Mn expulsion is unclear. Furthermore, the mass spectrum showed that no significant ions were evolved during heating. As no impurity peaks were observed in the diffraction patterns, the manganese was likely to be present as an amorphous phase.

To quantify the amount of amorphous material present in the sample, "$RbMn_{0.04}Fe_{0.96}P_2O_7$" was ground with a K_2SO_4 crystalline reference material in a 4:1 weight % ratio, respectively. X-ray diffraction data were collected on the resulting sample and a two-phase Rietveld refinement employed (see Appendix 2 for details). In allowing the phase fractions to vary, the refinement suggested that 75% of the sample was composed of the $RbMn_{0.04}Fe_{0.96}P_2O_7$ phase while 25% was the K_2SO_4 reference material, which confirmed the presence of amorphous material. The Rietveld method calculates the weight fraction, w_i, of a crystalline phase, i, by the following equation[17]: -

$$w_i = \frac{S_i M_i V_i}{\sum_j S_j M_j V_j} \times 100\% \qquad \text{[Equation 4.1]}$$

where S is a phase fraction scale factor, M is the mass of the formula unit and V is the volume of the unit cell, summed over all crystalline phases present, j. This is on the condition that $\sum(w_i) = 100\%$. As the Rietveld method only models the crystalline phases present, if their weight fractions do not total to 100% then the scale factor is simply increased. Given that we are certain of the amount of reference material present in the sample, we know that the K_2SO_4 phase has been overestimated by 25%. Therefore the 75% assigned to the $RbMn_{0.04}Fe_{0.96}P_2O_7$ phase has also been overestimated by 25%, meaning that the sample actually contains 60% $RbMn_{0.04}Fe_{0.96}P_2O_7$, 20% K_2SO_4 and 20% of amorphous material. Thus if we consider the $RbMn_{0.04}Fe_{0.96}P_2O_7$ sample alone, then 25% of it is actually an amorphous component.

We can also use the phase fractions obtained from the neutron diffraction data to provide us with an estimate of the amount of amorphous material present. This can be done by assuming that upon heating to 1100°C, all of the iron is retained in the host structure. Indeed, the Mössbauer spectrum (Figure 4.24) showed that iron remained in the +3 oxidation state, giving no obvious reason for it to form a separate amorphous phase in the sample. In scaling the composition based on the Fe content we then obtain: -

$$RbMn_{0.25}Fe_{0.75}P_2O_7 \xrightarrow{\Delta\ 1100°C} 0.78[RbMn_{0.04}Fe_{0.96}P_2O_7] + 0.22[\text{amorphous}]$$

[Equation 4.2]

The 22% calculated here is in good agreement with the 25% suggested by the X-ray diffraction data.

x = 0.5

The TGA curves in Figure 4.27 show that $RbMn_{0.5}Fe_{0.5}P_2O_7$ also exhibited similar mass stability in both nitrogen and oxygen atmospheres.

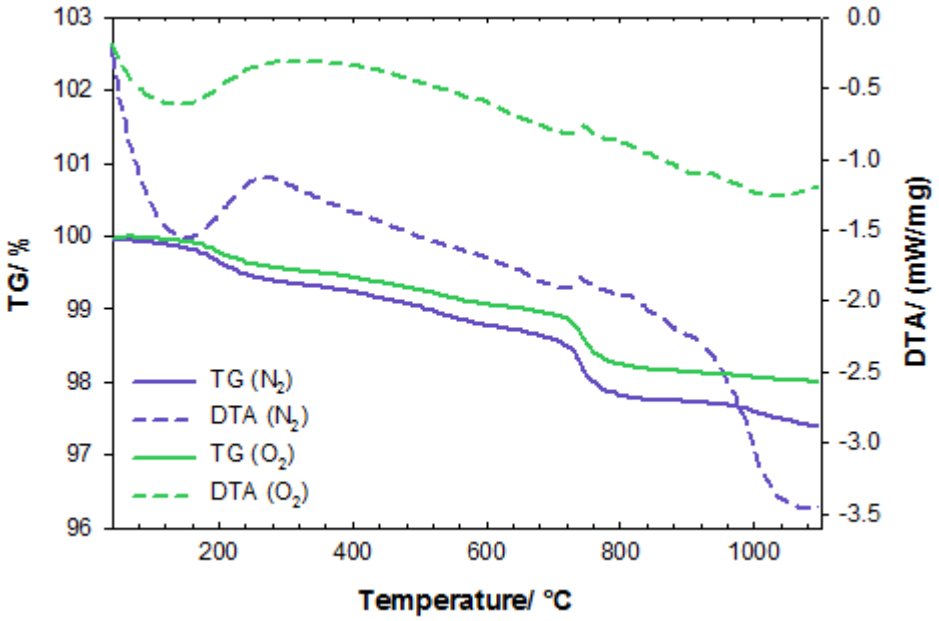

Figure 4.27: *TGA plots of $RbMn_{0.5}Fe_{0.5}P_2O_7$ heated in nitrogen and oxygen*

The compound remained reasonably stable up to ~700°C, whereupon a mass loss of *ca.* 0.75% occurred. However, the DTA signal showed no clear event occurring at this point and the mass spectrum showed that no significant ions were evolved during the course of heating.

Similarly to x = 0.25, *ex-situ* heat treatments under standard laboratory conditions were carried out in a furnace, with the colouration and lattice parameters of the products monitored once they had cooled to room temperature. The indigo colour of the host remained stable up to 700°C, but after heating between 800-1100°C, pale blue sintered products were recovered. The UV-Vis spectra shown in Figure 4.28 show that a decrease in intensity of the d→d transitions occurred particularly by 800°C, suggesting that a change in the manganese oxidation state had taken place.

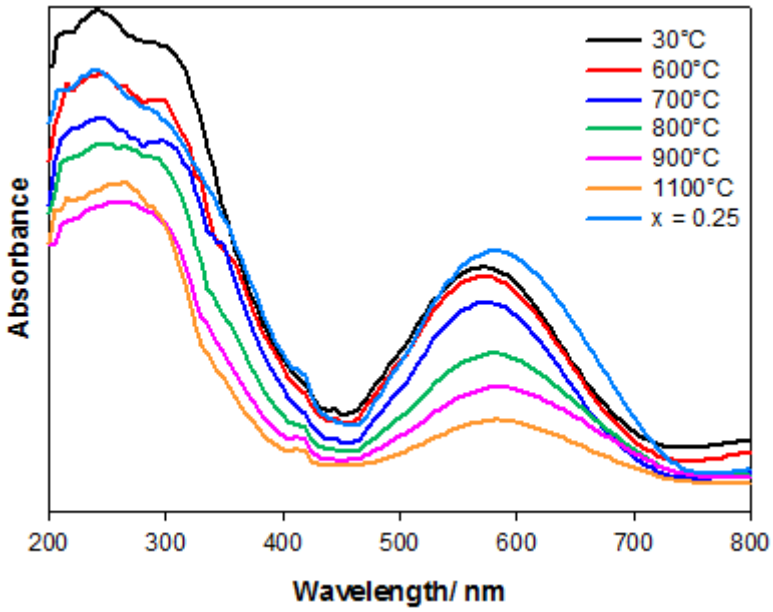

Figure 4.28: *UV-Vis spectra of $RbMn_{0.5}Fe_{0.5}P_2O_7$ heated to various temperatures in air. The spectrum of $RbMn_{0.25}Fe_{0.75}P_2O_7$ is shown for comparison.*

A small change in the X-ray diffraction patterns was seen at 700°C; by 800°C this became more marked and impurity peaks became apparent in the powder patterns (Figure 4.29). By 1100°C the impurity peaks were no longer evident, suggesting that the additional phase(s) had become amorphous. Further heating to 1200°C led to the compound melting.

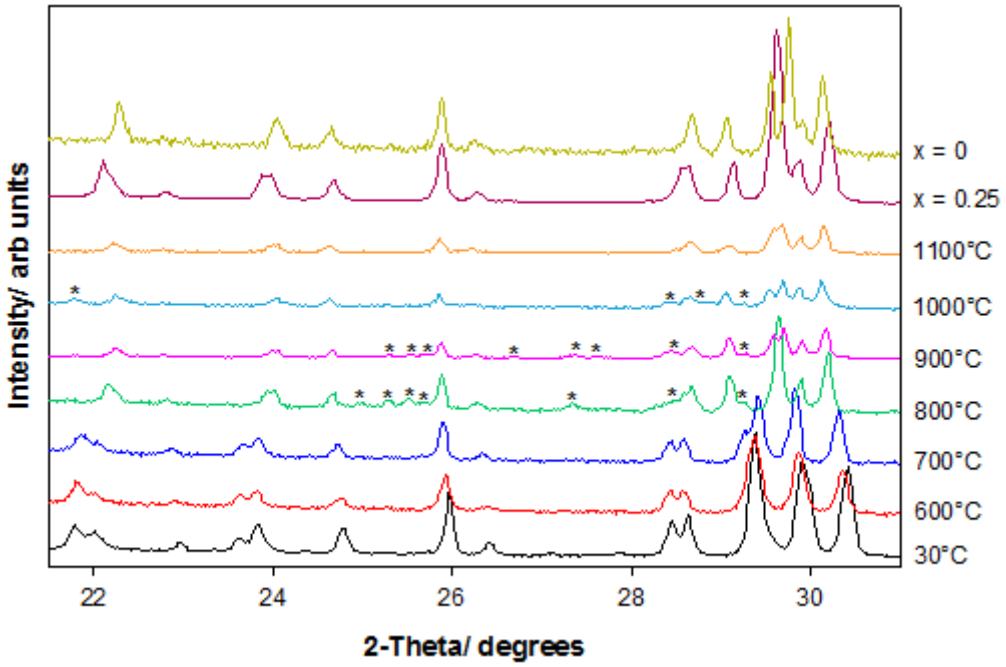

Figure 4.29: *XRD patterns of $RbMn_{0.5}Fe_{0.5}P_2O_7$ heated to various temperatures in air (* indicates impurity peaks). The patterns of $RbMn_{0.25}Fe_{0.75}P_2O_7$ and $RbFeP_2O_7$ are also shown for comparison.*

Similarly to x = 0.25, the lattice parameters of the phases heated to ≥ 800°C showed greater deviations from the host phase, tending closer to the parameters of the as-synthesised $RbMn_{0.25}Fe_{0.75}P_2O_7$ and $RbFeP_2O_7$ compounds (see Figure 4.30). Based on this it can be estimated that the level of manganese fell from 50% to below 25%.

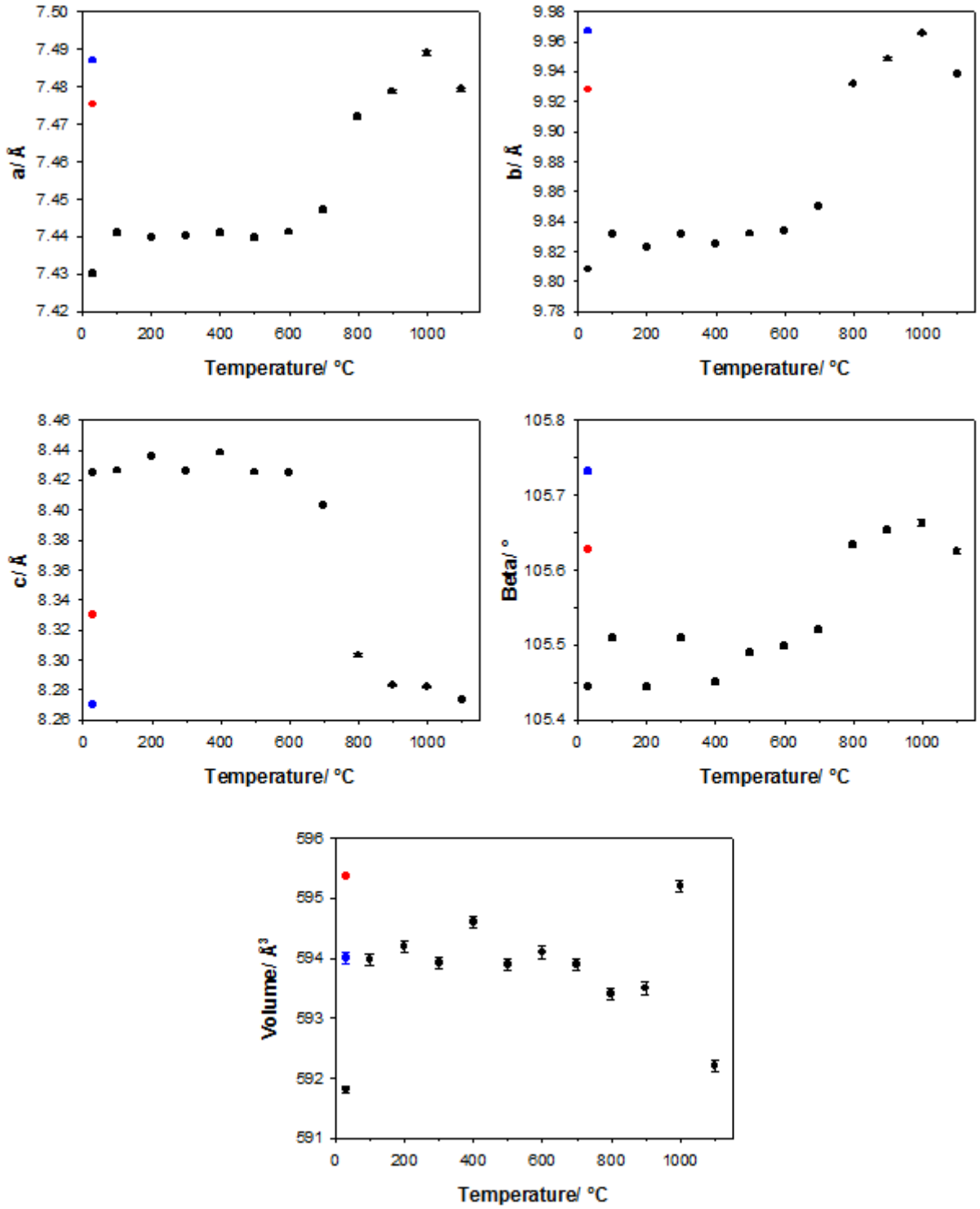

Figure 4.30: *XRD lattice parameters of $RbMn_{0.5}Fe_{0.5}P_2O_7$ heated to various temperatures in air, with those of $RbMn_{0.25}Fe_{0.75}P_2O_7$ (●) and $RbFeP_2O_7$ (●) shown for comparison.*

x = 0.75

The TGA plots for $RbMn_{0.75}Fe_{0.25}P_2O_7$ (Figure 4.31) showed that the compound remained reasonably stable up to ~670°C, whereupon a mass loss of 1.3% was seen in both N_2 and O_2 atmospheres. This corresponded to a broad endothermic event in accordance with the host phase melting. Again the mass spectrum showed that no significant ions were evolved during heating.

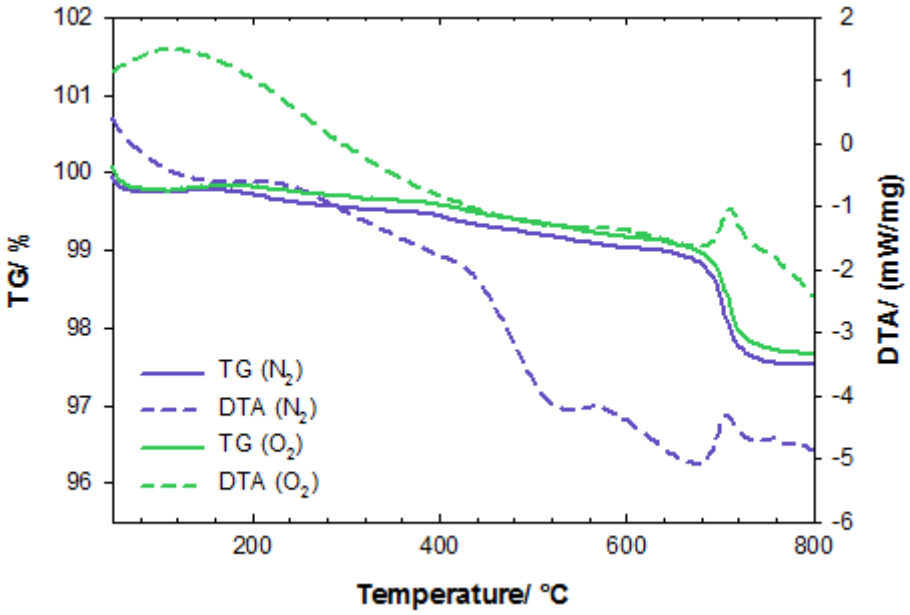

Figure 4.31: *TGA plots of $RbMn_{0.75}Fe_{0.25}P_2O_7$ heated in nitrogen and oxygen*

After the host was heated to 700°C in a furnace and allowed to cool, a colour change from violet to indigo was observed and the final product found to be sintered, suggesting that the compound had been close to melting. At this stage at least two phases were present in the X-ray diffraction pattern (Figure 4.32), one which resembled $RbMn_{0.5}Fe_{0.5}P_2O_7$ and another which could not be identified using the JCPDS[16] database. By 800°C the host had completely decomposed to give a pale blue sintered product which could also not be identified from the X-ray diffraction pattern.

The UV-Vis spectra showed that a small shift of the broad feature in the visible region had occurred at 700°C, towards that of the x = 0.5 compound (Figure 4.33). The lattice parameters obtained from X-ray diffraction also showed evidence for manganese expulsion at 700°C, becoming more like the as-synthesised x = 0.6 and x = 0.5 parameters (Figure 4.34).

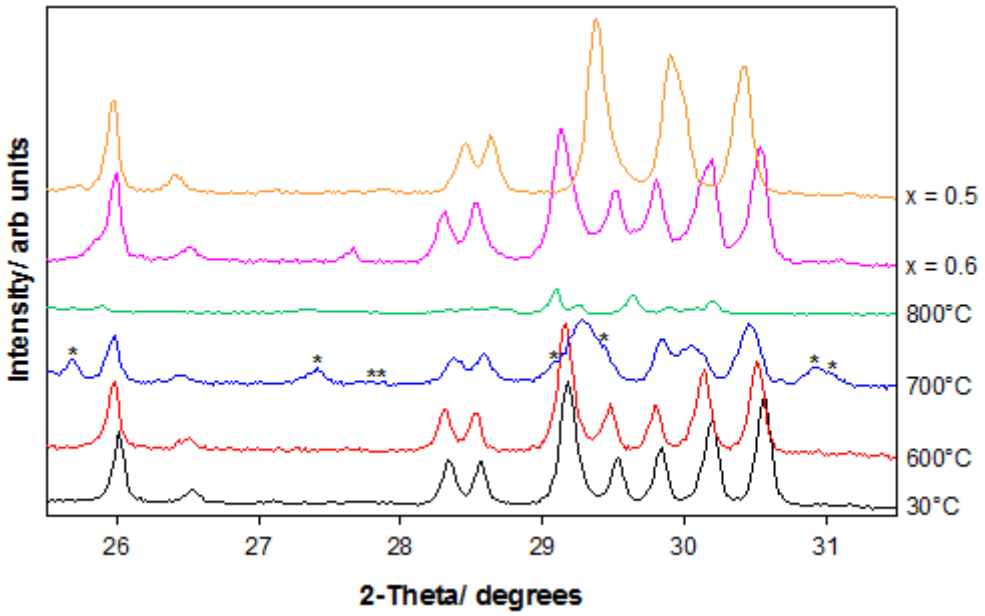

Figure 4.32: *XRD patterns of $RbMn_{0.75}Fe_{0.25}P_2O_7$ heated to various temperatures in air (* indicates impurity peaks). The patterns of x = 0.6 and 0.5 are shown for comparison.*

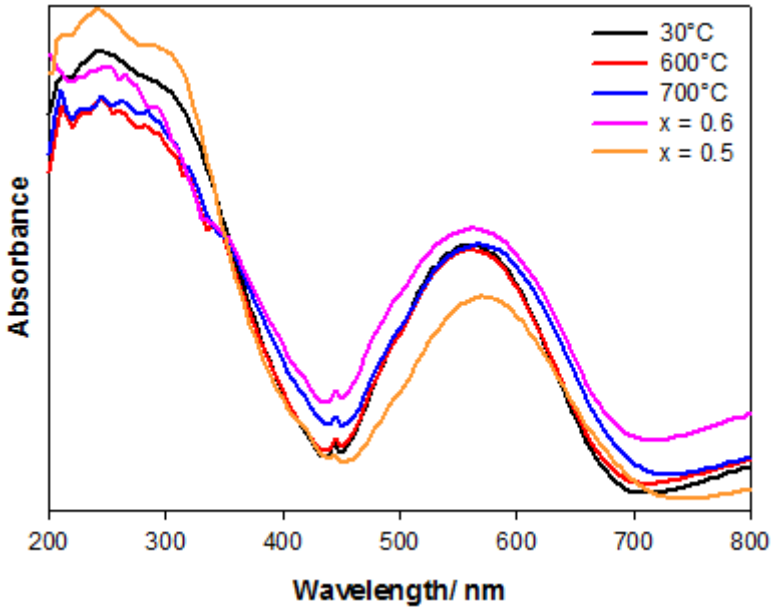

Figure 4.33: *UV-Vis spectra of $RbMn_{0.75}Fe_{0.25}P_2O_7$ heated to various temperatures in air. The spectra of $RbMn_{0.6}Fe_{0.4}P_2O_7$ and $RbMn_{0.5}Fe_{0.5}P_2O_7$ are shown for comparison.*

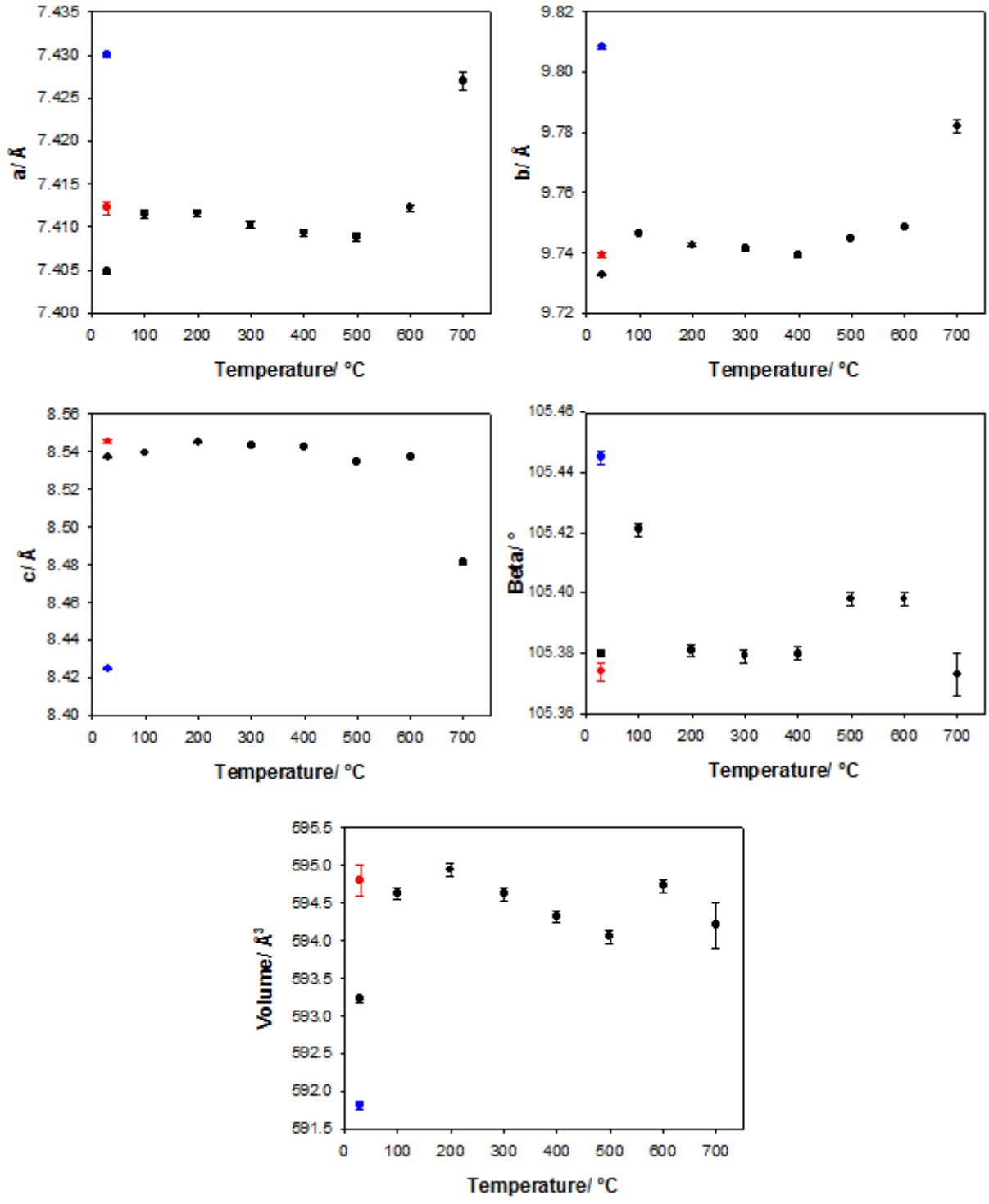

Figure 4.34: *XRD lattice parameters of $RbMn_{0.75}Fe_{0.25}P_2O_7$ heated to various temperatures in air, with those of $RbMn_{0.6}Fe_{0.4}P_2O_7$ (●) and $RbMn_{0.5}Fe_{0.5}P_2O_7$ (●) shown for comparison.*

4.3.4 Magnetic Analysis of the $RbMn_xFe_{1-x}P_2O_7$ System

Figure 4.35 shows the magnetic susceptibility measurements for the x = 0.75, 0.5 and 0.25 members and the Curie-Weiss fits to the data, while Table 4.7 summarises the parameters calculated from the latter. $RbMnP_2O_7$[2] and $RbFeP_2O_7$[6] have been previously shown to order antiferromagnetically, exhibiting similar behaviour in both the zero-field cooled/ field warmed (ZFCFW) and field cooled/ field warmed (FCFW) measurements.

Table 4.7: *Summary of parameters determined from the susceptibility data on the $RbMn_xFe_{1-x}P_2O_7$ series*

x	T_N/ K	θ/ K	μ_{eff}/μ_B	μ_{so}/μ_B	μ_{obs}/μ_B[18]
1[2]	20	-10.9(2)	4.54	4.90	4.80-4.90
0.75	22.4	-37(1)	5.85(2)	5.16	
0.5	16.3	-35.4(7)	5.23(1)	5.41	
0.25	N/A	-79(1)	6.77(2)	5.67	
0[6]	24	-	5.637(3)	5.92	5.70-6.00

Both the x = 0.75 and 0.5 members showed an antiferromagnetic (AFM) response in the ZFCFW measurement and a ferromagnetic (FM) component in the FCFW measurement, indicative of canted antiferromagnetism or spin glass behaviour. The effective magnetic moment for the x = 0.75 compound was found to be higher than the expected spin only moment, while for x = 0.5 it was found to be in reasonable agreement with μ_{so}. It should be noted that there were slight curvatures to the Curie-Weiss fits for these datasets, suggesting small deviations from the Curie-Weiss law.

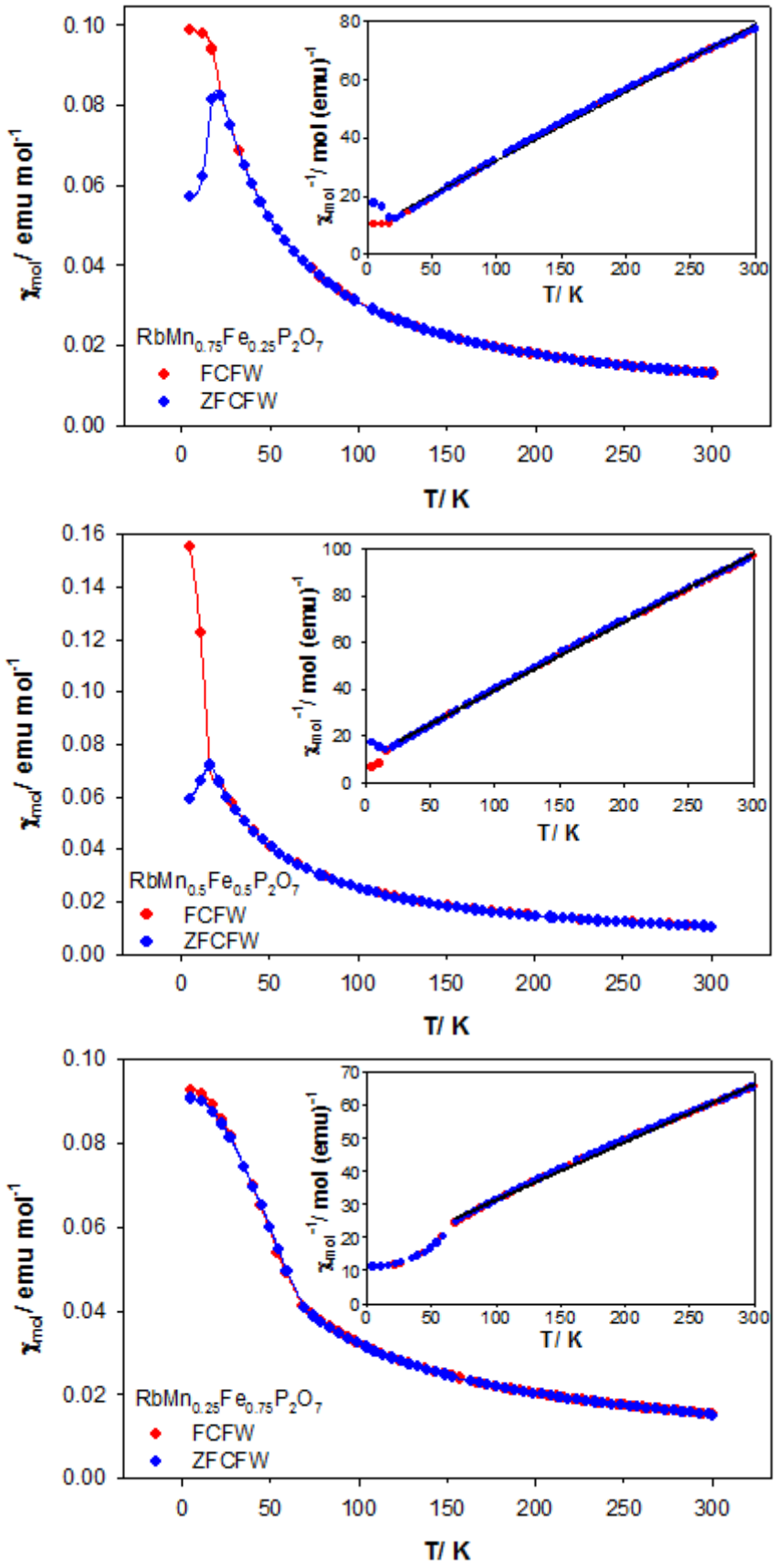

Figure 4.35: *Plots of molar susceptibility against temperature for the $RbMn_xFe_{1-x}P_2O_7$ series (x = 0.75, 0.5 and 0.25), with insets showing Curie-Weiss fits.*

For the x = 0.25 compound, the susceptibility data implied the presence of frustrated magnetic interactions, as evidenced by deviations from paramagnetic behaviour at T < 68 K. The Curie-Weiss curve fitted at T > 69 K gave a relatively large Weiss temperature of -79(1) K, which suggested inherent AFM interactions. The effective moment of 6.77(2) μ_B was however much higher than even that of a pure Fe^{3+} compound, suggesting that the Curie-Weiss law was not satisfactory in describing the magnetic behaviour of this compound.

The magnetic susceptibility of the $RbMn_xFe_{1-x}P_2O_7$ compounds can be contrasted to those of the isostructural α-$NH_4Mn_xFe_{1-x}P_2O_7$ series, where the Mn end member was found to be AFM, the intermediate members essentially paramagnetic and the Fe end member showing some evidence for frustrated magnetic interactions. For the intermediate members of these two systems it appears that the interactions are stronger where M^I = Rb, as indicated by SQUID measurements detecting ordering in these samples. This could be related to differing degrees of covalency imparted on the TM-O bonds by the two M^I cations. However, the magnetic interactions in these compounds are considered to be a result of “super-superexchange”, occurring over extended TM-O-P-O-TM pathways, and so the nature of the M^I cation is not expected to have a significant influence on the relative strength of these interactions.

4.3.4.1 Magnetic Structures from Neutron Diffraction

After the nuclear contribution was fitted to the 2 K neutron diffraction data on the x = 0.25, 0.5 and 0.75 compounds, the patterns showed evidence for additional peaks and intensity. For the x = 0.25 compound, these magnetic peaks could not be indexed on a commensurate unit cell to the nuclear cell. Due to the limited number of peaks present, we were also unable to obtain a cell from the Crysfire[19] indexing program. A similar case was also observed for $RbFeP_2O_7$[6] and a comparison of the diffraction patterns shows that both compounds exhibit analogous magnetic peaks (Figure 4.36). This suggests that a similar incommensurate magnetic structure type is adopted by both the x = 0 and 0.25 members.

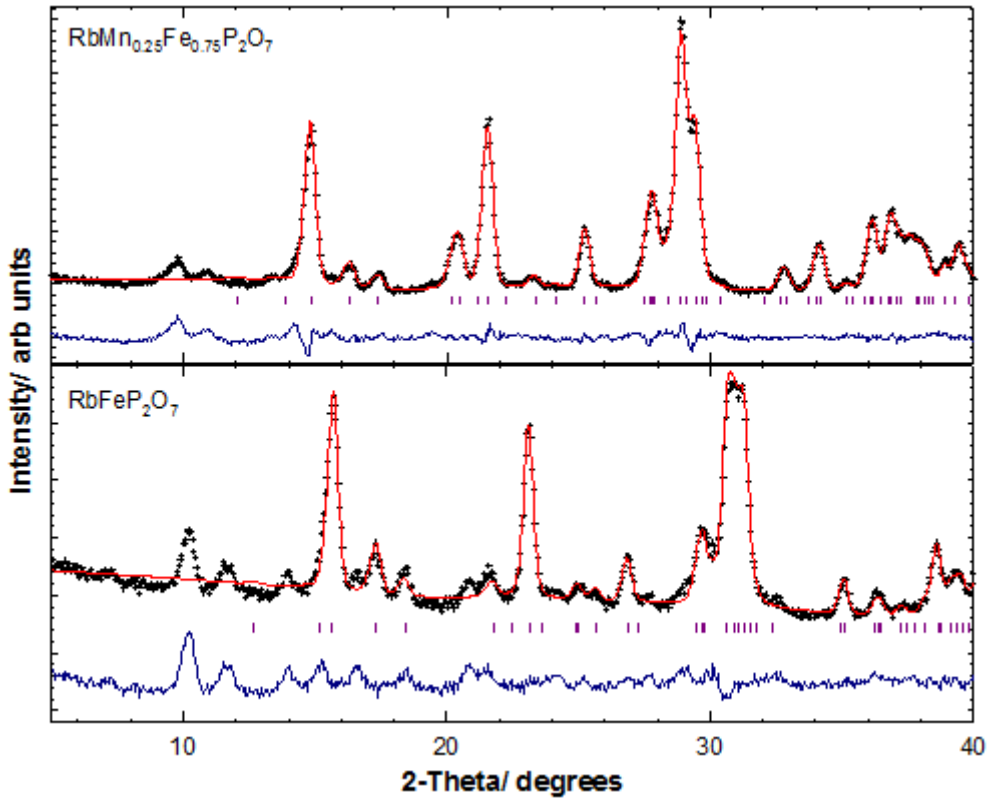

Figure 4.36: *Nuclear structural model (-) fitted to the 2 K neutron diffraction data (+) on x = 0.25 and 0. Difference plots (-) and nuclear reflection positions (l) are also shown.*

For the x = 0.75 and 0.5 compounds, the magnetic unit cells were found to be commensurate with the nuclear cells and consistent with the magnetic space group $P2_1'/c$. The relative orientations of the four TM spins in the unit cell were found to be (0.24, 0.60, 0.76)+, (0.76, 0.10, 0.74)+, (0.76, 0.40, 0.24)- and (0.24, 0.90, 0.26)-, with the magnetic intensities fitted with a calculated form factor for Mn^{3+} and Fe^{3+}.[20] The final refinements are shown in Figures 4.37-4.38, structural parameters in Table 4.8 and 4.10 and selected bond lengths and angles in Table 4.9 and 4.11, respectively. It should be noted that for the x = 0.75 composition, the atomic coordinates and fractional occupancies of the TM atoms were set to the values obtained from the joint ND/ XRD RT refinement, and U_{iso} fixed at 0.005 $Å^2$.

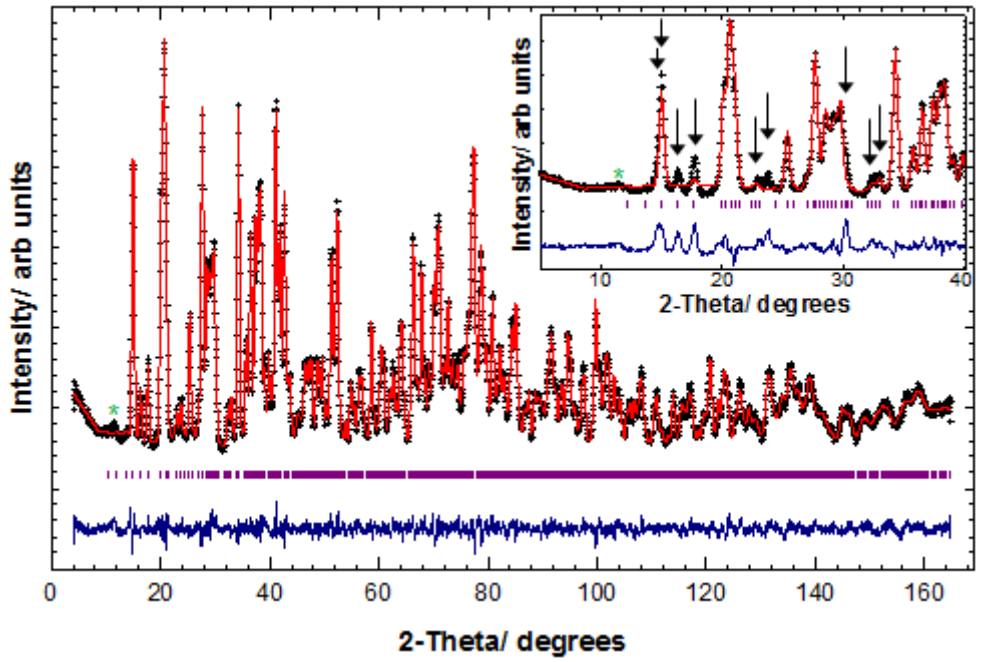

Figure 4.37: *Observed (+), calculated (-), difference profiles (-) and reflection positions (l) for the 2 K Rietveld refinement carried out on $RbMn_{0.75}Fe_{0.25}P_2O_7$ (* shows an impurity peak). The inset indicates the appearance of the profile without a magnetic contribution fitted, with arrows indicating magnetic peaks with significant intensity.*

Table 4.8: *Refined structural parameters for $RbMn_{0.75}Fe_{0.25}P_2O_7$ obtained from a Rietveld refinement of the 2 K neutron diffraction data.*

Atom	Site	Occupancy	*x*	*y*	*z*	U_{iso}/ Å^2	BVS[7]
Mn/ Fe	4*e*	0.761/ 0.239	0.2367	0.6024	0.7575	0.005	3.19/ 3.18
Rb	4*e*	1.0	0.1821(4)	0.3124(2)	0.0442(4)	0.0039(6)	1.27
P(1)	4*e*	1.0	0.4354(5)	0.6310(4)	0.1898(4)	0.0021(7)	4.89
P(2)	4*e*	1.0	0.1314(5)	0.9061(4)	0.8315(4)	0.0001(8)	5.05
O(1)	4*e*	1.0	0.3305(5)	0.9497(3)	0.8065(4)	0.0032(8)	2.11
O(2)	4*e*	1.0	0.0875(5)	0.7363(3)	0.2572(4)	0.0039(7)	2.26
O(3)	4*e*	1.0	0.6364(4)	0.5752(3)	0.2342(4)	0.0031(7)	2.02
O(4)	4*e*	1.0	0.1460(4)	0.5888(3)	0.5074(4)	0.0046(8)	1.96
O(5)	4*e*	1.0	0.3244(4)	0.6052(3)	0.0191(4)	0.0058(8)	1.86
O(6)	4*e*	1.0	0.9894(4)	0.4953(3)	0.2259(4)	0.0027(7)	2.14
O(7)	4*e*	1.0	0.4463(4)	0.7822(3)	0.2423(4)	0.0018(8)	2.03

Space group $P2_1'/c$, a = 7.3960(2) Å, b = 9.7535(3) Å, c = 8.5467(2) Å, β = 105.503(2)°
Magnetic moments: M_x = -0.16(9) μ_B, M_y = 0.0 μ_B, M_z = 3.48(3) μ_B, $|M|$ = 3.48(3) μ_B
GII[8] = 0.15 vu
Fitting factors: R_{wp} = 2.49%, R_p = 1.98%, χ^2 = 2.910

Table 4.9: *Selected Bond Distances (Å) and Angles (degrees) for $RbMn_{0.75}Fe_{0.25}P_2O_7$ measured at 2 K*

TM-O(2)	1.921(3)	**TM-O(5)**	2.155(3)
TM-O(3)	1.962(3)	**TM-O(6)**	1.963(3)
TM-O(4)	2.066(3)	**TM-O(7)**	1.948(3)
O(2)-TM-O(3)	172.7(1)	**O(3)-TM-O(7)**	97.5(1)
O(2)-TM-O(4)	91.3(1)	**O(4)-TM-O(5)**	176.7(1)
O(2)-TM-O(5)	90.3(1)	**O(4)-TM-O(6)**	89.8(1)
O(2)-TM-O(6)	84.1(1)	**O(4)-TM-O(7)**	90.7(1)
O(2)-TM-O(7)	89.6(1)	**O(5)-TM-O(6)**	87.6(1)
O(3)-TM-O(4)	90.0(1)	**O(5)-TM-O(7)**	92.2(1)
O(3)-TM-O(5)	88.0(1)	**O(6)-TM-O(7)**	173.8(1)
O(3)-TM-O(6)	88.7(1)		
P(1)-O(1)	1.621(5)	**P(2)-O(1)**	1.601(4)
P(1)-O(3)	1.533(4)	**P(2)-O(2)**	1.525(5)
P(1)-O(5)	1.492(4)	**P(2)-O(4)**	1.480(4)
P(1)-O(7)	1.537(5)	**P(2)-O(6)**	1.528(4)
O(1)-P(1)-O(3)	105.5(3)	**O(1)-P(2)-O(2)**	106.7(3)
O(1)-P(1)-O(5)	106.9(3)	**O(1)-P(2)-O(4)**	107.9(3)
O(1)-P(1)-O(7)	106.4(3)	**O(1)-P(2)-O(6)**	105.4(2)
O(3)-P(1)-O(5)	115.2(3)	**O(2)-P(2)-O(4)**	113.8(3)
O(3)-P(1)-O(7)	107.3(3)	**O(2)-P(2)-O(6)**	106.9(3)
O(5)-P(1)-O(7)	114.8(3)	**O(4)-P(2)-O(6)**	115.5(3)

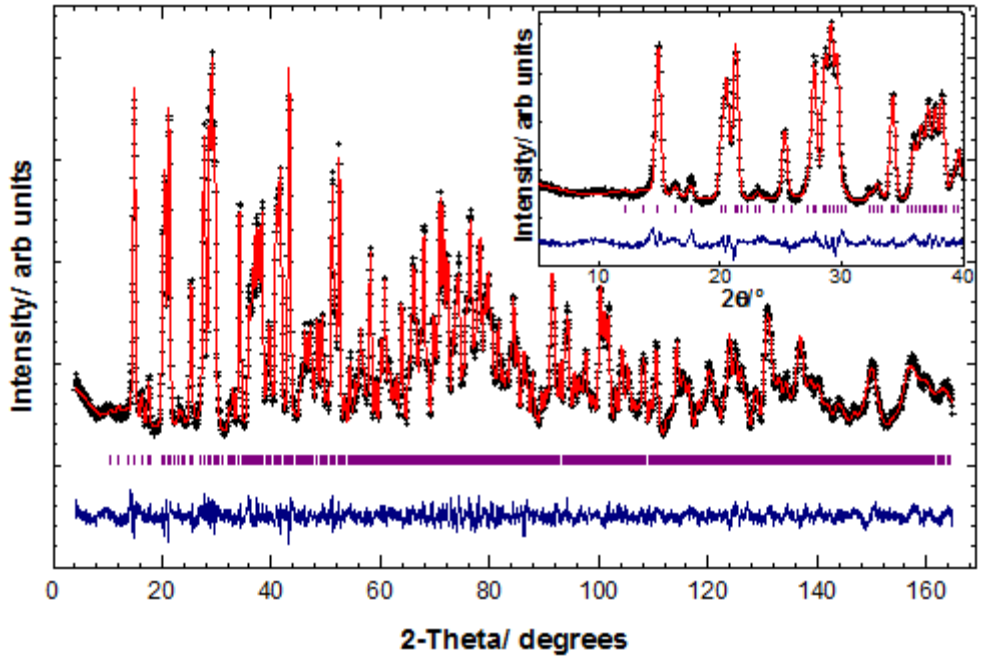

Figure 4.38: *Observed (+), calculated (-), difference profiles (-) and reflection positions (l) for the 2 K Rietveld refinement carried out on $RbMn_{0.5}Fe_{0.5}P_2O_7$. The inset indicates the appearance of the profile without a magnetic contribution fitted.*

Table 4.10: *Refined structural parameters for $RbMn_{0.5}Fe_{0.5}P_2O_7$ obtained from a Rietveld refinement of the 2 K neutron diffraction data.*

Atom	Site	Occupancy	*x*	*y*	*z*	U_{iso}/ Å^2	BVS[7]
Mn/ Fe	4*e*	0.501(3)/ 0.499(3)	0.242(1)	0.5981(8)	0.7628(9)	0.001(2)	3.15/ 3.15
Rb	4*e*	1.0	0.1816(4)	0.3107(3)	0.0434(4)	0.0016(7)	1.27
P(1)	4*e*	1.0	0.4356(6)	0.6317(4)	0.1898(5)	0.005(1)	4.94
P(2)	4*e*	1.0	0.1317(5)	0.9074(4)	0.8310(4)	0.0024(9)	4.90
O(1)	4*e*	1.0	0.3319(5)	0.9496(3)	0.8080(4)	0.0029(8)	2.09
O(2)	4*e*	1.0	0.0875(5)	0.7368(3)	0.2550(4)	0.0031(8)	2.09
O(3)	4*e*	1.0	0.6340(5)	0.5774(4)	0.2317(4)	0.0079(7)	2.10
O(4)	4*e*	1.0	0.1444(5)	0.5880(4)	0.5137(5)	0.0127(9)	1.85
O(5)	4*e*	1.0	0.3224(4)	0.6043(4)	0.0160(4)	0.0074(9)	1.89
O(6)	4*e*	1.0	0.9936(5)	0.4960(4)	0.2274(4)	0.0061(8)	2.20
O(7)	4*e*	1.0	0.4447(5)	0.7807(3)	0.2388(4)	0.0052(9)	2.04

Space group $P2_1'/c$, a = 7.4262(2) Å, b = 9.8352(3) Å, c = 8.4439(2) Å, β = 105.577(2)°
Magnetic moments: M_x = -0.42(9) μ_B, M_y = 0.0 μ_B, M_z = 1.88(5) μ_B, $|M|$ = 1.93(5) μ_B
GII[8] = 0.14 vu
Fitting factors: R_{wp} = 2.67%, R_p = 2.13%, χ^2 = 2.919

Table 4.11: *Selected Bond Distances (Å) and Angles (degrees) for $RbMn_{0.5}Fe_{0.5}P_2O_7$ measured at 2 K*

TM-O(2)	1.977(8)	**TM-O(5)**	2.061(8)
TM-O(3)	1.953(8)	**TM-O(6)**	1.998(8)
TM-O(4)	2.034(8)	**TM-O(7)**	1.975(8)
O(2)-TM-O(3)	173.1(5)	**O(3)-TM-O(7)**	99.6(3)
O(2)-TM-O(4)	88.0(3)	**O(4)-TM-O(5)**	176.2(4)
O(2)-TM-O(5)	90.8(3)	**O(4)-TM-O(6)**	87.1(3)
O(2)-TM-O(6)	82.9(3)	**O(4)-TM-O(7)**	89.5(3)
O(2)-TM-O(7)	87.2(3)	**O(5)-TM-O(6)**	89.1(3)
O(3)-TM-O(4)	90.9(3)	**O(5)-TM-O(7)**	94.1(4)
O(3)-TM-O(5)	89.9(3)	**O(6)-TM-O(7)**	169.7(4)
O(3)-TM-O(6)	90.2(4)		
P(1)-O(1)	1.625(5)	**P(2)-O(1)**	1.604(5)
P(1)-O(3)	1.517(5)	**P(2)-O(2)**	1.556(5)
P(1)-O(5)	1.507(5)	**P(2)-O(4)**	1.521(5)
P(1)-O(7)	1.519(5)	**P(2)-O(6)**	1.496(5)
O(1)-P(1)-O(3)	105.9(3)	**O(1)-P(2)-O(2)**	106.6(3)
O(1)-P(1)-O(5)	106.1(3)	**O(1)-P(2)-O(4)**	107.9(3)
O(1)-P(1)-O(7)	107.5(3)	**O(1)-P(2)-O(6)**	106.1(3)
O(3)-P(1)-O(5)	114.6(3)	**O(2)-P(2)-O(4)**	113.2(3)
O(3)-P(1)-O(7)	107.9(3)	**O(2)-P(2)-O(6)**	107.6(3)
O(5)-P(1)-O(7)	114.2(3)	**O(4)-P(2)-O(6)**	114.9(3)

For x = 0.75, the magnitude of the moments was found to be 3.48(3) μ_B, *cf.* the saturated moment of 4.25 μ_B expected for high spin Mn^{3+}/ Fe^{3+} ions in a 3:1 ratio. The reduced moment could be due to covalency effects, though there is also the possibility of disorder and/ or competing interactions introduced by the presence of Fe^{3+} in the structure. For x = 0.5, $|M|$ = 1.93(5) μ_B, which was much lower than the expected saturated moment of 4.5 μ_B. This value was not surprising considering that there was little evidence for magnetic peaks in the 2 K diffraction pattern (Figure 4.38; inset). However, MPMS SQUID measurements confirmed the presence of magnetic ordering and this was also detected by the Rietveld refinement. As with all magnetic refinements concerned, various magnetic models were introduced by trial

and error, and that which gave the best fit was chosen in an unbiased fashion- this transpired to be a model isostructural with the x = 1 and 0.75 phases. At 50% occupancy each, we would expect the competing magnetic interactions between Mn^{3+} and Fe^{3+} to be at a maximum, which could in part explain the relatively small moment that was observed.

Upon reducing the temperature, a similar pattern of TM-O_6 bond lengths was observed to those at room temperature, comprising of two relatively long and four short bond lengths. Overall both compounds adopt the same magnetic structure type as $RbMnP_2O_7$[2] and α-$NH_4MnP_2O_7$, with the easy axis of magnetisation found to be orientated along the *c*-axis of the structure; the direction also associated with the axial elongation of the TM-O_6 octahedra (Figure 4.39). A detailed discussion of these interactions was given in Chapter 3, section 3.3.4.4.1.

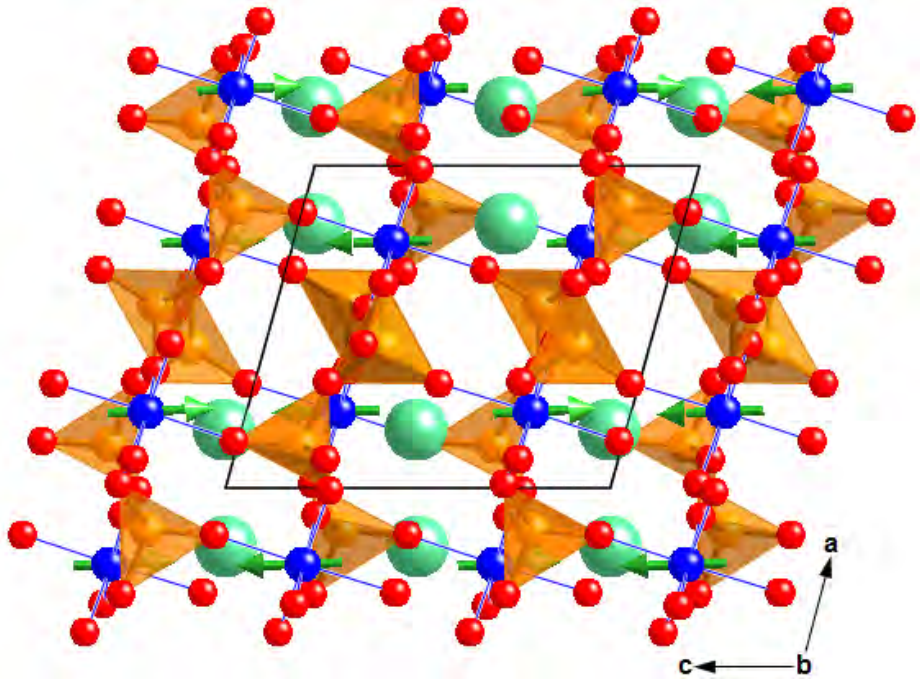

Figure 4.39: *Magnetic structure adopted by $RbMnP_2O_7$, $RbMn_{0.75}Fe_{0.25}P_2O_7$ and $RbMn_{0.5}Fe_{0.5}P_2O_7$, viewed down the b-direction. The orientations of the magnetic moments on the TM ions are shown with green arrows.*

Each TM spin was found to participate in twelve different TM-O-P-O-TM "super-superexchange" interactions, four of which appeared to be FM in nature and occurred within the *ab*-plane and eight of which were directed along the *c*-axis of the structure and showed an AFM relationship (Figure 4.40). However, the connectivity through the orthophosphate entities is such that each PO_4 unit of the diphosphate group simultaneously connects three TM ions *via* the terminal oxygen atoms. Two of these ions have their spins aligned ferromagnetically with respect to each other but antiferromagnetically to the third TM ion, giving rise to AFM ordering overall, as can be seen in Figure 4.41.

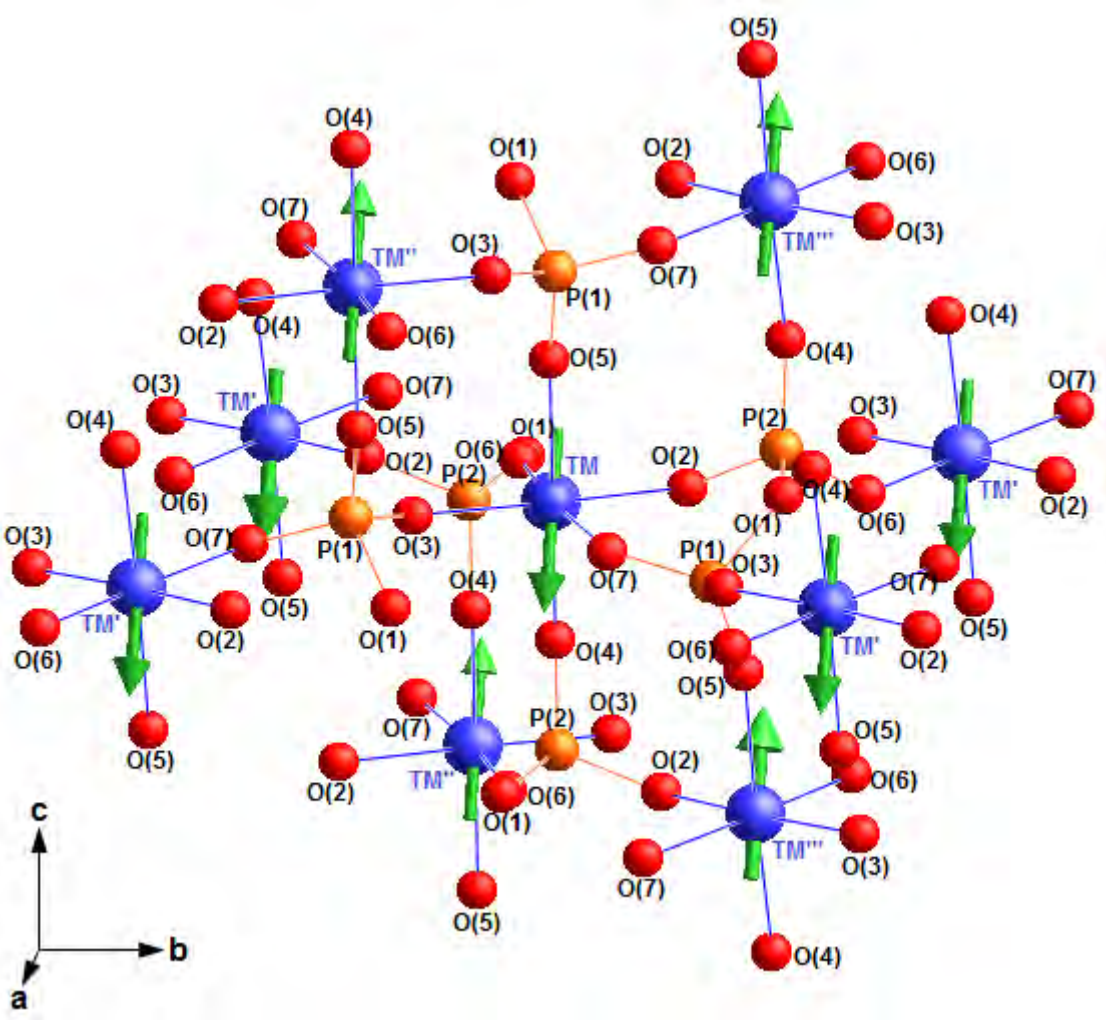

Figure 4.40: *Nearest neighbour TM---TM interactions in x = 1, 0.75 and 0.5 compounds. TM, P and O atoms are shown as blue, orange and red spheres, respectively.*

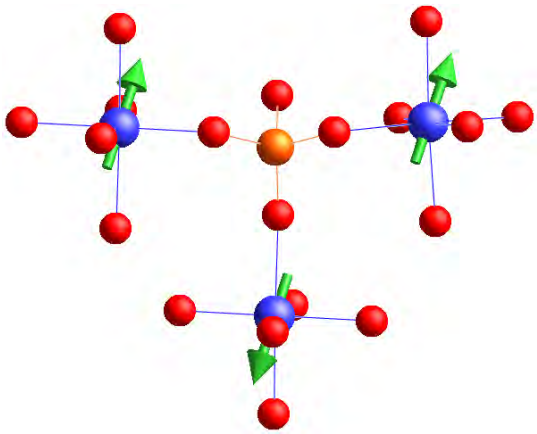

Figure 4.41: *Triad of interactions occurring through the orthophosphate units in the x = 1, 0.75 and 0.5 compounds*

The apparent FM interactions are mediated by the shorter TM-O bonds while one short and one long bond are involved in the AFM interactions. If we consider the orbital occupancies of Mn^{3+} and Fe^{3+}, then this suggests the following possibilities for the FM and AFM interactions, though clearly for x = 1 and 0.75 the Mn---Mn interactions will be dominant: -

FM: $Mn^{3+}\ d^0_{x^2-y^2}$ - - - $Mn^{3+}\ d^0_{x^2-y^2}$

$Mn^{3+}\ d^0_{x^2-y^2}$ - - - $Fe^{3+}\ d^1_{e_g}$

$Fe^{3+}\ d^1_{e_g}$ - - - $Fe^{3+}\ d^1_{e_g}$

AFM: $Mn^{3+}\ d^0_{x^2-y^2}$ - - - $Mn^{3+}\ d^1_{z^2}$

$Mn^{3+}\ d^0_{x^2-y^2}$ - - - $Fe^{3+}\ d^1_{e_g}$

$Fe^{3+}\ d^1_{e_g}$ - - - $Mn^{3+}\ d^1_{z^2}$

$Fe^{3+}\ d^1_{e_g}$ - - - $Fe^{3+}\ d^1_{e_g}$

We therefore generally note that FM interactions involve either two unoccupied, two singly occupied or an unoccupied-singly occupied e_g orbital, while AFM interactions involve either two singly occupied or an unoccupied-singly occupied

e_g orbital. Thus for a pure Fe^{3+} system where all 5 d-orbitals are singly occupied, we may expect to see both FM and AFM interactions. The magnetic structures reported for $NaFeP_2O_7$[21] and $LiFeP_2O_7$[22] are consistent with this and also show a similar triad of interactions occurring through each orthophosphate unit.

The geometry of the TM-O-P-O-TM unit was also investigated to explore whether this had any effect on the sign of the interaction. Table 4.12 shows that for both the x = 0.75 and 0.5 compounds, FM interactions involve O-P-O angles < 107.9° and O---O separations < 2.5 Å, while AFM interactions involve O-P-O angles > 113.2° and O---O separations > 2.5 Å. In the case of equatorial TM-O bonds, the TM-O-P angles for both FM and AFM interactions range from 126.4-140.5°. However, for the axial TM-O bonds an almost linear TM-O-P array is observed with angles of 160.2° and above. Furthermore, TM---TM distances are found to be > 5.9 Å and < 5.3 Å for FM and AFM interactions, respectively. However, a comparison to the 2 K neutron diffraction data on $RbFeP_2O_7$ (for which the magnetic structure is unknown) shows that similar geometrical differences occur between the different Fe-O-P-O-Fe exchange pathways, the only exception being a relatively long O---O separation (> 2.5 Å) in the Fe-O(3)-P(1)-O(7)-Fe pathway.

Table 4.12: *Summary of the exchange pathways present in $RbMn_xFe_{1-x}P_2O_7$ (x = 0.75, 0.5 and 0) and geometries of the interacting species.*

Exchange Pathway	x	O-P-O	TM-O-P	TM-O*-P	O---O	TM---TM	Interaction
TM-O(3)-P(1)-O(7)-TM' **TM-O(7)-P(1)-O(3)-TM'**	0.75	107.3°	138.2°	126.4°	2.472 Å	6.264 Å	FM
	0.5	107.9°	137.8°	129.1°	2.454 Å	6.278 Å	FM
	0	107.3°	138.9°	128.0°	2.510 Å	6.395 Å	/
TM-O(2)-P(2)-O(6)-TM' **TM-O(6)-P(2)-O(2)-TM'**	0.75	106.9°	133.4°	136.7°	2.453 Å	5.985 Å	FM
	0.5	107.6°	132.8°	137.7°	2.463 Å	6.057 Å	FM
	0	103.6°	130.6°	140.5°	2.432 Å	6.092 Å	/
TM-O(4)-P(2)-O(6)-TM'' **TM-O(6)-P(2)-O(4)-TM''**	0.75	115.5°	164.7°	136.7°	2.544 Å	5.233 Å	AFM
	0.5	114.9°	162.8°	137.7°	2.542 Å	5.267 Å	AFM
	0	110.6°	160.2°	140.5°	2.531 Å	5.200 Å	/
TM-O(5)-P(1)-O(3)-TM'' **TM-O(3)-P(1)-O(5)-TM''**	0.75	115.2°	138.2°	162.0°	2.554 Å	5.264 Å	AFM
	0.5	114.6°	137.8°	161.2°	2.545 Å	5.123 Å	AFM
	0	114.8°	138.9°	161.5°	2.556 Å	5.138 Å	/
TM-O(4)-P(2)-O(2)-TM''' **TM-O(2)-P(2)-O(4)-TM'''**	0.75	113.8°	133.4°	164.7°	2.517 Å	5.153 Å	AFM
	0.5	113.2°	132.8°	162.8°	2.569 Å	5.173 Å	AFM
	0	112.1°	130.6°	160.2°	2.525 Å	5.118 Å	/
TM-O(5)-P(1)-O(7)-TM''' **TM-O(7)-P(1)-O(5)-TM'''**	0.75	114.8°	162.0°	126.4°	2.552 Å	5.153 Å	AFM
	0.5	114.2°	161.2°	129.1°	2.540 Å	5.173 Å	AFM
	0	114.2°	161.5°	128.0°	2.594 Å	5.118 Å	/

For TM-O*-P, * indicates oxygen labelled with higher number

As mentioned, the magnetic structures of the $RbMn_xFe_{1-x}P_2O_7$ and α-$NH_4Mn_xFe_{1-x}P_2O_7$ compounds (where known) appear to be governed by a triad of interactions occurring through each orthophosphate unit. Given that the same triad is also observed in the magnetic structures of $NaFeP_2O_7$[21] and $LiFeP_2O_7$,[22] clearly the orbital occupancies of both Mn^{3+} and Fe^{3+} are able to facilitate this type of interaction. The exchange pathways in $NaFeP_2O_7$ and $LiFeP_2O_7$ were further investigated in order to establish whether there were any differences that could explain why the x = 0.25 and 0 members of the Rb system appear to adopt incommensurate magnetic structures. Whilst $RbFeP_2O_7$ and $RbMn_{0.25}Fe_{0.75}P_2O_7$

crystallise as type-I pyrophosphates (space group $P2_1/c$), the aforementioned compounds adopt type-II ($P2_1/c$) and type-III ($P2_1$) structures, respectively. All three structure types consist of FeO_6 octahedra corner-linked to five different pyrophosphate units, one of them being linked in a bidentate fashion. This results in tunnels running throughout the structure which contain the M^I cations in different arrangements. For type-I and type-II, the M^I cations run through the tunnels in a zigzag fashion, whereas for type-III they form a linear array. The configuration of the pyrophosphate group is also different; whilst for type-I the arrangement is semi-staggered, for type-II and type-III it is almost eclipsed. Tables 4.13 and 4.14 show that for $NaFeP_2O_7$ and $LiFeP_2O_7$, only the Fe---Fe separation can be directly correlated with the sign of the interaction. For both compounds, this separation is < 4.86 Å for FM interactions but > 5.16 Å for AFM interactions. This is an opposite effect to that observed for x = 0.25 and 0, where if the same magnetic structure type as the Mn end member was adopted, then FM interactions would involve TM---TM separations > 6.09 Å and AFM interactions would involve separations < 5.20 Å. However, given that there is such a large separation between the TM ions, we would not expect relatively small variations in this to have a significant influence on the sign of the interaction, and so the critical factor governing these interactions is at present unclear from these empirical observations.

Table 4.13: *Exchange pathways present in $NaFeP_2O_7$ and geometries of interacting species.*

Exchange Pathway	O-P-O	Fe-O-P	Fe-O*-P	O---O	Fe---Fe	Interaction
Fe-O(2)-P(1)-O(3)-Fe' **Fe-O(3)-P(1)-O(2)-Fe'**	112.0°	135.8°	129.2°	2.519 Å	4.859 Å	FM
Fe-O(5)-P(2)-O(6)-Fe' **Fe-O(6)-P(2)-O(5)-Fe'**	114.5°	150.7°	126.7°	2.558 Å	4.788 Å	FM
Fe-O(3)-P(1)-O(4)-Fe'' **Fe-O(4)-P(1)-O(3)-Fe''**	113.1°	129.2°	159.6°	2.520 Å	5.498 Å	AFM
Fe-O(5)-P(2)-O(7)-Fe'' **Fe-O(7)-P(2)-O(5)-Fe''**	113.3°	150.7°	126.6°	2.527 Å	5.260 Å	AFM
Fe-O(2)-P(1)-O(4)-Fe''' **Fe-O(4)-P(1)-O(2)-Fe'''**	111.3°	135.8°	159.6°	2.439 Å	6.116 Å	AFM
Fe-O(6)-P(2)-O(7)-Fe''' **Fe-O(7)-P(2)-O(6)-Fe'''**	109.6°	126.7°	126.6°	2.503 Å	6.277 Å	AFM

For Fe-O*-P, * indicates oxygen labelled with higher number

Table 4.14: *Exchange pathways present in $LiFeP_2O_7$ and geometries of interacting species.*

Exchange Pathway	O-P-O	Fe-O-P	Fe-O*-P	O---O	Fe---Fe	Interaction
Fe-O(4)-P(1)-O(7)-Fe **Fe-O(7)-P(1)-O(4)-Fe**	112.9°	139.8°	131.5°	2.507 Å	4.809 Å	FM
Fe-O(1)-P(2)-O(2)-Fe **Fe-O(2)-P(2)-O(1)-Fe**	114.1°	135.2°	131.4°	2.541 Å	4.809 Å	FM
Fe-O(1)-P(2)-O(5)-Fe' **Fe-O(5)-P(2)-O(1)-Fe'**	111.7°	135.2°	131.7°	2.498 Å	6.311 Å	AFM
Fe-O(2)-P(2)-O(5)-Fe' **Fe-O(5)-P(2)-O(2)-Fe'**	112.6°	131.4°	131.7°	2.516 Å	5.163 Å	AFM
Fe-O(4)-P(1)-O(3)-Fe' **Fe-O(3)-P(1)-O(4)-Fe'**	112.5°	146.6°	139.8°	2.505 Å	6.280 Å	AFM
Fe-O(3)-P(1)-O(7)-Fe' **Fe-O(7)-P(1)-O(3)-Fe'**	110.0°	146.6°	131.5°	2.477 Å	5.522 Å	AFM

For Fe-O*-P, * indicates oxygen labelled with higher number

4.4 Conclusions

The $RbMn_xFe_{1-x}P_2O_7$ solid solution was successfully synthesised by an acid melt method and the x = 1, 0.75, 0.5, 0.25 and 0 members characterised by neutron and X-ray diffraction. It was found that the x = 1 end member possesses a distorted MnO_6 coordination sphere that can be described by a [4+2] or [4+1+1] pattern of bond lengths. The average distortion at the transition metal centre decreases with an increasing amount of Fe^{3+} in the system and explains the change in unit cell parameters as the series is traversed.

For all compositions with x > 0, EXAFS and XANES showed that the MnO_6 coordination sphere can be described by a [4+2] elongation. The Mn-O bond lengths obtained from EXAFS suggested that there is a decrease in this distortion with an increasing amount of Fe in the system. UV-Vis spectroscopy was also used to probe the Mn^{3+} centres in these materials, with the spectra suggesting a [4+2] elongation for x = 0.5 and 0.25 and a more distorted octahedral coordination sphere for x = 1 and 0.75. In crossing the series, a colour change from violet to blue was observed and is likely to be related to the subtle changes in the MnO_6 coordination sphere.

With respect to the local Fe^{3+} environment, EXAFS and XANES showed that a regular octahedral coordination sphere is adopted by all compositions with x < 1. The more sensitive technique of ^{57}Fe Mössbauer spectroscopy showed that Fe^{3+} is in a distorted environment when there is a greater amount of Mn^{3+} present in the system, with data on the x = 0 compound showing that the Fe^{3+} here exists in a highly symmetric environment. The origin of the distortion at the Fe^{3+} centres is at present unclear, though it is thought to be caused by the surrounding asymmetric electronic charge distribution.

The results from Mn/ Fe EXAFS and XANES as well as UV-Vis spectroscopy suggest that of the two transition metals within the $RbMn_xFe_{1-x}P_2O_7$ system, the Mn^{3+} coordination sphere shows the more marked change as the series is traversed, which has consequences for the optical properties of these materials. Indeed, this is perhaps as a result of it being able to adopt a plastic coordination sphere, as opposed to Fe^{3+} which is more prone to adopt a regular octahedral coordination sphere.

The thermal stability of these compounds was investigated to ascertain the temperature range within which the phases remain stable and at what point changes in colouration occur. It was generally found that the stability was limited by the amount of Mn^{3+} present in the system, which unlike Fe^{3+}, appeared to be prone to a change in oxidation state. Despite this, the stability of all of these phases was much higher than that of some similarly coloured commercial pigments, such as manganese violet which is reported to be stable only up to 280°C.[23] To summarise, $RbMnP_2O_7$ was found to remain stable up to 660°C while $RbFeP_2O_7$ up to 1050°C. For the intermediate compounds it was found that by 700°C, some of the manganese was beginning to be expelled from the host structure, forming either an amorphous phase or a poorly crystalline phase, the nature of which was unknown. After being heated to 1000°C, the blue colouration of the x = 0.25 compound remained stable, though changed to pale blue upon further heating to 1100°C. Neutron diffraction measurements confirmed that the level of manganese had fallen to 4.2(4)%, which was also supported by a change in the XRD lattice parameters and UV-Vis spectra. For x = 0.5 and 0.75, the original colour of the hosts only remained stable up to ~700°C and ~600°C, respectively. XRD lattice parameters suggested that the level of

manganese had fallen to < 25% in the former case and between 50-60% in the latter case. The $RbMn_xFe_{1-x}P_2O_7$ structure type eventually collapsed by 1200°C for x = 0.25 and 0.5 and by 800°C for x = 0.75, which can be explained by the latter compound retaining a greater amount of manganese.

The mechanism for manganese expulsion is at present unclear. Given that it begins to occur by ~700°C, it is likely to be driven by a change in manganese oxidation state, which occurs by this temperature for $RbMnP_2O_7$. Further information could be obtained were the nature of the amorphous/ impurity phase known and also if the manganese oxidation state could be determined. However, the latter is complicated by the fact that there are at least two (if not more) Mn-containing phases present past 700°C.

The magnetic properties of x = 0.75, 0.5 and 0.25 were investigated and it was established that the former two compounds adopt the same magnetic structure as the Mn end member. Both FM and AFM TM-O-P-O-TM "super-superexchange" pathways were present but it was found that each PO_4 unit simultaneously links three TM centres such to give AFM ordering overall. The signs of the interactions suggested that FM interactions involved two unoccupied, two singly occupied or one unoccupied, one singly occupied e_g orbital and that AFM interactions involved two singly occupied or one singly occupied, one unoccupied e_g orbital. The susceptibility data suggested a canting of the moments for x = 0.75 and 0.5, though this was not further investigated as it was expected to be relatively small. For x = 0.25, the susceptibility data indicated the presence of frustrated magnetic interactions. Despite the 2 K neutron diffraction pattern showing evidence for magnetic ordering, like the Fe end member, the magnetic structure could not be solved. However, from our other

findings we would expect the pure Fe^{3+} system to possess both FM and AFM exchange pathways. A further comparison to the magnetic structures of $NaFeP_2O_7$ and $LiFeP_2O_7$ showed that FM interactions in these two compounds involved shorter Fe---Fe separations and AFM interactions longer separations. The converse was observed for x = 0.25 and 0, were they to adopt the same triad of interactions seen for the other members of the $RbMn_xFe_{1-x}P_2O_7$ solid solution. However, the long TM---TM separations observed within these compounds are unlikely to be critical factors in governing the exchange interactions.

From these studies we have been able to provide some tentative empirical observations on Mn^{3+} and Fe^{3+} "super-superexchange" interactions; indeed, it would be interesting to see whether these are evident in other condensed phosphate systems possessing similar exchange pathways. At present the strongest interaction in these systems has not been identified, though it is likely that the other interactions arrange themselves so as to allow this to dominate, particularly if there is little energy difference between these weaker interactions.

References

[1] L. S. Guzeeva and I. V. Tananaev, *Inorg. Mater.*, 1988, **24**, 538-542.

[2] F. C. Coomer, N. J. Checker and A. J. Wright, *Inorg. Chem.*, 2010, **49**, 934-942.

[3] A. J. Wright and J. P. Attfield, *Inorg. Chem.*, 1998, **37**, 3858-3861.

[4] J. M. M. Millet and B. F. Mentzen, *Eur. J. Solid State Inorg. Chem.*, 1991, **28**, 493-504.

[5] E. Dvoncova and K. H. Lii, *J. Solid State Chem.*, 1993, **105**, 279-286.

[6] N. J. Checker, *The Synthesis and Properties of Novel Condensed Phosphates*, PhD Thesis, University of Birmingham, 2006.

[7] I. D. Brown and D. Altermatt, *Acta Crystallogr.*, 1985, **B41**, 244-247.

[8] A. Salinas-Sanchez, J. L. Garcia-Munoz, J. Rodriguez-Carvajal, R. Saez-Puche and J. L. Martinez, *J. Solid State Chem.*, 1992, **100**, 201-211.

[9] H. N. Ng and C. Calvo, *Can. J. Chem.*, 1973, **51**, 2613-2620.

[10] R. D. Shannon, *Acta Crystallogr.*, 1976, **A32**, 751-767.

[11] A. A. Khan and W. H. Baur, *Acta Crystallogr.*, 1972, **B28**, 683-693.

[12] K. Fejfarova, R. Essehli, B. El Bali and M. Dusek, *Acta. Crystallogr.*, 2008, **E64**, I85-I86.

[13] *PeakFit Version 4.12*; Seasolve, 1999-2003.

[14] A. B. P. Lever, *Inorganic Electronic Spectroscopy*; Elsevier: Amsterdam, 1984.

[15] T. Moya-Pizarro, S. Salmon, L. Fournes, G. Le Flem, B. Wanklyn and P. Hagenmuller, *J. Solid State Chem.*, 1984, **53**, 387-397.

[16] JCPDS, *International Centre for Diffraction Data*, 1999, P.1., Swathmore, Pennsylvania, PA 19081, USA, 11990.

[17] A. F. Gualtieri, *A guided training exercise of quantitative phase analysis using EXPGUI*, www.ccp14.ac.uk/solution/gsas/files/expgui_quant_gualtieri.pdf.

[18] C. E. Housecroft and A. G. Sharpe, *Inorganic Chemistry*; Pearson Education: Harlow, 2001.

[19] R. Shirley, *The CRYSFIRE System for Automatic Powder Indexing: User's Manual*, 2002, The Lattice Press, 41 Guildford Park Avenue, Guildford, Surrey, GU2 7NL, England.

[20] P. J. Brown, *International Tables of Crystallography, Vol.C*; Kluwer: Dordrecht, 1992.

[21] R. C. Mercader, L. Terminiello, G. J. Long, D. G. Reichel, K. Dickhaus, R. Zysler, R. Sanchez and M. Tovar, *Phys. Rev. B*, 1990, **42**, 25-32.

[22] G. Rousse, J. Rodríguez-Carvajal, C. Wurm and C. Masquelier, *Solid State Sciences*, 2002, **4**, 973-978.

[23] Holliday Pigments, http://www.holliday-pigments.com/manganese-violets.

Chapter Five

Structure and Properties of the α-$RbMn_xFe_{1-x}HP_3O_{10}$ System

5.1 Introduction

The rich structural diversity of transition metal condensed phosphates has led to interest in their properties as electrode materials in lithium rechargeable batteries,[1-4] their ionic conductivity at high temperatures[5-6] and for their use as catalysts.[7-8] The most frequently encountered linear condensed phosphate units are those of the pyrophosphate ($P_2O_7^{4-}$) and triphosphate ($P_3O_{10}^{5-}$) anions, with further degrees of condensation often leading to the formation of ultraphosphates and cyclophosphates. Generally, these frameworks, at least in part, consist of transition metal (TM) octahedra corner-linked to PO_4 tetrahedra, resulting in structures of either a 3-dimensional porous nature[9-10] or a layered nature,[11] leading to potential ion exchange, intercalation and exfoliation properties.

Guzeeva and Tananaev[12] were the first to investigate the Rb-Mn-P-O condensed phosphate system, and in 1988 reported that three phases could be synthesised through varying the Rb:Mn:P molar ratio. Subsequent studies by Checker[13] detailed the optimum ratios to synthesise these three phases, presently referred to as α-$RbMnHP_3O_{10}$, β-$RbMnHP_3O_{10}$ and $RbMnP_2O_7$ (Table 5.1). The

nuclear and magnetic structures of all three compounds have been reported by Wright and Attfield[14] (α-$RbMnHP_3O_{10}$) and Coomer *et al*[15] (β-$RbMnHP_3O_{10}$ and $RbMnP_2O_7$). The $RbMn_xFe_{1-x}P_2O_7$ system was discussed in detail in Chapter 4 and as such the focus here lies with the triphosphate phases. Both polymorphs possess the same framework topology of MnO_6 octahedra corner-linked to hydrogen triphosphate anions, resulting in a three-dimensional network containing channels in which the Rb^+ cations reside. α-$RbMnHP_3O_{10}$ has been found to crystallise in space group *C*2/*c* and possesses one unique Mn site within the unit cell, located on an inversion centre. In contrast β-$RbMnHP_3O_{10}$ crystallises in space group *C*2 and possesses two unique Mn environments, both located on diads. Whilst α-$RbMnHP_3O_{10}$ contains only one type of channel, β-$RbMnHP_3O_{10}$ contains two, all of which show different dimensions to each other. To date, only one form of the iron analogue, $RbFeHP_3O_{10}$ has been reported. The compound was first isolated by Grunze and Grunze[16] as part of a wider study into the synthesis of various triphosphates. Later a structural determination by Checker[13] found this phase to be isostructural to α-$RbMnHP_3O_{10}$.

Table 5.1: *Optimum Rb:TM:P molar ratios to synthesise different Mn^{3+} and Fe^{3+} condensed phosphate phases.[13]*

Rb:Mn:P	Isolated phase	Rb:Fe:P	Isolated phase
5:1:15	α-$RbMnHP_3O_{10}$	5:1:15	$RbFeHP_3O_{10}$
7.5:1:15	β-$RbMnHP_3O_{10}$	9:1:15	$RbFeP_2O_7$
9:1:15	$RbMnP_2O_7$		

Given the interesting properties shown by the α-$NH_4Mn_xFe_{1-x}P_2O_7$ and $RbMn_xFe_{1-x}P_2O_7$ systems, it was of relevance to us to investigate whether $RbMn_xFe_{1-x}HP_3O_{10}$ solid solutions could also be formed. Again the study was to

emphasise the structural, optical, thermal and magnetic properties of the materials obtained. With the extra degree of condensation *cf.* the pyrophosphate unit, it would be of particular interest to examine whether similar trends were observed in the magnetic properties of triphosphate systems; the overall aim being to obtain sufficient data on magnetically dilute frameworks in order to be able to predict exchange interactions.

5.2 Experimental

α-$RbMn_xFe_{1-x}HP_3O_{10}$ compounds were prepared in a similar fashion to the end members, using a phosphoric acid melt method and a Rb:TM:P molar ratio of 5:1:15. Rb_2CO_3, Mn_2O_3 and Fe_2O_3 were ground together before being added to H_3PO_4 (86.5 wt %) in a porcelain crucible. The resulting mixture was transferred to an oven and heated at 250°C for 48 h and then cooled to RT over 24 h. The resulting products were then collected by suction filtration and washed with water. Attempts to synthesise β-$RbMn_xFe_{1-x}HP_3O_{10}$ ($x < 1$) compounds under similar conditions proved unsuccessful. Although Rb:TM:P molar ratios between 5:1:15 and 9:1:15 were explored, they were found to either form α-$RbMn_xFe_{1-x}HP_3O_{10}$, $RbMn_xFe_{1-x}P_2O_7$ or a mixture of these two phases.

Powder X-ray diffraction data were collected on a Bruker AXS: D8 Advance diffractometer in transmission mode with a 2θ scan range of 5-80°. Both RT and 2 K neutron diffraction data were recorded on the x = 0.75, 0.5 and 0.25 compounds on the HRPT instrument at the Paul Scherrer Institute, Switzerland. An incident neutron wavelength of 1.494 Å was employed over the range $5 \leq 2\theta \leq 160°$. RT neutron diffraction data on x = 1 and 0 were recorded over the same 2θ range on the D2B instrument at the Institut Laue-Langevin, Grenoble, using a wavelength of 1.5943 Å.

5.3 Results and Discussion

Structural details on the x = 1, 0.75, 0.5, 0.25 and 0 compounds were obtained from Rietveld refinements of the 300 K neutron diffraction data, using α-$RbMnHP_3O_{10}$[14] as a starting model (space group *C*2/*c*). For x = 0.75, the coherent scattering length of neutrons[17] from the TM site is very small, being approximately -0.3125 fm. Therefore a joint XRD/ ND refinement was employed here in order to obtain accurate details on the Mn and Fe atoms within the structure. The final refinements are shown in Figure 5.1, structural parameters in Table 5.2 and selected bond lengths and angles in Table 5.3. It should be noted that the x = 0 sample contained an impurity which could not be identified using the JCPDS[18] database, and so due to being unable to model the second phase present, the value of χ^2 was relatively high for this phase.

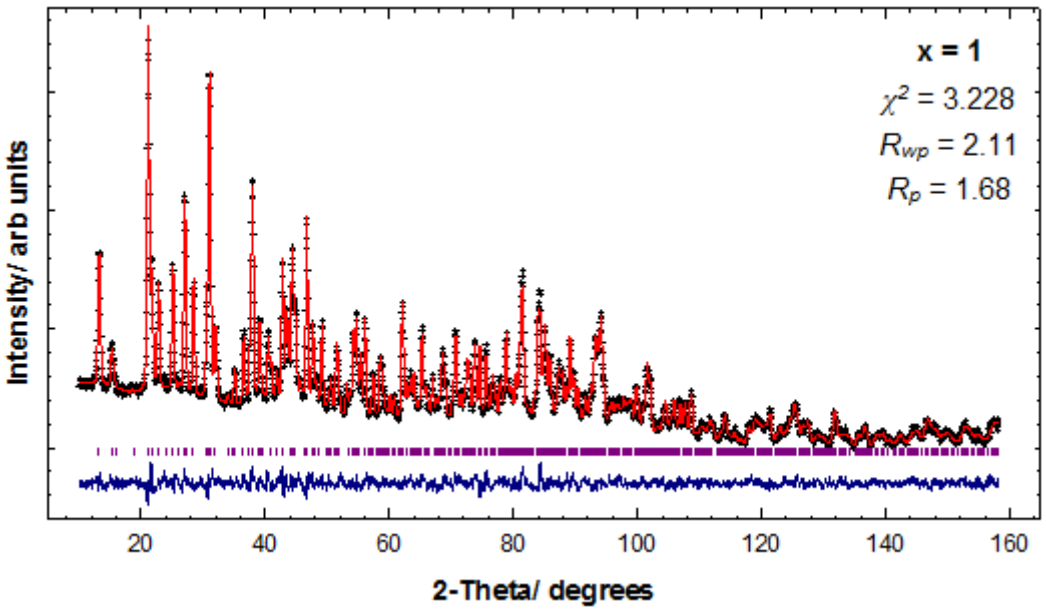

Figure 5.1: *Observed (+), calculated (-), difference profiles (-) and reflection positions (|) for the 300 K Rietveld refinements carried out on the α-$RbMn_xFe_{1-x}HP_3O_{10}$ (x = 1, 0.75, 0.5, 0.25 and 0) series. The inset for x = 0.75 shows the XRD data refinement.*

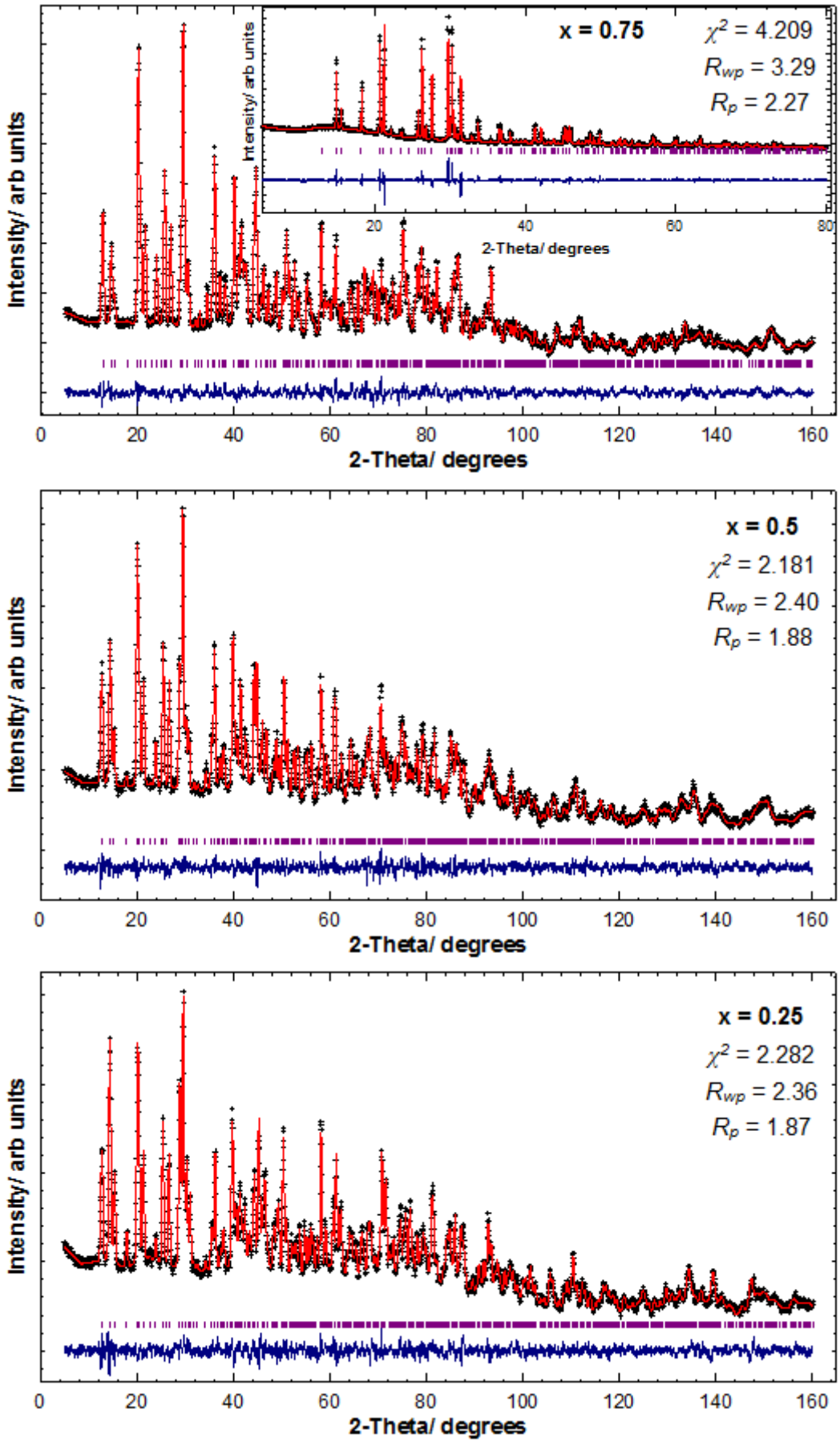
x = 0.75
χ^2 = 4.209
R_{wp} = 3.29
R_p = 2.27
Intensity/ arb units
2-Theta/ degrees
x = 0.5
χ^2 = 2.181
R_{wp} = 2.40
R_p = 1.88
Intensity/ arb units
2-Theta/ degrees
x = 0.25
χ^2 = 2.282
R_{wp} = 2.36
R_p = 1.87
Intensity/ arb units
2-Theta/ degrees

Figure 5.1 continued...

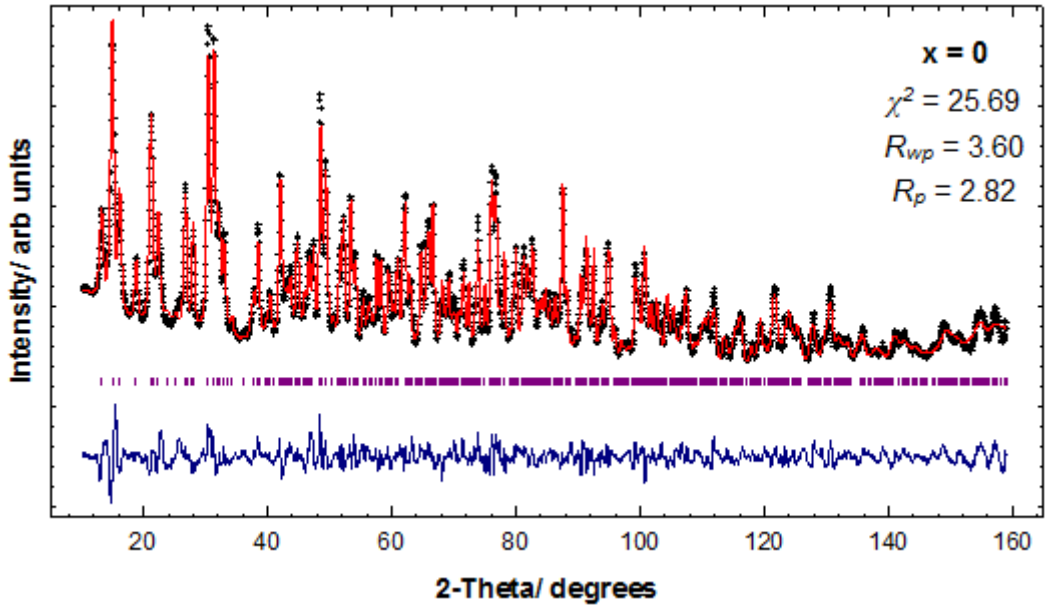

Table 5.2: *Refined structural parameters from the 300 K diffraction data on the α-$RbMn_xFe_{1-x}HP_3O_{10}$ series (x = 1, 0.75, 0.5, 0.25 and 0) with Bond Valence Sums*[19]

		x = 1	x = 0.75	x = 0.5	x = 0.25	x = 0
Space group *C2/c*	***a/ Å***	12.1825(5)	12.1004(3)	12.0775(5)	12.0448 (5)	12.0261(6)
	b/ Å	8.3517(3)	8.3949(2)	8.4468(4)	8.4798(4)	8.5047(4)
	c/ Å	9.0698(3)	9.1250(3)	9.1944(4)	9.2297(4)	9.2765(4)
	β/ °	109.038(2)	110.013(1)	110.718(3)	111.317(3)	111.931(3)
Mn/ Fe *4c*	***x***	0.25	0.25	0.25	0.25	0.25
	y	0.25	0.25	0.25	0.25	0.25
	z	0	0	0	0	0
	U_{iso}/ Å^2	0.010(2)	0.026(2)	0.017(4)	0.012(2)	0.010(1)
	Occ (Mn)	1	0.740(4)	0.506(5)	0.274(6)	0
	Occ (Fe)	0	0.260(4)	0.494(5)	0.726(6)	1
	BVS (Mn/ Fe)	3.32/ 0	3.27/ 3.26	3.23/ 3.22	3.29/ 3.28	0/ 3.14
Rb *4e*	***x***	0	0	0	0	0
	y	0.4375(6)	0.4382(3)	0.4405(6)	0.4395(8)	0.440(1)
	z	0.25	0.25	0.25	0.25	0.25
	U_{iso}/ Å^2	0.047(1)	0.049(1)	0.040(2)	0.044(2)	0.037(2)
	Occ	1	1	1	1	1
	BVS	0.91	0.95	0.95	0.95	0.96
P(1) *8f*	***x***	0.2924(3)	0.2935(3)	0.2921(3)	0.2894(4)	0.2898(6)
	y	0.5637(4)	0.5629(4)	0.5631(5)	0.5621(6)	0.5647(8)
	z	0.2049(4)	0.2090(4)	0.2056(5)	0.2024(5)	0.2063(7)
	U_{iso}/ Å^2	0.0109(8)	0.0089(9)	0.008(1)	0.011(1)	0.007(1)
	Occ	1	1	1	1	1
	BVS	5.02	5.08	4.94	4.93	5.06

Table 5.2 continued...

		x = 1	x = 0.75	x = 0.5	x = 0.25	x = 0
	x	0.5	0.5	0.5	0.5	0.5
P(2)	***y***	0.3696(6)	0.3732(5)	0.3733(6)	0.3749(7)	0.3773(9)
4*e*	***z***	0.25	0.25	0.25	0.25	0.25
	U_{iso}/ Å^2	0.010(1)	0.009(1)	0.007(1)	0.008(1)	0.003(2)
	Occ	1	1	1	1	1
	BVS	5.07	4.88	5.02	4.92	4.88
	x	0.4170(3)	0.4169(3)	0.4177(3)	0.4178(4)	0.4155(5)
O(1)	***y***	0.4846(4)	0.4845(4)	0.4834(4)	0.4858(5)	0.4840(6)
8*f*	***z***	0.3038(4)	0.3029(4)	0.3035(4)	0.3048(5)	0.3025(7)
	U_{iso}/ Å^2	0.0176(8)	0.0140(9)	0.0114(9)	0.014(1)	0.009(1)
	Occ	1	1	1	1	1
	BVS	2.06	2.24	2.17	2.10	2.20
O(2)	***x***	0.2161(3)	0.2120(3)	0.2126(3)	0.2120(3)	0.2102(5)
8*f*	***y***	0.4344(4)	0.4372(4)	0.4386(5)	0.4396(5)	0.4432(7)
	z	0.1054(4)	0.1024(4)	0.0994(4)	0.0974(5)	0.0978(6)
	U_{iso}/ Å^2	0.0115(7)	0.0154(8)	0.0124(8)	0.012(1)	0.007(1)
	Occ	1	1	1	1	1
	BVS	2.04	1.91	1.96	2.05	1.93
O(3)	***x***	0.3230(3)	0.3240(3)	0.3219(3)	0.3224(3)	0.3229(5)
8*f*	***y***	0.6974(4)	0.6970(5)	0.7006(5)	0.7007(5)	0.6989(6)
	z	0.1159(4)	0.1180(4)	0.1173(5)	0.1183(5)	0.1164(6)
	U_{iso}/ Å^2	0.0213(9)	0.026(1)	0.025(1)	0.022(1)	0.016(1)
	Occ	1	1	1	1	1
	BVS	1.97	1.89	1.87	1.85	1.82
O(4)	***x***	0.2413(3)	0.2389(3)	0.2385(3)	0.2400(4)	0.2403(4)
8*f*	***y***	0.6133(4)	0.6148(4)	0.6152(4)	0.6169(5)	0.6181(6)
	z	0.3283(4)	0.3233(4)	0.3221(5)	0.3231(5)	0.3214(6)
	U_{iso}/ Å^2	0.0195(8)	0.0171(9)	0.018(1)	0.017(1)	0.012(1)
	Occ	1	1	1	1	1
	BVS	2.11	2.18	2.07	2.01	2.14
O(5)	***x***	0.4340(3)	0.4296(3)	0.4288(3)	0.4279(4)	0.4280(5)
8*f*	***y***	0.2772(4)	0.2802(4)	0.2809(4)	0.2804(5)	0.2789(6)
	z	0.1095(4)	0.1046(4)	0.1075(4)	0.1087(5)	0.1096(6)
	U_{iso}/ Å^2	0.0136(8)	0.0174(9)	0.0134(9)	0.013(1)	0.012(1)
	Occ	1	1	1	1	1
	BVS	1.89	1.81	1.90	1.92	1.90
H	***x***	0.25	0.25	0.25	0.25	0.25
4*d*	***y***	0.25	0.25	0.25	0.25	0.25
	z	0.5	0.5	0.5	0.5	0.5
	U_{iso}/ Å^2	0.046(3)	0.040(3)	0.043(3)	0.042(3)	0.030(4)
	Occ	1	1	1	1	1
	BVS	0.81	0.79	0.86	0.85	0.87

Table 5.3: *Selected Bond Distances (Å) and Angles (degrees) for the α-$RbMn_xFe_{1-x}HP_3O_{10}$ series (x = 1, 0.75, 0.5, 0.25 and 0) and Global Instability Index[20] Values*

	x = 1	**x = 0.75**	**x = 0.5**	**x = 0.25**	**x = 0**
TM-O(2) × 2	1.927(3)	1.961(3)	1.967(4)	1.975(4)	2.019(6)
TM-O(4) × 2	1.906(4)	1.938(4)	1.957(4)	1.952(4)	1.968(6)
TM-O(5) × 2	2.148(3)	2.068(3)	2.049(4)	2.025(4)	2.012(5)
O(2)-TM-O(2')	180	180	180	180	180
O(2)-TM-O(4)	87.9(1)	88.1(1)	87.5(1)	87.5(2)	88.0(2)
O(2)-TM-O(4')	92.1(1)	91.9(1)	92.5(1)	92.5(2)	92.0(2)
O(2)-TM-O(5)	92.7(1)	93.6(1)	92.8(1)	92.8(2)	93.4(2)
O(2)-TM-O(5')	87.3(1)	86.4(1)	87.2(1)	87.2(2)	86.6(2)
O(4)-TM-O(4')	180	180	180	180	180
O(4)-TM-O(5)	94.9(1)	94.2(1)	94.6(1)	94.2(2)	94.2(2)
O(4)-TM-O(5')	85.1(1)	85.7(1)	85.4(1)	85.8(2)	85.8(2)
O(5)-TM-O(5')	180	180	180	180	180
P(1)-O(1)	1.630(5)	1.587(4)	1.612(5)	1.625(6)	1.595(8)
P(1)-O(2)	1.515(4)	1.541(4)	1.522(5)	1.493(6)	1.509(8)
P(1)-O(3)	1.495(5)	1.518(5)	1.531(6)	1.538(7)	1.551(8)
P(1)-O(4)	1.506(5)	1.478(4)	1.500(5)	1.515(6)	1.475(8)
P(2)-O(1) × 2	1.583(4)	1.565(5)	1.562(4)	1.576(5)	1.570(7)
P(2)-O(5) × 2	1.482(4)	1.523(4)	1.506(4)	1.508(5)	1.518(6)
O(1)-P(1)-O(2)	108.6(3)	109.7(3)	109.0(3)	109.8(4)	108.1(5)
O(1)-P(1)-O(3)	104.4(3)	104.1(3)	105.1(3)	103.4(4)	103.8(5)
O(1)-P(1)-O(4)	103.8(3)	107.9(3)	106.4(3)	103.8(3)	106.4(5)
O(2)-P(1)-O(3)	115.1(3)	112.7(3)	113.4(3)	114.8(4)	111.8(5)
O(2)-P(1)-O(4)	108.5(3)	107.7(3)	109.1(3)	111.8(4)	111.5(5)
O(3)-P(1)-O(4)	115.6(3)	114.7(3)	113.4(3)	112.3(4)	114.6(5)
O(1)-P(2)-O(1')	105.2(4)	106.7(4)	107.0(4)	106.8(5)	109.3(6)
O(1)-P(2)-O(5)	111.1(2)	110.3(2)	110.6(2)	111.3(2)	110.9(3)
O(1)-P(2)-O(5')	105.8(2)	105.3(2)	105.4(2)	105.7(2)	106.3(3)
O(5)-P(2)-O(5')	117.2(4)	118.4(4)	117.6(5)	115.8(5)	113.1(7)
Rb-O(2) × 2	3.303(3)	3.279(3)	3.321(3)	3.334(4)	3.324(5)
Rb-O(2') × 2	3.596(3)	3.516(3)	3.482(3)	3.450(4)	3.420(6)
Rb-O(3) × 2	2.905(5)	2.885(4)	2.892(4)	2.875(6)	2.879(9)
Rb-O(4) × 2	3.153(4)	3.111(4)	3.092(4)	3.108(5)	3.109(6)
Rb-O(5) × 2	3.106(5)	3.155(4)	3.151(4)	3.161(7)	3.15(1)
H-O(3) × 2	1.216(4)	1.224(4)	1.196(4)	1.198(4)	1.190(5)
O(3)-H-O(3')	180	180	180	180	180
GII	0.14	0.17	0.12	0.12	0.13

The structure (as shown in Figure 5.2) can be described as a three-dimensional network of TM-O_6 octahedra corner-linked to four different hydrogen triphosphate groups, two of them being connected in a bidentate fashion along a

common edge of the octahedron *i.e.* in a cis configuration (see Figure 5.3). Strong symmetric O(3)-H---O(3) hydrogen bonds link these anions into chains, resulting in a framework of channels running through the structure which hold the Rb^+ cations in 10-fold coordination. This can be contrasted to the structures adopted by other $M^{I}M^{III}HP_3O_{10}$ compounds, such as $KAlHP_3O_{10}$,[21] 1M-$CsGaHP_3O_{10}$[22] and $CsGaHP_3O_{10}$-III,[23] where the $HP_3O_{10}^{4-}$ and $M^{III}O_6$ units form layers held together by hydrogen bonding and separated by the M^{I} cations.

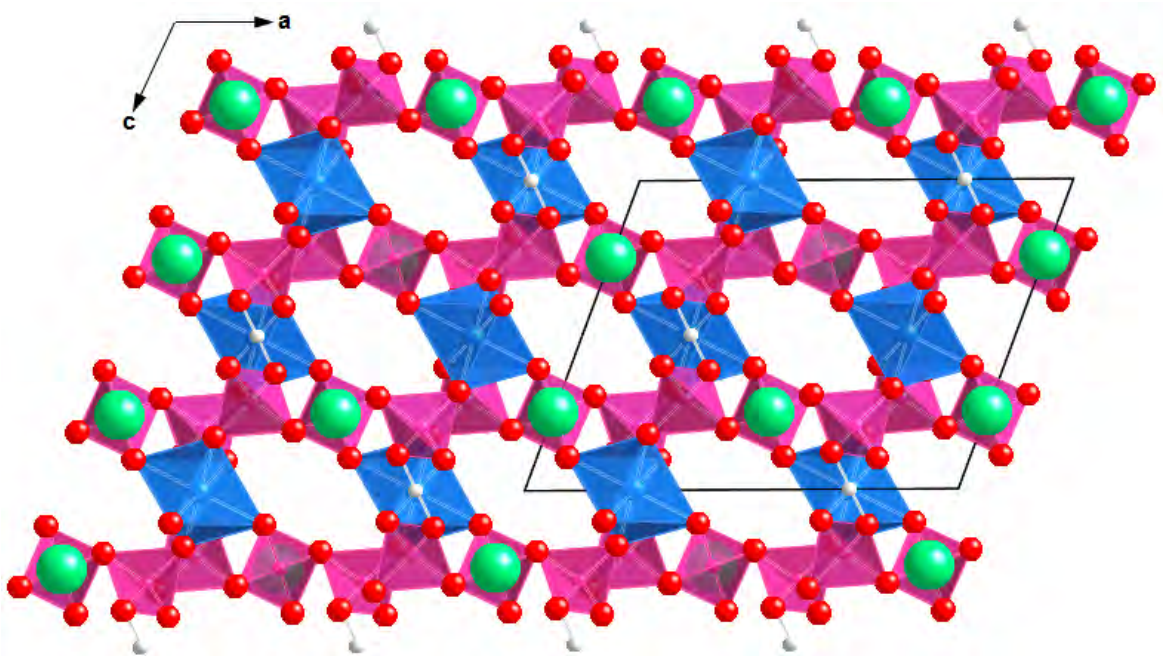

Figure 5.2: *Structure adopted by α-RbMn$_x$Fe$_{1-x}$HP$_3$O$_{10}$ compounds showing TM-O$_6$ octahedra (blue), P$_3$O$_{10}$ condensed phosphate tetrahedra (pink), rubidium cations (green spheres) and hydrogen atoms (white spheres). The thin black line defines the unit cell.*

Within the structure the hydrogen and transition metal atoms are located on inversion centres whilst rubidium and P(2) are located on a diad. This results in the triphosphate group exhibiting a 2-fold axis of symmetry through the central phosphorus atom, P(2). Indeed, this feature is also found amongst a number of other triphosphate compounds.[24-25] The PO_4 tetrahedra constituting the triphosphate units show longer P-O(1) bonds to the bridging oxygen and shorter P-O bonds to the

terminal oxygens that are shared with the TM centre. The P-O(3)H lengths are comparable to or slightly longer than the P-O(terminal) bond lengths, which is consistent with observations made of other well known triphosphates such as CsMnHP$_3$O$_{10}$.[26]

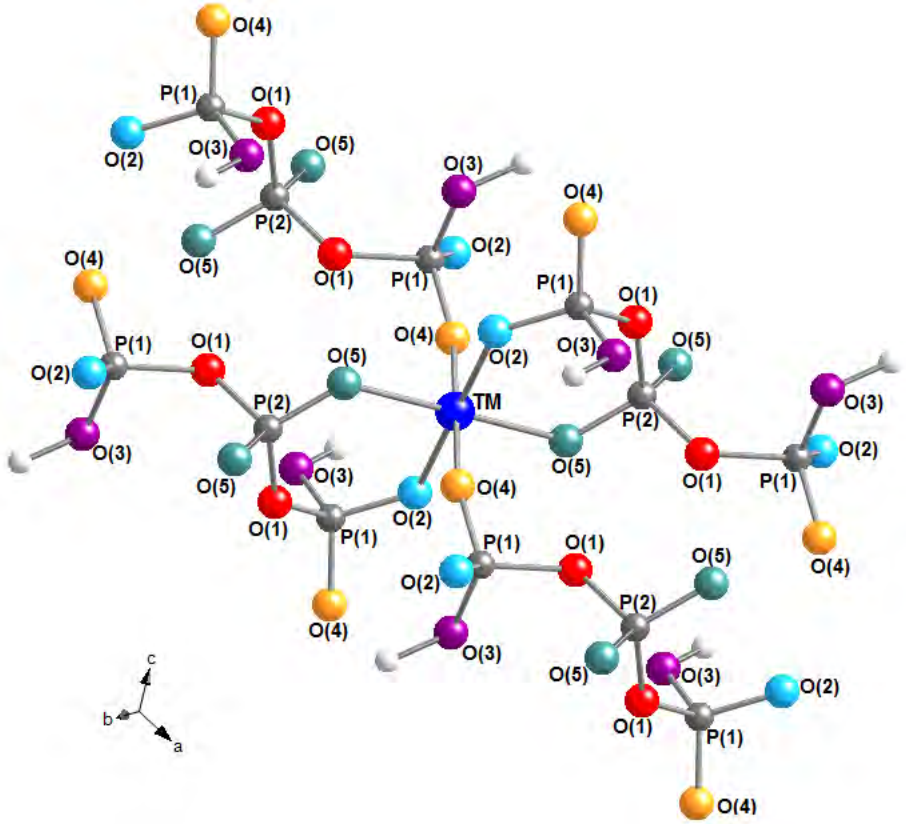

Figure 5.3: *Orientation of the triphosphate ligands about the TM centre in the α-RbMn$_x$Fe$_{1-x}$HP$_3$O$_{10}$ structure type. The TM atom (centre), phosphorus and hydrogen atoms are shown as dark blue, grey and white spheres, respectively.*

Across all compositions of α-RbMn$_x$Fe$_{1-x}$HP$_3$O$_{10}$, BVS calculations (Table 5.2) according to the values provided by Brown and Altermatt[19] showed most atoms to be slightly overbonded or underbonded, and so GII[20] calculations were performed in order to explore whether these effects were related to the crystal structure. Values ranged from 0.12-0.17 vu (Table 5.3), suggesting that the structure was relatively stable and that deviations from the valence sum rule were small. No clear change in GII values was observed as the series was traversed.

5.3.1 Trends and Electronic Distortions

Figure 5.4 shows that for the x = 1, 0.75, 0.5 and 0.25 compounds, the TM-O_6 coordination sphere can be described by a [4+2] elongation of bond lengths. A more regular octahedral coordination sphere was observed with an increasing amount of iron in the system, though for x = 0 the TM-O(4) bond lengths of 1.968(6) Å were found to be shorter than the remaining four and lower than the expected value of ~1.99 Å. An explanation for this could not be found in the corresponding P(1)-O(4) and Rb-O(4) bond lengths, as the former was shorter than the other P-O bonds (Figure 5.5), while the latter remained similar in length to that observed for the other members of the solid solution (Table 5.3). Fe^{3+} (d^5) exists in a non-degenerate electronic state in which the five d-orbitals are equally populated, and so it is not subject to a Jahn-Teller distortion. From Figure 5.3 it can be seen that within the structure, the transition metal ion is bonded to O(4) through a singularly connected triphosphate group but to the O(2) and O(5) atoms of a triphosphate group bonded in a bidentate fashion. It is therefore possible that the pattern of Fe-O bond lengths seen for x = 0 occurs in order to satisfy the coordination preferences of the triphosphate group. Indeed, a similar distortion of the FeO_6 octahedra has also been reported for the isostructural compound $NH_4FeHP_3O_{10}$,[25] whereas for $CsVHP_3O_{10}$[27] (also isostructural but containing Jahn-Teller active V^{3+}) a less pronounced [4+2] elongation of the VO_6 octahedra has been seen, with V-O bond lengths of 1.951(5) Å × 2, 1.973(5) Å × 2 and 2.028(6) Å × 2. It is therefore possible that for the compounds containing Mn^{3+}, the requirements of the triphosphate group are modified by the strong preference of this transition metal ion to adopt two long and four short Mn-O bond lengths.

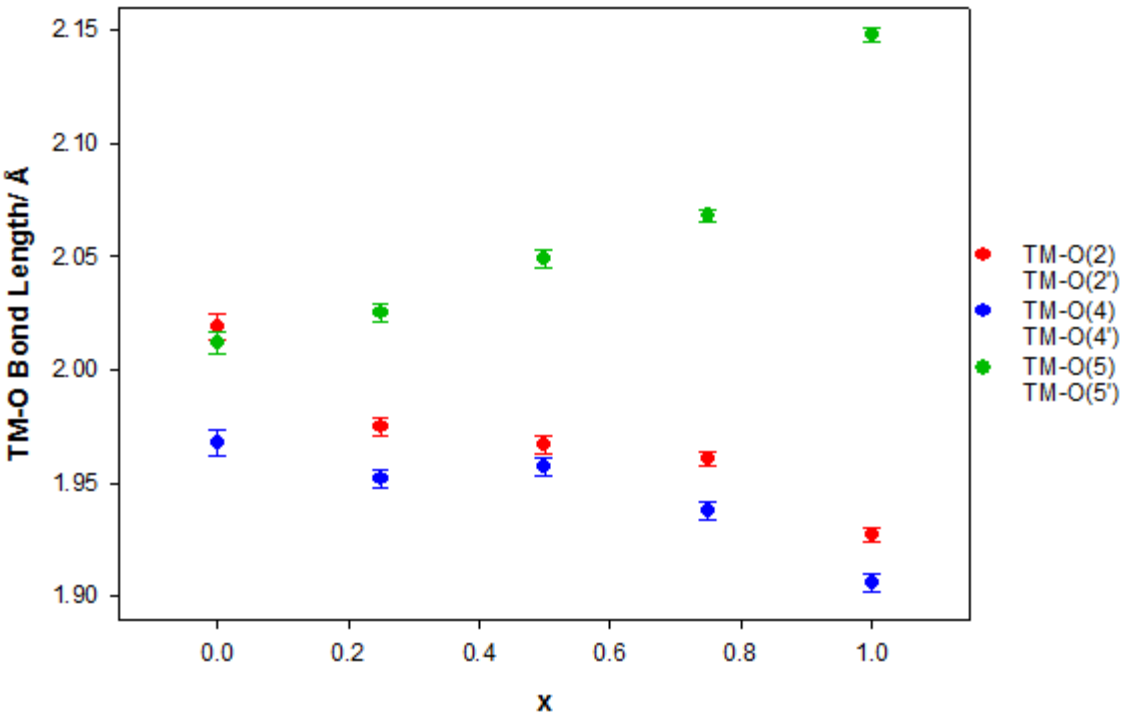

Figure 5.4: *Average bond lengths of the TM-O_6 octahedron as a function of varying Mn^{3+} content in the α-$RbMn_xFe_{1-x}HP_3O_{10}$ solid solution.*

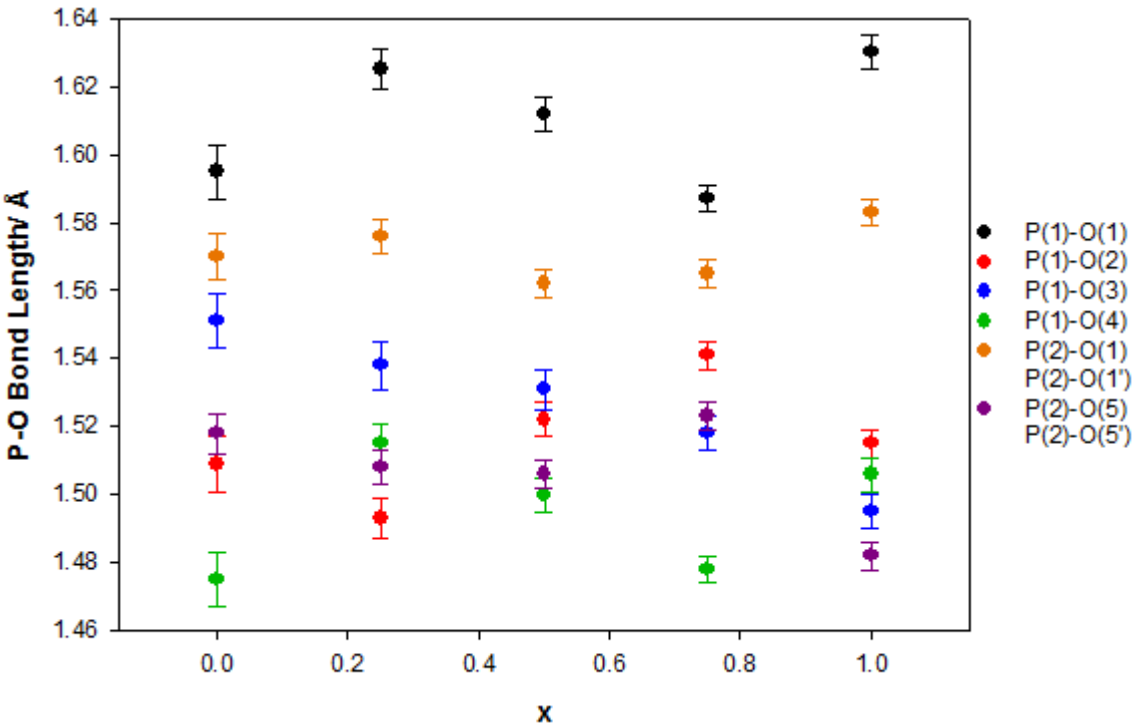

Figure 5.5: *Average P-O bond lengths as a function of varying Mn^{3+} content in the α-$RbMn_xFe_{1-x}HP_3O_{10}$ solid solution.*

Figure 5.5 shows that no clear trend occurred in the P-O bond lengths across the series except for a decrease in P-O(3) with increasing x, which can be related to a corresponding increase in the H-O(3) bond length (Table 5.3). In addition, no trend was seen amongst the O-P-O angles (Figures 5.6 and 5.7), which were found to range between 103.4-115.6° and 105.2-118.4° for the $P(1)O_4$ and $P(2)O_4$ tetrahedrons, respectively. These values are not unusual for condensed phosphate systems, with a range of 105-118° being reported for the $P(2)O_4$ tetrahedron in $NH_4BiHP_3O_{10}$.[28] The cis O-TM-O bond angles remained reasonably identical across the series and close to the ideal value of 90°, as can be seen from Figure 5.8, whilst the angles between the trans ligands were constrained to 180° by the point symmetry of the TM atom.

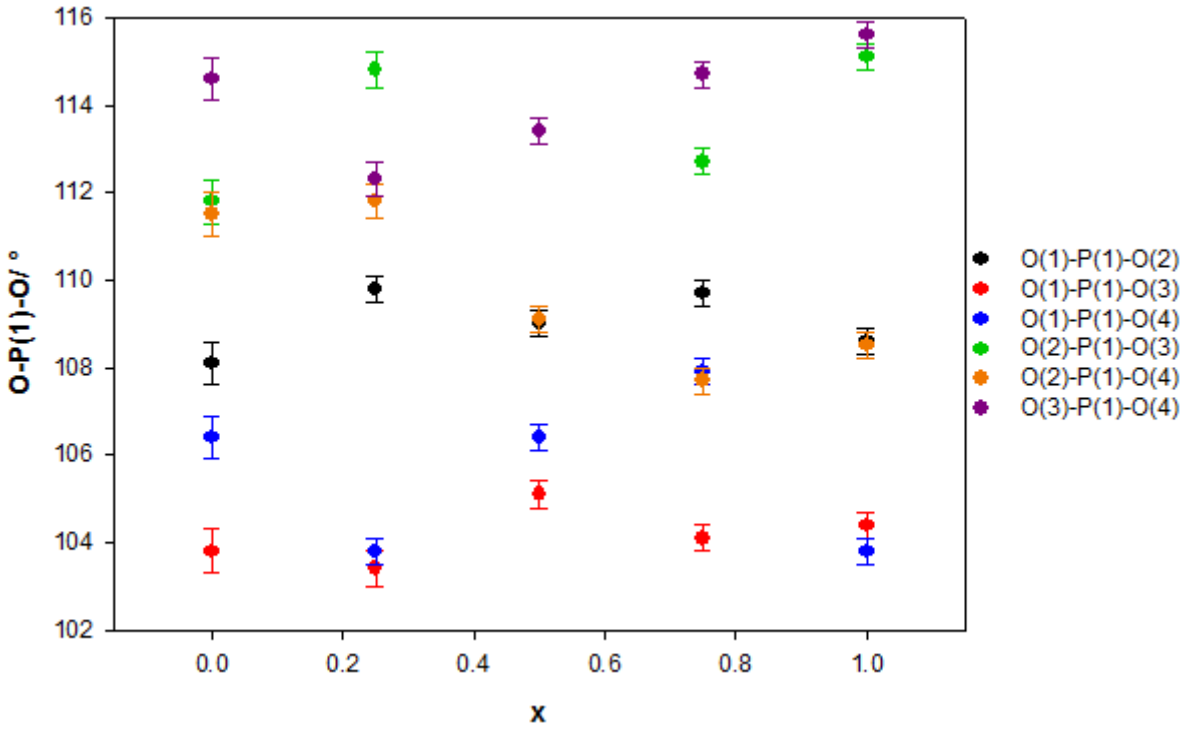

Figure 5.6: *Average O-P(1)-O bond angles as a function of varying Mn^{3+} content in the α-$RbMn_xFe_{1-x}HP_3O_{10}$ solid solution.*

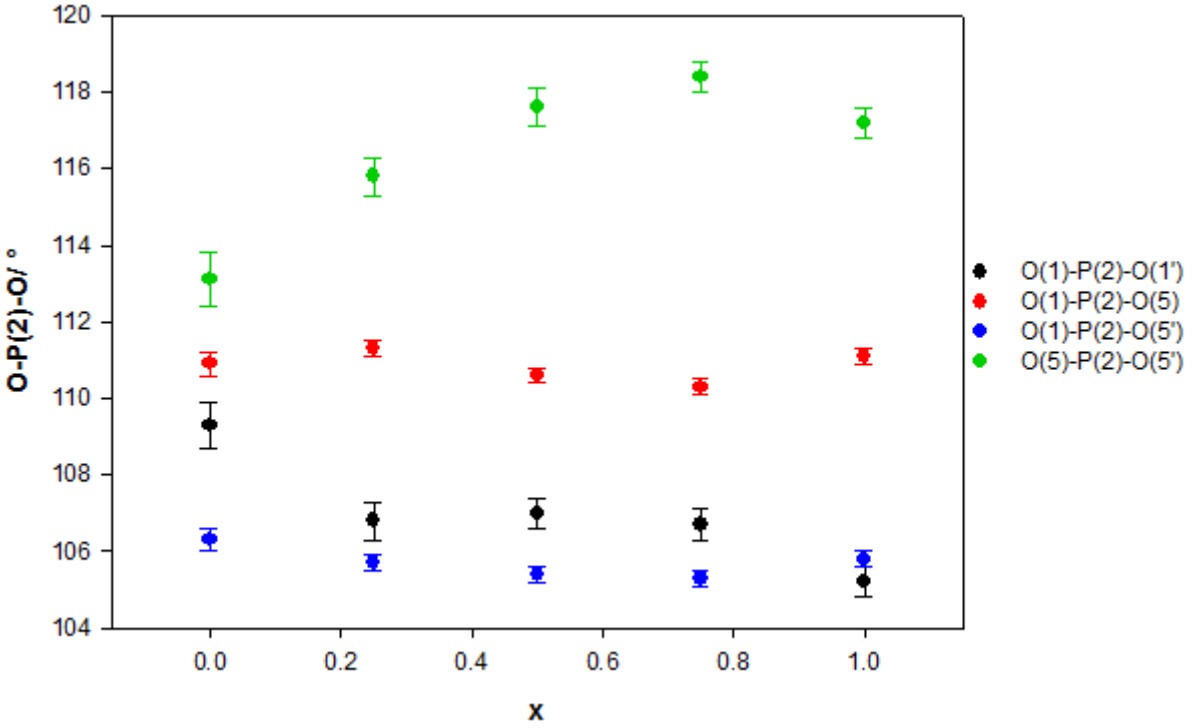

Figure 5.7: *Average O-P(2)-O bond angles as a function of varying Mn^{3+} content in the α-$RbMn_xFe_{1-x}HP_3O_{10}$ solid solution.*

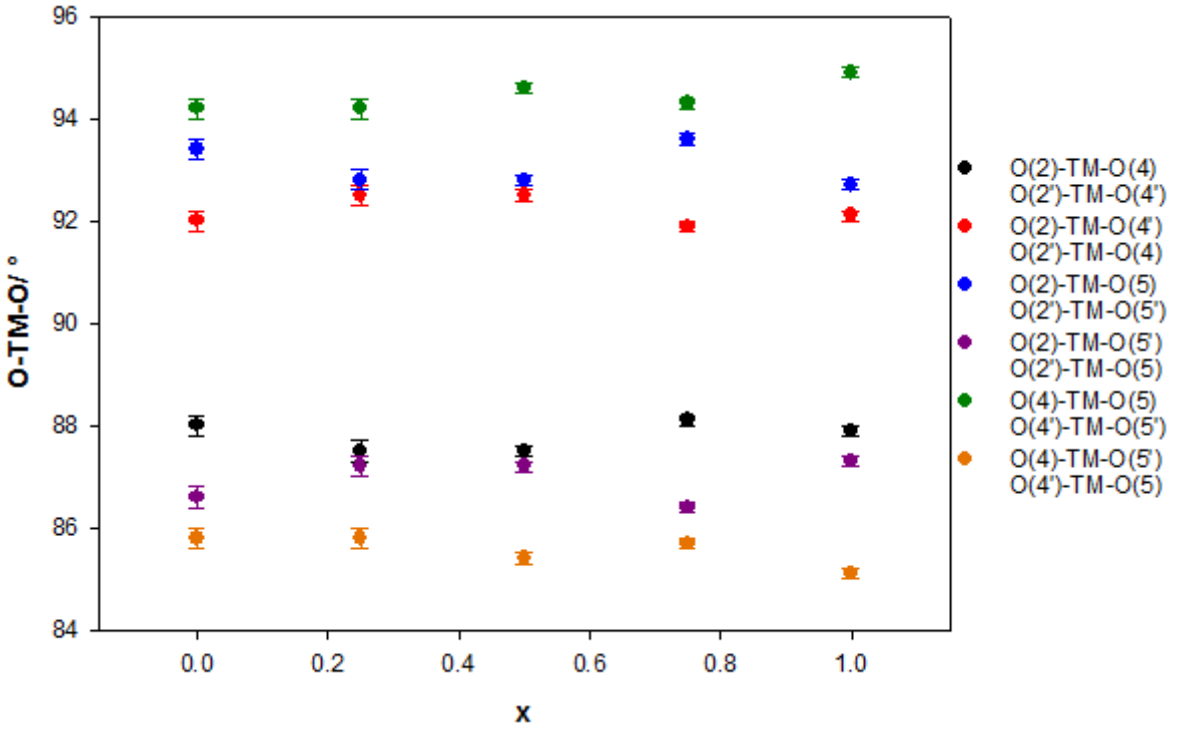

Figure 5.8: *Average cis O-TM-O bond angles as a function of varying Mn^{3+} content in the α-$RbMn_xFe_{1-x}HP_3O_{10}$ solid solution.*

Octahedral Mn^{3+} and Fe^{3+} have similar ionic radii of 0.65 Å,[29] and as such size effects are not expected to have a significant influence on the lattice. In traversing the α-$RbMn_xFe_{1-x}HP_3O_{10}$ series, Figures 5.9 and 5.10 show that a general increase in the *a*- lattice parameter occurred but a decrease in the *b*-, *c*- and *β*-parameters. A closer inspection of the TM coordination sphere (Figure 5.11) shows that the TM-O(5) bonds, which are those that are prone to elongation for x > 0, are essentially directed along the *a*-axis of the structure whilst the TM-O(2) and TM-O(4) bonds lie in between the trajectories of the *b*- and *c*-axes. From Figure 5.4 it was seen that the former bonds increase in length with the greater amount of Mn in the system whereas the latter generally decrease in length- this can therefore explain the increase in *a* coupled to a decrease in the *b*- and *c*-parameters with increasing Mn content.

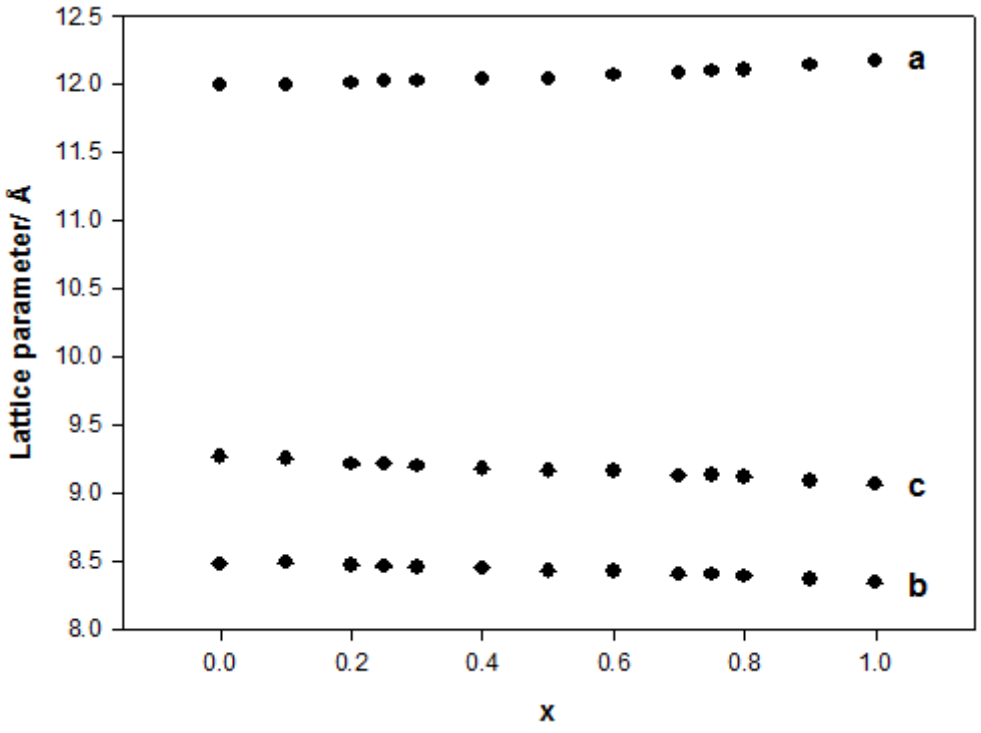

Figure 5.9: *Change in the a-, b- and c-lattice parameters with varying Mn^{3+} content in the α-$RbMn_xFe_{1-x}HP_3O_{10}$ solid solution (XRD data).*

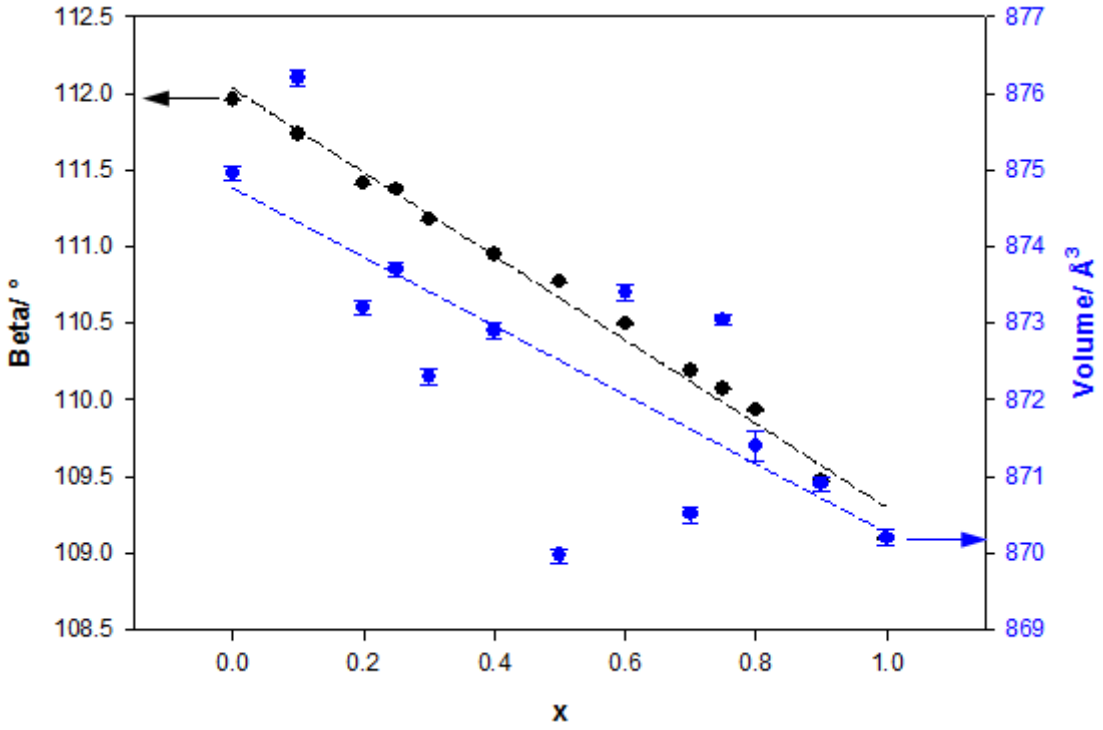

Figure 5.10: *Change in β-parameter (●) and volume (●) of unit cell with varying Mn^{3+} content in the α-$RbMn_xFe_{1-x}HP_3O_{10}$ solid solution (XRD data). Arrows indicate direction of axes.*

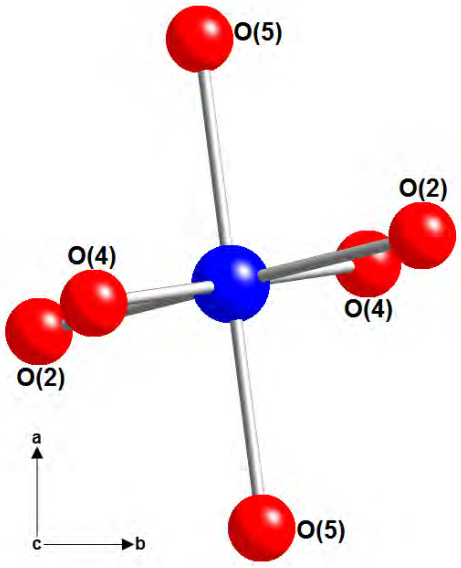

Figure 5.11: *The orientation of the TM-O_6 octahedron with respect to the unit cell axes in the α-$RbMn_xFe_{1-x}HP_3O_{10}$ system.*

A decrease in β-angle with increasing x is then observed in parallel with the greatest difference in length occurring between the *a*- and *c*-axes. In theory, as the axial

oxygens are at their furthest from the TM centre at this point, the equatorial oxygens can be bought closer to them without substantially increasing the electrostatic repulsion between the two sets.

As with the α-$NH_4Mn_xFe_{1-x}P_2O_7$ and $RbMn_xFe_{1-x}P_2O_7$ systems, it was also apparent here that the electronic properties of the two TM centres dictate the observed trend in unit cell parameters. However, their impact is clearly limited by the requirement of the P-O bond lengths to remain within a certain range for effective covalent bonding to occur. A general decrease in volume of the unit cell was observed with increasing Mn content (Figure 5.10), perhaps reflecting these competing effects.

^{57}Fe Mössbauer spectroscopy was used to investigate the local iron environment while UV-Vis spectroscopy was used to further probe the manganese centres in these materials. The position of the peaks in the Mössbauer spectra (Figure 5.12) confirmed that iron exists in the +3 oxidation state. A small increase in quadrupole splitting from 0.39 mm s^{-1} for x = 0 to 0.46 mm s^{-1} for x = 0.75 indicated that Fe^{3+} was in a more irregular environment when there was a greater amount of Mn^{3+} present in the system. Indeed, as x increases we would expect Fe^{3+} to be in a more distorted octahedral environment due to the coordination preferences of Mn^{3+} being dominant. However, the effect seen here was relatively small when compared to the $RbMn_xFe_{1-x}P_2O_7$ system (Chapter 4, section 4.3.2), where across the same composition the quadrupole splitting ranged from 0.20-0.57 mm s^{-1}.

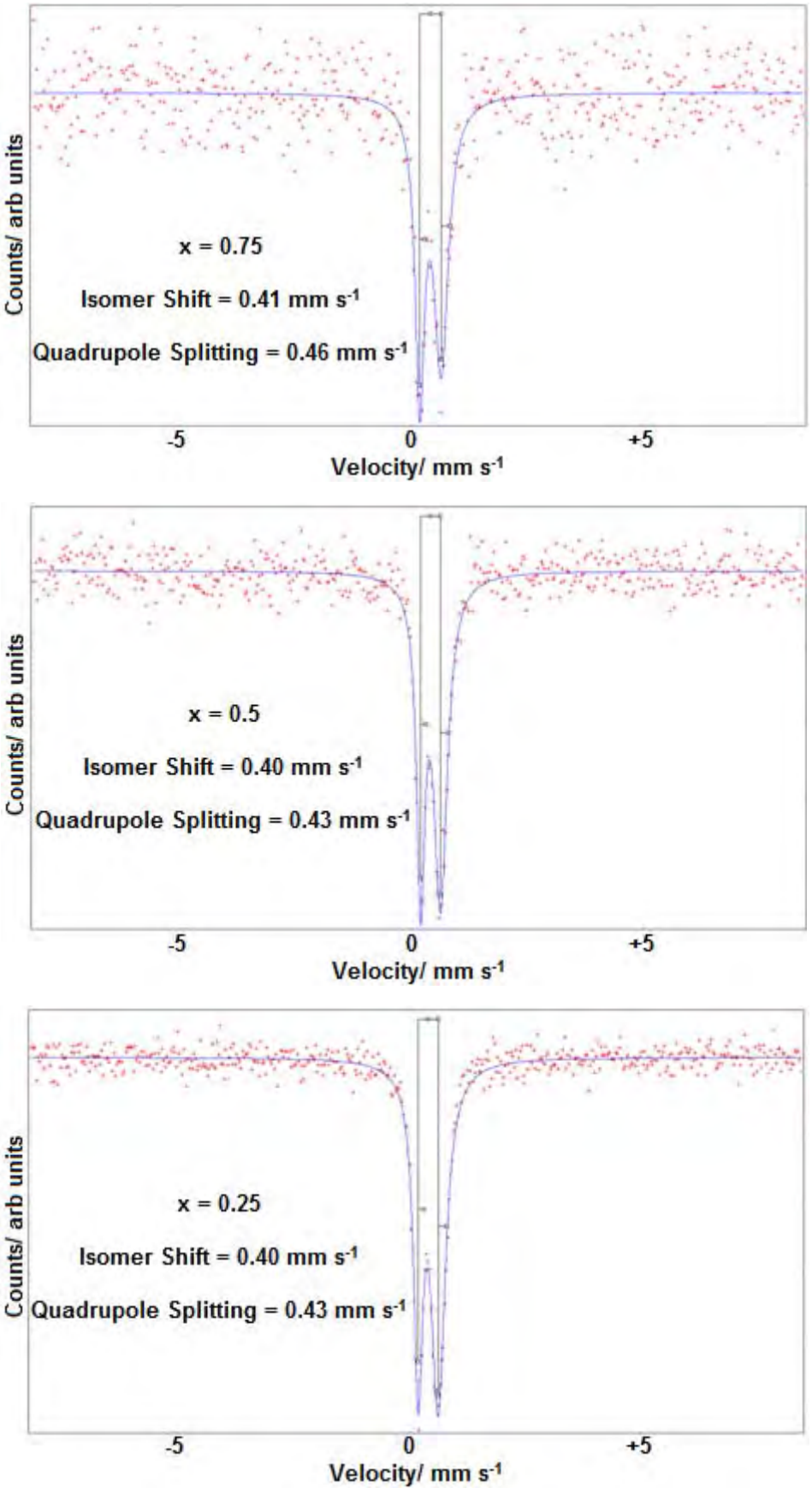

Figure 5.12: *Mössbauer spectra for the α-$RbMn_xFe_{1-x}HP_3O_{10}$ series*

Figure 5.12 continued...

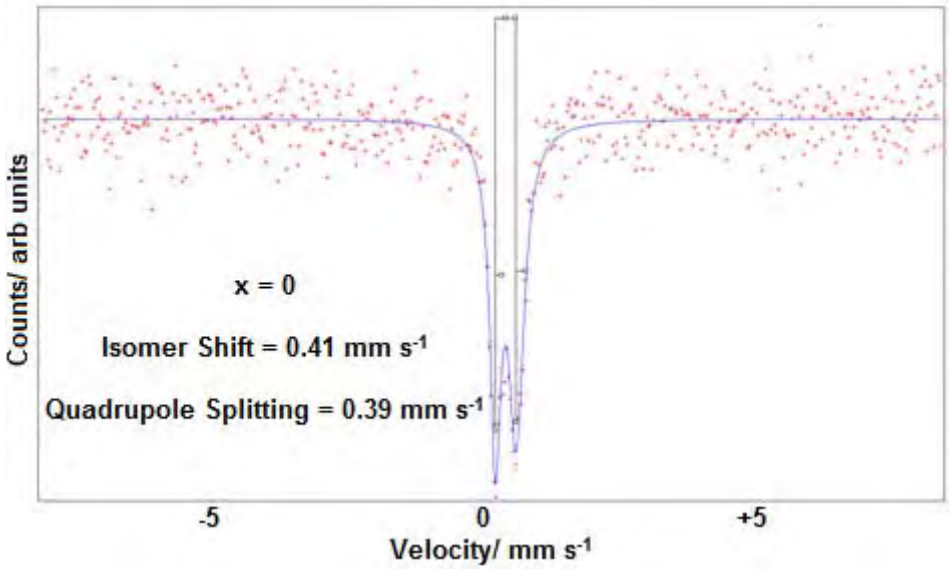

The UV-Vis spectra of the α-$RbMn_xFe_{1-x}HP_3O_{10}$ series are shown in Figure 5.13. All transitions occurring in the UV region were tentatively assigned as ligand to metal charge transfer (LMCT) given that Mn^{3+} and Fe^{3+} are in relatively high oxidation states and are directly coordinated to oxygen anions. As was seen for the α-$NH_4Mn_xFe_{1-x}P_2O_7$ and $RbMn_xFe_{1-x}P_2O_7$ systems, for x > 0, the intensity of these bands was not found to be significantly greater than that of the d→d bands seen in the visible region. The reason for this is at present unclear, though is likely in part to be due to a strong Jahn-Teller effect significantly reducing the symmetry of the MnO_6 unit. A similar assignment of bands has been made for the Mn^{3+} spectra of $MnPO_4 \cdot 1.3H_2O$[30] and $K_xMn_yHf_{1-y}(PO_4)_3$[31] compounds, where a significant difference in intensity between the LMCT and d→d bands was also not observed, perhaps suggesting that this is a feature of Mn^{3+} phosphate compounds.

The x = 0 end member showed a weak d→d transition in the visible region, consistent with the $^6A_{1g}$ ground state of Fe^{3+}. As this ion possesses no low lying excited states with a spin multiplicity of 6, any d→d transitions that occur are spin as

well as Laporte forbidden, consequently being weak in intensity. Indeed, Figure 5.14 shows that the Fe end member exhibited no significant colouration while all compounds containing Mn showed a brown colouration. It was therefore assumed that for the intermediate members, bands due to Fe^{3+} would be obscured by those arising from Mn^{3+}, which would be expected to be more intense. In an octahedral crystal field the ground state of Mn^{3+} is ^5E_g, from which one transition to the $^5T_{2g}$ level can occur. If tetragonally distorted, these energy levels are further split and give the possibility of three transitions which are spin allowed but Laporte forbidden (see Figure 5.15). As the spectra of all compounds showed broad unresolved features, the PeakFit[32] program was used to fit a sum of Gaussian bands on a constant baseline to the observed transitions (Table 5.4). Details on how this fitting was performed were given in Chapter 3, section 3.3.4.2. For the compounds containing Mn^{3+}, this resulted in three d→d transitions and confirmed the D_{4h} symmetry of the MnO_6 octahedra. It should be noted that for x = 1, 0.75 and 0.5, there was potentially an additional, weak transition at ~800 nm, though the relatively low intensity of the peak meant that its width could not be sufficiently modelled. Given the poor intensity of this fourth transition, the possibility of there being slight deviations from D_{4h} symmetry was considered to be negligible.

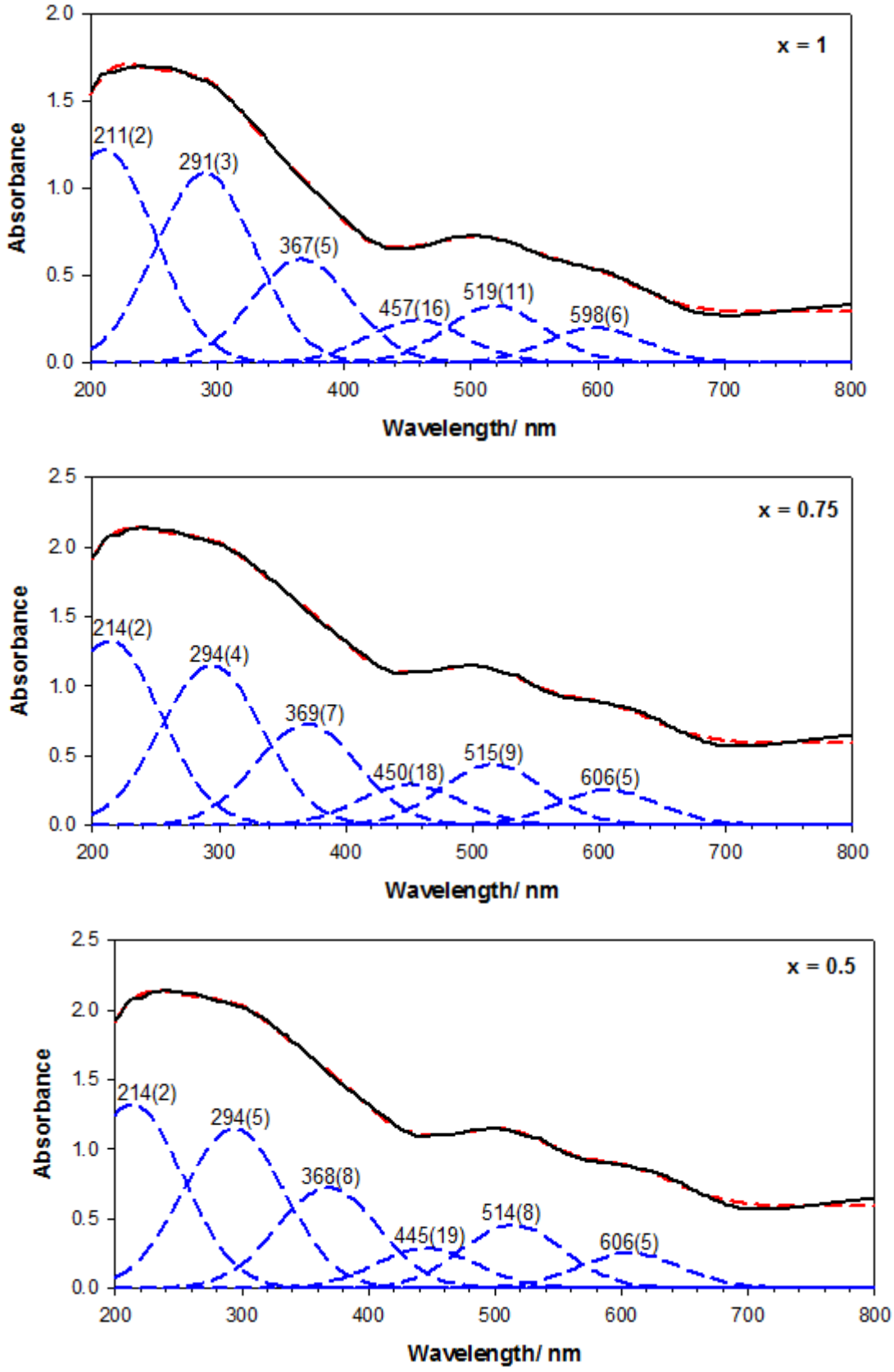

Figure 5.13: *UV-Vis spectra of the α-$RbMn_xFe_{1-x}HP_3O_{10}$ series, showing raw data (–), fitted Gaussian bands (---) and sum of the fitted Gaussian bands (---). Peak positions are marked.*

Figure 5.13 continued...

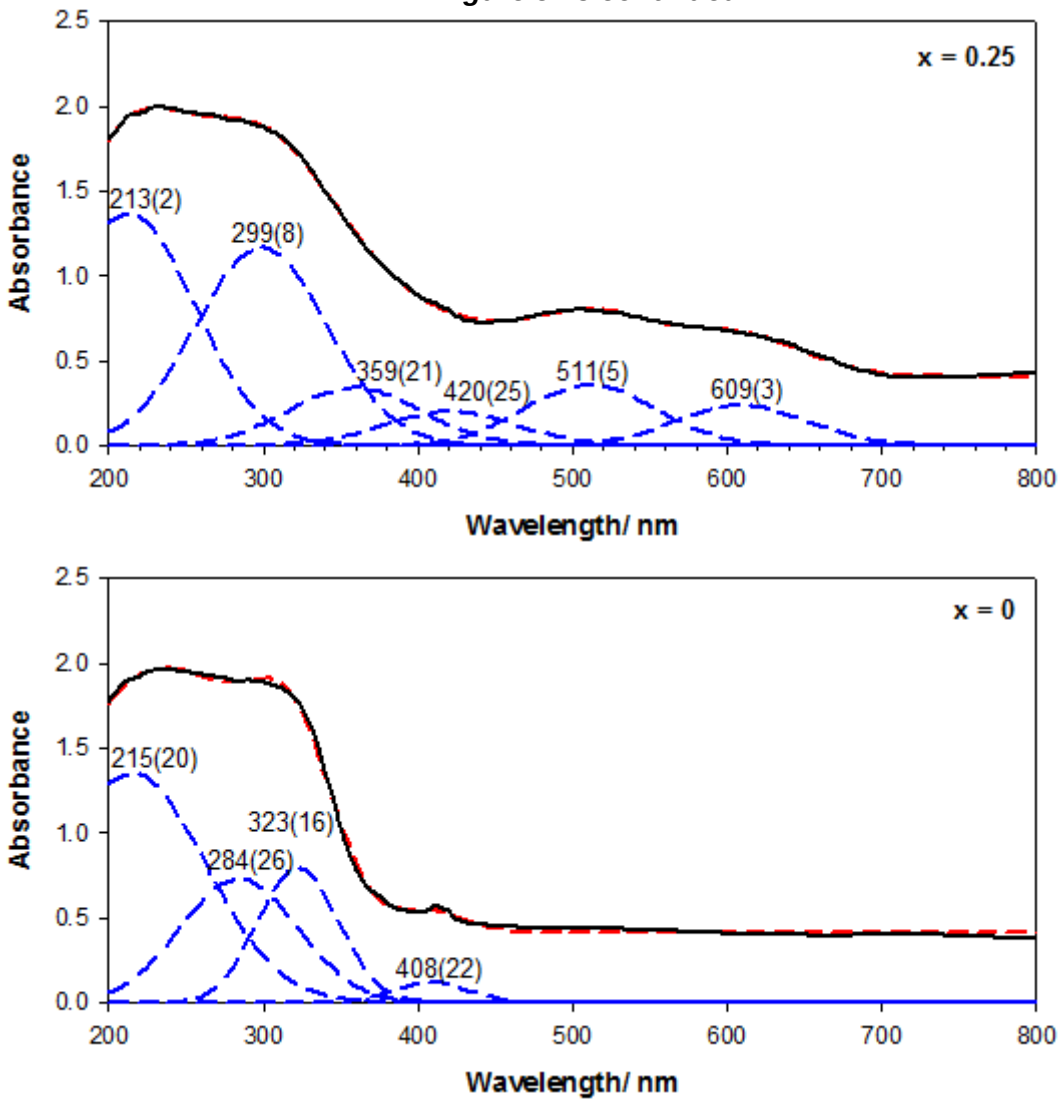

x = 1 x = 0.75 x = 0.5 x = 0.25 x = 0

Figure 5.14: *Colouration of the α-$RbMn_xFe_{1-x}HP_3O_{10}$ series*

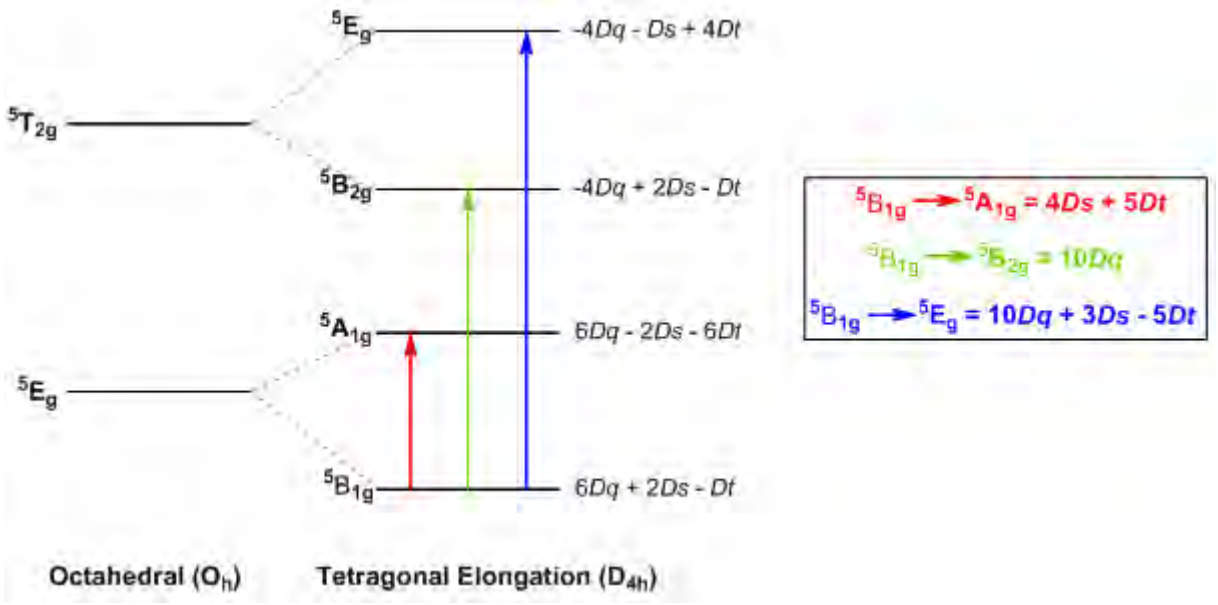

Figure 5.15: *Ligand field energy separations for a Mn^{3+} ion in a tetragonally elongated octahedron. Dq describes the crystal field splitting while Ds and Dt are parameters used to describe the energies of the 3d orbitals in a tetragonal field.*

Table 5.4: *Wavelengths (nm) and assignments of d→d transitions in the electronic spectra of α-$RbMn_xFe_{1-x}HP_3O_{10}$ compounds. 10Dq, Ds* and *Dt parameters are also shown.*

	x = 1	**x = 0.75**	**x = 0.5**	**x = 0.25**		**x = 0**
$^5B_{1g}$→$^5A_{1g}$	598(6)	606(5)	606(5)	609(3)	**d→d**	408(22)
$^5B_{1g}$→$^5B_{2g}$	519(11)	515(9)	514(8)	511(5)		
$^5B_{1g}$→^5E_g	457(16)	450(18)	445(19)	420(25)		
10*Dq*/ kJ mol^{-1}	230(5)	232(4)	233(4)	234(2)		
***Ds*/ kJ mol^{-1}**	33(2)	33(2)	33(2)	35(2)		
***Dt*/ kJ mol^{-1}**	14(1)	13(1)	13(1)	11(2)		

Table 5.4 shows that the values of 10*Dq* ranged between 230-234 kJ mol^{-1} for the α-$RbMn_xFe_{1-x}HP_3O_{10}$ compounds (x > 0), which was within the general range of 191-251 kJ mol^{-1} often observed for Mn^{3+} complexes.[33] The small increase in 10*Dq* across the series suggested an increase in the crystal field splitting with decreasing Mn content, which occurred in accordance with a less pronounced elongation of the Mn-O(5) bonds. As these bonds become shorter in length there is increased

electrostatic repulsion between the corresponding oxygens and the electron in the Mn^{3+} d_{z^2} orbital. Thus as the Mn-O(5) bonds become shorter, there is a less stabilising effect on d-orbitals possessing a z-component. Although the equatorial bonds become longer in length with decreasing Mn content, a larger change is seen in the axial bond lengths. Furthermore, the equatorial oxygens face the empty $d_{x^2-y^2}$ orbital and so a lengthening of these bond lengths is not expected to have a significant influence on the relative energies of the e_g orbitals.

It is worth commenting on the intensity in colouration exhibited by the α-$RbMn_xFe_{1-x}HP_3O_{10}$ compounds, which was less than that observed for compounds of the α-$NH_4Mn_xFe_{1-x}P_2O_7$ and $RbMn_xFe_{1-x}P_2O_7$ systems ($x > 0$) discussed in Chapters 3 and 4. Clearly this system is more dilute than the pyrophosphate systems and furthermore, in the structure type considered here, Mn^{3+} is located on an inversion centre, meaning that with the exception of some local disorder, the centre of symmetry in the MnO_6 unit is fixed. For the pyrophosphates, Mn^{3+} is located on a general position and in theory can take up six different Mn-O bond lengths. Thus the Laporte centrosymmetric selection rule is more applicable to the α-$RbMn_xFe_{1-x}HP_3O_{10}$ system, but does not necessarily hold for the pyrophosphate systems.

5.3.2 Thermal Stability

The TGA-MS plots in Figure 5.16 show that all α-$RbMn_xFe_{1-x}HP_3O_{10}$ compounds evolved surface water between ~120-280°C in a broad endothermic process. Indeed, this temperature is too low for condensation of the triphosphate units to occur, with separate heats to 450°C confirming that the host phases remained intact at this stage. In addition, neutron diffraction measurements did not reveal the presence of extra peaks to suggest that this water was part of the crystal structure. Table 5.5 shows that the surface water lost from each compound was minimal, ranging from 0.06-0.18 moles per formula unit of host.

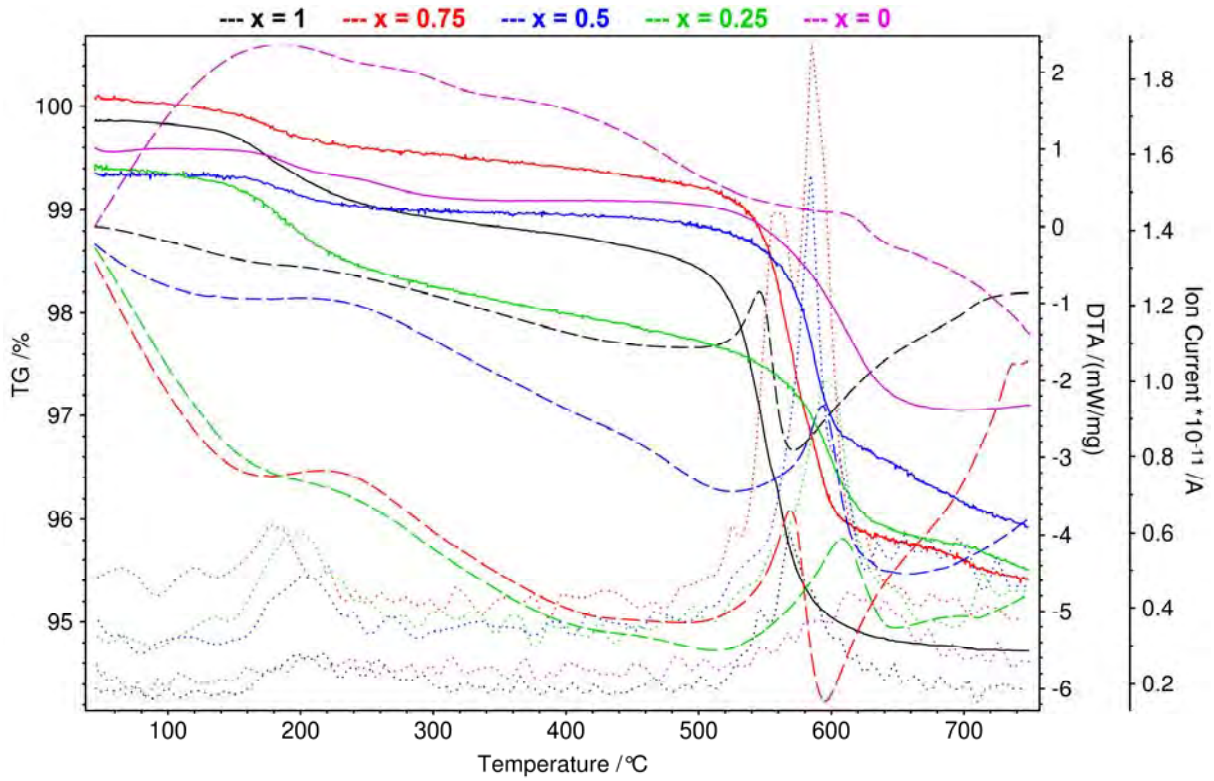

Figure 5.16: *TGA-MS plots for α-$RbMn_xFe_{1-x}HP_3O_{10}$ compounds. Solid, dashed and dotted lines show TG, DTA and mass 18 signals, respectively.*

Table 5.5: *Summary of thermal decomposition of α-$RbMn_xFe_{1-x}HP_3O_{10}$ compounds*

x	Mass loss 1	Moles surface water	Mass loss 2	Final product(s) after decomposition
1	0.69%	0.15	4.20%	$RbMnP_3O_9$*
0.75	0.32%	0.07	4.14%	$RbMnP_3O_9$*
0.5	0.27%	0.06	3.07%	$RbMnP_3O_9 + RbFeP_2O_7$*
0.25	0.84%	0.18	2.74%	$RbMnP_3O_9 + RbFeP_2O_7$*
0	0.29%	0.06	2.03%	$RbFeP_2O_7$*

** indicates that not all decomposition products were identified*

The stability of all compounds was inherently limited by the presence of a proton in the structure, which made them prone to condensation. As such, all compounds began to decompose at ~480°C. The x = 1 and 0.75 compounds lost water in two consecutive steps, corresponding to an endothermic process followed in quick succession by an exothermic process. For the x = 0.5, 0.25 and 0 compounds, the loss of water appeared to occur in one broad endothermic event, suggesting a different decomposition pathway. Table 5.5 summarises the mass losses observed and the final products formed. Although the latter could not all be identified using the JCPDS[18] database, the general observation was that a condensed phosphate had formed. For x = 1, a possible decomposition pathway is given by Equation 5.1: -

$$2RbMnHP_3O_{10} \xrightarrow[-\frac{1}{2}O_2]{-H_2O} 2RbMnP_3O_9 \qquad \textbf{Equation 5.1}$$

A similar decomposition route has also been proposed for the isostructural compound $KMnHP_3O_{10}$.[34] It should be noted though that despite the observed mass loss of 4.20% being consistent with the expected 4.31%, a loss of oxygen from the sample was not detected by the mass spectrum. Furthermore, there appeared to be two phases present in the decomposition product of α-$RbMnHP_3O_{10}$. Although the structure of $RbMnP_3O_9$ has been previously unknown, we were able to model this on

the isostructural compound $TlMnP_3O_9$,[35] and confirm that this was a major phase present in the heated compound (see Appendix 2 for Rietveld refinement). However, there were also a small number of additional peaks present in the X-ray diffraction pattern, which could not be identified. It is possible that these belonged to a phase that had crystallised from an amorphous component in the sample, or alternatively it may be that α-$RbMnHP_3O_{10}$ decomposes by a different mechanism to that proposed in Equation 5.1.

A possible decomposition pathway for x = 0 is given below, with the observed mass loss of 2.03% being in reasonable agreement with the 2.28% expected: -

$$2RbFeHP_3O_{10} \xrightarrow{-H_2O} RbFeP_2O_7 + RbFe(PO_3)_4 \qquad \textbf{Equation 5.2}$$

The X-ray diffraction pattern of the heated compound confirmed the presence of $RbFeP_2O_7$ but also showed a large number of additional peaks which could not be identified (see Appendix 2). It is possible that these peaks belonged to $RbFe(PO_3)_4$, though as this compound and related analogues have not been reported, we were unable to verify this.

5.3.3 Magnetic Analysis

Figure 5.17 shows the magnetic susceptibility measurements for the x = 0.75, 0.5 and 0.25 compounds and the Curie-Weiss fits to the data. The magnetic properties of α-$RbMnHP_3O_{10}$[14] and $RbFeHP_3O_{10}$[13] have been previously investigated and the structures solved, with the former compound found to order antiferromagnetically at T_N = 10 K and the latter showing canted antiferromagnetism, with T_N = 25 K. The x = 0.75 compound also showed antiferromagnetic behaviour whereas x = 0.5 and 0.25 gave evidence for canted antiferromagnetism or spin glass behaviour, as seen from deviations in the zero-field cooled/ field warmed (ZFCFW) and field cooled/ field warmed (FCFW) measurements. In contrast to the Mn and Fe end members, the intermediate members showed strong deviations from the Curie-Weiss law, with the inverse susceptibility plots possessing a significant degree of curvature. This suggested the presence of complex magnetic interactions between Mn^{3+} and Fe^{3+}. Separate Curie-Weiss fits to the upper and lower temperature regions of the plots gave moments > 7.6 μ_B and > 6.0 μ_B, respectively. These moments were higher than those expected, with μ_{SO} = 5.15, 5.41 and 5.66 μ_B for the x = 0.75, 0.5 and 0.25 compositions, respectively. The negative Weiss constants in all cases did however confirm the predominance of antiferromagnetic interactions. It was somewhat surprising to find that the Néel temperature for x = 0.75 (~17 K) was higher than that of x = 0.5 and 0.25 (~12 K). This suggested that weaker interactions were present in the latter two compounds, though we would expect them to be stronger given the extra d-electron introduced by Fe^{3+}.

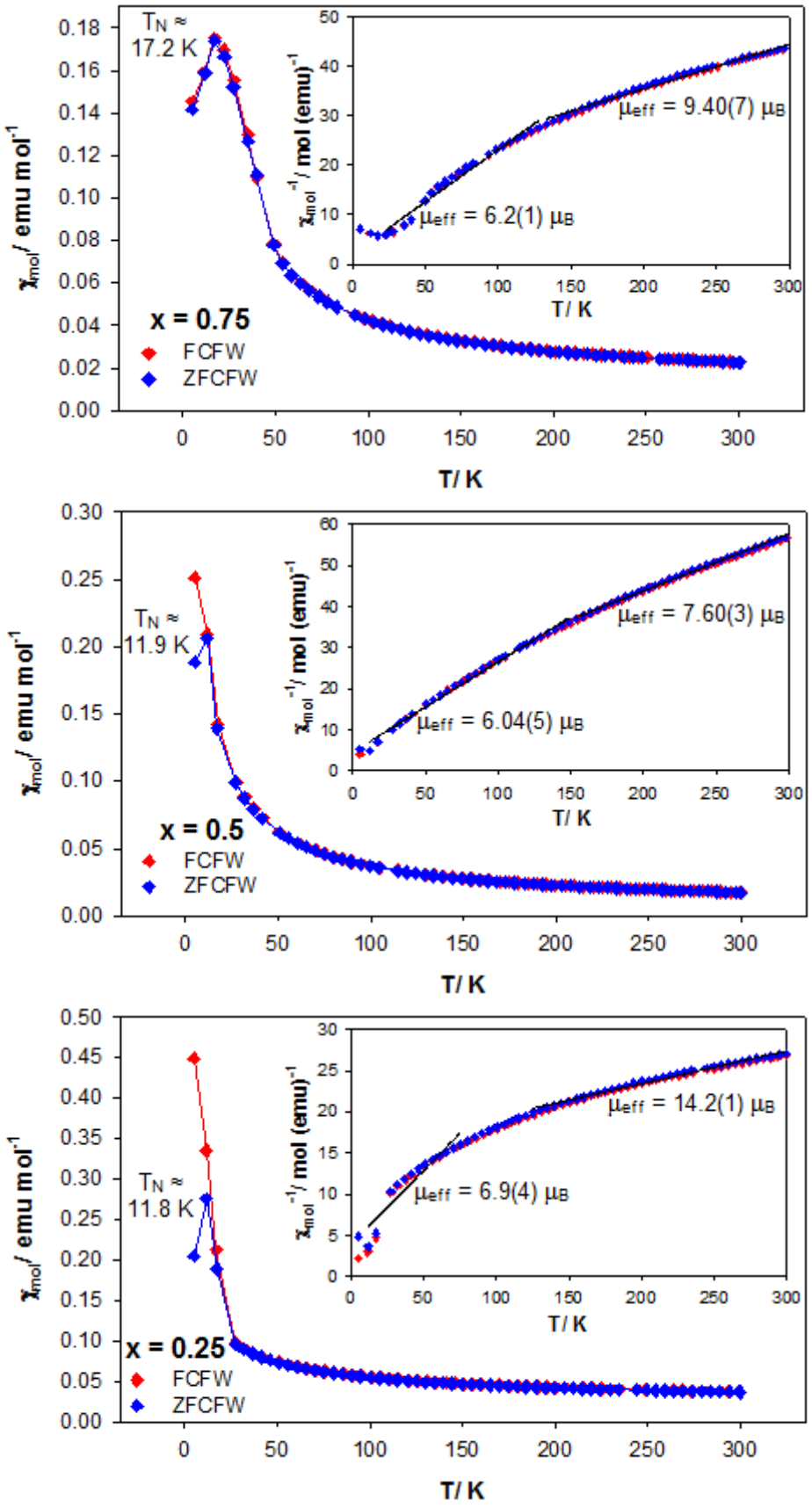

Figure 5.17: *Plots of molar susceptibility against temperature for the α-$RbMn_xFe_{1-x}HP_3O_{10}$ series (x = 0.75, 0.5 and 0.25), with insets showing Curie-Weiss fits to the data.*

5.3.3.4 Magnetic Structures from Neutron Diffraction

After the nuclear contribution was fitted to the 2 K neutron diffraction data on x = 0.5, the pattern gave no evidence for magnetic ordering, despite the MPMS measurements indicating a response at ~12 K. For the x = 0.75 and 0.25 compounds, magnetic peaks were evident in the diffraction patterns and indexed on commensurate unit cells to the nuclear cells. Magnetic intensities were fitted with a calculated form factor[36] for Mn^{3+} and Fe^{3+}, with the final refinements shown in Figure 5.18, structural parameters in Table 5.6 and selected bond distances and angles in Table 5.7.

For x = 0.75, like the Mn end member, the magnetic reflections were consistent with the magnetic space group P_C2/c', with the relative orientations of the four TM spins in the unit cell found to be (¼,¼, 0)+, (¾,¾, 0)-, (¾, ¼, ½)- and (¼, ¾, ½)+. It is worth noting that given the poor coherent scattering of neutrons from the TM site at this composition, the fractional occupancies of Mn and Fe were fixed to the values obtained from the 300 K refinement and isotropic temperature factors fixed at 0.005 $Å^2$. In contrast, the magnetic reflections exhibited by the x = 0.25 compound, like the Fe end member, were found to be consistent with space group *C*2/*c*, with the relative orientations of the four TM spins now being (¼,¼, 0)+, (¾,¾, 0)+, (¾, ¼, ½)- and (¼, ¾, ½)-. It is therefore likely that at x = 0.5, a crossover in the magnetic structures occurs. Indeed, at this composition the competing magnetic interactions between Mn^{3+} and Fe^{3+} would be expected to be at a maximum, but due to equal occupancy it is probably not possible for the preferences of one TM ion to dominate over the other. As such some local frustration may occur, leading to a lack of long range magnetic order which would be evident in the ND data.

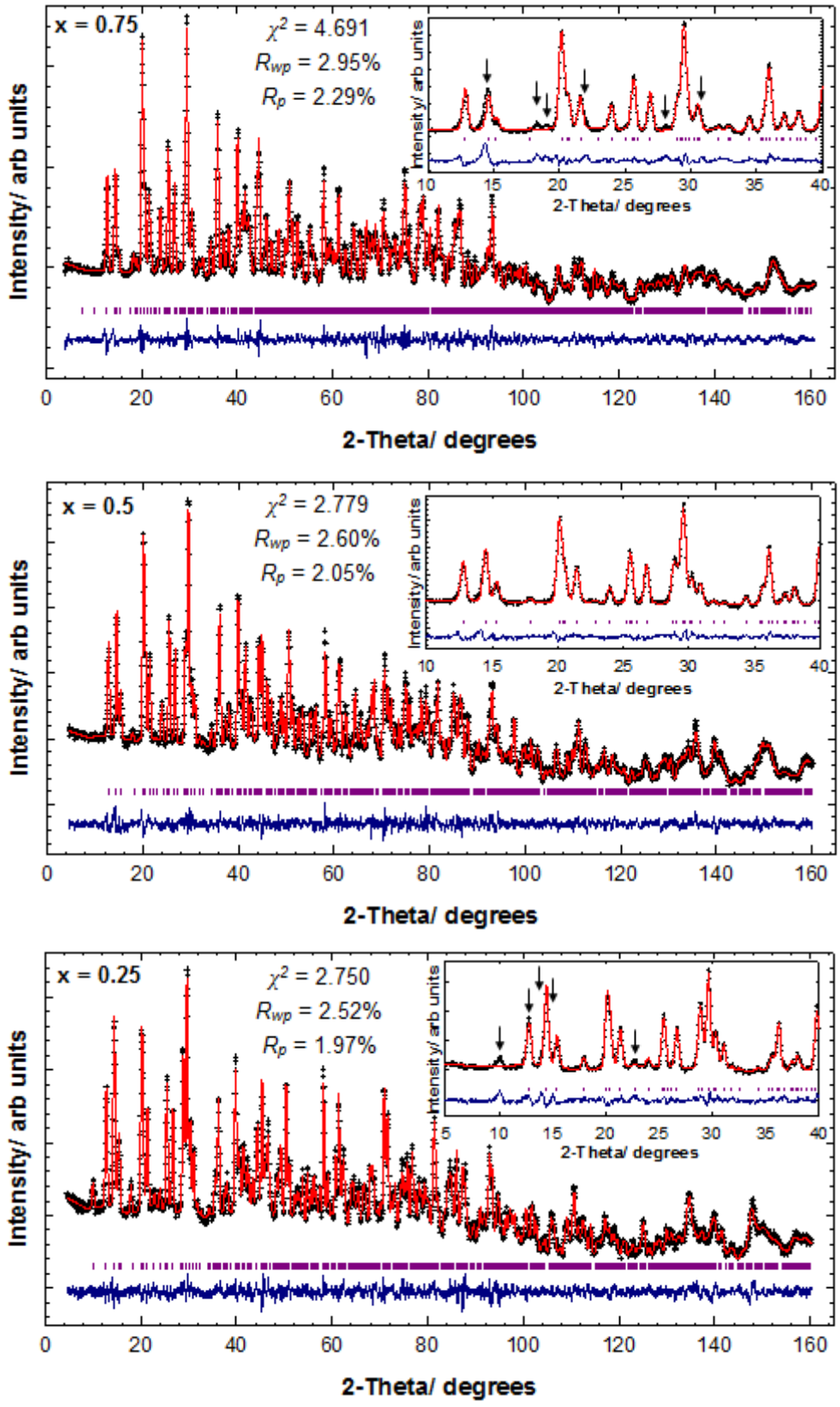

Figure 5.18: *Observed (+), calculated (-), difference profiles (-) and reflection positions (|) for the 2 K Rietveld refinements carried out on α-$RbMn_{0.75}Fe_{0.25}HP_3O_{10}$ compounds (x = 0.75, 0.5 and 0.25). The insets indicate the appearance of the profiles without a magnetic contribution fitted and arrows show peaks with significant magnetic intensity.*

Table 5.6: *Refined structural parameters from the 2 K neutron diffraction data on the α-$RbMn_xFe_{1-x}HP_3O_{10}$ series (x = 0.75, 0.5 and 0.25) with Bond Valence Sums.*[19]

		x = 0.75	**x = 0.5**	**x = 0.25**
	Space group	P_C2/c'	*C*2/*c* (nuclear)	*C*2/*c*
	***a*/ Å**	12.1000(5)	12.0482(4)	12.0195(4)
	***b*/ Å**	8.3945(4)	8.4360(3)	8.4674(3)
	***c*/ Å**	9.1366(4)	9.1935(3)	9.2306(3)
	***β*/ °**	109.882(2)	110.677(2)	111.299(2)
	x	0.25	0.25	0.25
Mn/ Fe	***y***	0.25	0.25	0.25
4*c*	***z***	0	0	0
	U_{iso}**/ Å²**	0.005	0.003(3)	0.005(1)
	Occ	0.740/ 0.260	0.515(5)/ 0.485(5)	0.278(6)/ 0.722(6)
	BVS	3.30/ 3.29	3.27/ 3.27	3.32/ 3.31
	M_x**/** μ_B	2.98(7)	-	2.17(6)
	M_y**/** μ_B	0.0	-	0.0
	M_z**/** μ_B	1.3(1)	-	1.0(2)
	$\lvert M \rvert$ **/** μ_B	3.25(5)	-	2.40(8)
	x	0	0	0
Rb	***y***	0.4420(5)	0.4448(4)	0.4451(5)
4*e*	***z***	0.25	0.25	0.25
	U_{iso}**/ Å²**	0.006(1)	0.0090(9)	0.013(1)
	Occ	1	1	1
	BVS	0.97	0.99	0.98
	x	0.2926(3)	0.2907(3)	0.2890(4)
P(1)	***y***	0.5638(5)	0.5650(5)	0.5643(5)
8*f*	***z***	0.2063(5)	0.2052(4)	0.2021(5)
	U_{iso}**/ Å²**	0.0046(9)	0.0053(8)	0.0057(9)
	Occ	1	1	1
	BVS	4.94	4.97	4.93
	x	0.5	0.5	0.5
P(2)	***y***	0.3727(6)	0.3725(6)	0.3760(7)
4*e*	***z***	0.25	0.25	0.25
	U_{iso}**/ Å²**	0.0004(1)	0.005(1)	0.004(1)
	Occ	1	1	1
	BVS	5.01	4.92	4.83
	x	0.4169(3)	0.4169(3)	0.4177(3)
O(1)	***y***	0.4859(4)	0.4853(4)	0.4870(4)
8*f*	***z***	0.3039(3)	0.3047(3)	0.3060(4)
	U_{iso}**/ Å²**	0.0044(8)	0.0032(7)	0.0048(9)
	Occ	1	1	1
	BVS	2.15	2.09	2.06

Table 5.6 continued...

		x = 0.75	x = 0.5	x = 0.25
	x	0.2144(3)	0.2124(3)	0.2117(3)
O(2)	***y***	0.4370(4)	0.4398(4)	0.4397(4)
8*f*	***z***	0.1014(3)	0.0993(4)	0.0973(4)
	U_{iso}/ Å^2	0.0070(7)	0.0075(7)	0.0069(8)
	Occ	1	1	1
	BVS	1.98	1.97	2.02
O(3)	***x***	0.3231(3)	0.3222(3)	0.3230(3)
8*f*	***y***	0.7021(4)	0.7022(4)	0.7010(4)
	z	0.1174(4)	0.1186(4)	0.1185(4)
	U_{iso}/ Å^2	0.0095(9)	0.0104(8)	0.0085(9)
	Occ	1	1	1
	BVS	1.86	1.88	1.88
O(4)	***x***	0.2394(3)	0.2377(3)	0.2391(3)
8*f*	***y***	0.6152(4)	0.6158(4)	0.6172(4)
	z	0.3253(4)	0.3225(4)	0.3224(4)
	U_{iso}/ Å^2	0.0075(8)	0.0047(8)	0.0059(9)
	Occ	1	1	1
	BVS	2.11	2.10	2.04
O(5)	***x***	0.4318(3)	0.4282(3)	0.4269(3)
8*f*	***y***	0.2789(4)	0.2810(4)	0.2811(4)
	z	0.1092(4)	0.1079(4)	0.1080(4)
	U_{iso}/ Å^2	0.0057(8)	0.0065(7)	0.0065(8)
	Occ	1	1	1
	BVS	1.90	1.94	1.92
H	***x***	0.25	0.25	0.25
4*d*	***y***	0.25	0.25	0.25
	z	0.5	0.5	0.5
	U_{iso}/ Å^2	0.027(2)	0.025(2)	0.028(3)
	Occ	1	1	1
	BVS	0.84	0.85	0.84

Table 5.7: *Selected Bond Distances (Å) and Angles (degrees) for the α-$RbMn_xFe_{1-x}HP_3O_{10}$ series (x = 0.75, 0.5 and 0.25) and Global Instability Index[20] Values.*

	x = 0.75	**x = 0.5**	**x = 0.25**
TM-O(2) × 2	1.944(3)	1.973(4)	1.975(4)
TM-O(4) × 2	1.925(4)	1.947(3)	1.953(3)
TM-O(5) × 2	2.097(3)	2.038(3)	2.011(4)
O(2)-TM-O(2')	180	180	180
O(2)-TM-O(4)	87.6(1)	87.4(1)	87.6(2)
O(2)-TM-O(4')	92.4(1)	92.6(1)	92.4(2)
O(2)-TM-O(5)	92.7(1)	92.6(1)	92.7(1)
O(2)-TM-O(5')	87.3(1)	87.4(1)	87.3(1)
O(4)-TM-O(4')	180	180	180
O(4)-TM-O(5)	95.2(1)	95.1(1)	94.4(1)
O(4)-TM-O(5')	84.9(1)	84.9(1)	85.6(1)
O(5)-TM-O(5')	180	180	180
P(1)-O(1)	1.603(5)	1.617(5)	1.632(5)
P(1)-O(2)	1.526(5)	1.517(5)	1.503(6)
P(1)-O(3)	1.532(5)	1.526(5)	1.527(6)
P(1)-O(4)	1.502(4)	1.497(4)	1.510(5)
P(2)-O(1) × 2	1.579(4)	1.586(4)	1.581(5)
P(2)-O(5) × 2	1.494(4)	1.500(4)	1.516(4)
O(1)-P(1)-O(2)	109.2(3)	108.7(3)	109.2(3)
O(1)-P(1)-O(3)	104.7(3)	104.7(3)	103.3(3)
O(1)-P(1)-O(4)	105.4(3)	105.4(3)	103.4(3)
O(2)-P(1)-O(3)	113.9(3)	114.0(3)	115.1(3)
O(2)-P(1)-O(4)	109.1(3)	109.6(3)	111.3(4)
O(3)-P(1)-O(4)	114.0(3)	114.0(3)	113.4(3)
O(1)-P(2)-O(1')	106.0(4)	106.3(4)	107.1(4)
O(1)-P(2)-O(5)	111.2(2)	110.5(2)	111.2(2)
O(1)-P(2)-O(5')	105.8(2)	105.5(2)	105.5(2)
O(5)-P(2)-O(5')	116.4(4)	118.1(5)	116.0(5)
Rb-O(2) × 2	3.311(3)	3.312(3)	3.326(3)
Rb-O(2') × 2	3.521(3)	3.464(3)	3.432(4)
Rb-O(3) × 2	2.886(4)	2.898(4)	2.897(5)
Rb-O(4) × 2	3.101(4)	3.062(4)	3.071(4)
Rb-O(5) × 2	3.099(5)	3.113(5)	3.122(5)
H-O(3) × 2	1.204(4)	1.199(3)	1.201(3)
O(3)-H-O(3')	180	180	180
GII	0.14	0.12	0.13

It is worth commenting that these compounds showed a similar pattern of bond lengths and angles to those observed at 300 K. The TM-O$_6$ coordination sphere consisted of four short and two long TM-O bonds, again with the elongation becoming less pronounced with decreasing x. GII values were not too dissimilar to those observed at room temperature, suggesting that a reduction in temperature did not significantly alter the structure.

The magnetic structures adopted by the α-RbMn$_x$Fe$_{1-x}$HP$_3$O$_{10}$ compounds are shown in Figure 5.19. Given that the TM ions within the structure are too far apart for direct exchange to occur, only those interactions occurring through TM-O-P-O-TM linkages were investigated. Indeed, interactions occurring through multiple phosphate linkages are likely to much weaker and so were not considered here.

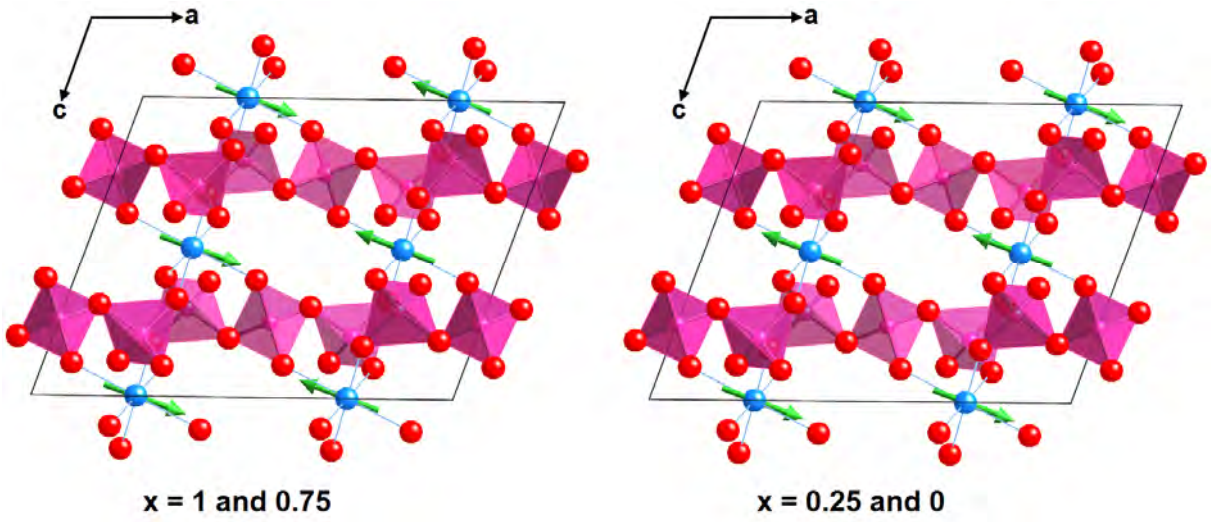

Figure 5.19: *Magnetic structures of α-RbMn$_x$Fe$_{1-x}$HP$_3$O$_{10}$ compounds. TM ions are shown as blue spheres, magnetic moments with green arrows and condensed triphosphate units as pink tetrahedra. The thin black lines define the unit cell.*

For the x = 0.75 compound, like the Mn end member, each TM spin was found to be connected to six others; four of these interactions were in the *bc*-plane and appeared to be ferromagnetic (FM) in nature and two occurred in the *ac*-plane and

were antiferromagnetic (AFM). For the x = 0.25 compound, like the Fe end member, each TM spin was also found to be linked to six others in a similar fashion, but this time all interactions appeared to be AFM in nature (see Figure 5.20). In all compounds the magnetic moments were directed in the *ac*-plane of the structure, with the major component being along the *a*-axis; for x > 0, this was the direction also associated with the axially elongated TM-O bonds. The refined moments of 3.25(5) μ_B for x = 0.75 and 2.40(8) μ_B for x = 0.25 were lower than the respective saturated moments of 4.25 μ_B and 4.75 μ_B. This was most likely as a result of the moments between Mn^{3+} and Fe^{3+} being disordered.

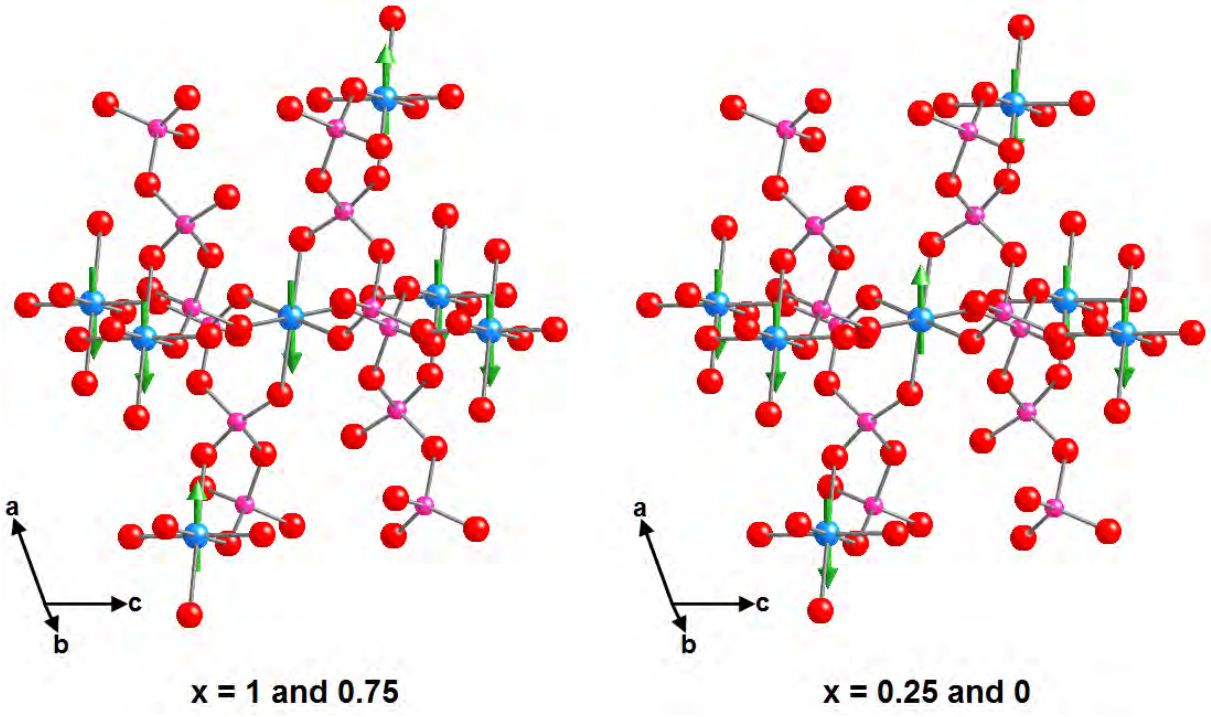

Figure 5.20: *Nearest neighbour interactions in α-$RbMn_xFe_{1-x}HP_3O_{10}$ compounds. TM, phosphorus and oxygen atoms are shown as blue, pink and red spheres, respectively and magnetic moments are shown with green arrows.*

Table 5.8 shows that all compounds contain six different exchange pathways, with two equivalent interactions occurring *via* TM-O(5)-P(2)-O(5)-TM linkages and four equivalent interactions occurring *via* TM-O(2)-P(1)-O(4)-TM linkages. For the x =

1 and 0.75 compounds, it can be seen that the former interactions are apparently AFM and mediated by the elongated TM-O bonds whereas the latter are apparently FM and mediated by the shorter TM-O bonds. For x = 0.25 and 0, all of these interactions are apparently AFM.

Table 5.8: *Summary of the exchange pathways present in α-$RbMn_xFe_{1-x}HP_3O_{10}$ (x = 1, 0.75, 0.25 and 0) compounds and geometries of the interacting species.*

	x	O-P-O	TM-O-P	TM-O*-P	O---O	TM---TM	Interaction
	1	117.7°	132.1°	132.1°	2.47 Å	6.30 Å	AFM
TM-O(5)-P(2)-O(5')-TM'	0.75	116.4°	130.7°	130.7°	2.54 Å	6.22 Å	AFM
TM-O(5')-P(2)-O(5)-TM'	0.25	118.1°	132.4°	132.4°	2.57 Å	6.11 Å	AFM
	0	116.6°	133.0°	133.0°	2.56 Å	6.06 Å	AFM
TM-O(2)-P(1)-O(4')-TM''	1	110.9°	133.2°	149.2°	2.49 Å	6.17 Å	FM
TM-O(2')-P(1)-O(4)-TM''	0.75	109.1°	132.2°	147.6°	2.47 Å	6.20 Å	FM
TM-O(4)-P(1)-O(2')-TM''	0.25	109.6°	132.2°	149.9°	2.49 Å	6.26 Å	AFM
TM-O(4')-P(1)-O(2)-TM''	0	110.1°	131.3°	149.4°	2.49 Å	6.30 Å	AFM

For TM-O*-P, * indicates oxygen labelled with the higher number

If we consider the orbital occupancies of Mn^{3+} and Fe^{3+}, then this suggests the following possibilities for the FM and AFM interactions: -

FM: -

	x = 1	x = 0.75	x = 0.25	x = 0
$Mn^{3+}\ d^0_{x^2-y^2}$ - - - $Mn^{3+}\ d^0_{x^2-y^2}$	Major	Major	N/ A	N/ A
$Mn^{3+}\ d^0_{x^2-y^2}$ - - - $Fe^{3+}\ d^1_{e_g}$	None	Minor	N/ A	N/ A
$Fe^{3+}\ d^1_{e_g}$ - - - $Fe^{3+}\ d^1_{e_g}$	None	Very minor	N/ A	N/ A

AFM: -

	x = 1	x = 0.75	x = 0.25	x = 0
$Mn^{3+}\ d^1_{z^2}$ - - - $Mn^{3+}\ d^1_{z^2}$	Major	Major	Very minor	None
$Mn^{3+}\ d^1_{z^2}$ - - - $Fe^{3+}\ d^1_{e_g}$	None	Minor	Minor	None
$Fe^{3+}\ d^1_{e_g}$ - - - $Fe^{3+}\ d^1_{e_g}$	None	Very minor	Major	Major

Therefore the FM interactions appear to involve either two unoccupied, two singly occupied or an unoccupied-singly occupied e_g orbital, while AFM interactions only involve two singly occupied e_g orbitals. However, it is apparent that a d^0---d^0 interaction dominates the FM interactions while a d^1---d^1 interaction dominates the AFM interactions. If we consider superexchange involving the same d-orbitals interacting *via* a single intervening oxygen *i.e.* TM-O-TM, then for bond angles > 100° Goodenough-Kanamori[37-38] rules predict AFM coupling in all cases except a Mn^{3+} $d^0_{x^2-y^2}$---Fe^{3+} $d^1_{e_g}$ interaction, for which FM coupling would be expected. Given that the α-$RbMn_xFe_{1-x}HP_3O_{10}$ system possesses a lengthened TM-O-P-O-TM exchange pathway, it is likely that subtle differences in geometry result in different exchange interactions being observed.

Table 5.8 shows that there was no correlation between the sign of interaction and the geometries of the interacting species. For x = 1 and 0.75, the AFM interactions that occurred through the TM-O(5)-P(2)-O(5)-TM pathways involved O-P-O angles > 116.4°, TM-O-P angles < 132.1° and TM---TM separations > 6.2 Å, while FM interactions occurring through TM-O(2)-P(1)-O(4)-TM pathways involved O-P-O angles < 110.9°, a TM-O-P angle > 147.6° and slightly shorter TM---TM separations of < 6.2 Å. However, the x = 0.25 and 0 compounds also showed similar bond angles and separations within the TM-O(2)-P(1)-O(4)-TM pathways, but this time the interactions were AFM. It is therefore likely that orbital occupancy effects dominate the sign of the exchange interaction, with the geometries of the interacting species having relatively little effect. Given that the susceptibility data on all compounds implied AFM ordering overall, it is likely that AFM interactions are stronger than FM in the x = 1 and 0.75 compounds.

5.4 Conclusions

The α-$RbMn_xFe_{1-x}HP_3O_{10}$ solid solution was successfully synthesised and the structural properties investigated. The structure can be described as a three-dimensional network of TM-O_6 octahedra corner-linked to hydrogen triphosphate units, with the Rb cations located in the resulting channels. GII values across the series were found to range between 0.12-0.17 vu, suggesting that the structure is relatively stable. For $x > 0$, the TM-O_6 coordination sphere was found to consist of four short and two long bonds, with the elongation becoming less pronounced with the greater amount of Fe^{3+} in the system. This in turn could be related to the change in unit cell parameters as the series was traversed. Mössbauer spectroscopy confirmed that the oxidation state of iron was +3 and showed a small increase in quadrupole splitting with increasing x. This suggested that Fe^{3+} was in a more distorted octahedral environment when there was a greater amount of Mn present in the system. UV-Vis spectroscopy confirmed the +3 oxidation state of manganese and the D_{4h} symmetry of the MnO_6 unit, as evidenced by three d→d transitions occurring in the visible region of the spectra. These transitions were assigned and showed an increase in 10*Dq* with decreasing Mn content, which could be related to a corresponding decrease in the axially elongated bond lengths across the series.

The thermal stability of these compounds was investigated and it was found that all remained stable up to ~500°C, after which point the host structures decomposed and evolved water. The main decomposition products were found to be $RbMnP_3O_9$ and $RbFeP_2O_7$.

Magnetic susceptibility measurements on the x = 0.75, 0.5 and 0.25 compounds revealed that the former compound ordered antiferromagnetically

whereas the latter two showed evidence for canted antiferromagnetism. Despite this, no magnetic ordering was detected in the 2 K neutron diffraction pattern of the x = 0.5 compound. The magnetic structures of the x = 0.75 and 0.25 compounds were solved and found to be isostructural with the Mn end member and Fe end member, respectively. All compounds were found to contain six different TM-O-P-O-TM exchange pathways; for x = 1 and 0.75, two of these interactions were AFM and occurred within the *ac*-plane and four were FM and occurred within the *bc*-plane of the structure. For x = 0.25 and 0, all interactions were found to be AFM. The geometries of the interacting species were found to have little effect on the sign of interaction, with FM interactions being dominated by two unoccupied e_g orbitals and AFM interactions being dominated by two singly occupied e_g orbitals.

References

[1] F. Yu, J. J. Zhang, C. Y. Wang, J. Yuan, Y. F. Yang and G. Z. Song, *Prog. Chem.*, 2010, **22**, 9-18.

[2] S. Nishimura, M. Nakamura, R. Natsui and A. Yamada, *J. Am. Chem. Soc.*, 2010, **132**, 13596-13597.

[3] F. Wang, J. Yang, Y. NuLi and J. Wang, *J. Power Sources*, 2011, **196**, 4806-4810.

[4] Gangulibabu, D. Bhuvaneswari and N. Kalaiselvi, *Appl. Phys. A- Mater.*, 2009, **96**, 489-493.

[5] D. M. Bykov, G. S. Shekhtman, A. L. Orlova, V. S. Kurazhkovskaya, E. Y. Borovikova and V. Y. Volgutov, *Solid State Ionics*, 2011, **182**, 47-52.

[6] G. Vītiņš, Z. Kaņepe, A. Vītiņš, J. Ronis, A. Dindūne and A. Lūsis, *J. Solid State Electrochem.*, 2000, **4**, 146-152.

[7] R. Y. Chen, J. W. Wang, H. N. Wang, W. Yao and J. Zhong, *Solid State Sciences*, 2011, **13**, 630-635.

[8] M. W. Kanan and D. G. Nocera, *Science*, 2008, **321**, 1072-1075.

[9] L. Adam, A. Guesdon and B. Raveau, *J. Solid State. Chem.*, 2008, **181**, 3110-3115.

[10] M. T. Averbuch and J. C. Guitel, *Acta Crystallogr.*, 1977, **B33**, 1613-1615.

[11] S. K. Rishi, B. M. Kariuki, N. J. Checker, J. Godber and A. J. Wright, *Chem. Commun.*, 2006, 747-749.

[12] L. S. Guzeeva and I. V. Tananaev, *Inorg. Mater.*, 1988, **24**, 538-542.

[13] N. J. Checker, *The Synthesis and Properties of Novel Condensed Phosphates*, PhD Thesis, University of Birmingham, 2006.

[14] A. J. Wright and J. P. Attfield, *Inorg. Chem.*, 1998, **37**, 3858-3861.

[15] F. C. Coomer, N. J. Checker and A. J. Wright, *Inorg. Chem.*, 2010, **49**, 934-942.

[16] I. Grunze and H. Grunze, *Z. Anorg. Allg. Chem.*, 1984, **512**, 39-47.

[17] Data accessed from NIST, *Neutron Scattering Lengths and Cross Sections*, www.ncnr.nist.gov/resources/n-lengths/.

[18] JCPDS, *International Centre for Diffraction Data*, 1999, P.1., Swathmore, Pennsylvania, PA 19081, USA, 11990.

[19] I. D. Brown and D. Altermatt, *Acta Crystallogr.*, 1985, **B41**, 244-247.

[20] A. Salinas-Sanchez, J. L. Garcia-Munoz, J. Rodriguez-Carvajal, R. Saez-Puche and J. L. Martinez, *J. Solid State Chem.*, 1992, **100**, 201-211.

[21] M. T. Averbuch- Pouchot, A. Durif and J. C. Guitel, *Acta Crystallogr.*, 1977, **B33**, 1436-1438.

[22] J. X. Mi, H. Borrmann, Y. X. Huang, J. T. Zhao and R. Kniep, *Z. Kristallogr.*, 2003, **218**, 169-170.

[23] N. Anisimova, M. Bork, R. Hoppe and M. Meisel, *Z. Anorg. Allg. Chem.*, 1995, **621**, 1069-1074.

[24] D. R. Davies and D. E. C. Corbridge, *Acta Crystallogr.*, 1958, **11**, 315-319.

[25] V. V. Krasnikov, Z. A. Konstant and V. S. Fundamenskii, *Inorg. Mater.*, 1983, **19**, 1231-1235.

[26] A. J. Wright and J. P. Attfield, *J. Solid State Chem.*, 1998, **141**, 160-163.

[27] B. Klinkert and M. Jansen, *Z. Anorg. Allg. Chem.*, 1988, **567**, 77-86.

[28] M. T. Averbuch- Pouchot and M. Bagieu-Beucher, *Z. Anorg. Allg. Chem.*, 1987, **552**, 171-180.

[29] R. D. Shannon, *Acta Crystallogr.*, 1976, **A32**, 751-767.

[30] M. A. G. Aranda and S. Bruque, *Inorg. Chem.*, 1990, **29**, 1334-1337.

[31] I. V. Ogorodnyk, I. V. Zatovsky, V. N. Baumer, N. S. Slobodyanik, O. V. Shishkin and I. P. Vorona, *J. Solid State Chem.*, 2007, **180**, 2838-2844.

[32] *PeakFit Version 4.12*; Seasolve, 1999-2003.

[33] A. B. P. Lever, *Inorganic Electronic Spectroscopy*; Elsevier: Amsterdam, 1984.

[34] J. Mechergui and W. Belam, *Mat. Res. Bull.*, 2008, **43**, 3358-3367.

[35] E. V. Murashova, N. N. Chudinova and B. S. Zakharova, *Inorg. Mater.*, 2001, **37**, 1170-1174.

[36] P. J. Brown, *International Tables of Crystallography, Vol.C*; Kluwer: Dordrecht, 1992.

[37] J. B. Goodenough, *Phys. Rev.*, 1955, **100**, 564-573.

[38] J. Kanamori, *J. Phys. Chem. Solids*, 1959, **10**, 87-98.

Chapter Six

The $MnPO_4 \cdot H_2O$-Fe_2O_3-H_3PO_4 Reaction System

6.1 Introduction

Condensed phosphate systems possessing high spin $3d^4$ Mn^{3+} ions are an appealing area of interest because of their broad range of structural, optical and magnetic properties. Indeed, the presence of Jahn-Teller distortions and orbital ordering, along with variations in colouration appear to be strongly inter-related. To date, the full nuclear and magnetic structures of α-$NH_4MnP_2O_7$ (section 3.3.1), $RbMnP_2O_7$,[1] $KMnHP_3O_{10}$,[2-3] α-$RbMnHP_3O_{10}$,[4] β-$RbMnHP_3O_{10}$[1] and $CsMnHP_3O_{10}$[5] have been determined whilst only the nuclear structures of α-$HMnP_2O_7$,[6] β-$HMnP_2O_7$,[7] $LiMnP_2O_7$[6] and MnP_3O_9[8] have been reported. There are also literature reports of other Mn^{3+} condensed phosphates such as γ-$HMnP_2O_7$,[9] δ-$HMnP_2O_7$,[10] $MnH_2P_3O_{10}$,[9] $MnH_2P_3O_{10} \cdot 2H_2O$,[9,11] $Mn_2(H_2P_2O_7)_3$[12] and $Mn_4(P_2O_7)_3$,[10,13] which have been characterised but have had no structural determinations performed.

Trivalent manganese phosphates are generally synthesised by heating a manganese salt or oxide with orthophosphoric acid (H_3PO_4), with additional

ammonium or alkali metal salts used depending on the product desired. If the oxidation state of manganese in the starting reagent is not +3, then it is often also necessary to add an oxidising or reducing agent. The reaction of $MnPO_4 \cdot H_2O$ with H_3PO_4 was first reported by Ivashkevich *et al*[6] as a route to synthesise α-$HMnP_2O_7$. They reported that this phase could be isolated by heating these reagents in a Mn:P molar ratio of 1:6 at 250°C with constant stirring. Once a product crystallised, the reaction mixture was rapidly cooled and washed with acetone/ water before being recovered by suction filtration.

It was of interest to us to investigate the reaction between $MnPO_4 \cdot H_2O$ and H_3PO_4 at different temperatures in order to explore whether other Mn^{3+} condensed phosphate phases could be isolated *via* this route. Attempts to introduce iron into these systems would also be made, and as before, any compounds that were isolated would be subject to a full structural and magnetic analysis, as well as investigation of their optical properties and thermal stability.

6.2 Experimental

$MnPO_4 \cdot H_2O$ was prepared according to the method published by Lightfoot *et al*.[14] A mixture of Mn_3O_4, H_3PO_4 (86.5 wt %) and H_2O in a molar ratio of 1:10:50 was sealed in a Teflon-lined stainless steel autoclave and heated at 200°C for 72 h. The resulting green suspension was washed with water and recovered by filtration. $MnPO_4 \cdot H_2O$ and Fe_2O_3 were then ground together before being added to H_3PO_4 (86.5 wt %) in a TM:P molar ratio of 1:6 in a porcelain crucible. The mixture was heated on a hotplate at temperatures ranging from 150-350°C with constant stirring for 6 h, with the resulting products (β-$HMnP_2O_7$, $Mn_xFe_{1-x}H_2P_3O_{10}$ (x = 0.5, 0.25 and

0) and $Mn_xFe_{1-x}P_3O_9$ (x = 1, 0.75, 0.25 and 0)) washed with water and recovered by suction filtration. Details on optimum reaction conditions are given in Table 6.1.

Powder X-ray diffraction data were collected on a Bruker AXS: D8 Advance diffractometer in transmission mode with a 2θ scan range of 5-80°. Both RT and 2 K neutron diffraction data were recorded on the β-$HMnP_2O_7$ and $Mn_xFe_{1-x}H_2P_3O_{10}$ (x = 0.5, 0.25 and 0) compounds as well as RT data on $Mn_xFe_{1-x}P_3O_9$ phases (x = 1, 0.75, 0.25 and 0) on the D2B instrument at the Institut Laue-Langevin, Grenoble. An incident neutron wavelength of 1.5943 Å was employed over the range $5 \leq 2\theta \leq 160°$.

6.3 Results and Discussion

The products obtained from the $MnPO_4 \cdot H_2O$-Fe_2O_3-H_3PO_4 reaction system are shown in Table 6.1. It is worth noting that α-$HMnP_2O_7$ was not observed as a product, contrary to reports by Ivashkevich *et al*.[6] With regards to the pure Mn and Fe systems, single phase compounds of β-$HMnP_2O_7$,[7] MnP_3O_9,[8] $FeH_2P_3O_{10}$[15] and FeP_3O_9[16] were isolated using this route. Although the nuclear structures of all of these phases have been determined by single crystal X-ray diffraction, attempts to replicate the reported synthetic procedures in some cases did not yield the desired products or gave additional phases. We have therefore identified a reproducible route for the synthesis of these phases in polycrystalline form.

Table 6.1: *Summary of products from the $MnPO_4 \cdot H_2O$-Fe_2O_3-H_3PO_4 reaction system*

Mn:Fe:P molar ratio	150°C	200°C	250°C	300°C	350°C
1:0:6	β-$HMnP_2O_7$	β-$HMnP_2O_7$	$MnH_2P_3O_{10} \cdot 2H_2O$* MnP_3O_9	MnP_3O_9	MnP_3O_9
3:1:24	/	β-$HMnP_2O_7$ $FeH_2P_3O_{10}$	$Mn_{0.75}Fe_{0.25}P_3O_9$	$Mn_{0.75}Fe_{0.25}P_3O_9$	$Mn_{0.75}Fe_{0.25}P_3O_9$
1:1:12	/	$Mn_{0.5}Fe_{0.5}H_2P_3O_{10}$	$Mn_{0.5}Fe_{0.5}H_2P_3O_{10}$	MnP_3O_9 FeP_3O_9	MnP_3O_9 FeP_3O_9
1:3:24	/	$Mn_{0.25}Fe_{0.75}H_2P_3O_{10}$	$Mn_{0.25}Fe_{0.75}H_2P_3O_{10}$	$Mn_{0.25}Fe_{0.75}P_3O_9$	$Mn_{0.25}Fe_{0.75}P_3O_9$
0:1:6	/	$FeH_2P_3O_{10}$	$FeH_2P_3O_{10}$	$FeH_2P_3O_{10}$ FeP_3O_9	FeP_3O_9

/ indicates no product was formed.
*This phase could not be isolated at intermediate reaction temperatures.

Given that there has been relatively little characterisation of these phases, it was of interest to us to further explore the properties of these systems, the studies of which are detailed in the sections below.

6.3.1 β-$HMnP_2O_7$

6.3.1.1 Nuclear Structure

Structural details on β-$HMnP_2O_7$ were obtained from a Rietveld refinement of the 300 K neutron diffraction data, with the refinement shown in Figure 6.1, structural parameters in Table 6.2 and selected bond lengths and angles in Table 6.3. The resulting structural information was found to be in good agreement with the previously reported single crystal XRD[7] analysis. Despite β-$HFeP_2O_7$ being shown to be isostructural with this phase, mixed compositions of $HMn_xFe_{1-x}P_2O_7$ could not be formed, with the introduction of iron leading to the formation of a separate triphosphate phase. It has been postulated that β-$HFeP_2O_7$ is metastable and indeed, single crystals for structural determination have only been obtained by using β-$HMnP_2O_7$ as a seed in the reaction mixture.[17-18]

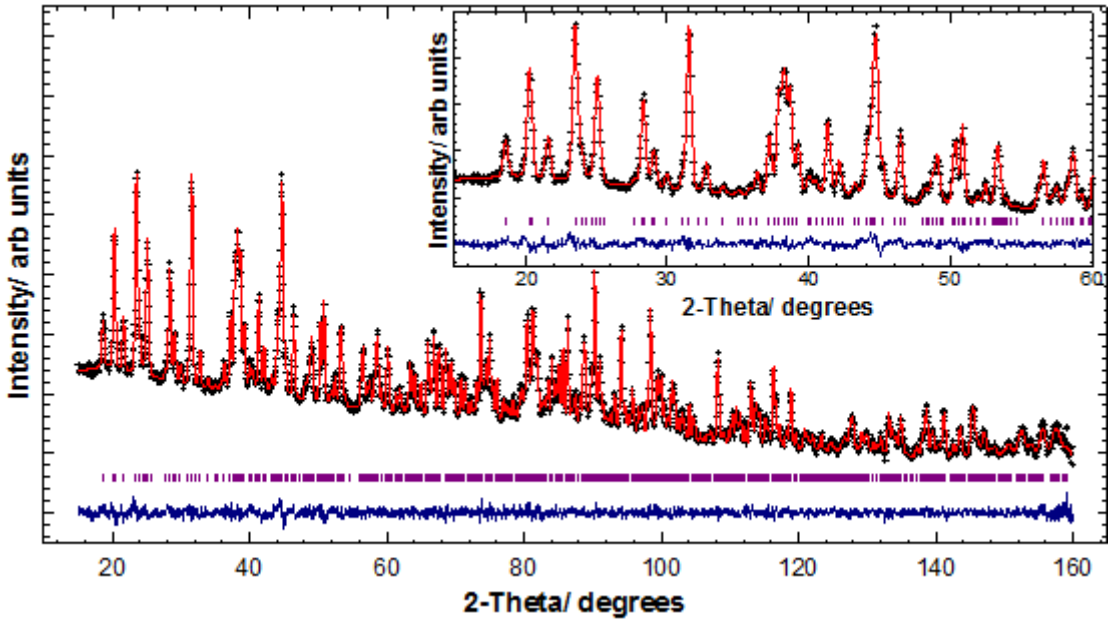

Figure 6.1: *Observed (+), calculated (-), difference profiles (-) and reflection positions (|) for the Rietveld refinement on β-$HMnP_2O_7$. The 15-60° 2θ region is expanded in the inset.*

Table 6.2: *Refined structural parameters from 300 K neutron diffraction data on β-$HMnP_2O_7$*

Atom	Site	Occupancy	*x*	*y*	*z*	U_{iso}/ Å^2	BVS[19]
Mn	4*e*	1.0	-0.0054(7)	0.3743(4)	0.126(1)	0.008(1)	3.29
P(1)	4*e*	1.0	0.2505(4)	0.4628(2)	0.6505(7)	0.0026(8)	4.94
P(2)	4*e*	1.0	0.2420(5)	0.1756(3)	0.0627(8)	0.0072(8)	5.00
O(1)	4*e*	1.0	0.1639(4)	0.0707(3)	0.9085(6)	0.0085(7)	2.17
O(2)	4*e*	1.0	0.1974(4)	0.4019(3)	0.3859(8)	0.0114(8)	2.05
O(3)	4*e*	1.0	0.3904(4)	0.2085(3)	0.9264(7)	0.0100(8)	1.71
O(4)	4*e*	1.0	0.0995(4)	0.4880(3)	0.7959(7)	0.0081(7)	1.96
O(5)	4*e*	1.0	0.2940(4)	0.1498(2)	0.3678(7)	0.0092(7)	2.05
O(6)	4*e*	1.0	0.0953(5)	0.2528(3)	0.0052(7)	0.0123(8)	2.06
O(7)	4*e*	1.0	0.3969(4)	0.4086(3)	0.8485(7)	0.0117(7)	2.01
H	4*e*	1.0	0.3937(8)	0.3313(4)	0.870(1)	0.025(2)	0.79

Space group $P2_1/n$, a = 7.9620(1) Å, b = 12.6530(2) Å, c = 4.9237(1) Å and β = 100.805(1)°.
Figures of merit: R_{wp} = 1.77%, R_p = 1.44%, χ^2 = 1.830.

Table 6.3: *Selected Bond Distances (Å) and Angles (degrees) for β-$HMnP_2O_7$*

Mn-O(2)	1.895(7)	**Mn-O(4')**	1.962(6)
Mn-O(3)	2.105(6)	**Mn-O(5)**	1.871(7)
Mn-O(4)	2.433(6)	**Mn-O(6)**	1.881(7)
O(2)-Mn-O(3)	90.9(3)	**O(3)-Mn-O(6)**	93.6(2)
O(2)-Mn-O(4)	90.7(3)	**O(4)-Mn-O(4')**	78.3(3)
O(2)-Mn-O(5)	178.8(3)	**O(4)-Mn-O(5)**	88.2(3)
O(2)-Mn-O(6)	90.3(3)	**O(4)-Mn-O(6)**	171.2(3)
O(3)-Mn-O(4)	95.1(3)	**O(5)-Mn-O(6)**	90.7(3)
O(3)-Mn-O(5)	89.9(3)		
P(1)-O(1)	1.577(4)	**P(2)-O(1)**	1.596(5)
P(1)-O(2)	1.504(5)	**P(2)-O(3)**	1.523(5)
P(1)-O(4)	1.544(4)	**P(2)-O(5)**	1.517(5)
P(1)-O(7)	1.534(4)	**P(2)-O(6)**	1.509(5)
O(1)-P(1)-O(2)	110.2(3)	**O(1)-P(2)-O(3)**	106.5(3)
O(1)-P(1)-O(4)	107.9(2)	**O(1)-P(2)-O(5)**	107.6(2)
O(1)-P(1)-O(7)	101.6(3)	**O(1)-P(2)-O(6)**	103.3(3)
O(2)-P(1)-O(4)	113.0(3)	**O(3)-P(2)-O(5)**	113.9(3)
O(2)-P(1)-O(7)	112.2(3)	**O(3)-P(2)-O(6)**	112.2(3)
O(4)-P(1)-O(7)	111.3(3)	**O(5)-P(2)-O(6)**	112.5(3)
H-O(7)	0.985(7)	**O(3)-H-O(7)**	175.9(7)
H---O(3)	1.580(6)		

The structure, as shown in Figures 6.2 and 6.3, consists of MnO_6 octahedra corner-linked to five hydrogen diphosphate units, one of them being connected in a bidentate fashion. Pairs of MnO_6 octahedra also share an edge to form isolated Mn_2O_{10} dimers bound by six diphosphate groups in total. The conformation of the diphosphate groups is virtually eclipsed, with O(7)-H---O(3) hydrogen bonding connecting these units into infinite chains that run along the *b*-axis of the structure. As with most diphosphate systems, longer P-O(1) bonds (> 1.57 Å) were observed to the bridging oxygen, intermediate bond lengths to P-OH and shorter P-O bonds (< 1.52 Å) to the terminal oxygens. Although O(4) is also a terminal oxygen, a relatively long P-O bond length of 1.544 Å was observed here as a consequence of this atom also being bonded to two Mn^{3+} ions. The O-P-O angles were found to range from

~102-113° and 103-114° for the $P(1)O_4$ and $P(2)O_4$ tetrahedra respectively, which is a similar range to that reported for KYP_2O_7.[20]

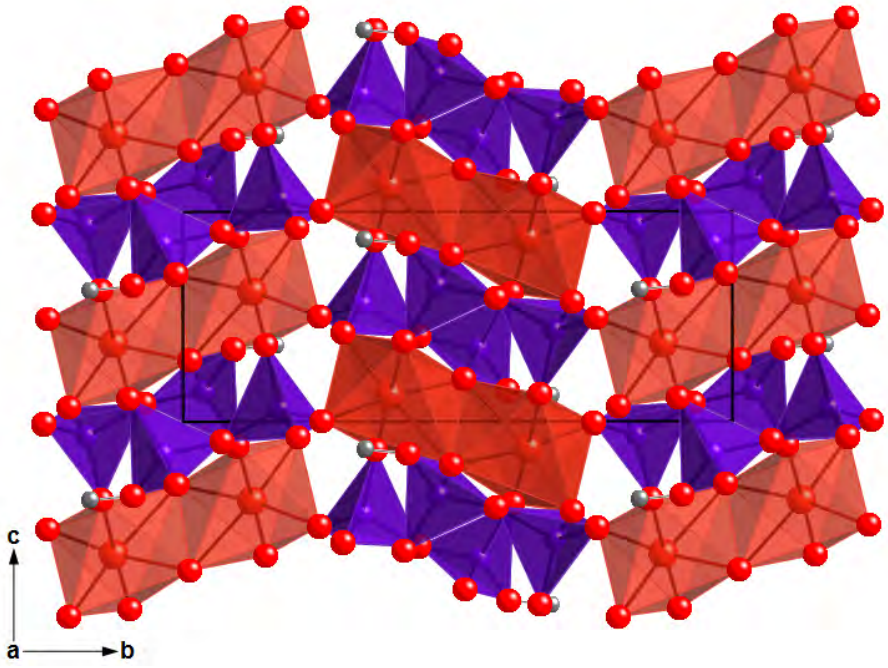

Figure 6.2: *Structure of β-$HMnP_2O_7$ viewed down the a-axis, showing MnO_6 octahedra (red), P_2O_7 condensed phosphate tetrahedra (blue) and protons as grey spheres. The thin black line defines the unit cell.*

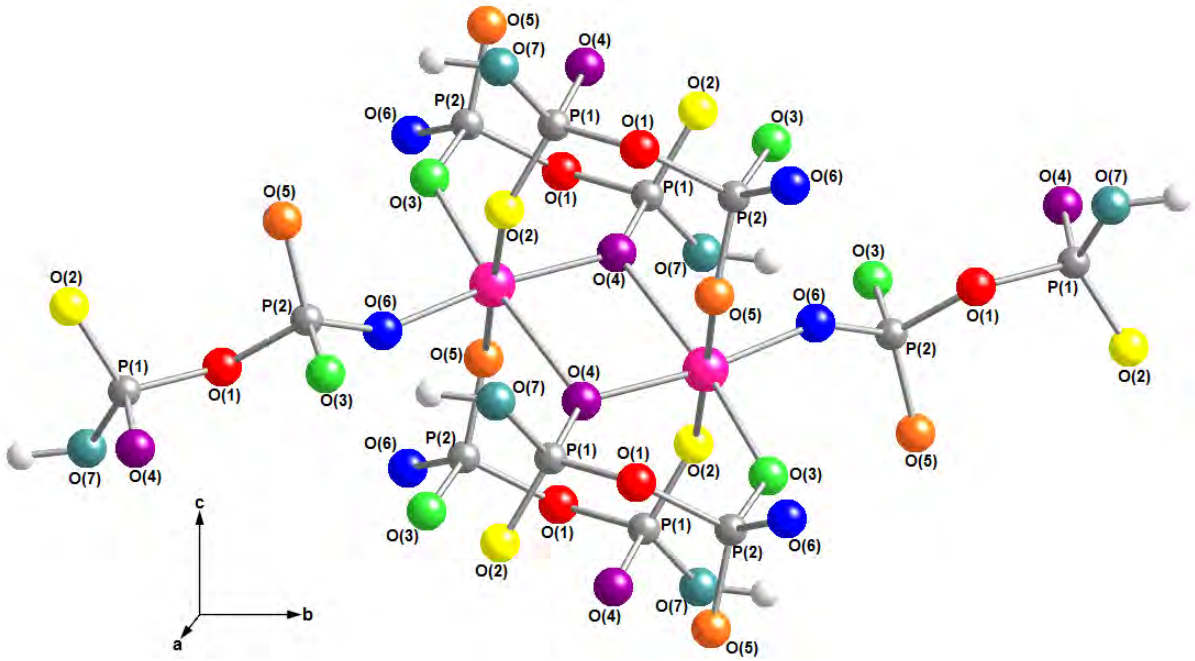

Figure 6.3: *Orientation of the diphosphate groups about the Mn_2O_{10} dimers in β-$HMnP_2O_7$. Mn, P and H atoms are shown as pink, grey and white spheres, respectively.*

The MnO_6 octahedra appear to possess an irregular arrangement of bond lengths, with three relatively short Mn-O bonds (< 1.90 Å) formed with O(2), O(5) and O(6), an intermediate bond length of 1.96 Å and a long bond of 2.43 Å formed to O(4') and O(4), respectively (the oxygens edge-shared with an adjacent MnO_6 unit) and a relatively long bond of 2.11 Å formed to O(3). This suggests that an axial elongation occurs along the Mn-O(3) and Mn-O(4) bonds. The O-Mn-O angles showed small deviations from an ideal octahedron, but this is not unusual in a system containing edge-sharing MnO_6 octahedra.

Bond Valence Sum calculations according to the values provided by Brown and Altermatt[19] showed some of the atoms in the structure to be slightly overbonded or underbonded (Table 6.2). The Global Instability Index (GII)[21] was therefore used to measure the extent to which the valence sum rule was violated over the whole structure (see Appendix 1) and gave a value of 0.15 vu, indicating that the structure is relatively stable but possesses a significant degree of lattice strain.

6.3.1.2 UV-Vis Spectroscopy

Figure 6.4 shows the UV-Vis spectrum of β-$HMnP_2O_7$. The PeakFit[22] program was used to resolve the spectrum and gave three transitions in the UV region and four in the visible region. The former were attributed to $O^{2-} \rightarrow Mn^{3+}$ ligand to metal charge transfer (LMCT), whilst the latter were assigned as d→d transitions occurring at Mn^{3+} and were consistent with a highly distorted 6-coordinate MnO_6 site, as was also seen from the diffraction data. A detailed discussion on the electronic properties of 6-coordinate Mn^{3+} was given in Chapter 3, section 3.3.2.1.

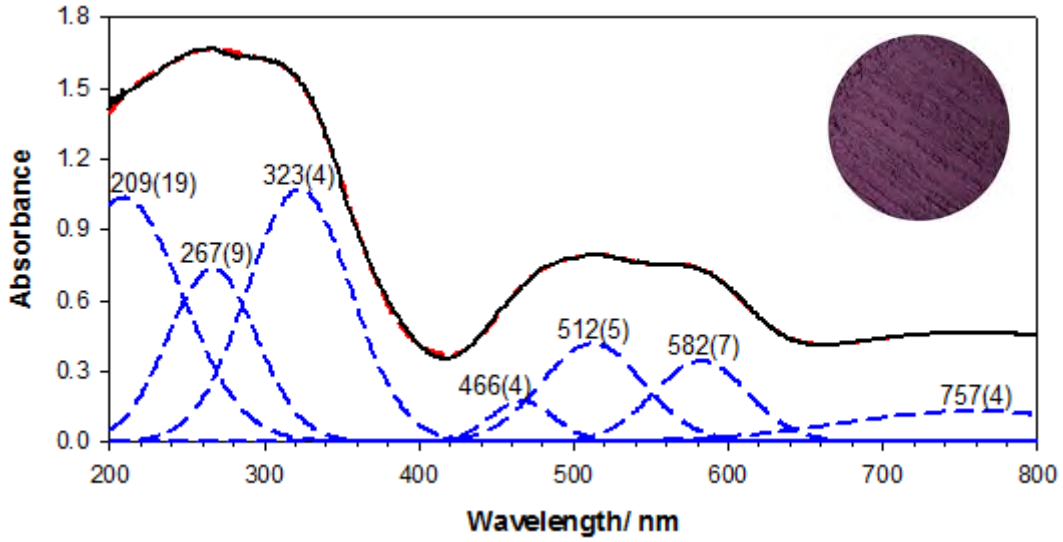

Figure 6.4: *UV-Vis spectrum of β-$HMnP_2O_7$, showing raw data (—), fitted Gaussian bands (---) and sum of the fitted Gaussian bands (---). Peak positions are marked and the colouration exhibited by this compound is shown in the top right corner.*

It is worth noting that the transitions seen in the visible region of this compound were not particularly intense, especially when compared to the pyrophosphates $NH_4MnP_2O_7$ (section 3.3.4.2) and $RbMnP_2O_7$ (section 4.3.2). Clearly a different structure type is adopted here, and so the surrounding ligand environment of the Mn^{3+} ion as well as particle size could be critical factors in governing the optical properties of the material.

6.3.1.3 Thermal Stability

The variable temperature XRD measurements in N_2 (Figure 6.5) showed that β-$HMnP_2O_7$ remained present up to 348°C but began to lose crystallinity above this temperature. By 552°C complete loss of peaks belonging to this phase occurred, to leave a virtually amorphous intermediate sample. Crystallisation of at least two new phases occurred by 575°C, as confirmed by some of the peaks in the diffraction pattern matching $Mn_4(P_2O_7)_3$ from the JCPDS[23] database, which suggested

retention of Mn^{3+}. Attempts to index the remaining peaks using Crysfire[24] did not provide any plausible unit cells, and so the other phase(s) present could not be identified. By 650°C, peaks belonging to $Mn_2P_4O_{12}$ began to appear in the diffraction pattern, indicating reduction to Mn^{2+}, and by 715°C, this was the only crystalline phase present and remained up to the final measurement temperature of 805°C.

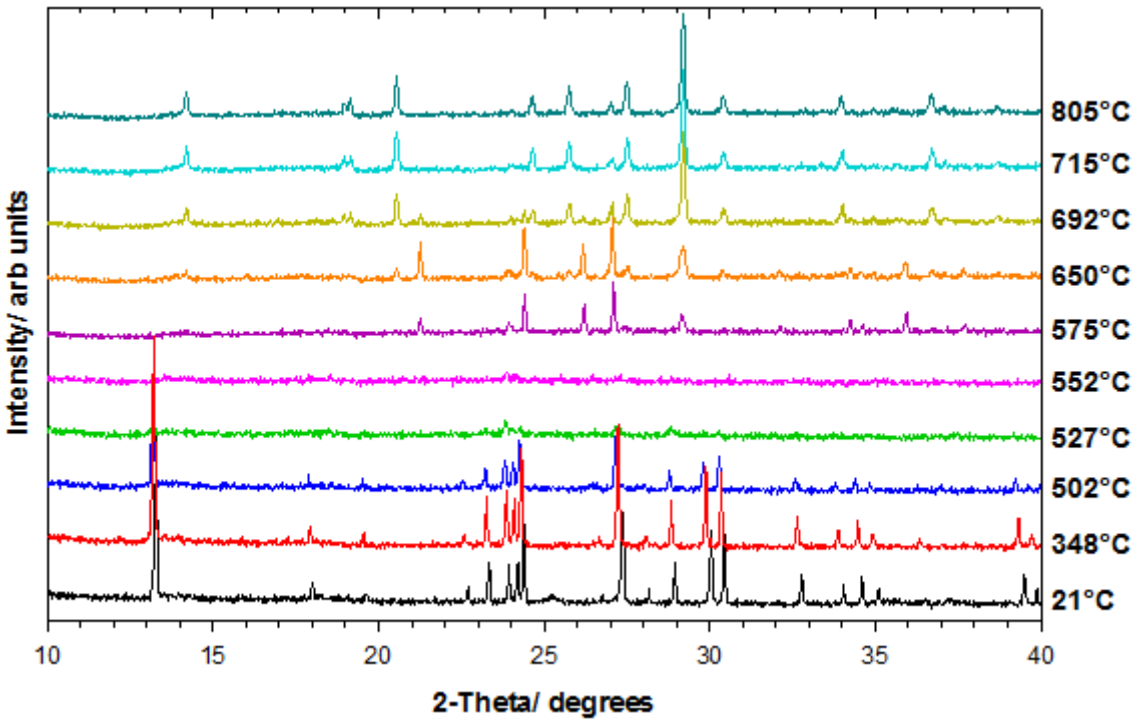

Figure 6.5: *Variable Temperature XRD of β-$HMnP_2O_7$ showing thermal decomposition to manganese (II) cyclotetraphosphate.*

The TGA-MS measurement (Figure 6.6) showed that a small loss of water (~2.29%) occurred between 130-240°C in an endothermic event. Variable temperature XRD measurements confirmed that no change had occurred to the host over this temperature range, and so this water loss was assigned as either surface water belonging to the host or possibly water loss from an amorphous phase that was not evident in the diffraction patterns.

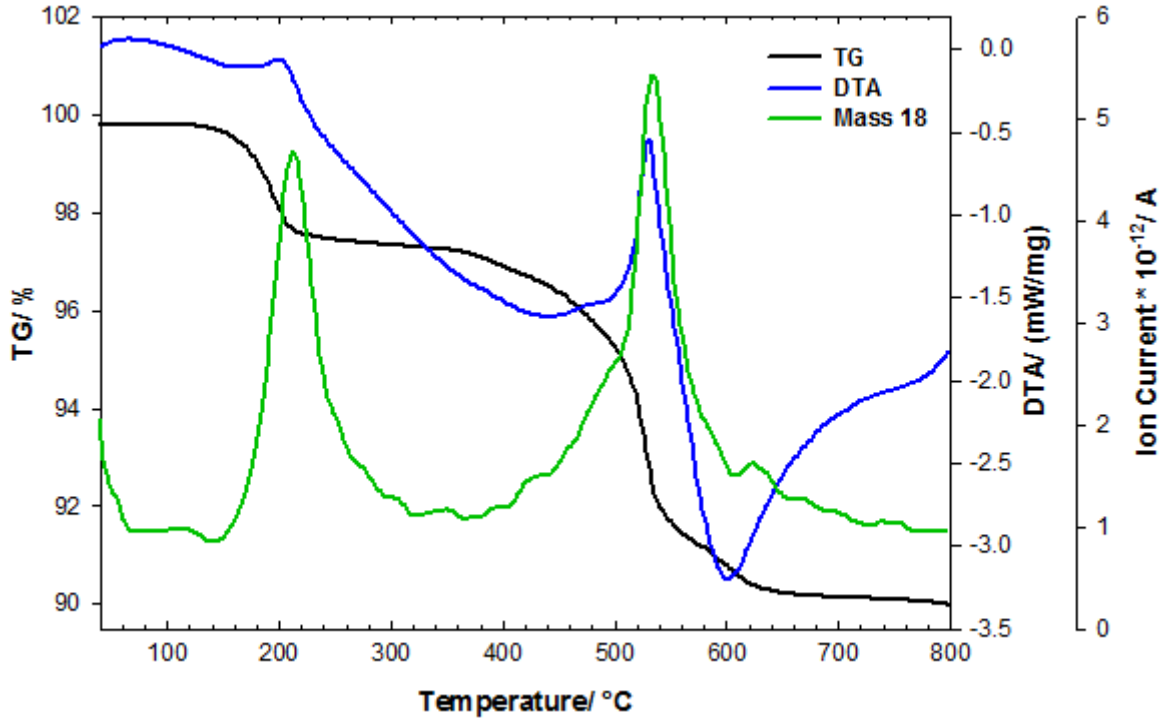

***Figure* 6.6:** *TGA-MS Plot for β-$HMnP_2O_7$*

A gradual mass loss was seen past 370°C, which was in accordance with variable temperature XRD measurements showing that the host phase began to lose crystallinity at this stage. The TGA-MS plot then indicated that a broad loss of water occurred over two consecutive mass loss steps, one occurring between ~410-550°C and corresponding to an endothermic event, and the other occurring over ~550-680°C and corresponding to an exothermic event. These two steps are likely to correspond to formation of the amorphous intermediate and then crystallisation of the reduced Mn phase, respectively. A mass loss of 7.35% was observed above 300°C, which is in good agreement with the 7.4% expected for conversion of β-$HMnP_2O_7$ to $Mn_2P_4O_{12}$. The exact mechanism for this decomposition is at present unclear, though given the reduction of Mn, it possibly involves a loss of oxygen from the host, as detailed in equation 6.1; this however was not detected by the mass spectrum.

$$2HMnP_2O_7 \longrightarrow Mn_2P_4O_{12} + H_2O + \tfrac{1}{2}O_2 \qquad \textbf{Equation 6.1}$$

6.3.1.4 Magnetic Properties

The magnetic susceptibility data on β-$HMnP_2O_7$ is shown in Figure 6.7, with a Curie-Weiss fit to the data given in the inset. Both the field cooled/ field warmed (FCFW) and zero-field cooled/ field warmed (ZFCFW) measurements were in agreement, giving negative Weiss constants and showing that the sample orders antiferromagnetically with a Néel temperature of 17 K. The effective magnetic moment of 4.816(7) μ_B was found to be in good agreement with the spin-only moment of 4.90 μ_B and experimentally observed moments of 4.80-4.90 μ_B seen for high spin Mn^{3+} complexes.[25]

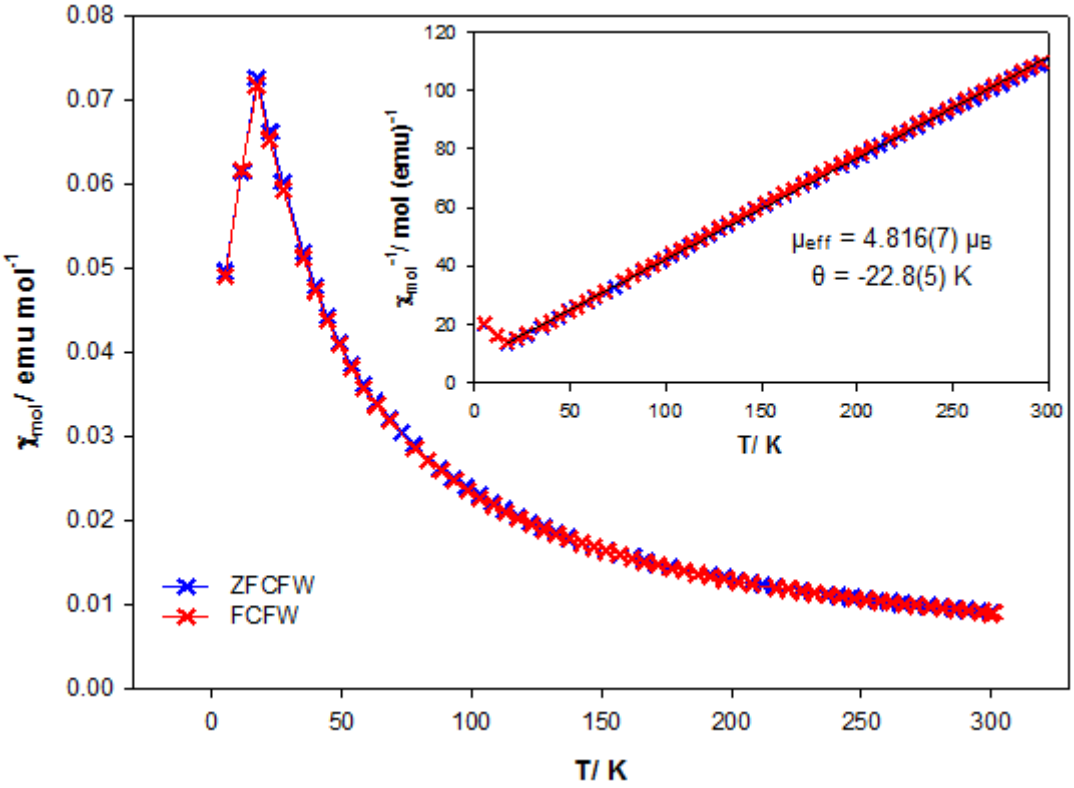

Figure 6.7: *Plot of molar susceptibility against temperature for β-$HMnP_2O_7$, with the inset showing a Curie-Weiss fit to the data.*

After the nuclear contribution was fitted to the 2 K neutron diffraction data, the pattern showed evidence for additional peaks and intensity (Figure 6.8). This allowed a magnetic unit cell to be determined which was found to be commensurate with the nuclear cell. The magnetic structure was refined as a separate, purely magnetic phase with *P*1 symmetry, leaving the directions of the magnetic moments unrestricted. The magnitude of the moments was found to be 3.24(9) μ_B, which is slightly lower than the saturated moment of 4.0 μ_B expected for high spin Mn^{3+} ions, and is possibly due to disorder between the moments and/ or competing interactions. The final refined structural parameters are shown in Table 6.4, with selected bond lengths and angles given in Table 6.5.

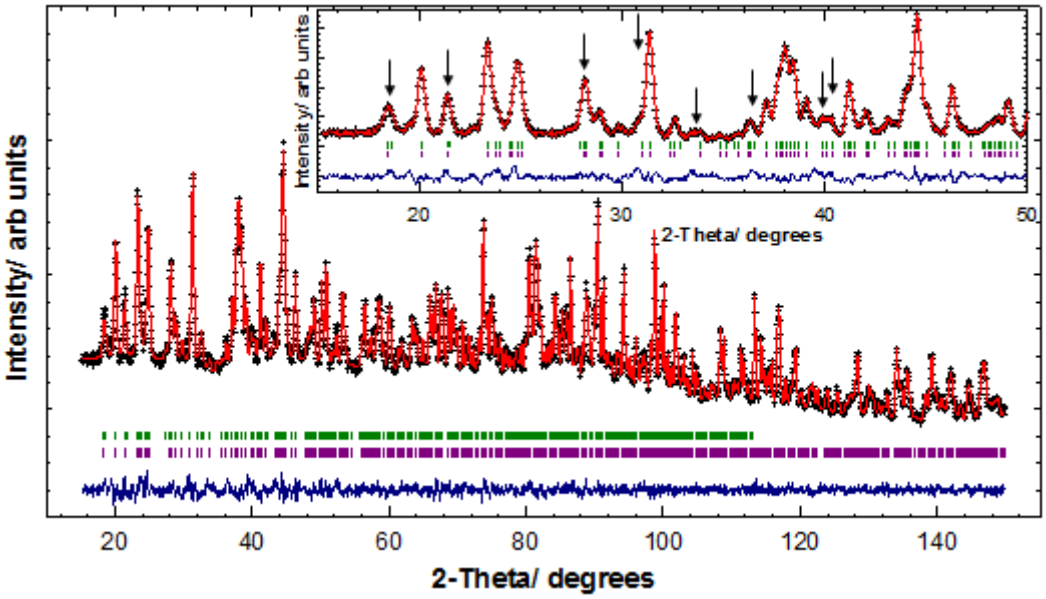

Figure 6.8: *Observed (+), calculated (-) and difference profiles (-) for the 2 K Rietveld refinement carried out on β-$HMnP_2O_7$. Reflections positions for the magnetic and nuclear phases are shown with green and purple markers, respectively and the low angle region is enlarged in the inset, with arrows indicating peaks with significant magnetic intensity.*

Table 6.4: *Refined structural parameters from 2 K neutron diffraction data on β-$HMnP_2O_7$*

Nuclear phase (space group $P2_1/n$)							
Atom	**Site**	**Occupancy**	***x***	***y***	***z***	**U_{iso}/ Å^2**	**BVS[19]**
Mn	4*e*	1.0	-0.0047(7)	0.3759(4)	0.126(1)	0.002(1)	3.28
P(1)	4*e*	1.0	0.2504(5)	0.4629(3)	0.6507(8)	0.0020(8)	4.98
P(2)	4*e*	1.0	0.2408(5)	0.1752(3)	0.0630(8)	0.0016(8)	5.04
O(1)	4*e*	1.0	0.1618(4)	0.0707(3)	0.9058(7)	0.0041(8)	2.17
O(2)	4*e*	1.0	0.1992(5)	0.4022(3)	0.3849(9)	0.0037(7)	2.07
O(3)	4*e*	1.0	0.3899(5)	0.2071(3)	0.9278(8)	0.0054(8)	1.74
O(4)	4*e*	1.0	0.1000(4)	0.4871(3)	0.7944(7)	0.0018(7)	2.04
O(5)	4*e*	1.0	0.2923(4)	0.1483(2)	0.3686(7)	0.0028(7)	2.04
O(6)	4*e*	1.0	0.0935(5)	0.2525(3)	0.0012(7)	0.0057(8)	2.03
O(7)	4*e*	1.0	0.3981(5)	0.4077(3)	0.8502(7)	0.0039(7)	1.95
H	4*e*	1.0	0.3974(8)	0.3295(4)	0.874(1)	0.016(1)	0.77
Magnetic phase (space group *P*1)							
Atom	**Site**	**Occupancy**	***x***	***y***	***z***	**U_{iso}/ Å^2**	**BVS[19]**
			M_x / μ_B	**M_y / μ_B**	**M_z / μ_B**	**$\lvert M \rvert$ / μ_B**	
Mn(1)	1*a*	1.0	-0.0047(7)	0.3759(4)	0.126(1)	0.002(1)	3.28
			1.5(3)	2.6(1)	1.0(3)	3.24(9)	
Mn(2)	1*a*	1.0	0.5047(4)	0.8760(2)	0.3731(6)	0.002(1)	3.28
			-1.5(3)	-2.6(1)	-1.0(3)	3.24(9)	
Mn(3)	1*a*	1.0	0.0047(7)	0.6241(4)	0.874(1)	0.002(1)	3.28
			1.5(3)	2.6(1)	1.0(3)	3.24(9)	
Mn(4)	1*a*	1.0	0.4953(4)	0.1240(2)	0.6269(6)	0.002(1)	3.28
			-1.5(3)	-2.6(1)	-1.0(3)	3.24(9)	

a = 7.9233(1) Å, b = 12.6305(2) Å, c = 4.9064(1) Å, α = 90°, β = 100.764(1)° and γ = 90°
Figures of merit: R_{wp} = 1.93%, R_p = 1.49%, χ^2 = 2.729.

Table 6.5: *Selected Bond Distances (Å) and Angles (degrees) for β-$HMnP_2O_7$ at 2K*

Mn-O(2)	1.888(7)	**Mn-O(4')**	1.956(6)
Mn-O(3)	2.109(6)	**Mn-O(5)**	1.876(7)
Mn-O(4)	2.411(7)	**Mn-O(6)**	1.896(7)
O(2)-Mn-O(3)	91.0(3)	**O(3)-Mn-O(6)**	93.3(2)
O(2)-Mn-O(4)	91.4(3)	**O(4)-Mn-O(4')**	79.1(3)
O(2)-Mn-O(5)	179.3(4)	**O(4)-Mn-O(5)**	88.0(3)
O(2)-Mn-O(6)	90.6(3)	**O(4)-Mn-O(6)**	171.6(4)
O(3)-Mn-O(4)	94.7(3)	**O(5)-Mn-O(6)**	90.0(3)
O(3)-Mn-O(5)	89.4(3)		
P(1)-O(1)	1.577(5)	**P(2)-O(1)**	1.596(5)
P(1)-O(2)	1.502(5)	**P(2)-O(3)**	1.513(5)
P(1)-O(4)	1.525(5)	**P(2)-O(5)**	1.517(5)
P(1)-O(7)	1.544(5)	**P(2)-O(6)**	1.508(5)
O(1)-P(1)-O(2)	110.2(3)	**O(1)-P(2)-O(3)**	106.1(3)
O(1)-P(1)-O(4)	108.5(3)	**O(1)-P(2)-O(5)**	107.5(3)
O(1)-P(1)-O(7)	101.2(3)	**O(1)-P(2)-O(6)**	102.7(3)
O(2)-P(1)-O(4)	113.3(4)	**O(3)-P(2)-O(5)**	113.9(3)
O(2)-P(1)-O(7)	111.7(3)	**O(3)-P(2)-O(6)**	112.2(3)
O(4)-P(1)-O(7)	111.3(3)	**O(5)-P(2)-O(6)**	113.5(3)
H-O(7)	0.995(7)	**O(3)-H-O(7)**	176.4(7)
H---O(3)	1.571(7)		

The magnetic structure of β-$HMnP_2O_7$ is shown in Figure 6.9. A similar pattern of bond lengths and angles to those seen at room temperature was observed, as well as an identical GII value of 0.15 vu. The major component of the moments was found to be directed along the *b*-axis of the structure, which unlike the Mn^{3+} condensed phosphates encountered in the previous chapters, was not the direction associated with the axial elongation of the MnO_6 octahedra.

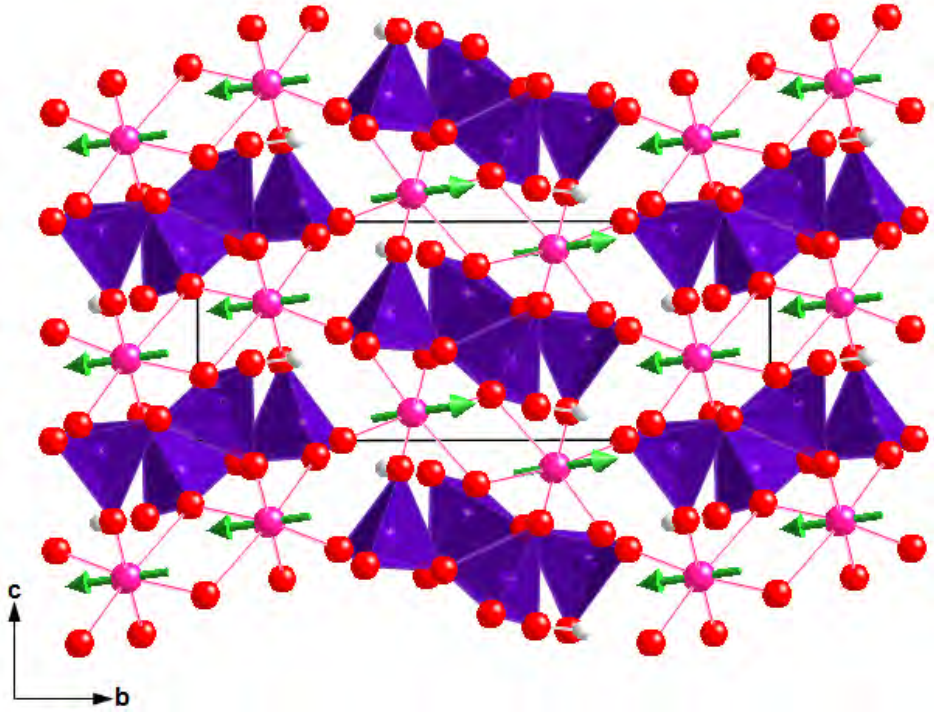

Figure 6.9: *Magnetic structure of β-$HMnP_2O_7$ viewed down the a-direction, with the orientation of magnetic moments on the Mn^{3+} ions (pink spheres) shown with green arrows and condensed phosphate tetrahedra shown in blue. The thin black line defines the unit cell.*

Within the Mn_2O_{10} dimers, the Mn ions were found to be linked in a FM fashion. The separation between these ions is ~3.38 Å, and as such we would expect the magnetic interaction to be the result of a superexchange mechanism or possibly direct exchange. If we contemplate superexchange occurring through the Mn-O-Mn linkages, then from crystal field considerations we would expect the equatorial Mn-O bonds to be situated in the direction of the empty $d_{x^2-y^2}$ orbital and the axially

elongated Mn-O bonds to be in the direction of the singly occupied d_{z^2} orbital. Thus within the dimer there are two superexchange interactions occurring between an empty $d_{x^2-y^2}$ orbital of one Mn ion and the singly occupied d_{z^2} orbital of the other, and *vice versa*, both mediated by intermediate oxygen anions. Assuming that the oxygen anions are diamagnetic, then for Hund's rule to be obeyed we would expect an AFM alignment of the moments, as seen schematically in Figure 6.10.

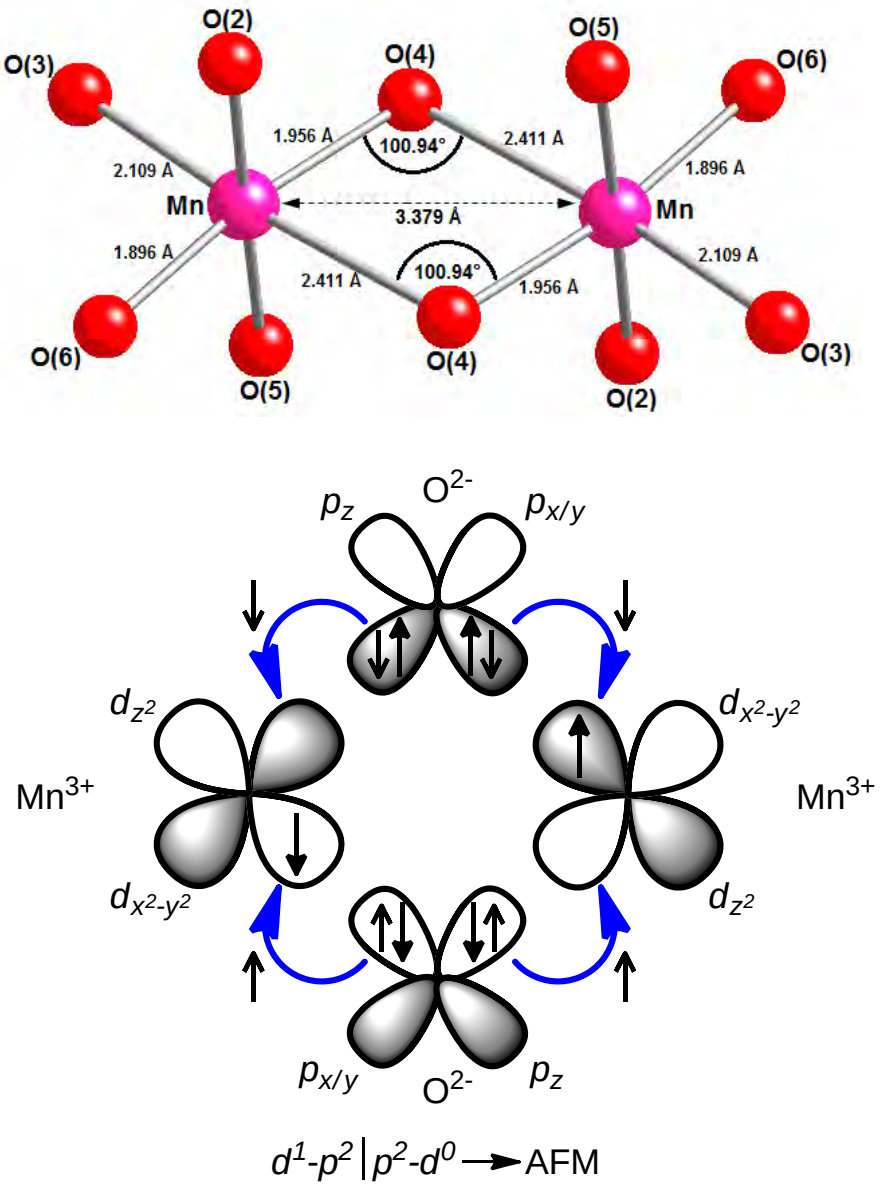

Figure 6.10: *Possible mechanism for superexchange in the Mn_2O_{10} dimers of β-$HMnP_2O_7$, giving rise to AFM ordering.*

With regards to direct exchange, as the MnO_6 octahedra within the dimers share a common edge, the singly occupied t_{2g} orbitals of the two Mn ions should point directly at each other and also overlap to give rise to an AFM interaction. A FM interaction can only be envisaged when there is overlap of a singly occupied t_{2g} orbital on one ion with an empty $d_{x^2-y^2}$ or d_{z^2} orbital on the other, in which case the spin direction of the electron to be transferred would not need to be changed. The magnetic properties of a small number of binuclear Mn^{3+} complexes containing edge-shared MnL_6 (L = ligand) octahedra with similar Mn-O-Mn angles and Mn---Mn distances have been investigated, with the interaction also found to be FM.[26-28] It has been suggested that this interaction is likely to be due to the efficient "crossed interaction" between the singly occupied d_{xy} orbital on one ion and the empty $d_{x^2-y^2}$ orbital on the other.[26,29] Clearly these findings are consistent with the FM interaction observed in β-$HMnP_2O_7$, though orbital analysis would have to be conducted in order to verify that the same orbital overlap occurs here.

Each Mn ion within the structure of β-$HMnP_2O_7$ was also found to be linked to another seven *via* Mn-O-P-O-Mn "super-superexchange" pathways. Interactions with three of these ions were FM in nature while those remaining were AFM (Figure 6.11). Table 6.6 summarises the exchange pathways present.

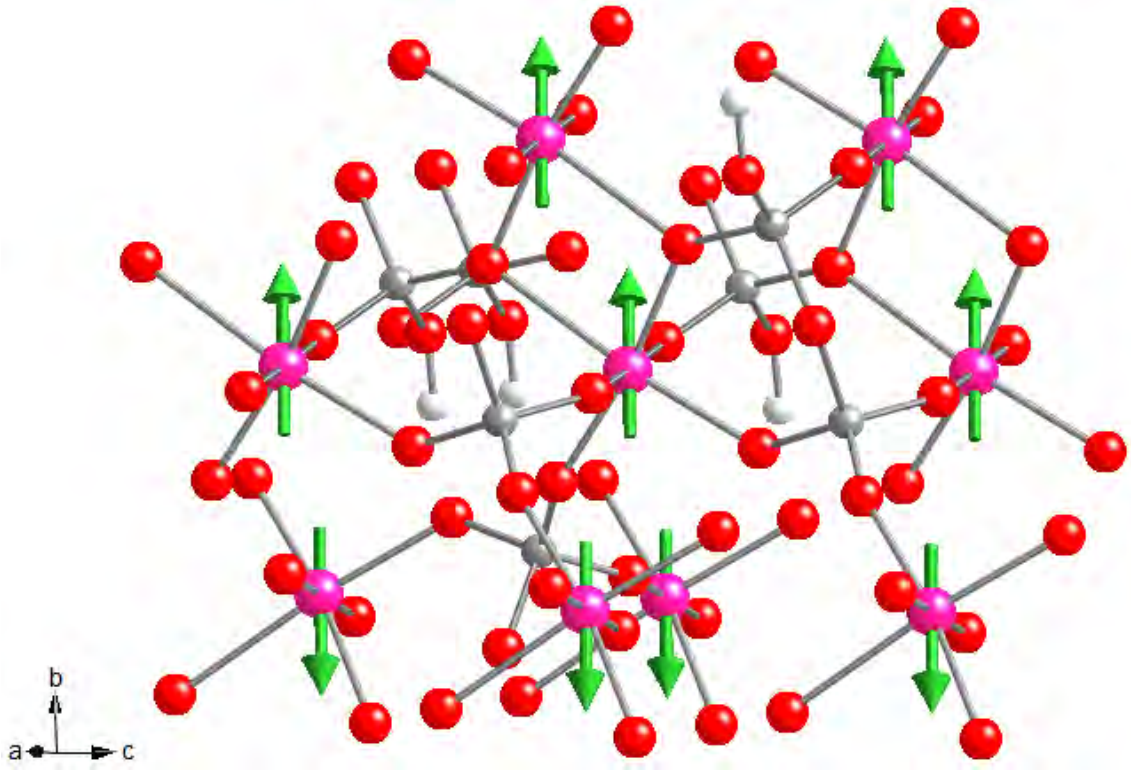

Figure 6.11: *Nearest neighbour Mn---Mn interactions in β-$HMnP_2O_7$. Mn, P, O and H atoms are shown as pink, grey, red and white spheres, respectively.*

It is interesting to note that all interactions mediated by the $P(1)O_4$ tetrahedron were FM in nature. Indeed, the bridging O(4) atoms of the Mn_2O_{10} dimers are also bonded to P(1), and so it is possible that the FM interactions within the dimer force the interactions occurring through the phosphate unit to also be FM. Interactions mediated by the $P(2)O_4$ tetrahedra were found to be a combination of FM and AFM. Each $P(2)O_4$ tetrahedron was found to simultaneously connect three Mn centres *via* the terminal oxygen atoms. The spin directions of this triad were such that two Mn ions were linked in a FM fashion with respect to each other but antiferromagnetically to the third Mn ion (Figure 6.12). Similar triads have also been observed in the structures of α-$NH_4MnP_2O_7$ (Chapter 3, section 3.3.4.4.1) and $RbMnP_2O_7$.[1] This feature results in an AFM alignment of the Mn_2O_{10} dimers along the *a*- and *b*-

directions of the structure (see Figure 6.9 also), resulting in bulk AFM ordering being observed for this material.

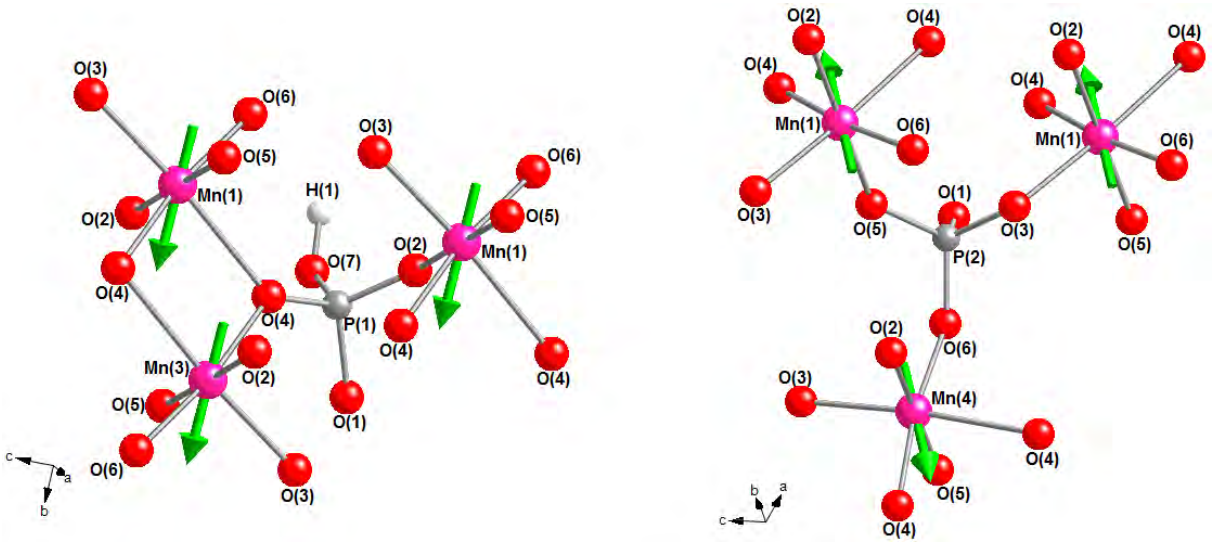

Figure 6.12: *Interactions occurring through the $P(1)O_4$ and $P(2)O_4$ units in β-$HMnP_2O_7$. Mn, P, O and H atoms are shown as pink, grey, red and white spheres, respectively.*

Table 6.6: *Summary of the exchange pathways present in β-$HMnP_2O_7$ and geometries of the interacting species.*

Mn(1)-O(2)-P(1)-O(4)-Mn(1) **Mn(1)-O(4)-P(1)-O(2)-Mn(1)**	O(2)-P(1)-O(4) = 113.3(4)° Mn(1)-O(2)-P(1) = 137.1° Mn(1)-O(4)-P(1) = 126.4°	O(2)---O(4) = 2.53 Å Mn(1)---Mn(1) = 4.91 Å	FM
Mn(1)-O(2)-P(1)-O(4')-Mn(3) **Mn(1)-O(4')-P(1)-O(2)-Mn(3)**	O(2)-P(1)-O(4') = 113.3(4)° Mn(1)-O(2)-P(1) = 137.1° Mn(1)-O(4')-P(1) = 129.1°	O(2)---O(4') = 2.53 Å Mn(1)---Mn(3) = 4.81 Å	FM
Mn(1)-O(3)-P(2)-O(5)-Mn(1) **Mn(1)-O(5)-P(2)-O(3)-Mn(1)**	O(3)-P(2)-O(5) = 113.9(3)° Mn(1)-O(3)-P(2) = 128.0° Mn(1)-O(5)-P(2) = 138.0°	O(3)---O(5) = 2.54 Å Mn(1)---Mn(1) = 4.91 Å	FM
Mn(1)-O(3)-P(2)-O(6)-Mn(4) **Mn(1)-O(6)-P(2)-O(3)-Mn(4)**	O(3)-P(2)-O(6) = 112.2(3)° Mn(1)-O(3)-P(2) = 128.0° Mn(1)-O(6)-P(2) = 144.6°	O(3)---O(6) = 2.51 Å Mn(1)---Mn(4) = 5.96 Å	AFM
Mn(1)-O(5)-P(2)-O(6)-Mn(4) **Mn(1)-O(6)-P(2)-O(5)-Mn(4)**	O(5)-P(2)-O(6) = 113.5(3)° Mn(1)-O(5)-P(2) = 138.0° Mn(1)-O(6)-P(2) = 144.6°	O(5)---O(6) = 2.54 Å Mn(1)---Mn(4) = 5.31 Å	AFM
Mn(1)-O(4)-Mn(3) **Mn(1)-O(4')-Mn(3)**	Mn(1)-O-Mn(3) = 100.9°	Mn(1)---Mn(3)= 3.38 Å	FM

From Table 6.6 it can be seen that the sign of the super-superexchange interaction was not related to orbital occupancy, with FM and AFM interactions both involving either two equatorial Mn-O bonds or one axial and one equatorial Mn-O bond. Furthermore, there appeared to be no direct relationship between the sign of the interaction and geometries of the interacting species, with O---O separations and O-P-O angles being similar in both FM and AFM pathways. The Mn-O-P angles were slightly shorter for FM interactions and the Mn---Mn separations ≤ 4.9 Å, compared to being ≥ 5.3 Å for AFM interactions. However, given the relatively large separation between the Mn ions within these pathways, it is unlikely that these small variations have a significant influence on the exchange interaction.

The magnetic structure of β-$HMnP_2O_7$ determined from neutron diffraction was in accordance with AFM ordering, as was also suggested by the susceptibility measurements. The FM interaction within the Mn_2O_{10} dimers would be expected to be stronger than super-superexchange interactions occurring through extended orthophosphate linkages. However, when considering the long range magnetic ordering between the dimers, the connectivity through the latter results in an AFM alignment. This compound is therefore clearly an example of where magnetic interactions occurring through extended linkages should not be ignored in the presence of possible superexchange and/ or direct exchange mechanisms.

6.3.2 $Mn_xFe_{1-x}H_2P_3O_{10}$ ($x \leq 0.5$)

An increase in temperature in the $MnPO_4 \cdot H_2O$-Fe_2O_3-H_3PO_4 reaction system led to $Mn_xFe_{1-x}H_2P_3O_{10}$ ($x \leq 0.5$) phases being exclusively observed over the 200-250°C temperature range. Compositions with $x > 0.5$ could not be formed, with the reactions giving either a mixture of β-$HMnP_2O_7$/ $FeH_2P_3O_{10}$, $MnH_2P_3O_{10} \cdot 2H_2O$/ $FeH_2P_3O_{10}$ or the corresponding polyphosphate. The fact that $MnH_2P_3O_{10}$ ($x = 1$) was not observed is consistent with literature observations that the two polymorphs of this compound (referred to as type I and II) are metastable. Indeed, type I is reported to rapidly absorb water to form $MnH_2P_3O_{10} \cdot 2H_2O$ while type-II has only been prepared by using a $FeH_2P_3O_{10}$ seed in the reaction mixture.[12]

6.3.2.1 Nuclear Structure

Structural details on the $Mn_xFe_{1-x}H_2P_3O_{10}$ ($x = 0.5$, 0.25 and 0) compounds were obtained from Rietveld refinements of the 300 K neutron powder diffraction data, using single crystal XRD data on $FeH_2P_3O_{10}$[15] (space group $P2_1/c$) as a starting model. The refinements are shown in Figure 6.13, structural parameters in Table 6.7, selected bond lengths and angles in Table 6.8 and the structure in Figure 6.14.

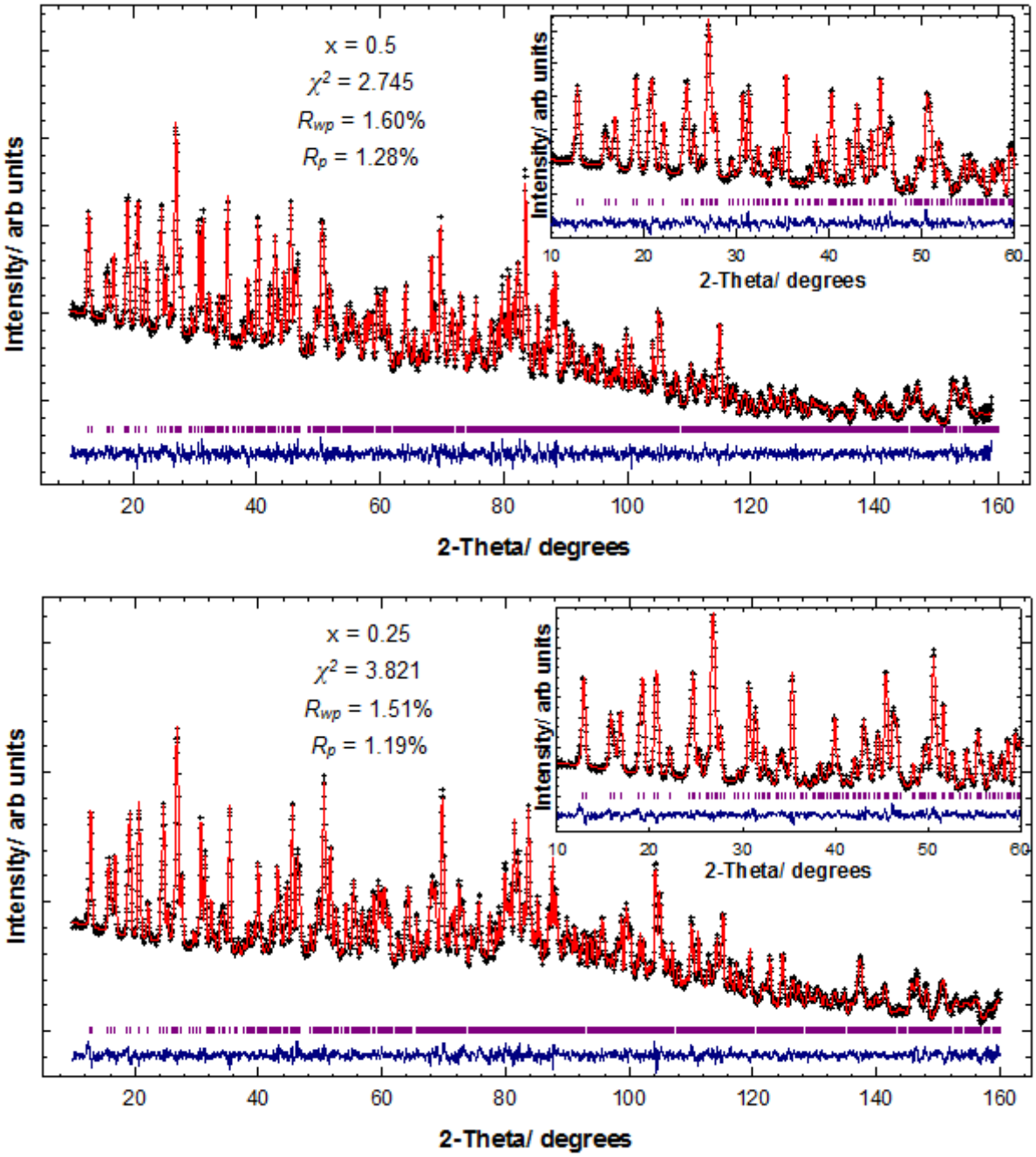

Figure 6.13: *Observed (+), calculated (-), difference profiles (-) and reflection positions (I) for the 300 K Rietveld refinements carried out on the $Mn_xFe_{1-x}H_2P_3O_{10}$ series (x = 0.5, 0.25 and 0). The 10-60° 2θ regions are expanded in the insets.*

Figure 6.13 continued...

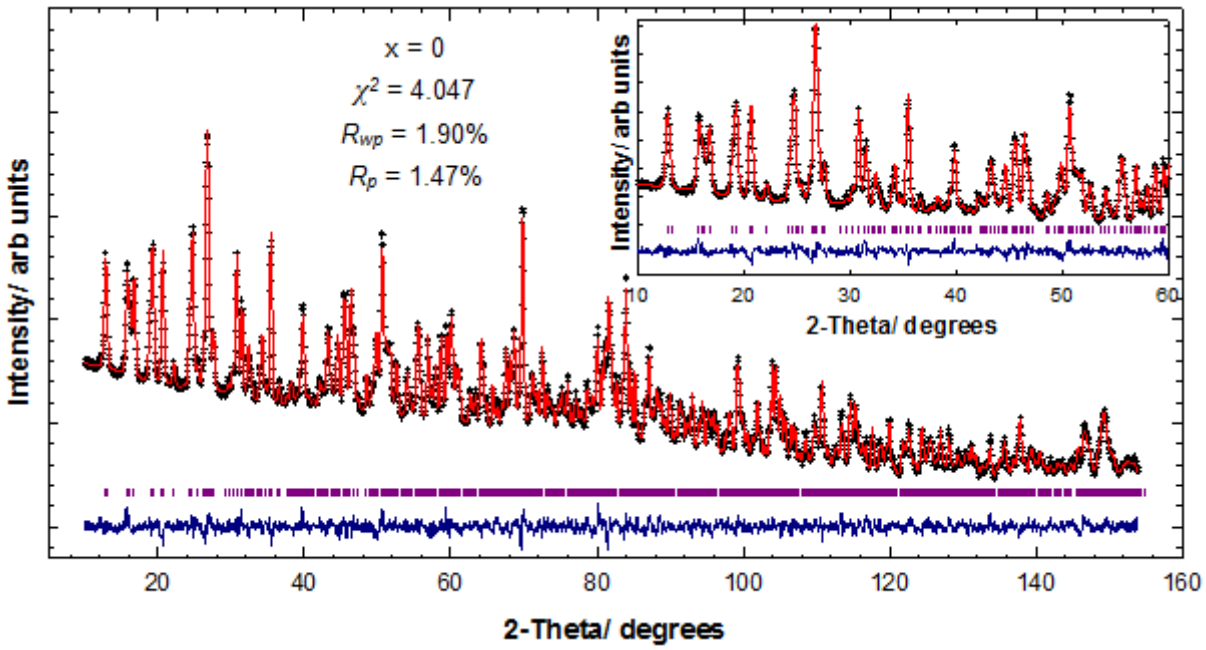

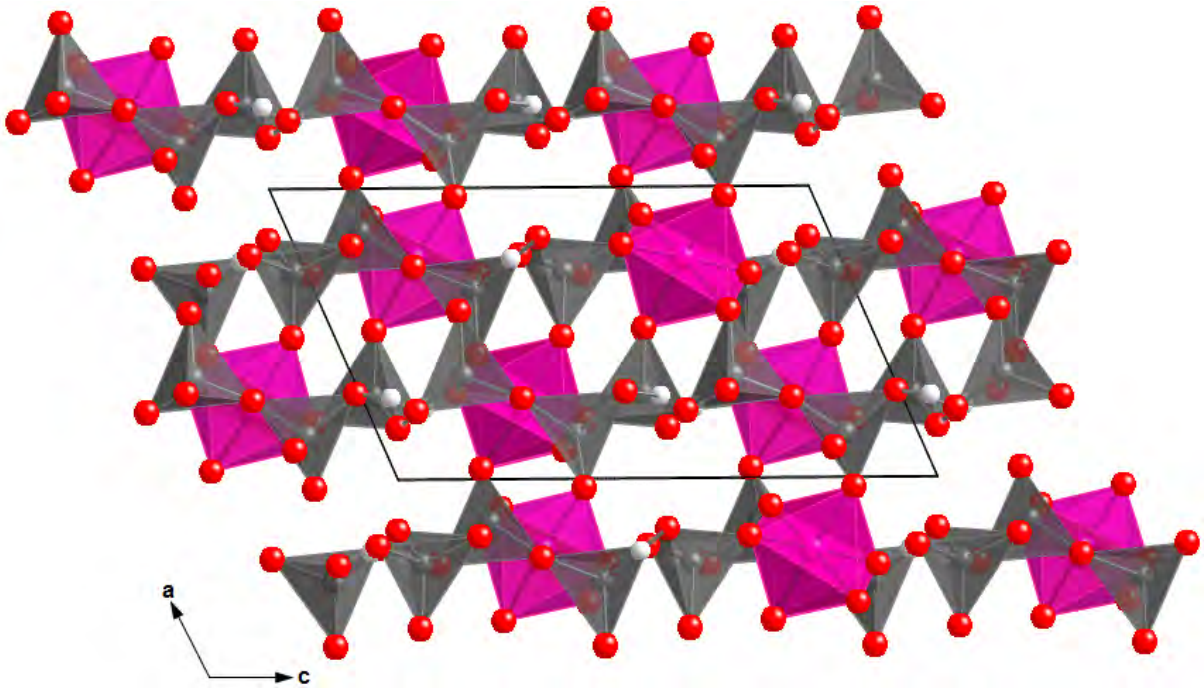

Figure 6.14: *Structure adopted by $Mn_xFe_{1-x}H_2P_3O_{10}$ compounds, showing TM-O_6 octahedra (pink), P_3O_{10} condensed phosphate tetrahedra (grey) and hydrogen atoms as white spheres. The thin black line defines the unit cell.*

Table 6.7: *Refined structural parameters from the 300 K diffraction data on the $Mn_xFe_{1-x}H_2P_3O_{10}$ series (x = 0.5, 0.25 and 0) with Bond Valence Sums[19] and Global Instability Index[21] Values*

		x = 0.5	x = 0.25	x = 0
Space group $P2_1/c$	***a*/ Å**	7.3351(2)	7.3584(1)	7.3702(2)
	***b*/ Å**	8.8079(3)	8.7935(1)	8.7861(2)
	***c*/ Å**	12.4331(4)	12.4008(2)	12.3736(3)
	***β*/ °**	113.531(1)	113.091(1)	112.758(1)
Mn/ Fe **4*e***	***x***	0.244(1)	0.2521(6)	0.2522(6)
	y	0.0752(9)	0.0732(4)	0.0719(4)
	z	0.2907(8)	0.2934(4)	0.2927(4)
	U_{iso}/ Å^2	0.008(2)	0.0019(9)	0.0091(7)
	Occupancy	0.462(5)/ 0.538(5)	0.236(5)/ 0.764(5)	0/ 1
	BVS	3.32/ 3.31	3.27/ 3.26	0/ 3.23
P(1) **4*e***	***x***	0.1492(8)	0.1442(7)	0.143(1)
	y	0.1071(6)	0.1035(5)	0.1038(7)
	z	0.8654(5)	0.8650(4)	0.8654(5)
	U_{iso}/ Å^2	0.011(1)	0.006(1)	0.011(1)
	BVS	4.95	4.94	5.12
P(2) **4*e***	***x***	0.3511(8)	0.3545(7)	0.3561(9)
	y	0.1064(6)	0.1033(5)	0.1090(6)
	z	0.7042(4)	0.7082(4)	0.7069(6)
	U_{iso}/ Å^2	0.005(1)	0.005(1)	0.003(1)
	BVS	5.01	4.88	4.95
P(3) **4*e***	***x***	0.7087(8)	0.7072(7)	0.711(1)
	y	0.1246(5)	0.1237(5)	0.1251(7)
	z	0.4768(5)	0.4769(4)	0.4797(6)
	U_{iso}/ Å^2	0.010(1)	0.004(1)	0.008(1)
	BVS	4.85	5.02	4.86
O(1) **4*e***	***x***	0.2706(8)	0.2708(7)	0.271(1)
	y	0.0375(5)	0.0343(5)	0.0331(6)
	z	0.7964(5)	0.7973(5)	0.7979(6)
	U_{iso}/ Å^2	0.015(1)	0.014(1)	0.011(1)
	BVS	2.13	2.15	2.00
O(2) **4*e***	***x***	0.2922(8)	0.2888(7)	0.2875(9)
	y	0.0804(6)	0.0784(5)	0.0732(7)
	z	0.9933(5)	0.9954(4)	0.9958(5)
	U_{iso}/ Å^2	0.016(1)	0.0108(9)	0.011(1)
	BVS	2.04	2.03	1.87
O(3) **4*e***	***x***	0.2334(8)	0.2379(6)	0.2366(9)
	y	0.4875(6)	0.4867(5)	0.4856(7)
	z	0.0914(5)	0.0921(4)	0.0920(5)
	U_{iso}/ Å^2	0.017(1)	0.0101(9)	0.010(1)
	BVS	2.15	2.13	2.01
O(4) **4*e***	***x***	0.0323(7)	0.0338(6)	0.0328(8)
	y	-0.0009(5)	-0.0033(5)	-0.0073(6)
	z	0.1619(4)	0.1601(4)	0.1614(5)
	U_{iso}/ Å^2	0.012(1)	0.011(1)	0.006(1)
	BVS	1.97	2.00	2.10

Table 6.7 continued...

		x = 0.5	x = 0.25	x = 0
	x	0.0993(7)	0.1035(6)	0.1042(8)
O(5)	***y***	0.2306(5)	0.2316(5)	0.2344(7)
4*e*	***z***	0.3324(4)	0.3355(4)	0.3372(5)
	U_{iso}/ Å^2	0.009(1)	0.008(1)	0.013(1)
	BVS	2.04	1.96	2.03
	x	0.4860(8)	0.4904(6)	0.4918(9)
O(6)	***y***	0.3548(6)	0.3526(5)	0.3478(7)
4*e*	***z***	0.9198(5)	0.9221(4)	0.9218(6)
	U_{iso}/ Å^2	0.018(1)	0.010(1)	0.020(2)
	BVS	1.92	2.01	1.86
	x	0.2976(8)	0.2988(6)	0.2995(8)
O(7)	***y***	0.2333(6)	0.2325(5)	0.2315(7)
4*e*	***z***	0.1806(4)	0.1837(4)	0.1867(5)
	U_{iso}/ Å^2	0.016(1)	0.011(1)	0.009(1)
	BVS	1.93	1.82	2.03
	x	0.5718(9)	0.5750(7)	0.5715(9)
O(8)	***y***	0.4318(6)	0.4329(5)	0.4313(7)
4*e*	***z***	0.2512(5)	0.2531(4)	0.2502(5)
	U_{iso}/ Å^2	0.014(1)	0.008(1)	0.014(1)
	BVS	1.74	1.78	1.86
	x	0.8003(7)	0.7972(6)	0.7987(8)
O(9)	***y***	0.4154(6)	0.4165(5)	0.4200(7)
4*e*	***z***	0.1049(4)	0.1044(4)	0.1053(5)
	U_{iso}/ Å^2	0.012(1)	0.0105(9)	0.013(1)
	BVS	1.85	1.90	1.98
	x	0.8240(8)	0.8233(7)	0.8282(9)
O(10)	***y***	0.2631(7)	0.2606(5)	0.2631(7)
4*e*	***z***	0.4575(5)	0.4576(4)	0.4614(5)
	U_{iso}/ Å^2	0.019(1)	0.014(1)	0.015(2)
	BVS	1.92	2.11	2.03
	x	0.278(2)	0.276(1)	0.277(2)
H(1)	***y***	0.141(1)	0.1395(9)	0.138(1)
4*e*	***z***	0.0548(9)	0.0536(7)	0.058(1)
	U_{iso}/ Å^2	0.036(3)	0.022(2)	0.031(3)
	BVS	0.80	0.89	0.76
	x	0.750(2)	0.754(2)	0.755(3)
H(2)	***y***	0.330(2)	0.329(1)	0.328(2)
4*e*	***z***	0.391(1)	0.4002(9)	0.399(1)
	U_{iso}/ Å^2	0.055(4)	0.045(3)	0.059(4)
	BVS	0.75	0.91	0.86
	GII	0.15	0.12	0.12

Table 6.8: *Selected Bond Distances (Å) and Angles (degrees) for the $Mn_xFe_{1-x}H_2P_3O_{10}$ series (x = 0.5, 0.25 and 0)*

	x = 0.5	x = 0.25	x = 0		x = 0.5	x = 0.25	x = 0
				O(4)-TM-O(5)	97.4(4)	96.5(2)	97.0(3)
				O(4)-TM-O(6)	173.9(6)	174.9(3)	175.8(4)
				O(4)-TM-O(7)	89.2(4)	88.3(3)	90.2(3)
				O(4)-TM-O(8)	88.1(4)	87.0(2)	88.4(3)
TM-O(4)	1.855(9)	1.918(6)	1.925(6)	**O(4)-TM-O(9)**	90.5(4)	90.3(2)	89.4(3)
TM-O(5)	1.925(9)	1.964(5)	2.000(7)	**O(5)-TM-O(6)**	88.4(4)	87.8(2)	86.3(3)
TM-O(6)	1.96(1)	1.963(6)	1.997(8)	**O(5)-TM-O(7)**	88.3(4)	87.0(2)	86.2(3)
TM-O(7)	2.10(1)	2.072(6)	2.039(7)	**O(5)-TM-O(8)**	172.0(5)	172.6(3)	172.0(3)
TM-O(8)	2.063(9)	2.012(5)	2.008(7)	**O(5)-TM-O(9)**	94.3(4)	93.6(2)	92.7(3)
TM-O(9)	2.027(9)	2.000(5)	1.970(7)	**O(6)-TM-O(7)**	88.9(4)	89.1(2)	87.3(3)
				O(6)-TM-O(8)	85.9(4)	88.5(2)	88.1(3)
				O(6)-TM-O(9)	91.0(4)	92.3(2)	93.2(3)
				O(7)-TM-O(8)	86.0(4)	86.6(2)	88.0(3)
				O(7)-TM-O(9)	177.4(5)	178.6(3)	178.8(3)
				O(8)-TM-O(9)	91.4(4)	92.9(2)	93.2(3)
				O(1)-P(1)-O(2)	101.7(4)	100.9(4)	99.6(5)
P(1)-O(1)	1.585(8)	1.599(7)	1.608(9)	**O(1)-P(1)-O(4)**	105.5(4)	107.9(4)	107.6(5)
P(1)-O(2)	1.534(8)	1.564(6)	1.575(9)	**O(1)-P(1)-O(5)**	110.5(4)	110.0(4)	110.6(5)
P(1)-O(4)	1.550(7)	1.506(7)	1.476(9)	**O(2)- P(1)-O(4)**	107.8(4)	108.4(4)	108.6(5)
P(1)-O(5)	1.491(7)	1.497(6)	1.465(8)	**O(2)-P(1)-O(5)**	115.1(5)	112.3(4)	113.7(5)
				O(4)-P(1)-O(5)	115.0(5)	116.2(4)	115.4(5)
				O(1)-P(2)-O(3)	102.3(4)	103.0(4)	100.1(4)
P(2)-O(1)	1.604(7)	1.582(6)	1.627(8)	**O(1)-P(2)-O(7)**	111.2(4)	111.1(4)	110.6(5)
P(2)-O(3)	1.559(7)	1.570(6)	1.587(9)	**O(1)-P(2)-O(8)**	106.3(4)	108.3(4)	106.9(5)
P(2)-O(7)	1.464(7)	1.500(6)	1.455(8)	**O(3)- P(2)-O(7)**	108.8(4)	107.0(4)	109.1(5)
P(2)-O(8)	1.523(7)	1.528(6)	1.508(9)	**O(3)-P(2)-O(8)**	110.5(4)	110.5(3)	109.8(4)
				O(7)-P(2)-O(8)	116.7(5)	116.2(4)	118.7(5)
				O(3)-P(3)-O(6)	107.7(4)	108.0(4)	107.1(5)
P(3)-O(3)	1.626(7)	1.618(6)	1.645(8)	**O(3)-P(3)-O(9)**	106.2(4)	106.5(3)	105.5(5)
P(3)-O(6)	1.510(7)	1.483(6)	1.511(9)	**O(3)-P(3)-O(10)**	103.4(4)	103.3(4)	104.0(5)
P(3)-O(9)	1.503(7)	1.497(6)	1.488(8)	**O(6)-P(3)-O(9)**	117.9(4)	117.9(4)	119.3(6)
P(3)-O(10)	1.557(7)	1.548(6)	1.556(8)	**O(6)-P(3)-O(10)**	112.7(4)	112.3(4)	111.1(5)
				O(9)-P(3)-O(10)	107.8(4)	107.7(4)	108.5(5)
H(1)-O(2)	0.97(1)	0.93(1)	0.99(1)	**O(2)-H(1)-O(7)**	169(1)	167.3(8)	168(1)
H(1)---O(7)	1.72(1)	1.758(9)	1.74(1)				
H(2)-O(10)	0.99(1)	0.92(1)	0.94(2)	**O(8)-H(2)-O(10)**	170(1)	166.4(9)	169(1)
H(2)---O(8)	1.93(1)	2.01(1)	2.03(2)				

The structure (as shown in Figures 6.14 and 6.15) can be described as a three-dimensional network of TM-O_6 octahedra corner-linked to four dihydrogen triphosphate units, two of them being connected in a bidentate fashion along a common edge of the octahedron. The OH groups of the triphosphate units are

located at the terminal $P(1)O_4$ and $P(3)O_4$ tetrahedra, with hydrogen bonds formed to the central $P(2)O_4$ tetrahedron of other triphosphate units to give infinite chains. Longer P-O bond lengths were observed to the bridging oxygen, intermediate bond lengths to those oxygens participating in hydrogen bonding and shorter P-O bonds to the terminal oxygen atoms. The triphosphate group possesses no internal symmetry, giving rise to three distinct phosphorus atoms and ten oxygen atoms. This is a common feature amongst a number of triphosphate systems,[30] though can be contrasted to the α-$RbMn_xFe_{1-x}HP_3O_{10}$ system (Chapter 5) in which the triphosphate unit possesses a binary axis of symmetry to give five distinct oxygen atoms.

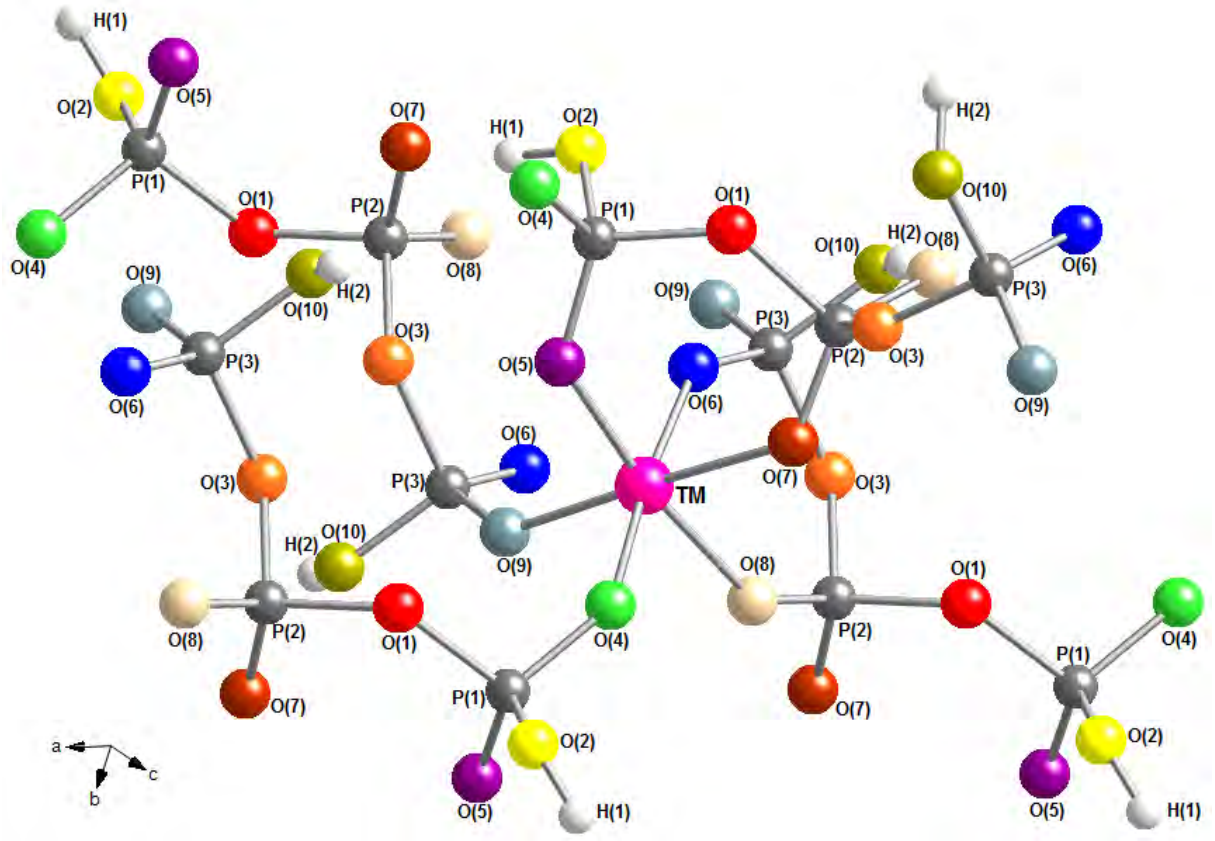

Figure 6.15: *Orientation of the triphosphate ligands about the TM centre in the $Mn_xFe_{1-x}H_2P_3O_{10}$ structure type. The TM atom (centre), phosphorus and hydrogen atoms are shown as pink, grey and white spheres, respectively.*

Across the x = 0.5, 0.25 and 0 compositions of $Mn_xFe_{1-x}H_2P_3O_{10}$, BVS[19] calculations (Table 6.7) showed most atoms in the structure to be slightly overbonded or underbonded. GII[21] values of 0.15 vu for x = 0.5 and 0.12 vu for x = 0.25 and 0 showed that these discrepancies were relatively small for the latter two compounds, with no significant lattice strain present in the structure.

6.3.2.2 Trends and Distortions

Figure 6.16 shows that within the $Mn_xFe_{1-x}H_2P_3O_{10}$ system, the x = 0.5 compound adopts a highly distorted octahedral coordination sphere, with one short TM-O bond length, two intermediate bond lengths and three relatively long bonds.

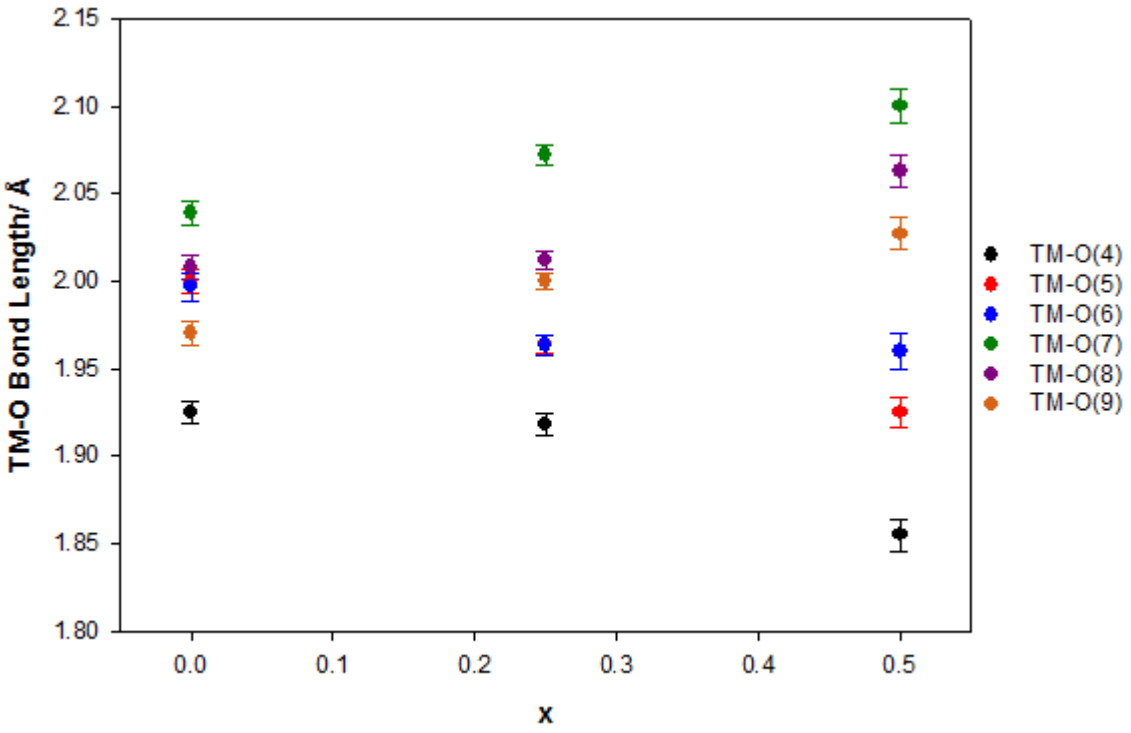

Figure 6.16: *Average bond lengths of the TM-O_6 octahedron as a function of varying Mn^{3+} content in the $Mn_xFe_{1-x}H_2P_3O_{10}$ system.*

As the amount of iron in the system was increased, an increase in the TM-O(4), TM-O(5) and TM-O(6) bond lengths occurred but a decrease in TM-O(7), TM-O(8)

and TM-O(9), overall giving a more regular octahedral environment for x = 0. It should be noted however that even in the pure iron compound the six bond lengths were not completely matched in length, with the largest distance being ~2.04 Å and the shortest being ~1.93 Å *cf.* ~1.99 Å expected for a typical Fe-O bond length. It is possible that this distorted arrangement occurs in order to satisfy the steric requirements of the triphosphate anions. Figure 6.17 shows that the corresponding P-O bond lengths (except P(2)-O(7) and P(3)-O(6), which showed no clear trend) decreased with increasing Fe content. While these bond lengths within the PO_4 tetrahedra decreased, the effect appeared to be compensated for by a general increase in the remaining P-O bond lengths with increasing iron content.

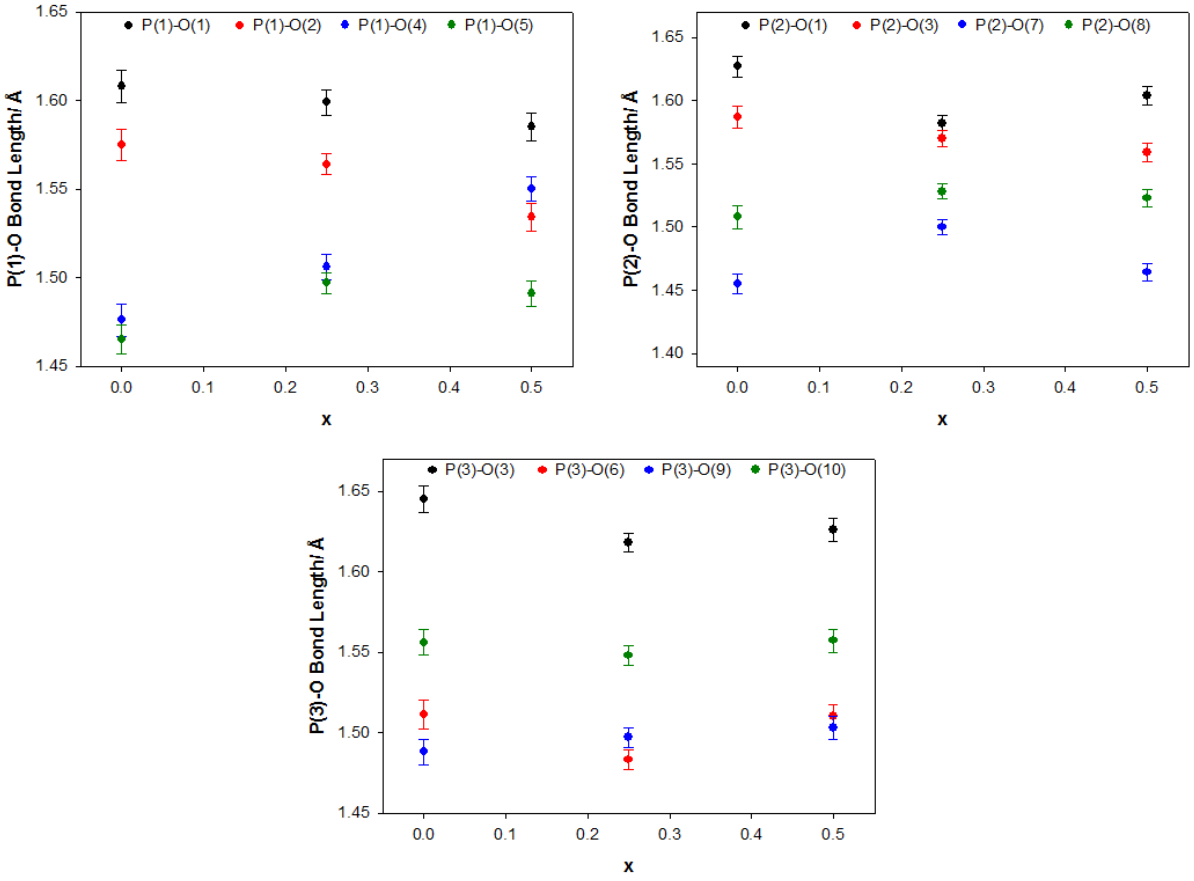

Figure 6.17: *Average O-P-O bond lengths as a function of varying Mn^{3+} content in the $Mn_xFe_{1-x}H_2P_3O_{10}$ solid solution.*

Table 6.8 shows that small variations occurred in the O-TM-O angles across the series though in general these angles were close to the values of an ideal octahedron, ranging from ~86-97° and ~172-179°. The O-P-O angles remained similar across the series, ranging from ~100-116°, ~100-119° and ~103-119° for the $P(1)O_4$, $P(2)O_4$ and $P(3)O_4$ tetrahedrons, respectively.

Figures 6.18 and 6.19 show that with increasing Fe content, there was a general increase in the *a* lattice parameter and volume of the unit cell but a decrease in *b*, *c* and *β*. Octahedral Mn^{3+} and Fe^{3+} have virtually identical ionic radii of 0.65 Å,[31] and so we would not expect size differences between these two cations to have a significant influence on the lattice parameters.

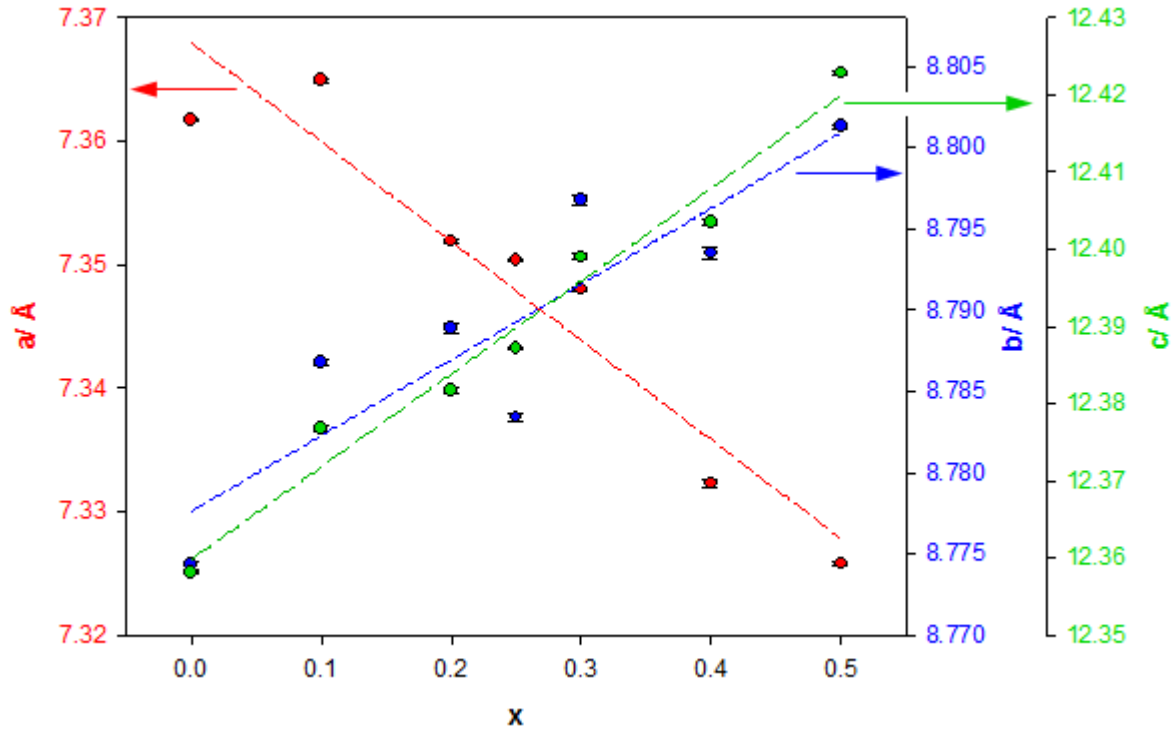

Figure 6.18: *Change in the a-, b- and c-lattice parameters with varying Mn^{3+} content in the $Mn_xFe_{1-x}H_2P_3O_{10}$ system (XRD data). Arrows indicate the direction of the axes.*

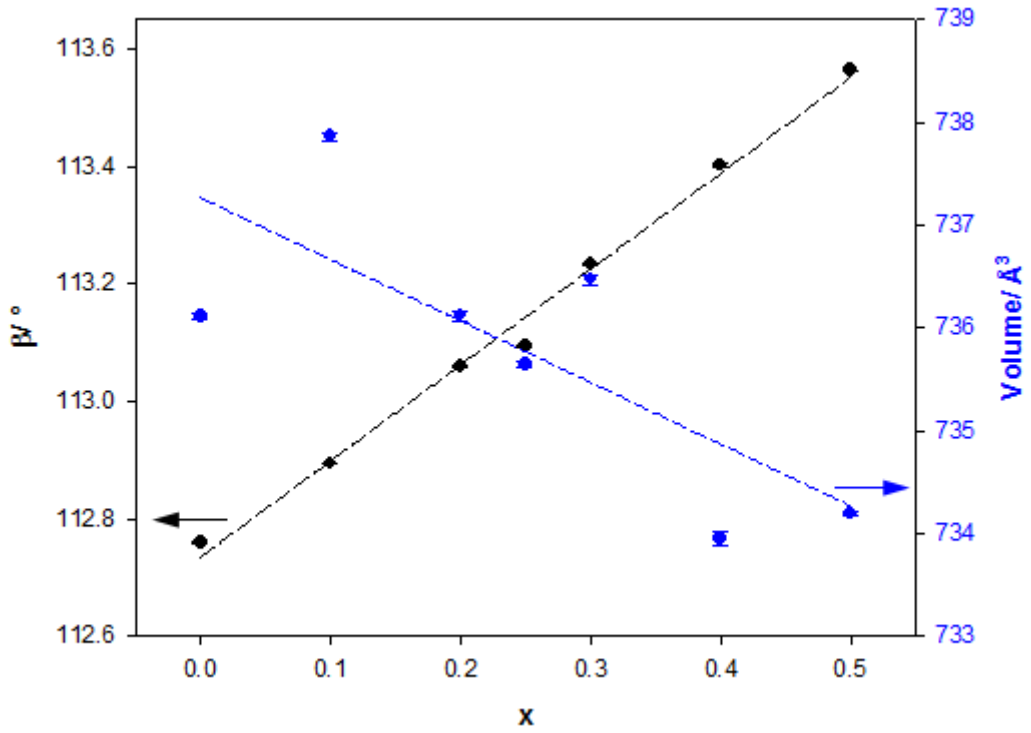

Figure 6.19: *Change in β-parameter and volume of unit cell with varying Mn^{3+} content in the $Mn_xFe_{1-x}H_2P_3O_{10}$ system (XRD data). Arrows indicate direction of the axes.*

A closer inspection of the TM coordination sphere (Figure 6.20(a)) shows that the direction of the TM-O(4)/ TM-O(6) and TM-O(5)/ TM-O(8) bonds crosses the trajectory of the *a*-axis of the structure and as such an increase in these bond lengths with increasing Fe content (except TM-O(8)) can explain the corresponding increase in the *a*-parameter. Similarly Figure 6.20(b) shows that the TM-O(5)/ TM-O(8) and TM-O(7)/ TM-O(9) bonds are directed across the *b*-axis of the structure, and so a decrease in the latter three with increasing Fe content can explain the corresponding decrease in the *b*-parameter. TM-O(4)/ TM-O(6) and TM-O(7)/ TM-O(9) cross the *c*-axis of the structure (Figure 6.20(c)), but this time the former two bond lengths increase with iron content while the latter two decrease. Overall a decrease in the *c*-parameter is observed, most likely because the direction of the TM-O(7)/ TM-O(9) bonds is more closely correlated with the *c*-axis, thereby exhibiting a greater influence.

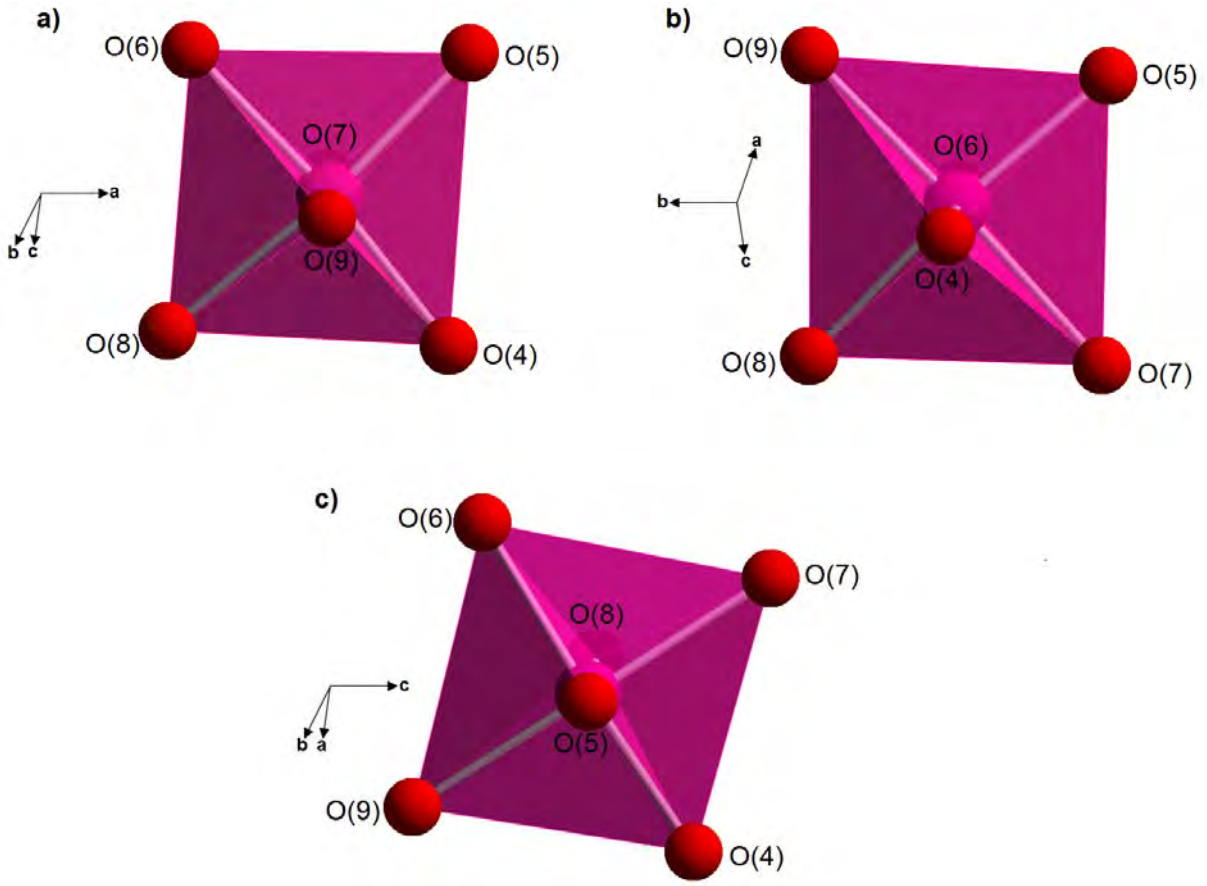

Figure 6.20: *The orientation of the TM-O_6 octahedron with respect to the unit cell axes in the $Mn_xFe_{1-x}H_2P_3O_{10}$ system.*

Clearly there are a number of competing effects at the TM coordination sphere which influence the unit cell parameters of the $Mn_xFe_{1-x}H_2P_3O_{10}$ system. A decrease in β-angle and increase in volume is observed with increasing Fe content, but as there are no TM-O bonds directly situated along the unit cell axes, it is difficult to assess the extent of their impact and the reason for this change. Within the TM-O_6 coordination sphere, with an increasing amount of Fe, three of the bonds move further away from the TM centre, with the total increase in their length being 9.6%, while three move closer in and give a total decrease in length of 8.4%. Indeed, the average TM-O bond length changes from ~1.988 Å for x = 0.5 and 0.25 to ~1.990 Å for x = 0. It is therefore possible that this very small expansion of the TM coordination

sphere gives less repulsion between the oxygen ligands, allowing the *a*- and c-axes to be bought closer together i.e. for β to decrease and resulting in a small increase in the volume.

UV-Vis spectroscopy was used to further probe the Mn^{3+} environment in the $Mn_xFe_{1-x}H_2P_3O_{10}$ compounds. Transitions occurring in the UV region of the spectra (Figure 6.21) were tentatively assigned as $O^{2-} \rightarrow Mn^{3+}$ and/ or $O^{2-} \rightarrow Fe^{3+}$ LMCT while those occurring in the visible region as d→d transitions. For x = 0 the PeakFit[22] program modelled two transitions in the visible region, which was consistent with the $^6A_{1g}$ ground state of Fe^{3+}. For compounds with x > 0, these peaks were expected to be obscured by the more intense, spin allowed d→d transitions exhibited by Mn^{3+}, allowing the spectra to reveal details on the manganese coordination environment.

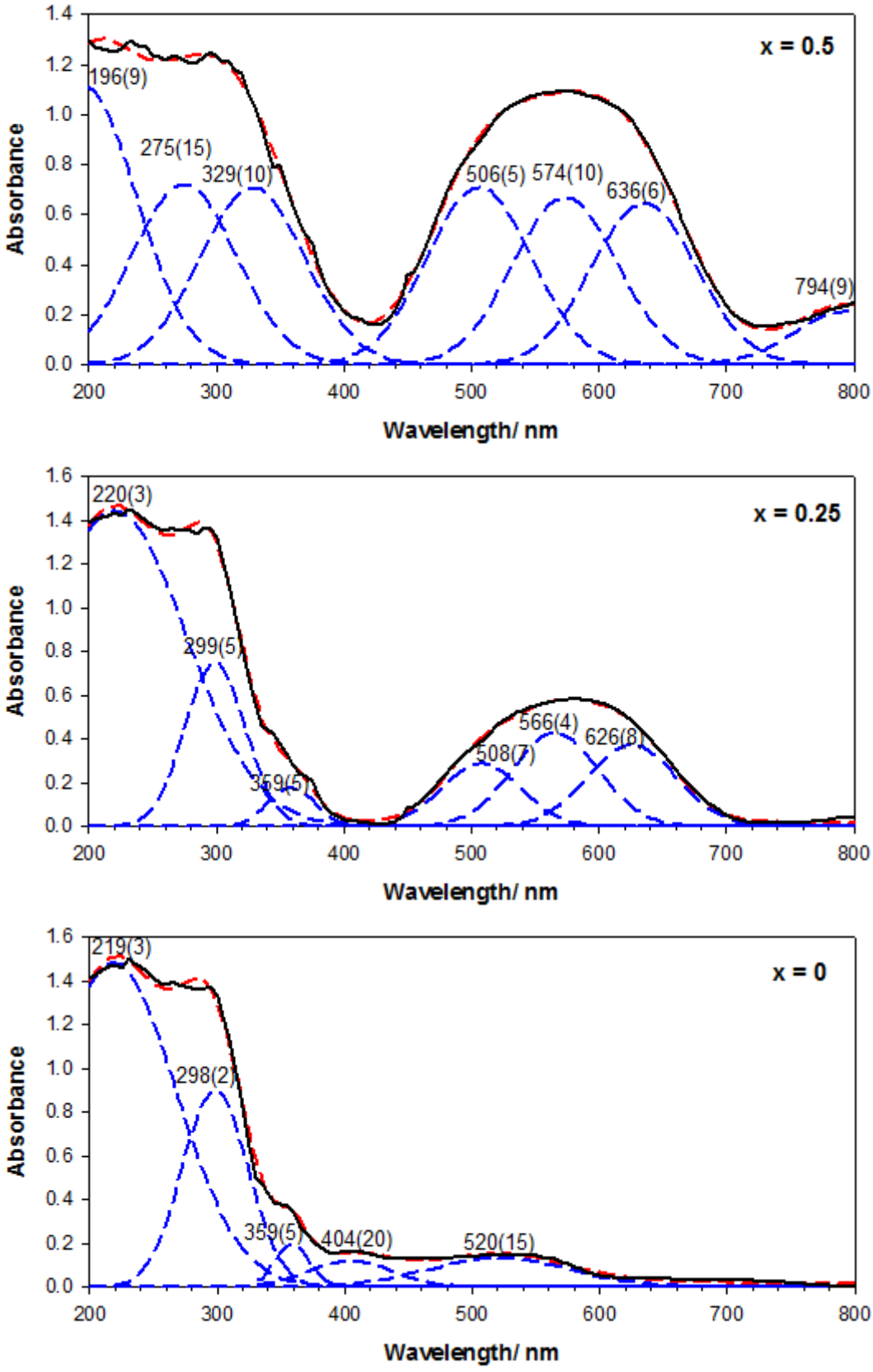

Figure 6.21: *UV-Vis spectra of the $Mn_xFe_{1-x}H_2P_3O_{10}$ series, showing raw data (—), fitted Gaussian bands (---) and sum of the fitted Gaussian bands (---). Peak positions are marked.*

For x = 0.5 four transitions were modelled in the visible region, suggesting a highly distorted MnO_6 coordination sphere, beyond a standard [4+2] elongation. As the centre of inversion in the MnO_6 unit is lost, such transitions become both spin and Laporte allowed and contribute to the intense colouration exhibited by this particular member, as can be seen in Figure 6.22. For x = 0.25 three d→d transitions were seen, suggesting a [4+2] elongation of the MnO_6 coordination sphere. As there is now a centre of inversion present, transitions are Laporte forbidden and as such this member exhibited a different, less intense purple colouration which could be related to the change in the manganese coordination sphere. Given that the second transition ($^5B_{1g} \rightarrow {}^5B_{2g}$) coincides with the average value of 10*Dq*, the value was calculated to be 211(1) kJ mol^{-1} for x = 0.25, which is in the range of 191-251 kJ mol^{-1} expected for high spin Mn^{3+} complexes.[32] Finally, the Fe end member showed a weak pink-brown colouration, consistent with the transitions seen in the visible region of its spectrum.

x = 0.5 x = 0.25 x = 0

Figure 6.22: *Colouration of the $Mn_xFe_{1-x}H_2P_3O_{10}$ series*

6.3.2.3 Thermal Stability

Figure 6.23 shows that the thermal stability of the $Mn_xFe_{1-x}H_2P_3O_{10}$ phases in N_2 increased slightly with the greater amount of iron in the system, though was inherently limited by the presence of protons in the structure, which led to condensation in an endothermic event above ~430°C; a similar decomposition

temperature to that observed for the α-$RbMn_xFe_{1-x}HP_3O_{10}$ system (Chapter 5, section 5.3.2). Table 6.9 summarises the decomposition temperatures and the mass losses observed. In all cases the mass spectrum confirmed that a loss of water occurred in the principal mass loss step, and XRD showed the final product to be the corresponding polyphosphate. Indeed, the mass losses observed were close to the expected 1 mole of water being lost from the host, as detailed in Equation 6.2: -

$$Mn_xFe_{1-x}H_2P_3O_{10} \xrightarrow{-H_2O} Mn_xFe_{1-x}P_3O_9 \qquad \textbf{Equation 6.2}$$

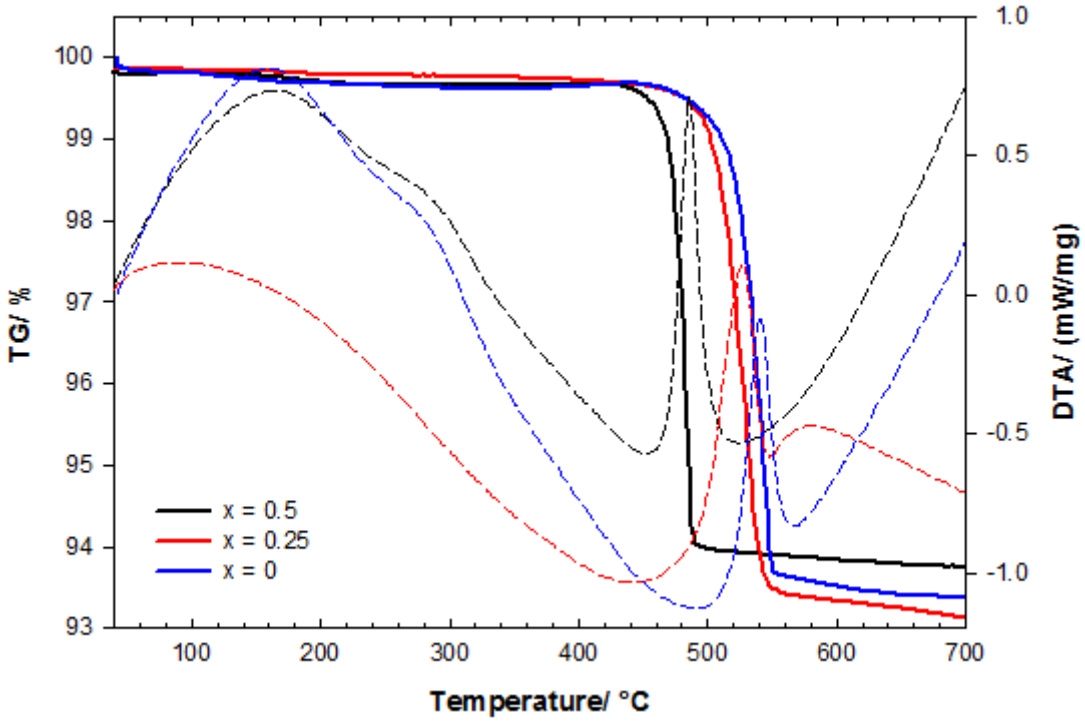

Figure 6.23: *TGA plots for $Mn_xFe_{1-x}H_2P_3O_{10}$ compounds. Solid and dashed lines show TG and DTA signals, respectively.*

Table 6.9: *Summary of thermal decomposition of $Mn_xFe_{1-x}H_2P_3O_{10}$ phases. Decomposition products in inverted commas indicate that the Mn:Fe ratio was not quantified.*

x	Approximate decomposition temperature/ °C	% mass loss	Moles water lost	Product after thermal decomposition
0.5	430	5.90	1.02	"$Mn_{0.5}Fe_{0.5}P_3O_9$"
0.25	460	6.49	1.13	"$Mn_{0.25}Fe_{0.75}P_3O_9$"
0	460	6.26	1.09	FeP_3O_9

6.3.2.4 Magnetic Properties

Figure 6.24 shows the magnetic susceptibility measurements for the x = 0.5, 0.25 and 0 members and the Curie-Weiss fits to the data, while Table 6.10 summarises the parameters calculated from the latter. The x = 0.5 and 0 members showed an antiferromagnetic (AFM) response in the ZFCFW measurement and a ferromagnetic (FM) component in the FCFW measurement, suggesting canted antiferromagnetism. For x = 0.25, a small divergence was seen between the ZFCFW and FCFW measurements, suggesting spin glass behaviour. The Néel temperatures for x = 0.5 and 0.25 (~11.8 K) were found to be lower than that of x = 0 ($T_N \approx 17$ K), suggesting disorder and/ or competing interactions between Mn^{3+} and Fe^{3+}. For x = 0.25, the effective moment was found to be close to the expected spin-only moment, while for x = 0.5 and 0 it was found to be slightly higher and lower than μ_{SO}, respectively.

Table 6.10: *Summary of parameters determined from the susceptibility data on the $Mn_xFe_{1-x}H_2P_3O_{10}$ series*

x	θ/ K	$\mu_{eff}/\ \mu_B$	$\mu_{so}/\ \mu_B$	$\mu_{obs}/\ \mu_B$ [25]
0.5	-35(1)	5.73(2)	5.41	
0.25	-23.5(3)	5.643(4)	5.67	
0	-27.2(3)	5.568(4)	5.92	5.70-6.00

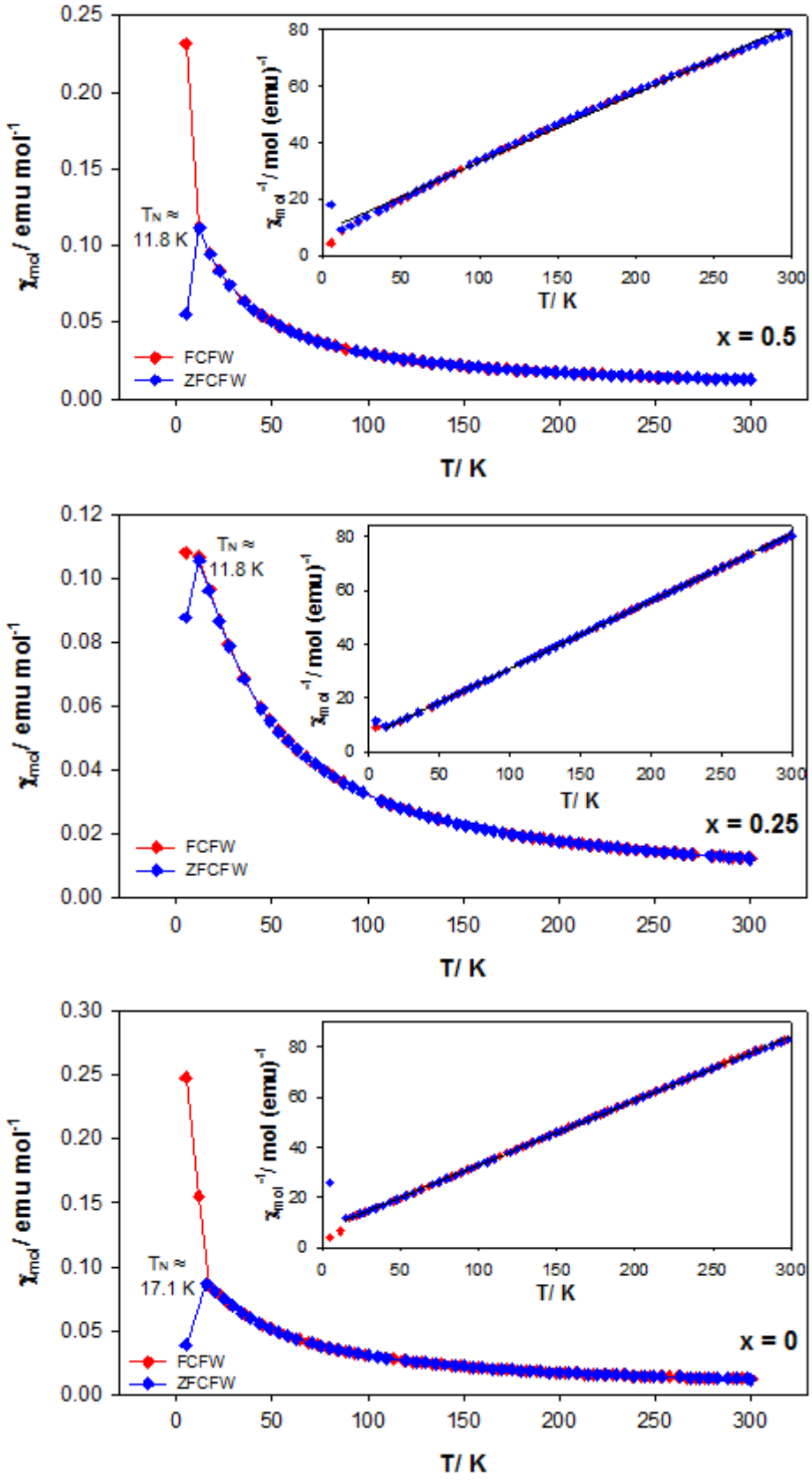

Figure 6.24: *Plots of molar susceptibility against temperature for the $Mn_xFe_{1-x}H_2P_3O_{10}$ system (x = 0.5, 0.25 and 0), with insets showing Curie-Weiss fits to the data.*

After the nuclear contribution was fitted to the 2 K neutron diffraction data, the patterns showed evidence for additional peaks and intensity. This allowed a magnetic unit cell to be determined which was found to be commensurate with the nuclear cell. The magnetic phase was modelled separately in space group *P*1, with the magnetic intensities fitted with a calculated form factor for Mn^{3+} and Fe^{3+}.[33] The relative orientations of the four TM spins in the unit cell were found to be (0.25, 0.07, 0.29)+, (0.75, 0.57, 0.21)-, (0.75, 0.93, 0.71)- and (0.25, 0.43, 0.79)+, though the components of the moments along the *x*, *y* and *z* directions differed across the series. The final refinements are shown in Figure 6.25, structural parameters of the magnetic phase in Table 6.11 and selected bond lengths and angles in Table 6.12.

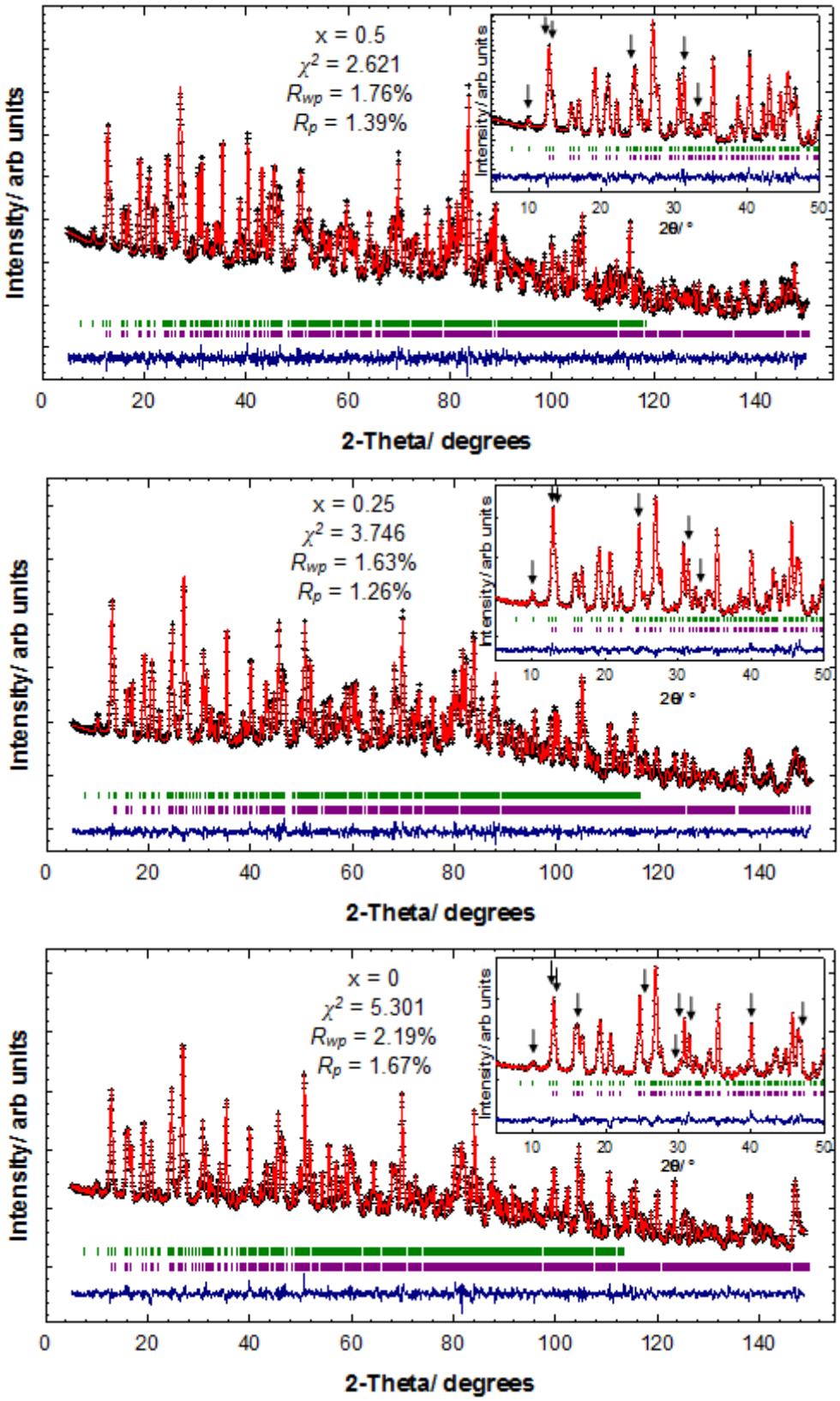

Figure 6.25: *Observed (+), calculated (-) and difference profiles (-) for the 2 K Rietveld refinements carried out on the $Mn_xFe_{1-x}H_2P_3O_{10}$ series. Reflections for the magnetic and nuclear phases are shown with green and purple markers, respectively. The inset shows the low angle region enlarged, with arrows indicating peaks with significant magnetic intensity.*

Table 6.11: *Structural parameters for the magnetic phases of $Mn_xFe_{1-x}H_2P_3O_{10}$ compounds*

		x = 0.5	**x = 0.25**	**x = 0**
Space group *P*1	***a*/ Å**	7.3141(2)	7.3411(1)	7.3520(2)
	***b*/ Å**	8.8033(2)	8.7900(2)	8.7820(2)
	***c*/ Å**	12.4285(3)	12.3854(3)	12.3476(3)
	***α, β, γ* / °**	90, 113.804(1), 90	90, 113.299(1), 90	90, 113.023(1), 90
Mn(1)/ Fe(1) 1*a*	***x***	0.249(1)	0.2506(7)	0.2481(6)
	y	0.0734(8)	0.0727(4)	0.0710(4)
	z	0.2943(8)	0.2934(4)	0.2935(4)
	U_{iso}/ Å^2	0.009(2)	0.002(1)	0.0032(7)
	Occupancy	0.460(6)/ 0.540(6)	0.246(6)/ 0.754(6)	1
	M_x / μ_B	-1.3(2)	1.6(2)	1.5(2)
	M_y / μ_B	1.5(2)	1.3(3)	2.7(2)
	M_z / μ_B	2.9(2)	-3.3(1)	2.4(3)
	$\|M\|$ / μ_B	3.50(6)	3.86(5)	3.93(8)
Mn(2)/ Fe(2) 1*a*	***x***	0.751(1)	0.7494(7)	0.7519(6)
	y	0.5742(4)	0.5718(2)	0.5702(2)
	z	0.2046(4)	0.2058(2)	0.2059(2)
	U_{iso}/ Å^2	0.009(2)	0.002(1)	0.0032(7)
	Occupancy	0.460(6)/ 0.540(6)	0.246(6)/ 0.754(6)	1
	M_x / μ_B	1.3(2)	-1.6(2)	-1.5(2)
	M_y / μ_B	-1.5(2)	-1.3(3)	-2.7(2)
	M_z / μ_B	-2.9(2)	3.3(1)	-2.4(3)
	$\|M\|$ / μ_B	3.50(6)	3.86(5)	3.93(8)
Mn(3)/ Fe(3) 1*a*	***x***	0.751(1)	0.7494(7)	0.7519(6)
	y	0.9266(8)	0.9273(4)	0.9290(4)
	z	0.7057(8)	0.7066(8)	0.7065(4)
	U_{iso}/ Å^2	0.009(2)	0.002(1)	0.0032(7)
	Occupancy	0.460(6)/ 0.540(6)	0.246(6)/ 0.754(6)	1
	M_x / μ_B	1.3(2)	-1.6(2)	-1.5(2)
	M_y / μ_B	-1.5(2)	-1.3(3)	-2.7(2)
	M_z / μ_B	-2.9(2)	3.3(1)	-2.4(3)
	$\|M\|$ / μ_B	3.50(6)	3.86(5)	3.93(8)
Mn(4)/ Fe(4) 1*a*	***x***	0.249(1)	0.2506(7)	0.2481(6)
	y	0.4258(4)	0.4282(2)	0.4297(2)
	z	0.7954(4)	0.7942(2)	0.7941(2)
	U_{iso}/ Å^2	0.009(2)	0.002(1)	0.0032(7)
	Occupancy	0.460(6)/ 0.540(6)	0.246(6)/ 0.754(6)	1
	M_x / μ_B	-1.3(2)	1.6(2)	1.5(2)
	M_y / μ_B	1.5(2)	1.3(3)	2.7(2)
	M_z / μ_B	2.9(2)	-3.3(1)	2.4(3)
	$\|M\|$ / μ_B	3.50(6)	3.86(5)	3.93(8)

Table 6.12: *Selected Bond Distances (Å) and Angles (degrees) for the $Mn_xFe_{1-x}H_2P_3O_{10}$ series at 2 K*

	x = 0.5	x = 0.25	x = 0		x = 0.5	x = 0.25	x = 0
				O(4)-TM-O(5)	96.4(4)	97.0(3)	97.5(3)
				O(4)-TM-O(6)	174.0(6)	174.1(3)	173.4(4)
				O(4)-TM-O(7)	88.0(4)	88.0(3)	88.2(3)
				O(4)-TM-O(8)	86.7(4)	86.2(3)	87.5(3)
TM-O(4)	1.913(9)	1.914(6)	1.926(6)	**O(4)-TM-O(9)**	89.1(3)	90.0(2)	90.8(3)
TM-O(5)	1.940(8)	1.957(6)	1.979(6)	**O(5)-TM-O(6)**	88.7(4)	88.3(2)	87.2(3)
TM-O(6)	1.93(1)	1.961(7)	1.997(7)	**O(5)-TM-O(7)**	87.8(4)	87.6(3)	86.2(3)
TM-O(7)	2.11(1)	2.078(6)	2.051(7)	**O(5)-TM-O(8)**	172.5(5)	173.2(3)	169.9(3)
TM-O(8)	2.044(9)	2.023(6)	2.033(7)	**O(5)-TM-O(9)**	94.1(4)	93.5(3)	95.3(3)
TM-O(9)	2.02(1)	2.011(6)	1.955(7)	**O(6)-TM-O(7)**	89.2(4)	89.6(3)	87.4(3)
				O(6)-TM-O(8)	87.8(4)	88.3(2)	87.2(3)
				O(6)-TM-O(9)	93.6(5)	92.4(2)	93.4(3)
				O(7)-TM-O(8)	85.5(4)	86.4(3)	85.2(3)
				O(7)-TM-O(9)	176.6(5)	177.7(3)	178.3(3)
				O(8)-TM-O(9)	92.7(4)	92.6(2)	93.4(3)
				O(1)-P(1)-O(2)	101.4(4)	102.5(4)	99.8(4)
P(1)-O(1)	1.610(7)	1.597(7)	1.598(8)	**O(1)-P(1)-O(4)**	105.9(4)	106.8(4)	107.8(5)
P(1)-O(2)	1.541(8)	1.544(7)	1.545(8)	**O(1)-P(1)-O(5)**	110.5(4)	111.1(4)	108.9(5)
P(1)-O(4)	1.523(7)	1.554(7)	1.491(9)	**O(2)- P(1)-O(4)**	108.7(4)	108.1(4)	109.9(5)
P(1)-O(5)	1.485(7)	1.497(7)	1.462(8)	**O(2)-P(1)-O(5)**	114.7(4)	115.0(4)	113.6(5)
				O(4)-P(1)-O(5)	114.5(4)	112.6(4)	115.5(5)
				O(1)-P(2)-O(3)	102.7(4)	103.8(4)	102.7(5)
P(2)-O(1)	1.599(7)	1.574(6)	1.625(8)	**O(1)-P(2)-O(7)**	110.9(4)	111.8(4)	111.4(4)
P(2)-O(3)	1.567(6)	1.548(7)	1.573(9)	**O(1)-P(2)-O(8)**	106.4(4)	107.6(4)	105.7(5)
P(2)-O(7)	1.488(7)	1.503(7)	1.491(8)	**O(3)- P(2)-O(7)**	109.1(4)	106.9(4)	109.1(5)
P(2)-O(8)	1.508(6)	1.539(7)	1.532(9)	**O(3)-P(2)-O(8)**	110.9(4)	111.3(4)	110.8(5)
				O(7)-P(2)-O(8)	116.0(4)	114.9(4)	116.3(5)
				O(3)-P(3)-O(6)	108.3(4)	108.8(4)	107.8(5)
P(3)-O(3)	1.600(6)	1.633(6)	1.634(8)	**O(3)-P(3)-O(9)**	106.4(4)	106.3(4)	106.9(4)
P(3)-O(6)	1.506(7)	1.485(7)	1.513(9)	**O(3)-P(3)-O(10)**	105.0(4)	104.0(4)	104.1(4)
P(3)-O(9)	1.503(7)	1.495(7)	1.479(8)	**O(6)-P(3)-O(9)**	117.4(4)	117.5(4)	118.7(5)
P(3)-O(10)	1.559(7)	1.569(6)	1.583(7)	**O(6)-P(3)-O(10)**	111.0(4)	112.4(4)	110.2(4)
				O(9)-P(3)-O(10)	108.0(4)	106.7(4)	108.2(5)
H(1)-O(2)	0.96(1)	0.94(1)	0.96(1)	**O(2)-H(1)-O(7)**	167.3(9)	166(1)	172(1)
H(1)---O(7)	1.70(1)	1.72(1)	1.70(1)				
H(2)-O(10)	1.00(1)	0.97(1)	1.00(2)	**O(8)-H(2)-O(10)**	172(1)	167.5(8)	172(1)
H(2)---O(8)	1.87(1)	1.93(1)	1.92(2)				

A similar pattern of bond lengths and angles to those observed at room temperature was seen, though GII values were found to be a little higher for x = 0.25 and 0 (GII = 0.14 vu (x = 0.5), 0.15 vu (x = 0.25) and 0.16 vu (x = 0)). All compounds were found to adopt the same magnetic structure type, shown in Figure 6.26.

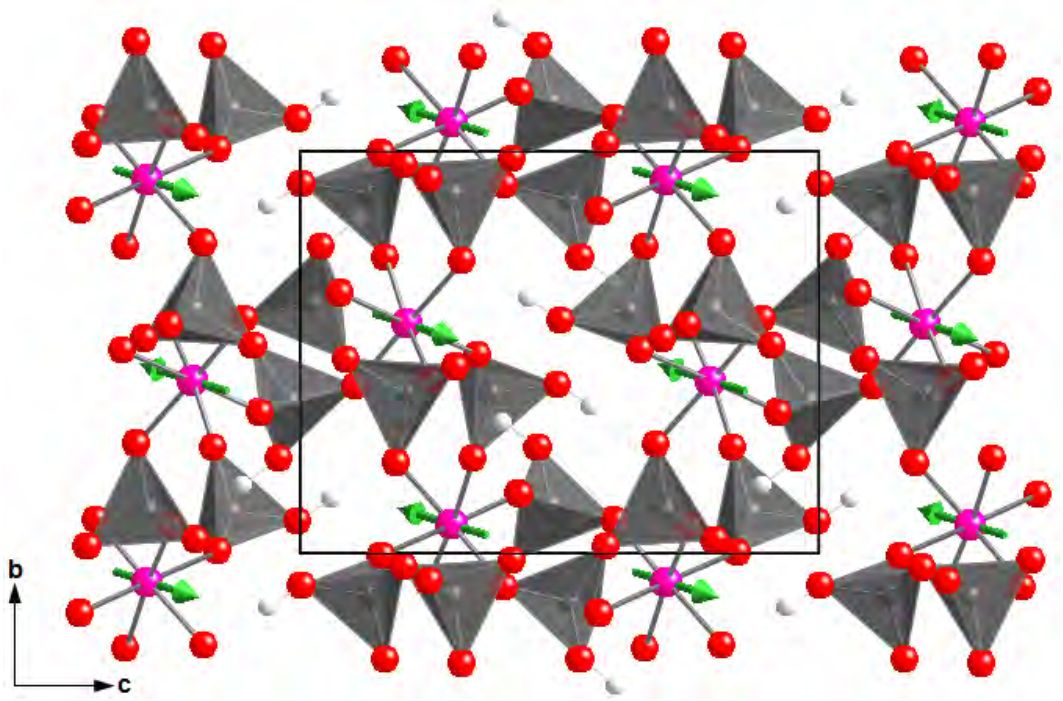

Figure 6.26: *Magnetic structure type adopted by $Mn_xFe_{1-x}H_2P_3O_{10}$ compounds, with the orientation of magnetic moments on the TM ions (pink spheres) shown with green arrows and condensed phosphate tetrahedra shown in grey. The thin black line defines the unit cell.*

The TM ions within the structure are situated too far apart for direct exchange to occur, and as such only the shortest entity linking them was considered *i.e.* an orthophosphate unit. Each TM ion was found to be linked to five others *via* six different TM-O-P-O-TM pathways, with all interactions found to be AFM, as can be seen in Figure 6.27. A similar observation was also made for the x = 0.25 and 0 members of the α-$RbMn_xFe_{1-x}HP_3O_{10}$ system (Chapter 5, section 5.3.3.4). The magnitude of the moments was found to be 3.50(6) μ_B for x = 0.5, 3.86(5) μ_B for x =

0.25 and 3.93(8) μ_B for x = 0, which were lower than the respective saturated moments of 4.5 μ_B, 4.75 μ_B and 5.0 μ_B, suggesting disorder between the moments.

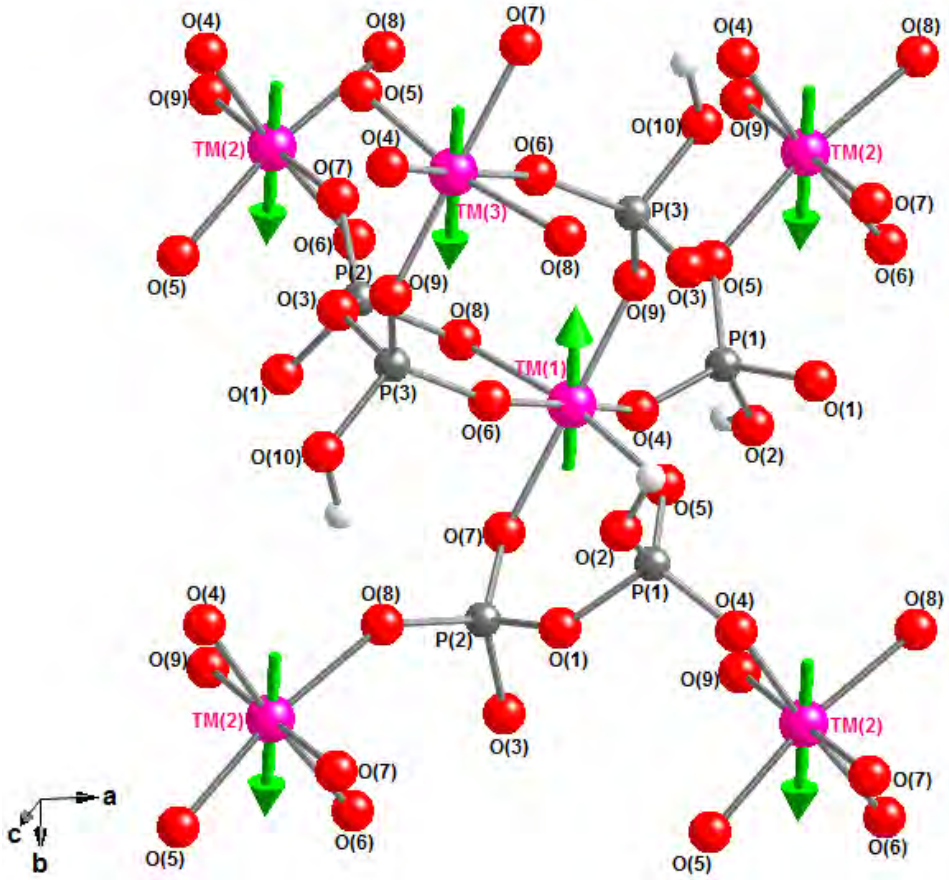

Figure 6.27: *Nearest neighbour TM---TM interactions in $Mn_xFe_{1-x}H_2P_3O_{10}$ compounds. TM, P, O and H atoms are shown as pink, grey, red and white spheres, respectively.*

Table 6.13 shows that within the TM-O-P-O-TM linkages, the geometries of the interacting species remained similar across the series. O---O separations ranged from 2.49-2.58 Å, TM---TM separations between 5.11-6.11 Å and the TM-O-P angles between 127.6-142.2°, with these variations having no effect on the sign of the interaction.

Table 6.13: *Summary of the antiferromagnetic exchange pathways present in $Mn_xFe_{1-x}H_2P_3O_{10}$ (x = 0.5, 0.25 and 0) and geometries of the interacting species.*

Exchange Pathway	x	O-P-O	TM-O-P	TM-O*-P	O---O	TM---TM
TM(1)-O(4)-P(1)-O(5)-TM(2) **TM(1)-O(5)-P(1)-O(4)-TM(2)**	0.5	114.5°	138.8°	130.5°	2.53 Å	5.54 Å
	0.25	112.6°	138.6°	129.9°	2.54 Å	5.56 Å
	0	115.5°	138.1°	133.9°	2.49 Å	5.54 Å
TM(1)-O(7)-P(2)-O(8)-TM(2) **TM(1)-O(8)-P(2)-O(7)-TM(2)**	0.5	116.0°	127.6°	136.3°	2.54 Å	6.11 Å
	0.25	114.9°	127.9°	135.8°	2.57 Å	6.08 Å
	0	116.3°	130.6°	137.6°	2.57 Å	6.10 Å
TM(1)-O(6)-P(3)-O(9)-TM(3) **TM(1)-O(9)-P(3)-O(6)-TM(3)**	0.5	117.4°	142.2°	134.1°	2.57 Å	5.11 Å
	0.25	117.5°	141.2°	134.2°	2.55 Å	5.13 Å
	0	118.7°	140.6°	135.0°	2.58 Å	5.15 Å

For TM-O*-P, * indicates oxygen labelled with higher number

6.3.3 $Mn_xFe_{1-x}P_3O_9$ ($0 \leq x \leq 0.4$ and $0.75 \leq x \leq 1$)

Within the $MnPO_4 \cdot H_2O$-Fe_2O_3-H_3PO_4 reaction system, at temperatures ≥ 250°C transition metal polyphosphates with composition $Mn_xFe_{1-x}P_3O_9$ were observed. Interestingly the full solid solution could not be synthesised, with the acid melt reaction favouring separate Mn and Fe phases in the case of x = 0.5 (Table 6.1), 0.6 and 0.7. It should be noted that $Mn_{0.5}Fe_{0.5}P_3O_9$ was observed as a decomposition product of $Mn_{0.5}Fe_{0.5}H_2P_3O_{10}$ (section 6.3.2.3), most likely because the amount of phosphorus was fixed, whereas in the acid melt reaction a six-fold excess of phosphorus to metal was available.

The Mn rich phases were found to adopt a different crystal structure to those with x ≤ 0.5, with the miscibility gap suggesting that the Mn host is only able to accommodate 25% of iron into the structure whereas the Fe host can accommodate up to 50% of Mn.

6.3.3.1. $Mn_xFe_{1-x}P_3O_9$ ($0.75 \leq x \leq 1$)

Structural details on the x = 1 compound were obtained from a Rietveld refinement of the 300 K neutron diffraction data, while those on x = 0.75 from a joint ND/ XRD refinement, using single crystal XRD data on MnP_3O_9[8] as a starting model. The refinements are shown in Figure 6.28, structural parameters in Table 6.14 and selected bond lengths and angles in Table 6.15.

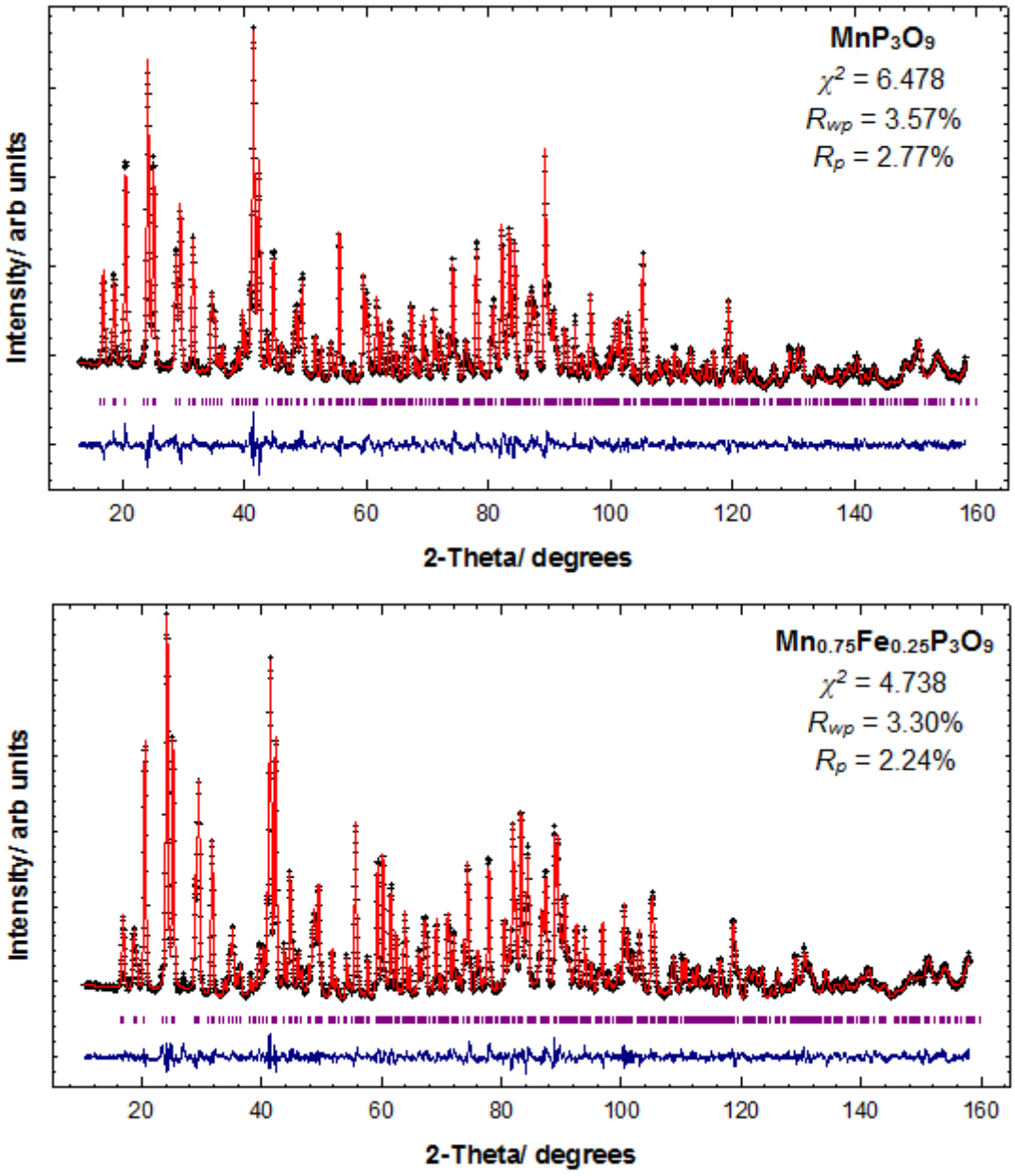

Figure 6.28: *Observed (+), calculated (-), difference profiles (-) and reflection positions (l) for the 300 K Rietveld refinements carried out on MnP_3O_9 and $Mn_{0.75}Fe_{0.25}P_3O_9$.*

Table 6.14: *Refined structural parameters from the 300 K diffraction data on MnP_3O_9 and $Mn_{0.75}Fe_{0.25}P_3O_9$, with Bond Valence Sums[19]*

Atom and site symmetry	x in $Mn_xFe_{1-x}P_3O_9$	Occupancy	*x*	*y*	*z*	U_{iso}/ Å^2	BVS
Mn/ Fe	1	1/ 0	0	0	0	0.009(1)	3.45
4*a*	0.75	0.747(2)/ 0.253(2)	0	0	0	0.016(2)	3.42/ 3.41
P(1)	1	1	0.5844(4)	0	0	0.0057(7)	5.16
4*c*	0.75	1	0.5831(3)	0	0	0.0042(6)	5.24
P(2)	1	1	0.2151(3)	0.6335(2)	0.1333(4)	0.0080(6)	5.07
8*e*	0.75	1	0.2125(2)	0.6341(2)	0.1343(3)	0.0075(4)	5.05
O(1)	1	1	0.0034(3)	0.1518(2)	0.1505(4)	0.0125(5)	2.13
8*e*	0.75	1	0.0043(2)	0.1528(2)	0.1500(3)	0.0145(4)	2.13
O(2)	1	1	0.0828(3)	0.9007(2)	0.2677(4)	0.0141(6)	1.81
8*e*	0.75	1	0.0822(2)	0.9008(2)	0.2646(3)	0.0172(4)	1.86
O(3)	1	1	0.3200(3)	0.9663(2)	0.3921(4)	0.0120(6)	2.11
8*e*	0.75	1	0.3198(2)	0.9655(1)	0.3891(3)	0.0106(4)	2.03
O(4)	1	1	0.3106(3)	0.3092(2)	0.4068(4)	0.0161(6)	2.26
8*e*	0.75	1	0.3130(2)	0.3095(2)	0.4071(3)	0.0171(4)	2.29
O(5)	1	1	0.2843(4)	0.75	0.25	0.0185(9)	2.12
4*d*	0.75	1	0.2829(3)	0.75	0.25	0.0201(6)	2.13

Space group *Pnaa.* x = 1: *a* = 9.6939(2) Å, *b* = 10.6636(3) Å and *c* = 6.3605(2) Å

x = 0.75: *a* = 9.7097(2) Å, *b* = 10.6975(2) Å and *c* = 6.3324(1) Å

Table 6.15: *Selected Bond Distances (Å) and Angles (°) for MnP_3O_9 and $Mn_{0.75}Fe_{0.25}P_3O_9$*

	x = 1	x = 0.75		x = 1	x = 0.75
			O(1)-TM-O(1')	180	180
			O(1)-TM-O(2)	90.8(1)	91.54(7)
			O(1)-TM-O(2')	89.2(1)	88.46(7)
TM-O(1) × 2	1.881(2)	1.891(2)	**O(1)-TM-O(3)**	90.3(1)	89.85(7)
TM-O(2) × 2	2.160(3)	2.138(2)	**O(1)-TM-O(3')**	89.7(1)	90.15(7)
TM-O(3) × 2	1.910(3)	1.921(2)	**O(2)-TM-O(2')**	180	180
			O(2)-TM-O(3)	92.1(1)	92.38(8)
			O(2)-TM-O(3')	87.9(1)	87.62(8)
			O(3)-TM-O(3')	180	180
			O(1)-P(1)-O(1')	110.4(3)	110.2(2)
P(1)-O(1) × 2	1.490(3)	1.484(2)	**O(1)-P(1)-O(4)**	111.2(1)	111.0(1)
P(1)-O(4) × 2	1.559(4)	1.553(2)	**O(1)-P(1)-O(4')**	112.7(1)	112.67(9)
			O(4)-P(1)-O(4')	98.3(3)	99.0(2)
			O(2)-P(2)-O(3)	117.8(2)	117.5(2)
P(2)-O(2)	1.475(3)	1.466(2)	**O(2)-P(2)-O(4)**	110.3(2)	111.1(2)
P(2)-O(3)	1.480(3)	1.498(2)	**O(2)-P(2)-O(5)**	111.1(2)	111.5(2)
P(2)-O(4)	1.584(3)	1.580(2)	**O(3)-P(2)-O(4)**	106.6(2)	106.9(2)
P(2)-O(5)	1.595(3)	1.594(2)	**O(3)-P(2)-O(5)**	108.8(2)	107.5(2)
			O(4)-P(2)-O(5)	100.9(2)	100.9(1)

Like the previous condensed phosphate systems encountered, the structure of $Mn_xFe_{1-x}P_3O_9$ ($x \geq 0.75$) can be described as a three-dimensional network of TM-O_6 octahedra corner-linked to four polyphosphate units, two of them being connected in a bidentate fashion along a common edge of the octahedron, as can be seen in Figure 6.29.

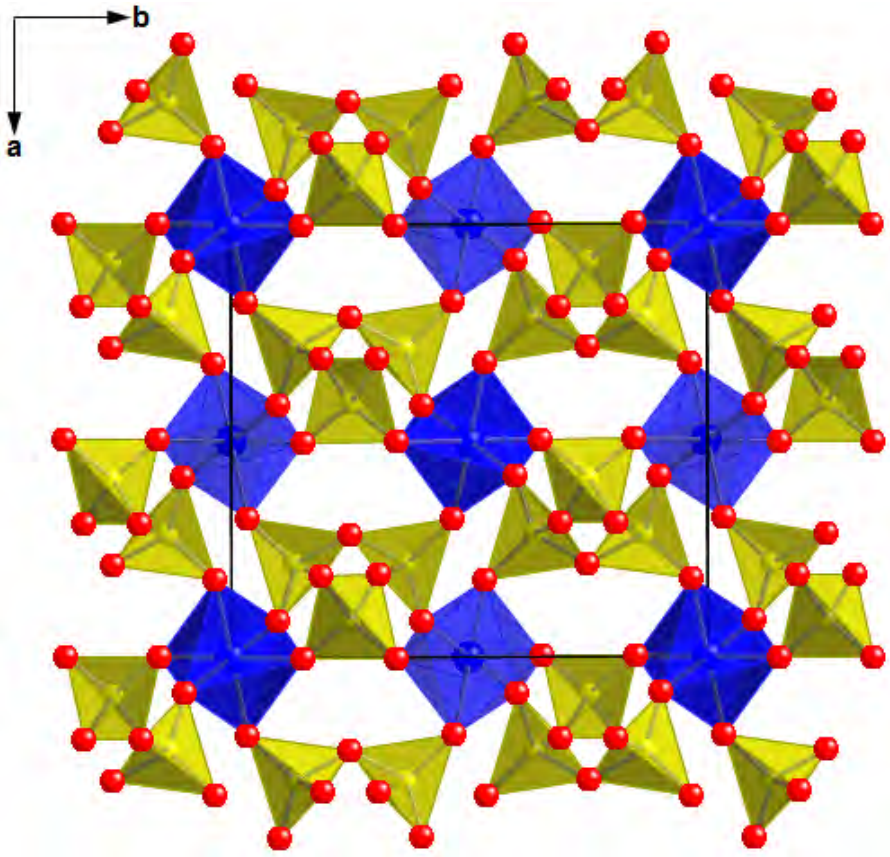

Figure 6.29: *Structure adopted by MnP_3O_9 and $Mn_{0.75}Fe_{0.25}P_3O_9$, showing TM-O_6 octahedra (blue) and condensed phosphate tetrahedra (yellow). The thin black line defines the unit cell.*

The polyphosphate units themselves are formed from corner-shared PO_4 tetrahedra which create infinite chains running parallel to the *c*-axis (Figure 6.30). The relatively high symmetry of the structure means that each polyphosphate unit only possesses two distinct phosphorus atoms, with P(1) found to lie on a binary axis and P(2) located on a general position. O(4) is the bridging atom between P(1) and P(2) while O(5) (also located on a binary axis) bridges P(2) centres throughout the

structure. Longer P-O bond lengths were observed to these bridging oxygens and shorter bonds to the terminal oxygens, with O-P-O angles found to be in the range of ~98-113° and ~101-118° for the $P(1)O_4$ and $P(2)O_4$ tetrahedrons, respectively.

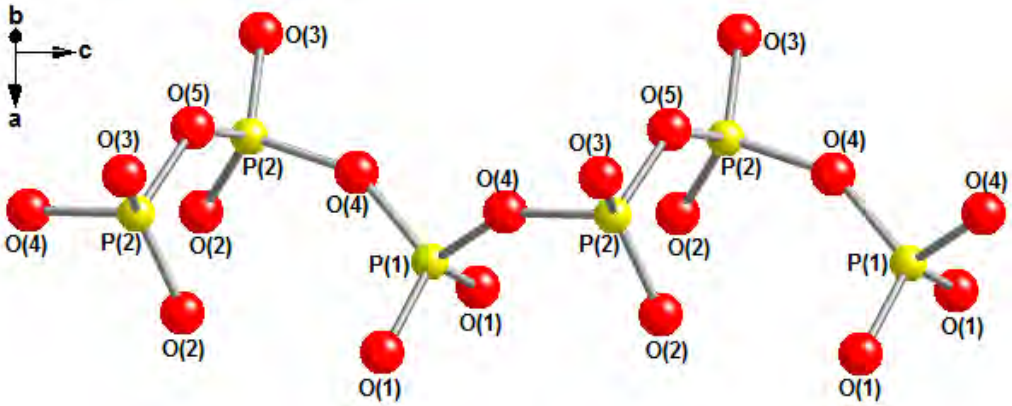

Figure 6.30: *Orientation of the polyphosphate ligands within the MnP_3O_9 structure type. Phosphorus and oxygen atoms are shown as yellow and red spheres, respectively.*

The TM ions are located on inversion centres throughout the structure and showed a [2+2+2] tetragonal elongation, with two long TM-O bonds > 2.13 Å, two bonds ~1.91 Å and two bonds < 1.89 Å, with the four shorter bonds closely matched in length. As expected, this elongation was slightly less pronounced for x = 0.75. In both cases the O-TM-O angles were found to be close to that of an ideal octahedron. BVS calculations showed the TM ions to be significantly overbonded within the structure, with valencies of ~3.4 compared to the expected oxidation state of +3. GII values for both members were found to be 0.22 vu, suggesting that there is a large degree of lattice strain present in the structure, which is most likely a result of the TM ions having to adapt their coordination sphere to fulfil the structural requirements of the polyphosphate anions, which extend infinitely throughout the structure. This is possibly the reason for there being a limit to the amount of iron that could be taken up by the structure.

The UV-Vis spectra (Figure 6.31) showed four d→d transitions occurring in the visible region, consistent with the [2+2+2] pattern of TM-O bond lengths seen from the diffraction data. The MnO_6 unit has D_{2h} symmetry in which there is a centre of inversion, meaning that electronic transitions are spin allowed but Laporte forbidden. As expected, the spectra of both compounds were found to be very similar, with no obvious differences seen in their colouration (Figure 6.32).

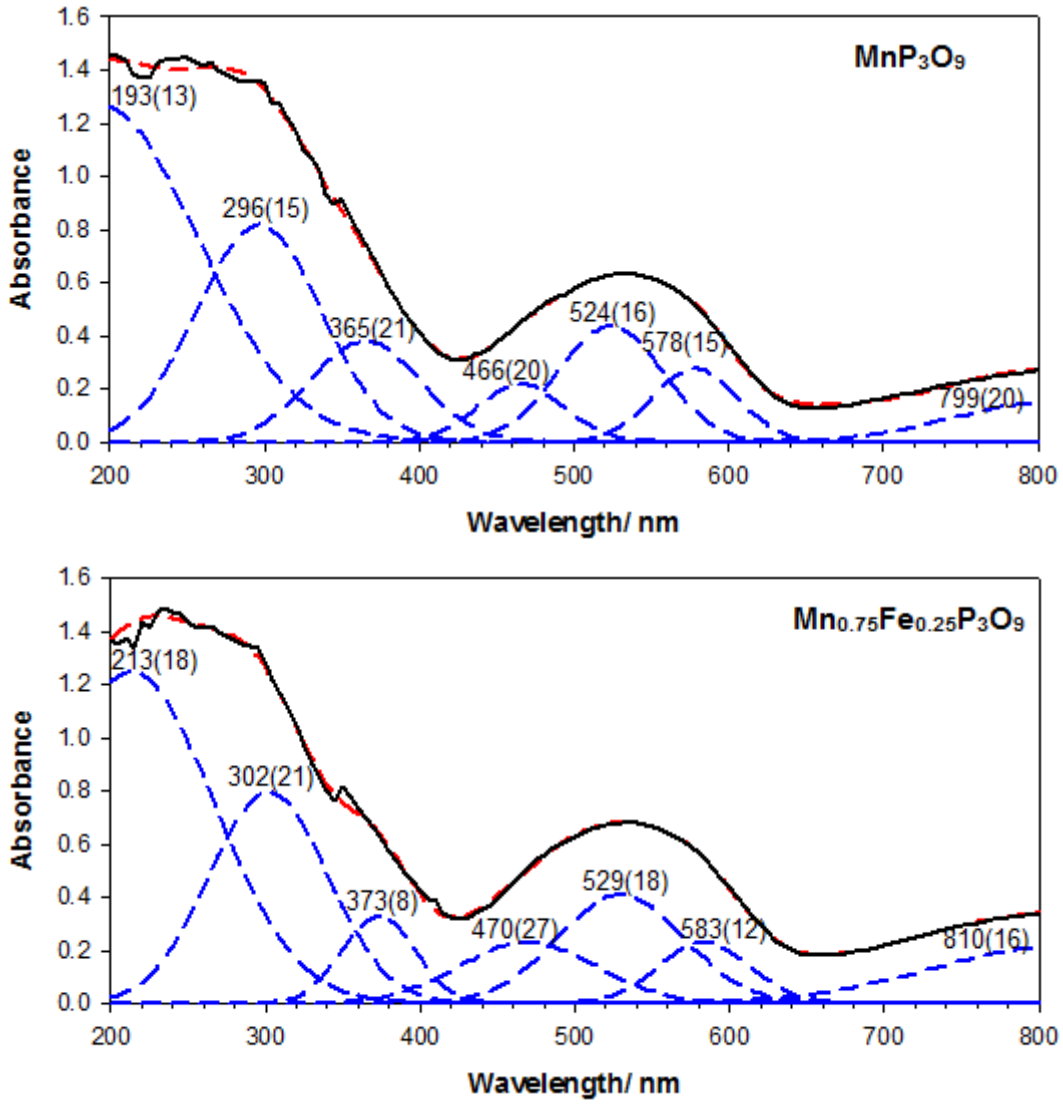

Figure 6.31: *UV-Vis spectra of MnP_3O_9 and $Mn_{0.75}Fe_{0.25}P_3O_9$, showing raw data (—), fitted Gaussian bands (---) and sum of the fitted Gaussian bands (---). Peak positions are marked.*

Figure 6.32: *Colouration of $Mn_xFe_{1-x}P_3O_9$ compounds*

Figures 6.33 and 6.34 show that with decreasing manganese content in the MnP_3O_9 structure type, a general decrease in the *c*-lattice parameter occurred but an increase in *a* and *b*, which led to an overall increase in volume of the unit cell. A closer inspection of the structure (as shown in Figure 6.35) reveals that the direction of the TM-O(3), TM-O(1) and TM-O(2) bonds is closely correlated with the *a*-, *b*- and *c*-axes, respectively. With decreasing Mn content the TM-O_6 coordination sphere becomes less distorted, with the former two bond types increasing in length and the latter decreasing (Table 6.15). This therefore explains the corresponding increase in the *a*- and *b*-parameters coupled to a decrease in *c*.

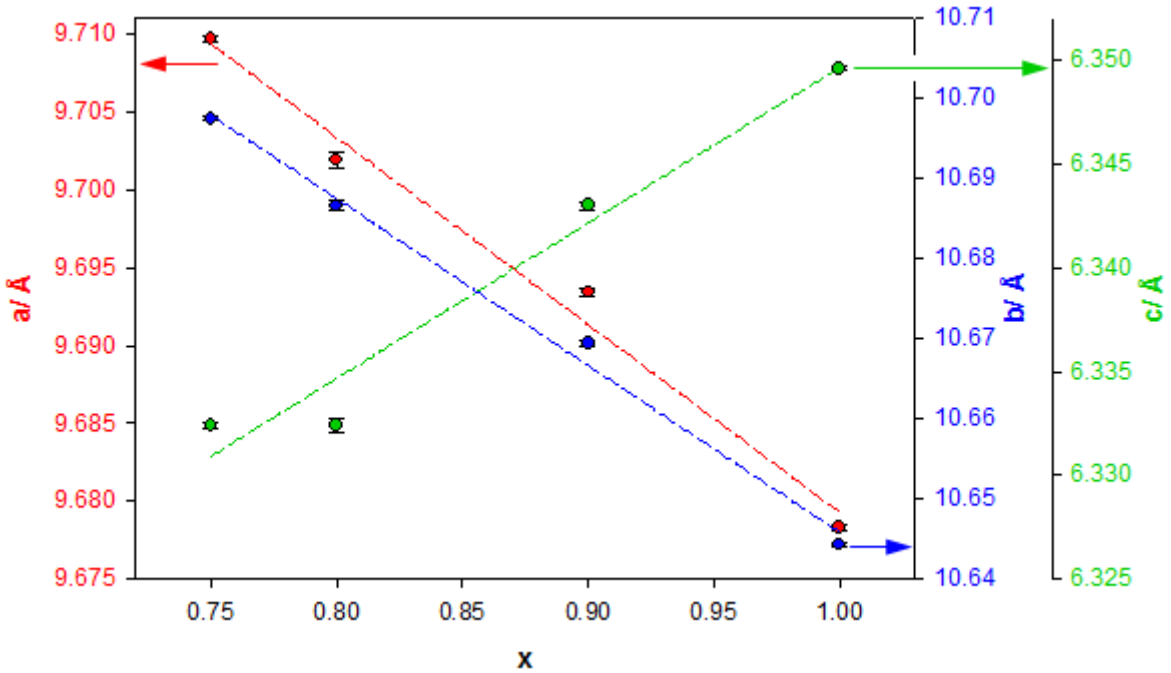

Figure 6.33: *Change in the a-, b- and c-lattice parameters with varying Mn^{3+} content in the $Mn_xFe_{1-x}P_3O_9$ system (XRD data). Arrows indicate direction of axes.*

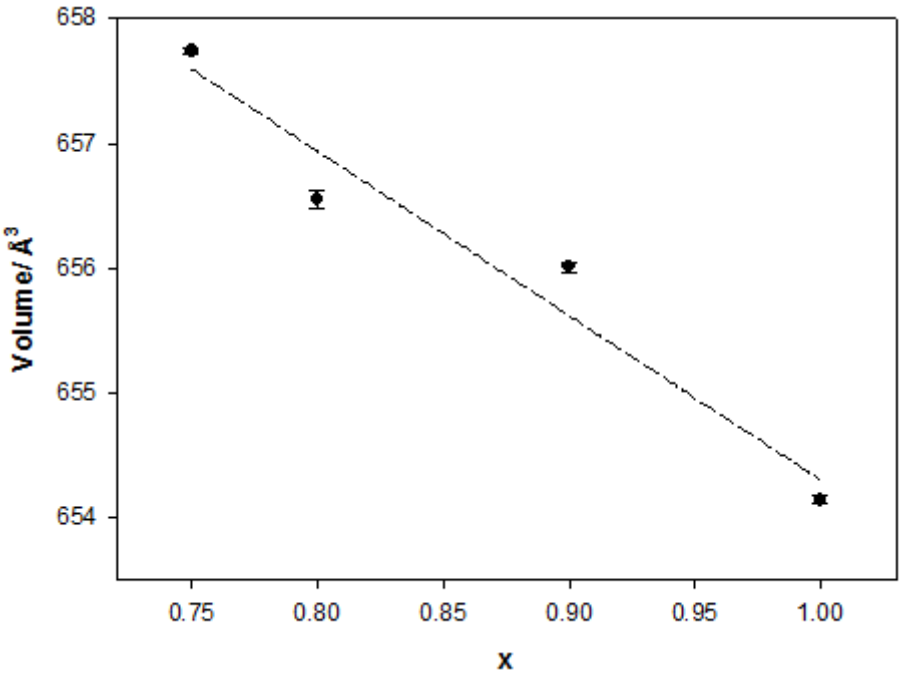

Figure 6.34: *Change in volume of the unit cell with varying Mn^{3+} content in the $Mn_xFe_{1-x}P_3O_9$ system (XRD data).*

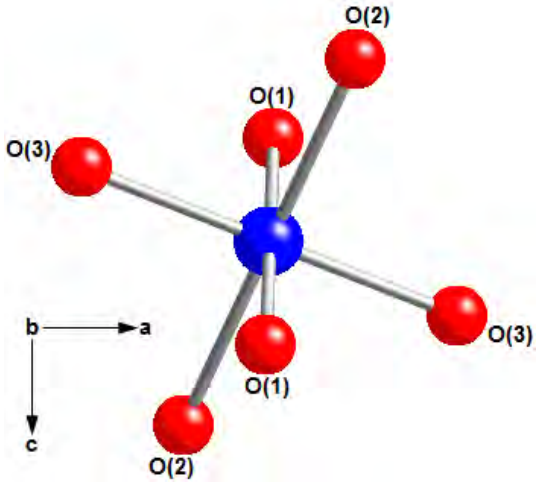

Figure 6.35: *The orientation of the TM-O_6 octahedron with respect to the unit cell axes in the MnP_3O_9 structure type.*

6.3.3.2. $Mn_xFe_{1-x}P_3O_9$ ($0 \leq x \leq 0.4$)

Within the $MnPO_4 \cdot H_2O$-Fe_2O_3-H_3PO_4 reaction system, $Mn_xFe_{1-x}P_3O_9$ polyphosphates with $x \leq 0.4$ were found to crystallise in a different structure type to those with $x \geq 0.75$. Although neutron diffraction data on the $x = 0$ and 0.25 phases were collected, the complexity of the structural model (single crystal data on FeP_3O_9[16]) meant that it was difficult to achieve stable refinements. Whilst the refinement for $x = 0$ reached convergence (Figure 6.36), for $x = 0.25$ the refinement was unable to converge when the atomic coordinates were allowed to vary. This suggested that the data were not of sufficient quality to detect subtle changes in the structure that had occurred with the introduction of manganese into the system. Table 6.16 lists the structural parameters for $x = 0$ while Table 6.17 gives selected bond lengths and angles. The neutron diffraction data were found to be in reasonable agreement with the single crystal data on this phase.

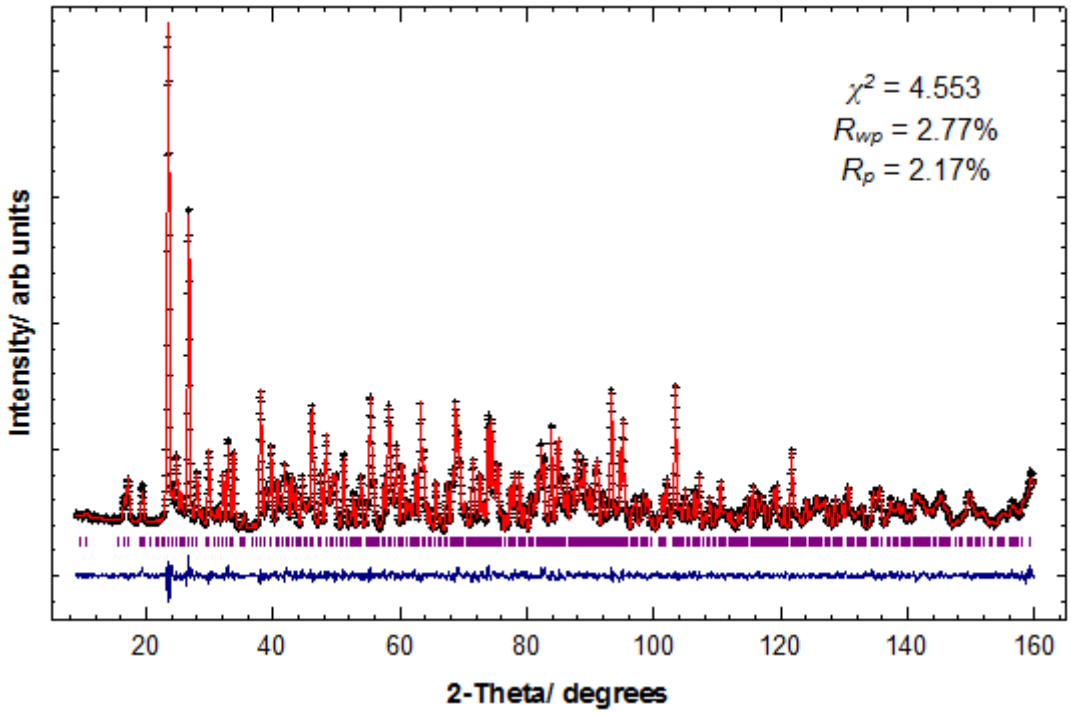

Figure 6.36: *Observed (+), calculated (-), difference profiles (-) and reflection positions (|) for the 300 K Rietveld refinement carried out on FeP_3O_9.*

Table 6.16: *Refined structural parameters from the 300 K neutron diffraction data on FeP_3O_9 with BVS's[19]. Isotropic displacement factors of like atoms were constrained to be equal.*

Atom	Site	Occupancy	*x*	*y*	*z*	U_{iso}/ Å^2	BVS
Fe(1)	4*a*	1	0.8381(9)	0.0815(5)	0.066(1)	0.0034(5)	3.33
Fe(2)	4*a*	1	0.8232(7)	0.2424(4)	0.5389(9)	0.0034(5)	3.19
Fe(3)	4*a*	1	0.3497(8)	0.0869(4)	0.580(1)	0.0034(5)	3.25
P(1)	4*a*	1	0.708(1)	-0.0293(7)	0.751(2)	0.0052(5)	5.10
P(2)	4*a*	1	0.695(1)	0.3053(7)	0.727(2)	0.0052(5)	4.83
P(3)	4*a*	1	0.693(1)	0.3609(8)	0.226(2)	0.0052(5)	5.42
P(4)	4*a*	1	0.108(1)	0.0199(7)	0.843(1)	0.0052(5)	5.22
P(5)	4*a*	1	0.599(1)	0.1849(6)	0.833(2)	0.0052(5)	5.02
P(6)	4*a*	1	0.488(1)	0.0301(9)	0.406(2)	0.0052(5)	5.18
P(7)	4*a*	1	0.569(1)	0.1441(7)	0.279(2)	0.0052(5)	5.18
P(8)	4*a*	1	0.477(1)	0.3038(8)	0.886(2)	0.0052(5)	4.64
P(9)	4*a*	1	0.972(1)	0.1306(7)	0.882(2)	0.0052(5)	5.12
O(1)	4*a*	1	0.617(1)	0.0909(7)	0.203(2)	0.0105(3)	2.31
O(2)	4*a*	1	0.686(1)	0.1340(6)	0.963(1)	0.0105(3)	2.30
O(3)	4*a*	1	0.876(1)	0.1088(6)	0.902(2)	0.0105(3)	2.19
O(4)	4*a*	1	0.682(1)	0.1723(6)	0.437(1)	0.0105(3)	2.17
O(5)	4*a*	1	0.300(1)	0.2085(6)	0.205(2)	0.0105(3)	1.75
O(6)	4*a*	1	0.395(1)	0.0353(6)	0.444(2)	0.0105(3)	2.04
O(7)	4*a*	1	0.494(1)	0.0993(6)	0.332(1)	0.0105(3)	2.38
O(8)	4*a*	1	0.814(1)	0.0567(6)	0.251(1)	0.0105(3)	1.93
O(9)	4*a*	1	0.472(1)	0.1931(6)	0.135(2)	0.0105(3)	1.88
O(10)	4*a*	1	0.671(1)	0.2282(5)	0.779(1)	0.0105(3)	2.11
O(11)	4*a*	1	0.296(1)	0.1350(6)	0.713(1)	0.0105(3)	2.15
O(12)	4*a*	1	0.206(1)	0.0217(6)	0.496(2)	0.0105(3)	2.06
O(13)	4*a*	1	0.622(1)	0.0240(8)	0.602(2)	0.0105(3)	2.22
O(14)	4*a*	1	0.471(1)	0.1631(5)	0.649(1)	0.0105(3)	1.72
O(15)	4*a*	1	0.572(1)	0.2392(6)	0.933(1)	0.0105(3)	2.10
O(16)	4*a*	1	0.062(1)	0.1439(6)	0.549(1)	0.0105(3)	2.35
O(17)	4*a*	1	0.057(1)	0.1884(6)	0.039(2)	0.0105(3)	2.01
O(18)	4*a*	1	0.219(1)	0.1428(5)	0.355(2)	0.0105(3)	2.07
O(19)	4*a*	1	0.467(1)	0.0326(6)	0.796(1)	0.0105(3)	1.97
O(20)	4*a*	1	0.858(1)	0.2130(5)	0.372(1)	0.0105(3)	1.81
O(21)	4*a*	1	0.741(1)	0.0013(7)	0.924(2)	0.0105(3)	1.90
O(22)	4*a*	1	0.938(1)	0.1673(6)	0.211(2)	0.0105(3)	1.85
O(23)	4*a*	1	0.936(1)	0.1686(6)	0.719(1)	0.0105(3)	1.88
O(24)	4*a*	1	0.2048(9)	0.1899(6)	0.853(1)	0.0105(3)	2.05
O(25)	4*a*	1	0.174(1)	0.0620(5)	0.775(1)	0.0105(3)	2.12
O(26)	4*a*	1	0.078(1)	0.0763(6)	0.941(1)	0.0105(3)	2.19
O(27)	4*a*	1	-0.001(1)	0.0192(5)	0.198(1)	0.0105(3)	2.00

Space group *Cc*: a = 13.1681(2) Å, b = 19.0996(3) Å, c = 9.4234(2) Å and β = 127.029(1)°

Table 6.17: *Selected Bond Distances (Å) and Angles (degrees) for FeP_3O_9*

Fe(1)-O(2)	1.90(2)	**Fe(2)-O(4)**	2.01(1)	**Fe(3)-O(6)**	1.98(2)
Fe(1)-O(3)	1.96(2)	**Fe(2)-O(5)**	2.00(2)	**Fe(3)-O(11)**	1.99(2)
Fe(1)-O(8)	2.00(2)	**Fe(2)-O(9)**	2.01(2)	**Fe(3)-O(12)**	1.99(2)
Fe(1)-O(21)	1.93(2)	**Fe(2)-O(20)**	1.96(2)	**Fe(3)-O(14)**	1.96(1)
Fe(1)-O(22)	2.03(2)	**Fe(2)-O(23)**	2.01(1)	**Fe(3)-O(18)**	2.05(1)
Fe(1)-O(27)	2.07(2)	**Fe(2)-O(24)**	1.97(1)	**Fe(3)-O(19)**	1.95(2)
O(2)-Fe(1)-O(3)	98.3(6)	**O(4)-Fe(2)-O(5)**	98.7(6)	**O(6)-Fe(3)-O(11)**	176.8(7)
O(2)-Fe(1)-O(8)	84.5(7)	**O(4)-Fe(2)-O(9)**	175.0(7)	**O(6)-Fe(3)-O(12)**	90.9(6)
O(2)-Fe(1)-O(21)	90.8(7)	**O(4)-Fe(2)-O(20)**	91.2(6)	**O(6)-Fe(3)-O(14)**	94.6(6)
O(2)-Fe(1)-O(22)	88.6(6)	**O(4)-Fe(2)-O(23)**	86.3(6)	**O(6)-Fe(3)-O(18)**	88.8(5)
O(2)-Fe(1)-O(27)	173.4(8)	**O(4)-Fe(2)-O(24)**	90.2(5)	**O(6)-Fe(3)-O(19)**	93.0(6)
O(3)-Fe(1)-O(8)	175.1(8)	**O(5)-Fe(2)-O(9)**	85.9(6)	**O(11)-Fe(3)-O(12)**	85.9(6)
O(3)-Fe(1)-O(21)	92.1(7)	**O(5)-Fe(2)-O(20)**	168.4(6)	**O(11)-Fe(3)-O(14)**	88.6(6)
O(3)-Fe(1)-O(22)	86.9(6)	**O(5)-Fe(2)-O(23)**	92.9(5)	**O(11)-Fe(3)-O(18)**	90.9(6)
O(3)-Fe(1)-O(27)	88.3(6)	**O(5)-Fe(2)-O(24)**	88.7(5)	**O(11)-Fe(3)-O(19)**	87.1(5)
O(8)-Fe(1)-O(21)	91.9(7)	**O(9)-Fe(2)-O(20)**	84.5(6)	**O(12)-Fe(3)-O(14)**	170.8(7)
O(8)-Fe(1)-O(22)	89.1(6)	**O(9)-Fe(2)-O(23)**	91.5(6)	**O(12)-Fe(3)-O(18)**	84.8(5)
O(8)-Fe(1)-O(27)	89.0(6)	**O(9)-Fe(2)-O(24)**	92.0(6)	**O(12)-Fe(3)-O(19)**	93.0(6)
O(21)-Fe(1)-O(22)	178.7(9)	**O(20)-Fe(2)-O(23)**	93.8(6)	**O(14)-Fe(3)-O(18)**	88.0(5)
O(21)-Fe(1)-O(27)	88.2(7)	**O(20)-Fe(2)-O(24)**	85.2(5)	**O(14)-Fe(3)-O(19)**	94.0(6)
O(22)-Fe(1)-O(27)	92.6(6)	**O(23)-Fe(2)-O(24)**	176.3(6)	**O(18)-Fe(3)-O(19)**	177.1(8)
P(1)-O(1)	1.54(2)	**P(2)-O(5)**	1.54(2)	**P(3)-O(11)**	1.44(2)
P(1)-O(8)	1.49(2)	**P(2)-O(10)**	1.64(2)	**P(3)-O(16)**	1.52(2)
P(1)-O(13)	1.55(2)	**P(2)-O(17)**	1.60(2)	**P(3)-O(24)**	1.47(2)
P(1)-O(21)	1.53(2)	**P(2)-O(18)**	1.44(2)	**P(3)-O(25)**	1.61(2)
P(4)-O(12)	1.46(2)	**P(5)-O(2)**	1.44(2)	**P(6)-O(6)**	1.47(2)
P(4)-O(25)	1.58(2)	**P(5)-O(10)**	1.56(2)	**P(6)-O(7)**	1.52(2)
P(4)-O(26)	1.61(2)	**P(5)-O(14)**	1.57(2)	**P(6)-O(13)**	1.61(2)
P(4)-O(27)	1.45(2)	**P(5)-O(15)**	1.58(2)	**P(6)-O(19)**	1.50(2)
P(7)-O(1)	1.59(2)	**P(8)-O(15)**	1.62(2)	**P(9)-O(3)**	1.44(2)
P(7)-O(4)	1.43(2)	**P(8)-O(16)**	1.60(2)	**P(9)-O(17)**	1.63(2)
P(7)-O(7)	1.59(2)	**P(8)-O(20)**	1.54(2)	**P(9)-O(23)**	1.50(2)
P(7)-O(9)	1.50(2)	**P(8)-O(22)**	1.50(2)	**P(9)-O(26)**	1.56(2)

The structure of FeP_3O_9 is a three-dimensional network of three distinct FeO_6 octahedra corner-linked to the PO_4 tetrahedra of infinite polyphosphate chains (Figure 6.37). There are two distinct polyphosphate chains, the first being three-membered and consisting of P(1), P(6) and P(7) and the second being six-membered and comprising P(2), P(3), P(4), P(5), P(8) and P(9), with both running along the *c*-axis of the structure (Figure 6.38). Longer P-O bonds were observed to the bridging oxygens of the phosphate units and shorter bonds to the terminal oxygens, as is seen in most condensed phosphate systems.[30] The three crystallographically distinct FeO_6 octahedra alternate along the [010] direction and like the PO_4 tetrahedra, showed a relatively irregular arrangement of bond lengths.

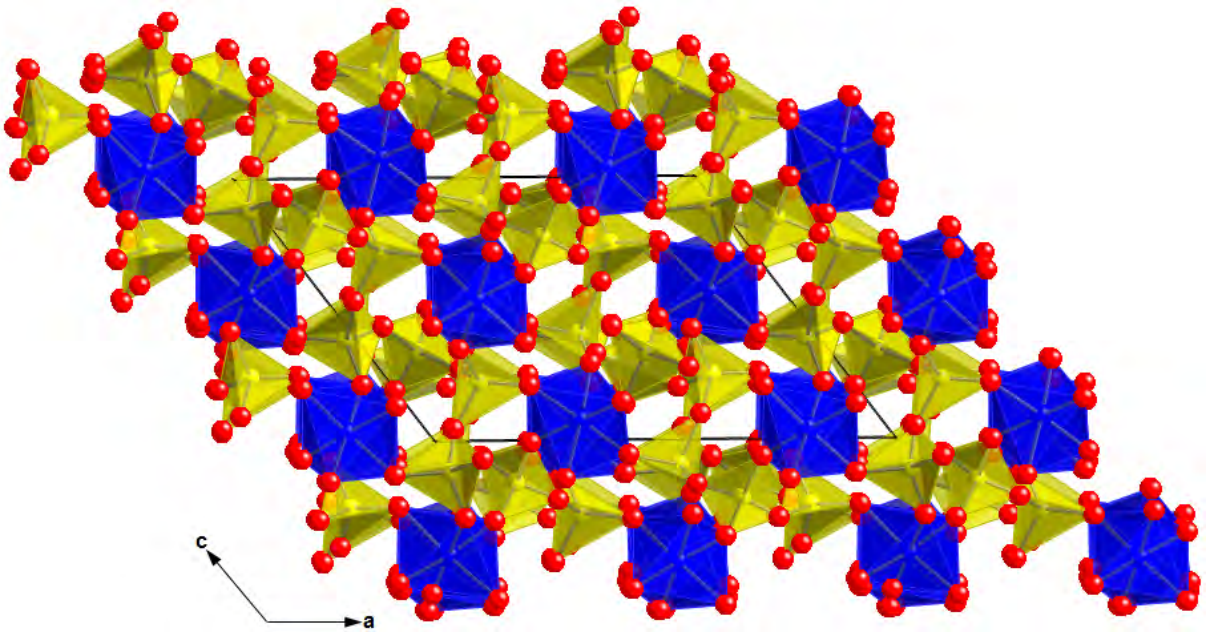

Figure 6.37: *FeP_3O_9 structure type, showing TM-O_6 octahedra (blue) and condensed phosphate tetrahedra (yellow). The thin black line defines the unit cell.*

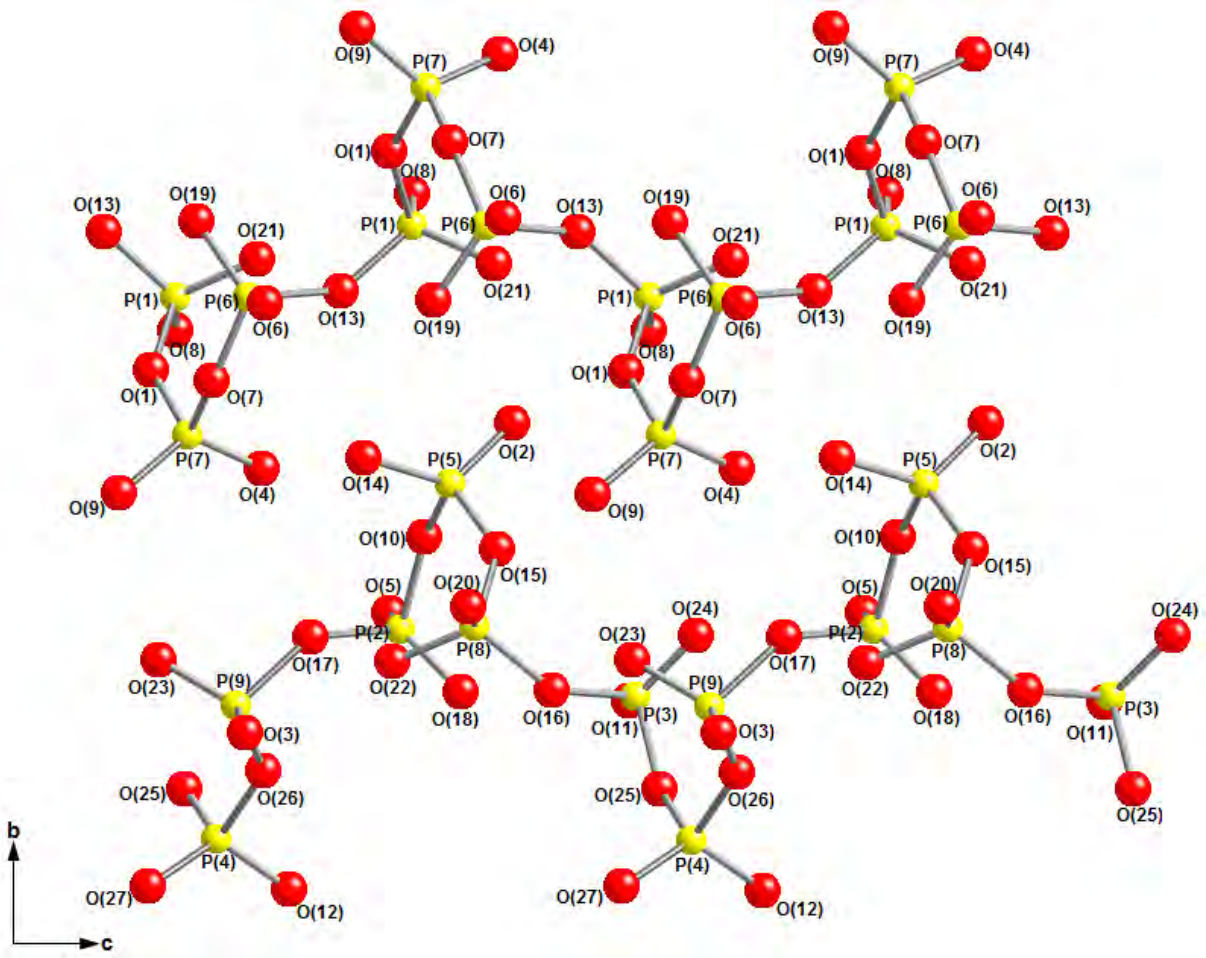

Figure 6.38: *Orientation of the polyphosphate ligands within the FeP_3O_9 structure type. Phosphorus and oxygen atoms are shown as yellow and red spheres, respectively.*

BVS[19] calculations (Table 6.16) showed some of the atoms within the structure to be highly overbonded or underbonded, and a GII[21] value of 0.20 vu suggested a significant degree of lattice strain present. The value obtained for the iron system was only slightly lower than that obtained for MnP_3O_9, which gave a GII of 0.22 vu. This small difference is unlikely to provide a possible explanation for the former structure type being able to accommodate a greater level of manganese. Table 6.18 shows that a general decrease in the unit cell parameters occurred with the incorporation of Mn, though no clear trend in the volume was observed. As reliable structural details on the Mn containing members *i.e.* x = 0.25 could not be

obtained, we were unable to further comment on the lattice parameters at this stage. The UV-Vis spectrum (Figure 6.39) for this compound did however suggest a [4+2] tetragonal elongation of the MnO_6 coordination sphere, with three d→d transitions modelled in the visible region, corresponding to an average 10*Dq* value of 218(6) kJ mol^{-1}.

Table 6.18: *XRD lattice parameters for the $Mn_xFe_{1-x}P_3O_9$ series ($x \leq 0.4$)*

$Mn_xFe_{1-x}P_3O_9$	*a*/ Å	*b*/ Å	*c*/ Å	*β*/ °	Volume/ $Å^3$
x = 0	13.1447(3)	19.0657(5)	9.4065(2)	127.030(3)	1881.96(7)
x = 0.1	13.1453(8)	19.075(1)	9.4076(6)	126.927(3)	1885.8(2)
x = 0.2	13.1362(9)	19.074(2)	9.4018(7)	126.831(3)	1885.5(3)
x = 0.3	13.124(1)	19.066(2)	9.3947(9)	126.708(3)	1884.6(3)
x = 0.4	13.111(1)	19.059(2)	9.385(1)	126.575(3)	1883.2(4)

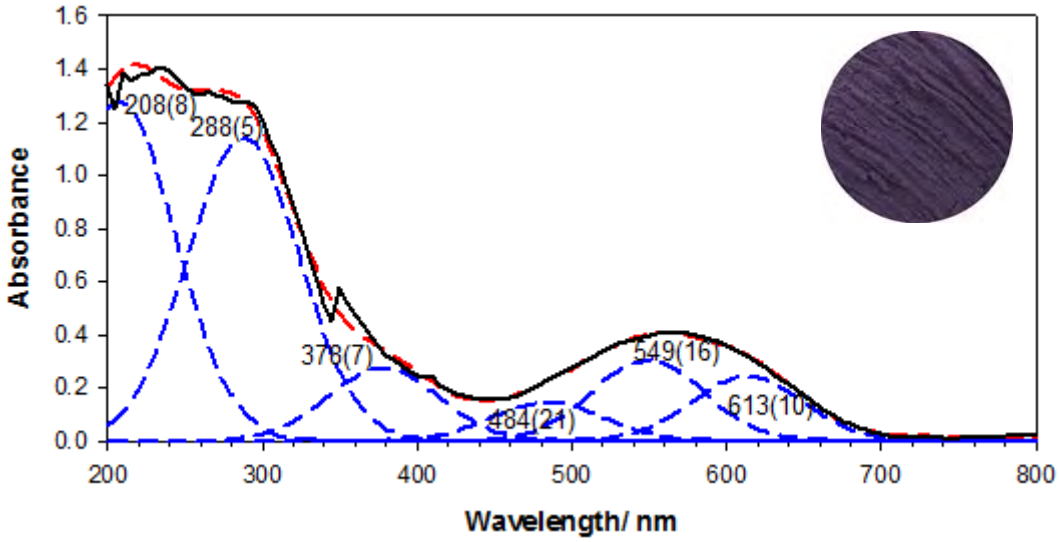

Figure 6.39: *UV-Vis spectrum of $Mn_{0.25}Fe_{0.75}P_3O_9$, showing raw data (—), fitted Gaussian bands (---) and sum of the fitted Gaussian bands (---). Peak positions are marked and the colouration exhibited by this member is shown in the top right corner.*

6.3.3.3 Thermal Stability

The TGA plots for the x =1, 0.75, 0.25 and 0 polyphosphates heated in nitrogen are shown in Figure 6.40. The x = 1 and 0.75 compounds evolved a small amount of water between ~170-260°C, which was possibly surface water or water belonging to an amorphous phase in the sample. After being heated to 750°C, these

compounds remained intact albeit with reduced crystallinity, but further heating to 800°C led to these phases melting. The FeP_3O_9 structure type showed a much greater stability, with x = 0.25 remaining stable up to ~1000°C and x = 0 up to ~1050°C before melting.

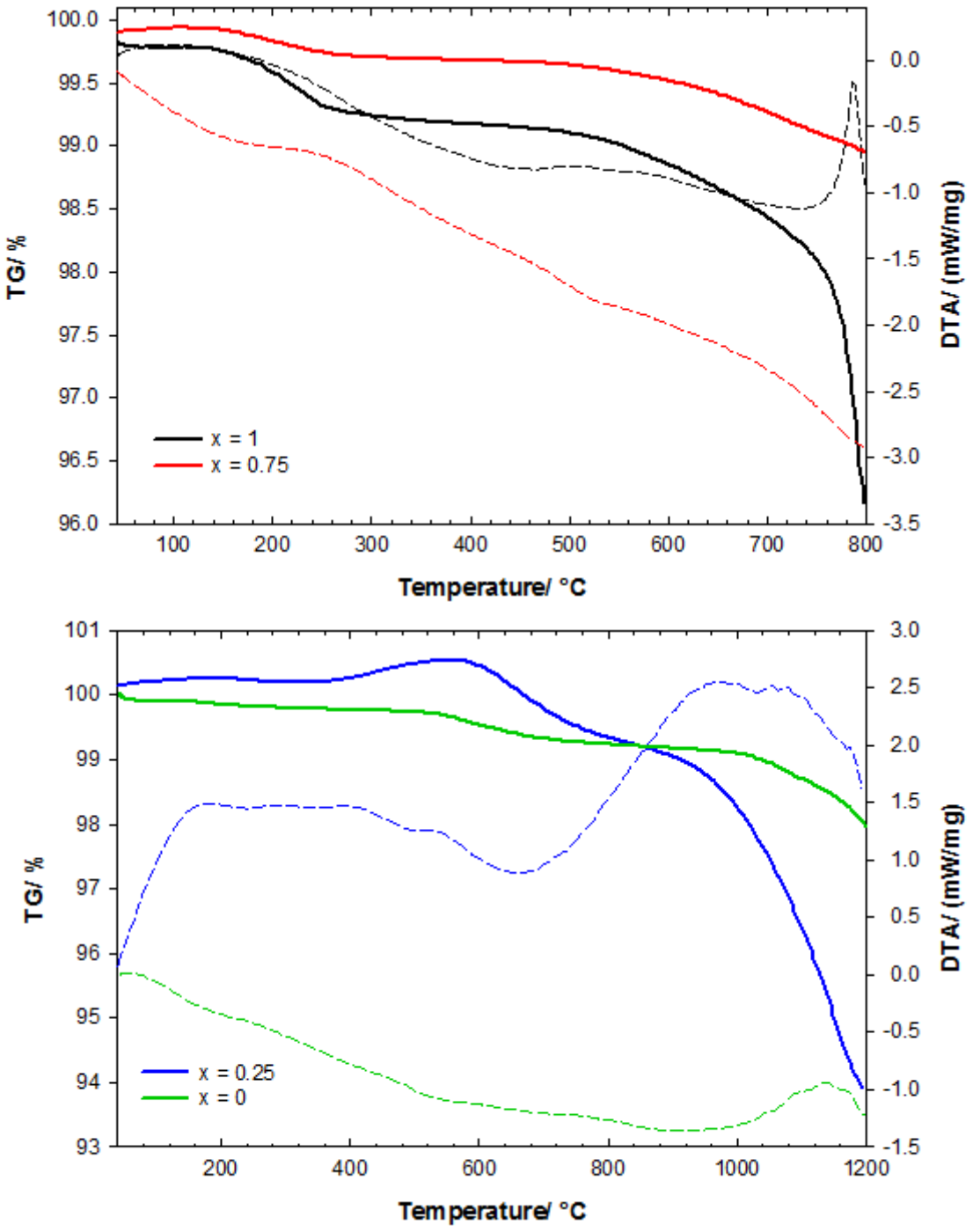

Figure 6.40: *TGA plots for $Mn_xFe_{1-x}P_3O_9$ compounds. Solid and dashed lines show TG and DTA signals, respectively.*

6.3.3.4 Magnetic Properties

Figure 6.41 shows the magnetic susceptibility measurements for the x = 1, 0.75 and 0.25 compounds and Curie-Weiss fits to the data. The magnetic structure of FeP_3O_9[16] has been previously solved, with the compound found to possess purely AFM Fe-O-P-O-Fe exchange pathways. A relatively low Néel temperature of 10 K was reported, and is likely to be a result of the highly diluted framework. As such, the paramagnetic behaviour exhibited by the polyphosphates containing manganese was in part expected, given that these systems contain fewer unpaired electrons than the Fe end member. The x = 1 and 0.75 compounds showed strong deviations from the Curie-Weiss law while x = 0.25 exhibited a relatively small curvature in the inverse susceptibility plot. In all cases the moments determined were much higher than those expected based on the spin-only formula, particularly for x = 1 which showed the most marked curvature. This confirmed that the Curie-Weiss law was not ideal for describing the paramagnetic behaviour of these compounds.

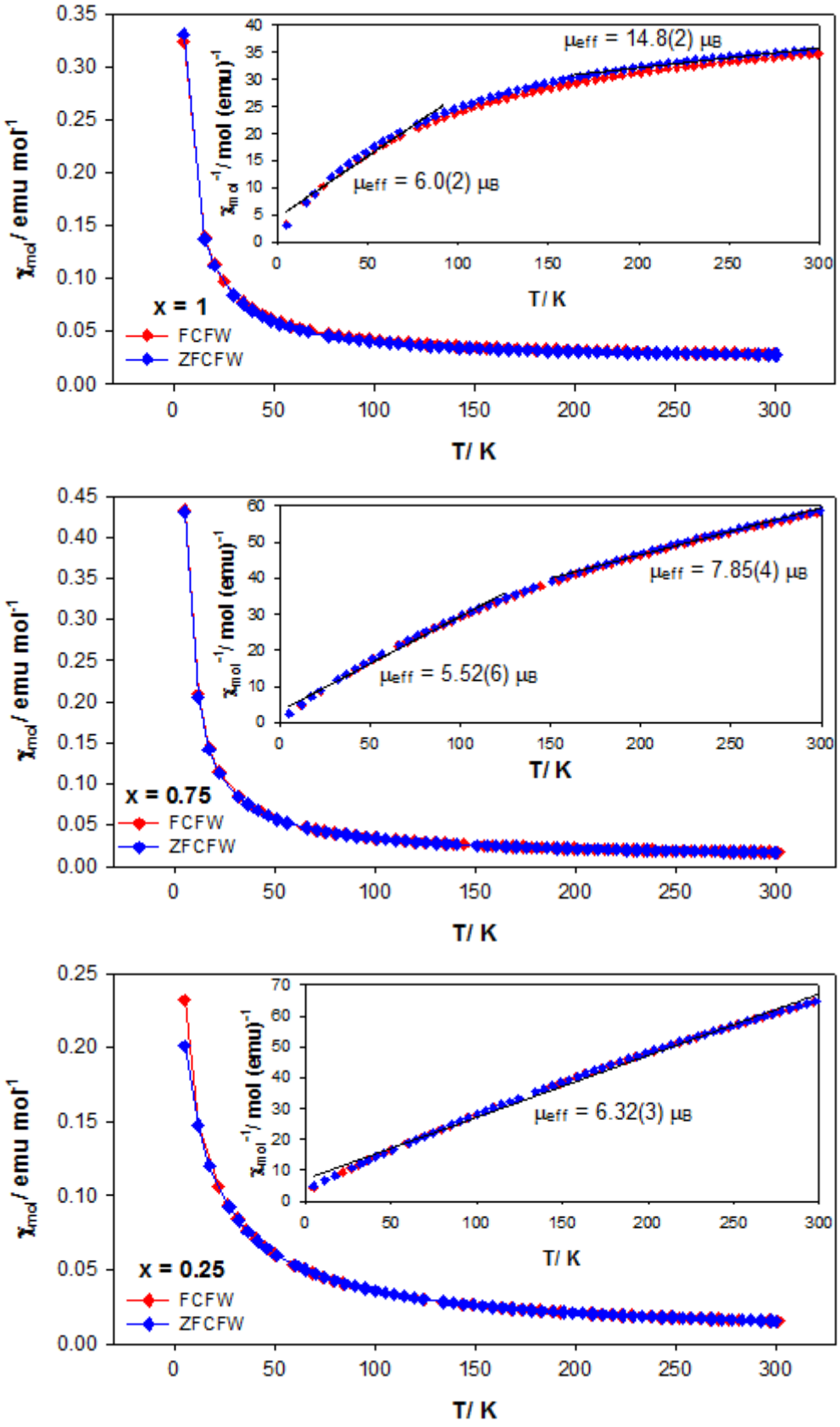

Figure 6.41: *Plots of molar susceptibility against temperature for $Mn_xFe_{1-x}P_3O_9$ compounds (x = 1, 0.75 and 0.25), with insets showing Curie-Weiss fits to the data.*

6.4 Conclusions

In investigating the $MnPO_4{\cdot}H_2O$-Fe_2O_3-H_3PO_4 reaction system we have been able to access a number of Mn/ Fe condensed phosphate phases which show interesting structural, optical and magnetic properties. Through using Mn^{3+} orthophosphate as a starting reagent, a relatively short reaction time of ~6 h sufficed in yielding a product, with the extent of condensation being controlled by the reaction temperature that was used.

At 150-200°C and with a Mn:P molar ratio of 1:6, we were able to isolate β-$HMnP_2O_7$, though could not form mixed compositions with iron. Although the aforementioned compound has been structurally characterised, we were unable to replicate the reported synthetic procedure and so have identified an alternative method for the synthesis of this compound in polycrystalline form. The structure type is quite unusual amongst Mn^{3+} condensed phosphates, with each MnO_6 octahedron edge-shared with one other to give Mn_2O_{10} dimers as well being corner-linked to hydrogen diphosphate units. As such Mn^{3+} finds itself in a highly distorted 6-coordinate site, which was also seen from the UV-Vis spectrum of this material.

The thermal stability of this phase was investigated and it was found that decomposition occurred over ~348-502°C to give an amorphous intermediate. Crystallisation of at least two new phases then occurred, one of which was unknown and the other which appeared to be $Mn_4(P_2O_7)_3$. Degradation of these phases gave a final product of $Mn_2P_4O_{12}$.

The magnetic properties of β-$HMnP_2O_7$ were also investigated and its magnetic structure solved at 2 K. The magnetic structure was in accordance with three-dimensional AFM ordering, though the structure was found to consist of both

FM and AFM exchange pathways. Interactions within the Mn_2O_{10} dimers were found to be FM in nature, though the mechanism for this exchange was unclear; an AFM interaction would be expected for superexchange or t_{2g}-t_{2g} direct exchange, while the FM interaction observed possibly originates from the "crossed interaction" between a d_{xy} orbital on one ion and the empty $d_{x^2-y^2}$ orbital on the other. It is possible that more than one exchange mechanism occurs, with the competing effects weakening the magnetic interaction within the Mn_2O_{10} dimers. In terms of "super-superexchange" occurring through extended Mn-O-P-O-Mn linkages, purely FM interactions were found to occur through the $P(1)O_4$ tetrahedron while the $P(2)O_4$ tetrahedron presented a triad of interactions, two of which were AFM and one of which was FM. This resulted in an AFM arrangement of the Mn_2O_{10} dimers along the *a*- and *b*-directions of the structure. The signs of the interactions were not correlated with orbital occupancy or the geometries of the interacting species.

An increase in the $MnPO_4 \cdot H_2O$-Fe_2O_3-H_3PO_4 reaction temperature to 250°C led to $Mn_xFe_{1-x}H_2P_3O_{10}$ ($x \leq 0.5$) phases being observed. In brief, the structure adopted is a three-dimensional network of TM-O_6 octahedra corner-linked to dihydrogen triphosphate units. The x = 0.5 member showed a distorted octahedral coordination sphere which became more regular with an increasing amount of Fe in the system. This could be related in part to the change in unit cell parameters as the series was traversed, though it was difficult to assess the extent of this influence. UV-Vis spectroscopy confirmed that the manganese coordination sphere was distorted beyond a [4+2] elongation for x = 0.5, while for x = 0.25 it suggested a [4+2] pattern of bond lengths. All phases remained stable up to ~430°C before condensation occurred to give the corresponding polyphosphate. The x = 0.5

member exhibited a particularly intense colouration and as such has the potential to be used in low temperature pigment applications.

The magnetic structures of the x = 0.5, 0.25 and 0 compounds were solved with all members found to adopt the same structure type. The TM-O-P-O-TM exchange pathways were all found to be AFM in nature. The canting of the moments suggested by the susceptibility data was not detected by the neutron diffraction measurements and was not further investigated.

A further increase in the reaction temperature of the $MnPO_4 \cdot H_2O$-Fe_2O_3-H_3PO_4 system to 300°C led to polyphosphates with composition $Mn_xFe_{1-x}P_3O_9$ being observed. A miscibility gap between $0.5 \leq x < 0.75$ occurred with the members on either end adopting two different structure types. Both structures were found to be similar, consisting of TM-O_6 octahedra corner linked to the PO_4 tetrahedra of infinite polyphosphate chains. Within the FeP_3O_9 structure type (space group *Cc*) there were three distinct TM atoms and two distinct polyphosphate chains, while the MnP_3O_9 structure type crystallised in higher symmetry (space group *Pnaa*), and possessed only one distinct TM site and polyphosphate chain.

For x = 1 and 0.75, UV-Vis spectroscopy confirmed a [2+2+2] distortion of the MnO_6 coordination sphere, while for x = 0.25 it suggested a [4+2] pattern of bond lengths. The unusual dark pink colouration exhibited by x = 1 and 0.75 also gives these compounds potential to be used as inorganic pigments. Indeed, these members were found to remain stable up to a relatively high temperature of ~800°C before melting. Compounds with the FeP_3O_9 structure type were found to remain stable up to a higher temperature of ~1000°C.

The magnetic properties of the x = 1, 0.75 and 0.25 compounds were investigated. All members were found to exhibit paramagnetic behaviour with the former two showing strong deviations from the Curie-Weiss law.

References

[1] F. C. Coomer, N. J. Checker and A. J. Wright, *Inorg. Chem.*, 2010, **49**, 934-942.

[2] J. Mechergui and W. Belam, *Mat. Res. Bull.*, 2008, **43**, 3358-3367.

[3] A. J. Wright, C. Ruiz-Valero and J. P. Attfield, *J. Solid State Chem.*, 1999, **145**, 479-483.

[4] A. J. Wright and J. P. Attfield, *Inorg. Chem.*, 1998, **37**, 3858-3861.

[5] A. J. Wright and J. P. Attfield, *J. Solid State Chem.*, 1998, **141**, 160-163.

[6] L. S. Ivashkevich, K. A. Selevich, A. I. Lesnikovich, A. F. Selevich and A. S. Lyakhov, *Z. Kristallogr.*, 2006, **221**, 115-121.

[7] P. A. Durif and M. T. Averbuch-Pouchot, *Acta Crystallogr.*, 1982, **B38**, 2883-2885.

[8] M. Bagieu-Beucher, *Acta Crystallogr.*, 1978, **B34**, 1443-1446.

[9] A. F. Selevich and V. D. Lyutsko, *Russ. J. Inorg. Chem.*, 1984, **29**, 364-369.

[10] V. A. Lyutsko, A. F. Selevich and E. R. Kutseva, *Russ. J. Inorg. Chem.*, 1990, **35**, 343-345.

[11] M. A. G. Aranda, J. Chaboy and S. Bruque, *Inorg. Chem.*, 1991, **30**, 2394-2397.

[12] A. F. Selevich and A. I. Lesnikovich, *Russ. J. Inorg. Chem.*, 1994, **39**, 1322-1326.

[13] A. I. Teterevkov and A. V. Chubarov, *Russ. J. Inorg. Chem.*, 1982, **27**, 529-531.

[14] P. Lightfoot, A. K. Cheetham and A. W. Sleight, *Inorg. Chem.*, 1987, **26**, 3544-3547.

[15] V. Lutsko and G. Johansson, *Acta Chem. Scand. Ser. A*, 1984, **38**, 663-669.

[16] L. K. Elbouaanani, B. Malaman and R. Gerardin, *J. Solid State Chem.*, 1999, **148**, 455-463.

[17] A. F. Selevich and A. I. Lesnikovich, *Zh. Neorg. Khim.*, 1995, **40**, 849-852.

[18] K. A. Selevich, L. S. Ivashkevich, A. F. Selevich and A. I. Lesnikovich, *Russ. J. Inorg. Chem.*, 2007, **52**, 1125-1130.

[19] I. D. Brown and D. Altermatt, *Acta Crystallogr.*, 1985, **B41**, 244-247.

[20] A. Hamady, M. F. Zid and T. Jouini, *J. Solid State Chem.*, 1994, **113**, 120-124.

[21] A. Salinas-Sanchez, J. L. Garcia-Munoz, J. Rodriguez-Carvajal, R. Saez-Puche and J. L. Martinez, *J. Solid State Chem.*, 1992, **100**, 201-211.

[22] *PeakFit Version 4.12*; Seasolve, 1999-2003.

[23] JCPDS, *International Centre for Diffraction Data*, 1999, P.1., Swathmore, Pennsylvania, PA 19081, USA, 11990.

[24] R. Shirley, *The CRYSFIRE System for Automatic Powder Indexing: User's Manual*, 2002, The Lattice Press, 41 Guildford Park Avenue, Guildford, Surrey, GU2 7NL, England.

[25] C. E. Housecroft and A. G. Sharpe, *Inorganic Chemistry*; Pearson Education: Harlow, 2001.

[26] C. Beghidja, G. Rogez, J. Kortus, M. Wesolek and R. Welter, *J. Am. Chem. Soc.*, 2006, **128**, 3140-3141.

[27] H. Miyasaka, R. Clerac, W. Wernsdorfer, L. Lecren, C. Bonhomme, K. Sugiura and M. Yamashita, *Angew. Chem. Int. Edit.*, 2004, **43**, 2801-2805.

[28] R. Karmakar, C. R. Choudhury, G. Bravic, J. P. Sutter and S. Mitra, *Polyhedron*, 2004, **23**, 949-954.

[29] R. Hotzelmann, K. Wieghardt, U. Florke, H. J. Haupt, D. C. Weatherburn, J. Bonvoisin, G. Blondin and J. J. Girerd, *J. Am. Chem. Soc.*, 1992, **114**, 1681-1696.

[30] M. T. Averbuch-Pouchot and A. Durif, *Topics in Phosphate Chemistry*; World Scientific Publishing Co. Pte. Ltd.: Singapore, 1996.

[31] R. D. Shannon, *Acta Crystallogr.*, 1976, **A32**, 751-767.

[32] A. B. P. Lever, *Inorganic Electronic Spectroscopy*; Elsevier: Amsterdam, 1984.

[33] P. J. Brown, *International Tables of Crystallography, Vol.C*; Kluwer: Dordrecht, 1992.

Chapter Seven

Characterisation of $MnH_2P_3O_{10}\cdot 2H_2O$ and Manipulation of its Interlayer Region

7.1 Introduction

To date, there are reports of a relatively small number of condensed phosphate phases containing manganese solely in the +3 oxidation state. Where structural determinations have been performed, these phases have generally been shown to be three-dimensional frameworks of MnO_6 octahedra corner-linked to PO_4 tetrahedra, with the exception of β-$HMnP_2O_7$,[1] which also possesses edge-shared Mn_2O_{10} dimers. The compound $MnH_2P_3O_{10}\cdot 2H_2O$[2] has been previously characterised in the literature, though the structure has remained unknown. A recent structural determination of the layered compound $AlH_2P_3O_{10}\cdot 2H_2O$[3] (AlTP) led us to explore whether the two phases were isostructural. In brief, the structure of AlTP consists of layers of dihydrogen triphosphate units providing octahedral coordination to Al^{3+}, with the terminal hydroxyl groups directed in the interlamellar region. The layers are held together by hydrogen bonding between these hydroxyl groups and the waters of hydration, which are situated within the interlayer region (Figure 7.1).

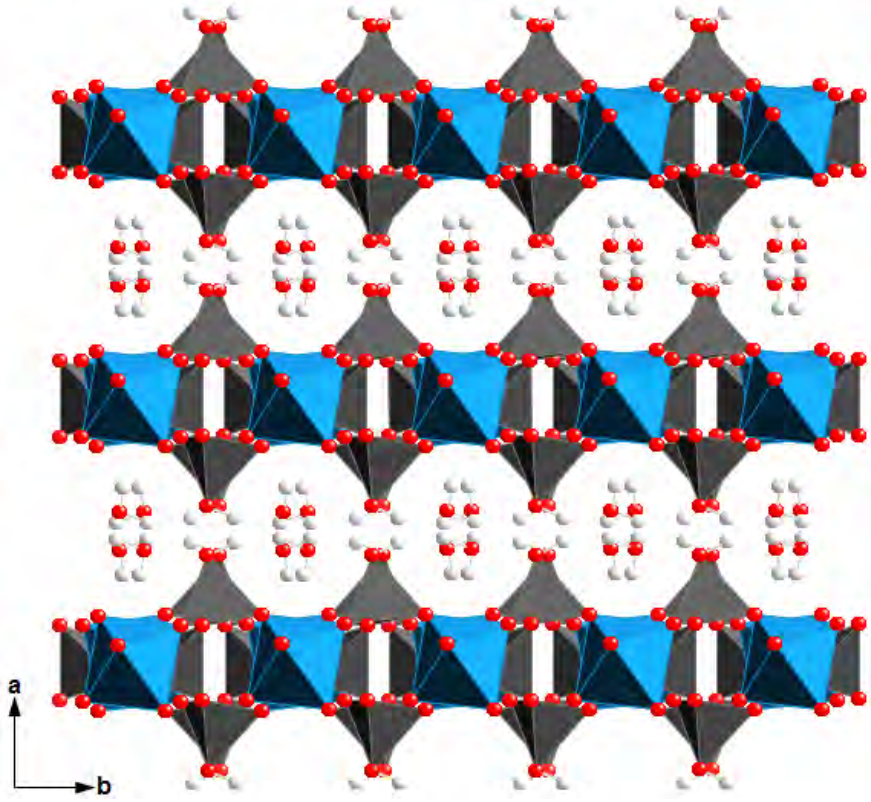

Figure 7.1: *Structure of $AlH_2P_3O_{10}\cdot 2H_2O$, showing AlO_6 octahedra (blue), condensed triphosphate tetrahedra (grey) and hydrogen atoms as white spheres.*

The AlTP structure type is similar to that of α-$Zr(HPO_4)_2\cdot H_2O$[4] (α-ZrP) and α-$Ti(HPO_4)_2\cdot H_2O$[5] (α-TiP), both of which are isostructural and consist of layers of MO_6 octahedra corner-linked to PO_4 tetrahedra. The hydroxyl groups also protrude into the interlamellar region and hydrogen bond with the interlayer water.

The $M^{III}H_2P_3O_{10}\cdot 2H_2O$ family of compounds has been relatively unexplored but is particularly appealing as the Al, Ga and Cr analogues have been shown to undergo chemical manipulations such as ion exchange,[6-8] intercalation,[6-14] and exfoliation.[9] The presence of transition metal ions could give these structures magnetic and/ or electronic properties in addition to the features they already possess. $CrH_2P_3O_{10}\cdot 2H_2O$[15] has been previously found to be isostructural with the Al analogue, with subsequent susceptibility measurements showing the phase to be

paramagnetic.[16] As such, our focus was with the synthesis of the Mn and Fe members of this family, referred to as MnTP and FeTP, respectively. Previous attempts by Checker[9] to synthesise these compounds have either led to poorly crystalline phases or phases that lack stability, making it difficult to manipulate the interlayer region. It was therefore of interest to us to explore whether we could identify reaction conditions that would allow chemical modification of these compounds. Attempts would also be made to incorporate magnetically active species into the interlayer region, which could potentially lead to a rearrangement of the layers and interesting magnetic properties. A similar approach to that reported for α-ZrP and α-TiP compounds was to be used, which involved first intercalating a basic organic molecule into the host in order to expand the layers and then contacting this intercalate with a transition metal solution.[17-20] Shpeizer *et al*[21-22] have reported using amine intercalates of α-ZrP in order to accommodate nickel ions into the structure. A three-tiered layer in between the zirconium phosphate layers was formed. The terminal tiers contained nickel atoms bonded to the phosphate layers while the middle tier was in isolation, possessing nickel atoms linked by hydroxo, aquo or acetato bridges. The material was found to be paramagnetic, but after heating to ~400°C, condensation of the central layer occurred to create three-tiered NiO like layers in between the zirconium phosphate layers, with the material now showing magnetic ordering similar to that of a ferromagnet. Isostructural compounds containing copper, cobalt and mixed cation composites were also prepared. In other studies Olivera-Pastor *et al*[23] synthesised a mixed alumina-chromia pillared α-ZrP as a potential material for catalysis and adsorption. Alfonso *et al*[24] have prepared α-TiP/ propylamine intercalation compounds containing Co^{2+}, Ni^{2+}, Fe^{3+} and Cr^{3+} ions. The

materials were found to be paramagnetic, but did impart optical properties on the host material.

It is therefore apparent that studies on the incorporation of magnetic species within layered metal phosphates have received relatively little attention. Much of the work so far has focused on using ZrP/ TiP hosts, though the obvious similarities of their structure to AlTP indicates that compounds of the latter type could also be manipulated in an analogous way, potentially giving novel magnetic compounds.

7.2 Experimental

A modified method based on that reported by Checker[9] was used to synthesise MnTP. Polyphosphoric acid (84% P_2O_5) and Mn_2O_3, in a P:Mn ratio of 8:1, were stirred at 150°C in a porcelain crucible. The resulting melt was transferred to a preheated oven where it was heated at 180°C for 72 h and cooled to room temperature over 24 h. The purple product was recovered by vacuum filtration and washed with acetone. Attempts to form sufficiently crystalline FeTP using similar reaction conditions were unsuccessful.

The series of monoamines $C_nH_{2n+1}NH_2$ (n = 3, 4, 6, 7, 8, 9) were intercalated into MnTP by adding 10 cm^3 of a concentrated solution of the respective amine to 0.5 g of the host. The mixture was stirred at room temperature for 1 h, with longer reaction times leading to a breakdown of the host phase. The purple products were recovered by vacuum filtration and washed with ethanol. Attempts to intercalate diamines into MnTP led to amorphous products being formed.

The hexylamine intercalate of MnTP (MnTP-hex) was refluxed with aqueous and methanolic solutions of $Cu(CH_3COO)_2\cdot H_2O$ or $Mn(CH_3COO)_2\cdot 4H_2O$ for durations of 1-120 h. The concentration of the acetate solutions ranged from 0.02–0.40 mol

dm^{-3}. In all cases the products were recovered by vacuum filtration and washed with water and ethanol.

Powder X-ray diffraction (XRD) data on MnTP were collected on a Bruker AXS: D8 Advance diffractometer in transmission mode with a 2θ scan range of 5-60°. All other XRD data were collected on a Siemens D5000 diffractometer in transmission mode with a 2θ scan range of 3-60°.

7.3 Results and Discussion

7.3.1 Characterisation of $MnH_2P_3O_{10}\cdot 2H_2O$

Under the reaction conditions employed, MnTP was synthesised in a relatively crystalline form, with the XRD pattern shown in Figure 7.2. Attempts to synthesise more crystalline forms through varying the reaction conditions were unsuccessful. A Rietveld refinement of the XRD data using AlTP[3] as a structural model indicated that MnTP adopts the same structure type, with space group *P*2/*c* and *a* = 7.803(3) Å, *b* = 4.942(1) Å, *c* = 12.226(2) Å and *β* = 95.76(1)° (see Appendix 2). However, allowing the atomic coordinates and thermal factors of the phase to freely refine caused instabilities, which were mostly evident from a divergence in the least squares refinement. When convergence was achieved, the model contained thermal factors with highly negative coefficients and some unusual bond lengths and therefore, these solutions were discounted. These instabilities are likely to be a result of the relatively poor quality of the data and the number of variables necessary for a full refinement. The situation could be improved by synthesising a more crystalline sample or by employing neutron diffraction on a deuterated sample, which would permit a more accurate location of the oxygen positions.

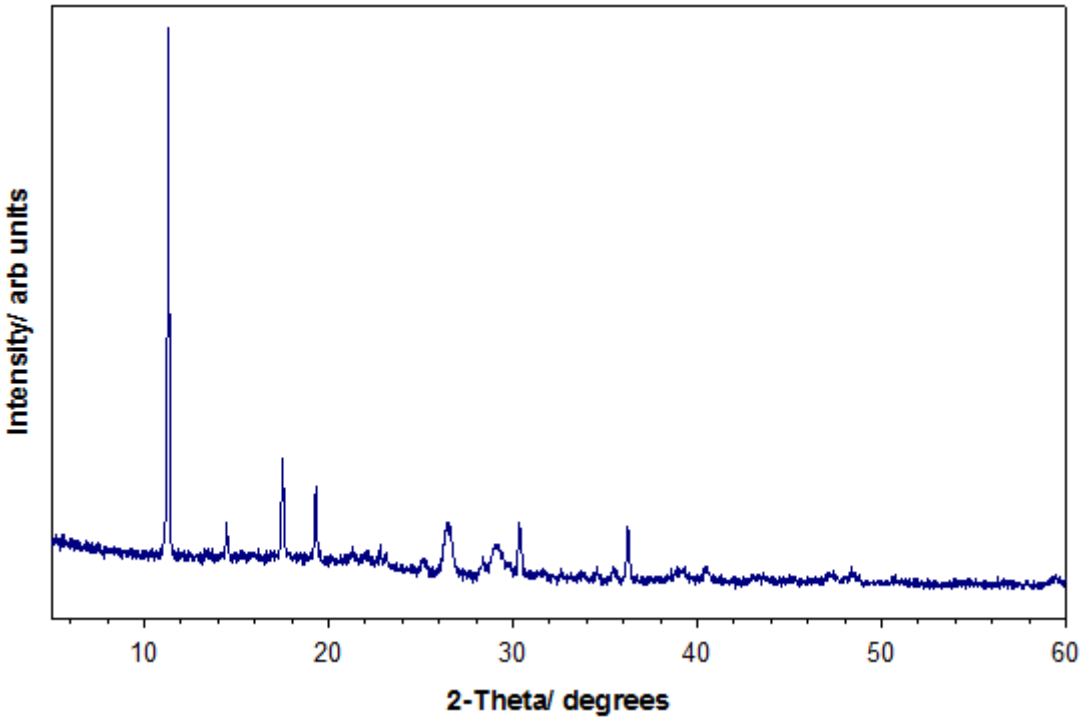

Figure 7.2: *XRD pattern of MnTP*

It was evident from the diffraction pattern of MnTP that some peaks were broader than others, and a closer inspection of the full width at half maximum (FWHM) showed that peaks were broader for those reflections possessing a (112) component (Table 7.1). Similar anisotropic broadening was reported in the analysis of AlTP,[6] and is likely to be a feature of these layered hydrated structures.

Table 7.1: *FWHMs for selected reflections from the MnTP phase*

hkl	**2θ/ °**	**FWHM/ °**
100	11.320	0.089
002	14.483	0.092
$10\bar{2}$	17.503	0.132
102	19.316	0.146
$11\bar{2}$	25.187	**0.309**
112	26.465	**0.465**
013	28.355	0.061

Scanning Electron Microscopy (SEM) showed that MnTP consists of rod-shaped crystals (Figure 7.3). The anisotropic particle size is not surprising and is likely to be the cause of the anisotropic line broadening observed in the XRD powder pattern. Generally, factors affecting peak widths are the instrument characteristics and specimen nature. For the latter case, anisotropic broadening is usually seen if there is an anisotropic particle size, anisotropic strains present or stacking faults in the sample structure.

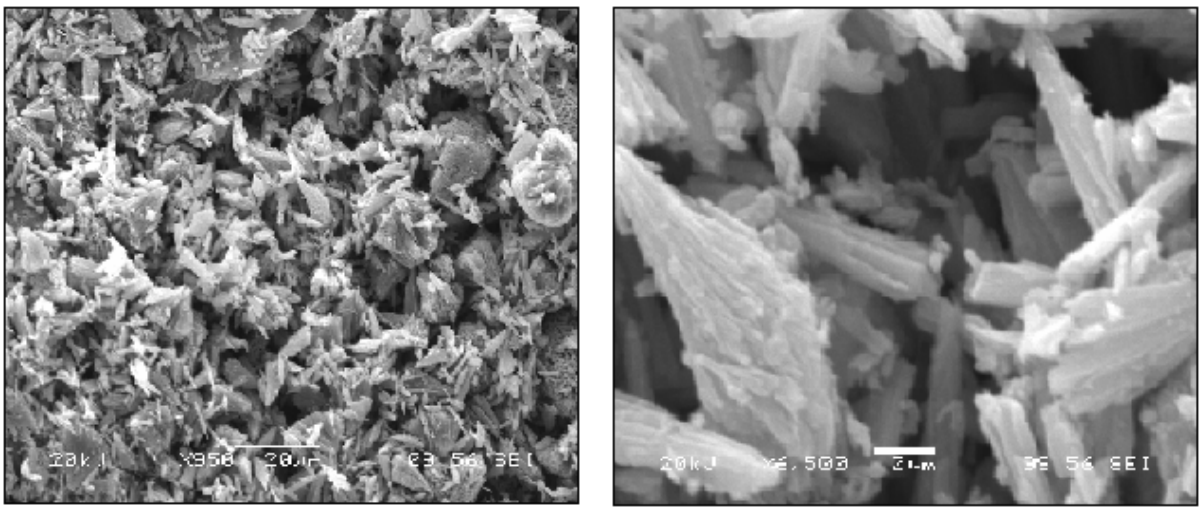

Figure 7.3: *SEM images of MnTP showing rod-shaped crystals*

IR spectroscopy was employed so that the spectra of products from subsequent reactions on MnTP could be compared to that of the original host phase (see Appendix 3). A broad band centred at approximately 3358 cm^{-1} confirmed the presence of hydrogen bonded water while a band at ~1667 cm^{-1} was assigned to the deformation vibrations of the water molecules. A band at *ca.* 3554 cm^{-1} was assigned to the –OH vibration in the triphosphate chain and bands in the region of 1220-1000 cm^{-1} were associated with the P-O vibrations of the phosphate groups.

7.3.1.1 Thermal Stability

The TGA-MS plot for MnTP heated in N_2 is shown in Figure 7.4. The mass spectrum showed that water was evolved from the compound during each mass loss step. The first loss of ~10.6% occurred in an endothermic event over 120°C-280°C, corresponding to ~2.0 moles of water of hydration being lost to give $MnH_2P_3O_{10}$. Decomposition then occurred above 350°C to give a final product of MnP_3O_9. The DTA signal showed an endothermic event followed by an exothermic event, which was in accordance with decomposition and then crystallisation of the polyphosphate, respectively. A mass loss of ~5.0% was observed, corresponding to ~0.96 moles of water being lost, which was close to the expected 1 mole of water of constitution. The evolution of water molecules of constitution is understood to be the result of a condensation polymerisation reaction of the triphosphate units, which leads to the formation of further P-O-P linkages, as shown schematically in Figure 7.5.

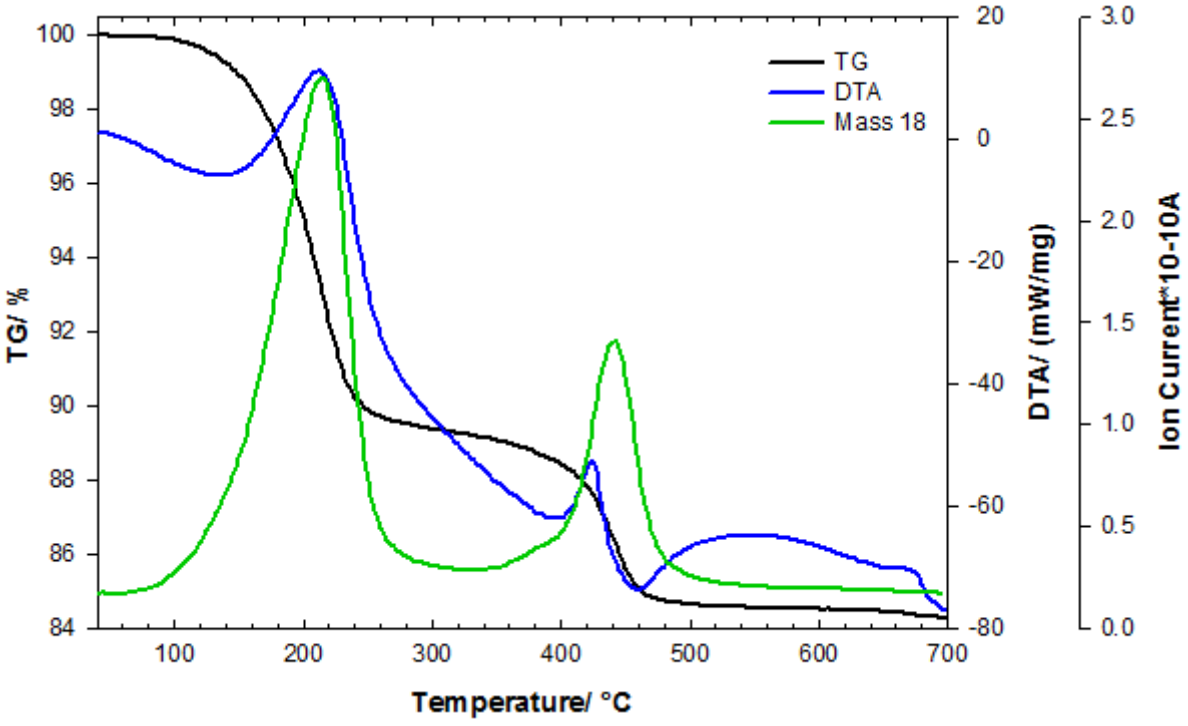

Figure 7.4: *TGA-MS Plot for MnTP*

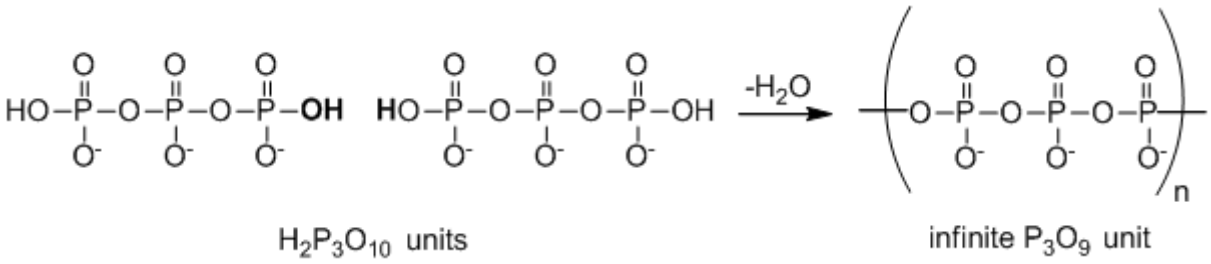

Figure 7.5: *Condensation polymerisation of the triphosphate unit to form P-O-P linkages*

7.3.1.2 Magnetic Measurements

Figure 7.6 shows the magnetic susceptibility measurements for MnTP and the Curie-Weiss fit to the data. The compound showed an antiferromagnetic response in the zero-field cooled/ field warmed (ZFCFW) measurement and a ferromagnetic component in the field cooled/ field warmed (FCFW) measurement, indicative of canted antiferromagnetism or spin glass behaviour. A Néel temperature of ~6 K was observed and a small Weiss constant of -7.8(5) K, suggesting that the magnetic interactions in this compound are relatively weak. At higher temperatures the sample behaved as a typical Curie-Weiss paramagnet, with a calculated μ_{eff} of 4.776(7) μ_B that was in good agreement with the spin-only moment of high spin Mn^{3+} complexes and observed moments of 4.80-4.90 μ_B.[25]

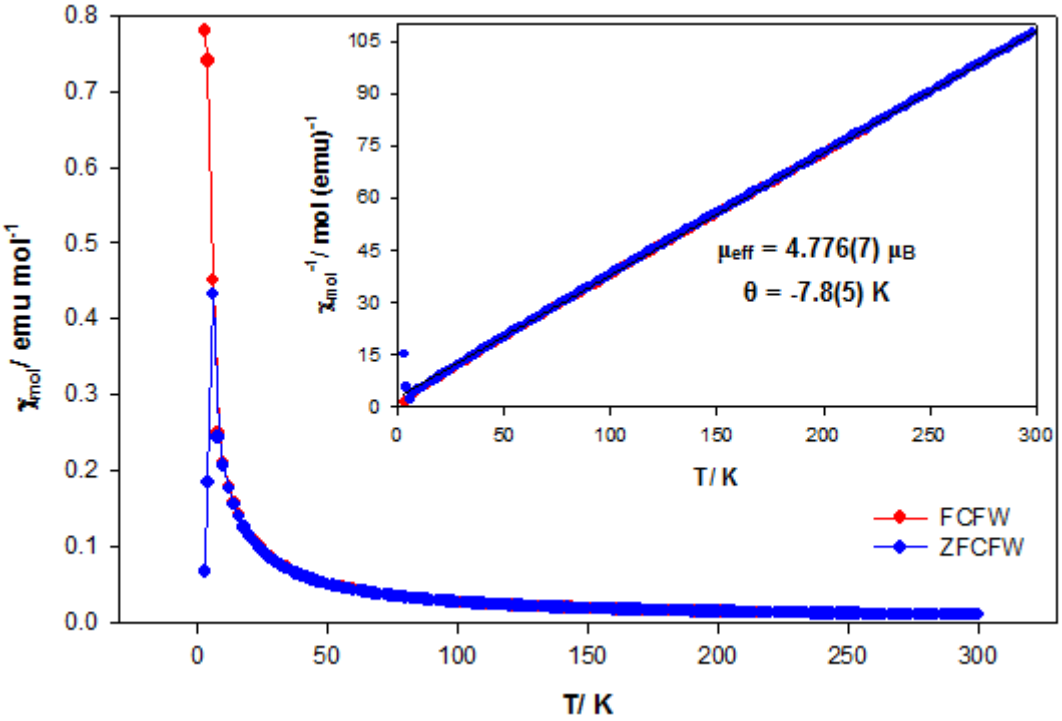

Figure 7.6: *Plot of molar susceptibility against temperature for MnTP, with inset showing the Curie-Weiss fit to the data.*

7.3.2 Intercalation of monoamines into MnTP

The driving force behind amine intercalation is worth speculating on before a more detailed discussion of the various aspects is employed. A range of favourable interactions are possible which result in amines residing in the interlayer spacing as opposed to simply existing as a separate entity to the MnTP phase. Amines exhibit basic behaviour, and in MnTP the P-OH groups that protrude into the interlayer region will be relatively acidic. Thus an acid-base type interaction or at least hydrogen bonding is possible between the two functional groups. Each triphosphate unit is capable of interacting with two amine molecules to give a bilayer in which it is expected that the hydrophobic chains will sit together and allow the hydrophilic groups to interact with each other. Indeed, it has been well reported that diamines form a monolayer and that monoamines form a bilayer in these layered structure

types.[10,26-30] There are various arrangements that the amine molecules could have with respect to each other. That is to say that the hydrocarbon chains could be stacked or interdigitated, either way giving rise to favourable van der Waal's interactions. Two layers where the alkyl chains face against each other have been found to increase colloid stability[31-32] and to have use in nanoencapsulation.[32]

It is worth noting that the maximum intercalation capacity of the host material may not necessarily be fulfilled. The formation of stoichiometric compounds highly depends on the cross section of the guest being less than the free area of each active site; this is known as the "covering effect".[33] If the cross section of the amine entity exceeds the free area available to it, then this may result in adjacent sites becoming unavailable for bonding to other amine molecules. If the maximum intercalation capacity is not fulfilled then this gives rise to the possibility of a porous material which can potentially be used as a catalyst, molecular sieve, sorbent or as the inorganic component of inorganic-organic hybrids.

Figure 7.7 shows the powder patterns of the monoamine intercalation compounds of MnTP. Upon intercalation, the dominant diffraction peak of the MnTP host with d_{100} = 7.82 Å disappeared and a new dominant peak appeared at a lower angle. The d_{100} peak is related to the interlayer separation (see Figure 7.8), and so it is therefore likely that the new dominant peak that appeared was d_{100} of the intercalated phase. The positions of these peaks were consistent with the MnTP phase being expanded to accommodate the amine molecules. Each amine entity can be likened to a pillar, holding the layers apart for the incoming of further species.

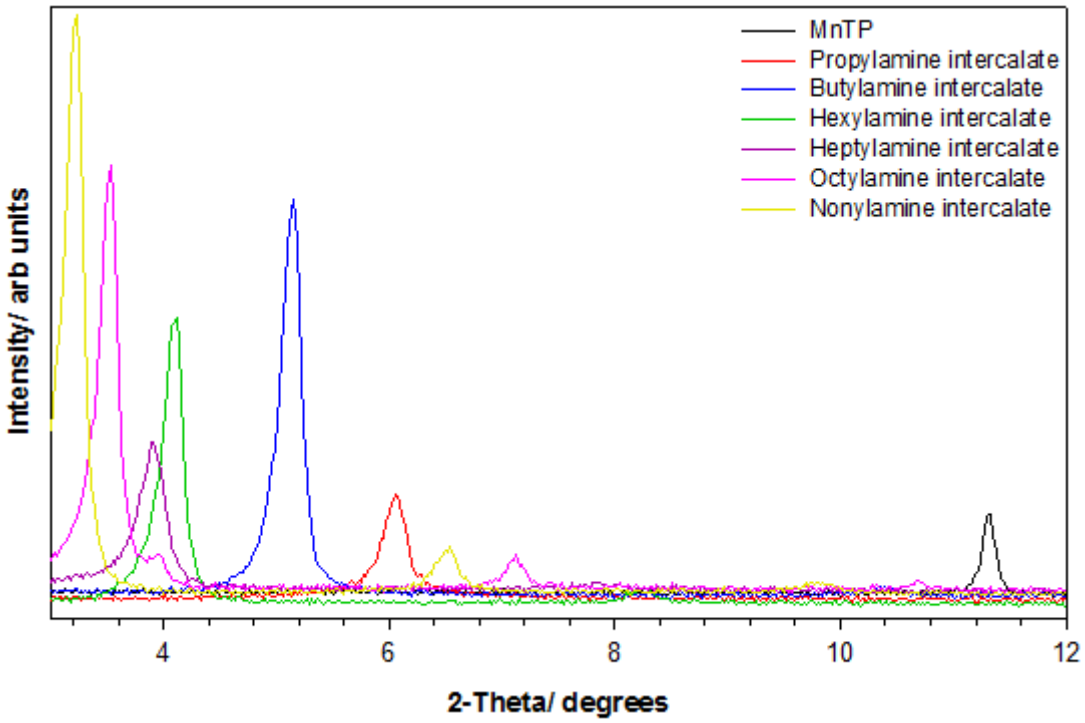

Figure 7.7: *XRD powder patterns of the amine intercalates*

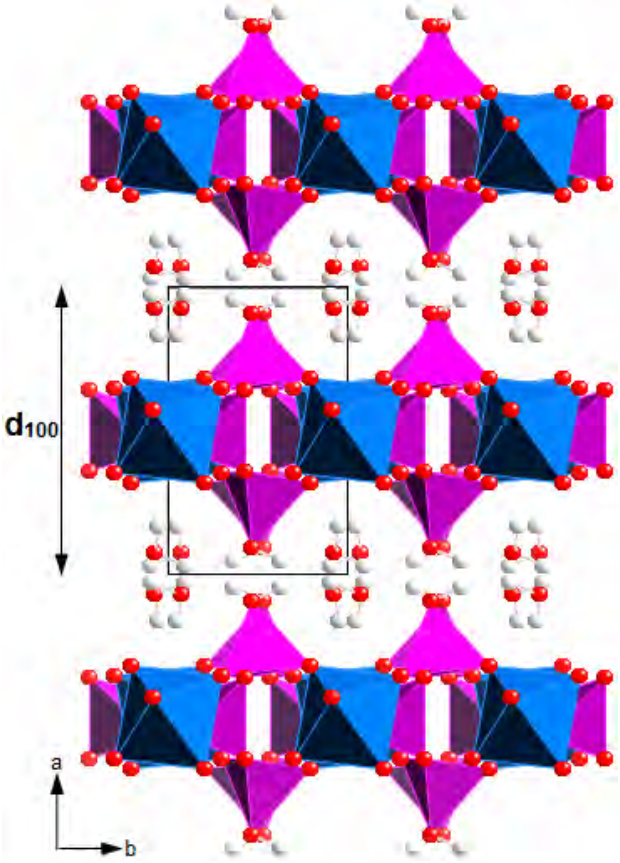

Figure 7.8: *The relationship between the d_{100} peak and the interlayer separation of MnTP.*

As can be seen from Table 7.2, the interlayer spacing increased as the carbon chain length was increased; the fact that some order remained in the host material demonstrates the adaptability of the metal phosphate layers. The linear relationship indicated that the amines were regularly oriented in the interlayer region and that the angle to the phosphate layer remained constant.

Table 7.2: *The interlayer separations of the intercalated phases, with estimated errors in parentheses*

Phase	Measured interlayer distance (d-spacing) from XRD/ Å
MnTP	7.82(2)
MnTP + propylamine	14.57(10)
MnTP + butylamine	17.19(15)
MnTP + hexylamine	21.59(10)
MnTP + heptylamine	22.63(16)
MnTP + octylamine	25.15(11)
MnTP + nonylamine	27.46(16)

The expected increase in chain length of the amine with adding a carbon atom to the chain was estimated by taking a typical sp^3 hybridised C-C bond length[34] and C-C-C bond angle[34] and using trigonometry. As can be seen from Figure 7.9, the length of the chain should increase by approximately 1.27 Å per carbon atom added (assuming the conformation of the alkyl chain is all trans).

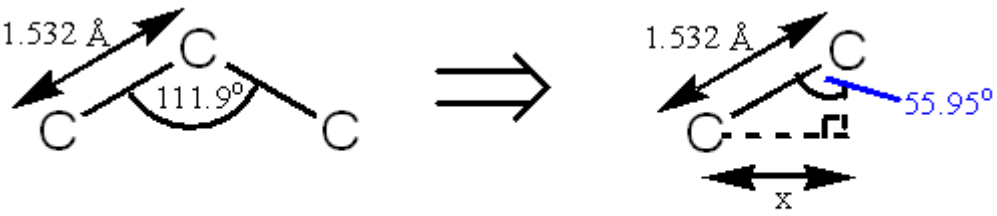

$$Sin(55.95) = \frac{x}{1.532}$$

$$x = 1.27 \text{ Å}$$

Figure 7.9: *Calculation of the increase in amine chain length due to the addition of one carbon atom to the unit*

Plots of interlayer spacing against chain length are often informative as they allow one to assess the incline angle of the intercalated guest. The gradient of such plots indicates the change in d-spacing with the addition of a carbon atom to the chain. It is evident in Table 7.2 that the increase in interlayer separation for each additional carbon was greater than 1.27 Å. Therefore a bilayer structure was assumed so that for example, the interlayer spacing observed for the propylamine intercalate was due to six carbons rather than three. It was also assumed that the amine bilayer had a stacked arrangement as opposed to an interdigitated one. The plot obtained revealed that as the carbon chain increased by one *i.e.* by 1.27 Å, the interlayer spacing increased by 2 × 1.074 Å due to the formation of a bilayer. Using this information trigonometry was again employed to estimate an incline angle of ~58(1)°; this is described in Figure 7.10 and the result has been shown in Figure 7.11. The angle is similar to that observed from a previous study on AlTP.[10] A similar angle of inclination was also reported for the related analogues α-ZrP[27,35] and α-

TiP.[29] For the former it was approximately 55-56° and for the latter approximately 59°.

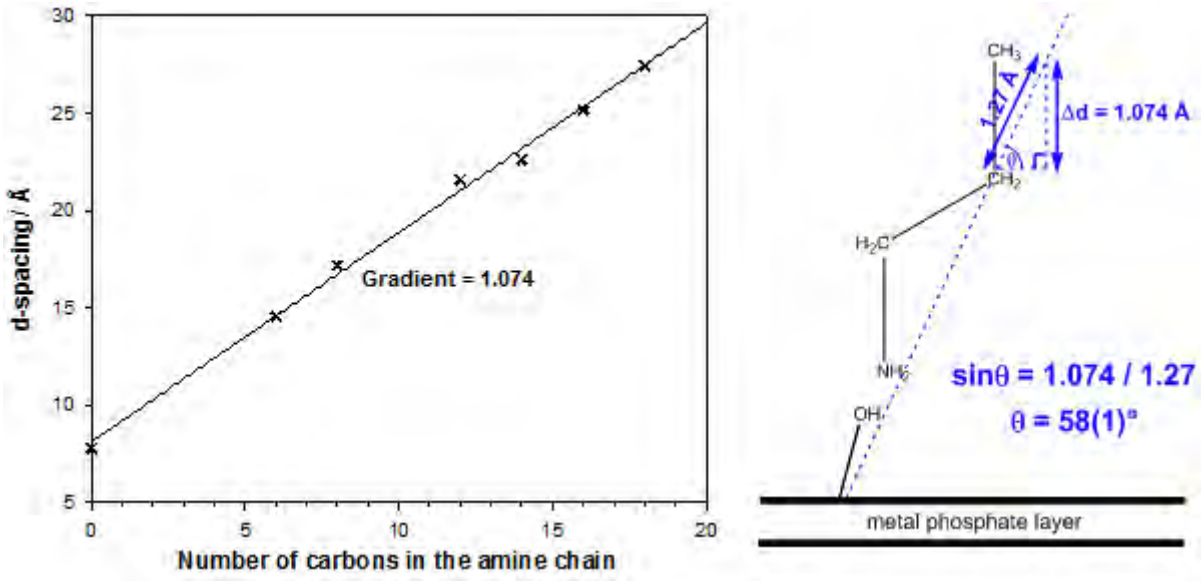

Figure 7.10: *Increase in the interlayer separation with increasing chain length of the amine and subsequent estimation of the incline angle of the intercalated amine.*

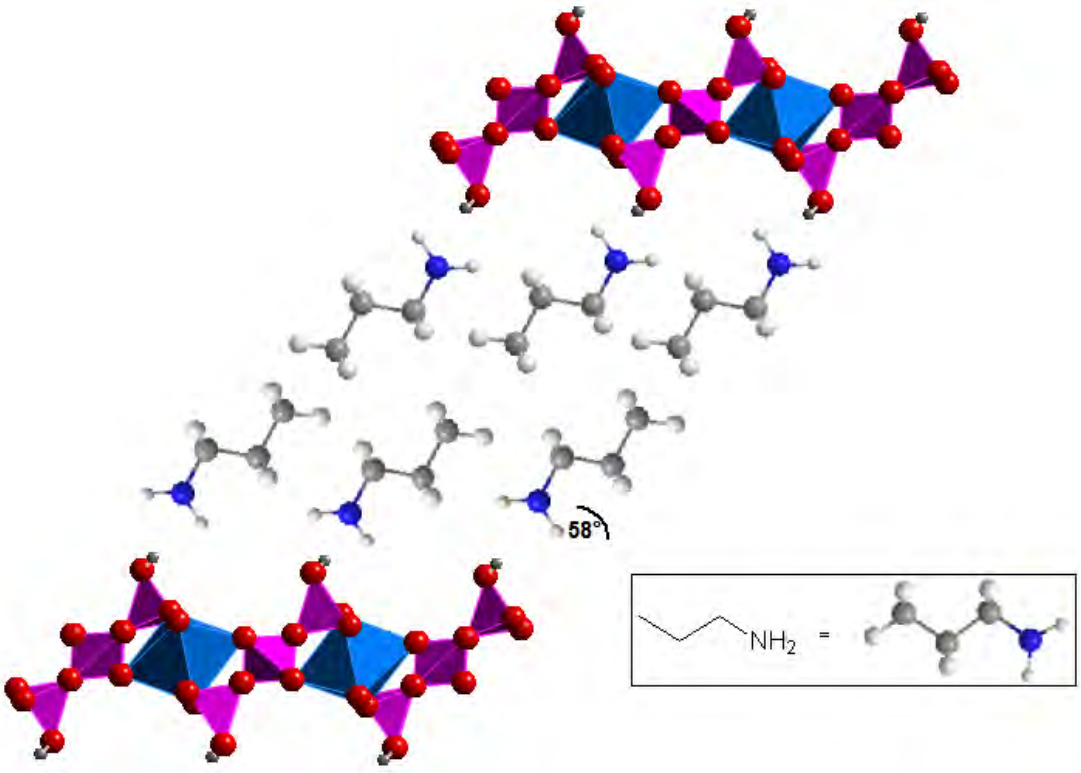

Figure 7.11: *Schematic showing the arrangement of a monoamine bilayer in MnTP; amines are not to scale and for clarity water molecules have been omitted*

7.3.3. Incorporation of TM ions into MnTP-hex

The hexylamine intercalate of MnTP (MnTP-hex) was chosen as the pillared host material as it could obtained in a relatively high yield and purity. This host was then used to attempt incorporation of further TM ions between its layers. Detailed characterisation of the host material was undertaken prior to further reaction so that any subsequent changes could be clearly distinguished.

SEM pictures shown in Figure 7.12 confirmed that the layered structure of the material remained intact, with the crystal shapes appearing plate-like.

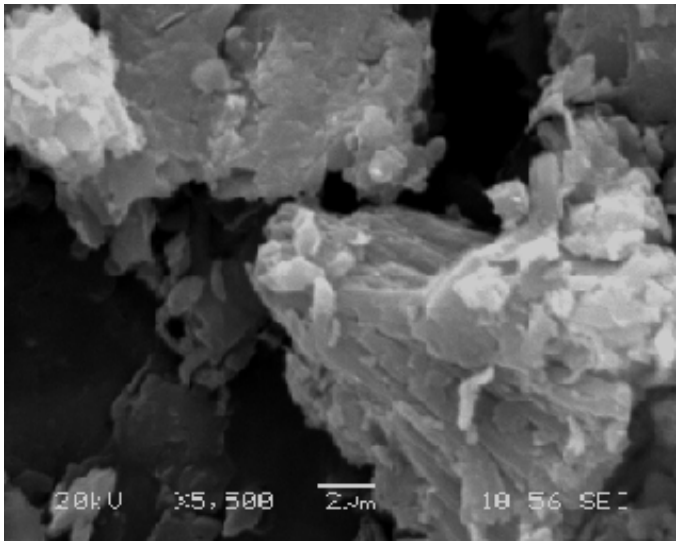

Figure 7.12: *SEM image of MnTP-hex*

The IR spectrum of MnTP-hex (Appendix 3) showed that as expected, the phosphate groups remained present in the structure, with bands evident in the region of 1220-1000 cm^{-1}. Upon intercalation, the bands due to lattice water became more broadened and poorly resolved, with the deformation vibration of water shifting to a lower frequency of 1628 cm^{-1}. Although bands due to the $–NH_2$ functional group were masked by the broad O-H band, the presence of amine was confirmed by the appearance of bands in the area of ~2950-2850 cm^{-1}, which corresponds to the C-H

stretching region. A peak at 1467 cm^{-1} was assigned to the C-H bending mode. There was also appearance of peaks that could be assigned to $-NH_3^+$, for example, a peak at 1523 cm^{-1} was attributed to its asymmetric bending mode.

7.3.3.1 The use of aqueous solutions of the metal acetate

As mentioned in section 7.2, MnTP-hex was initially refluxed with aqueous solutions of metal acetate. It was found that the concentration of the solutions did not particularly affect the product outcome, but reflux times were important. Figures 7.13 and 7.14 show the XRD patterns of the products from the reactions with Cu^{II} acetate and Mn^{II} acetate, respectively. These products were isolated after a reflux time of 1 h. The product from the reaction of MnTP-hex with Cu acetate was found to match $Cu_2P_2O_7\cdot 3H_2O$ in the JCPDS[36] database, the structure of which is unknown. Although the product from reaction with Mn acetate could not be identified, the similarity of the diffraction patterns suggested that an analogous manganese pyrophosphate had formed. As the reflux times were increased, the crystallinity of the product gradually deteriorated to give an amorphous phase which was typically evident after a reflux time of 24 h. Refluxing for up to 120 h caused complete hydrolysis of the triphosphate unit to give $MnPO_4\cdot H_2O$, which was seen as a crystalline phase in the diffraction pattern. From these results it was clear that these reaction conditions were leading to breakdown of the host manganese triphosphate layers.

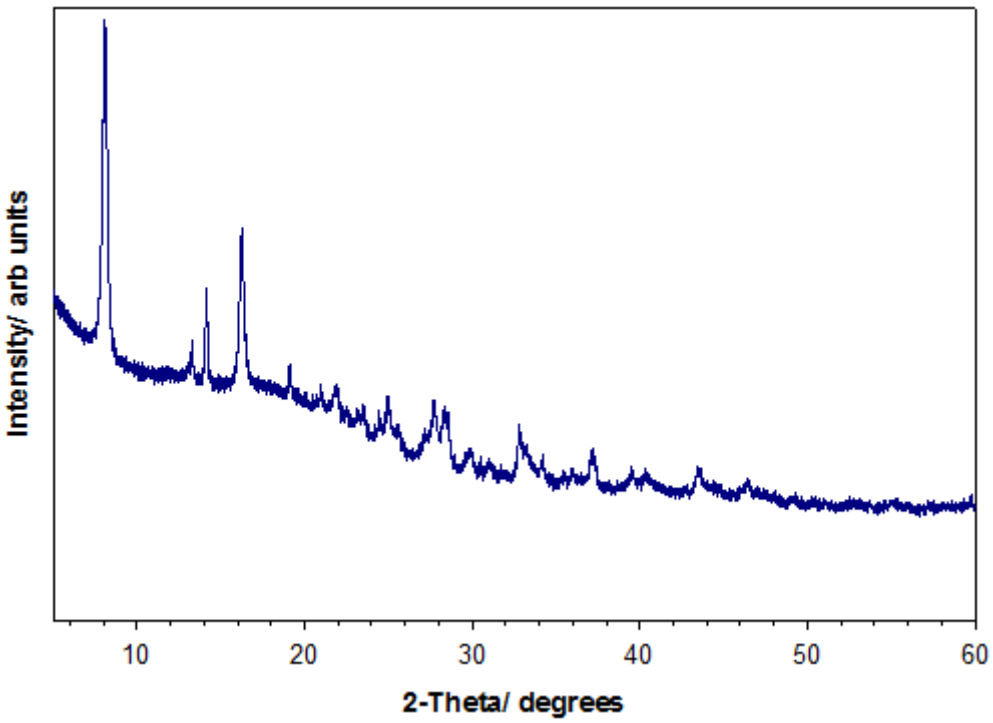

Figure 7.13: *Product from the reaction of MnTp-hex with aq. Cu acetate after 1 h reflux*

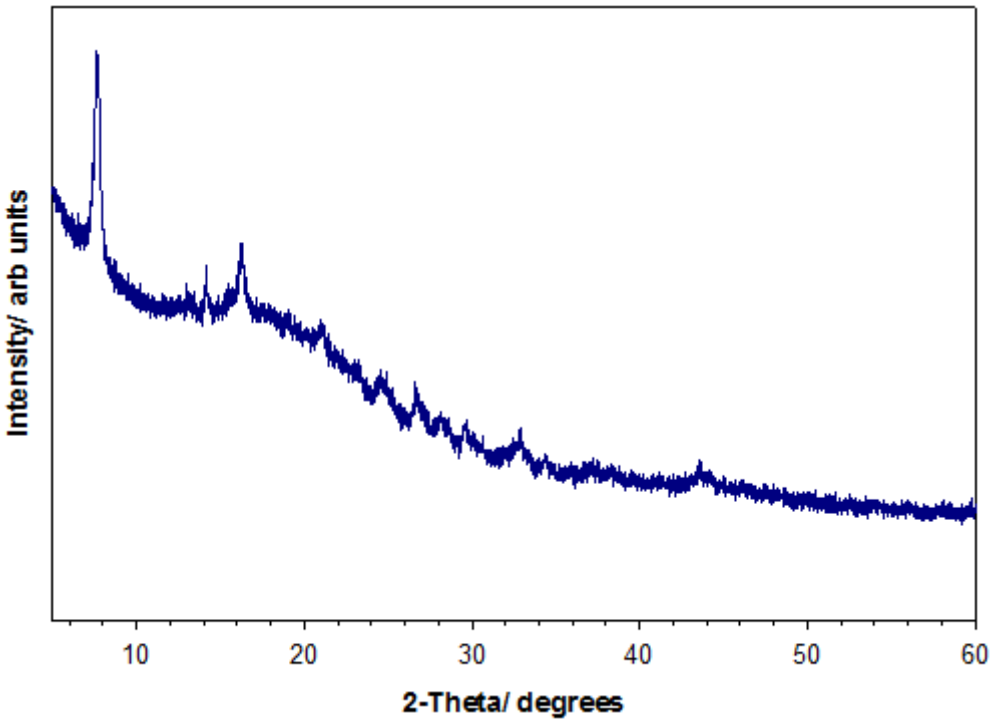

Figure 7.14: *Product from the reaction of MnTp-hex with aq. Mn acetate after 1 h reflux*

7.3.3.2. The use of methanolic solutions of the metal acetate

To explore whether the presence of water was influencing the stability of the host structure, methanol solvent was used to dissolve the metal acetate and act as the solvent medium. Encouragingly, MnTP-hex was found to remain intact after 1 h of refluxing in methanol, with no hydrolysis products observed. Indeed, the layered structure of MnTP-hex was still retained even after 28 h of refluxing in methanolic solutions. However, as can be seen from Figure 7.15, increasing the reflux time beyond 4 h led to a gradual reduction in its crystallinity. The instability of the amine intercalate to aqueous solutions suggests that significant hydrolysis reactions readily occur which not only remove the intercalate, but likely hydrolyse the metal triphosphate layers to amorphous products.

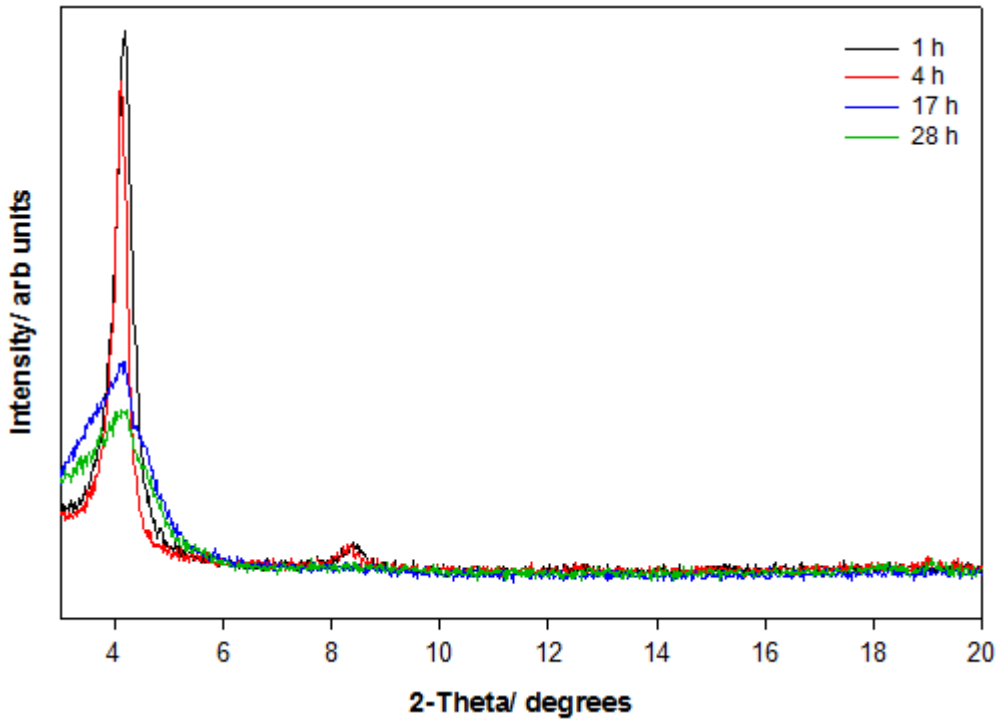

Figure 7.15: *The effect of different reflux times on the reaction of MnTP-hex with methanolic Cu acetate*

Samples refluxed in methanolic solutions for 4 h were analysed by XRF in order to ascertain whether further TM ions had been incorporated into the structure. It should be noted that measurements were performed without external calibration, so should be treated more as a qualitative rather than quantitative analysis. The results are summarised in Table 7.3 and include those of pre-reaction host MnTP-hex, which was measured for comparison purposes. For the reaction with Cu acetate, Cu had indeed been incorporated into the final product while for the reaction with Mn acetate, there was more Mn present in the product *cf.* MnTP-hex. It is possible that the additional TM ions form part of a separate phase that is X-ray amorphous, or alternatively they could be situated within the interlayer region of MnTP-hex, where a random arrangement would mean that they are not easily detected by XRD. It is not possible to distinguish these possibilities from XRF however.

Table 7.3: *XRF results for MnTP-hex and products after reaction with methanolic solutions of Cu acetate and Mn acetate.*

	Measured Elemental Weight %		
	Mn	**P**	**Cu**
MnTp-hex	21.46	23.33	0
MnTp-hex + Cu^{II} acetate	20.79	20.33	16.56
MnTp-hex + Mn^{II} acetate	33.27	18.64	0

IR spectroscopy was also performed on the products in order to investigate whether the TM ions had been incorporated in the acetate form (Appendix 3). The spectra showed no evidence for a C=O functionality existing in the structure, though did confirm the presence of amine in the products.

Given the possibility that the TM ions existed in the interlayer region alongside the amine, the products after reflux were heated in an attempt to "burn off" the amine to leave behind a TM entity between the layers. Slow heat treatments to 300°C were unsuccessful, with the layered structure collapsing to give an amorphous material (see Figure 7.16 as an example). This suggests that once the amine pillars are removed, the material can no longer retain any long-range order.

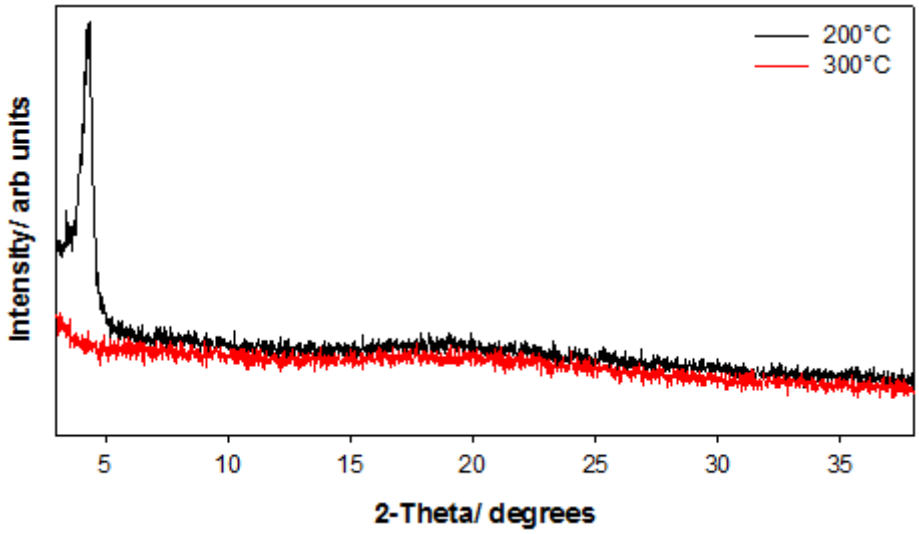

Figure 7.16: *Heat treatments of the product from reaction of MnTP-hex with methanolic Cu acetate after 4 h reflux*

7.4 Conclusions

MnTP was synthesised in a relatively crystalline form, with initial results from the Rietveld refinement suggesting that the phase is isostructural to AlTP. The compound was found to remain stable up to ~120°C before the water of crystallisation was lost, with condensation of the triphosphate unit occurring above 350°C. Magnetic measurements revealed that the phase magnetically orders at ~6 K and exhibits either canted antiferromagnetism or spin glass behaviour.

The phase appeared to be relatively stable in that it could undergo intercalation with monoamines, which has previously been reported to be

unsuccessful.[9] XRD data suggested that a bilayer was formed from which an inclination angle of 58(1)° was calculated. Attempts were made to incorporate Cu^{II} and Mn^{II} ions into the structure of the hexylamine intercalate. Where aqueous solutions of the transition metals were used, it was found that the excess water present caused hydrolysis of the host phase. The reason for this hydrolytic instability is at present unclear; it could be that MnTP-hex is predominantly hydrophobic and so breaks down in the presence of an aqueous solution. Indeed, the pillared intercalate remained relatively stable in the presence of methanolic solutions, with XRF showing that copper and manganese ions had been incorporated into the products. IR spectroscopy on these products showed that the acetate ion was absent, though it remained unclear as to whether the TM ions had been incorporated into the host structure or whether they were part of a separate phase. Heat treatments of the compounds in an attempt to remove hexylamine from the layers led to a loss of the long range order, suggesting that the metal phosphate layers collapse randomly when the amine is removed. These studies therefore show that in attempting to incorporate TM ions into the interlayer region of MnTP, it is difficult to retain the long range order of the host and determine if the manganese triphosphate layers remain intact.

References

[1] P. A. Durif and M. T. Averbuch-Pouchot, Acta Crystallogr., 1982, **B38**, 2883-2885.

[2] M. A. G. Aranda, J. Chaboy and S. Bruque, Inorg. Chem., 1991, **30**, 2394-2397.

[3] S. K. Rishi, B. M. Kariuki, N. J. Checker, J. Godber and A. J. Wright, Chem. Commun., 2006, 747-749.

[4] A. Clearfield and G. D. Smith, Inorg. Chem., 1969, **8**, 431-436.

[5] A. N. Christensen, E. K. Andersen, I. G. K. Andersen, G. Alberti, M. Nielsen and M. S. Lehmann, Acta Chem. Scand., 1990, **44**, 865-872.

[6] S. K. Rishi, Synthesis and Characterisation of a series of layered trivalent metal triphosphates, PhD Thesis, University of Birmingham, 2006.

[7] T. P. Marsh, Studies into the Ion Exchange and Intercalation Properties of $AlH_2P_3O_{10}\cdot 2H_2O$, PhD Thesis, University of Birmingham, 2011.

[8] A. Hayashi, H. Saimen, N. Watanabe, H. Kimura, A. Kobayashi, H. Nakayama and M. Tsuhako, Langmuir, 2005, **21**, 7238-7242.

[9] N. J. Checker, The Synthesis and Properties of Novel Condensed Phosphates, PhD Thesis, University of Birmingham, 2006.

[10] A. Hayashi, H. Nakayama, M. Tsuhako, T. Eguchi and N. Nakamura, J. Inclusion Phenom. Macrocyclic Chem., 1999, **34**, 401-412.

[11] V. A. Lyutsko and A. V. Tuchkovskaya, Russ. J. Inorg. Chem., 1985, **30**, 1284-1287.

[12] V. A. Lyutsko, A. V. Tuchkovskaya and A. L. Shifrina, Russ. J. Inorg. Chem., 1987, **32**, 1541-1544.

[13] V. A. Lyutsko, A. V. Tuchkovskaya and A. L. Shifrina, Russ. J. Inorg. Chem., 1988, **33**, 1431-1433.

[14] V. A. Lyutsko, A. V. Tuchkovskaya and O. L. Novash, Russ. J. Inorg. Chem., 1991, **36**, 641-643.

[15] L. S. Ivashkevich, A. S. Lyakhov and A. F. Selevich, Phos. Res. Bull., 2010, **24**, 6-11.

[16] F. C. Coomer, Y. Begum and A. J. Wright, Unpublished Results, 2008.

[17] C. Ferragina, A. L. Ginestra, M. A. Massucci, P. Patrono and A. A. G. Tomlinson, J. Phys. Chem., 1985, **89**, 4762-4769.

[18] M. Alcántara-Rodríguez, P. Olivera-Pastor, E. Rodríguez-Castellón, A. Jiménez-López, M. Lenarda, L. Storaro and R. Ganzerla, J. Mater. Chem., 1998, **8**, 1625-1630.

[19] F. J. Perez-Reina, P. Olivera-Pastor, P. Maireles-Torres, E. Rodriguez-Castellon and A. Jimenez-Lopez, Langmuir, 1998, **14**, 4017-4024.

[20] P. Maireles-Torres, P. Olivera-Pastor, E. Rodríguez-Castellón and A. Jiménez-López, J. Solid State. Chem., 1991, **94**, 368-380.

[21] B. Shpeizer, D. M. Poojary, K. Ahn, C. E. R. Jr and A. Clearfield, Science, 1994, **266**, 1357-1359.

[22] B. G. Shpeizer, P. Sylvester, R. A. Cahill and A. Clearfield, Chem. Mater., 1999, **11**, 1201-1209.

[23] P. Olivera-Pastor, J. Maza-Rodríguez, P. Maireles-Torres, E. Rodríguez-Castellón and A. Jiménez-López, J. Mater. Chem., 1994, **4**, 179-184.

[24] B. F. Alfonso, C. Trobajo, M. A. Salvadó, P. Pertierra, S. García-Granda, J. Rodríguez-Fernández, J. A. Blanco and J. R. García, Z. Anorg. Allg. Chem., 2005, **631**, 2174-2180.

[25] C. E. Housecroft and A. G. Sharpe, Inorganic Chemistry; Pearson Education: Harlow, 2001.

[26] M. Casciola, U. Constantino, L. Dicroce and F. Marmottini, J. Inclusion Phenom., 1988, **6**, 291-306.

[27] D. J. MacLachlan and K. R. Morgan, J. Phys. Chem., 1992, **96**, 3458-3464.

[28] M. Danjo, M. Tsuhako, H. Nakayama, T. Eguchi, N. Nakamura, S. Yamaguchi, H. Nariai and I. Motooka, Bull. Chem. Soc. Jpn., 1997, **70**, 1053-1060.

[29] A. Espina, C. Trobajo, S. A. Khainakov, J. R. García and A. I. Bortun, J. Chem. Soc., Dalton Trans., 2001, **5**, 753-757.

[30] F. Menéndez, A. Espina, C. Trobajo and J. Rodríguez, Mat. Res. Bull., 1990, **25**, 1531-1539.

[31] A. Swami, A. Kumar and M. Sastry, Langmuir, 2003, **19**, 1168-1172.

[32] E. T. Kisak, B. Coldren and J. A. Zasadzinski, Langmuir, 2002, **18**, 284-288.

[33] M. S. Whittingham and A. J. Jacobson, Intercalation Chemistry; Academic Press Inc: New York, 1982.

[34] D. Nasipuri, Stereochemistry of Organic Compounds, Principles and Applications; John Wiley and Sons: Chichester, 1991.

[35] G. Alberti and U. Constantino, J. Molec. Cat., 1984, **27**, 235-250.

[36] JCPDS, International Centre for Diffraction Data, 1999, P.1., Swathmore, Pennsylvania, PA 19081, USA, 11990.

Chapter Eight

Conclusions and Further Work

This thesis has focused on the synthesis and characterisation of Mn^{3+} condensed phosphate phases and substitution with Fe^{3+}. Where there was scope, attempts were also made to chemically modify these hosts through ion exchange and intercalation.

8.1 Conclusions

For compounds containing a mixed cation composition, it was generally found that the introduction of Fe into the system led to a more regular octahedral TM-O_6 coordination sphere being observed, which in turn could be related to changes in the unit cell parameters. Many of the compounds encountered showed interesting colourations and as such, detailed analyses of their thermal stability and optical properties were conducted. These can be considered preliminary characterisations were these compounds to be applied as non-toxic inorganic pigments. Within these structure types it was found that the symmetry of the MnO_6 unit relates to the number and intensity of d→d transitions occurring in the visible region, and hence strongly influences the colouration. Intense colourations were often observed when the MnO_6 unit was highly distorted.

In addition, the magnetic properties of these condensed phosphate phases were studied. The magnetic ordering in these dilute systems is not well understood compared to systems displaying superexchange, and so the systems described in this thesis offer an opportunity where empirical observations can be derived that would allow these exchange interactions to be predicted, *cf.* Goodenough-Kanamori[1-2] rules for oxide systems. However, from the analysis of a number of systems, no clear trend emerged between the geometries of the interacting species within the TM-O-P-O-TM pathway and the sign of the interaction. It was generally found though that Mn^{3+} was able to participate in both ferromagnetic (FM) and antiferromagnetic (AFM) interactions whereas Fe^{3+} had a tendency to adopt AFM interactions. An exception to this appears to be Fe^{3+} pyrophosphate systems where the orthophosphate unit presents a triad of interactions; as the triad cannot be purely AFM it seems that FM interactions are imposed on the structure. As expected, for compounds containing mixed cation compositions, where the magnetic structure was solved it was found that the TM present in greater quantity dominated the magnetic interactions. All compounds studied showed AFM ordering overall, suggesting that these interactions are stronger and/ or weakly preferred over those that are FM in nature.

In **Chapter 3** α-$NH_4MnP_2O_7$ was successfully synthesised in a pure, crystalline form and its structure determined by neutron diffraction. This compound and a second polymorph designated as β-$NH_4MnP_2O_7$ were found to be key components of a commercial manganese violet sample used in pigment applications. A unit cell and structure type was identified for the β-polymorph, but reliable structural details could not be determined due to being unable to synthesise the material in single phase

form. Further work on the synthetic procedure is required to explore whether this phase can be isolated or whether it can be synthesised as the dominant polymorph in the sample.

K^+ and Rb^+ exchange in α-$NH_4MnP_2O_7$ were achieved through a nitrate melt reaction, but accompanied by the formation of significant amorphous material. The full α-$NH_4Mn_xFe_{1-x}P_2O_7$ solid solution was synthesised in sufficiently crystalline form by an acid melt method. The optical properties of the materials appeared to change in accordance with the Mn content and its local environment. α-$NH_4MnP_2O_7$ remained stable up to ~340°C while the phases containing iron remained stable up to slightly higher temperatures. This was attributed to the greater stability of iron in the +3 oxidation state. The magnetic structure of α-$NH_4MnP_2O_7$ was solved and found to be isostructural with $RbMnP_2O_7$,[3] possessing both FM and AFM exchange pathways. A detailed analysis of the bond lengths and angles involved in these pathways was conducted. The remaining members of the solid solution were found to be paramagnetic.

In **Chapter 4** the $RbMn_{1-x}Fe_{1-x}P_2O_7$ solid solution was investigated. The nuclear structures of the x = 0.75, 0.5 and 0.25 members were solved and the trends as the series was traversed discussed. The intense colouration exhibited by members with $x \geq 0.25$ and the distinct colour change from violet (x = 1) to blue (x = 0.25) led us to further investigate the TM coordination sphere by means of XANES, EXAFS and ^{57}Fe Mössbauer spectroscopy. XANES showed that the Mn and Fe edges remained identical across the series. EXAFS suggested a [4+2] pattern of Mn-O bond lengths and six identical Fe-O bond lengths across the series. The elongation of the MnO_6 octahedron became slightly less pronounced with an

increasing amount of Fe in the system. These observations were consistent with results from neutron diffraction and UV-Vis spectroscopy. Mössbauer spectroscopy showed that with decreasing x the iron became much more regularly ordered. In considering all of these findings it was therefore apparent that in traversing the series, the most marked change occurs at the MnO_6 coordination sphere, which in turn accounts for the colour change that was observed.

The thermal stability of these compounds was found to be similar in reducing and oxidising atmospheres, being limited by the amount of Mn^{3+} present in the system, which appeared to be prone to a change in oxidation state. $RbMnP_2O_7$ was found to remain stable up to 660°C while $RbFeP_2O_7$ up to 1050°C. The original colour of x = 0.75, 0.5 and 0.25 was found to remain stable up to ~600°C, ~700°C and ~1000°C, respectively. For these intermediate compounds it was found that by 700°C, some of the manganese had been expelled from the host structure, forming either a separate amorphous phase or a poorly crystalline phase. The $RbMn_xFe_{1-x}P_2O_7$ structure type eventually collapsed by *ca.* 800°C for x = 0.75 and 1200°C for x = 0.25 and 0.5. Further work is required to quantify the level of Mn retained in the host structures and to ascertain whether it is all expelled at once or gradually whilst the compounds are heated. This would most easily be achieved by collecting neutron diffraction data on the hosts heated to various temperatures. It would also be useful to determine the oxidation state of manganese in the heated compounds, possibly through XANES or X-ray Photoelectron Spectroscopy.

The magnetic structures of the x = 0.75 and 0.5 members were solved and found to be isostructural with the Mn end member. The magnetic structure of x =

0.25, like the Fe end member could not be solved. Possible reasons for this were investigated by analysing the structures of $LiFeP_2O_7$[4] and $NaFeP_2O_7$.[5]

In **Chapter 5** the $RbMn_{1-x}Fe_{1-x}HP_3O_{10}$ solid solution was synthesised and the trends as the series traversed investigated. The brown colouration of compounds with $x > 0$ was in contrast to the violet and blue colourations seen for the aforementioned pyrophosphate compounds. UV-Vis spectroscopy suggested a [4+2] tetragonal elongation of the MnO_6 coordination sphere. The crystal field splitting was found to show a small increase with decreasing Mn content, which was attributed to a less pronounced elongation. All compounds remained stable up to ~480°C before evolving water.

The magnetic structures of the $x = 0.75$ and 0.25 members were solved. The former, like the Mn end member was found to possess both FM and AFM interactions while the latter, like the Fe end member only possessed AFM interactions. No magnetic ordering was evident from the 2 K neutron diffraction pattern of $x = 0.5$, despite susceptibility measurements suggesting canted antiferromagnetism.

In **Chapter 6** the $MnPO_4 \cdot H_2O$-Fe_2O_3-H_3PO_4 reaction system was investigated as a route to otherwise inaccessible trivalent condensed phosphates. In increasing the reaction temperature, products with a greater degree of condensation were obtained. Pure phase compounds of β-$HMnP_2O_7$, $Mn_xFe_{1-x}H_2P_3O_{10}$ ($x \leq 0.5$) and $Mn_xFe_{1-x}P_3O_9$ ($0 \leq x \leq 0.4$ and $0.75 \leq x \leq 1$) were isolated and further characterised.

The structure of β-$HMnP_2O_7$ is relatively rare amongst condensed phosphates, possessing edge-shared Mn_2O_{10} dimers as well MnO_6 octahedra corner-linked to PO_4 tetrahedra. The phase was found to remain stable up to ~350°C. The magnetic structure was solved and found to consist of FM and AFM interactions occurring

through the orthophosphate units. The interaction within the Mn_2O_{10} dimers was found to be FM in nature and attributed to direct exchange occurring between the d_{xy} orbital on one ion and the $d_{x^2-y^2}$ orbital on the other. This would need to be further investigated by conducting an orbital analysis.

Within the $Mn_xFe_{1-x}H_2P_3O_{10}$ system the structures of the x = 0.5, 0.25 and 0 compounds were determined by neutron diffraction. The magnetic structures were also solved, with all phases adopting the same structure type and possessing purely AFM interactions. These phases remained stable up to ~430°C before evolving water to form the corresponding polyphosphate.

Within the $Mn_xFe_{1-x}P_3O_9$ system two different structure types were observed. The MnP_3O_9 structure type was able to take 25% Fe into the structure while FeP_3O_9 could accommodate up to 50% Mn. These differences were attributed to MnP_3O_9 possessing a greater degree of lattice strain than FeP_3O_9. The structures of x = 1, 0.75 and 0 were determined by neutron diffraction while that of x = 0.25 could not be determined due to the complexity of the structural model for this phase. The x = 1 and 0.75 members were found to remain stable up to ~800°C while x = 0.25 and 0 to ~1000°C. Susceptibility measurements showed all members containing Mn to be paramagnetic, which was in contrast to FeP_3O_9 which has been found to order antiferromagnetically.[6]

In **Chapter 7** the synthesis and characterisation of $MnH_2P_3O_{10}\cdot 2H_2O$ (MnTP) was carried out. The compound was synthesised in a pure and relatively crystalline form by adapting a method reported by Checker.[7] Attempts to synthesise $FeH_2P_3O_{10}\cdot 2H_2O$ were unsuccessful. A preliminary Rietveld refinement on MnTP indicated that the structure is isostructural with the layered compound

$AlH_2P_3O_{10}·2H_2O$.[8] An accurate structural determination of MnTP ideally requires neutron diffraction data to be collected on this phase, which would in turn need a deuterated sample to be synthesised due to the relatively high proton content. This would also allow the magnetic structure to be determined, with susceptibility measurements indicating three-dimensional AFM ordering.

Monoamines were successfully intercalated into MnTP with an incline angle of 58(1)°. Diamine intercalation was unsuccessful, though future attempts could be made to intercalate other organic molecules into the host phase such as alcohols. The hexylamine intercalate of MnTP was used as a pillared material to allow subsequent incorporation of Cu^{2+} and Mn^{2+} ions into the interlayer region. A reflux reaction was employed but it was found that aqueous solutions of the TM led to hydrolysis of the host phase. Methanolic solutions of the TM allowed the host structure to be retained to a degree, but it was unclear as to whether the additional TM ions had been incorporated into the interlayer region or whether they formed a separate amorphous phase. This could be further studied using techniques such as microscopy, EXAFS and XANES. Heat treatments of the products from MnTP-hex refluxed with methanolic TM solutions led to the likely collapse of the layered structure, giving amorphous materials. These studies therefore suggest that a different approach is required to incorporate TM ions into the interlayer region of MnTP.

8.2 Further Work on All Systems

The thermal stability of most compounds was only investigated in nitrogen, and so it would be worthwhile to explore whether a similar decomposition mechanism occurs in oxidising atmospheres.

Further work that could be conducted with respect to the optical properties of all materials is an accurate quantification of their colour, intensity and particle size. Modification of particle size through variations in the synthetic procedure or *via* processes such as ball milling could allow the optical properties to be fine-tuned, while introduction of other cations such as V^{3+} and Cr^{3+} into the structures could lead to different colourations and an alteration in the thermal stability. In order to better understand the optical properties, it would be useful to explore the band structure of these materials. Density Functional Theory (DFT) could be used to calculate the relative energies of the molecular orbitals, from which band gaps could be obtained and an estimation of the optical spectra; this could then be compared to the measured data.

Where susceptibility measurements indicated canted antiferromagnetism or spin glass behaviour, hysteresis or AC susceptibility measurements could be carried out in order to further probe this. DFT calculations could be used to estimate the relative strengths of the exchange interactions, from which an expected magnetic ground state could be derived. If the calculated model was to be consistent with that observed experimentally, then the magnetic structures of $RbFeP_2O_7$ and $RbMn_{0.25}Fe_{0.75}P_2O_7$ could also be predicted and perhaps provide an explanation as to why incommensurate magnetic structures appear to be adopted. Also, the magnetic properties of analogous systems such as arsenates could be compared to the phosphates discussed here in order to assess the influence of phosphorus, if any on the exchange interaction.

References

[1] J. B. Goodenough, *Phys. Rev.*, 1955, **100**, 564-573.

[2] J. Kanamori, *J. Phys. Chem. Solids*, 1959, **10**, 87-98.

[3] F. C. Coomer, N. J. Checker and A. J. Wright, *Inorg. Chem.*, 2010, **49**, 934-942.

[4] G. Rousse, J. Rodríguez-Carvajal, C. Wurm and C. Masquelier, *Solid State Sciences*, 2002, **4**, 973-978.

[5] R. C. Mercader, L. Terminiello, G. J. Long, D. G. Reichel, K. Dickhaus, R. Zysler, R. Sanchez and M. Tovar, *Phys. Rev. B*, 1990, **42**, 25-32.

[6] L. K. Elbouaanani, B. Malaman and R. Gerardin, *J. Solid State Chem.*, 1999, **148**, 455-463.

[7] N. J. Checker, *The Synthesis and Properties of Novel Condensed Phosphates*, PhD Thesis, University of Birmingham, 2006.

[8] S. K. Rishi, B. M. Kariuki, N. J. Checker, J. Godber and A. J. Wright, *Chem. Commun.*, 2006, 747-749.

Appendix 1

The Bond Valence Sum (BVS) Model and Global Instability Index (GII)

The bond valence model[1] states that the atomic valence (V_i) of an ion, *i* is equal to the sum of the individual bond valences (S_{ij}) surrounding that ion: -

$$V_i = \sum_j S_{ij} \qquad \text{Equation A1}$$

The relationship between bond valence and bond length is empirically found to be: -

$$S_{ij} = \exp\left(\frac{R_0 - R_{ij}}{B}\right) \qquad \text{Equation A2}$$

where R_{ij} is the experimentally determined bond length between atoms *i* and *j*, R_0 is the characteristic bond length and *B* is an empirical constant, found to be 0.37 Å for most compounds.

If the calculated valence from Equation A2 is close to the expected valence of an atom, then this is generally a good sign that the correct oxidation state and coordination environment of the ion has been assumed. BVS calculations can also provide a useful indication of whether there is lattice strain present in a given structure. This is evident through there being low valence sums around some cations and high valence sums around others. The GII,[2-3] derived from the BVS model, measures the extent to which the valence sum rule is violated over the whole structure, and can be used as a measure of lattice strain.

$$\text{GII} = \left\langle \left(\sum_j S_{ij} - V_i \right)^2 \right\rangle^{1/2} \qquad \text{Equation A3}$$

where V_i is the formal valence and <> indicates an average taken over all atoms in the formula unit.

GII values < 0.05 valence units (vu) suggest that little or no strain is present while values > 0.20 vu indicate a structure that is so strained it is unstable. Such large values are rarely found in correctly determined crystal structures.

References

[1] I. D. Brown and D. Altermatt, *Acta Crystallogr.*, 1985, **B41**, 244-247.

[2] A. Salinas-Sanchez, J. L. Garcia-Munoz, J. Rodriguez-Carvajal, R. Saez-Puche and J. L. Martinez, *J. Solid State Chem.*, 1992, **100**, 201-211.

[3] I. D. Brown, *The Chemical Bond in Inorganic Chemistry*; Oxford University Press: Oxford, 2002.

Appendix 2

Miscellaneous Rietveld Refinements and XRD Patterns

A2.1 K-exchanged α-$NH_4MnP_2O_7$

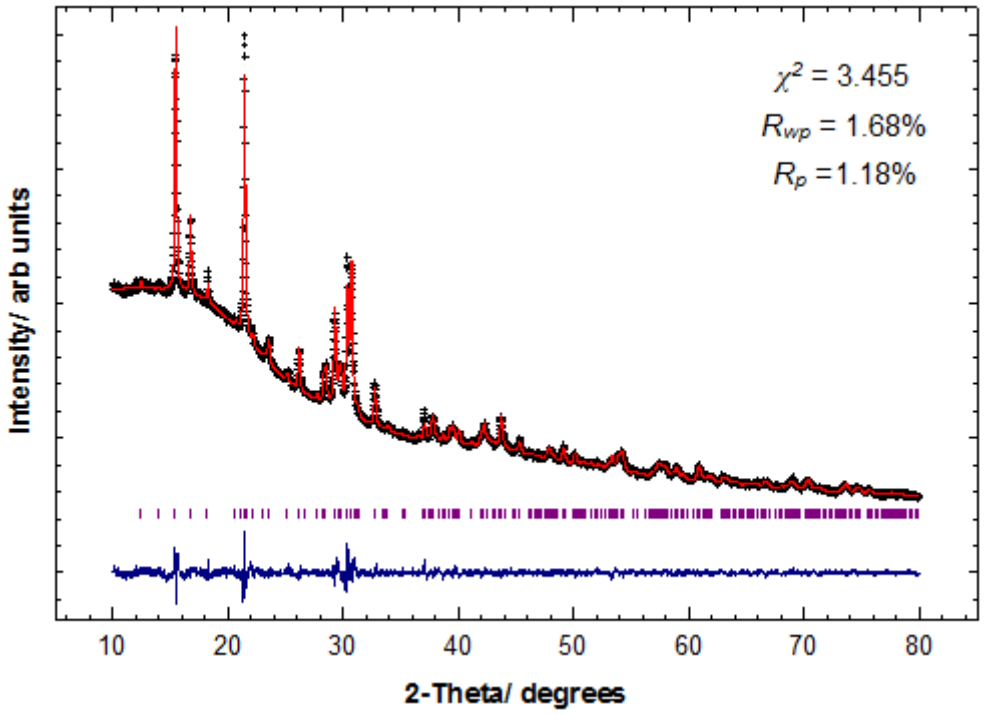

Figure A2.1: *Observed (+), calculated (-), difference profiles (-) and reflection positions (l) for the XRD Rietveld refinement on K-exchanged α-$NH_4MnP_2O_7$.*

Table A2.1: *Structural parameters for K-exchanged α-$NH_4MnP_2O_7$. Isotropic displacement factors (U_{iso}) were constrained to be equal and not refined.*

Atom	Site	Occupancy	*x*	*y*	*z*	U_{iso}/ Å^2
Mn	4*e*	1.0	0.731(1)	0.1034(7)	0.758(1)	0.01
P(1)	4*e*	1.0	0.628(2)	0.415(1)	0.824(1)	0.01
P(2)	4*e*	1.0	0.938(2)	0.357(1)	0.699(2)	0.01
O(1)	4*e*	1.0	0.589(3)	0.237(3)	0.760(3)	0.01
O(2)	4*e*	1.0	0.633(4)	0.414(2)	1.015(3)	0.01
O(3)	4*e*	1.0	0.821(4)	0.453(2)	0.804(3)	0.01
O(4)	4*e*	1.0	0.479(4)	0.497(2)	0.732(3)	0.01
O(5)	4*e*	1.0	0.975(3)	0.208(2)	0.767(3)	0.01
O(6)	4*e*	1.0	0.828(4)	0.390(3)	0.539(2)	0.01
O(7)	4*e*	1.0	1.114(3)	0.437(2)	0.731(3)	0.01
N	4*e*	0.70(1)	0.321(3)	0.316(1)	0.444(2)	0.01
K	4*e*	0.30(1)	0.321(3)	0.316(1)	0.444(2)	0.01

Space group $P2_1/c$, a = 7.3494(5) Å, b = 9.6847(6) Å, c = 8.5955(5) Å and β = 105.905(5)°

Table A2.2: *Selected Bond Distances (Å) for K-exchanged α-$NH_4MnP_2O_7$*

Mn-O(1)	1.67(2)	**Mn-O(5)**	2.04(2)
Mn-O(2)	2.02(2)	**Mn-O(6)**	2.32(2)
Mn-O(4)	1.88(3)	**Mn-O(7)**	1.97(3)
P(1)-O(1)	1.81(3)	**P(2)-O(3)**	1.68(2)
P(1)-O(2)	1.63(3)	**P(2)-O(5)**	1.55(2)
P(1)-O(3)	1.52(2)	**P(2)-O(6)**	1.42(2)
P(1)-O(4)	1.40(2)	**P(2)-O(7)**	1.46(3)

A2.2 Rb-exchanged α-$NH_4MnP_2O_7$

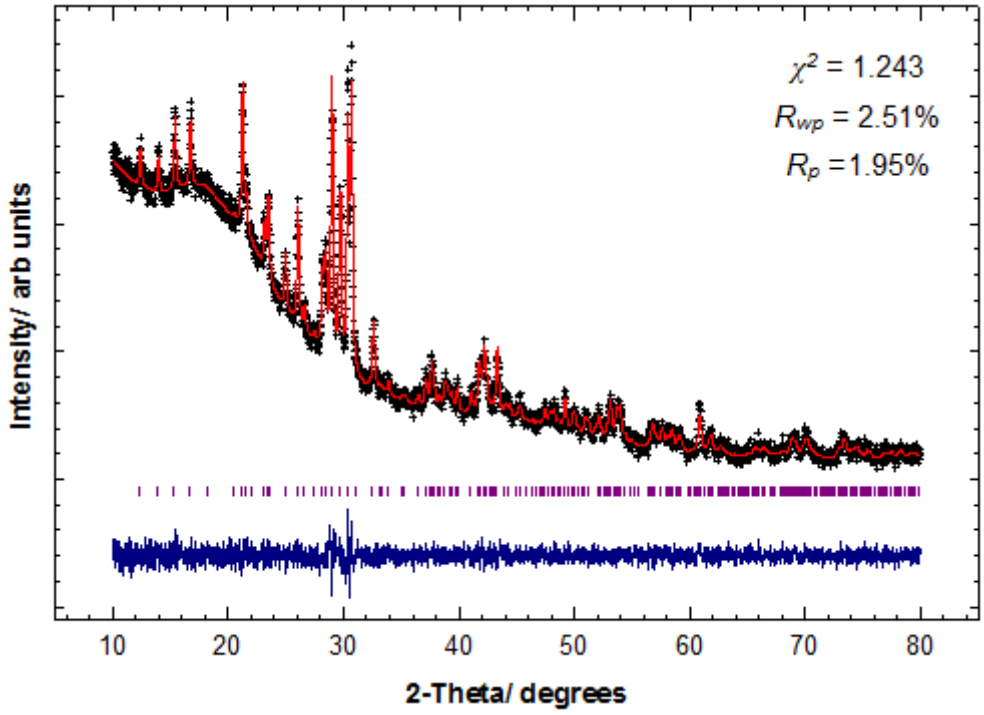

Figure A2.2: *Observed (+), calculated (-), difference profiles (-) and reflection positions (|) for the XRD Rietveld refinement on Rb-exchanged α-$NH_4MnP_2O_7$.*

Table A2.3: *Selected Bond Distances (Å) for Rb-exchanged α-$NH_4MnP_2O_7$*

Mn-O(2)	1.925(3)	**Mn-O(5)**	2.16(3)
Mn-O(3)	1.99(4)	**Mn-O(6)**	1.95(4)
Mn-O(4)	2.11(3)	**Mn-O(7)**	1.89(4)
P(1)-O(1)	1.66(3)	**P(2)-O(1)**	1.57(3)
P(1)-O(3)	1.51(3)	**P(2)-O(2)**	1.60(4)
P(1)-O(5)	1.48(3)	**P(2)-O(4)**	1.48(3)
P(1)-O(7)	1.68(4)	**P(2)-O(6)**	1.61(4)

Table A2.4: *Refined structural parameters for Rb-exchanged α-$NH_4MnP_2O_7$. Oxygen displacement factors (U_{iso}) were constrained to be equal.*

Atom	Site	Occupancy	*x*	*y*	*z*	U_{iso}/ Å^2
Mn	4*e*	1.0	0.237(2)	0.603(1)	0.755(2)	0.034(5)
P(1)	4*e*	1.0	0.430(3)	0.627(2)	0.185(2)	0.039(8)
P(2)	4*e*	1.0	0.136(3)	0.908(2)	0.832(2)	0.055(9)
O(1)	4*e*	1.0	0.333(6)	0.953(3)	0.813(4)	0.016(6)
O(2)	4*e*	1.0	0.076(4)	0.740(3)	0.252(3)	0.016(6)
O(3)	4*e*	1.0	0.633(4)	0.579(4)	0.229(4)	0.016(6)
O(4)	4*e*	1.0	0.136(5)	0.588(3)	0.503(4)	0.016(6)
O(5)	4*e*	1.0	0.330(5)	0.608(4)	0.013(4)	0.016(6)
O(6)	4*e*	1.0	0.988(6)	0.489(4)	0.217(4)	0.016(6)
O(7)	4*e*	1.0	0.449(4)	0.791(4)	0.251(3)	0.016(6)
N	4*e*	0.21(1)	0.185(1)	0.3070(8)	0.044(1)	0.042(5)
Rb	4*e*	0.79(1)	0.185(1)	0.3070(8)	0.044(1)	0.042(5)

Space group $P2_1/c$, a = 7.3778(8) Å, b = 9.6656(9) Å, c = 8.646(1) Å and β = 105.423(5)°.

A2.3 Amorphous content determination in $RbMn_{0.25}Fe_{0.75}P_2O_7$ heated to 1100°C

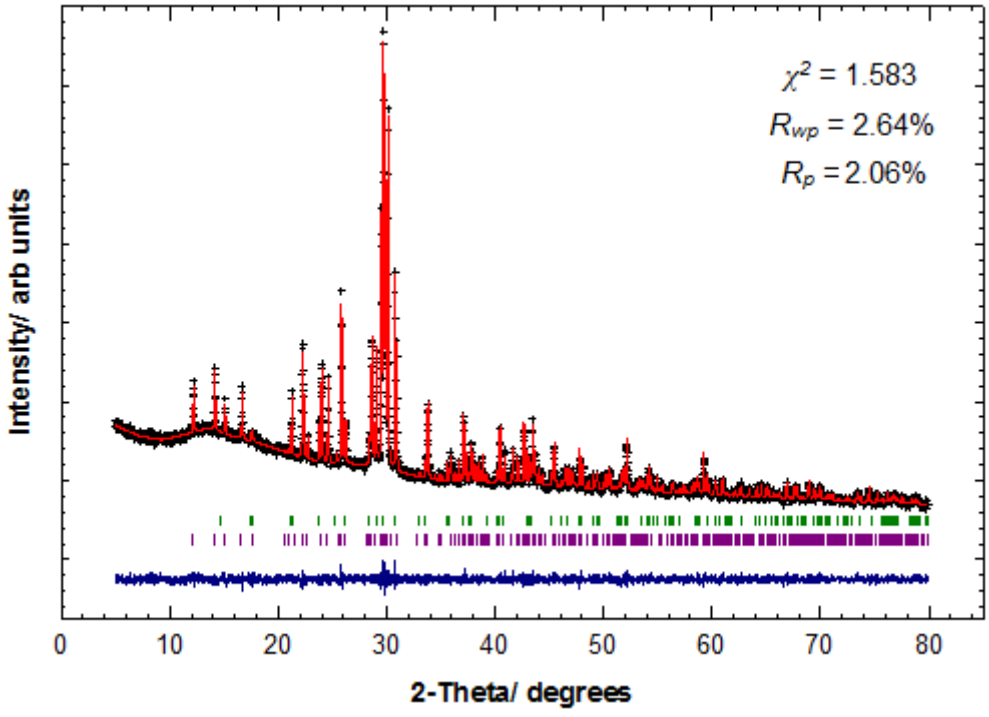

Figure A2.3: *Observed (+), calculated (-) and difference profiles (-) for the two-phase XRD Rietveld refinement on $RbMn_{0.25}Fe_{0.75}P_2O_7$ Δ to 1100°C + K_2SO_4, ground in a 4:1 weight % ratio, respectively. Reflections are shown with purple and green markers, respectively.*

Table A2.5: *Refined structural parameters for $RbMn_{0.25}Fe_{0.75}P_2O_7$ Δ to 1100°C. Mn and Fe fractional occupancies were set to those obtained from the neutron diffraction data and isotropic displacement factors of like atoms were constrained to be equal.*

Atom	Site	Occupancy	*x*	*y*	*z*	U_{iso}/ Å^2
Mn/ Fe	4*e*	0.042/ 0.958	0.2399(9)	0.5995(7)	0.760(1)	0.050(3)
Rb	4*e*	1.0	0.1858(5)	0.3114(3)	0.0478(5)	0.050(3)
P(1)	4*e*	1.0	0.438(2)	0.632(1)	0.189(1)	0.045(2)
P(2)	4*e*	1.0	0.131(2)	0.905(1)	0.829(2)	0.042(3)
O(1)	4*e*	1.0	0.323(4)	0.951(2)	0.811(3)	0.042(3)
O(2)	4*e*	1.0	0.087(2)	0.739(2)	0.260(2)	0.035(3)
O(3)	4*e*	1.0	0.630(3)	0.574(2)	0.238(2)	0.035(3)
O(4)	4*e*	1.0	0.159(3)	0.586(2)	0.517(3)	0.035(3)
O(5)	4*e*	1.0	0.328(3)	0.603(2)	0.008(2)	0.035(3)
O(6)	4*e*	1.0	0.993(3)	0.495(2)	0.228(2)	0.035(3)
O(7)	4*e*	1.0	0.438(2)	0.774(2)	0.237(2)	0.035(3)

Space group $P2_1/c$, a = 7.4888(2) Å, b = 9.9640(2) Å, c = 8.2714(2) Å, β = 105.667(1)°

Weight fraction = 75%

Table A2.6: *Refined structural parameters for K_2SO_4 crystalline reference phase. Oxygen displacement factors were constrained to be equal.*

Atom	Site	Occupancy	*x*	*y*	*z*	U_{iso}/ Å^2
K(1)	4*c*	1.0	0.25	0.088(1)	0.170(1)	0.029(5)
K(2)	4*c*	1.0	0.25	0.7940(9)	0.488(1)	0.028(4)
S(1)	4*c*	1.0	0.25	0.425(2)	0.241(2)	0.034(5)
O(1)	4*c*	1.0	0.25	0.404(2)	0.046(3)	0.017(5)
O(2)	4*c*	1.0	0.25	0.559(3)	0.289(3)	0.017(5)
O(3)	8*d*	1.0	0.028(3)	0.354(2)	0.305(2)	0.017(5)

Space group *Pmcn*, a = 5.7659(1) Å, b = 10.0621(3) Å and c = 7.4699(2) Å

Weight fraction = 25%

A2.4 α-$RbMnHP_3O_{10}$ post TGA product modelled as $RbMnP_3O_9$

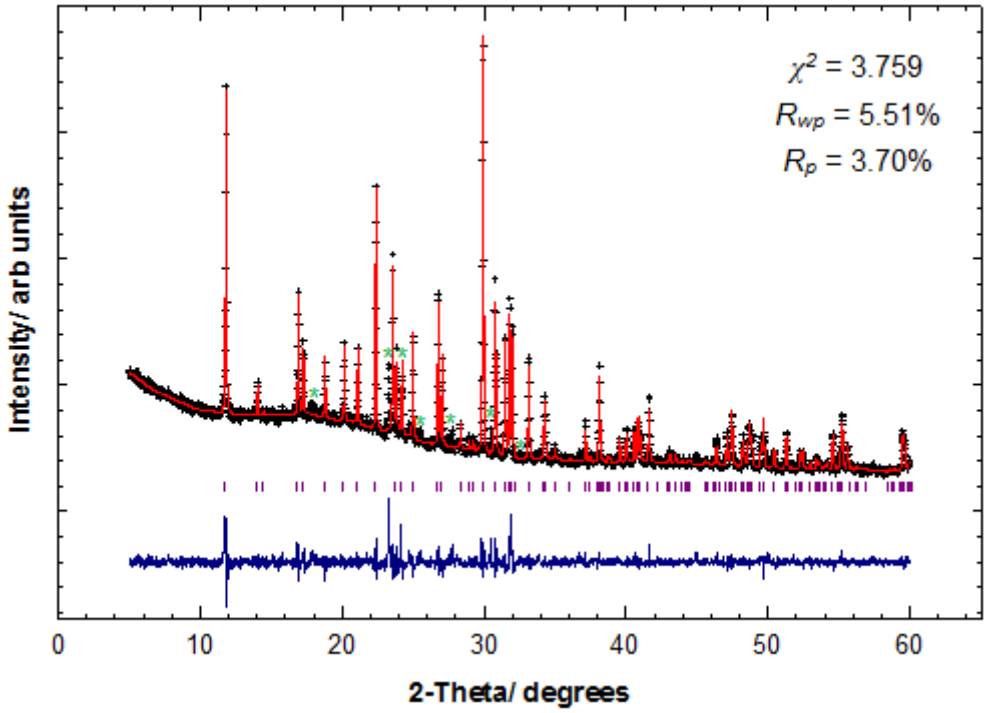

Figure A2.4: *Observed (+), calculated (-), difference profiles (-) and reflection positions (l) for $RbMnP_3O_9$. * indicates peaks that do not belong to this phase.*

Table A2.7: *Structural parameters for $RbMnP_3O_9$. Isotropic displacement factors were fixed and not refined.*

Atom	Site	Occupancy	*x*	*y*	*z*	U_{iso}/ Å^2
Mn	4*c*	1.0	-0.015(1)	0.25	0.7820(8)	0.01
Rb	4*c*	1.0	0.6006(5)	0.25	0.4162(4)	0.01
P(1)	4*c*	1.0	0.201(2)	0.25	0.543(2)	0.01
P(2)	8*d*	1.0	0.248(1)	0.052(1)	0.348(1)	0.01
O(1)	4*c*	1.0	0.103(3)	0.25	0.633(3)	0.01
O(2)	8*d*	1.0	0.169(2)	0.076(3)	0.467(2)	0.01
O(3)	4*c*	1.0	0.345(3)	0.25	0.574(3)	0.01
O(4)	4*c*	1.0	0.277(3)	0.25	0.314(2)	0.01
O(5)	8*d*	1.0	0.377(2)	-0.061(2)	0.371(1)	0.01
O(6)	8*d*	1.0	0.141(2)	-0.025(3)	0.273(2)	0.01

Space group *Pnma*, *a* = 9.4153(3) Å, *b* = 7.3279(2) Å and *c* = 12.1960(4) Å

Table A2.8: *Selected Bond Distances (Å) for $RbMnP_3O_9$*

Mn-O(1)	2.14(3)	**Mn-O(5)**	2.19(2)
Mn-O(3)	2.19(3)	**Mn-O(6)**	2.14(2)
Mn-O(5)	2.19(2)	**Mn-O(6)**	2.14(2)
P(1)-O(1)	1.43(3)	**P(2)-O(2)**	1.63(2)
P(1)-O(2)	1.61(2)	**P(2)-O(4)**	1.54(1)
P(1)-O(2)	1.61(2)	**P(2)-O(5)**	1.50(2)
P(1)-O(3)	1.41(3)	**P(2)-O(6)**	1.47(2)

A2.5 $RbFeP_2O_7$ in $RbFeHP_3O_{10}$ post TGA product

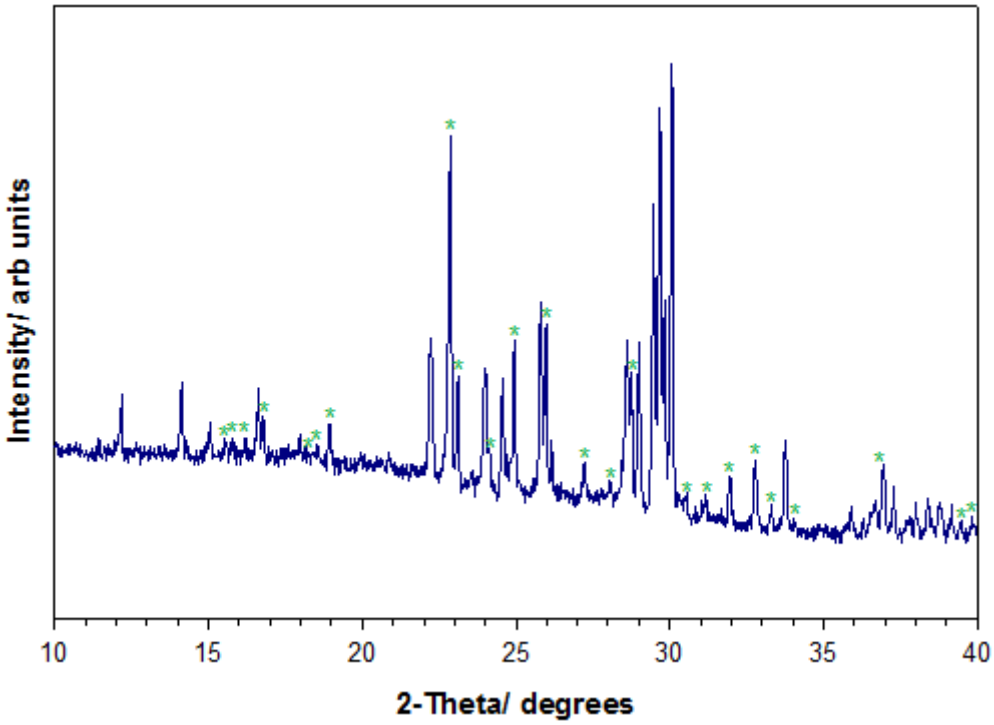

Figure A2.5: *XRD pattern of product from $RbFeHP_3O_{10}$ heated to 750°C.*
** indicates peaks that do not belong to $RbFeP_2O_7$.*

A2.6 MnTP

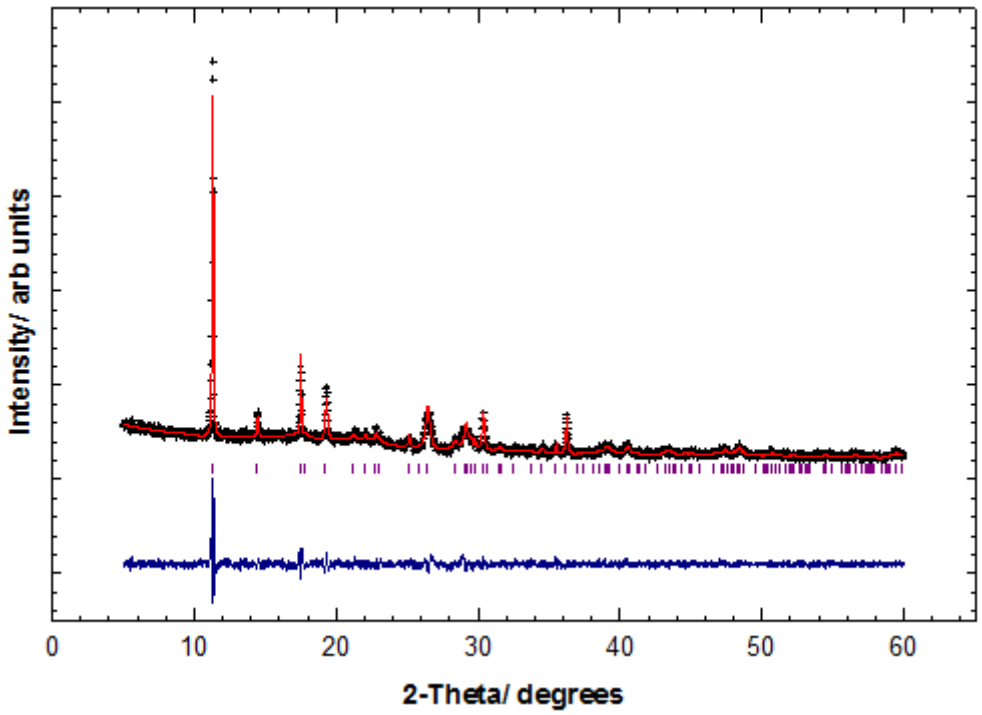

Figure A2.6: *Observed (+), calculated (-), difference profiles (-) and reflection positions (|) for preliminary Rietveld refinement of MnTP based on AlTP structure type.*

Appendix 3

IR Spectra of $MnH_2P_3O_{10}\cdot 2H_2O$ (MnTP) and Subsequent Reaction Products

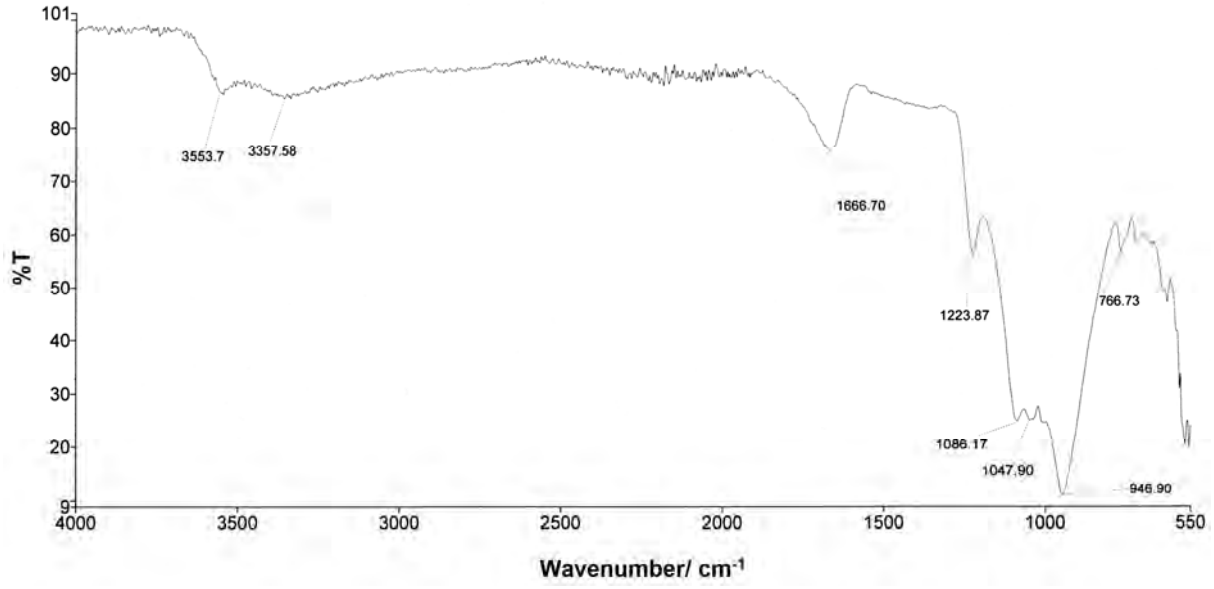

Figure A3.1: *IR spectrum of $MnH_2P_3O_{10}\cdot 2H_2O$ (MnTP)*

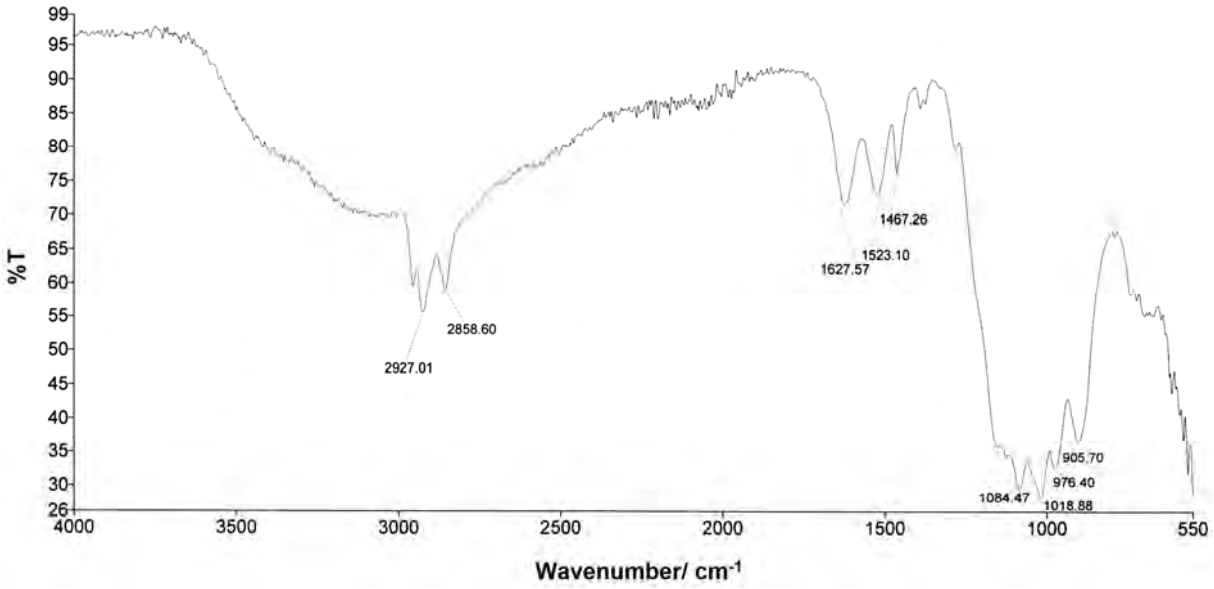

Figure A3.2: *IR spectrum of MnTP intercalated with hexylamine (MnTP-hex)*

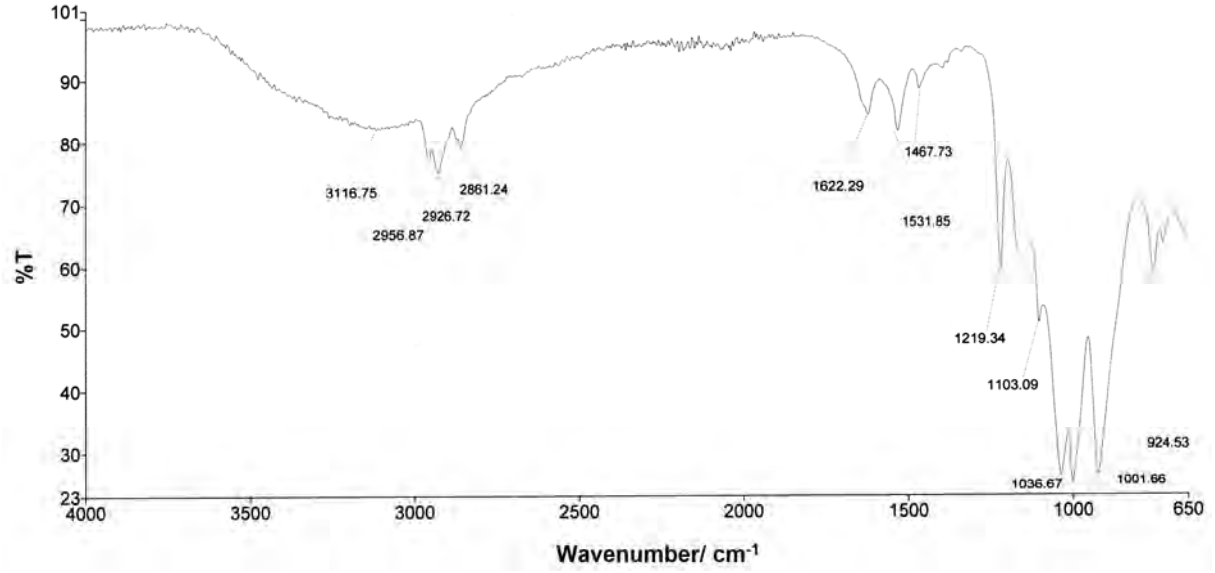

Figure A3.3: *IR spectrum of product from reaction of MnTP-hex with methanolic Cu acetate after 4 h reflux*

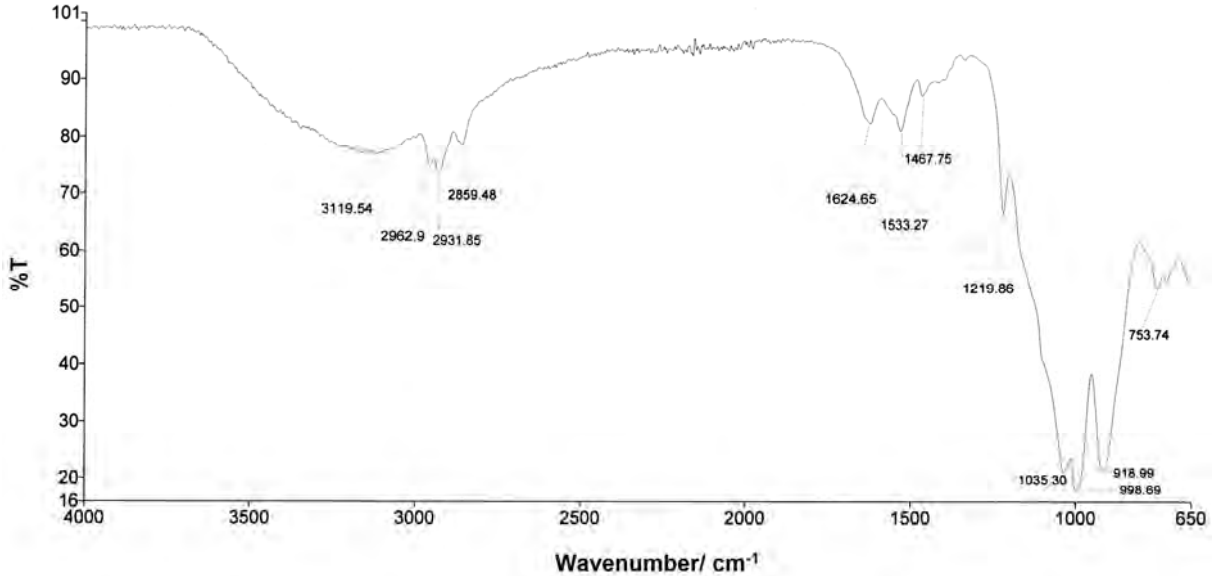

Figure A3.4: *IR spectrum of product from reaction of MnTP-hex with methanolic Mn acetate after 4 h reflux*

Appendix 4

Papers

Papers published: -

- Y. Begum and A. J. Wright, "Relating Highly Distorted Jahn-Teller MnO_6 to Colouration in Manganese Violet Pigments," *J. Mater. Chem.*, 2012, **22**, 21110-21116.

Papers in preparation: -

- Structure-Property Relationships in the $RbMn_xFe_{1-x}P_2O_7$ System
- Structural and Magnetic Properties of the $RbMn_{1-x}Fe_xHP_3O_{10}$ System
- Structural and Magnetic Properties of β-$HMnP_2O_7$ and $Mn_xFe_{1-x}H_2P_3O_{10}$ ($x \leq 0.5$) Condensed Phosphate Phases